Interférométrie atomique : applications aux capteurs inertiels

Arnaud Landragin

SYSTÈMES DE RÉFÉRENCE TEMPS-ESPACE

HABILITATION À DIRIGER LES RECHERCHES

présentée par

Arnaud Landragin

Interférométrie atomique : applications aux capteurs inertiels

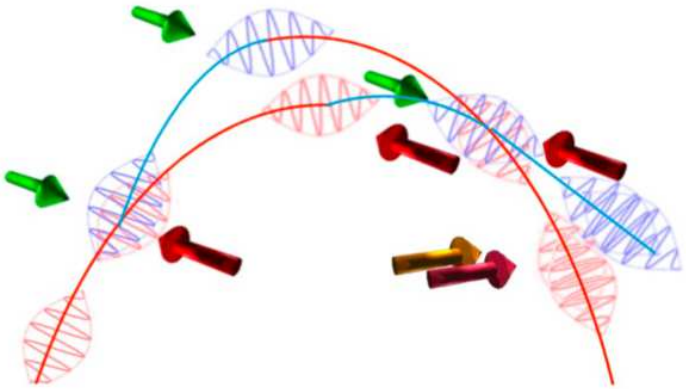

Soutenue le 18 décembre 2009 devant le jury composé de :

M. Alain Aspect	Examinateur
M. François Biraben	Président
M. Christian Bordé	Examinateur
M. F. Bretenaker	Rapporteur
M. Ernst Rasel	Rapporteur
M. Christoph Westbrook	Rapporteur

Remerciements

Tout d'abord je voudrais remercier Fabien Bretenaker, Ernst Rasel et Christoph Westbrook d'avoir accepté d'être mes rapporteurs pour ce mémoire, et d'avoir marqué ainsi leur intérêt pour mon travail de recherche. Je suis également reconnaissant à Alain Aspect, François Biraben et Christian Bordé d'avoir accepté de participer à mon jury.

Bien que ce manuscrit ne concerne pas mes travaux de recherche pendant ma thèse de doctorat, celle-ci a été déterminante dans le choix de continuer une carrière de chercheur dans la thématique de la physique atomique, et en particulier de l'interférométrie atomique. C'est pourquoi, je remercie très chaleureusement Alain Aspect, qui a été mon directeur de thèse à l'Institut d'Optique, mais aussi Nathalie et Christoph Westbrook, qui m'ont également encadré, pour m'avoir fait découvrir ce monde passionnant de la recherche, pour leur enthousiasme et leur esprit scientifique à la fois rigoureux et très pédagogique.

J'ai ensuite pleinement découvert la thématique de l'interférométrie atomique lors de mon séjour post-doctoral dans l'équipe de Mark Kasevich à l'université de Yale. Je le remercie de m'avoir fait confiance en m'y accueillant et en me donnant rapidement une indépendance dans les choix expérimentaux. J'ai beaucoup apprécié ses grandes qualités scientifiques et sa très grande réactivité. Je voudrais également associer Todd Gustavson que j'ai eu le plaisir d'encadrer et qui est en grande partie responsable des résultas obtenus durant cette période.

Mon arrivée et mon intégration au laboratoire, qui ne s'appelait pas encore le SYRTE, doit beaucoup à André Clairon et Noël Dimarcq. Je les remercie de m'avoir fait confiance pour le développement de cette nouvelle activité au laboratoire mais également de leurs soutiens et leurs précieux conseils. J'espère avoir appris des vastes connaissances d'André aussi bien expérimentales qu'en physique en générale, et souhaite en bénéficier encore longtemps. Quant à Noël, j'apprécie beaucoup son dynamisme, son goût pour la nouveauté et l'indépendance qu'il m'a rapidement accordé. Je voudrais associer l'ensemble de mes collègues du laboratoire : "horlogers", théoriciens et astronomes, avec qui j'ai eu la chance de travailler ainsi

que l'ensemble des services techniques, indispensables à la réussite de nos expériences. Je m'excuse de ne pas les citer tous dans ces quelques lignes, mais ils se reconnaitront. Pour les autres, merci de contribuer à cette ambiance à la fois stimulante et chaleureuse que j'apprécie au laboratoire.

Les résultats de ces expériences ont largement bénéficié du travail de l'ensemble de mes collaborateurs au sein de l'équipe. En premier lieu, je remercie Franck Pereira Dos Santos pour sa rigueur scientifique et sa grande efficacité qui en font un collaborateur que je souhaite à tout le monde. Je remercie également Christian Bordé pour ces discussions passionnantes en physique et en interférométrie atomique en particulier, elles m'incitent toujours à regarder plus loin. Merci également à Sébastien Merlet, qui bien qu'encore récent dans notre équipe a déjà pris une place importante. Je suis convaincu que nos collaborations ne font que commencer. Il est indéniable que l'avancement des projets doit beaucoup aux post-doctorants et doctorants qui sont les véritables "chevilles ouvrières" de nos expériences, ils en sont parfois bien plus. Merci donc à Walid Chaibi et Tanja Mehlstäubler qui ont su apporter leur expérience et leur contribution originale. David Holleville et Jérôme Fils ont eu la lourde tâche de commencer l'expérience du gyromètre, et par la même, l'ensemble des activités de l'équipe, et les en remercie sincèrement. Florence Yver-Leduc, Benjamin Canuel et Alexandre Gauguet ont su valoriser ce travail sur le gyromètre, permettant d'approfondir la physique qui y est liée. Je remercie également Thomas Lévèque qui prépare activement la prochaine étape. Merci à Patrick Cheinet qui a eu la charge de débuter l'expérience de gravimètre et a obtenu rapidement les premiers signaux. Je souhaiterais également remercier Julien Le Gouët, Quentin Bodard et Nicolas Malossi pour leur contribution au gravimètre, bien que ne les ayant pas encadré directement.

Mes recherches m'ont mené à débuter de nombreuses collaborations à la fois nationales et internationales. A nouveau, il serait difficile de citer tout le monde sans oublier quelqu'un. Ces collaborations m'ont, non seulement, ouvert à d'autres façons de mener mes recherches, mais également à découvrir d'autres thématiques hors de la physique atomique voire même en dehors de la physique. Je n'y serais sans doute jamais un expert, mais cela me permet de situer mon travail personnel dans un cadre plus large. Comme après toute règle en français, il faut quelques exceptions, je remercie donc particulièrement Philippe Bouyer et Ernst Rasel avec qui mes collaborations ont commencé à travers le projet HYPER, qui restent mes principaux collaborateurs hors du laboratoire et qui, je l'espère, le resteront. J'y associe les doctorants et post-doctorants des deux expériences ICE et BIARO, situées à l'Institut d'Optique, avec qui j'ai eu ou j'ai de très nombreux contacts : merci donc à Gaël, Robert, Rémi, Guillaume, Baptiste et Vincent d'un côté et à Simon, Thomas et Andrea de l'autre.

Enfin, je souhaite remercier ma famille, Véronique, Etienne, Lucile et Laurine pour leur soutien et leur compréhension, tout à fait indispensables pendant ces années. J'y associe mes parents, qui bien qu'étrangers au monde de la recherche, ont su m'apprendre des valeurs qui y sont bien utiles.

Table des matières

Chapitre 1

Présentation générale des travaux

Ce manuscrit présente un résumé de mes activités de recherche depuis ma soutenance de thèse de doctorat fin 1997. La partie concernant ma thèse [Landragin thèse] dans l'équipe d'Optique Atomique d'Alain Aspect à l'Institut d'Optique n'y est pas décrite et a porté sur l'étude d'un miroir à atomes à onde évanescente qui s'avérait comme un candidat prometteur pour la manipulation cohérente des paquets d'ondes atomiques. Les études ont permis de caractériser les propriétés de ce miroir : son efficacité, la force de van der Waals entre les atomes et la paroi diélectrique [Landragin 1996a], les problèmes de décohérence dus à des phénomènes de réflexion diffuse [Landragin 1996b], et la possibilité de l'utiliser comme comme un réseau de diffraction en réflexion [Landragin 1997].

A la fin de ma thèse, j'ai poursuivi mes recherches en optique atomique en les orientant vers le domaine de l'interférométrie atomique, fondée sur la manipulation des ondes de de Broglie. Je suis parti près de deux ans (1998-99) dans le groupe de Mark Kasevich à l'université de Yale (USA) ou j'ai étudié le fonctionnement d'un gyromètre atomique, fondé sur l'utilisation de jets atomiques refroidis transversalement. Mon travail sur le gyromètre a notamment démontré que l'interférométrie atomique permet de réaliser un gyromètre dépassant l'état de l'art en terme de sensibilité.

Il faut noter que les résultats publiés par les équipes de S. Chu [Peters 1997] et M. Kasevich [Gustavson 1997] en 1997 avaient montré, pour la première fois, que les performances des interféromètres pouvaient concurrencer les technologies standard : gravimètres à coin de cube en chute libre et gyromètres optiques. Les travaux réalisés par les mêmes équipes entre 1997 et 2000 ont permis de démontrer qu'ils pouvaient même les dépasser [Gustavson 1998, Peters 1999, Gustavson 2000, Peters 2001]. Ces deux équipes utilisaient des méthodes de manipulation des ondes atomiques fondées sur des transitions Raman stimulées [Kasevich 1991b], permettant, à la fois, un bon rapport signal à bruit et un contrôle fin du processus de diffraction

nécessaires pour des mesures de grande précision. Bien que de nombreuses autres solutions aient été étudiées entre 1991 et 1997 [Berman 1997], la plupart ont été arrêtées à cette période. Ce n'est qu'au début des années 2000 que l'activité du domaine a repris de manière significative, mais en utilisant les interféromètres atomiques comme outils pour des applications spécifiques en navigation inertielle, physique fondamentale ou géophysique. Toutes ces applications peuvent, en effet, bénéficier de la stabilité à long terme et de l'exactitude apportées par ce type de capteur.

A partir de fin 1999, j'ai commencé l'étude du gyromètre-accéléromètre à atomes froids au SYRTE. Ce projet a débuté fin 1997 et j'en ai pris la charge dès mon arrivée. Il fait donc partie des premières expériences de cette nouvelle génération d'interféromètre. Son développement a été motivé par des applications en navigation inertielle. Il a permis la première caractérisation des performances d'un gyromètre à atomes froids puis son étude détaillée, conduisant notamment à l'identification des différentes limites expérimentales. Par ailleurs, il a démontré la possibilité de mesurer l'ensemble des six composantes d'inertie à l'aide du même instrument, qui est un point important pour les applications et en particulier en navigation inertielle. Au moins deux autres expériences de gyromètre à atomes froids ont débuté depuis, une dans l'équipe de E. Rasel à l'université de Hanovre (Allemagne) en 2001 [Müller 2007, Müller 2009] et l'autre dans celle de M.S. Zhan à l'université de Wuhan (Chine) [Wang 2007], mais n'ont donné que des résultats préliminaires pour l'instant.

Le développement du gravimètre atomique est également motivé par une application spécifique dans le projet de balance du watt du LNE (Laboratoire Nationale de Métrologie et d'Essai) [Geneves 2005] de redéfinition du kilogramme. Cette expérience a également des implications en géophysique puisqu'elle va conduire à une mesure des fluctuations de la gravité sur un site fixe et pendant une très longue période (plusieurs années). L'expérience a permis d'obtenir rapidement des performances au niveau de l'état de l'art [de Angelis 2009], similaire à celles obtenues dans l'équipe de S. Chu à l'université de Stanford [H-Müller 2008]. Plusieurs expériences similaires sont en cours de montage à travers le monde, mais n'ont pas encore donné lieu à publication. L'une de ces expériences est à Berlin (Allemagne) dans l'équipe de A. Peters, deux autres sont en Chine et au Japon. On peut également noter le développement de gradiomètres, mesurant l'accélération différentielle entre deux nuages séparés spatialement. Ceux de M. Kasevich [Snadden 1998, McGuirk 2002, Fixler 2007] et de G. Tino [Fattori03, Bertoldi 2006, Bertoldi 2008] (université de Florence) ont donné des mesures prometteuses pour la détermination de la constante de gravitation G. Celui de N. Yu [Yu 2006] est développé en vue de gradiométrie spatiale (JPL, USA). Une autre expérience a débuté depuis deux ans dans l'équipe de Z. Wang à l'université du Zhejing (Chine).

Une spécificité de mes activités de recherche vient de l'étude métrologique du fonctionnement de ces capteurs inertiels, nécessaire à l'obtention des meilleures performances et aux développements en vue des différentes applications. Ces études ont notamment porté sur la compréhension fine de l'interaction atomes-lasers pendant les impulsions Raman utilisées pour la manipulation des paquets d'ondes atomiques, qui s'est révélée être le point critique pour la réduction des sources de bruit et des biais.

Le manuscrit comporte quatre chapitres en plus de cette présentation générale. Dans le chapitre deux, je présente une rapide introduction historique suivie du principe de fonctionnement des interféromètres fondés sur l'utilisation de transition Raman stimulées. Je présente enfin la méthode de la fonction de sensibilité permettant d'identifier et de quantifier les différentes sources de bruits et de biais. Le chapitre trois présente les principaux résultats obtenus pendant mon séjour post-doctoral portant sur le gyromètre à jets refroidis d'une part et sur le gyromètre-accéléromètre à atomes froids d'autre part. Le chapitre quatre est consacré aux résultats du gravimètre absolu. Enfin, un dernier chapitre présente les perspectives en terme de performances limites et de nouveaux concepts, notamment quant à l'utilisation d'atomes ultra-froids, ainsi qu'un certain nombre d'applications de l'interférométrie atomique aux capteurs inertiels dans l'espace.

Chapitre 2

Interférométrie atomique : principe et sensibilité

2.1 Introduction à l'interferométrie atomique

Depuis les travaux théoriques de L. de Broglie (1923) [de Broglie 1923] et la célèbre expérience de Davidson et Germer (1927) [Davisson 1927], on sait qu'à toute particule matérielle est associée une onde, l'*onde de de Broglie*. Les premières expériences d'interférométrie à ondes de matière ont utilisé des particules élémentaires comme l'électron [Marton 1952] puis les neutrons [Rauch 1974]. Ces interféromètres à ondes de matière sont semblables à l'interféromètre de Mach-Zehnder en optique photonique (figure 2.1). Pour ces expériences, la manipulation des ondes de de Broglie est réalisée par des réseaux de diffraction élaborés à partir d'un cristal. Rapidement, ces interféromètres ont été utilisés pour mesurer les accélérations et l'effet Sagnac [Sagnac 1913] avec des neutrons [Colella 1975, Werner 1979] ou des paires de Cooper [Zimmerman 1965]. L'interférométrie atomique, quant à elle, débute en 1990-91 avec un ensemble d'expériences pionnières utilisant différentes techniques. Enfin, la première expérience d'interférométrie avec des molécules est réalisée en 1994 [Bordé 1994a].

La manipulation cohérente d'ondes atomiques par des structures matérielles

Les premières expériences d'interférométrie atomique ont débuté au début des années 1990, avec l'expérience J. Mlynek et O. Carnal [Carnal 1991], qui utilise la diffraction d'Young d'un jet d'hélium par une double fente. Peu de temps après, une expérience du même type a été réalisée par Shimizu *et al.* [Shimizu 1992], avec des atomes de néon refroidis, issus d'un piège magnéto-optique.

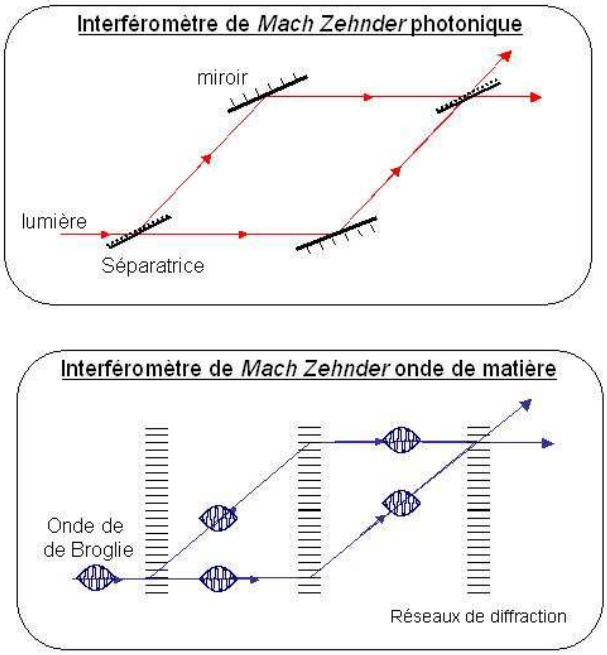

FIG. 2.1 : *Il est possible de créer l'analogue des interféromètres de Mach Zehnder avec des ondes de matière. Les ondes de matière sont manipulées avec des réseaux de diffraction (matériel ou lumineux).*

La même année, 1991, un interféromètre atomique fonctionnant avec trois réseaux de diffraction, directement inspiré des interféromètres à neutrons, est conçu dans l'équipe de D. Pritchard [Keith 1991]. Les réseaux matériels utilisés sont fabriqués avec des techniques de nanolithographie sur des membranes très fines. Ces techniques de diffraction, indépendantes de la structure interne de la particule, ont pu être généralisées pour des particules plus complexes que des atomes. C'est ainsi que la diffraction de la molécule de sodium [Chapman 1995, Schöllkopf 2004] ou de molécules de C_{60} [Arndt 2001] a été également utilisée pour la réalisation d'interféromètres.

La manipulation cohérente d'ondes atomiques par réseaux optiques

Une alternative aux réseaux matériels est l'utilisation de réseaux lumineux. L'idée d'utiliser une onde stationnaire pour créer un réseau de diffraction pour les ondes électroniques a été proposée par Kapitza et Dirac en 1933 [Kapitza 1933] dans le but de mettre en évidence l'émission stimulée. Cependant, le très faible couplage entre la lumière et les électrons libres n'a permis la mise en évidence de cet effet qu'après l'invention du laser en 2001 [Freimund 2001]. Néanmoins, en 1966 Altshuler [Altshuler 1966] met en évidence la

possibilité de réaliser la diffraction d'onde atomique, en profitant de la structure interne des atomes qui permet d'induire des transitions entre ces niveaux avec des champs lumineux résonants ou quasi-résonants. La diffraction d'atomes par une onde stationnaire a été mise en évidence, expérimentalement, pour la première fois en 1983 dans l'équipe de D. Pritchard [Moskowitz 1983]. La réalisation d'un interféromètre atomique avec un réseau lumineux stationnaire a été publiée pour la première fois en 1995 dans [Rasel 1995] et [Giltner 1995] en utilisant des séparatrices optiques dans le régime d Bragg (réseau épais), en 1996 en modulant un miroir à atomes à onde évanescente [Szriftgiser 1996], puis en 1997 dans le régime de Kapitza-Dirac [Cahn 1997](réseau mince équivalent au régime de Raman-Nath en optique).

La manipulation cohérente d'ondes atomiques par des transitions Raman stimulées

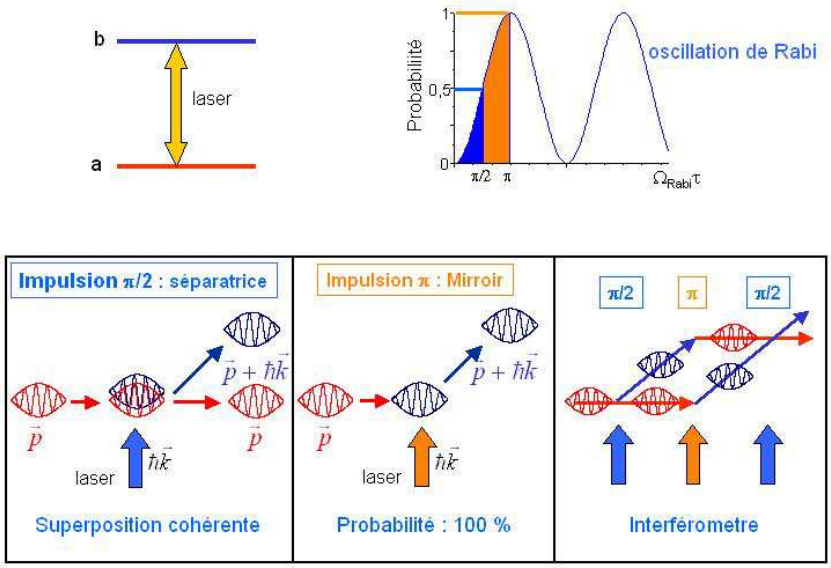

FIG. 2.2 : *Le changement d'état interne entre deux états d'un atome couplé avec un laser s'accompagne d'un transfert d'impulsion. Par conséquent, en créant une superposition cohérente entre les deux états par une impulsion $\pi/2$, on réalise l'équivalent d'une séparatrice. Dans le cas d'un transfert cohérent avec une impulsion π, on réalise l'équivalent d'un miroir. Un interféromètre similaire à celui de Mach-Zenhder en optique est créé avec une succession d'impulsions $\pi/2 - \pi - \pi/2$.*

Une autre approche, pour réaliser des séparatrices cohérentes d'ondes atomiques, utilise le couplage, via un champ laser, entre deux niveaux internes distincts, $|a\rangle$ et $|b\rangle$ (c.f. figure2.2).

Ce couplage permet de créer une superposition cohérente entre ces deux états et a été initialement utilisée pour réaliser des horloges optiques. La fonction d'onde atomique se sépare grâce à la différence de quantité de mouvement entre ces deux états atomiques, qui est liée au recul dû au photon absorbé pour passer de l'état fondamental à l'état excité. Il y a ainsi une parfaite correspondance entre l'état interne et l'état externe (état d'impulsion) de l'atome, les deux états couplés pouvant s'écrire $|a, \vec{p}\rangle$ et $|b, \vec{p} + \hbar\vec{k}\ \rangle$. Cette méthode présente, en outre, l'avantage d'obtenir deux voies de sorties de l'interféromètre dans des états atomiques internes différents, facilitant la détection [Bordé 1989]. Les interféromètres atomiques utilisant ce type de séparatrices sont appelés dans la littérature *interféromètres de Ramsey-Bordé*. Ces séparatrices atomiques ont été utilisées pour réaliser un interféromètre atomique, qui a permis de mettre en évidence pour la première fois (aussi en 1991) l'effet Sagnac pour les ondes atomiques [Riehle 1991].

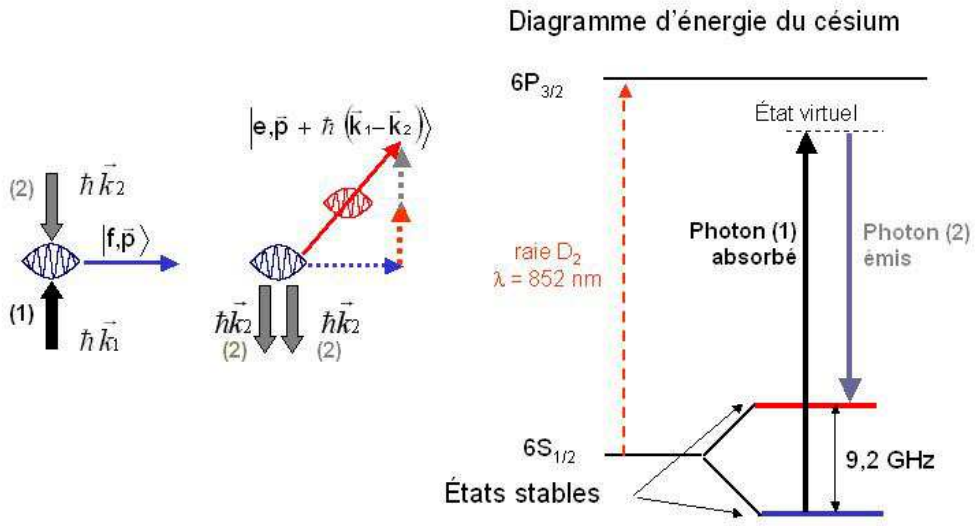

FIG. 2.3 : *Principe d'une séparatrice atomique Raman. L'atome absorbe un photon dans le mode du laser (1) et émet (de façon stimulée) dans le mode laser (2). Du fait de la conservation de la quantité de mouvement, l'atome encaisse un recul* $\hbar\vec{k}_{eff} = \hbar(\vec{k}_1 - \vec{k}_2)$.

Cependant, avec ce type de séparatrices atomiques, la durée de vie de l'état excité utilisé doit être plus longue que la durée de l'interféromètre pour éviter les pertes de cohérence par émission spontanée. Par ailleurs, comme nous le verrons par la suite, l'interaction atome-

laser ne se limite pas au transfert d'impulsion, mais ajoute en plus un déphasage sur l'onde atomique diffractée, qui dépend de la phase laser ; ce qui implique de très bien contrôler la fréquence absolue du laser. Une méthode pour diminuer ces contraintes a été proposée dans [Bordé 1989, Bordé 1991], et consiste à utiliser des transitions Raman pour coupler les deux états atomiques évoluant dans l'interféromètre. Dans ce type de transition, deux états métastables $|a\rangle$ et $|b\rangle$ sont couplés par une transition à deux photons, utilisant deux lasers dont la différence de fréquence $\omega_2 - \omega_1$ est égale à la différence de fréquence entre les deux niveaux $|a\rangle$ et $|b\rangle$ (c.f. figure 2.3). Cet effet correspond à l'absorption d'un photon dans le mode du laser (1) et à l'émission stimulée d'un photon dans le mode du laser (2). Par conséquent, lorsque les faisceaux lasers sont contra-propageants, c'est-à-dire $\vec{k}_1 \simeq -\vec{k}_2$, l'impulsion communiquée à l'onde atomique, correspond à environ deux fois l'impulsion d'un photon $2\hbar\vec{k} \simeq \hbar(\vec{k}_1 - \vec{k}_2)$. Le premier interféromètre atomique utilisant des transitions Raman a été mis au point en 1991 par S. Chu et M. Kasevich [Kasevich 1991b] pour mesurer des accélérations. Ce type d'interféromètre, utilisant des séparatrices Raman, est actuellement le plus répandu, notamment pour les mesures inertielles, et correspond à celui que nous utilisons dans nos expériences.

Evolution du domaine

Entre 1991 et 1997, de nombreuses expériences ont été réalisées pour tester de nouvelles configurations d'interféromètres atomiques, qui sont décrites dans [Berman 1997] ou dans les références incluses. Une revue plus récente des différents types d'interféromètre est donnée dans [Miffre 2006a]. Après 1997, la plupart des nouvelles expériences sont réalisées dans le but d'applications en navigation inertielle, en géophysique ou en physique fondamentale et utilisent des sources d'atomes en chute libre. L'utilisation de transition à deux photons s'y est imposée pour la plupart des applications : les transitions Raman stimulées pour la réalisation de capteurs inertiels [Peters 1997, Gustavson 1997, Snadden 1998], l'utilisation d'onde stationnaire pour les mesures de polarisabilité électrique [Ekstrom 1995, Miffre 2006b] ou d'indice de réfraction lors de la collision avec un autre gaz [Schmiedmayer 1995, Jacquey 2007], les transitions avec passage adiabatique [Weitz 1994] ou des oscillations de Bloch pour la mesure de structure fine [Weiss 1994, Wicht 2002, Cladé 2006, Cadoret 2008]. Depuis 2005, l'utilisation de source d'atomes ultra-froids a ouvert un nouveau champ de recherche en interférométrie atomique dans lesquels les atomes ne sont plus en chute libre mais sont guidés ou piégés [Madison 2000, Schumm 2005, Wang 2005, Garcia 2006, Jo 2007, Wu 2007, Impens 2006, Arnold 2006, Hughes 2009].

2.2 Interféromètres fondés sur l'utilisation de transitions Raman stimulées

Le choix d'interféromètres atomiques fondés sur l'utilisation de transitions Raman stimulées est lié à plusieurs arguments. Premièrement, l'utilisation de séparatrices optiques permet un très bon contrôle de la séparation entre les paquets d'onde atomique et donc du facteur d'échelle pour les mesures d'inertie. Deuxièmement, l'utilisation de réseau d'indice permet d'obtenir une bonne transmission de l'interféromètre, ce qui n'est pas le cas avec les réseaux mécaniques. Contrairement à la diffraction de Bragg qui couple deux états externes de même état interne, l'utilisation de transitions entre deux états internes différents, transitions à un photon optique ou transitions Raman, permet "l'étiquetage" de l'état externe par l'état interne, rendant extrêmement facile et performante la détection de l'état de sortie de l'interféromètre. Ce point est d'autant plus important que la séparation des paquets d'ondes est délicate avec des atomes froids pour lesquels la distribution en vitesse de la source est plus large que la vitesse de recul. il est alors nécessite de réaliser une sélection en vitesse initiale pour utiliser la diffraction de Bragg. Cet argument est moins pertinent lorsque la source atomique est un jet collimaté, ou au contraire une source ultra-froide dans laquelle la distribution en vitesse devient très petite devant la vitesse de recul associée à la transition optique. Enfin l'utilisation de transitions Raman est beaucoup plus facile expérimentalement que celle de transition optique à un photon car il n'est pas nécessaire de stabiliser la fréquence absolue du laser mais seulement la différence de fréquence entre les deux lasers Raman (rapport des fréquences entre 10^4 et 10^5).

2.2.1 Les transitions Raman stimulées comme séparatrices atomiques

Une transition Raman stimulée est un processus à deux photons, où le changement d'état interne est lié au changement de quantité de mouvement [Kasevich 1991b]. Les atomes alcalins se prêtent très bien aux transitions Raman : leurs deux sous-niveaux hyperfins sont métastables, si bien que la cohérence du processus ne sera jamais limitée par leur durée de vie.

Considérons un atome dans un état atomique pur, éclairé simultanément par deux faisceaux lasers, dont la différence de fréquence concorde avec la différence de fréquence des états inférieurs $|f\rangle$ et $|e\rangle$ (fig. 2.4). Les lasers sont accordés proche d'une transition optique avec un niveau d'énergie virtuel $|i\rangle$ et ont pour fréquences respectives ω_1 et ω_2. On définit ainsi le désaccord Raman Δ entre la pulsation du laser 1 et la transition électronique $|f\rangle \rightarrow |i\rangle$:

$$\Delta = \omega_1 - (\omega_i - \omega_f) \tag{2.1}$$

Si l'atome, d'impulsion $\mathbf{p}$, est initialement dans l'état métastable fondamental $|f\rangle$, il diffuse un photon du champ classique $\mathbf{E}_1(\mathbf{r},t) \propto e^{i(\omega_1 t - \mathbf{k_1}.\mathbf{r}+\phi_1)}$ et acquiert l'impulsion $\hbar\mathbf{k_1}$ du champ. Le photon est diffusé par émission stimulée dans le champ $\mathbf{E}_2(\mathbf{r},t) \propto e^{i(\omega_2 t - \mathbf{k_2}.\mathbf{r}+\phi_2)}$. Par conservation de la quantité de mouvement, il acquiert cette fois l'impulsion $-\hbar\mathbf{k_2}$. L'impulsion totale de l'atome à l'issue de la transition est donc $\mathbf{p}' = \mathbf{p} + \hbar\mathbf{k}_{\text{eff}}$, où $\mathbf{k}_{\text{eff}} = \mathbf{k_1} - \mathbf{k_2}$.

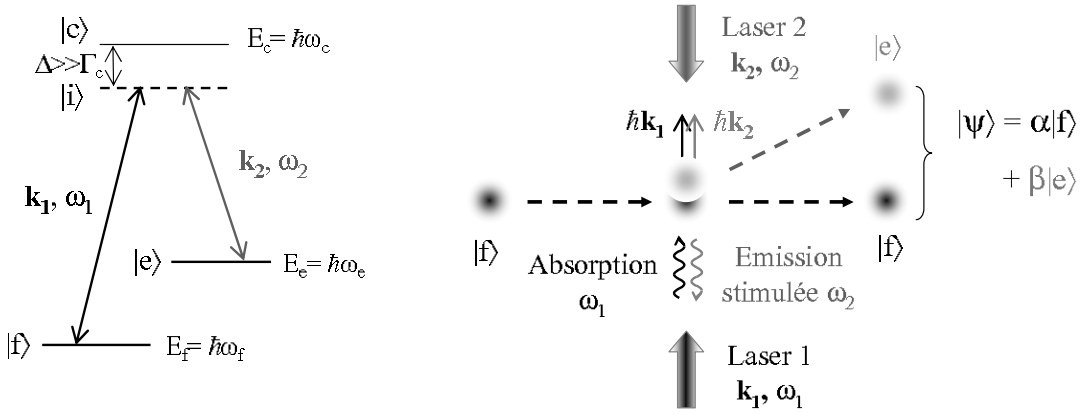

FIG. 2.4 : *Gauche : diagramme énergétique en lambda d'un atome alcalin. Droite : schéma de la séparation cohérente effectuée par une transition Raman stimulée.*

Si les lasers sont contra-propageants, les deux impulsions transférées sont dirigées dans le même sens, et le module de l'impulsion totale est égal à la somme des modules. La vitesse supplémentaire communiquée aux atomes est de deux fois la vitesse de recul v_{rec}, soit environ 1 cm/s dans le cas du césium et du rubidium.

La condition de résonance exacte entre les lasers est dictée par les conservations de la quantité de mouvement et de l'énergie au cours du processus, entre l'état initial et final :

$$\hbar\omega_1^0 + \hbar\omega_f + \frac{\mathbf{p}^2}{2m} = \hbar\omega_2^0 + \hbar\omega_e + \frac{(\mathbf{p} + \hbar\mathbf{k}_{\text{eff}})^2}{2m} \tag{2.2}$$

que l'on peut écrire en fonction de la différence de pulsation des lasers à résonance, ω_1^0 et ω_2^0 :

$$\begin{aligned} \omega_1^0 - \omega_2^0 &= \omega_e - \omega_f + \frac{\mathbf{p}.\mathbf{k}_{\text{eff}}}{m} + \frac{\hbar\mathbf{k}_{\text{eff}}{}^2}{2m} \\ &= \omega_{\text{HFS}} + \omega_{\text{D}} + \omega_{\text{rec}} \end{aligned} \tag{2.3}$$

où l'on a défini les pulsations ω_{HFS} correspondant à la transition hyperfine, ω_{D} au désaccord Doppler et ω_{rec} au déplacement de recul.

Dans le cas général, où la différence de fréquence des lasers ne satisfait pas la condition de résonance Raman, le désaccord $\delta\omega$ est défini par :

$$\omega_1 - \omega_2 = \omega_1^0 - \omega_2^0 + \delta\omega$$

Lorsque le désaccord Raman Δ est grand devant la largeur naturelle Γ des transitions, l'état excité $|i\rangle$ est très peu peuplé et l'émission spontanée est négligeable [Moler 1992]. Dans ce cas, la cohérence de la superposition des états métastables n'est pas limitée par Γ, et on montre que le système des équations de Schrödinger se ramène à celui d'un atome à deux niveaux $|f\rangle$ et $|e\rangle$. Le vecteur décrivant l'état du système à un instant t s'écrit alors en fonction des amplitudes de probabilité C_f et C_e dans chaque état propre : $|\Psi(t)\rangle = C_f(t)|f\rangle + C_e(t)|e\rangle$.

En effectuant le changement de variable $C_k = c_k e^{-i\omega_k t}$, le système des équations couplées se met habituellement sous la forme :

$$\left\{ \begin{array}{rcl} \dot{c_f} & = & -i \left(\delta\omega_f \, c_f + \dfrac{\Omega^*_{\text{eff}}}{2} \, e^{i(\delta\omega \, t + \phi)} \, c_e \right) \\ \dot{c_e} & = & -i \left(\dfrac{\Omega_{\text{eff}}}{2} \, e^{-i(\delta\omega \, t + \phi)} \, c_f + \delta\omega_e \, c_e \right) \end{array} \right. \tag{2.4}$$

où les décalages $\delta\omega_f$ et $\delta\omega_e$ correspondent aux déplacements lumineux induits par les deux champs électriques sur les niveaux d'énergie hyperfins, s'écrivent :

$$\delta\omega_f = \frac{|\Omega_{f1}|^2}{4\,\Delta} + \frac{|\Omega_{f2}|^2}{4\,(\Delta - \omega_{\text{HFS}})} \qquad \delta\omega_e = \frac{|\Omega_{e1}|^2}{4\,(\Delta + \omega_{\text{HFS}})} + \frac{|\Omega_{e2}|^2}{4\,\Delta} \tag{2.5}$$

Les fréquences de Rabi décrivant l'interaction d'un champ k ($k = 1$ ou 2) avec un niveau $|j\rangle$ ($j = f$ ou e) sont définies par :

$$\Omega_{jk} = -\frac{2}{\hbar} \, \langle i|\mathbf{d}.\epsilon_{\mathbf{k}}\mathbf{E}^{\mathbf{0}}_{\mathbf{k}}|j\rangle \tag{2.6}$$

où $\epsilon_{\mathbf{k}}$ représente la polarisation du champ. Le système 2.4 fait aussi apparaître la différence de phase $\phi = \phi_1 - \phi_2$ entre les lasers, et la pulsation de Rabi effective :

$$\Omega_{\text{eff}} = \frac{\Omega_{f1} \, \Omega^*_{e2}}{2\Delta} \tag{2.7}$$

On définit alors les déplacements lumineux différentiel $\delta\omega_{\text{LS1}}$ et moyen μ_{LS1} (pour "Light Shift à 1 photon"), et la pulsation de Rabi généralisée comme :

$$\begin{array}{rcl} \delta\omega_{\text{LS1}} & = & \delta\omega_e - \delta\omega_f \\ \mu_{\text{LS1}} & = & \delta\omega_e + \delta\omega_f \\ \Omega_R & = & \sqrt{\Omega^2_{\text{eff}} + (\delta\omega - \delta\omega_{\text{LS1}})^2} \end{array} \tag{2.8}$$

La résolution du système 2.4 est bien connue [Moler 1992]. Elle mène aux équations d'évolution suivantes, pour les amplitudes de probabilité C_f et C_e :

$$
\begin{aligned}
C_f(t_0+\tau) = &\left\{ \left(\cos\frac{\Omega_R\tau}{2} - i\cos\theta\sin\frac{\Omega_R\tau}{2} \right) C_f(t_0) \right. \\
&\left. -i\, e^{i((\omega_1-\omega_2)t_0+\phi)} \sin\theta \sin\frac{\Omega_R\tau}{2}\, C_e(t_0) \right\} e^{-i(\mu_{LS1}-\delta\omega+2\omega_f)\frac{\tau}{2}} \\
C_e(t_0+\tau) = &\left\{ -i\, e^{-i((\omega_1-\omega_2)t_0+\phi)} \sin\theta \sin\frac{\Omega_R\tau}{2}\, C_f(t_0) \right. \\
&\left. + \left(\cos\frac{\Omega_R\tau}{2} + i\cos\theta\sin\frac{\Omega_R\tau}{2} \right) C_e(t_0) \right\} e^{-i(\mu_{LS1}+\delta\omega+2\omega_e)\frac{\tau}{2}}
\end{aligned}
\tag{2.9}
$$

où est introduit le paramètre θ, défini par $\cos\theta = \dfrac{\delta\omega - \delta\omega_{LS1}}{\Omega_R}$ et $\sin\theta = \dfrac{|\Omega_{\text{eff}}|}{\Omega_R}$.

Pour illustrer ce résultat, considérons les probabilités de présence dans chaque état hyperfin, en supposant que l'atome est initialement dans l'état $|f,\mathbf{p}\rangle$, soit $C_f(t_0)=1$ et $C_e(t_0)=0$:

$$
\left\{
\begin{array}{rcl}
|C_f(t_0+\tau)|^2 &=& 1 - \dfrac{\Omega_{\text{eff}}^2}{\Omega_R^2}\sin^2\left(\Omega_R\dfrac{\tau}{2}\right) \\
|C_e(t_0+\tau)|^2 &=& \dfrac{\Omega_{\text{eff}}^2}{\Omega_R^2}\sin^2\left(\Omega_R\dfrac{\tau}{2}\right)
\end{array}
\right.
\tag{2.10}
$$

Nous obtenons des oscillations de Rabi entre les populations des deux états de la superposition, comme pour un atome à deux niveaux.

Deux cas nous intéressent particulièrement. D'abord une impulsion de durée $\tau_{\pi/2}$ telle que $\Omega_R\tau = \pi/2$, où la répartition des populations est équiprobable. L'état final s'écrit

$$|\psi\rangle = \frac{1}{\sqrt{2}}(|f,\mathbf{p}\rangle + |e,\mathbf{p}+\hbar\mathbf{k}_{\text{eff}}\rangle),$$

où les paquets d'ondes s'éloignent l'un de l'autre du fait de leur différence d'impulsion $\Delta\mathbf{p} = \hbar\mathbf{k}_{\text{eff}}$. Une telle transition Raman, dite '$\pi/2$', est l'équivalent atomique d'une séparation 50/50 par un cube polarisant en optique. De façon similaire, une transition 'π' désigne une impulsion dont la durée (ou la fréquence de Rabi) est deux fois plus grande $\Omega_R\tau = \pi$. Dans ce cas, le transfert de population est complet, et tous les atomes arrivant dans l'état $|f,\mathbf{p}\rangle$ sont défléchis dans l'état $|e,\mathbf{p}+\hbar\mathbf{k}_{\text{eff}}\rangle$. Ce sont ces deux types de transitions que nous utilisons pour réaliser l'interféromètre.

2.2.2 L'interféromètre atomique

Nous obtenons un interféromètre atomique similaire à un interféromètre optique de Mach-Zehnder grâce à une séquence temporelle de trois impulsions Raman. Une première impulsion

$\pi/2$ sépare les deux composantes de la fonction d'onde. Après une durée T, une impulsion π, d'aire deux fois plus grande que la première, les redirige l'une vers l'autre. Les deux paquets d'ondes se rejoignent au bout d'un nouveau temps T, et la dernière impulsion $\pi/2$ permet de les faire interférer (fig. 2.5).

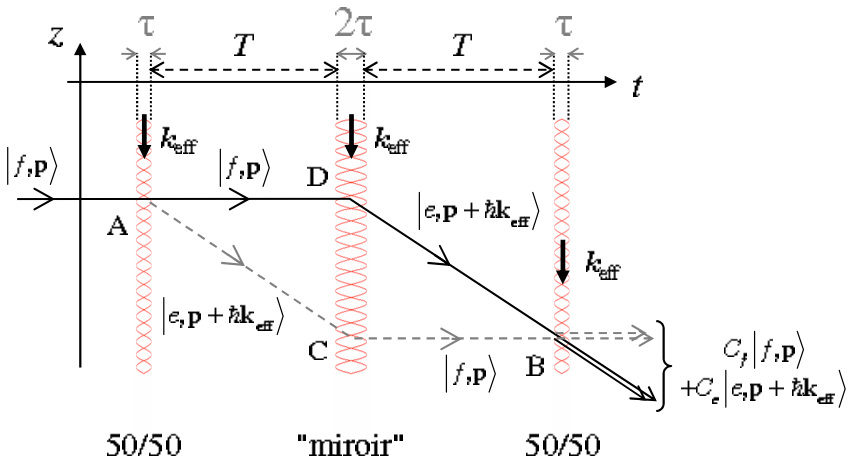

FIG. 2.5 : *Schéma d'un interféromètre atomique où les ondes de matières sont séparées puis redirigées et recombinées par des transitions Raman stimulées. Ces séparatrices lumineuses sont sélectives en vitesse et établissent une relation univoque entre les états d'impulsion qui forment l'interféromètre et les états d'énergie interne.*

L'effet d'une transition Raman seule sur une fonction d'onde peut être modélisé par une matrice, tirée des équations 2.9. Nous supposons dans ce paragraphe que le désaccord total $\delta\omega - \delta\omega_{LS1}$ est nul. Soit $V(t_0)$ le vecteur désignant la fonction d'onde initiale, et qui est composé des deux amplitudes de probabilité $C_f(t_0)$ et $C_e(t_0)$. Le vecteur $V(t_0+\tau)$ issu d'une transition Raman stimulée s'écrit, d'après ce qui précède :

$$V(t_0+\tau) = \begin{pmatrix} C_f(t_0+\tau) \\ C_e(t_0+\tau) \end{pmatrix} = M(t_0,\phi,\tau).V(t_0) \tag{2.11}$$

où la matrice $M(t_0,\phi,\tau)$ est donnée par :

$$\begin{pmatrix} \cos|\Omega_{\text{eff}}|\dfrac{\tau}{2}\, e^{-i\omega_f\tau} & -ie^{i((\omega_1-\omega_2)t_0+\phi)}\sin|\Omega_{\text{eff}}|\dfrac{\tau}{2}\, e^{-i\omega_f\tau} \\ -ie^{-i((\omega_1-\omega_2)t_0+\phi)}\sin|\Omega_{\text{eff}}|\dfrac{\tau}{2}\, e^{-i\omega_e\tau} & \cos|\Omega_{\text{eff}}|\dfrac{\tau}{2}\, e^{-i\omega_e\tau} \end{pmatrix} \tag{2.12}$$

Entre chaque transition, les lasers sont éteints et la fonction d'onde évolue librement pendant un intervalle de temps T. La matrice d'évolution sans couplage s'écrit alors simplement :

$$M_l(T) = \begin{pmatrix} e^{-i\omega_f T} & 0 \\ 0 & e^{-i\omega_e T} \end{pmatrix} \tag{2.13}$$

Finalement, la matrice du transfert de l'état initial de la fonction d'onde vers l'état final s'écrit comme le produit de trois matrices de transitions Raman de durées τ et 2τ, et de deux matrices d'évolution libre de durée T. Considérant que l'interféromètre commence au temps t_0, le vecteur décrivant l'état final de l'interféromètre est $V(t_0 + 2T + 4\tau) = M_{\text{tot}}.V(t_0)$, avec

$$\begin{aligned} M_{\text{tot}} = \quad & M(t_0 + 2T + 3\tau, \phi(t_0 + 2T + 3\tau), \tau).M_l(T). \\ & M(t_0 + T + \tau, \phi(t_0 + T + \tau), 2\tau).M_l(T).M(t_0, \phi(t_0), \tau) \end{aligned} \tag{2.14}$$

On tire ensuite de ce calcul la probabilité de transition de l'état initial $|\psi(t)\rangle = |f, \mathbf{p}\rangle$ vers l'état $|e, \mathbf{p} + \hbar\mathbf{k}_{\text{eff}}\rangle$:

$$P(t_f = t_0 + 2T + 4\tau) = \frac{|C_e(t_f)|^2}{|C_f(t_f)|^2 + |C_e(t_f)|^2} = \frac{1}{2}\left(1 - \cos\Delta\Phi\right) \tag{2.15}$$

Cette expression correspond au résultat d'un interféromètre à deux ondes. Dans la limite où l'on néglige la durée des impulsions devant T, le déphasage s'écrit :

$$\Delta\Phi = \phi(t_0) - 2\phi(t_0 + T) + \phi(t_0 + 2T) = \phi_1(t_0) - 2\phi_2(t_0 + T) + \phi_3(t_0 + 2T) \tag{2.16}$$

où $\phi_i(t_i)$ représente la différence de phase entre les deux faisceaux lasers Raman au centre du paquet d'onde atomique et au moment de l'impulsion i.

2.2.3 Sensibilité aux forces d'inertie

La très grande sensibilité des interféromètres atomiques aux forces d'inertie a été prévue avant les premières expériences [Clauser 1988]. Différentes méthodes ont été développées pour calculer les déphasages attendus, comme par exemple en utilisant la méthode des intégrales de chemin de Feynmann [Storey 1994]. Nous allons ici suivre une méthode relativement simple qui permet de calcuer cette sensibilité et de relier les déphasages aux expériences.

Le terme de phase laser qui apparaît dans 2.16 peut s'écrire sous la forme :

$$\phi_i(t_i) = \mathbf{k}^{\mathbf{i}}_{\mathbf{eff}}.\mathbf{r_i} + \phi_{laser}(t_i) \tag{2.17}$$

où $\mathbf{k}^{\mathbf{i}}_{\mathbf{eff}}$ et $r_i = r(t_i)$ sont respectivement le vecteur d'onde effectif de la transition et la position du centre du paquet d'onde au moment de l'impulsion i, et $\phi_{laser}(t_i)$ la différence de phase des deux lasers Raman.

De manière générale, il faut également tenir compte du terme d'action accumulé le long des deux bras de l'interféromètre et du déphasage lié au décalage spatial entre les deux ondes partielles qui interfèrent en sortie de l'interféromètre. Or il est possible de démontrer que ces deux derniers termes se compensent pour tout type d'interaction dont l'Hamiltonien est au plus quadratique en $\mathbf{R}$ et en $\mathbf{P}$ [Fils thèse, Antoine 2003a] , et donc pour les accélérations, les rotations et les gradients d'accélération, dépendants du temps ou non [Antoine 2003b]. Le formalisme utilisé pour ces démonstrations est similaire au formalisme ABCD en optique photonique [Bordé 2001]. Il permet également de mettre en évidence une analogie complète entre les capteurs inertiels et les horloges [Bordé 2002] et même de généraliser les résultats des déphasages à tout type d'interféromètre, à ondes de matière ou lumineuses, dans un espace à cinq dimensions [Bordé 2008].

Il apparaît alors clairement dans 2.16 et 2.17 que le déphasage à la sortie de l'interféromètre dépend d'une part de la stabilité de phase relative entre les deux faisceaux Raman $\phi_{laser}(t)$ et d'autre part du déplacement relatif du paquet d'onde atomique par rapport aux équi-phases lasers $\mathbf{k_{eff}}.\mathbf{r(t)}$: les atomes en chute libre définissent un référentiel d'inertie alors que les équi-phases lasers sont liées au référentiel du laboratoire. Nous pouvons également remarquer que si les équi-phases ne sont pas parfaitement planes, un déphasage parasite lié aux défauts de front d'onde apparaît. Nous verrons par la suite qu'il représente la principale limite à l'exactitude et à la stabilité long terme de ce type d'interféromètre. L'interféromètre est donc sensible aux accélérations le long de la direction de propagation des faisceaux lasers Raman. Cette sensibilité est mise à profit pour la mesure de la gravité (voir chapitre 4). En présence d'un gradient d'accélération, le terme correctif est donné dans [Wolf 1999].

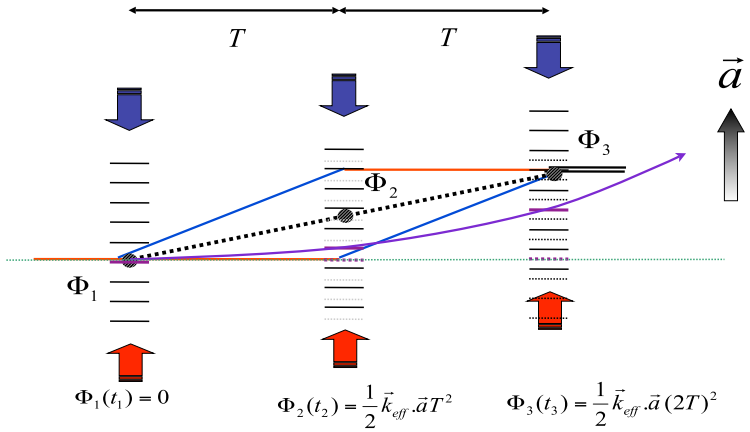

FIG. 2.6 : *Principe de la sensibilité de l'interféromètre aux accélérations. Le schéma représente l'accélération des faisceaux Raman dans le référentiel en chute libre avec le centre de masse des paquets d'ondes atomiques.*

Dans le cas d'une accélération $\mathbf{a}$, il est très facile, à partir du défilement de la phase laser dans le référentiel des atomes $\phi_{laser}(t) = \frac{1}{2}\mathbf{k_{eff}}.\mathbf{a}.t^2$ (Fig. 2.6), de calculer le déphasage à la sortie de l'interféromètre :

$$\Delta\Phi = \mathbf{k_{eff}}.\mathbf{a}T^2 \tag{2.18}$$

De même, dans le cas d'une rotation de vitesse de rotation Ω, il est possible d'en déduire très facilement le déphasage à partir du déplacement du centre du paquet d'onde atomique par rapport aux équi-phases laser (Fig. 2.7) :

$$\Delta\Phi = k_{eff}VT(\theta_3 - \theta_1) \tag{2.19}$$

Comme le montre le schéma 2.7, l'angle des faisceaux lasers Raman lors de la seconde impulsion n'a pas d'effet sur le déphasage atomique et la mesure correspond de fait à la variation d'angle entre la première et la dernière impulsion, c'est-à-dire à la rotation moyenne. Le déphasage dû à la rotation dépend de la vitesse moyenne des atomes $\mathbf{v}$, et plus particulièrement de la projection du déplacement entre les impulsions Raman dans le plan orthogonal à la direction de propagation des lasers Raman. Nous retrouvons ici le fait qu'un interféromètre doit avoir une aire physique non nulle pour être sensible à l'effet Sagnac [Sagnac 1913].

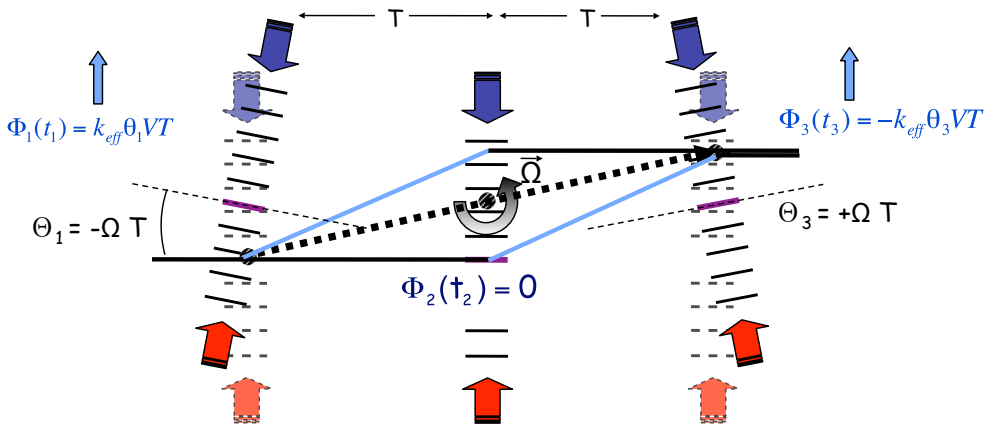

FIG. 2.7 : *Principe de la sensibilité de l'interféromètre aux rotations. Le schéma représente la rotation des faisceaux Raman dans un référentiel en chute libre avec le centre de masse des paquets d'ondes atomiques, dans le cas spécifique ou les faisceaux lasers sont dirigés perpendiculairement à la trajectoire atomique au moment de l'impulsion centrale.*

Dans le cas d'une vitesse de rotation constante $\mathbf{\Omega}$ nous retrouvons l'expression habituelle [Storey 1994] :

$$\Delta\Phi = -2(\mathbf{k_{eff}} \times \mathbf{v}).\mathbf{\Omega}T^2 \tag{2.20}$$

2.3 Fonction de sensibilité

Afin d'utiliser les interféromètres atomiques pour des mesures de précision, il faut pouvoir calculer l'impact des différentes sources expérimentales de bruit ou de biais. Pour cela, il faut considérer les trois durées caractéristiques de l'interféromètre : la durée des impulsions Raman τ, la durée entre deux impulsions T et la durée d'un cycle de mesure T_c incluant les phases de préparation des sources atomiques et de détection.

Considérant l'équation 2.16, les effets d'échantillonnage liés à la nature séquentielle de l'expérience, utilisant trois impulsions séparées par des durées de vol libre d'une part et avec des temps morts pendant le chargement et la détection d'autre part, peuvent être calculés assez facilement ($T < T_c$) [Yver-Leduc 2005].

La prise en compte de la durée finie des impulsions lasers est plus complexe et notamment en présence de forces d'inertie. En utilisant la méthode dite de la fonction de sensibilité, initialement développée pour les horloges atomiques [Dick 1987, Santarelli 1998, Quessada 2003], il est possible de prendre en compte à la fois les effets d'échantillonnage et de durée finie des impulsions. Cette méthode consiste à calculer la fonction de sensibilité à un saut de phase prenant en compte la durée finie des impulsions lasers [Cheinet 2008]. Elle permet ensuite d'en déduire l'effet de toute perturbation temporelle ou de calculer la réponse spectrale aux fluctuations de phase. Par la suite, cette méthode a été étendue à l'impact de toute perturbation se traduisant par une fluctuation de phase vue par les atomes : accélérations, rotations et fluctuations de la fréquence de transition dues aux champs magnétiques ou aux déplacements lumineux des niveaux atomiques par les faisceaux Raman [Cheinet thèse, Canuel thèse].

Ce formalisme s'est avéré un outil extrêmement pratique pour l'optimisation des deux expériences de gyromètre à atomes froids (voire paragraphe 3.3) et du gravimètre (chapitre 4), pour la caractérisation des erreurs systématiques et surtout pour l'amélioration du rapport signal à bruit des expériences, permettant notamment d'analyser séparément les contributions des différentes sources de bruit.

2.3.1 Sensibilité au bruit de phase

Nous calculons la variation de probabilité de transition, δP, de l'interféromètre pour une variation infinitésimale de phase laser $\delta\phi$ imprimée à l'instant t sur la phase atomique. La fonction de sensibilité de l'interféromètre $g_\phi(t)$ est définie par :

$$g_\phi(t) = 2 \lim_{\delta\phi \to 0} \frac{\delta P(\delta\phi, t)}{\delta\phi} \tag{2.21}$$

Expérimentalement, les mesures sont réalisées à flanc de frange pour maximiser la sensibilité. Pour cela, un déphasage de $\frac{\pi}{2}$ est introduit entre deux impulsions Raman tel que $(\phi_1 - 2\phi_2 + \phi_3 = \frac{\pi}{2})$. Dans ce cas la sensibilité à la phase peut être linéarisée :

$$g_\phi(t) = \lim_{\delta\phi \to 0} \frac{\delta\Phi(\delta\phi, t)}{\delta\phi} \tag{2.22}$$

Dès lors, le déphasage en sortie de l'interféromètre pour une évolution quelconque de la phase des lasers est donné par :

$$\Delta\Phi = \int_{-\infty}^{+\infty} g_\phi(t) d\phi(t) = \int_{-\infty}^{+\infty} g_\phi(t) \frac{d\phi(t)}{dt} dt \tag{2.23}$$

Pour calculer l'impact d'un saut de phase $\delta\phi$ à l'instant t pendant une impulsion, il suffit de remplacer la matrice d'évolution (eq.2.12) de cette impulsion par un produit de deux matrices, l'une faisant évoluer l'état atomique entre le début de l'impulsion et l'instant t avec la phase ϕ_i et l'autre entre l'instant t jusqu'à la fin de l'impulsion avec la phase $\phi_i + \delta\phi$. Pour connaître l'effet de ce saut de phase à l'instant t sur l'interféromètre, il suffit de réutiliser la matrice de transfert de l'interféromètre $M_{\text{tot}}(t)$ (eq.2.14) avec ce changement.

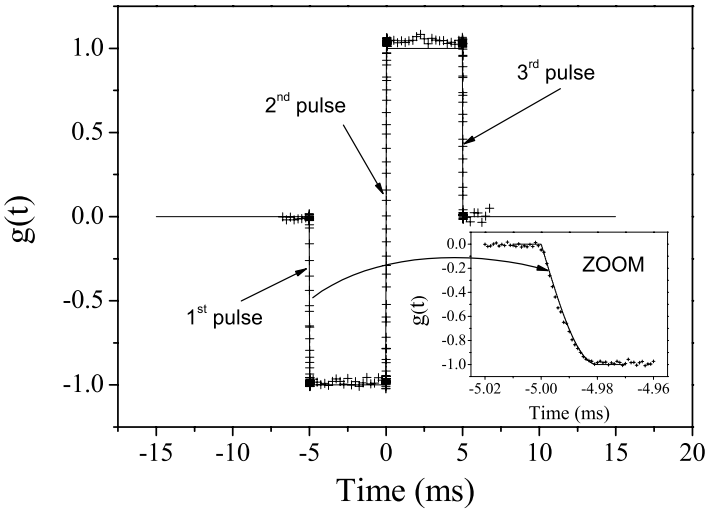

FIG. 2.8 : *Mesure de la fonction de sensibilité. La probabilité de transition est enregistrée en fonction du moment auquel le saut de phase est appliqué. Les données (croix) sont ensuite normalisées par l'amplitude du saut de phase et comparées à la courbe théorique (ligne).*

Dans le cas où les l'intensités des faisceaux lasers sont identiques lors des trois impulsions (Ω_R constant)[1], les durées des trois impulsions Raman valent respectivement $\tau - 2\tau - \tau$. Ainsi, en prenant l'origine des temps au milieu de l'impulsion π nous obtenons pour $g_\phi(t)$ une fonction impaire [Cheinet 2008] :

$$g_\phi(t) = \begin{cases} \sin(2\Omega_R t) & 0 < t < \tau \\ 1 & \tau < t < T + \tau \\ \sin(\Omega_R(t - T - \frac{\tau}{2}) + \frac{\pi}{2}) & T + \tau < t < T + \frac{3\tau}{2} \end{cases} \tag{2.24}$$

où $\Omega_R \tau = \frac{\pi}{2}$.

2.3.2 Calcul du facteur d'échelle aux forces d'inertie

Nous nous intéressons maintenant à la modification du facteur d'échelle, à la rotation et à l'accélération liée à la durée finie des impulsions lasers.

Nous avons vu que l'effet d'une accélération pouvait être traité comme un déplacement des équi-phases lasers dans le référentiel des atomes en chute libre ; la phase Raman instantanée imprimée sur la phase atomique $\phi_{\text{eff}}(t)$:

$$\phi_{\text{eff}}(t) = \frac{k_{\text{eff}} a t^2}{2} + k_{\text{eff}} v_0 t + \phi^0(t) \tag{2.25}$$

Le déphasage interférométrique est calculé avec l'équation 2.23 :

$$\Delta\Phi_{acc} = \int_{-\infty}^{+\infty} g_\phi(t) k_{\text{eff}}(at + v_0) dt \tag{2.26}$$

La symétrie impaire de la fonction de sensibilité $g_\phi(t)$ implique que le déphasage ne dépend pas de la vitesse initiale v_0 des atomes. La sensibilité de l'interféromètre est alors donnée en intégrant l'équation 2.26. La durée finie des impulsions lasers modifie légèrement le facteur d'échelle :

$$\Delta\Phi_{acc} = k_{\text{eff}} a (T + 2\tau)(T + \frac{4}{\pi}\tau) \tag{2.27}$$

Pour des paramètres correspondant à l'expérience du gravimètre : $\tau = 6$ µs et $T = 50$ms, la correction apportée par la durée finie des impulsions est de 4 10^{-4}.

Nous reprenons le même calcul pour obtenir la modification du facteur d'échelle lié à une vitesse de rotation constante. La phase instantanée des lasers s'écrit :

[1] Notons que dans l'expérience de gyromètre à atomes froids, c'est la durée des impulsions τ qui est constante, les formules données dans [Canuel thèse] sont donc légèrement différentes

$$\phi_{\text{eff}}(t) = \frac{2k_{\text{eff}}v\Omega t^2}{2} + k_{\text{eff}}v_0 t + \phi^0(t) \tag{2.28}$$

En tenant compte de la modification de la sensibilité de l'interféromètre induit par la durée finie des impulsions Raman (équation 2.23), le déphasage atomique mesuré en présence d'une rotation uniforme et constante Ω est donnée par :

$$\Delta\Phi_{rot} = 2k_{\text{eff}}v\Omega(T + 2\tau)(T + \frac{4}{\pi}\tau) \tag{2.29}$$

Pour des paramètres correspondant à l'expérience du gyromètre $\tau = 15$ µs et $T = 40$ ms la correction apportée par la durée finie des impulsions est de 0,1%. Cette modification du facteur d'échelle liée à la durée finie des impulsions lasers peut aussi être interprétée comme une modification de l'aire interférométrique lors de l'interaction avec les paquets d'ondes [Antoine 2006, Antoine 2007]. De manière générale, pour un interféromètre utilisant des impulsions de durées τ_1, τ_2 et $\tau_3 = \tau_1$, la sensibilité devient :

$$\Delta\Phi_{rot} = 2k_{\text{eff}}v\Omega(T + \tau_2)(T + \frac{4}{\pi}\tau_1) \tag{2.30}$$

2.3.3 Impact sur l'interféromètre des différentes sources de bruit

De façon similaire à celle utilisée pour la sensibilité aux forces d'inertie, nous pouvons évaluer le déphasage induit par les différentes sources d'erreur systématique (gradient de champ magnétique, déplacement lumineux à un ou deux photons, interaction entre atomes froids...). Il faut alors calculer la fonction de sensibilité à chaque perturbation puis intégrer l'effet sur la trajectoire atomique. Cela nous permet de quantifier les spécifications sur le contrôle des différents paramètres expérimentaux : du champ magnétiques, du rapport d'intensité entre les faisceaux lasers Raman, de l'intensité totale ou du désaccord Raman.

Dans le cas de perturbations temporelles aléatoires, il n'est plus possible de calculer exactement le déphasage, mais nous pouvons l'estimer à partir de la densité spectrale de bruit dans l'ensemble de la gamme d'intérêts pour l'interféromètre. Il faut pour cela pouvoir mesurer de façon indépendante l'ordre de grandeur des fluctuations du ou des paramètres expérimentaux impliqués (intensité, fréquence ou phase des faisceaux lasers Raman, champ magnétique, vibrations...). Il est alors possible d'en déduire l'impact sur le rapport signal à bruit en utilisant la transformée de Fourrier de la fonction de sensibilité [Cheinet 2008], puis d'optimiser l'expérience en réduisant chaque source de bruit, sans pour autant utiliser l'interféromètre directement.

L'impact sur le déphasage de l'interféromètre d'un bruit de phase des lasers Raman de densité spectrale de puissance $S_\phi(\omega)$ vaut :

$$(\sigma_\Phi^{rms})^2 = \int_0^{+\infty} |H(\omega)|^2 S_\phi(\omega) d\omega \tag{2.31}$$

où $H(\omega)$, la fonction de transfert s'écrit :

$$H(\omega) = \frac{4i\omega\Omega_R}{\omega^2 - \Omega_R^2} \sin(\frac{\omega(T+2\tau_R)}{2})(\cos(\frac{\omega(T+2\tau_R)}{2}) + \frac{\Omega_R}{\omega}\sin(\frac{\omega T}{2})) \tag{2.32}$$

La première partie de ces études a concerné la stabilité relative de phase entre les deux faisceaux lasers Raman, de longueur d'onde autour de 852 (resp. 780 nm) pour le césium (resp. le rubidium), et dont l'écart en fréquence est de 9,2 GHz (resp. 6,8 GHz). L'un des deux faisceaux lasers Raman est asservi en phase par rapport à l'autre via un battement optique et une référence de fréquence micro-onde. Les références de fréquences micro-ondes et les asservissements de phase des faisceaux lasers Raman ont été spécifiquement optimisés pour l'interférométrie atomique [Cheinet 2008, Nyman 2006, Le Gouët 2008]. La contribution totale de ces deux termes au déphasage des interféromètres a été ramenée en dessous de 1 mrad pour des paramètres typiques (temps d'interrogation 2T de l'ordre de 100 ms et durée des impulsions de l'ordre de 10 μs).

Nous avons également mis en évidence et caractérisé l'effet d'un délai de propagation différent entre les deux faisceaux lasers Raman qui transforme le bruit de fréquence du laser de référence en bruit de phase sur l'interféromètre et qui avait toujours été considéré comme non critique [Le Gouët 2007].

Une troisième partie a porté sur l'étude et la réduction des déplacements de fréquences, qui sont dus aux champs magnétiques et aux fluctuations des puissances des faisceaux lasers Raman, et pour lesquels l'utilisation de blindages magnétiques et du contrôle de la puissance des faisceaux Raman se sont avérés nécessaires [Canuel thèse].

L'ensemble de ces études a permis d'améliorer le rapport signal à bruit pour ne plus être limité que par les accélérations parasites pour l'accélération et le bruit de détection pour les mesures de rotation. Dans le cas du gyromètre, un rapport signal à bruit coup à coup de 200 (5 mrad de bruit de phase) a été obtenu pour la mesure de la rotation (c.f. chap.3.3). Pour l'accélération, le rapport signal à bruit obtenu sur le gravimètre est de 70, permettant d'obtenir une sensibilité au niveau de l'état de l'art tout en utilisant un temps de mesure relativement réduit (100 ms) [Le Gouët 2008].

2.4 Articles relatifs à la fonction de sensibilité

Les trois articles, reproduits et ajoutés à ce chapitre, concernent des mesures spécifiquement liées à la fonction de sensibilité. Le premier article (JOPB 2003) constitue une approche simplifiée qui nous a permis de quantifier les différentes sources de bruit dues aux effets d'échantillonnage et l'impact de la durée finie des impulsions lasers. Dans le second article (IEEE 2008), le lecteur pourra trouver le calcul et les mesures de la fonction de sensibilité à la différence de phase des faisceaux lasers Raman, à la fois dans le domaine temporel et dans le domaine spectral. Le troisième article (EPJD 2007) est spécifiquement consacré à l'effet d'un délai de rétro-réflection des faisceaux lasers Raman qui convertit les fluctuations de fréquence du laser Raman de référence en une fluctuation de phase vue par les atomes. Ces expériences montrent que la largeur de raie des lasers Raman peut limiter les performances de ce type d'interféromètre, et notamment celles des gradiomètres dans lesquels il devient d'autant plus limitant que les deux nuages d'atomes sont séparés. Beaucoup d'autres résultats utilisant la fonction de sensibilité pourront être trouvés dans les autres publications concernant le gyromètre (chapitre 3) à atomes froids ou le gravimètre (chapitre 4), mais également l'expérience ICE (paragraphe 5.5).

INSTITUTE OF PHYSICS PUBLISHING JOURNAL OF OPTICS B: QUANTUM AND SEMICLASSICAL OPTICS

J. Opt. B: Quantum Semiclass. Opt. **5** (2003) S136–S142 PII: S1464-4266(03)56905-1

Reaching the quantum noise limit in a high-sensitivity cold-atom inertial sensor

Florence Yver-Leduc[1], Patrick Cheinet[1], Jérôme Fils[1], André Clairon[1], Noël Dimarcq[1], David Holleville[1], Philippe Bouyer[2] and Arnaud Landragin[1]

[1] BNM-SYRTE, UMR 8630, Observatoire de Paris, 61 avenue de l'Observatoire, 75014 Paris, France

[2] Laboratoire Charles Fabry, UMR 8501, Centre Scientifique d'Orsay, Bât 503, BP 147, 91403 Orsay, France

E-mail: florence.yver@obspm.fr

Received 28 November 2002, in final form 3 February 2003
Published 2 April 2003
Online at stacks.iop.org/JOptB/5/S136

Abstract

In our high-precision atom interferometer, the measured atomic phase shift is sensitive to rotations and accelerations of the apparatus, and also to phase fluctuations of the Raman lasers. In this paper we study two principal noise sources affecting the atomic phase shift, induced by optical phase noise and vibrations of the setup. Phase noise is reduced by carrying out a phase lock of the Raman lasers after the amplification stages. We also present a new scheme to reduce noise due to accelerations by using a feed-forward on the phase of the Raman beams. With these methods, it should be possible to reach the range of the atomic quantum projection noise limit, which is about 1 mrad rms for our experiment, i.e. 30 nrad s^{-1} $Hz^{-1/2}$ for a rotation measurement.

Keywords: Atom interferometer, Raman transitions, laser phase lock, phase noise in optical fibres, acceleration compensation in precision measurements

1. Introduction

Recent progress in atom interferometry [1] enables the development of new inertial sensors, using the potential of matter-waves to lead to high-precision detectors. Since the first atom interferometer showing a phase shift owing to rotation in 1991 [2], several gyroscopes have been developed and their sensitivities are already similar to those obtained with the best optical gyroscopes [3]. The first high-sensitivity measurement of the local acceleration of gravity based on atom interferometry was achieved the same year, and has been strongly improved since [4].

In the last decade, the laser cooling techniques have been considerably improved and developed for metrological applications, as exemplified in the field of atomic clocks [5]. For inertial sensors based on de Broglie waves, they lead to drastic improvements in stability and sensitivity, while enabling a reduction of the dimensions of the apparatus.

High-sensitivity inertial sensors with good long-term stability have applications in various domains: gravimetry and gradiometry, inertial navigation, geophysics, measurements of fundamental constants [6] and tests of general relativity, like the equivalence principle and the Lense–Thirring effect [7].

2. Description of our apparatus

The design of our apparatus has been guided by two goals: long-term stability and compactness. The expected sensitivity is 30 nrad s^{-1} $Hz^{-1/2}$ as a rate-gyroscope and 4×10^{-8} m s^{-2} $Hz^{-1/2}$ as an accelerometer, when about 10^6 atoms are detected at the output of the interferometer. This corresponds to a signal-to-noise ratio of 1000, so that the atomic quantum projection noise limit is 1 mrad rms.

A scheme of the setup is shown in figure 1. The atomic sources are caesium atoms cooled in a magneto-optical trap to a few microkelvin. Then, the atoms are launched by a moving molasses technique at 2.4 m s^{-1} with a repetition rate of 2 Hz. This value corresponds to the first characteristic frequency of the instrument, leading to a pass band of the

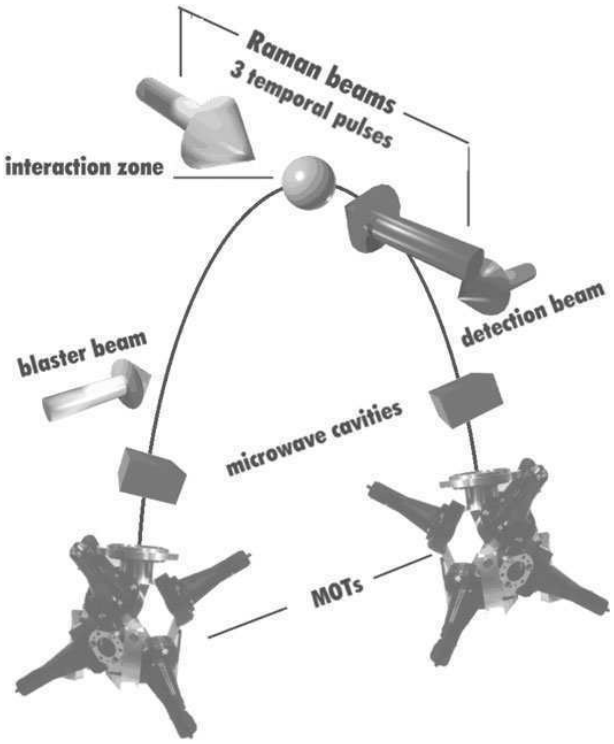

Figure 1. Principle of our cold atom inertial sensor. It uses two atomic sources launched in opposite trajectories and sharing the same Raman lasers. Horizontal velocity: 0.3 m s^{-1}.

interferometer of about 1 Hz. The atoms are prepared in the ($6S_{1/2}$, $F = 3, m_F = 0$) state by using microwave and optical pulses, and then reach the interferometer zone. The duration of one measurement in this zone is $2T \leqslant 100$ ms, which defines the second characteristic frequency of the instrument.

The interferometer configuration is similar to an optical Mach–Zehnder interferometer, and uses a $\pi/2-\pi-\pi/2$ sequence of counterpropagating laser pulses to induce stimulated Raman transitions [8] and coherently manipulate the atomic wavepackets (splitting, deviation and recombination). At the output of the interferometer, we measure the population of both hyperfine states ($6S_{1/2}$, $F = 3, m_F = 0$) and ($6S_{1/2}$, $F = 4, m_F = 0$) by laser-induced fluorescence and calculate the transition probability P between the two states.

The transition probability P is a function (1) of accelerations in the direction of the Raman laser beams, (2) of the rotation rate around the axis normal to the oriented area enclosed between the two arms of the interferometer, and (3) of fluctuations of the phase difference between the Raman lasers [9]. This last point will be further discussed in section 3. The phase shifts induced on the atomic wave phase are respectively named $\Delta\Phi_{acc}$, $\Delta\Phi_{rot}$ and $\Delta\Phi_{laser}$. The transition probability induced by the Raman sequence can be written as

$$P = \tfrac{1}{2}[1 + C\cos(\Delta\Phi_{acc} + \Delta\Phi_{rot} + \Delta\Phi_{laser})] \qquad (1)$$

where C is the contrast of the atomic fringes.

In order to distinguish between atomic phase shifts induced by rotation and acceleration, the experiment uses two counterpropagating atomic clouds diffracted by the same Raman pulses. The phase shifts measured by the two interferometers are then opposite for rotations, while they are identical for both accelerations and laser fluctuations. We thus discriminate between acceleration and rotation by adding or subtracting the phase shifts extracted from the two atomic clouds signals, as already demonstrated in [10].

Atom interferometry using either time domain (pulsed laser beams) [11] or space domain (focussed continuous laser beams) [12] can be built. The interferometer phase shifts induced by rotation and acceleration are

$$\Delta\Phi_{rot} = 2k_{eff}\Omega V T^2 \qquad (2)$$

$$\Delta\Phi_{acc} = k_{eff} a T^2 \qquad (3)$$

for an interferometer operating in the time domain, and

$$\Delta\Phi_{rot} = 2k_{eff}\Omega\frac{L^2}{V} \qquad (4)$$

$$\Delta\Phi_{acc} = k_{eff} a\frac{L^2}{V^2} \qquad (5)$$

in the space domain. $k_{eff} \cong 2k_{laser}$ represents the effective wavevector of the Raman laser pair, Ω is the rotation rate, and a the acceleration. In normal operation, V is the horizontal projection of the atomic mean velocity. T corresponds to the time between two successive Raman pulses and L is the spatial distance between two successive Raman beams.

In the time domain, the parameter determining the scaling factors is the time T between two successive interactions, whereas the important parameter in the space domain is the distance L between them.

A precise measurement requires a good definition of the scaling factor. Compared to thermal atomic beams, cold atom sources enable a smaller velocity dispersion of the atomic cloud and a better defined velocity by the use of the moving molasses technique. This leads to a better definition of the rotation scaling factor. Also, acceleration rejection by the use of two counterpropagating atomic clouds is more efficient in the time domain, as the velocity of the atoms does not appear in the scaling factor, which is thus better defined. For these reasons we have chosen to work with cold atoms and in the time domain.

Time intervals can be measured with a very high precision: in our apparatus, Raman pulses are generated by an acousto-optic modulator (AOM) with less than 100 ns rise time. Moreover, when using cold atoms launched by a moving molasses, the velocity of the atoms is very well known and stable: we can reach a stability of 10^{-4} m s^{-1} or better from shot to shot. The scaling factor of the gyroscope is then very well defined, and we can expect to know the rotation scaling factor with a relative uncertainty of 4×10^{-5} or better in one cycle. In the case of the Earth rotation rate measurement, this ensures an uncertainty below 3 nrad s^{-1} per shot, which is ten times lower than the short-term interferometer sensitivity.

Furthermore, the three laser pulses are generated by switching on and off three times the same pair of large Raman laser beams. The rotation noise induced in space domain gyroscopes by misalignments of the Raman laser pairs between each other is thus strongly reduced in our case.

However, our setup is also sensitive to temporal fluctuations of the Raman phase difference, which can lead to a degradation of the signal-to-noise ratio.

3. Influence of phase noises on rotation and acceleration measurements

The atomic phase shift measured at the output of the interferometer is a function of the phase difference between the two counterpropagating Raman lasers [13]:

$$\Delta\Phi_{laser} = \Phi_1(t) - 2\Phi_2(t+T) + \Phi_3(t+2T) \qquad (6)$$

where $\Phi_i(t)$ represents the phase difference between the two Raman lasers during the ith pulse. This phase is considered at the location of the centre of the atomic wavepacket [14]. This means that the atomic phase shift measured is also sensitive to any fluctuations of the phase difference between the Raman pulses. As laser phase noise induces identical phase shifts for both atomic clouds, it is seen as acceleration by the interferometer.

For an acceleration measurement, phase noise on the Raman phase difference and vibrations of the setup have to be minimized so that their contributions to the atomic phase noise remain below the 1 mrad rms interferometer noise.

For a rotation measurement, laser phase noise is rejected by the use of two counterpropagating atomic clouds. However, the phase shifts induced by these perturbations must remain negligible compared with 2π, in order to avoid any ambiguity on the fringe number. Moreover, to simplify the extraction of rotation and acceleration phase shifts from the experimental signals, the interferometer's phase fluctuations and vibrations should be reduced to less than 0.1 rad rms, which allows a linearization of equation (1) near the operating point.

In our setup, we have implemented a phase lock scheme that enables a reduction of the phase noise induced by the semiconductor (SC) amplifiers. In addition to a passive isolation from the vibrations, we also show here the possibility to implement a feed-forward compensation of the effect of vibrations by directly acting on the phase of the Raman beams.

4. Measurement and rejection of the phase noise of the Raman beams

The difference between the two Raman laser frequencies must be stabilized at 9.19 GHz to be tuned to the clock transition frequency of the caesium atoms. This stabilization is also crucial to prevent any degradation of the signal-to-noise ratio in the interferometer.

Several noise sources could spoil the Raman phase difference: internal noise of the microwave generator, optical amplification by slave lasers, independent propagation of the beams through air and various optical elements (AOM, polarization maintaining fibre). In this study, we will focus on optical phase noise sources, such as optical amplification and propagation in the polarization maintaining fibre, and on their contributions to the interferometer noise.

In order to deduce the contribution of the optical phase noise to the noise degrading the atomic phase shift, the measured phase noise spectra have to be weighted by the interferometer transfer function. As shown in equation (6), the atomic phase shift measurement consists in reading the Raman phase difference at three times $t = 0, T, 2T$, because of the $\pi/2{-}\pi{-}\pi/2$ configuration. We calculate the transfer function by expressing the atomic phase shift as a function of fluctuations of the phase difference $\Phi_i(t)$ between the two Raman lasers during the ith pulse.

We first suppose that the three laser pulses have an infinitely short duration. When expressing the Fourier transform of the laser phase fluctuation, with amplitude Φ_f and arbitrary phase φ_f at frequency f, each $\Phi_i(t)$ corresponding to the phase difference between the two Raman lasers during the ith pulse can be written as

$$\Phi_i(t) = \int_f \Phi_f \cos\,(2\pi f t + \varphi_f)\,\mathrm{d}f. \qquad (7)$$

Calculated from equation (6), the atomic phase shift induced by the laser phase fluctuation component at frequency f is thus

$$\Delta\Phi_{laser}(f) = -4\Phi_f \sin^2(\pi f T)\cos(2\pi f T + \varphi_f). \qquad (8)$$

A quadratic average of equation (8) on the arbitrary phase φ_f gives the contribution of the laser phase fluctuation to the atomic phase shift at frequency f:

$$\sqrt{\langle \Delta\Phi^2_{laser}(f)\rangle_{\varphi_f}} = 2\sqrt{2}\Phi_f \sin^2(\pi f T). \qquad (9)$$

The rms atomic phase shift due to a laser phase fluctuation at frequency f is thus obtained by multiplying the amplitude Φ_f of the fluctuation by a transfer function defined by a square sine function of the frequency f. This implies that the interferometer transfer function cancels at frequency multiples of $1/T$ and expresses the fact that the atomic phase shift measurement results in a sampled measurement of the rotation rate or the acceleration [4].

Furthermore, the study of the real case of square Raman pulses with a finite duration τ induces a well-known first-order low-pass filter in the transfer function of the interferometer, with a cut-off frequency $f_c = 1/2\tau$. From equation (9), the transfer function of the interferometer can be written as

$$|H(f)|^2 = \frac{8\sin^4(\pi f T)}{1 + (\frac{f}{f_c})^2} \qquad (10)$$

where T is the time interval between two consecutive Raman pulses, and f_c the cut-off frequency of the low-pass filter due to the pulses' finite duration τ ($\tau = 30\ \mu$s in our experimental case).

Each measured phase noise spectrum has thus to be weighted by this transfer function in order to evaluate its contribution to the noise degrading the atomic phase shift.

Phase noise measurements due to the optical amplification and to the propagation in the fibre are detailed after a short description of the optical bench generating the Raman laser beams.

The Raman laser beams are generated with two extended cavity laser diodes (ECLD) emitting at 852 nm. ECLD outputs are amplified to get the optical power needed for about 30 μs Raman pulses (figure 2). Therefore we use a slave laser diode (SD) for one path, from which we get 200 mW. On the other path, a tapered SC amplifier increases the laser power up to 500 mW. After superimposition in a polarization beam splitting cube, both beams are deflected by an AOM used as an optical switch to generate the three pulses. They are then injected with

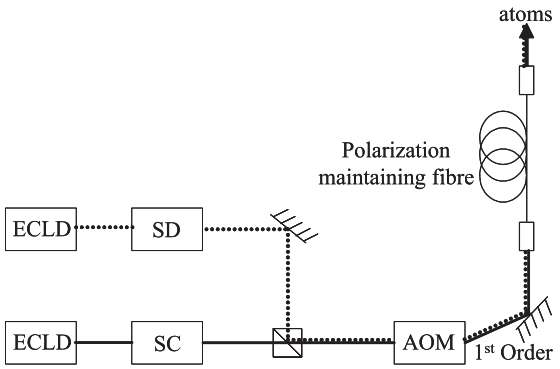

Figure 2. Principle of generation of the Raman laser beams. The laser frequency difference is 9.19 GHz and the AOM is used only as a switch of the Raman beams.

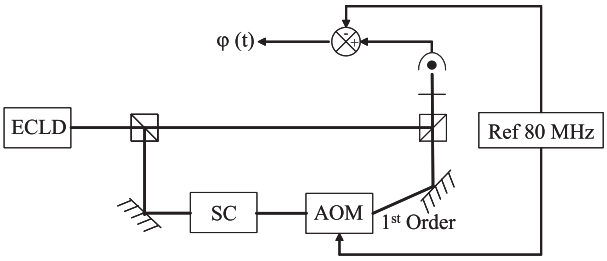

Figure 3. Scheme of the experiment used to measure the phase noise generated in the optical amplification path using the SC amplifier.

crossed polarizations into the two proper axes of a polarization maintaining fibre and propagate towards the interaction zone with the atoms.

The first step is to measure the phase noise induced by one of the two amplification stages, realized with the SC amplifier. The injection of the slave diode is supposed to add a similar phase noise. A photodiode detects the beat-note between the ECLD and the amplified laser beam, frequency shifted by 80 MHz using an AOM (figure 3). Phase noise is measured by mixing the photodiode output with a reference signal at 80 MHz.

The power spectral density (PSD) of the phase noise spoiling this beat-note is shown in figure 4. Low-frequency noise up to 3 kHz is due to temperature fluctuations on the optical bench and in the SC amplifier, and to mechanical vibrations. At higher frequencies, phase noise sources are mostly electrical and result in high narrow peaks of noise.

After weighting this spectrum by the interferometer transfer function to phase fluctuations described in equation (10), we estimate the atomic phase noise induced by the SC amplifier at the level of 180 mrad rms. This value greatly exceeds the limit of 1 mrad rms set by the expected signal-to-noise ratio of 1000.

We have to implement a method to imprint the phase quality of the microwave generator on the Raman phase difference. Usually, this Raman laser frequency stabilization is realized by phase locking one ECLD on the other [15]. But, doing so, the phase noise induced by the amplification stages is not compensated for, and degrades the phase difference between the laser beams at the level previously measured. That is the reason why we chose to phase lock the Raman laser beams after the optical amplification stages. With this method,

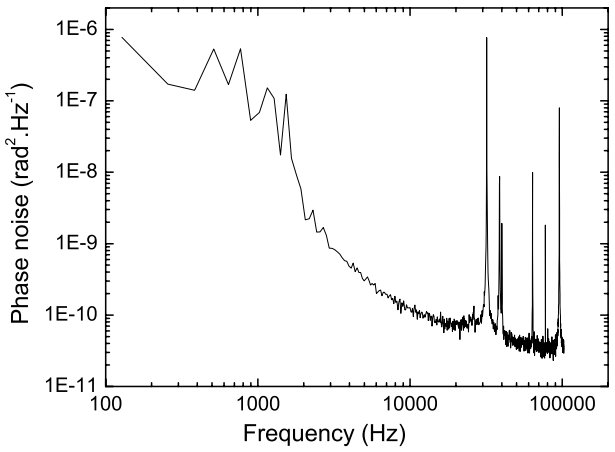

Figure 4. PSD measured in the experiment described in figure 3. The phase noise is mostly due to the SC amplifier and optical path fluctuations.

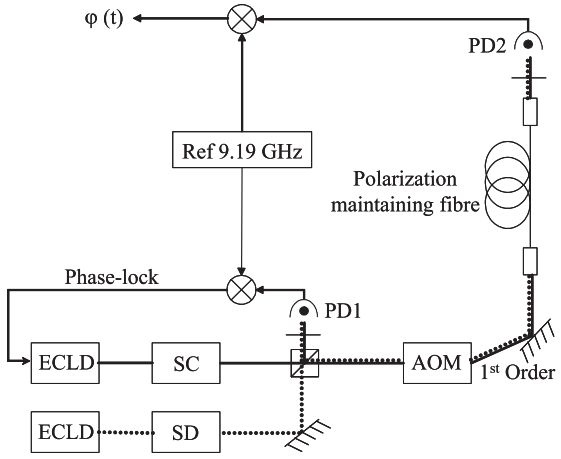

Figure 5. Principle of measurement of the residual phase noise between the two phase-locked Raman beams, directly imprinted on the atomic wave phase.

the loop delay is certainly increased, but all optical phase shifts introduced while the Raman beams do not copropagate are strongly reduced.

One could propose that the phase noise induced by the polarization maintaining fibre can also be rejected with a phase lock after the fibre. But, as Raman lasers are pulsed by the AOM, it is impossible to make any continuous servo-control including this AOM in the loop. The only way to servo-control the phase shift after the fibre is to use an external continuous laser, far detuned from the atomic transitions and copropagating in the optical fibre. For reasons of simplicity and easy implementation, the Raman laser beams are phase locked just before the AOM. Residual noise spoiling the phase difference between the phase-locked lasers is measured after propagation in the polarization maintaining fibre, in order to control whether this method is sufficient to preserve a high signal-to-noise ratio.

The phase difference between the two amplified laser beams is phase locked at the superimposition point by carrying out a beat-note between the laser beams on a Hamamatsu ultrafast photoconductor G4176, named PD1 (figure 5). The amplified beat-note is mixed with a reference signal at

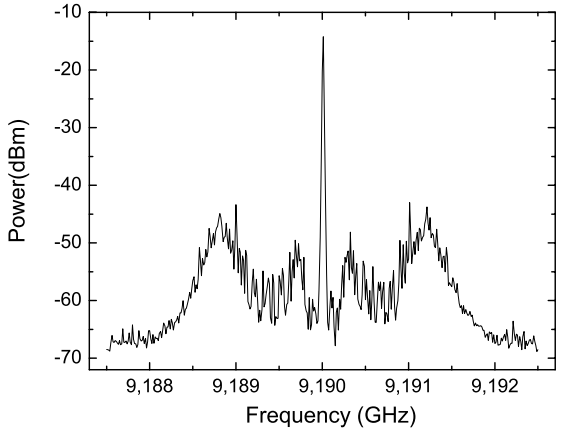

Figure 6. Beat-note detected on the photoconductor PD1, with a resolution bandwidth of 10 kHz. The central peak contains about 90% of the total power.

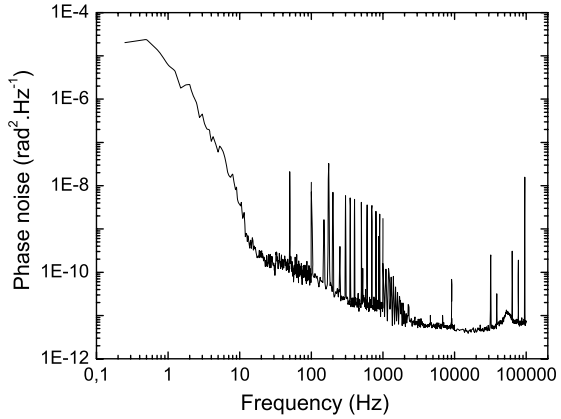

Figure 7. PSD of the phase noise measured on PD2 after the phase lock and propagation in the fibre. This Raman phase noise is directly seen by the atoms.

9.19 GHz. The error signal is then used to generate a correction signal fed back to the ECLD current and piezoelectric transductor (PZT).

Figure 6 shows the beat-note measured by a spectrum analyser with a resolution bandwidth of 10 kHz. We observe a lock bandwidth of 1.2 MHz. This is enough to reduce the phase noise of the Raman beams to the phase noise level of the microwave generator.

In figure 7 is shown the residual phase noise after propagation in a 3 m long optical fibre, and table 1 gives the induced phase noise in the atom interferometer after weighting by $H(f)$ (see equation (10)), for each frequency decade.

We can see a high phase noise at low frequencies up to 10 Hz. This phase noise is due to temperature fluctuations in the polarization maintaining fibre. For comparison, we measured the phase noise induced by propagation without any fibre, which showed a much lower contribution to the atomic phase noise in this decade (0.38 mrad rms compared to 1.01 mrad rms).

At Fourier frequencies from 100 Hz to 1 kHz, we measure many peaks at harmonic frequencies of 50 Hz. Their contribution to the atomic phase noise is significant (0.49 mrad rms) but does not represent the principal noise source. Moreover, they could come from electrical artefacts and their existence on the Raman phase difference is not certain. This means that the contribution of the frequency band from 100 Hz to 1 kHz to the atomic phase noise is probably lower than what we measured.

Table 1. Contribution of the Raman phase noise in each frequency decade calculated from the PSD (figure 7) weighted by the interferometer transfer function $H(f)$.

Frequency band	Atomic phase noise (mrad rms)
0–10 Hz	1.01
10– 100 Hz	0.37
100 Hz–1 kHz	0.87
1 kHz–10 kHz	0.48
10 kHz–100 kHz	0.37
Total	1.51

At frequencies higher than 1 kHz, the PSD reaches the noise level of the measurement setup.

Thus, a direct phase lock of optical amplified lasers enables a rejection of the major part of the phase noise induced by the amplification stages and non-counterpropagating paths. With this method, the contribution of the Raman lasers' phase noise falls down to the level of 1.5 mrad rms.

The optical fibre is the most important source of noise on the Raman laser phase difference. With a better control of the fibre temperature, we expect to reduce the interferometer phase noise to the range of 1.2 mrad rms.

5. Acceleration compensation

Because of an aliasing effect due to our sampling frequency of 2 Hz, the high-frequency part of the acceleration noise is transferred to the low frequencies (lower than 1 Hz) and can degrade the signal-to-noise ratio of the interferometer. In order to evaluate the effect of vibrations on the interferometer, we measured the acceleration noise and deduced its contribution to the interferometer phase shift by weighting it by equation (10). Because the interferometer signal depends only on the difference of position (or phase) between the three pulses (see equation (6)), the accelerometer signal has to be converted in a position (or phase) signal. This means that it has to be integrated in the frequency band from 0.1 to 200 Hz. Vibrations of the lab floor have been measured with an accelerometer (IMI model 626A04) and would contribute to the interferometer phase noise at the level of 1 rad rms. This value is too high compared with the limits of 1 mrad rms and 0.1 rad rms required respectively for acceleration and rotation measurements.

Two methods can be implemented to reduce vibrations of the setup: putting it on an isolation platform or compensating for vibrations actively. We installed our interferometer on an optimized NanoK isolation platform. This enabled us to reduce vibrations so that their contribution to the interferometer phase noise is estimated at about 0.1 rad rms. This method, alone, is not sufficient to reach the interferometer sensitivity. Moreover, the platform could lead to additional rotation noise [4]. For these reasons, we have tested a new scheme to reduce the effect of vibrations by using a feed-forward on the phase of the Raman beams. If the method is efficient and robust enough, it will be possible to avoid using any vibration isolation platform.

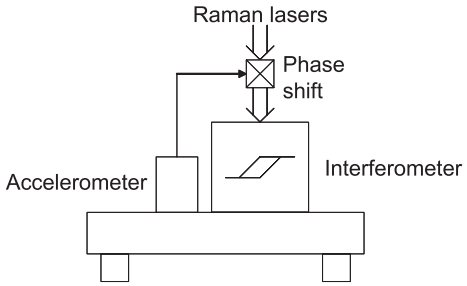

Figure 8. Principle of setup for acceleration compensation on the inertial sensor. The accelerometer signal is used to generate a correction signal on the Raman phase, which cancels the phase shift induced by vibrations.

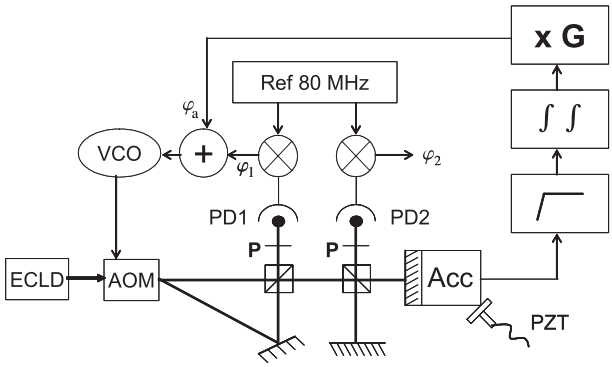

Figure 9. Auxiliary experiment testing the acceleration rejection. The accelerometer signal is used as a feed-forward correction signal and is added into the Raman phase lock loop.

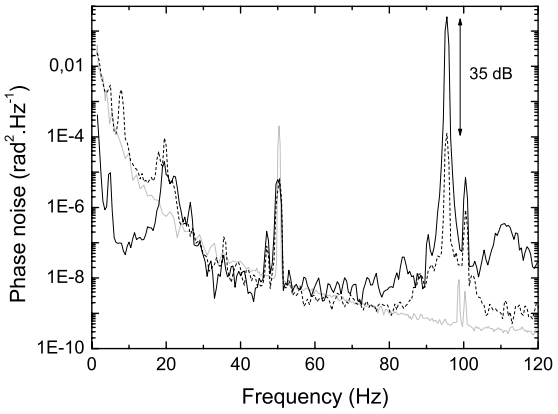

Figure 10. PSD of the phase noise measured on PD2 (figure 9). Solid curve: without rejection. Dashed curve: with rejection. Grey curve: accelerometer's internal noise.

The basic principle of the method is schematized in figure 8. A low-noise sensor is rigidly fixed on the table supporting the interferometer. This sensor provides an acceleration signal at high frequencies used in the feed-forward compensation on the phase of the Raman beams. After the two integrations and proper adjustment of the gain, it is applied to the phase lock setup of the Raman beams. This adjustment can be performed by minimizing the interferometer noise. By doing so, we have the advantage of the high sensitivity of mechanical accelerometers at high frequencies and the stability of atomic interferometers at low frequencies and continuous accelerations.

In order to test this method, we built the auxiliary experiment schematized in figure 9. The first step is to implement a setup similar to the original optical bench. The two laser beams representing the Raman lasers come from the same ECLD diffracted in zero and first orders of an AOM, fed with a voltage-controlled oscillator (VCO). The two laser beams are then recombined in a polarization beam splitting cube.

At one output of the cube, a first photodiode PD1 measures the beat-note between the two beams. This signal is mixed with an 80 MHz reference signal to obtain the phase error signal φ_1 used to drive the VCO feeding the AOM. In this way, we servo-lock the phase difference between the two beams at the location of the photodiode, as it is done in the original setup.

At the second output, the beams are separated again into a Michelson interferometer and we simulate vibrations of the setup by moving one mirror with a PZT. A second photodiode PD2 is placed at the output of the interferometer to measure the optical phase shift φ_2 that would be imprinted on the atomic wave phase.

Our method to compensate for this phase shift consists in measuring the mirror's vibrations with an accelerometer to generate a correction signal. For this study, we use an accelerometer working in the frequency range from 0.1 to 200 Hz. In order to suppress low frequencies below 0.1 Hz which lead to a drift of the correction signal, we use a high-pass filter with a cut-off frequency of 0.16 Hz. The signal has to be integrated twice and scaled in order to be compared with φ_2. The integration used a second-order low-pass filter with a cut-off frequency of 3 Hz. Finally, this correction signal, named φ_a, is added to the phase error signal φ_1 of the servo-loop. When the compensation is perfectly adjusted, no modulation induced by the PZT should appear on φ_2. The scaling factor G is chosen experimentally to minimize the modulation of φ_2.

We show in figure 10 the PSD of the phase noise measured on PD2 for an excitation frequency of 95 Hz, with and without feed-forward compensation, and the equivalent accelerometer's internal noise previously measured.

Any active rejection will add the noise of its reference. Here, the feed-forward compensation adds the accelerometer's noise to the final measured phase noise. One can notice that, at low frequency (below 60 Hz), the accelerometer's noise is at the level of or higher than the vibration noise. This leads to an increased noise level for frequencies lower than 20 Hz in this case. Wherever the accelerometer's noise is low enough, we observe a decrease of the noise level and we reach a 35 dB rejection efficiency for the frequency modulation of the PZT at 95 Hz.

To fully characterize the rejection process, the last step is to study the efficiency of the vibration compensation as a function of the modulation frequency. To do so, we use a PZT modulation amplitude high enough to be only partially rejected, so that the rejection process is not limited by the accelerometer's noise. We found a strong dependence on the modulation frequency. In order to better understand this result, we modelled the rejection efficiency, taking into account the processing of the acceleration signal before its addition in the servo-loop.

For low frequencies, the phase shift introduced by the high-pass filters and integration device prevents an exact cancellation. This will reduce the rejection efficiency. For

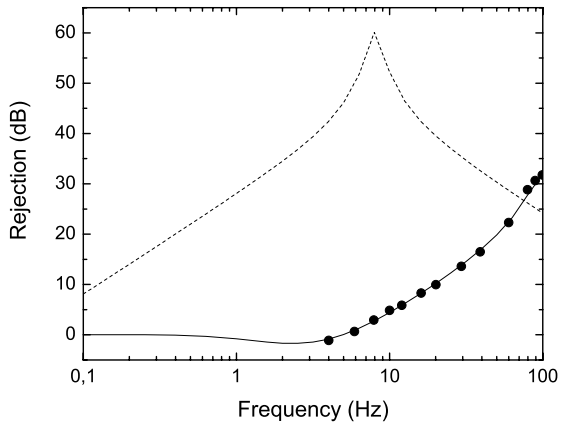

Figure 11. Phase noise rejection of the modulation induced by the PZT. Black dots: experimental result. Solid curve: simulated rejection in the actual experimental conditions. Dashed curve: calculated rejection that could be obtained by using a better accelerometer with a lower noise level and a lower working frequency (0.01 Hz cut-off frequency).

the best rejection efficiency, the scaling factor error will limit the rejection.

Finally, for the highest frequencies, the accelerometer's sensitivity presents a mechanical resonance around 2 kHz. This will induce a decrease of the rejection efficiency.

We can see in figure 11 that the simulation is in good agreement with the experimental results. This means that the rejection measured here is limited by the analogical processing of the signal.

We plan to replace the accelerometer by a seismometer working in the 0.01–50 Hz frequency range, which presents a lower noise level (Guralp CMG-T40). This will allow us to reduce the cut-off frequencies on the analogical filters, in order to optimize the rejection. We plotted also in figure 11 with a dashed curve the case with cut-off frequencies of 0.01 Hz, with a scaling error of 1:1000. This will lead at least to a 25 dB rejection from 1 to 100 Hz. We could further improve this result by using a numerical filtering instead of an analogical one. This would enable the use of the optimum filter taking into account the real transfer function of the setup.

Traditional criticisms made against feed-forward compensation schemes concern the difficulties due to the need for a very good knowledge of the scaling factors. They do not really apply here for at least three reasons: first, we only need to reduce the interferometer phase noise induced by high-frequency noise aliased to low frequency. Second, the compensation is not totally an open-loop configuration; a numerical minimization of the interferometer noise allows at least for gain adjustment of the vibration compensation in the long term. Third, we do not suspect the mechanical transfer function to vary significantly during the course of a measurement.

6. Conclusions

In this paper we have demonstrated our ability to reduce two principal noise sources in the atom interferometer. A phase lock after the amplification stages reduces the phase noise on the Raman phase difference. The residual noise contributes to the atomic phase noise at the level of 1.5 mrad rms.

A preliminary test of acceleration compensation by acting on the optical phase has been validated. The method enables us to reach a 35 dB rejection, and this value can be easily improved by using a seismometer with better low-frequency internal noise. This should allow us to operate the inertial sensor on the ground and perhaps to free the setup from potential rotation noise added by the isolation platform.

More work is necessary to fully demonstrate the efficiency of this feed-forward vibration compensation. However, it looks very promising and its implementation is much easier than the traditional method used for active vibration isolation. A generalization to three dimensions is possible, and it could also be applied in other high-precision measurements, particularly for vibration compensation of lasers stabilized in supercavities.

Thus, we expect that these two main noise sources can be reduced to the intrinsic limit of the interferometer sensitivity. The remaining main noise source is due to wavefront distortions of the Raman lasers. This can lead to a systematic error if the two atomic trajectories do not perfectly overlap [16].

Acknowledgments

The authors would like to thank CNRS, BNM, DGA, SAGEM and CNES for supporting this work. We would also like to thank the electronic staff of SYRTE for their help and advice.

References

[1] Berman P R (ed) 1997 *Atom Interferometry* (London: Academic)
[2] Riehle F, Kister Th, Witte A, Helmcke J and Bordé Ch J 1991 *Phys. Rev. Lett.* **67** 177
[3] Gustavson T L, Landragin A and Kasevich M 2000 *Class. Quantum Grav.* **17** 1
[4] Peters A, Chung K Y and Chu S 2001 *Metrologia* **38** 25
[5] Clairon A, Laurent Ph, Santarelli G, Ghezali S, Lea S N and Bahoura M 1995 *IEEE Trans. Instrum. Meas.* **44** 128
[6] Wicht A, Hensley J M, Sarajlic E and Chu S 2001 *Proc. 6th Symp. on Frequency Standards and Metrology* ed P Gill (Singapore: World Scientific) p 193
[7] *ESA Assessment Study Report* 2000 ESA-SCI 10
[8] Bordé Ch J 1991 *Laser Spectroscopy* vol 10, ed M Ducloy, E Giacobino and G Camy (Singapore: World Scientific) p 239
[9] Storey P and Cohen-Tannoudji C 1994 *J. Physique* II **4** 1999–2027
[10] Gustavson T L, Bouyer P and Kasevich M 1998 *Proc. SPIE* **3270** 62
[11] Sterr U, Sengstock K, Ertmer W, Riehle F and Helmcke J 1997 *Atom Interferometry* ed P R Berman (London: Academic)
[12] Udem Th, Diddams S A, Vogel K R, Oates C W, Curtis E A, Lee W D, Itano W M, Drullinger R E, Bergquist J C and Hollberg L 2001 *Phys. Rev. Lett.* **86** 4996
[13] Kasevich M and Chu S 1992 *Appl. Phys.* B **54** 321
[14] Antoine C and Bordé Ch J 2002 *Phys. Lett.* A **306** 277
[15] Santarelli G, Clairon A, Lea S N and Tino G 1994 *Opt. Commun.* **104** 339
[16] Landragin A, Fils J, Yver F, Holleville D, Dimarcq N and Clairon A 2001 *Proc. 6th Symp. on Frequency Standards and Metrology* ed P Gill (Singapore: World Scientific) p 532

Measurement of the Sensitivity Function in a Time-Domain Atomic Interferometer

Patrick Cheinet, Benjamin Canuel, Franck Pereira Dos Santos, Alexandre Gauguet, Florence Yver-Leduc, and Arnaud Landragin

***Abstract*—We present here an analysis of the sensitivity of a time-domain atomic interferometer to the phase noise of the lasers used to manipulate the atomic wave packets. The sensitivity function is calculated in the case of a three-pulse Mach–Zehnder interferometer, which is the configuration of the two inertial sensors we are building at the Laboratoire National de Métrologie et d'Essais-Système de Références Temps-Espace. We successfully compare this calculation to experimental measurements. The sensitivity of the interferometer is limited by the phase noise of the lasers as well as by residual vibrations. We evaluate the performance that could be obtained with state-of-the-art quartz oscillators, as well as the impact of the residual phase noise of the phase-locked loop. Requirements on the level of vibrations are derived from the same formalism.**

***Index Terms*—Atomic physics, gyroscopes, interferometry, laser noise, phase-locked loops (PLLs), phase noise, vibrations.**

I. Introduction

ATOM optics are a means to realize precision measurements in various fields. Atomic microwave clocks are the most precise realization of a Système Internationale unit, namely, the second [1], and high-sensitivity inertial sensors [2]–[4], based on atomic interferometry [5], already reveal accuracies that are comparable with state-of-the-art sensors [6], [7]. Two cold atom inertial sensors are currently under construction at the Laboratoire National de Métrologie et d'Essais-Système de Références Temps-Espace (LNE-SYRTE)—a gyroscope [8], which already reaches a sensitivity of 2.5×10^{-6} rad $\cdot$ s^{-1} $\cdot$ Hz$^{-1/2}$, and an absolute gravimeter [9], which will be used in the LNE watt Balance project [10]. Although based on different atoms and geometries, the atomic gyroscope and gravimeter rely on the same principle, which is presented in Fig. 1. Atoms are collected in a 3-D magnetooptical trap (3-D-MOT) in which the atoms are cooled down to a few microkelvins. In the gyroscope, ^{133}Cs atoms are launched upward with an angle of 8°, with respect to verticality using the technique of moving molasses, whereas in the gravimeter, ^{87}Rb atoms are simply allowed to fall. Then, the initial quantum state is prepared by a combination of microwave and optical pulses. The manipulation of the atoms is realized by stimulated Raman transition pulses [11], using two counterpropagating lasers, which drive coherent transitions between the two hyperfine levels of the alkali atom. Three laser pulses, of durations τ_R, $2\tau_R$, and τ_R, separated in time by T, respectively split, redirect, and recombine the atomic wave packets, creating an atomic interferometer [12]. Finally, a fluorescence detection gives a measurement of the transition probability from one hyperfine level to the other, which is given by $P = (1/2)(1 - \cos(\Phi))$, Φ being the interferometric phase. The phase difference between the two Raman lasers (which we will call the Raman phase throughout this paper, and will be denoted as ϕ) is imprinted at each pulse on the phase of the atomic wave function [13]. As ϕ depends on the position of the atoms, the interferometer is sensitive to inertial forces and can thus measure rotation rates and accelerations. A drawback of this technique is that the measurement of the interferometric phase is affected by the phase noise of the Raman lasers as well as parasitic vibrations. The aim of this paper is to investigate both theoretically and experimentally how these noise sources limit the sensitivity of such an atomic interferometer.

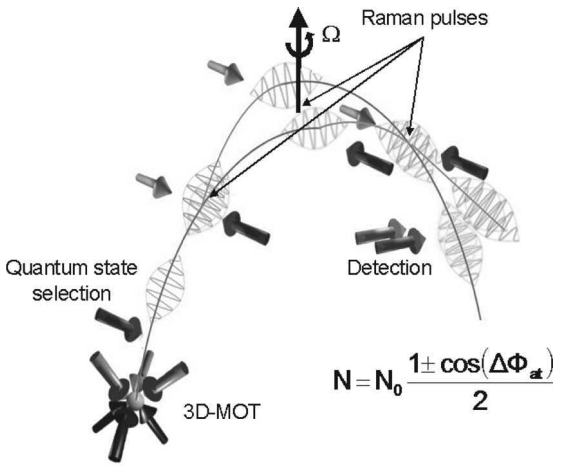

Fig. 1. Scheme of principle of our inertial sensors, which is illustrated for the gyroscope experiment. Cold atoms from the 3-D-MOT are launched upward, and a pure quantum state is selected. At the top of their trajectory, we apply three Raman laser pulses realizing the interferometer. Finally, a fluorescence detection allows measurement of the transition probability. Such an interferometer is sensitive to the rotation (Ω) perpendicular to the area enclosed between the two arms and to the acceleration along the laser's axis.

Manuscript received March 23, 2005; revised November 26, 2007. This work was supported in part by the Laboratoire National de Métrologie et d'Essais (LNE), by the Centre National de la Recherche Scientifique (CNRS), by the Délégation générale pour l'armement (DGA), and by the Centre National d'Études Spatiales (CNES).

P. Cheinet is with the University of Mainz, 55099 Mainz, Germany.

B. Canuel is with the European Gravitational Observatory, 56021 Pisa, Italy.

F. Pereira Dos Santos, A. Gauguet, F. Yver-Leduc, and A. Landragin are with the LNE-Système de Références Temps-Espace (SYRTE), CNRS UMR 8630, Observatoire de Paris, 75014 Paris, France (e-mail: franck.pereira@obspm.fr).

Color versions of one or more of the figures in this paper are available online at http://ieeexplore.ieee.org.

Digital Object Identifier 10.1109/TIM.2007.915148

II. Sensitivity Function

The sensitivity function is a natural tool to characterize the influence of the fluctuations in the Raman phase ϕ on the transition probability [14] and, thus, on the interferometric phase. Let us assume that a phase jump $\delta\phi$ occurs on the Raman phase ϕ at time t during the interferometer sequence, inducing a change of $\delta P(\delta\phi, t)$ in the transition probability. The sensitivity function is then defined by

$$g(t) = 2 \lim_{\delta\phi \to 0} \frac{\delta P(\delta\phi, t)}{\delta\phi}. \tag{1}$$

The sensitivity function can easily be calculated for infinitesimally short Raman pulses. In this case, the interferometric phase Φ can be deduced from the Raman phases ϕ_1, ϕ_2, and ϕ_3 during the three laser interactions, taken at the position of the center of the atomic wave packet, i.e., $\Phi = \phi_1 - 2\phi_2 + \phi_3$ [15]. Usually, the interferometer is operated at $\Phi = \pi/2$, for which the transition probability is one half, to get the highest sensitivity to interferometric phase fluctuations. If the phase step $\delta\phi$ occurs, for instance, between the first and the second pulses, the interferometric phase changes by $\delta\Phi = -\delta\phi$, and the transition probability by $\delta P = -\cos(\pi/2 + \delta\Phi)/2 \sim -\delta\phi/2$ in the limit of an infinitesimal phase step. Thus, in between the first two pulses, the sensitivity function is -1: the same way one finds for the sensitivity function between the last two pulses, i.e., $+1$.

In the general case of finite-duration Raman laser pulses, the sensitivity function depends on the evolution of the atomic state during the pulses. To calculate $g(t)$, we make several assumptions. First, the laser waves are considered as pure plane waves. The atomic motion is then quantized in the direction parallel to the laser beams. Second, we restrict our calculation to the case of a constant Rabi frequency (square pulses). Third, we assume that the resonance condition is fulfilled. The Raman interaction then couples the two states $|a\rangle = |g_1, \overrightarrow{p}\rangle$ and $|b\rangle = |g_2, \overrightarrow{p} + \hbar\overrightarrow{k}_{\text{eff}}\rangle$, where $|g_1\rangle$ and $|g_2\rangle$ are the two hyperfine levels of the ground state, $\overrightarrow{p}$ is the atomic momentum, and $\overrightarrow{k}_{\text{eff}}$ is the difference between the wave vectors of the two lasers.

We develop the atomic wave function on the basis set $\{|a\rangle, |b\rangle\}$ so that $|\Psi(t)\rangle = C_a(t)|a\rangle + C_b(t)|b\rangle$ and choose the initial state to be $|\Psi(t_i)\rangle = |\Psi_i\rangle = |a\rangle$. At the output of the interferometer, the transition probability is given by $P = |C_b(t_f)|^2$, where $t_f = t_i + 2T + 4\tau_R$. The evolution of C_a and C_b from t_i to t_f is given by

$$\begin{pmatrix} C_a(t_f) \\ C_b(t_f) \end{pmatrix} = M \begin{pmatrix} C_a(t_i) \\ C_b(t_i) \end{pmatrix} \tag{2}$$

where M is the evolution matrix through the whole interferometer. Solving the Schrödinger equation gives the evolution matrix (3), shown at the bottom of the page, during a Raman pulse [16], from time t_0 to time t, where $\Omega_R/2\pi$ is the Rabi frequency, and ω_L, which is the effective frequency, is the frequency difference between the two lasers $\omega_L = \omega_2 - \omega_1$. Setting $\Omega_R = 0$ in $M_p(t_0, t, \Omega_R, \phi)$ gives the free evolution matrix, which determines the evolution between the pulses. The evolution matrix for the full evolution is obtained by taking the product of several matrices. When t occurs during the ith laser pulse, we split the evolution matrix of this pulse at time t into two successive matrices—the first one with ϕ_i and the second one with $\phi = \phi_i + \delta\phi$.

Finally, we choose the time origin at the middle of the second Raman pulse. We thus have $t_i = -(T + 2\tau_R)$ and $t_f = T + 2\tau_R$. We then calculate the change in the transition probability for an infinitesimally small phase jump at any time t during the interferometer and deduce $g(t)$. It is an odd function, whose expression is given here for $t > 0$. Thus, we have

$$g(t) = \begin{cases} \sin(\Omega_R t), & 0 < t < \tau_R \\ 1, & \tau_R < t < T + \tau_R \\ -\sin\left(\Omega_R(T - t)\right), & T + \tau_R < t < T + 2\tau_R. \end{cases} \tag{4}$$

When the phase jump occurs outside the interferometer, the change in the transition probability is null, so that $g(t) = 0$ for $|t| > T + 2\tau_R$.

To validate this calculation, we use the gyroscope experiment to experimentally measure the sensitivity function. About 10^8 atoms from a background vapor are loaded in a 3-D-MOT within 125 ms, with six laser beams tuned to the red of the $F = 4 \to F' = 5$ transition at 852 nm. The atoms are then launched upward at $\sim$2.4 m/s within 1 ms and cooled down to an effective temperature of ~ 2.4 μK. After launch, the atoms are prepared into the $|F = 3, m_F = 0\rangle$ state using a combination of microwave and laser pulses. They first enter a selection cavity tuned to the $|F = 4, m_F = 0\rangle \to |F = 3, m_F = 0\rangle$ transition. The atoms left in the $F = 4$ state are pushed away by a laser beam tuned to the $F = 4 \to F' = 5$ transition, 11 cm above the selection cavity. The selected atoms then reach the apogee 245 ms after the launch, where they experience three interferometer pulses of duration $\tau_R - 2\tau_R - \tau_R$ with $\tau_R = 20$ μs separated in time by $T = 4.97$ ms. The number of atoms $N_{F=3}$ and $N_{F=4}$ are finally measured by detecting the fluorescence induced by a pair of laser beams located 7 cm below the apogee. From these measurements, we deduce the transition probability $N_{F=4}/(N_{F=3} + N_{F=4})$. The total number of detected atoms is about 10^5. The repetition rate of the experiment is 2 Hz.

The setup for the generation of the two Raman laser beams is displayed in Fig. 2. Two slave diode lasers of 150-mW output power are injected with extended cavity diode lasers. The polarizations of the slave diode output beams are made orthogonal so that the two beams can be combined onto a polarization beam splitter cube. The light at this cube is then split in two distinct unbalanced paths.

$$M_p(t_0, t, \Omega_R, \phi) = \begin{pmatrix} e^{-i\omega_a(t-t_0)} \cos\left(\frac{\Omega_R}{2}(t - t_0)\right) & -ie^{-i\omega_a(t-t_0)} e^{i(\omega_L t_0 + \phi)} \sin\left(\frac{\Omega_R}{2}(t - t_0)\right) \\ -ie^{-i\omega_b(t-t_0)} e^{-i(\omega_L t_0 + \phi)} \sin\left(\frac{\Omega_R}{2}(t - t_0)\right) & e^{-i\omega_b(t-t_0)} \cos\left(\frac{\Omega_R}{2}(t - t_0)\right) \end{pmatrix} \tag{3}$$

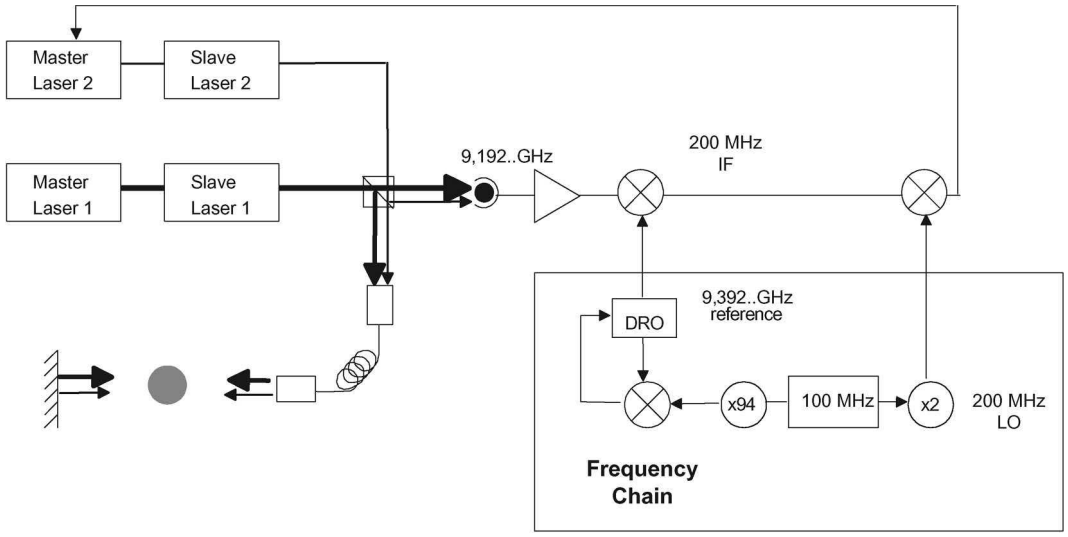

Fig. 2. Principle of the laser phase lock. The beatnote at 9.192 GHz between the two Raman lasers is observed on a fast response photodetector. After amplification, this beatnote is mixed with the reference frequency at 9.392 GHz from the frequency chain to obtain a signal at 200 MHz. This signal is compared with the reference frequency at 200 MHz from the same frequency chain to get an error signal. This error signal is then processed and sent to the current of the laser and to the PZT that controls the laser cavity length.

On the first path, most of the power of each beam is sent through an optical fiber to the vacuum chamber. The two beams are then collimated with an objective attached onto the chamber (waist $w_0 = 15$ mm). They enter together through a viewpoint, cross the atomic cloud, and are finally retroreflected by a mirror fixed outside the vacuum chamber. In this geometry, four laser beams are actually sent onto the atoms, which interact with only two of them, because of selection rules and resonance conditions. The interferometer can also be operated with copropagating Raman laser beams by simply blocking the light in front of the retroreflecting mirror. A remarkable feature of this experiment is that the three interferometer pulses are realized by this single pair of Raman lasers that is turned on and off three times, the middle pulse being at the top of the atoms' trajectory. For all the measurements described in this paper, the Raman lasers are used in the *copropagating* configuration. The interferometer is then no longer sensitive to inertial forces but remains sensitive to the relative phase of the Raman lasers. Moreover, as such Raman transitions are not velocity selective, more atoms contribute to the signal. All this allows us to reach a good signal to noise ratio of 150 per shot. We insist here on the fact that the formalism developed in this paper does not depend on the geometry of the Raman beams. We test the model with copropagating Raman measurements, but it applies as well to the case of counterpropagating measurements.

The second path is used to control the Raman laser phase difference, which needs to be locked [17] onto the phase of a very stable microwave oscillator. The phase-locked loop (PLL) scheme is also displayed in Fig. 2. The frequency difference is measured by a fast photodetector, which detects a beatnote at 9.192 GHz. This signal is then mixed with the signal of a dielectric resonator oscillator (DRO) tuned at 9.392 GHz. The DRO itself is phase locked onto the 94th harmonics of a very stable 100-MHz quartz. The output of the mixer (IF) is 200 MHz. A local oscillator (LO) at 200 MHz is generated by doubling the same 100-MHz quartz. IF and LO are compared

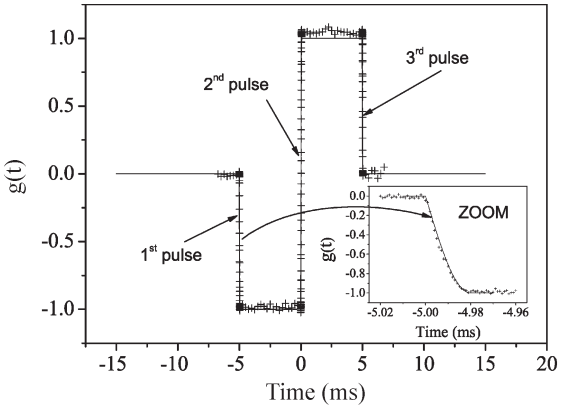

Fig. 3. Atomic sensitivity function $g(t)$ as a function of time for a three-pulse interferometer with a Rabi frequency $\Omega_R = (\pi/2\tau_R)$. The theoretical calculation is displayed in solid line and the experimental measurement in crosses. A zoom is made on the first pulse.

using a digital phase and frequency detector, whose output is used as the error signal of the PLL. The relative phase of the lasers is stabilized by reacting on the current of one of the two diode lasers, as well as on the voltage applied to the piezoelectric transducer (PZT) that controls the length of the extended cavity diode laser [17].

To measure $g(t)$, a small phase step of $\delta\phi = 0.107$ rad is applied at time t on the LO. The PLL copies this phase step onto the Raman phase within a fraction of a microsecond, which is much shorter than the Raman pulse duration of $\tau_R = 20$ μs. Finally, we measured the transition probability as a function of t and deduced the sensitivity function. We display in Fig. 3 the measurement of the sensitivity function compared with the theoretical calculation. We also realized a precise measurement during each pulse and clearly obtained the predicted sinusoidal rise of the sensitivity function.

For a better agreement of the experimental data with the theoretical calculation, the data are normalized to take into

account the interferometer's contrast, which was measured to be 78%. This reduction in the contrast with respect to 100% is due to the combined effect of inhomogeneous Rabi frequencies between the atoms and unbalanced Rabi frequencies between the pulses. Indeed, the atomic cloud size of 8 mm is not negligible with respect to the size of the single pair of Raman Gaussian beams: $w_0 = 15$ mm. Atoms at both sides of the atomic cloud will not see the same intensity, inducing variable transfer efficiency of the Raman transitions. Moreover, the cloud moves by about 3 mm between the first and the last pulse. In order for the cloud to explore only the central part of the Gaussian beams, we choose a rather small interaction time of $T = 4.97$ ms with respect to the maximum interaction time possible of $T = 40$ ms. Still, the quantitative agreement is not perfect. One particularly observes a significant asymmetry of the sensitivity function, which remains to be explained. A full numerical simulation could help in understanding the effect of the experimental imperfections.

III. Transfer Function of the Interferometer

From the sensitivity function, we can now evaluate the fluctuations of the interferometric phase Φ for an arbitrary Raman phase noise $\phi(t)$ on the lasers as

$$\delta\Phi = \int_{-\infty}^{+\infty} g(t)d\phi(t) = \int_{-\infty}^{+\infty} g(t)\frac{d\phi(t)}{dt}dt. \tag{5}$$

The transfer function of the interferometer can be obtained by calculating the response of the interferometer phase Φ to a sinusoidal modulation of the Raman phase, given by $\phi(t) = A_0\cos(\omega_0 t + \psi)$. We find $\delta\Phi = A_0\omega_0 Im(G(\omega_0))\cos(\psi)$, where G is the Fourier transform of the sensitivity function. Thus, we have

$$G(\omega) = \int_{-\infty}^{+\infty} e^{-i\omega t}g(t)dt. \tag{6}$$

When averaging over a random distribution of the modulation phase ψ, the rms value of the interferometer phase is $\delta\Phi^{\mathrm{rms}} = |A_0\omega_0 G(\omega_0)|$. The transfer function is thus given by $H(\omega) = \omega G(\omega)$. If we now assume uncorrelated Raman phase noise between successive measurements, the rms standard deviation of the interferometric phase noise $\sigma_\Phi^{\mathrm{rms}}$ is given by

$$(\sigma_\Phi^{\mathrm{rms}})^2 = \int_0^{+\infty} |H(\omega)|^2 S_\phi(\omega)d\omega \tag{7}$$

where $S_\phi(\omega)$ is the power spectral density of the Raman phase.

We calculate the Fourier transform of the sensitivity function and find

$$G(\omega) = \frac{4i\Omega_R}{\omega^2 - \Omega_R^2}\sin\left(\frac{\omega(T+2\tau_R)}{2}\right) \times\left(\cos\left(\frac{\omega(T+2\tau_R)}{2}\right) + \frac{\Omega_R}{\omega}\sin\left(\frac{\omega T}{2}\right)\right). \tag{8}$$

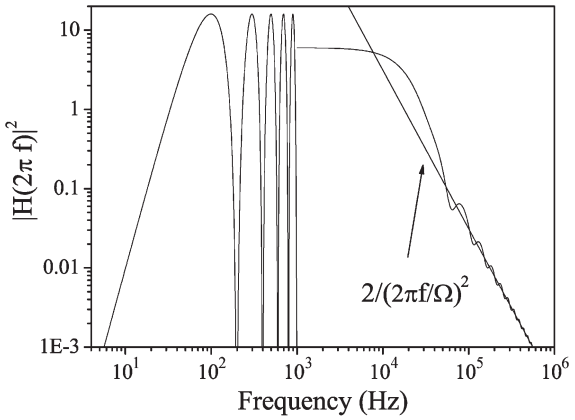

Fig. 4. Calculated weighting function for the Raman phase noise as a function of frequency. Below 1 kHz, the exact weighting function is displayed. It shows an oscillation with a period frequency of $\delta f = 1/(T + 2\tau)$. Above 1 kHz, only the mean value of the weighting function over δf is displayed. The weighting function acts as a first-order low-pass filter, with an effective cutoff frequency of $f_0 = (\sqrt{3}/3)(\Omega_R/2\pi)$.

At low frequency, where $\omega \ll \Omega_R$, the sensitivity function can be approximated by

$$G(\omega) = -\frac{4i}{\omega}\sin^2(\omega T/2). \tag{9}$$

The weighting function $|H(2\pi f)|^2$ versus the frequency f is displayed in Fig. 4. It has two important features. The first one is an oscillating behavior at a frequency given by $1/(T + 2\tau_R)$, leading to zeros at frequencies given by $f_k = k/(T + 2\tau_R)$. The second is a low-pass first-order filtering due to the finite duration of the Raman pulses, with an effective cutoff frequency f_0, given by $f_0 = (\sqrt{3}/3)(\Omega_R/2\pi)$. Above 1 kHz, only the mean value over one oscillation is displayed on the figure.

To measure the transfer function, a phase modulation $A_m\cos(2\pi f_m t + \psi)$ is applied on the Raman phase, triggered on the first Raman pulse. The interferometric phase variation is then recorded as a function of f_m. We then repeat the measurements for the phase modulation in quadrature $A_m\sin(2\pi f_m t + \psi)$. From the quadratic sum of these measurement, we extract $H(2\pi f_m)^2$. The weighting function was first measured at low frequency. The results, which are displayed in Fig. 5 together with the theoretical value, clearly demonstrate the oscillating behavior of the weighting function. Fig. 6 displays the measurements performed slightly above the cutoff frequency and shows two zeros. The first one corresponds to a frequency multiple of $1/(T + 2\tau)$. The second one is a zero of the last factor of (8). Its position depends critically on the value of the Rabi frequency.

When comparing the data with the calculation, the experimental imperfections already mentioned have to be accounted for. An effective Rabi frequency Ω_{eff} can be defined by the relation $\Omega_{\mathrm{eff}}\tau_0 = \pi$, where τ_0 is the duration of the single pulse, performed at the center of the Gaussian Raman beams, that optimizes the transition probability. For homogeneous Raman beams, this pulse would be a π pulse. This effective Rabi frequency is measured with an uncertainty of about 1%. It had to be corrected by only 1.5% in order for the theoretical and experimental positions of the second zero to match. The

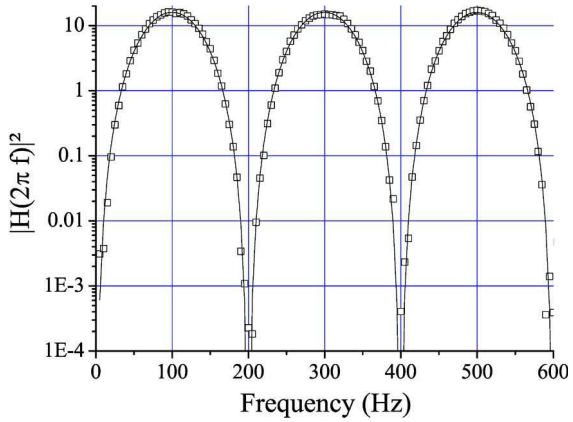

Fig. 5. Phase noise weighting function $|H(2\pi f)^2|$ for $T = 4.97$ ms and $\tau_R = 20$ μs at low frequency. The theoretical calculation is displayed in solid line and the experimental results in squares. We clearly see that the oscillating behavior of the weighting function and the experimental measurement are in good agreement with the theoretical calculation.

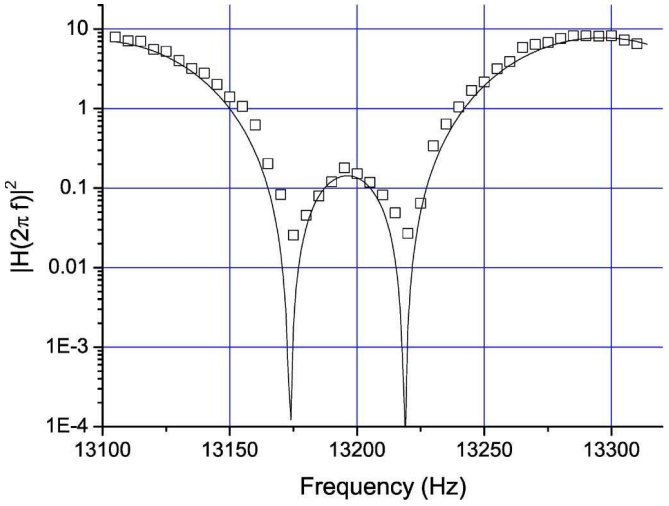

Fig. 6. Phase noise weighting function $|H(2\pi f)^2|$ for $T = 4.97$ ms and $\tau_R = 20$ μs displayed near the Rabi frequency. The theoretical calculation is displayed in solid line and the experimental results in squares. We identified the zero multiple of $(1/T + 2\tau)$ and experimentally observed both zeros with a good agreement with theory.

excellent agreement between the theoretical and experimental curves validates our model.

IV. Link Between the Sensitivity Function and the Sensitivity of the Interferometer

The sensitivity of the interferometer is characterized by the Allan variance of the interferometric phase fluctuations $\sigma_\Phi^2(\tau)$, which is defined as

$$\sigma_\Phi^2(\tau) = \frac{1}{2}\left\langle (\delta\bar{\Phi}_{k+1} - \delta\bar{\Phi}_k)^2 \right\rangle \tag{10}$$

$$= \frac{1}{2}\lim_{n\to\infty}\left\{ \frac{1}{n}\sum_{k=1}^{n} (\delta\bar{\Phi}_{k+1} - \delta\bar{\Phi}_k)^2 \right\} \tag{11}$$

where $\delta\bar{\Phi}_k$ is the average value of $\delta\Phi$ over the interval $[t_k, t_{k+1}]$ of duration τ. The Allan variance is equal, within a factor of two, to the variance of the differences in the successive average values $\delta\bar{\Phi}_k$ of the interferometric phase. Because the interferometer is sequentially operated at a rate $f_c = 1/T_c$, τ is a multiple of $T_c : \tau = mT_c$. Without losing generality, we can choose $t_k = -T_c/2 + kmT_c$. The average value $\delta\bar{\Phi}_k$ can now be expressed as

$$\begin{aligned}\delta\bar{\Phi}_k &= \frac{1}{m}\sum_{i=1}^{m}\delta\Phi_i \\ &= \frac{1}{m}\sum_{i=1}^{m}\int_{t_k+(i-1)T_c}^{t_k+iT_c} g\left(t - t_k - (i-1)T_c - T_c/2\right)\frac{d\phi}{dt}dt \\ &= \frac{1}{m}\int_{t_k}^{t_{k+1}} g_k(t)\frac{d\phi}{dt}dt \end{aligned} \tag{12}$$

where $g_k(t) = \sum_{i=1}^{m} g(t - kmT_c - (i-1)T_c)$. The difference between successive average values is then given by

$$\delta\bar{\Phi}_{k+1} - \delta\bar{\Phi}_k = \frac{1}{m}\int_{-\infty}^{+\infty}\left(g_{k+1}(t) - g_k(t)\right)\frac{d\phi}{dt}dt. \tag{13}$$

For long-enough averaging times, the fluctuations of the successive averages are not correlated, and the Allan variance is given by

$$\sigma_\Phi^2(\tau) = \frac{1}{2}\frac{1}{m^2}\int_0^{+\infty}|G_m(\omega)|^2\,\omega^2 S_\phi(\omega)d\omega \tag{14}$$

where G_m is the Fourier transform of the function $g_{k+1}(t) - g_k(t)$. After a little algebra, we find, for the squared modulus of G_m, the following expression:

$$|G_m(\omega)|^2 = 4\frac{\sin^4(\omega m T_c/2)}{\sin^2(\omega T_c/2)}|G(\omega)|^2. \tag{15}$$

When $\tau\to\infty$, $|G_m(\omega)|^2 \sim (2m/T_c)\sum_{j=-\infty}^{\infty}\delta(\omega - j2\pi f_c)$ $|G(\omega)|^2$. Thus, for large averaging times τ, the Allan variance of the interferometric phase is given by

$$\sigma_\Phi^2(\tau) = \frac{1}{\tau}\sum_{n=1}^{\infty}|H(2\pi n f_c)|^2\,S_\phi(2\pi n f_c). \tag{16}$$

Equation (16) shows that the sensitivity of the interferometer is limited by an aliasing phenomenon similar to the Dick effect in atomic clocks [14]. Only the phase noise at multiple of the cycling frequency appears in the Allan variance, and it is weighted by the Fourier components of the transfer function.

Various sources of phase noise will contribute to (16). Phase noise of the reference oscillator, electronic noise of the PLL, laser phase noise outside the PLL bandwidth, and difference of phase accumulated in the propagation of the two Raman beams to the vacuum chamber will contribute in the same way, whatever the configuration of the Raman beams (copropagating or counterpropagating) is.

In the case of inertial forces, the sensitivity arises from the Raman phase fluctuations of counterpropagating beams in

the referential frame of the atoms and can be treated with the same formalism. As the two laser beams are first overlapped before being sent onto the atoms, their phase difference is mostly affected by the movements of a single optical element, i.e., the mirror that finally retroreflects them. A displacement of the retroreflecting mirror by δz induces a Raman phase shift of $k_{\text{eff}}\delta z$.

V. Laser Phase Noise

In this section, we focus on the influence of the phase noise of the reference oscillator and on the limitations imposed by the PLL.

Let us examine first the case of white Raman phase noise $S_\phi(\omega) = S_\phi^0$. The interferometer sensitivity is given by

$$\sigma_\Phi^2(\tau) = \left(\frac{\pi}{2}\right)^2 \frac{S_\phi^0}{\tau}\frac{T_c}{\tau_R}. \tag{17}$$

In that case, the sensitivity of the interferometer depends not only on the Raman phase noise spectral density but also on the pulse duration τ_R. For a better sensitivity, one should use the largest pulse duration as possible. However, as the Raman transitions are velocity selective in the counterpropagating configuration, a very long pulse will reduce the number of useful atoms. This increases the detection noise contribution, so that there is an optimum value of τ_R that depends on the experimental parameters. In the case of the gyroscope, the optimum was found to be $\tau_R = 20\ \mu$s.

To reach a good sensitivity, the Raman phase needs to be locked to the phase of a very stable microwave oscillator (whose frequency is 6.834 GHz for ^{87}Rb and 9.192 GHz for ^{133}Cs). This oscillator can be generated by a frequency chain, where low phase noise quartz performances are transposed in the microwave domain. At low frequencies ($f < 10-100$ Hz), the phase noise spectral density of such an oscillator is usually well approximated by a $1/f^3$ power law (flicker noise), whereas at high frequency ($f > 1$ kHz), it is independent of the frequency (white noise). Using (16) and the typical parameters of our experiments ($\tau_R = 20\ \mu$s and $T = 50$ ms), we can calculate the phase noise spectral density required to achieve an interferometric phase fluctuation of 1 mrad/shot. This is equivalent to the quantum projection noise limit for 10^6 detected atoms. The flicker noise of the microwave oscillator should be lower than -53 dB $\cdot$ rad$^2 \cdot$ Hz^{-1} at 1 Hz from the carrier frequency and its white noise below -111 dB $\cdot$ rad$^2 \cdot$ Hz^{-1}. Unfortunately, there exists no quartz oscillator combining these two levels of performance. Thus, we plan to lock a SC Premium 100 MHz oscillator (from Wenzel Company) onto a low flicker noise 5 MHz Blue Top oscillator (Wenzel). From the specifications of this quartz, we calculate a contribution of 1.2 mrad to the interferometric phase noise.

Phase fluctuations also arise from residual noise in the servo-lock loop. We have experimentally measured the residual phase noise power spectral density of a phase-locked system analogous to the one described in Fig. 2. This system has been developed to phase lock the Raman lasers of the gravimeter experiment. The measurement was performed by mixing IF and LO onto an independent RF mixer, whose output phase fluctuations were analyzed onto a fast Fourier transform analyzer. The result of the measurement is displayed in Fig. 7. At low frequencies, below 100 Hz, the phase noise of our phase-locked system lies well below the required flicker noise. After a few kilohertz, it reaches a plateau of -119 dB $\cdot$ rad$^2 \cdot$ Hz^{-1}. The amplitude of this residual noise is not limited by the gain of the servo loop. Above 60 kHz, it increases up to -90 dB $\cdot$ rad$^2 \cdot$ Hz^{-1} at 3.5 MHz, which is the bandwidth of our servo-lock loop. Using (16), we evaluated to 0.72 mrad its contribution to the interferometer's phase noise.

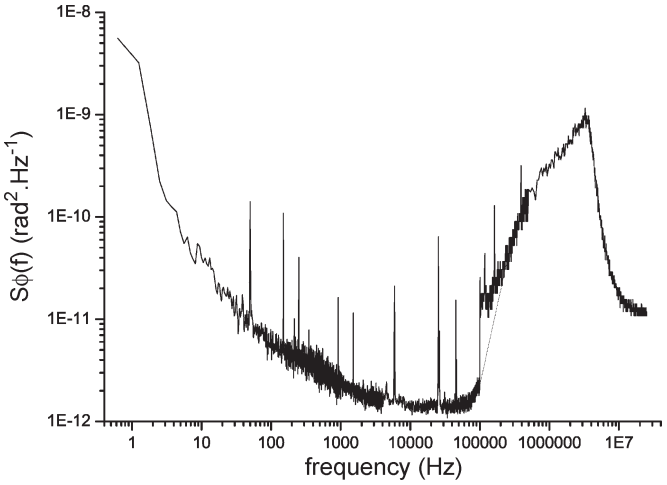

Fig. 7. Phase noise power spectral density between the two phase-locked diode lasers. Up to 100 kHz, we display the residual noise of the PLL, which is obtained by measuring the phase noise of the demodulated beatnote on a fast Fourier transform analyzer. There, the phase noise of the reference oscillator is rejected. Above 100 kHz, we display the phase noise measured directly on the beatnote observed onto a spectrum analyzer. In this case, the reference oscillator phase noise limits the Raman phase noise to 1.5×10^{-11} rad$^2 \cdot$ Hz^{-1}. An extrapolation of the phase noise due to the PLL alone between 100 and 300 kHz is displayed with dotted line.

Other sources of noise are expected to contribute, which are not investigated in this paper. The measurement presented here has been performed with a single optical beat setup, which rejects noise of the photoconductor as well as other noise sources inherent to the setup (vibrations of the mirrors and beamsplitters in the beat setup for instance). Independent measurements we have performed with two independent photoconductors show that these noise sources are anyway negligible—their contribution was found to be on the order of 0.1 mrad/shot. In addition, the phase noise due to the propagation of the Raman beams in free space and in optical fibers has already been studied in [18].

VI. Case of Parasitic Vibrations

As already stated before, the same formalism can be used to evaluate the degradation of the sensitivity to inertial forces caused by parasitic vibrations due to the movement of the retroreflecting mirror.

The sensitivity of the interferometer is then given by

$$\sigma_\Phi^2(\tau) = \frac{k_{\text{eff}}^2}{\tau}\sum_{n=1}^{\infty} |H(2\pi n f_c)|^2\, S_z(2\pi n f_c) \tag{18}$$

where $S_z(\omega)$ is the power spectral density of position noise. Introducing the power spectral density of acceleration noise $S_a(\omega)$, the previous equation can be written as

$$\sigma_\Phi^2(\tau) = \frac{k_{\text{eff}}^2}{\tau} \sum_{n=1}^{\infty} \frac{|H(2\pi n f_c)|^2}{(2\pi n f_c)^4} S_a(2\pi n f_c). \tag{19}$$

It is important to note here that the acceleration noise is severely filtered by the transfer function for acceleration which decreases as $1/f^4$.

In the case of white acceleration noise S_a, and to first order in τ_R/T, the limit on the sensitivity of the interferometer is given by

$$\sigma_\Phi^2(\tau) = \frac{k_{\text{eff}}^2 T^4}{2} \left(\frac{2T_c}{3T} - 1 \right) \frac{S_a}{\tau}. \tag{20}$$

To put this into numbers, we now calculate the requirements on the acceleration noise of the retroreflecting mirror to reach a sensitivity of 1 mrad/shot. For the typical parameters of our gravimeter, the amplitude noise should lie below 10^{-8} m $\cdot$ s^{-2} $\cdot$ Hz$^{-1/2}$. The typical amplitude of the vibration noise measured on the lab floor is 2×10^{-7} m $\cdot$ s^{-2} $\cdot$ Hz$^{-1/2}$ at 1 Hz and rises up to about 5×10^{-5} m $\cdot$ s^{-2} $\cdot$ Hz$^{-1/2}$ at 10 Hz. This vibration noise can be lowered to a few 10^{-7} m $\cdot$ s^{-2} $\cdot$ Hz$^{-1/2}$ in the 1- to 100-Hz frequency band with a passive isolation platform. To fill the gap and cancel the effect of vibrations, one could use the method proposed in [18], which consists of measuring the vibrations of the mirror with a very low noise seismometer and compensating the fluctuations of the position of the mirror by reacting on the Raman laser phase difference.

VII. Conclusion

We have here calculated and experimentally measured the sensitivity function of a three-pulse atomic interferometer. This enables us to determine the influence of the Raman phase noise, as well as of parasitic vibrations, on the noise on the interferometer phase. Reaching a 1 mrad/shot to shot fluctuation requires a very low phase noise frequency reference and an optimized PLL of the Raman lasers, together with a very low level of parasitic vibrations. With our typical experimental parameters, this would result in a sensitivity of 4×10^{-8} rad $\cdot$ s^{-1} $\cdot$ Hz$^{-1/2}$ for the gyroscope and of 1.5×10^{-8} m $\cdot$ s^{-2} $\cdot$ Hz$^{-1/2}$ for the gravimeter. One can then expect that, compared to previous experiments [4], the vibration noise will be, by far, the dominant limitation on the sensitivity of the gravimeter, as reaching the equivalent level of vibration is very difficult.

Improvements on the contribution of some of the noise sources are still possible. The frequency reference could be obtained from an ultrastable microwave oscillator, such as a cryogenic sapphire oscillator [19], whose phase noise lies well below the best quartz available. In addition, the requirements on the phase noise would be easier to achieve using atoms with a lower hyperfine transition frequency, such as Na or K. Trapping a very large initial number of atoms in the 3-D-MOT would enable a very drastic velocity selection. The duration of the Raman pulses could then be significantly increased, which makes the interferometer less sensitive to high-frequency Raman phase noise. The manipulation of the atoms can also be implemented using Bragg pulses [20], [21]. Because difference in the frequencies of the two beams is much smaller, the requirement on the stability of the relative phase is far less stringent. In that case, a different detection method needs to be implemented as atoms in both exit ports of the interferometer are in the same internal state. Using ultracold atoms with subrecoil temperature, atomic wave packets at the two exit ports can be spatially separated, which allows for a simple detection based on absorption imaging. Such an interferometer would benefit from the long interaction times available in space to reach a very high sensitivity.

We also want to emphasize that the sensitivity function can also be used to calculate the phase shifts arising from all possible systematic effects such as the light shifts, magnetic field gradients, and cold atom collisions.

Acknowledgment

The authors would like to thank A. Clairon for fruitful discussions and careful reading of the manuscript.

References

[1] A. Clairon, P. Laurent, G. Santarelli, S. Ghezali, S. N. Lea, and M. Bahoura, "A cesium fountain frequency standard: Preliminary result," *IEEE Trans Instrum. Meas.*, vol. 44, no. 2, pp. 128–131, Apr. 1995.

[2] F. Riehle, T. Kister, A. Witte, J. Helmcke, and C. J. Bordé, "Optical Ramsey spectroscopy in a rotating frame: Sagnac effect in a matter-wave interferometer," *Phys. Rev. Lett.*, vol. 67, no. 2, pp. 177–180, Jul. 1991.

[3] T. L. Gustavson, A. Landragin, and M. Kasevich, "Rotation sensing with a dual atom-interferometer Sagnac gyroscope," *Class. Quantum. Grav.*, vol. 17, no. 12, pp. 2385–2398, 2000.

[4] A. Peters, K. Y. Chung, and S. Chu, "High-precision gravity measurements using atom interferometry," *Metrologia*, vol. 38, no. 1, pp. 25–61, Feb. 2001.

[5] P. R. Berman, Ed., *Atom Interferometry*. Chestnut Hill, MA: Academic, 1997.

[6] T. M. Niebauer, G. S. Sasagawa, J. E. Faller, R. Hilt, and F. Klopping, "A new generation of absolute gravimeters," *Metrologia*, vol. 32, no. 3, pp. 159–180, 1995.

[7] G. E. Stedman, "Ring-laser tests of fundamental physics and geophyscics," *Rep. Prog. Phys.*, vol. 60, pp. 615–688, 1997.

[8] F. Leduc, D. Holleville, J. Fils, A. Clairon, N. Dimarcq, and A. Landragin, "Cold atom gyroscope for precision measurement," in *Proc. ICOLS*, 2003, pp. 68–70.

[9] P. Cheinet, F. Pereira Dos Santos, A. Clairon, N. Dimarcq, D. Holleville, and A. Landragin, "Gravimètre à atomes froids," *J. Phys. 4*, vol. 119, p. 153, 2004.

[10] G. Genevès, P. Gournay, A. Gosset, M. Lecollinet, F. Villar, P. Pinot, P. Juncar, A. Clairon, A. Landragin, D. Holleville, F. Pereira Dos Santos, J. David, M. Besbes, F. Alves, L. Chassagne, and S. Topçu, "The BNM Watt balance project," *IEEE Trans. Instrum. Meas.*, vol. 54, no. 2, pp. 850–853, Apr. 2005.

[11] M. Kasevich and S. Chu, "Atomic interferometry using stimulated Raman transitions," *Phys. Rev. Lett.*, vol. 67, no. 2, pp. 181–184, Jul. 1991.

[12] C. J. Bordé, "Atom interferometry and laser spectroscopy," in *Laser Spectroscopy X*, M. Ducloy, E. Giacobino, and G. Camy, Eds. Singapore: World Scientific, 1991, p. 239.

[13] C. Antoine and C. J. Bordé, "Quantum theory of atomic clocks and gravito-inertial sensors: An update," *J. Opt. B, Quantum Semiclass. Opt.*, vol. 5, no. 2, pp. 199–207, Apr. 2003.

[14] G. J. Dick, "Local oscillator induced instabilities," in *Proc. 19th Annu. Precise Time Time Interval*, 1987, pp. 133–147.

[15] M. Kasevich and S. Chu, "Measurement of the gravitational acceleration of an atom with a light-pulse atom interferometer," *Appl. Phys. B, Laser Opt.*, vol. 54, no. 5, pp. 321–332, May 1992.

[16] K. A. Moler, D. S. Weiss, M. Kasevich, and S. Chu, "Theoretical analysis of velocity-selective Raman transitions," *Phys. Rev. A, Gen. Phys.*, vol. 45, no. 1, pp. 342–348, Jan. 1992.
[17] G. Santarelli, A. Clairon, S. N. Lea, and G. M. Tino, "Heterodyne optical phase locking of extended-cavity semiconductor lasers at 9 GHz," *Opt. Commun.*, vol. 104, no. 4–6, pp. 339–344, Jan. 1994.
[18] F. Yver-Leduc, P. Cheinet, J. Fils, A. Clairon, N. Dimarcq, D. Holleville, P. Bouyer, and A. Landragin, "Reaching the quantum noise limit in a high-sensitivity cold-atom inertial sensor," *J. Opt. B, Quantum Semiclass. Opt.*, vol. 5, no. 2, pp. S136–S142, Apr. 2003.
[19] A. Mann, C. Sheng, and A. Luiten, "Cryogenic sapphire oscillator with exceptionally high frequency stability," *IEEE Trans. Instrum. Meas.*, vol. 50, no. 2, pp. 519–521, Apr. 2001.
[20] E. M. Rasel, M. K. Oberthaler, H. Batelaan, J. Schmiedmayer, and A. Zeilinger, "Atom wave interferometry with diffraction gratings of light," *Phys. Rev. Lett.*, vol. 75, no. 14, pp. 2633–2637, Oct. 1995.
[21] D. M. Giltner, R. W. McGowan, and S. A. Lee, "Atom interferometer based on Bragg scattering from standing light waves," *Phys. Rev. Lett.*, vol. 75, no. 14, pp. 2638–2641, Oct. 1995.

Patrick Cheinet received the Ph.D. degree in physics from the Université Paris VI, Paris, France, in 2006.

He is currently a Postdoctoral Fellow with the University of Mainz, Mainz, Germany. His research interests include Bose Einstein condensates, ultracold gases in optical lattices, and strongly correlated many body physics.

Benjamin Canuel received the degree in physics and the Ph.D. degree in physics from the Université Paris XI, Orsay, France, in 2003 and 2007.

He is currently an Applied Physicist with the European Gravitational Observatory, Pisa, Italy. His research interests include optical systems for gravitational wave detection, high-power stabilized lasers, and nonlinear optics.

Franck Pereira Dos Santos was born in Fontainebleau, France, on April 30, 1973. He received the degree from Ecole Normale Supérieure, Paris, France, and the Ph.D. degree in physics from the Université Pierre et Marie Curie, Paris VI, in 2002.

Since 2002, he has been with the Laboratoire National de Métrologie et d'Essais-Systèmes de Référence Temps Espace (LNE-SYRTE), Observatoire de Paris, Paris, France, where he currently works on the development of cold atomic sensors. Since October 2004, he has been a permanent Researcher with CNRS. His research interests include laser cooling and Bose Einstein condensation.

Alexandre Gauguet received the degree from the University of Orsay, Orsay, France, in 2004. He is currently working toward the Ph.D. degree with the Laboratoire National de Métrologie et d'Essais-Systèmes de Référence Temps Espace, (LNE-SYRTE), Observatoire de Paris, Paris, France.

Florence Yver-Leduc graduated from the Institut d'Optique, Orsay, France, in 2001 and received the Ph.D. degree in physics from the Université Paris XI, Orsay, in 2004.

He is currently with the Laboratoire National de Métrologie et d'Essais-Systèmes de Référence Temps Espace, (LNE-SYRTE), Observatoire de Paris, Paris, France.

Arnaud Landragin received the Ph.D. degree in physics from the Université Paris XI, Orsay, France, in 1997.

He is currently a permanent Researcher with the Laboratoire National de Métrologie et d'Essais-Systèmes de Référence Temps Espace, (LNE-SYRTE), Observatoire de Paris, Paris, France. His research interests include the realization and characterization of atom interferometers for application as inertial sensors.

Eur. Phys. J. D **44**, 419–425 (2007)
DOI: 10.1140/epjd/e2007-00218-2

THE EUROPEAN PHYSICAL JOURNAL D

Influence of lasers propagation delay on the sensitivity of atom interferometers

J. Le Gouët[a], P. Cheinet, J. Kim[b], D. Holleville, A. Clairon, A. Landragin, and F. Pereira Dos Santos

LNE-SYRTE, Observatoire de Paris, LNE, CNRS, UPMC, 61 avenue de l'Observatoire, 75014 Paris, France

Received 20 December 2006 / Received in final form 23 March 2007
Published online 29 June 2007 –

Abstract. In atom interferometers based on two photon transitions, the delay induced by the difference of the laser beams paths makes the interferometer sensitive to the fluctuations of the frequency of the lasers. We first study, in the general case, how the laser frequency noise affects the performance of the interferometer measurement. Our calculations are compared with the measurements performed on our cold atom gravimeter based on stimulated Raman transitions. We finally extend this study to the case of cold atom gradiometers.

PACS. 39.20.+q Atom interferometry techniques – 32.80.Pj Optical cooling of atoms; trapping – 06.20.-f Metrology

1 Introduction

Atom interferometry allows to realize measurements in the fields of frequency metrology [1], inertial sensors [2,3], tests of fundamental physics [4–6], by splitting an atomic wave function into separated wave packets. The difference in the quantum phases accumulated by the wave packets can be extracted from the interference pattern obtained when recombining them. Among the various types of coherent beam splitters developed for matter wave manipulation [7–11], two photon transitions have proven to be powerful tools for precise measurements. For instance, atom interferometers based on Bragg transitions [8] can be used for polarisability [12] and fundamental measurements [13]. On the other hand, stimulated Raman transitions [14] allowed the development of high precision inertial sensors [15–18], whose performances compete with state of the art instruments [19,20].

In the case of interferometers based on two photon transitions, atomic wave packets are split and recombined with light pulses of a pair of counter-propagating laser beams, which couple long lived atomic states. The sensitivity of such interferometers arises from the large momentum transfer of counter-propagating photons. A propagation delay is unavoidable between the two counter-propagating beams at the position of the atoms. As already stated in [17], this delay makes the interferometer measurement sensitive to the lasers frequency noise. This last paper considered the influence of a laser frequency jitter, and showed that the sensitivity degradation scales linearly with the propagation delay. In this paper, we investigate this effect for a very general laser frequency noise, and quantify its influence on the sensitivity of an interferometer. The study is realized in the case of our gravimeter, based on stimulated Raman transitions. However, the formalism presented here can be applied to any type of interferometer where two photon transitions are used as beam splitters.

The sensitivity to inertial forces of such an interferometer arises from the imprinting of the phase difference between the lasers onto the atomic wave function [21]. As temporal fluctuations in the laser phase difference affect the measurement of the atomic phase, a high degree of phase coherence is required. This coherence can be obtained either by using two sidebands of a single phase modulated laser [2], or by locking the phase difference between two independent lasers [22,23]. In both cases, the phase relation is well determined only at a specific position, where the laser is modulated or where the frequency difference is measured. Between this very position and the atoms, the phase difference will be affected by fluctuations of the respective paths of the two beams over the propagation distance. In most of the high sensitivity atom interferometers, the influence of path length variations is minimized by overlapping the two beams, and making them propagate as long as possible over the same path. The vibrations of any optical element shift the phase of each laser, but do not strongly disturb their phase difference as long as the lasers co-propagate, because their optical frequencies are very close. However, for the interferometer to be sensitive to inertial forces, the two beams (with wave vectors $\boldsymbol{k}_1$ and $\boldsymbol{k}_2$) have to be counter-propagating.

[a] e-mail: julien.legouet@obspm.fr
[b] *Present address*: Department of Physics, Myongji University, Yongin 449-728, Korea.

The two overlapped beams are thus directed to the atoms and retro-reflected. Among the four beams actually sent onto the atoms, two will realize the interferometer pulses. As a consequence, the reflected beam is delayed with respect to the other one. Then, the phase difference at the atoms position is affected by the phase noise of the lasers, accumulated during this reflection delay [17].

In this article, we pay more attention to this effect and investigate both theoretically and experimentally the influence of the delay on the sensitivity of an atom interferometer. In the following section, we briefly describe our experimental setup. The transfer function of the interferometer phase noise with respect to the Raman laser frequency noise is derived in Section 3, and compared with experimental measurements. In Section 4, we demonstrate the sensitivity limitations induced by the retro-reflection delay of the lasers in the case of our atomic gravimeter. We then discuss how such limitations could be overcome. The discussion is finally extended to the case of high precision gradiometers, whose performances might be limited by their intrinsic propagation delays.

2 Experimental setup

Our interferometer is a cold atom gravimeter based on stimulated Raman transitions, which address the two hyperfine sublevels $F = 1$ and $F = 2$ of the $^5S_{1/2}$ ground state of the ^{87}Rb atom. We use successively a 2D-MOT, a 3D-MOT and an optical molasses to prepare about 10^7 atoms at a temperature of 2.5 μK, within a loading time of 50 ms. The intensity of the lasers is then adiabatically decreased to drop the atoms, and we detune both the repumper and cooling lasers from the atomic transitions by about 1 GHz to obtain the two off-resonant Raman lasers. A description of the compact and agile laser system that we developed can be found in [24]. The preparation sequence ends with the selection of a narrow velocity distribution ($\sigma_v \leq v_r = 5.9$ mm/s) in the $|F = 1, m_F = 0\rangle$ state, using a combination of microwave and optical pulses.

A sequence of three pulses ($\pi/2 - \pi - \pi/2$) then splits, redirects and recombines the atomic wave packets. At the output of the interferometer, the transition probability from an hyperfine state to the other is given by the usual formula of two waves interferometers: $P = \frac{1}{2}(1 + C\cos\Delta\Phi)$, where C is the contrast of the fringes, and $\Delta\Phi$ the difference of the atomic phases accumulated along the two paths. We measure by fluorescence the populations of each of the two states and deduce the transition probability. The difference in the phases accumulated along the two paths depends on the acceleration $\boldsymbol{a}$ experienced by the atoms. It can be written as $\Delta\Phi = \phi(0) - 2\phi(T) + \phi(2T) = -\boldsymbol{k}_{\mathit{eff}} \cdot \boldsymbol{a}T^2$, where $\phi(0, T, 2T)$ is the phase difference of the lasers at the location of the center of the atomic wavepackets for each of the three pulses [25], $\boldsymbol{k}_{\mathit{eff}} = \boldsymbol{k}_1 - \boldsymbol{k}_2$ is the effective wave vector (with $|\boldsymbol{k}_{\mathit{eff}}| = k_1 + k_2$), and T is the time interval between two consecutive pulses [2].

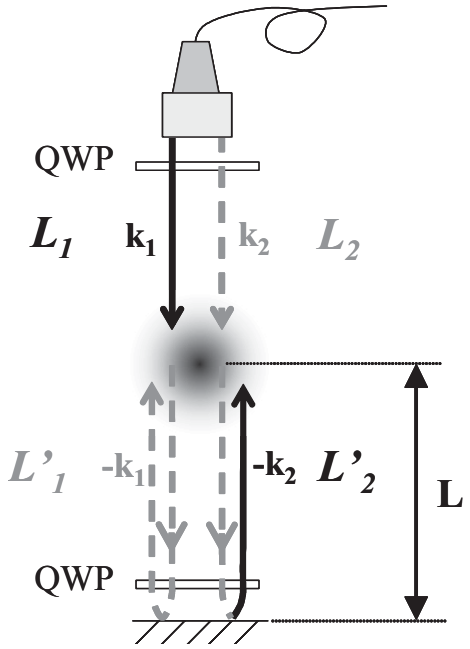

Fig. 1. Experimental scheme of the cold atom gravimeter. The two Raman lasers L_1 and L_2 are guided from the optical bench to the atoms by the same optical fiber, and the resonant counter-propagating beams are obtained by retro-reflecting the lasers with the mirror at the bottom of the vacuum chamber. Due to the Doppler shift of the falling atoms, only L_1 and L_2' can drive the Raman transitions. QWP: quarter wave plate.

The Raman light sources are two extended cavity diode lasers, amplified by two independent tapered amplifiers. Their frequency difference is phase locked onto a microwave reference source generated by multiplications of highly stable quartz oscillators. The two Raman laser beams are overlapped with a polarization beam splitter cube, resulting in two orthogonally polarized beams. First, a small part of the overlapped beams is sent onto a fast photodetector to measure an optical beat. This beat-note is mixed down with a reference microwave oscillator, and compared to a stable reference RF frequency in a Digital Phase Frequency Detector. The phase error signal is then used to lock the laser phase difference at the very position where the beat is recorded. The phase locked loop reacts onto the supply current of one of the two lasers (the "slave" laser), as well as on the piezo-electric transducer that controls the length of its extended cavity. The impact of the phase noise of the reference microwave oscillator on the interferometer sensitivity, as well as the performances of the PLL, has already been studied in [26]. Finally, the two overlapped beams are injected in a polarization maintaining fiber, and guided towards the vacuum chamber. We obtain the counter-propagating beams by laying a mirror and a quarterwave plate at the bottom of the experiment. As displayed in Figure 1, four beams (L_1, L_2, L_1', L_2') are actually sent onto the atoms. Because of the selection rules and the Doppler shift induced by the free fall of the atoms, only the counter-propagating pair

L_1/L_2' drives the Raman transitions. In the following, we define L_1 as the "master" laser, and L_2 as the "slave" one.

3 Influence of the propagation delay on the interferometer phase noise

3.1 Theoretical expression of the transfer function

The phase difference φ imprinted onto the atoms by the counter-propagating beams is given by $\varphi(t) = \varphi_1(t) - \varphi_{2'}(t)$, where φ_1 and $\varphi_{2'}$ are respectively the phases of the downward-propagating master laser and of the retro-reflected slave laser. Because of the retro-reflection, the phase of L_2' writes as $\varphi_{2'}(t) = \varphi_2(t - t_d)$. The retro-reflection delay t_d is given by $t_d = 2L/c$, where L is the distance between the atoms and the bottom mirror. We consider here a perfect phase locked loop, which guarantees the stability of the phase difference for copropagating lasers. Then $\varphi_2(t-t_d) = \varphi_1(t-t_d)+\omega_0(t-t_d)$, where ω_0 is the frequency difference between the two lasers. Since we assume ω_0 is perfectly stable, its contribution will vanish in the interferometer phase $\Delta\Phi$. Thus, we do not take it into account when writing the laser phase difference, and finally obtain $\varphi(t) = \varphi_1(t) - \varphi_1(t - t_d)$.

As shown in [26], the interferometer phase shift Φ induced by fluctuations of φ can be written as:

$$\Phi = \int_{-\infty}^{+\infty} g(t)\frac{d\varphi(t)}{dt}dt \tag{1}$$

where $g(t)$ is the sensitivity function of the interferometer. This function quantifies the influence of a relative laser phase shift $\delta\phi$ occurring at time t onto the transition probability $\delta P(\delta\phi, t)$. It is defined in [27] as:

$$g(t) = 2 \lim_{\delta\phi\to 0} \frac{\delta P(\delta\phi, t)}{\delta\phi}. \tag{2}$$

We consider an interferometer with three pulses $\pi/2-\pi-\pi/2$ of durations respectively $\tau_R - 2\tau_R - \tau_R$. If the time origin is chosen at the center of the π pulse, $t \mapsto g(t)$ is an odd function. Its following expression for positive time is derived in [26]:

$$g(t) = \begin{cases} \sin \Omega_R t & \text{for } 0 < t < \tau_R \\ 1 & \text{for } \tau_R < t < T + \tau_R \\ -\sin \Omega_R(T - t) & \text{for } T + \tau_R < t < T + 2\tau_R \end{cases} \tag{3}$$

where Ω_R is the Rabi pulsation.

In the presence of fluctuations of the master Raman laser frequency, the interferometer phase shift becomes:

$$\begin{aligned}\Phi &= \int_{-\infty}^{+\infty} dt\; g(t)\frac{d\varphi(t)}{dt} \\ &= \int_{-\infty}^{+\infty} dt\; g(t)\left[\frac{d\varphi_1(t)}{dt} - \frac{d\varphi_1(t-t_d)}{dt}\right].\end{aligned} \tag{4}$$

If no assumption is made on the distance L between the mirror and the atoms, the retro-reflection delay t_d is not the same for the three pulses. However, the maximum duration of our interferometer is 100 ms, corresponding to a 5 cm atomic path, much smaller than the distance $L \approx 50$ cm. We can thus consider t_d constant during the measurement, and write the interferometer phase shift as:

$$\begin{aligned}\Phi &= \int_{-\infty}^{+\infty} dt\; [g(t) - g(t + t_d)]\,\frac{d\varphi_1(t)}{dt} \\ &= 2\pi \int_{-\infty}^{+\infty} dt\; [g(t) - g(t + t_d)]\,\nu_1(t)dt.\end{aligned} \tag{5}$$

We deduce from (5) that the transfer function Z, which converts Raman laser frequency noise into interferometer phase noise, is given by the Fourier transform of the difference $g(t) - g(t + t_d)$. After some algebra, we find:

$$Z(f, t_d) = -ie^{-i\omega t_d/2} t_d H(2\pi f)\frac{\sin(\pi f t_d)}{\pi f t_d} \tag{6}$$

where $H(\omega) = \omega \int g(t)e^{i\omega t}dt$ is the weighting function describing the response of the interferometer phase to the fluctuations of the laser phase difference, as already described in [26]. A remarkable feature of the function $H(\omega)$ is a low pass first order filtering, arising from the fact that the response time of the atoms to a perturbation is necessarily limited by the Rabi frequency. The cutoff frequency is given by $f_c = \sqrt{3}\Omega_R/6\pi = \sqrt{3}/12\tau_R$.

In our experimental setup, the delay time is about $t_d = 3$ ns. Since the cut-off frequency f_c is roughly 20 kHz, we can assume that $f_c t_d \ll 1$. The amplitude of the transfer function is finally:

$$|Z(f, t_d)| \approx t_d\; |H(2\pi f)|\,. \tag{7}$$

3.2 Measurement of the transfer function

In order to measure the amplitude of $Z(f)$, we modulate the master laser frequency at a frequency f. The applied frequency modulation is detected in the beat-note between the master laser and a reference laser, locked on a atomic line of the ^{87}Rb by a saturated spectroscopy setup. The frequency of the beat-note is converted into a voltage modulation by a frequency to voltage converter (FVC). When the modulation is not synchronous with the cycle rate, the response of the interferometer appears as a periodic modulation of its phase. Its amplitude is the modulus of the transfer function, and the apparent period of the response depends on the ratio f/f_s, where f_s is the sampling rate of the experiment. For these measurements, the cycle rate was $f_s = 4$ Hz.

We choose the modulation frequency as $f = (n + 1/10)f_s$ and record the transition probability from which we extract the transfer function amplitude $|Z(f, t_d)|$. We run the experiment with a modest interrogation time of $2T = 2$ ms, which allows us to reach a good signal to noise ratio (SNR) of 250 per shot for the detection of the perturbation. As the interferometer phase shift scales as the square of T, best sensitivities to inertial forces are usually

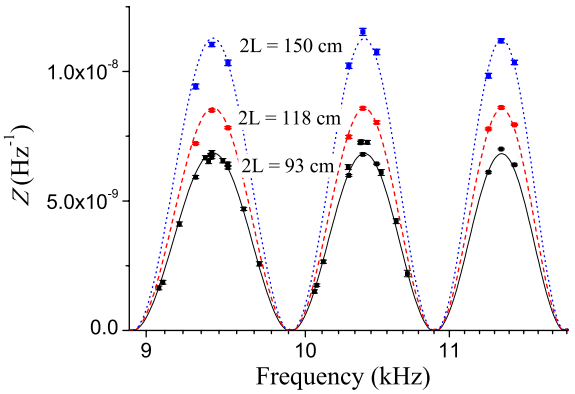

Fig. 2. Transfer function Z of the frequency noise of the laser for three optical lengths. The experimental points and the theoretical curves (see Eq. (7)) are in good agreement.

obtained for large values of T. However, in that case, the interferometer also becomes more sensitive to vibrations, which limit the SNR to about 50 in our experiment when $2T = 100$ ms.

Figure 2 displays the measured and calculated transfer function Z as a function of the modulation frequency f, for three values of the retro-reflection length: $2L = 93$, 118 and 150 cm. The weighting function zeros occur when the period of the perturbation is a multiple of $T+2\tau_R$. In that case, the phase of the perturbation is the same for each of the three pulses, and the corresponding interferometer phase shift $\Delta\Phi = \varphi_1 - 2\varphi_2 + \varphi_3$ vanishes. One can see in Figure 2 that the experimental points agree with the calculation (Eq. (7)), demonstrating that the amplitude of Z increases linearly with the time delay t_d.

We also test further the relation between our measurement of the transfer function and the weighting function $H(\omega)$ [26]. We measure the transfer function for a fixed value of t_d, for frequencies respectively lower and higher than the low pass cut-off frequency f_c. In our case, a $\pi/2$ pulse is 6 μs long, so f_c is about 24 kHz. The measurements are presented in Figure 3. For $f \gg f_c$, there is a slight shift between the measurement and the theoretical expression of Z. We tested out various possible origins like the duration and timings of the pulses, the synchronization of the frequency synthesizer we used to modulate the laser frequency and the clock frequency of the experiment, but this shift is still not understood. However it does not affect the value of the variance integrated over the whole spectrum (see Eq. (10)).

4 Limits on the interferometer sensitivity

4.1 Theoretical analysis

We finally quantify the degradation of the interferometer sensitivity as a function of laser frequency noise level and of the optical delay. Using equation (5), the variance of the phase fluctuation is given by:

$$\sigma_\Phi^2 = 4\pi^2 \int_0^{+\infty} |Z(\omega)|^2 \, S_{\nu_1}(\omega) \frac{d\omega}{2\pi} \qquad (8)$$

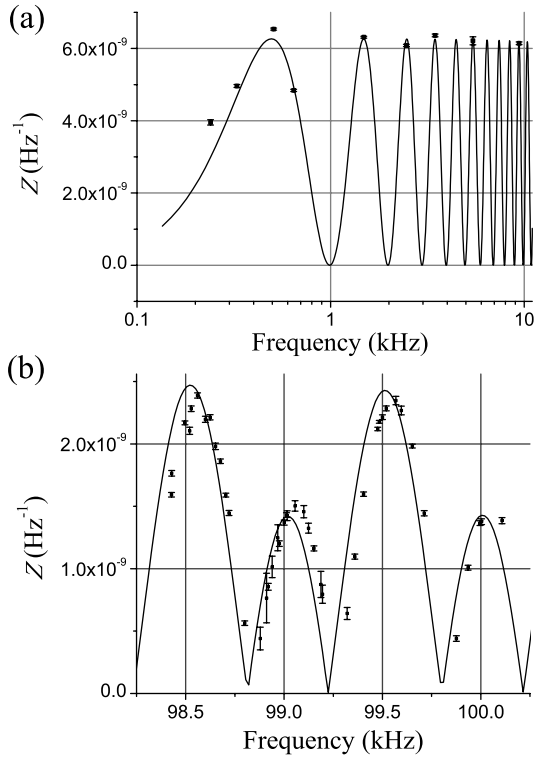

Fig. 3. Calculation and measurement of the transfer function for low (a) and high (b) frequencies (with respect to $f_c \approx 24$ kHz) of master frequency modulation. For these measurements, the back and forth distance between the atoms and the mirror is $2L = 93$ cm.

where S_{ν_1} is the power spectral density (PSD) of the master laser frequency noise. Then, using equation (6), one writes the variance as:

$$\sigma_\Phi^2 = 4\pi^2 \int_0^{+\infty} 4\sin^2\left(\frac{\omega t_d}{2}\right) \frac{|H(\omega)|^2}{\omega^2} S_{\nu_1}(\omega) \frac{d\omega}{2\pi}. \qquad (9)$$

The same approximation than before ($\pi f t_d \ll 1$) leads to the final expression:

$$\sigma_\Phi^2 \approx 4\pi^2 t_d^2 \int_0^{+\infty} |H(\omega)|^2 \, S_{\nu_1}(\omega) \frac{d\omega}{2\pi}. \qquad (10)$$

According to this formula, the interferometer sensitivity σ_Φ increases linearly with the retro-reflection length. In the case of a white frequency noise ($S_{\nu_1}(\omega) = S^0_{\nu_1}$), the variance is:

$$\sigma_\Phi^2 \approx \frac{\pi^4}{\tau_R} \, t_d^2 \, S^0_{\nu_1}. \qquad (11)$$

This last result provides a simple evaluation of the level of white frequency noise required to reach a given sensitivity, for given retro-reflection delay and Raman pulse duration.

4.2 Example of the laser frequency noise influence

In a second experiment, the frequency noise is deliberately degraded by adding noise on the master laser current. We

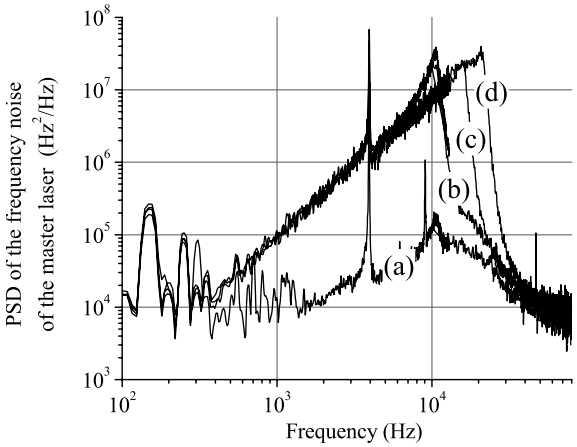

Fig. 4. PSD of the frequency noise of the master laser. The curve (a) shows a typical unperturbed power spectrum of the laser. The other curves correspond to the PSD with added noise on the laser current, for different cut-off frequencies of the low pass filter: (b) 10 kHz, (c) 15 kHz, (d) 20 kHz.

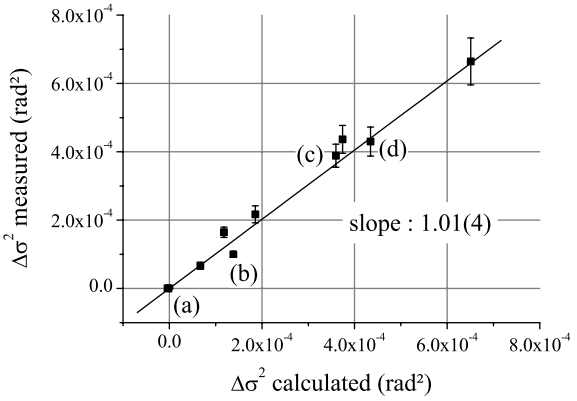

Fig. 5. Comparison between calculated and measured degradations of the phase sensitivity, for different added noise. The point (a), where $\Delta\sigma^2 = 0$, corresponds to the case where no frequency noise is added. The points (b), (c) and (d) correspond to the power spectra displayed in Figure 4.

use a high gain amplifier with an incorporated tunable low pass filter (Stanford Research System SR650) as the noise source, with its input connected to ground. We basically control the amount of RMS frequency noise by changing the cut-off frequency of the filter (see Fig. 4). The PSD of the master laser frequency noise is measured by analyzing the FVC output with a FFT analyzer (we made sure it is well above the PSD of the reference laser to which the master laser is compared). We also measure the power spectrum of the laser without additional noise, and we calculate the two corresponding variances, with or without added noise, using equation (10). The difference between the two variances gives the expected variance degradation $\Delta\sigma_\Phi^2$ of the interferometer phase noise. We compare this calculation with the experimental value of $\Delta\sigma_\Phi^2$ obtained by measuring the difference between the variances of the interferometer phase with and without added noise. The experiment was performed for $2L = 93$ cm, and Figure 5 shows the comparison between the calculated and the measured values of the variance degradation. The experimental values agree very well with the result of the calculation.

From the nominal frequency noise spectrum (curve (a) in Fig. 4), we estimate that the retro-reflection induces a laser frequency noise contribution of 2.0 mrad/shot to the total interferometer noise.

5 Discussion

5.1 Sensitivity limitation of the gravimeter measurement

This contribution of the frequency noise does not depend on the duration $2T$ of our interferometer. Indeed, as discussed before, the retro-reflection delay t_d can be considered as constant even for the longest interferometer we can perform. Moreover, dominant contributions to the variance arise from the high frequency part of the laser frequency noise spectrum, for which the fast oscillations of the transfer function average to the same value, regardless to $2T$.

The calculated laser frequency noise contribution induced by the retro-reflection is of the same order of magnitude than the other sources of phase noise also due to the lasers. Indeed, the PLL noise contributes for 2.1 mrad/shot [26], the various frequency references for 1.6 mrad/shot, and the propagation in the optical fiber for 1.0 mrad/shot. All these noise sources are independent, so the frequency noise of the Raman lasers represents a total contribution of $\sigma_\Phi = 3.5$ mrad/shot to the interferometer phase sensitivity.

With 2.0 mrad/shot, the retro-reflection contribution limits the sensitivity of the acceleration measurement up to $\sigma_g = 2.5 \times 10^{-9}$ g/$\sqrt{\text{Hz}}$ with our experimental parameters ($2T = 100$ ms, $\tau_R = 6$ μs, $L = 93$ cm, and cycle rate 4 Hz). However, the interferometer sensitivity is presently limited to 2×10^{-8} g/$\sqrt{\text{Hz}}$ by the vibration noise.

We want to emphasize here that our ECDL have excellent white frequency noise floor, which corresponds to a linewidth of only 5 kHz. Excess $1/f$ noise at low frequency is inherent to the diode lasers. It could be reduced more efficiently by using other locking techniques which allow larger bandwidths [28–30]. Other laser sources based on frequency doubled fiber lasers, whose frequency noise is extremely low, could be beneficial [31,32]. On the contrary, free DBR laser diodes, whose linewidth is typically a few MHz, are not recommended.

The sensitivity may be improved by using longer Raman pulses. In the case of a white frequency noise, equation (11) indicates that the sensitivity scales as $1/\sqrt{\tau_R}$. However, the frequency noise of a locked laser is generally colored, so that the gain in sensitivity depends on the features of the frequency spectrum. Considering the spectrum of our laser (curve (a) in Fig. 4), we can distinguish several cases. For cutoff frequencies f_c slightly

lower than the bandwidth of the frequency lock loop f_{BW} ($f_c \lesssim f_{BW}$), increasing τ_R (i.e. decreasing f_c) reduces the frequency noise contribution faster than $1/\sqrt{\tau_R}$. For example, we find $\sigma_\Phi = 1.5$ mrad/shot for $\tau_R = 20$ μs, and 0.57 mrad/shot for the fourfold duration $\tau_R = 80$ μs. On the contrary, when $f_c \gtrsim f_{BP}$ the phase noise decreases slower than $1/\sqrt{\tau_R}$. For a 1 μs (resp. 4 μs) pulse duration, $\sigma_\Phi = 2.7$ mrad/shot (resp. 2.2 mrad/shot). For the asymptotic cases $f_c \ll f_{BP}$ or $f_c \gg f_{BP}$, the interferometer phase noise is dominated by the frequency noise inside or far outside of the bandwidth, where the noise is in general white. Hence the sensitivity scales as $1/\sqrt{\tau_R}$ in both cases.

However, when the duration τ_R is larger, the velocity selectivity of the pulses becomes more stringent. Then the contribution of useful atoms to the signal is smaller, and the detection noise is larger. Even for the lowest temperatures one can reach with $\sigma_+ - \sigma_-$ cooling, the increase of τ_R reduces either the contrast when no primary velocity selection is performed, or the number of atoms in the measurement. Ultra-cold atoms, obtained by evaporative or sideband cooling, would be of interest [33,34].

The sensitivity can also be improved by bringing the mirror closer to the atoms. Presently, our mirror is located at the bottom of the experiment, out of the magnetic shields. Ultimately the mirror could be installed inside the vacuum chamber, very close to the atoms. In this ideal situation, the laser propagation delay cannot be considered constant for the three pulses anymore. The maximum delay scales as the trajectory length, which is proportional to T^2. On the other hand, the sensitivity to inertial forces also scales as T^2 when going to large interaction times. Hence, the sensitivity limit on the inertial measurement induced by the propagation delay, does not depend on T for ground instruments. The situation is more favorable for space based instruments [32] where the distance between the atoms and the retro-reflection mirror would scale like the separation of the wavepackets, meaning only like T.

5.2 Influence on gradiometers measurement

The formalism developed here could finally be useful to determine the ultimate performances of cold atom gradiometers. In such experiments, two atomic clouds are spatially separated and realize simultaneously gravity measurements [17,35]. Most of the phase noise contributions are rejected thanks to the differential measurement, when the clouds experience the same Raman lasers. However, as the lasers propagation delays are not the same for the two spaced interferometers, the laser frequency noise do not cancel. Let us consider the simple case where the atomic sample S_2 is very close to the retro-reflection mirror, whereas the other S_1 is half a meter above. While the phase noise induced by the laser L_2' propagation is negligible for S_2, for the other sample S_1 this phase noise contribution would reach the 2.0 mrad/shot that we calculated for a single sample located at $L = 93/2$ cm, with our laser setup. A remarkable point is that this phase noise contribution scales like the distance $L = ct_d/2$, just like

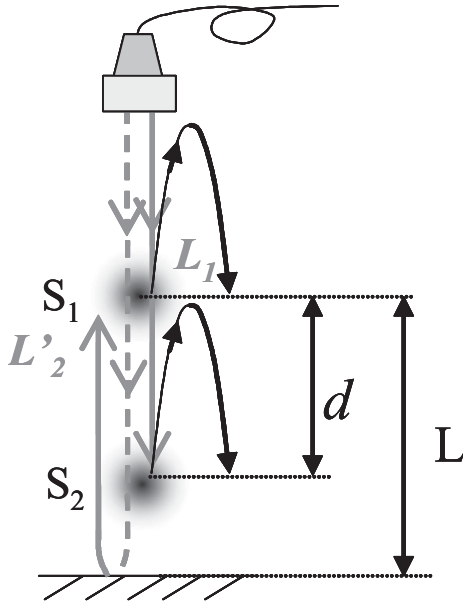

Fig. 6. Possible setup of a cold atom gradiometer, where two samples S_1 and S_2 are used for two simultaneous interferometers. Their separation d keeps constant all along their trajectories, and the phase noise induced by the frequency noise of L_2' during the retro-reflection only depends on d.

the sensitivity of the gradiometer measurement [17]. Hence there would be no advantage in increasing the separation between the samples, as long as one do not increase the interaction time $2T$.

In the more common configuration where the samples are given the same initial velocity, the distance d between them remains constant during their trajectories. It is then quite straightforward that the gradiometer phase noise induced by the lasers propagation delays only depend on the separation d. Thus the sensitivity limit is also given by the equation (10), with $t_d = 2d/c$. The variance in the case of a white frequency noise is then:

$$\sigma_\Phi^2 \approx 4\frac{\pi^4}{\tau_R}\frac{d^2}{c^2}S_{\nu_1}^0. \tag{12}$$

Using our experimental setup, with the parameters mentioned before, the best sensitivity would be thus 50 E/$\sqrt{\text{Hz}}$ (1 E = 10^{-9} s^{-2}). Let us consider now an atomic fountain configuration with a vertical separation $d = 1$ m of the two samples, and a trajectory height of 1 meter too (see Fig. 6). This trajectory is obtained for an initial velocity of 4 m/s, and the apogee is reached after a time interval of 450 ms, which defines the maximum interaction time T. A laser linewidth as small as 1 kHz (corresponding to a white frequency noise of about $S_\nu = 320$ Hz^2/Hz) would allow to obtain a stability measurement of 0.1 E/$\sqrt{\text{Hz}}$ (for a standard pulse duration $\tau_R = 10$ μs and a cycle rate of 1 shot/s).

6 Conclusion

We have investigated the influence of the optical propagation delays on the phase noise of an atom interferometer based on two photon transitions. The transfer function for the laser frequency fluctuations has been calculated and measured for various optical paths with our cold atom gravimeter. Quantitative measurements of the interferometer sensitivity have also been performed, which show that the laser frequency noise can limit the sensitivity of the interferometer. A necessary effort must therefore be placed to reduce the laser frequency noise. We apply the present formalism to the case of atomic gradiometers, where the other sources of interferometer phase noise are rejected. Our model can be used to estimate the required frequency laser noise for a given sensitivity. This work presents interest for space-borne experiments as well, where interaction times can be much longer, and where the effect of the lasers propagation could constitute a technical limitation.

The authors would like to thank the Institut Francilien pour la Recherche sur les Atomes Froids (IFRAF), the Centre National des Études Spatiales (contract no. 02/CNES/0282), the European Union (FINAQS) for financial support. P.C. and J.L.G. thank DGA for supporting their works.

References

1. G. Santarelli, Ph. Laurent, P. Lemonde, A. Clairon, Phys. Rev. Lett. **82**, 4619 (1999)
2. M. Kasevich, S. Chu, Phys. Rev. Lett. **67**, 181 (1991)
3. F. Riehle, Th. Kisters, A. Witte, J. Helmcke, Ch. J. Bordé, Phys. Rev. Lett. **67**, 177180 (1991)
4. D.S. Weiss, B.C. Young, S. Chu, Appl. Phys. B **59**, 217253 (1994)
5. H. Marion, F. Pereira Dos Santos, M. Abgrall, S. Zhang, Y. Sortais, S. Bize, I. Maksimovic, D. Calonico, J. Grünert, C. Mandache, P. Lemonde, G. Santarelli, Ph. Laurent, A. Clairon, Phys. Rev. Lett. **90**, 150801 (2003)
6. P. Wolf, F. Chapelet, S. Bize, A. Clairon, Phys. Rev. Lett. **96**, 060801 (2006)
7. D.W. Keith, M.L. Schattenburg, H.I. Smith, D.E. Pritchard, Phys. Rev. Lett. **61**, 1580 (1988)
8. E.M. Rasel, M.K. Oberthaler, H. Batelaan, J. Schmiedmayer, A. Zeilinger, Phys. Rev. Lett. **75**, 2633 (1995); D.M. Giltner, R.W. McGowan, S.A. Lee, Phys. Rev. Lett. **75**, 26382641 (1995)
9. Ch. Miniatura, J. Robert, S. Boiteux, J. Reinhardt, J. Baudon, Appl. Phys. B **54**, 347 (1992)
10. T. Schumm, S. Hofferberth, L.M. Andersson, S. Wildermuth, S. Groth, I. Bar-Joseph, J. Schmiedmayer, P. Krüger, Nature Phys. **1**, 57 (2005)
11. *Atom Interferometry*, edited by P.R. Berman (Academic Press, 1997)
12. A. Miffre, M. Jacquey, M. Büchner, G. Trénec, J. Vigué, Eur. Phys. J. D **38**, 353 (2006)
13. H. Müller, S.-W. Chiow, Q. Long, C. Vo, S. Chu, Appl. Phys. B **84**, 633 (2006)
14. K. Moler, D.S. Weiss, M. Kasevich, S. Chu, Phys. Rev. A **45**, 342 (1992)
15. A. Peters, K.Y. Chung, S. Chu, Nature **400**, 849 (1999)
16. T.L. Gustavson, P. Bouyer, M.A. Kasevich, Phys. Rev. Lett. **78**, 2046 (1997)
17. J.M. McGuirk, G.T. Foster, J.B. Fixler, M.J. Snadden, M.A. Kasevich, Phys. Rev. A **68**, 033608 (2002)
18. B. Canuel, F. Leduc, D. Holleville, A. Gauguet, J. Fils, A. Virdis, A. Clairon, N. Dimarcq, Ch.J. Bordé, A. Landragin, P. Bouyer, Phys. Rev. Lett. **97**, 010402 (2006)
19. T.M. Niebauer, G.S. Sasagawa, J.E. Faller, R. Hilt, F. Klopping, Metrologia **32**, 159 (1995)
20. K.U. Schreiber, A. Velikoseltsev, M. Rothacher, T. Klugel, G.E. Stedman, D.L. Wiltshire, J. Geophys. Res. **109** B06405 (2004)
21. C.J. Bordé, in *Laser Spectroscopy X*, edited by M. Ducloy, E. Giacobino, G. Camy (Singapore, World Scientific, 1991), pp. 239–245
22. G. Santarelli, A. Clairon, S.N. Lea, G. Tino, Opt. Comm. **104**, 339 (1994)
23. P. Bouyer, T.L. Gustavson, K.G. Haritos, M.A. Kasevich, Opt. Lett. **21**, 1502 (1996)
24. P. Cheinet, F. Pereira Dos Santos, T. Petelski, J. Le Gouët, J. Kim, K.T. Therkildsen, A. Clairon, A. Landragin, Appl. Phys. B **84**, 643 (2006)
25. C.J. Bordé, Metrologia **39**, 435 (2002)
26. P. Cheinet, B. Canuel, F. Pereira Dos Santos, A. Gauguet, F. Leduc, A. Landragin, IEEE Trans. Instrum. Meas. (submitted), `arXiv:physics/0510197` (2005)
27. G.J. Dick, *Local Oscillator induced instabilities, in Proc. Nineteenth Annual Precise Time, Time Interval* (1987) pp. 133–147
28. R.W.P. Drever, J.L. Hall, F.V. Kowalski, J. Hough, G.M. Ford, A.J. Munley, H. Ward, Appl. Phys. B **31**, 97 (1983)
29. B. Dahmani, L. Hollberg, R. Drullinger, Opt. Lett. **12**, 876 (1987)
30. V. Crozatier, F. de Seze, L. Haals, F. Bretenaker, I. Lorgeré, J.-L. Le Gouët, Opt. Comm. **241**, 203213 (2004)
31. R. Thompson, M. Tu, D. Aveline, N. Lundblad, L. Maleki, Opt. Exp. **11**, 1709 (2003)
32. R.A. Nyman, G. Varoquaux, F. Lienhart, D. Chambon, S. Boussen, J.-F. Clément, T. Müller, G. Santarelli, F. Pereira Dos Santos, A. Clairon, A. Bresson, A. Landragin, P. Bouyer, Appl. Phys. B **84**, 673 (2006)
33. N. Masuhara, J.M. Doyle, J.C. Sandberg, D. Kleppner, T.J. Greytak, H.F. Hess, G.P. Kochanski, Phys. Rev. Lett. **61**, 935 (1988)
34. H. Perrin, A. Kuhn, I. Bouchoule, T. Pfau, C. Salomon, Europhys. Lett. **46**, 141 (1999)
35. N. Yu, J.M. Kohel, J.R. Kellogg, L. Maleki, Appl. Phys. B **84**, 647 (2006)

Chapitre 3

Gyromètre à ondes de matière

3.1 Introduction

Les appareils de mesure des rotations peuvent être classés en deux types : ceux qui mesurent des angles, les gyroscopes, et ceux qui mesurent les vitesses de rotation, les gyromètres. Cette distinction dans la langue française n'existe pas en anglais mais est trés utile. Le mot *gyroscope*, du grec "qui regarde la rotation", a été proposé par Léon Foucault en 1852 lorsqu'il l'inventa et se rapporte donc à la mesure d'un angle. Les *gyromètres* mesurent les vitesses de rotation qui correspondent donc à la dérivée du signal d'angle. Tous les gyromètres sont fondés sur la mesure de l'effet Sagnac, initialement démontré pour les ondes lumineuses, mais qui est en fait indépendant de la nature des ondes utilisées et qui est à la base des expériences de gyrométrie à ondes de matière qui sont décrites dans la suite de ce chapitre.

Les gyroscopes sont donc intrinsèquement meilleurs pour des mesures de stabilité sur des temps longs alors que les gyromètres sont typiquement meilleurs sur les temps courts. Pour les applications nécessitant un très bonne stabilité à long terme, les gyroscopes mécaniques, bien que très chers à usiner, ont été très longtemps sans équivalent, notamment pour les applications en navigation inertielle de longues durées. Les gyromètres à atomes peuvent concurrencer les gyroscopes mécaniques pour ce type d'application.

3.1.1 L'effet Sagnac

Une histoire de l'effet Sagnac

Cet effet a été découvert en 1913 par G. Sagnac, dans le cadre de travaux visant à démontrer l'existence de l'éther. Pour cela, il réalise une expérience en utilisant un interféromètre optique en rotation rapide (2 Hz) [Sagnac 1913]. Le décalage des franges d'interférence, qui

est observé lorsque l'interféromètre d'aire A est soumis à une rotation Ω, correspond à celui qu'il avait prédit dans le cadre d'une théorie classique de l'éther :

$$\Delta\Phi = \frac{4\Omega A}{\lambda c} \tag{3.1}$$

Dans cette équation λ et c sont respectivement la longueur d'onde et la vitesse de la lumière dans le vide. L'interféromètre utilisé par Sagnac (figure 3.1) a une aire d'environ 866 cm^2, il est monté sur une table tournant à une fréquence de 2 Hz.

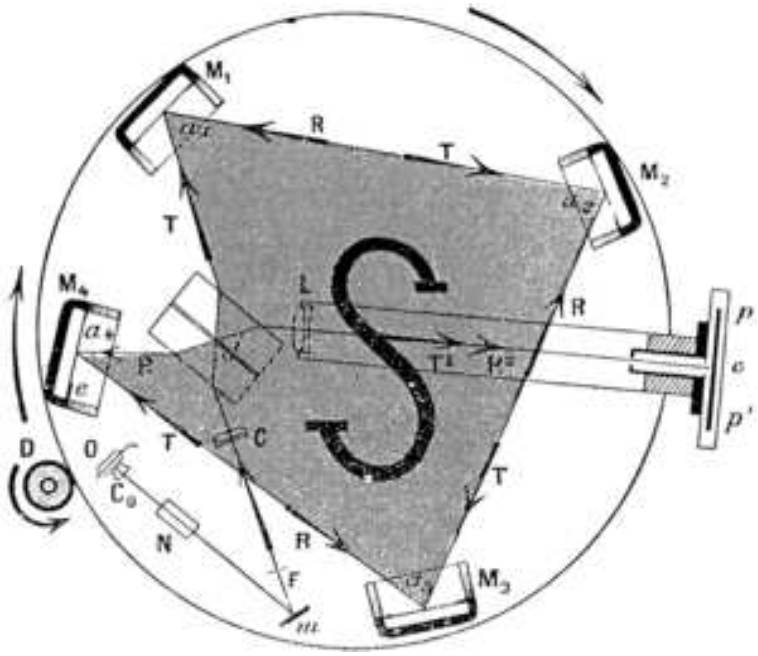

FIG. 3.1 : *Interféromètre de Sagnac*

Un an avant l'expérience de Sagnac, Haress réalise lui aussi une expérience d'interférométrie optique dans un référentiel en rotation. Il utilise un interféromètre constitué de prismes en verre pour guider la lumière, dans le but d'étudier les effets d'entraînement de la lumière dans le verre en mouvement. Il mesure alors un déphasage qu'il ne peut expliquer. Cet écart ne fut correctement interprété qu'en 1914 par Harzer comme étant l'effet Sagnac. En plus de démontrer l'effet Sagnac, cette expérience montre que ce dernier est indépendant de l'indice de réfraction du milieu dans lequel se propage la lumière, ce qui n'était pas le cas de l'expérience de Sagnac réalisée dans l'air.

La mesure de la rotation de la Terre avec un interféromètre optique fut proposée par O. Lodge en 1893 [Lodge 1893]. Il fallut attendre 1925, 30 ans après la proposition de Lodge, pour qu'une mesure de la vitesse de la Terre soit réalisée avec un interféromètre optique par

A. Michelson [Michelson 1925]. L'interféromètre construit est une prouesse expérimentale, il s'agit d'un interféromètre de 0,25 km^2, réalisé avec une lampe à arc de carbone ! Une description détaillée des premières études de l'effet Sagnac, et du contexte historique dans lequel elles se déroulent, peut être trouvée dans [Anderson 1994].

Quelques précisions à propos de l'effet Sagnac

L'effet Sagnac peut être défini comme le décalage temporel de la réception entre deux signaux émis et reçus dans un référentiel tournant. Pour mesurer cet effet, il est possible d'utiliser deux ondes (cohérentes), émises par une source attachée au référentiel tournant à la vitesse angulaire Ω, et se propageant en sens inverses dans un interféromètre d'aire non nulle. Les deux ondes arrivent alors sur un détecteur (attaché au référentiel tournant) avec un décalage temporel qui dépend de la rotation de l'interféromètre. Ce décalage se traduit par un déphasage entre les deux ondes qu'il est possible de mesurer en les faisant interférer[1]. L'invention du laser a permis un regain d'intérêt pour l'interférométrie Sagnac et conduit au développement de nouveaux gyromètres, comme les gyromètres à fibre optique [Vali 1976] et les gyro-lasers, aujourd'hui utilisés pour la navigation inertielle.

Cependant, l'effet Sagnac a donné lieu à de multiples interprétations et de nombreuses polémiques, rapportées par exemple dans [Post 1967] ou [Rizzi 2003]. Le déphasage Sagnac peut être dérivé dans le cadre de la relativité restreinte, en utilisant les formules de changement de référentiel en rotation. On montre alors (voir par exemple [Rizzi 2003]) que l'expression du déphasage Sagnac ne dépend pas de la nature de l'onde, il peut s'agir d'une onde lumineuse comme d'une ondes de matière. On trouve alors :

$$\boxed{\Delta\Phi = \frac{2AE}{\hbar c^2}\Omega} \tag{3.2}$$

où A est l'aire de l'interféromètre, Ω la vitesse de rotation de l'interféromètre par rapport à un référentiel inertiel, et E l'énergie totale des particules utilisées. Il est intéressant de noter que cette expression ne dépend pas de la vitesse de groupe pour les ondes lumineuses, mais uniquement de sa pulsation ω.

Dans le cas d'une ondes de matière associée à une particule de masse m, l'énergie est donnée par :

$$E = \frac{mc^2}{\sqrt{1 - \frac{v^2}{c^2}}} \tag{3.3}$$

[1] Avec le développement d'horloges de très grande exactitude, ce décalage temporel peut être mesuré directement et doit être pris en compte lors des transferts de temps sur de grandes distances.

On obtient donc l'expression du déphasage Sagnac pour une ondes de matière à un terme en $\frac{v^2}{c^2}$ près :

$$\boxed{\Delta\Phi_{\text{mat.}} = \frac{2Am}{\hbar}\Omega} \tag{3.4}$$

Le rapport des sensibilités intrinsèques entre un gyromètre réalisé avec des particules de masse M (pour le césium $M_{Cs} = 220,8.10^{-27}$ kg), et un gyromètre optique utilisant une onde de pulsation ω (de l'ordre de 10^{15} rad.s^{-1}) vaut :

$$\frac{\Delta\Phi_{\text{atomique}}}{\Delta\Phi_{\text{optique}}} = \frac{Mc^2}{\hbar\omega} \approx 10^{11} \tag{3.5}$$

Ainsi, pour une aire d'interféromètre égale, le facteur d'échelle du gyromètre à atomes est 10^{11} fois plus élevé que celui d'un gyromètre optique. Les gyromètres à atomes sont donc potentiellement beaucoup plus performants que les gyromètres optiques. Cependant, l'aire interférométrique réalisée avec un gyromètre optique peut atteindre 10 m^2, alors que les aires des interféromètres à ondes de matières ne dépassent pas pour l'instant le cm^2 (dans notre expérience, l'aire de l'interféromètre est de l'ordre de 4 mm^2). Par ailleurs, le rapport signal à bruit est beaucoup plus faible dans un interféromètre atomique comparé à celui d'un interféromètre optique, car il est difficile d'obtenir des sources intenses d'ondes de matière.

L'utilisation d'arguments relativistes permet de réaliser simplement une comparaison entre les gyromètres optiques et les gyromètres atomiques. Cependant, nous avons vu au paragraphe 2.2.3 que l'effet Sagnac pour les ondes de matières peut être dérivé avec une théorie non relativiste de la mécanique quantique. Nous pouvons d'ailleurs utiliser la formule 2.20 et retrouver le déphasage Sagnac eq. 3.4 en notant que l'aire de l'interféromètre s'écrit :

$$A = \frac{\hbar k_{eff}}{M}.V.T^2$$

3.1.2 Etat de l'art des gyromètres

Le type de gyromètre choisi pour une application donnée dépend de beaucoup de paramètres et notamment de la sensibilité, du coût ou de l'encombrement disponible. Mais, la sensibilité n'est pas le seul argument pertinent en terme de performance : la dérive de biais ou la stabilité du facteur d'échelle sont également importants dans le choix d'un type de gyro. Une discussion très détaillée de l'ensemble de ces paramètres et une comparaison entre les différents types de capteur incluant les interféromètres atomiques pourra être trouvée dans [Holleville thèse].

Dans le tableau 3.1, les performances des gyromètres atomiques sont comparées à celles des gyromètres optiques. En gyrométrie, les performances sont données en $°/\sqrt{\text{h}}$ pour la sen-

sibilité (bruit de marche aléatoire d'angle), en °/h pour la stabilité du biais (correspondant au palier de la variance d'Allan) et en % pour la stabilité du facteur d'échelle. Ici les performances sont données en système SI : 1 °/h correspond à 4,8.10^{-6} rad.s^{-1} et 1°/$\sqrt{\text{h}}$ correspond à 2,9.10^{-4} rad.s$^{-1}/\sqrt{\text{Hz}}$. Les valeurs données dans le tableau 3.1 doivent être prises avec précaution, car il est souvent difficile d'obtenir des informations sur les performances des dernières innovations. De plus, ces gyromètres ont des caractéristiques technologiques très différentes (dimensions, consommation en énergie, etc.) rendant certains de ces capteurs inutilisables pour de nombreuses applications. C'est le cas par exemple du problème d'encombrement du gyro-laser géant basés en Nouvelle Zélande [Hurst 2009] et an Allemagne [Schreiber 2008] ou dans une moindre mesure de ceux des interféromètres atomiques utilisant des jets d'atomes thermiques [Gustavson 1998] et [Lenef 1997]. Enfin, les performances dépendent également du niveau de maturité technologique. Par exemple, les gyrolasers sont maintenant à maturité technologique depuis plus de 10 ans alors que les gyromètres à fibre y arrivent seulement, et que les gyromètres atomiques n'y sont pas encore.

Type de gyromètre	Sensibilité (rad.s$^{-1}/\sqrt{\text{Hz}}$)	long terme (rad.s^{-1})	durée d'intégration
Gyro atomique Kasevich [Gustavson 2000] chapitre 3.2	6.10^{-10}	2.10^{-9}	100 s
Gyro atomique Kasevich [Durfee 2006]	8.10^{-8}	4.10^{-9}	30 minutes
Gyro SYRTE, chapitre 3.3, [Gauguet 2009]	$2,4.10^{-7}$	10^{-8}	30 minutes
Gyro atomique Pritchard [Lenef 1997]	4.10^{-6}	-	-
Gyro spin nucléaire [Kornack 2005]	5.10^{-7}	4.10^{-9}	-
Gyro à hélium superfluide	2.10^{-7}	-	-
Gyro à fibre IXSEA (IMU 120)	3.10^{-7}	10^{-8}	30 minutes
Gyro à fibre IXSEA (com. privée)	6.10^{-8}	6.10^{-10}	qq heures
Gyro laser navigation	(qq 10^{-8})	qq 10^{-9}	qq heures
Gyro laser géant [Schreiber 2008]	8 10^{-11}	8 10^{-13}	5 heures

TAB. 3.1 : *Comparaison des performances à court et à long terme de gyromètres optiques et à ondes de matière. La dernière colonne donne la durée typique pour atteindre le palier Flicker, dont la valeur est donnée dans la colonne "long terme".*

Les performances du gyromètre atomique de M. Kasevich furent présentées en deux temps. Une première publication en 2000 [Gustavson 2000] montre une sensibilité à court-terme optimale de 6.10^{-10} rad.s$^{-1}/\sqrt{\text{Hz}}$ et sera détaillée dans le paragraphe 3.2. En 2006,

une étude de la stabilité à long terme est présentée dans [Durfee 2006]. Afin d'obtenir un meilleur contrôle des paramètres expérimentaux, les performances à court terme furent limitées ($\sim 8.10^{-8}$ rad.s$^{-1}/\sqrt{\text{Hz}}$), les mesures de rotation se moyennent alors pendant 1000 secondes pour atteindre une sensibilité de 4.10^{-9} rad.s^{-1}.

Pour comparer les performances des gyromètres lasers et aux gyromètres à fibre (FOG), il est important de noter que les performances à très court terme (par exemple à 1 s) des gyrolasers ne sont pas limitées par le bruit de marche aléatoire (en $1/\sqrt{\tau}$) mais par le bruit de quantification qui décroît en $1/\tau$ et est donc plus élevé sur les temps courts (la performance à une seconde correspondant au tableau 3.1 est nettement moins bonne que qq. 10^{-8}). Par contre, les FOG sont beaucoup plus sensibles à l'environnement extérieur (température, vibrations), qui limite notamment la stabilité du facteur d'échelle. Pour conclure, dans un environnement très calme (sous-marin, satellite...) et/ou s'il y a un besoin de grande stabilité sur des temps courts les FOG sont de très bon candidats, alors que l'on préférera un gyrolaser dans un environnement perturbé (avion...) et/ou avec des vitesses de rotations élevées.

3.1.3 Applications

Navigation inertielle

Une des applications des gyromètres de très hautes performances est la navigation inertielle. Le principe de la navigation inertielle est simple, elle est fondée sur l'intégration des équations du mouvement de l'appareil (typiquement un avion, un sous-marin ou un satellite), connaissant sa position de départ. Pour cela, des centrales inertielles sont réalisées le plus souvent en associant trois accéléromètres et trois gyromètres (selon chacune des directions de l'espace) et une horloge pour réaliser l'échelle de temps nécessaire à l'intégration. Les performances de ces centrales sont limitées par les dérives des capteurs inertiels, qui imposent des recalages réguliers avec des moyens extérieurs (astronomie, GPS...) et par conséquent limitent l'autonomie des véhicules. C'est pourquoi, en plus d'une très bonne résolution, les capteurs inertiels destinés à la navigation de longue durée doivent aussi avoir une excellente stabilité à long terme permettant de limiter, voire de s'affranchir, des recalages.

Après plus de 60 ans d'études, les meilleures performances sur les temps longs sont aujourd'hui réalisées avec des gyroscopes mécaniques, bien qu'en passe d'être remplacés par des gyromètres optiques. Cependant, il aura fallu à peine 15 ans depuis la première démonstration de l'effet Sagnac atomique pour que les performances des gyromètres atomiques approchent celles des meilleurs gyroscopes. De plus, nous verrons que les études détaillées des limites des dispositifs actuels montrent qu'elles ne sont pas fondamentales et laissent envisager des performances bien supérieures.

Mesures en géophysique

A cause du mouvement de la Lune et du soleil autour de la Terre, l'attraction gravitationnelle change au cours du temps. Ces effets, communément appelés effets de marée, sont entre autres responsables de la variation de l'accélération de pesanteur locale g. Un autre effet lié à ces phénomènes de marées est la variation de la distribution des masses sur Terre, comme celle des océans, qui entraîne une modification de sa vitesse de rotation Ω_T. Ces fluctuations de vitesse de rotation de la Terre, de l'ordre de $10^{-8}\ \Omega_T$, sont très bien résolues avec des techniques d'observation astronomique VLBI (*Very Long Baseline Interferometry*) [Chao 1997] à des échelles de temps de l'ordre de plusieurs jours. Néanmoins, des interrogations persistent quant à l'origine et la nature de certaines fluctuations observées sur des échelles de temps plus courtes [Frede 2000]. L'utilisation de gyromètres avec une sensibilité inférieure à quelques $10^{-7}\ \Omega_T$ sur des échelles de temps de l'heure permettrait une étude plus précise de ces fluctuations et de tester les modèles théoriques [Lambeck 1980] de rotation de la Terre.

Par ailleurs, les gyromètres de très grande sensibilité pourraient contribuer à l'étude des séismes. En effet, contrairement aux mesures du type VLBI, il est possible de mesurer avec un gyromètre des vitesses de rotation locales, par exemple près d'une faille sismique. Les effets intéressants sont attendus dans la gamme de fréquence 3 mHz à 20 Hz du spectre de rotation des ondes sismiques [Schreiber 2006, Igel 2007], avec des vitesses de rotation allant de 10^{-14} rad.s^{-1} à 1 rad.s^{-1}. La mesure de ces effets, liés aux déformations de la croûte terrestre, pourraient contribuer à une meilleure compréhension de la propagation des ondes sismiques et de la physique de la croûte terrestre en général, et notamment de la réorganisation entre plaques tectoniques pendant un épisode sismique.

Mesures en physique fondamentale

La très grande sensibilité des capteurs inertiels à ondes de matière en font des outils adéquats pour tester certains effets prévus par la théorie de la relativité générale [Dimopoulos 2007, Tino 2007, Will 2006]. Le projet HYPER ([ESA-SCI 2000, Angonin 2006]), proposé à l' Agence Spatiale Européenne (ESA) en 2000, dont le but était de tester l'effet prévu par Lense et Thirring en 1918 [Lense 1918], qui prédit une précession du repère d'inertie locale à proximité d'une masse en rotation. Dans cette expérience, un gyromètre atomique envoyé dans l'espace en orbite autour de la Terre, permettrait de déterminer l'écart entre la mesure de rotation effectuée localement par le gyromètre et une mesure faite par rapport au référentiel non local défini par des étoiles fixes. L'effet attendu est de l'ordre de quelques 10^{-14} rad.s^{-1}. Ce projet sera discuté dans le paragraphe 5.4.

3.1.4 Atomes chauds ou atomes froids ?

Le choix du type de source d'atomes pour réaliser un gyromètre atomique de grande sensibilité n'est pas trivial. En effet, la sensibilité variant comme $V.T^2$, elle serait maximale pour une vitesse moyenne importante et un grand temps d'interrogation. Evidement, satisfaire en même temps ces deux conditions se traduirait par une augmentation drastique de la taille de l'expérience, qui n'est pas vraiment compatible avec une expérience de laboratoire, et encore moins pour certaines applications nécessitant un appareil transportable. A taille L d'expérience fixée, $L = V.T$, la sensibilité croît comme le temps de mesure T, indiquant que l'utilisation d'atomes froids, permettant de grand temps d'interrogation, est plus favorable. Néanmoins l'utilisation d'un jet atomique collimaté (refroidis suivant les directions transverses) permet d'obtenir un flux nettement plus important et donc d'améliorer le rapport signal à bruit.

Le choix du type de source, jet ou nuage, fixe également le type de fonctionnement des séparatrices Raman : fonctionnement spatial pour les jets (le temps d'interrogation est fixé par le temps de parcours entre deux paires de faisceaux Raman) et fonctionnement temporel pour les nuages d'atomes froids (les faisceaux lasers Raman sont successivement allumés puis éteints). Cette différence n'est pas anodine. En effet, le signal de rotation est issus de la différence entre les signaux de deux interféromètres utilisant des sources d'atomes contrapropageantes afin d'annuler le déphasage d'accélération ; il est donc important de s'assurer que les deux interféromètres ont la même sensibilité à l'accélération pour garantir cette annulation. Cette condition est bien mieux remplie avec un fonctionnement temporel, soit avec des atomes froids, qu'avec un fonctionnement spatial. De même pour la connaissance et la stabilité du facteur d'échelle, qui dépend de la vitesse des atomes, l'utilisation d'atomes froids est plus favorable. Nous sommes, de fait, dans une situation assez similaire à celle avec les horloges mirco-ondes, pour lesquelles l'utilisation d'atomes froids a d'abord et principalement permis d'améliorer la stabilité long terme et l'exactitude plutôt que la sensibilité à court terme.

Les deux expériences décrites dans les deux paragraphes suivants représentent pratiquement deux extrêmes : l'expérience sur jet utilise un interféromètre avec des atomes rapides (290 m.s^{-1}) et de très grande taille (2 m) alors que la seconde utilise des atomes froids très lents (0,33 m.s^{-1}) et un interféromètre de petite taille (3 cm).

3.2 Gyromètre à jets collimatés de Césium

3.2.1 Description de l'expérience

Description générale

L'interféromètre, développé initialement à l'université de Stanford puis à celle de Yale, est fondé sur l'utilisation de jets thermiques de Césium, refroidis dans les deux directions transverses. Les premiers résultats de 1997 ont démontré une très grande sensibilité [Gustavson 1997].

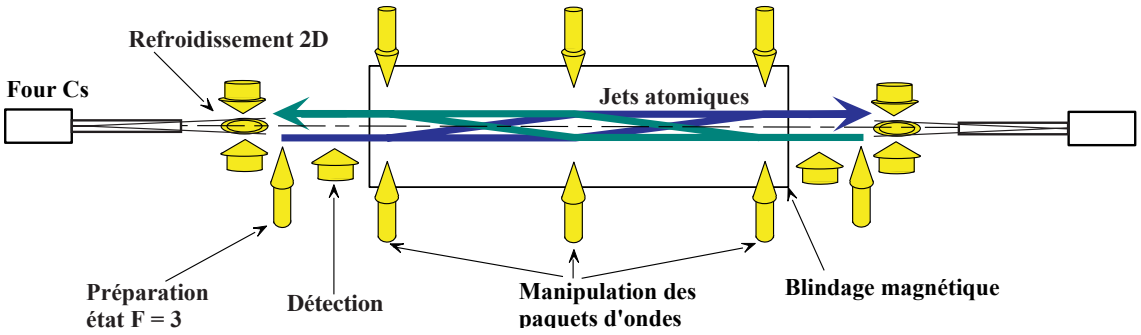

FIG. 3.2 : *Schéma de principe du gyromètre réalisé à l'université de Stanford puis de Yale. Les deux jets de Césium sont issus de fours à recirculation et se propagent suivant des directions opposées.*

Les atomes sont issus de fours à recirculation [Gustavson 1998] permettant d'obtenir un flux très élevé d'atomes. Les jets sont collimatés à l'aide d'une mélasse optique dans les deux directions transverses. Les atomes sont ensuite pompés dans le niveau hyperfin $F = 3$ avant d'entrer dans l'interféromètre. Il est réalisé à l'aide de trois paires de faisceaux Raman lasers, qui sont séparées respectivement d'une distance L d'un mètre. La détection est réalisée par fluorescence sur l'état $F = 4$. Les deux jets atomiques, de vitesse $\mathbf{v}_\pm$, se propagent suivant des directions opposées, permettent de réaliser deux interféromètres qui partagent les mêmes faisceaux lasers Raman et sont donc sensibles de façon identique à l'accélération (voir eq. 2.18) et avec des signes opposés aux rotations (voir eq. 2.20) :

$$\Delta\Phi = \mathbf{k_{eff}}.(\mathbf{a} - 2\mathbf{\Omega} \times \mathbf{v}_\pm)\frac{L^2}{v_\pm^2} \tag{3.6}$$

La somme (rep. la différence) des deux déphasages issus des deux interféromètres, donne accès aux accélérations (resp. aux rotations [Gustavson 1998]). L'utilisation d'un laser résonant avec la transition $F = 4$ vers $F' = 4$, pour réaliser l'étape de pompage optique dans le

niveau hypefin $F = 3$, permet aux atomes de traverser le faisceau laser de détection du jet se propageant dans la direction opposée et résonant avec la transition fermée $F = 4$ vers $F' = 5$, sans émettre de lumière parasite.

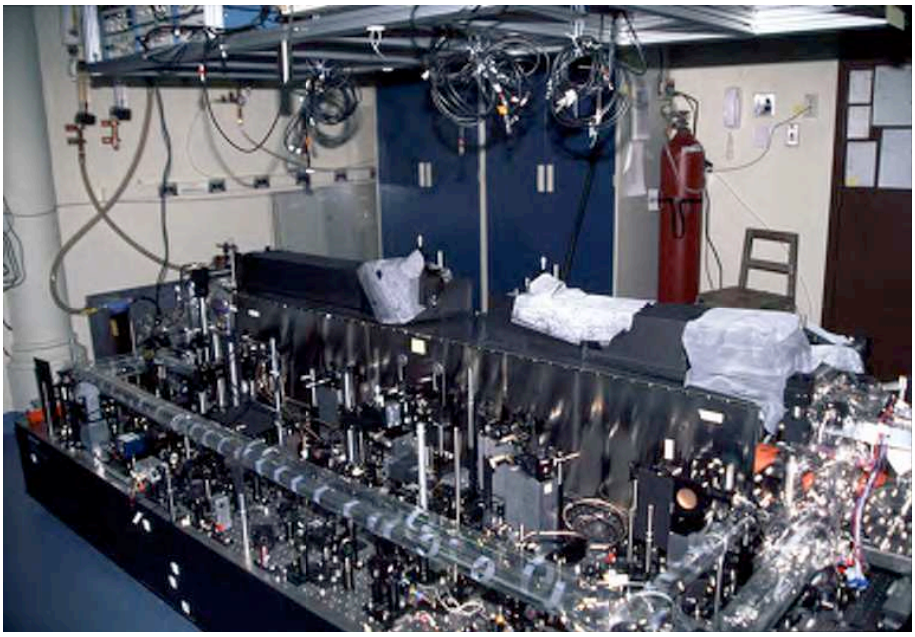

FIG. 3.3 : *Photographie de l'expérience.*

Sources atomiques

L'utilisation d'une source à recirculation et d'une phase de refroidissement transverse permet d'obtenir des jets à la fois très intenses et collimatés. Les fours sont chauffés à une température de 180°C donnant des jets thermiques avec un maximum de la distribution de vitesse à typiquement 290 m.s^{-1} (voir Fig. 3.4). L'utilisation d'une mélasse à deux dimensions permet de réduire la distribution en vitesse transverse à une largeur totale à demi-hauteur de 22 cm.s^{-1}, donnant une collimation de 2,9 10^{-7} steradians et correspondant à une amélioration d'un facteur 2500 par rapport à un jet thermique sans refroidissement. La température relativement élevée (160 μK) dans les deux directions transverses est liée au temps relativement court du processus de refroidissement (150 μs) ne permettant pas d'atteindre le régime de refroidissement sub-Doppler. Le flux détecté au niveau de la zone de détection est typiquement de 10^{11} at.s^{-1}, dans le sous-niveau magnétique m_F=0 utilisé dans l'interféromètre.

Pour bénéficier pleinement du flux important, il faut obtenir une très bonne stabilité du flux atomique et une grande efficacité de détection, recourant l'utilisation d'un laser à cavité

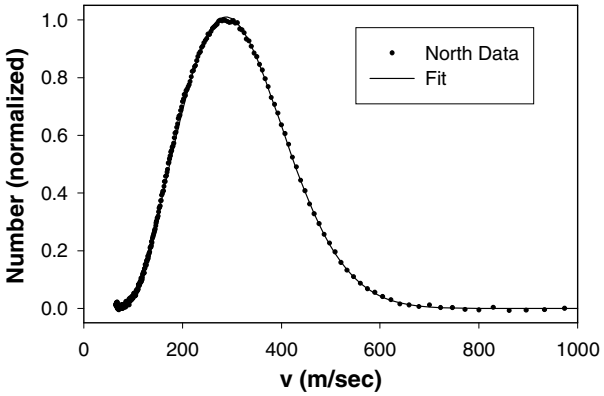

FIG. 3.4 : *Distribution de la vitesse longitudinale de l'un des deux jets atomiques, mesurée par temps de vol.*

étendue au lieu d'un laser DFB. De plus, une protection contre les mouvements d'air sur les faisceaux des mélasses optiques a été mise en place. Une stabilité du flux de 10^{-5} $\mathrm{Hz}^{-1/2}$ a été obtenue correspondant au bruit de projection quantique pour un flux de 10^{10} at.

3.2.2 Configuration co-propageante

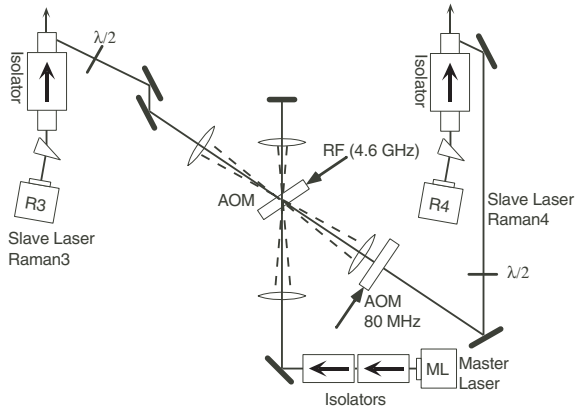

FIG. 3.5 : *Schéma de principe de la génération des deux faisceaux lasers Raman asservis en phase. L'ordre +1 du modulateur acousto-optique est utilisé pour injecter le premier laser Raman (R3). L'ordre 0 est alors rétro-réfléchi dans le modulateur pour générer l'ordre -1 qui sert à injecter le second laser (R4).*

Pour réaliser les séparatrices Raman, il est nécessaire de disposer de deux lasers dont la différence de fréquence correspond à la fréquence hyperfine (9,2 GHz pour le Cs) et asservies

en phase. Le fonctionnement de cet ensemble est décrit dans [Bouyer 1996] et est fondé sur l'injection de deux diodes lasers esclaves à l'aide de deux faisceaux issus du même laser maître et décalés en fréquence à l'aide d'un modulateur acousto-optique à $\pm$4,6 GHz (voir Fig. 3.5). Les deux lasers sont ensuite superposés pour être transportés jusqu'à l'enceinte à vide, évitant ainsi l'accumulation d'un déphasage relatif entre les deux faisceaux lors du transport. Un second modulateur à 80 MHz est ajouté avant l'injection du laser R4 afin de pouvoir changer rapidement la fréquence ou la phase relative entre les deux lasers Raman.

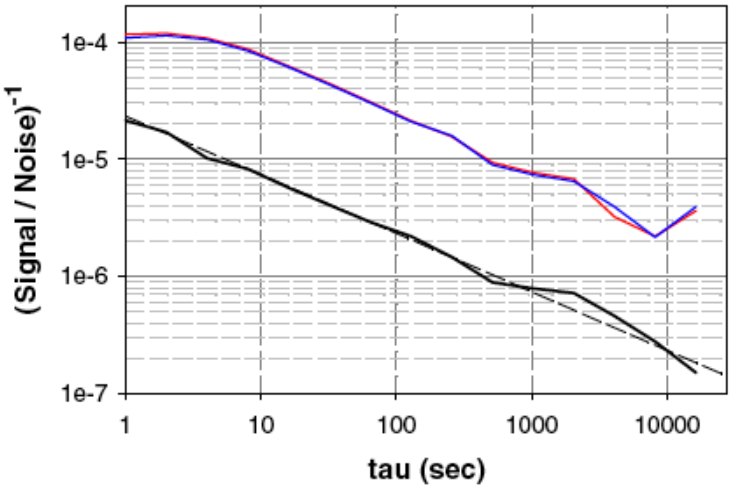

FIG. 3.6 : *Ecart type d'Allan du rapport signal à bruit. Les deux courbes supérieures (en rouge et en bleu) correspondent aux deux signaux issus des jets indépendants, après normalisation par le signal pic à pic, alors que la courbe en noir correspond à la demi-différences des deux signaux après normalisation.*

Pour tester l'ensemble des sources de bruit instrumentales de l'interféromètre sauf les déphasages inertiels, il est très pratique d'utiliser des configurations de faisceaux co-propageants avec trois impulsions $\pi/2 - \pi - \pi/2$. Comme les deux faisceaux conduisant à la transition Raman se propagent dans la même direction, le transfert d'impulsion est quasi-nul alors que l'appareil reste sensible de la même façon au bruit de phase entre les deux faisceaux lasers Raman, au déplacement à un photon ou aux fluctuations du champ magnétique. Pour s'affranchir des fluctuations à basses fréquences du flux atomique et/ou du contraste, une modulation de phase est introduite sur la différence de phase entre les deux faisceaux Raman (AOM à 80 MHz, voir Fig. 3.5). Le signal est alors démodulé à l'aide d'une détection synchrone. La figure 3.6 montre l'évolution du rapport signal à bruit (défini comme l'inverse à la stabilité de phase) des deux signaux issus des deux jets d'une part et de la demi-différence des déphasages d'autre part. Nous constatons que cette méthode permet d'améliorer d'un ordre de grandeur la

stabilité du signal qui nous intéresse. Le rapport signal à bruit s'améliore comme la racine du temps de mesure, caractéristique d'un bruit blanc. Il vaut 50 000 à une seconde, correspondant donc à une limite de résolution de 20 μrad de déphasage en une seconde.

3.2.3 Faisceaux Raman rétro-réfléchis

Génération des faisceaux Raman contra-propageants

Afin d'adresser la distribution en vitesse la plus large possible, les faisceaux lasers Raman sont rendus fortement elliptiques (rapport d'aspect de 10). En effet, en réduisant la taille des faisceaux lasers Raman dans la direction horizontale, l'intensité augmente de façon proportionnelle à la réduction de la durée des impulsions (temps de transit dans les faisceaux). La taille dans la direction horizontale est de 400 μm (rayon à 1/e^2 en intensité) pour environ 5 mm dans la direction verticale. De plus, le système optique a été conçu pour imager le col du faisceau au niveau de l'interaction avec les atomes pour les trois impulsions simultanément. La rétro-réflexion des faisceaux lasers Raman est réalisée de façon à imager le col de faisceau en retour à nouveau au niveau des jets atomiques (voir figure 3.7).

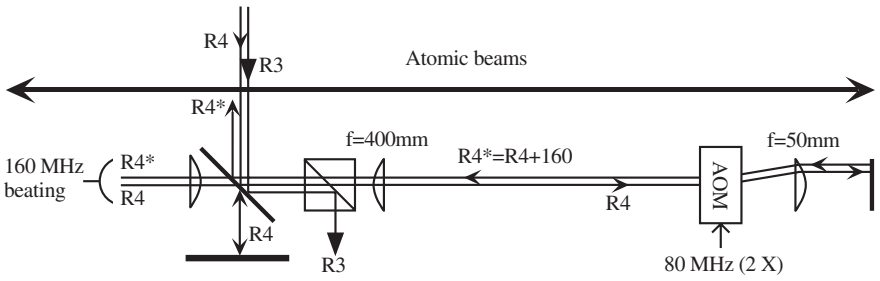

FIG. 3.7 : *Schéma de principe de l'optique de rétro-réflection de chaque paire de faisceaux lasers Raman.*

Un modulateur acousto-optique (MAO) est positionné sur le trajet et permet de décaler la fréquence du faisceau réfléchi de 160 MHz, permettant de garantir que seule une transition contra-propageante est résonante. Pour éviter des fluctuations de phases dues à des changements de longueur optique (effets thermiques dans les modulateurs acousto-optique, mouvements d'air...), un asservissement de cette longueur optique est réalisé en utilisant le battement à 160 MHz entre le faisceau réfléchi par le miroir de référence et celui réfléchi à travers le modulateur acousto-optique. Le signal est comparé à une référence à 80 MHz et la boucle de rétro-action agit sur la fréquence de pilotage du MAO.

Ce système permet de changer facilement la phase ou la fréquence de chaque faisceau laser Raman indépendamment des deux autres faisceaux. La figure 3.8 présente la probabilité de transition entre les niveaux $F = 3$ et $F = 4$ en fonction du désaccord Raman pour la seule paire de faisceau centrale réalisant l'impulsion π. Les sept pics correspondent aux sept transitions magnétiques possibles ($\Delta m = 0$) et sont séparés par effet Zeeman grâce à l'utilisation d'un champ magnétique de biais.

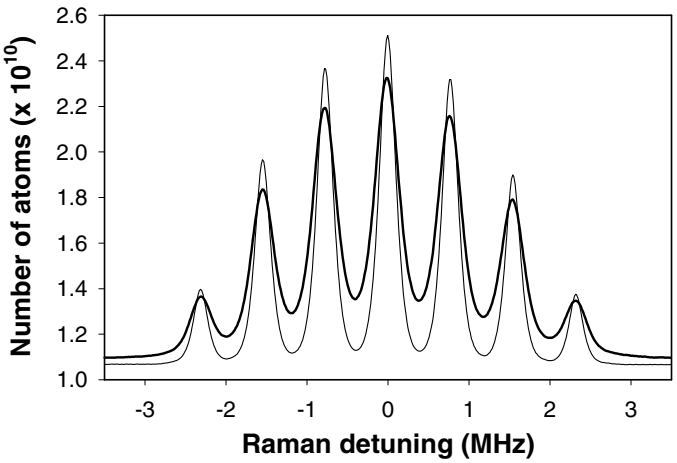

FIG. 3.8 : *Flux d'atomes transférés en fonction du désaccord Raman pour une transition π contra-propageante. Les deux courbes correspondent aux deux jets.*

Génération électronique des rotations et modulations

Le choix d'un système de rétro-réflexion relativement complexe, avec la présence du MAO, a été guidé par la possibilité de compenser de façon électronique les rotations. En effet, dans le référentiel des atomes, la rotation autour de la position de l'impulsion π apparaît comme un décalage de fréquence au niveau des impulsions $\pi/2$ de :

$$\delta = \pm k_{eff} \Omega L$$

où L est la distance entre deux impulsions successives. Comme montré sur la figure 3.9, le signe du désaccord dépend de la transition $\pi/2$ considérée.

Il est donc possible de simuler, au premier ordre, la rotation par des décalages opposés des désaccords Raman pour les deux impulsions $\pi/2$. Ceci est rendu possible grâce à l'utilisation de MAO dans le système de rétro-réflexion (voir figure 3.7) Il est important de noter que la rotation simulée ne dépend que de la distance entre les paires de faisceaux Raman et du vecteur d'onde de la transition, mais pas de la vitesse des atomes. Cela se traduit par le fait que la

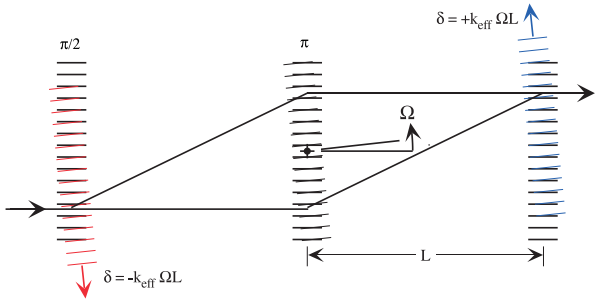

FIG. 3.9 : *Dans un référentiel inertiel, la rotation apparaît comme un décalage de fréquence de signes opposés pour les deux impulsions $\pi/2$*

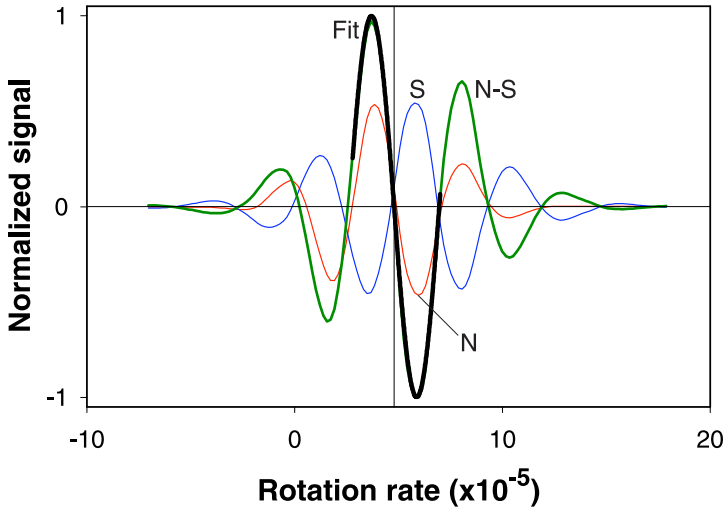

FIG. 3.10 : *Interférogramme obtenu en simulant de façon électronique la rotation. Les courbes rouge et bleue correspondent respectivement aux signaux issus des jets notés nord et sud. La courbe verte correspond à la différence des deux signaux, indépendante de l'accélération. Le zéro de rotation correspond à la projection de la rotation de la terre sur la verticale locale, qui vaut 4,8 10^{-5} rad.s^{-1} à l'université de Yale.*

rotation simulée est identique pour les deux interféromètres. Deuxièmement, si le décalage de fréquence est choisi pour compenser la rotation vue par l'interféromètre ($\delta = 108,8Hz$ pour l'expérience à l'université de Yale avec une distance L = 96,842 cm), il induit une compensation pour l'ensemble de la distribution de vitesse. Ce n'est pas uniquement un moyen de se placer à déphasage nul, mais également un moyen de se ramener sur la frange centrale, où le contraste est maximal (voir figure 3.10).

De la même façon, en changeant la phase relative entre les deux faisceaux lasers de la paire Raman correspondant à l'impulsion π, il est possible de générer un déphasage identique pour les deux interféromètres et donc par exemple de pouvoir se positionner à flanc de frange simultanément pour les deux interféromètres, là où la sensibilité est maximale. Il est également possible d'utiliser un décalage de fréquence pour moduler le signal de sortie des interféromètres et pouvoir ainsi s'affranchir des fluctuations à basses fréquences du flux ou du contraste des interféromètres. Le rapport signal à bruit obtenu avec ce fonctionnement (modulation à 30 Hz) est de 33 000 sur une seconde, correspondant à une sensibilité à une seconde pour le gyromètre atomique de 6 10^{-10} rad.s^{-1}.

3.2.4 Stabilité

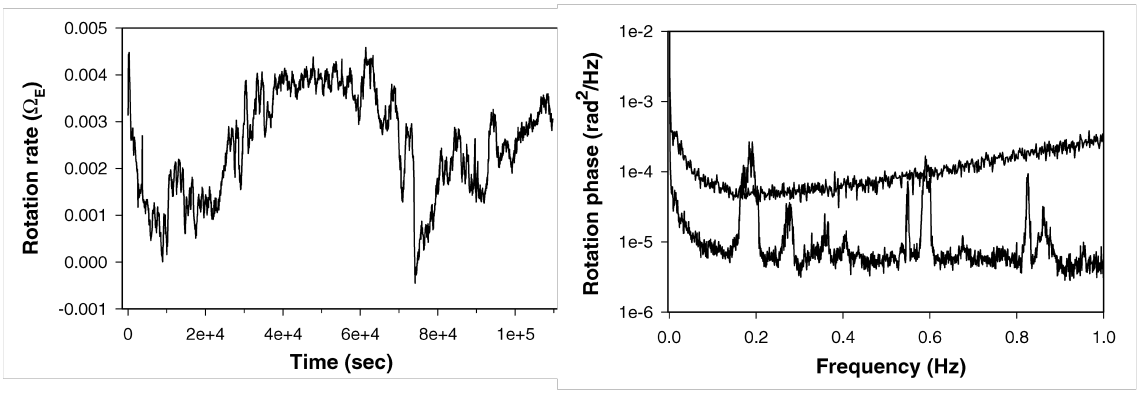

FIG. 3.11 : *A gauche : signal de rotation enregistré en continu, la table optique étant posée directement sur le sol. A droite : l'analyse spectrale du signal de gauche correspond à la courbe la plus basse, l'autre correspond au même signal sur la table flottante, qui présente une résonance mécanique à 1,7 Hz non visible sur ce graphique.*

Les mesures long terme sont effectuées en modulant la phase des interféromètres à une fréquence typique de modulation de 3,2 Hz et en asservissant la phase des faisceaux Raman de l'impulsion π afin de rester en permanence autour d'un déphasage équivalent d'accélération nul pour garder une sensibilité maximale (ce déphasage contient un terme arbitraire dû à la position relative des trois miroirs de référence). Les signaux des deux interféromètres sont donc modulés en phase, permettant de maximiser la réjection des bruits de phase ou de vibration parasites à hautes fréquences. Les fluctuations de vitesse de rotation n'ont pas besoin d'être asservies car elles restent très petites devant la dynamique de l'appareil, mais pourraient l'être également dans le cadre d'applications à la navigation par exemple. Le déphasage de

rotation est extrait par ajustement des modulations des deux interféromètre par une sinusoïde de fréquence 3,2 Hz.

Cette méthode de démodulation ajoute un bruit d'échantillonnage sur les mesures de rotation qui dégradent les performances de près d'un ordre de grandeur sur les temps courts (à 1 seconde). La stabilité de la mesure de rotation s'améliore ensuite comme la racine carrée du temps de mesure jusqu'à environ 100 secondes pour atteindre environ 2.10^{-9} rad.s^{-1}. Différentes sources de bruit ont été étudiées et peuvent expliquer la dérive du signal de rotation sur les temps longs. La principale concerne une variation de la distance entre les trois paires de faisceaux lasers Raman. Si les deux distances L ne sont plus identiques, il apparaît des biais de signes opposés sur les deux interféromètres, conduisant à un biais sur le signal de rotation. La plupart de ces sources de dérive disparaissent par contre en alternant des mesures avec des vecteurs d'onde opposés. C'est ce qui a été mis en place par la suite [Durfee 2006]. Cette méthode a effectivement permis de réduire les dérives sur les temps assez longs (10^3 à 10^4s).

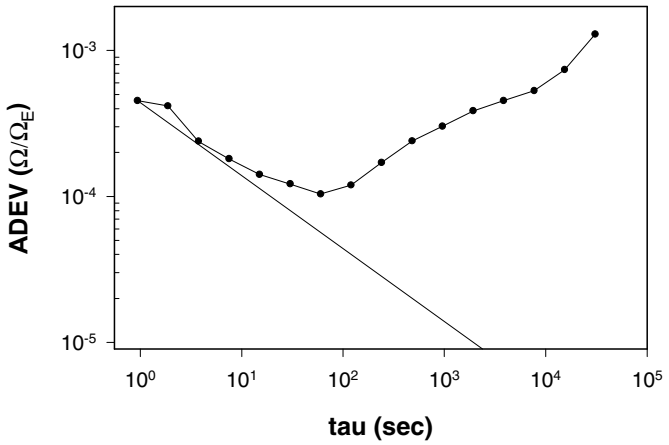

FIG. 3.12 : *Ecart type d'Allan correspondant au signal de la figure 3.11.*

3.3 Le Gyromètre-Accéléromètre à atomes froids

3.3.1 Description générale : capteur inertiel 6 axes

L'une des applications les plus prometteuses pour les gyromètres atomiques est leur utilisation à la navigation inertielle. Ce type d'application nécessite une très bonne stabilité sur des temps longs, et l'utilisation d'atomes froids est à priori favorable à un meilleur contrôle du facteur d'échelle et des effets systématiques : des trajectoires atomiques, via le contrôle de

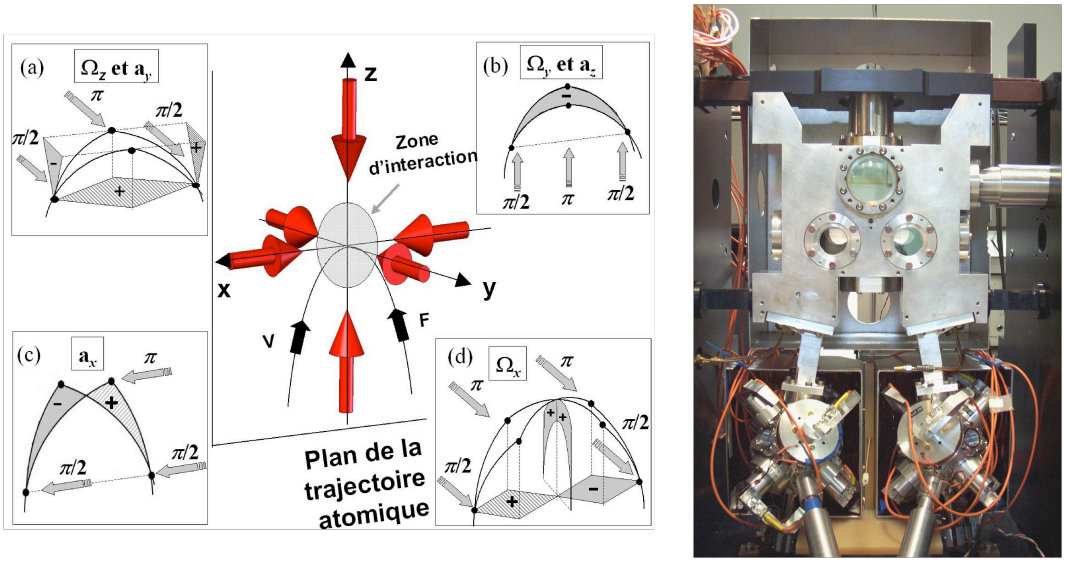

FIG. 3.13 : *A droite, photographie de l'enceinte à vide du gyromètre-accéléromètre (taille du blindage 50x30 cm). A gauche, schéma de principe montrant la possibilité de mesurer l'ensemble des six axes d'inertie sur le même appareil.*

fréquence lors de la phase de lancement, et surtout du temps d'interrogation puisque l'expérience est séquentielle (contrôle de la durée des impulsions et du temps entre impulsions). Ce raisonnement est identique à celui qui a conduit à la réalisation d'horloges à atomes froids, et particulier des fontaines atomiques. De plus, pour ce type d'application, il est nécessaire de pouvoir mesurer l'ensemble des axes d'inerties (trois composantes de rotation et trois composantes d'accélération). Enfin, il est nécessaire de réaliser un interféromètre de taille réduite.

L'utilisation d'atomes froids permet d'obtenir une vitesse moyenne très faible des atomes et donc une trajectoire très courbée permettant d'appliquer les faisceaux Raman dans trois directions de l'espace. Cette possibilité permet d'orienter un faisceau laser suivant la direction de la vitesse moyenne des atomes (axe x de la figure 3.13). Enfin, compte-tenu de la taille relativement faible de l'interféromètre (3 cm), il est possible d'utiliser un faisceau unique pour générer les trois impulsions lasers en l'allumant et l'éteignant successivement trois fois. L'utilisation d'une paire de faisceaux Raman unique garantit l'absence de fluctuation relative d'angle entre la première et la dernière impulsion. Les configurations a), b) et c) utilisent une séquence habituelle à trois impulsions lasers ($\pi/2 - \pi - \pi/2$) donnant accès à l'accélération suivant la direction de propagation des faisceaux lasers Raman (eq. 2.20) et à la rotation dans la direction normale à l'aire orientée (eq. 2.18) :

$$\Delta\Phi = \mathbf{k_{eff}}.\mathbf{a}T^2 - 2(\mathbf{k_{eff}} \times \mathbf{v}).\mathbf{\Omega}T^2. \tag{3.7}$$

Dans le cas c), l'aire physique est nulle et l'interféromètre n'est sensible qu'aux accélérations. La dernière composante de rotation (autour de x) n'est pas accessible avec ce type de séquence temporelle car elle est parallèle à la direction moyenne de propagation des atomes. A l'aide d'une séquence à quatre impulsions comme décrite dans d) (séquence $\pi/2-\pi-\pi-\pi/2$), il est par contre possible d'utiliser l'effet de l'accélération de la gravité, qui replie les trajectoires atomiques, pour apporter une sensibilité aux rotations suivant l'axe x, sans être sensible à une accélération continue si ce n'est à travers le facteur d'échelle. Les deux demi-interféromètres ont des aires dont les projections sur le plan vertical s'annulent mais s'ajoutent sur le plan horizontal [Canuel 2006] :

$$\Delta\Phi = \frac{1}{2}(\mathbf{k_{eff}} \times \mathbf{g}).\mathbf{\Omega} T^3. \tag{3.8}$$

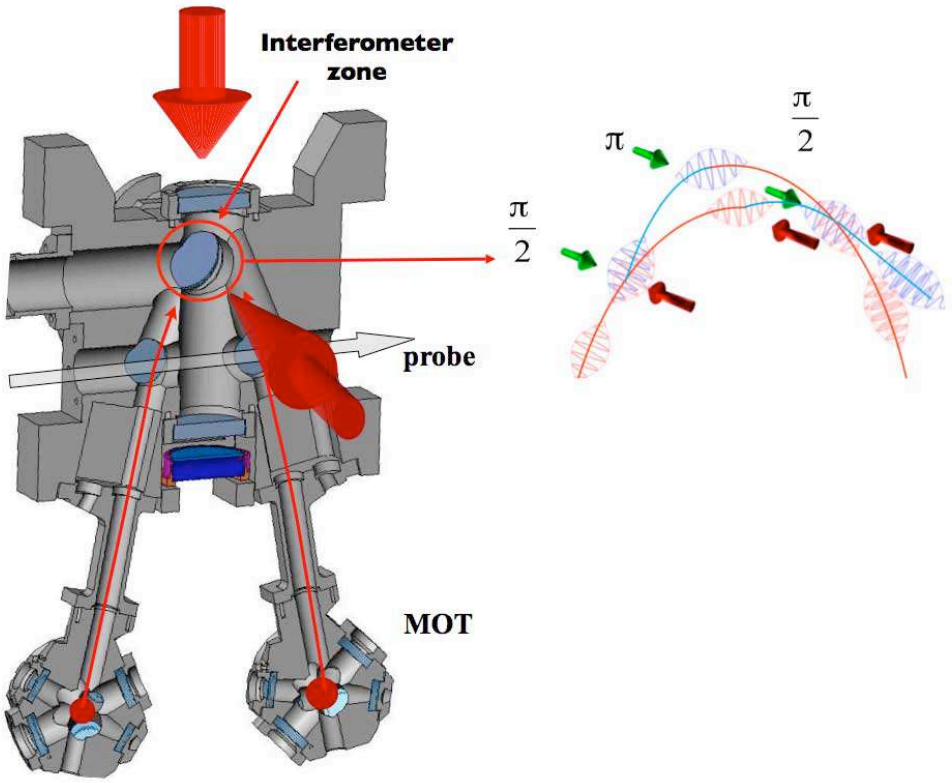

FIG. 3.14 : *Schéma du gyromètre à atomes froids. Les deux nuages d'atomes de césium froids sont produits par deux pièges magnéto-optiques et lancés suivant des trajectoires paraboliques. L'interféromètre est réalisé à l'apogée de la trajectoire, où les faisceaux lasers Raman (orientés suivant la direction x ou z) peuvent réaliser l'interféromètre.*

Les sources atomiques sont réalisées par deux pièges magnéto-optiques de césium chargés à partir d'une vapeur pendant typiquement 140 ms. Puis, ils sont lancés à l'aide d'une méthode de mélasse mouvante à une vitesse de 2,4 m.s^{-1} avec un angle de 8° par rapport à la verticale, conduisant à une vitesse horizontale de 0,33 m.s^{-1}. Les atomes sont alors refroidis dans le référentiel en mouvement à une température d'environ 1,2 μK puis pompés dans le niveau hyperfin F = 4. Les atomes passent dans une cavité micro-onde qui transfert ceux, initialement dans F = 4, m_F = 0, dans l'état F = 3, m_F = 0. Un faisceau pousseur permet alors d'éliminer tous les atomes restés dans F = 4. Les atomes entrent ensuite dans la zone interférométrique où il est possible de faire varier le temps d'interrogation de zéro à 2T = 80 ms de manière continue grâce à l'utilisation du faisceau laser unique. Les atomes retombent alors vers la zone de détection où la mesure de la probabilité de transition est réalisée par fluorescence à travers deux sondes, permettant une normalisation à chaque coup (temps de cycle 580 ms).

3.3.2 Caractérisation des sources atomiques

La mesure du nombre d'atomes peut être réalisée par absorption dans la sonde de détection et donne typiquement 10^6 atomes détectés dans la sonde dans m_F = 0 avec un temps de chargement des pièges de 140 ms.

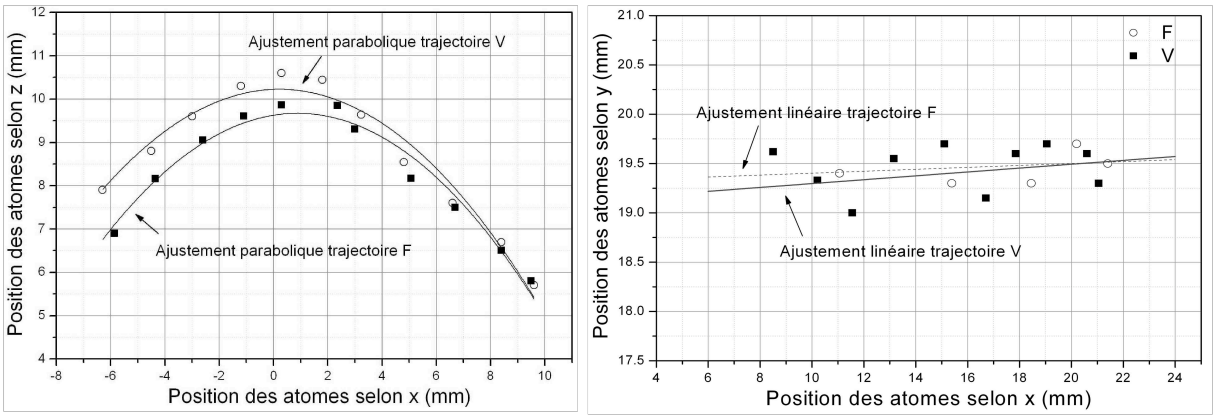

FIG. 3.15 : *Trajectoires des deux nuages d'atomes au niveau de la zone interférométrique pour les deux nuages issus des sources F et V : à gauche dans le plan vertical (OXZ) et à droite dans le plan horizontal (OXY).*

Bien que les interféromètres ne soient pas intrinsèquement sensibles à la position et à la vitesse initiale des atomes, nous verrons par la suite que les causes principales de biais et de dérives sont liées aux erreurs de trajectoire. En effet, les défauts de front d'onde des faisceaux Raman ne pouvant être distingués des accélérations, il apparaît un biais sur le signal

de rotation si les trajectoires des deux nuages ne se superposent pas parfaitement. La mesure des trajectoires des nuages au niveau de la zone interférométrique est présentée sur la figure 3.15. Nous observons que les trajectoires ne sont pas parfaitement superposées dans le plan vertical (écart inférieur à 1 mm), mais que dans le plan horizontal les différences de trajectoire ne sont pas résolues (<0,5 mm).

Si un défaut de trajectoire engendre un biais sur le signal de rotation dû aux défauts de front d'onde, une fluctuation relative des trajectoires se traduit par une variation de ce biais. De même si les trajectoires ne sont pas parfaitement superposées et que les défauts de front d'onde changent. Ce problème a été envisagé avant l'obtention des premiers signaux et une première étude sur l'influence de la stabilité en position du piège est présentée dans [Fils thèse] et [Fils 2005] (reproduit au chapitre 3.5).

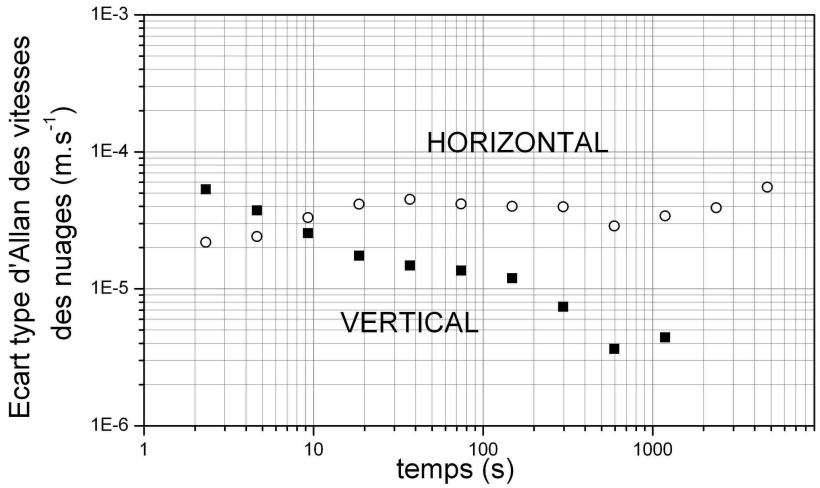

FIG. 3.16 : *Stabilité des vitesses d'un des nuages suivant les directions horizontale ou verticale.*

Le critère important est la fluctuation de la position des atomes au moment de chacune des trois impulsions (paragraphe 2.2.3), qui peut être due aux fluctuations de position initiale du nuage avant lancement ou aux fluctuations de vitesse initiale, le décalage s'accumulant alors d'autant plus que le temps de vol est grand. Des études plus approfondies ont été menées à la fois sur le gyromètre [Canuel thèse] et sur le gravimètre [Le Gouët thèse]. Elles ont clairement montré que les fluctuations en vitesses sont indépendantes de la vitesse de lancement (comparaison gyromètre et gravimètre d'une part et gyromètre dans la direction verticale et horizontale d'autre part), mais sont sans doute liées à l'utilisation de mélasses de type σ^+/σ^-, les mélasses de type "linéaire/linéaire orthogonale" étant moins sensibles. Nous avons également identifié qu'elles sont dues aux fluctuations de polarisation dans les fibres à maintien de polarisation utilisées pour transporter les faisceaux du banc laser au piège. Nous avons ob-

servé une sensibilité de la vitesse de lancement de 36 μm.s^{-1} par % de défaut de polarisation. L'utilisation d'un polariseur en sortie de fibre ne fait qu'accentuer le problème, sauf si on asservit les puissances des six faisceaux pièges. Les stabilités des vitesses moyennes d'un des nuages, représentées sur la figure 3.16, ont été obtenues en utilisant les transitions Raman. Par ailleurs, nous avons mesuré, dans le gyromètre, une dépendance des fluctuations de position à la fin de la phase de mélasse avec le rapport de puissance des trois faisceaux pièges du haut par rapport aux trois faisceaux du bas de 50 μm par %. Cette mesure correspond au cas ou les variations de puissance sont réalisées simultanément entre les trois faisceaux du haut et les aux trois faisceaux du bas. Ce décalage apparaît pendant la phase de lancement uniquement, pendant que les faisceaux hauts et bas ne sont plus équilibrés en puissance.

3.3.3 Sensibilité aux forces d'inertie

Acquisition des signaux

Pour réaliser un interférogramme, il est possible d'utiliser la dépendance du déphasage en sortie de l'interféromètre avec la différence de phase entre les faisceaux lasers Raman. En changeant la différence de phase entre la seconde et la troisième impulsion, nous ajoutons un terme de phase aux deux interféromètres simultanément. L'interférogramme est ensuite balayé en variant la valeur de ce saut de phase d'une mesure à la suivante (voir fig. 3.17).

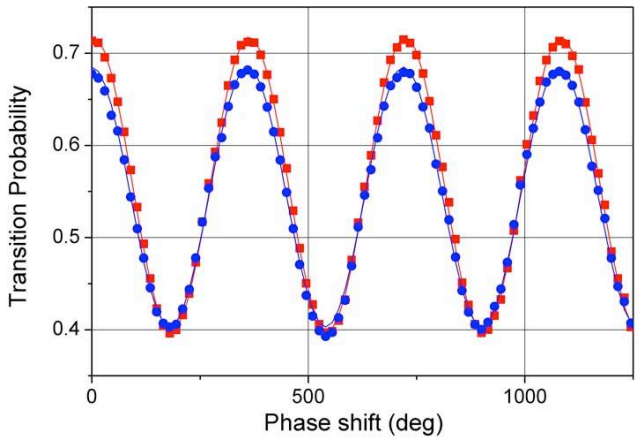

FIG. 3.17 : *Franges d'interférences obtenues dans la configuration avec les faisceaux Raman verticaux et pour le temps d'interrogation maximal de 80 ms. Les carrés rouges et les points bleus correspondent respectivement aux deux différents interféromètres.*

Pour enregistrer les signaux d'accélération et de rotation avec la meilleure sensibilité, nous ajustons le saut de phase pour être approximativement aux flancs des franges d'interférences. Une séquence temporelle, alternant à la fois des mesures sur les deux flancs de la même frange d'interférence et des mesures avec des vecteurs d'ondes orientés de façon opposés, permet de s'affranchir des dérives de contraste et des effets systématiques liés uniquement aux états internes (effet Zeeman, déplacement lumineux...). La figure 3.18 représente les signaux d'accélération et de rotation pendant une période de 34 heures consécutives. Nous observons nettement les variations des signaux dus aux marées sur le signal d'accélération.

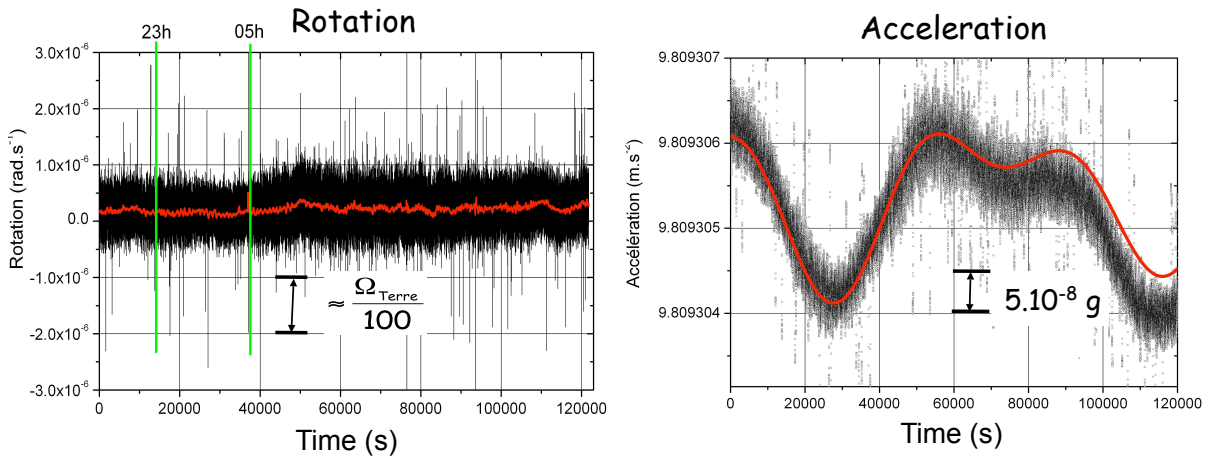

FIG. 3.18 : *Signaux de rotation et d'accélération en fonction du temps. Les données ne sont pas moyennées et correspondent à un temps d'interrogation 2T = 80 ms et une durée de cycle de 580 ms. Les barres verticales vertes schématisent la fin et le début du service du métro et du RER, à 23 h et 05 h.*

Stabilité

Une autre façon de présenter les résultats est d'utiliser l'écart-type d'Allan des signaux d'accélération et de rotation qui donne la sensibilité, c'est-à- dire la plus petite variation mesurable en fonction du temps de mesure (voir figure 3.19). La stabilité des mesures de rotation est de $2{,}4.10^{-7}$ rad.s^{-1} sur une seconde et s'améliore comme la racine carrée du temps de mesure jusqu'à environ 1000 s où elle atteint une stabilité de 10^{-8} rad.s^{-1}. Pour les accélérations, la stabilité à une seconde est de $5{,}5.10^{-7}$ m.s^{-2} et s'améliore pour atteindre typiquement 10^{-8} m.s^{-2} à 2000 s.

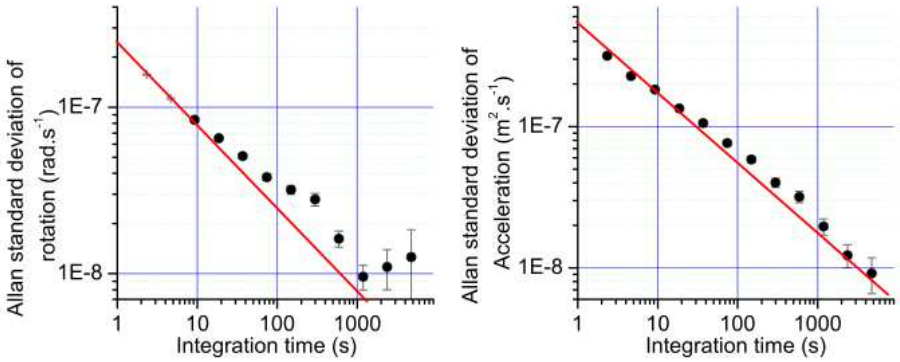

FIG. 3.19 : *Ecart-type d'Allan des signaux de rotation (à gauche) et d'accélération (à droite) correspondant aux données temporelles de la figure 3.18.*

Limites à la stabilité à court terme

La limite à la stabilité à court-terme de la mesure d'accélération s'explique très bien par les vibrations parasites résiduelles sur la plateforme d'isolation passive. Nous verrons que les résultats sont sensiblement meilleurs avec le gravimètre, bien qu'ils soient limités par les mêmes causes. La différence s'explique par un temps d'interrogation plus court sur le gyromètre-accéléromètre et une fréquence de cycle réduite. La stabilité à court-terme de la mesure de rotation s'explique par le bruit de détection, et plus particulièrement par le bruit de projection quantique dû au nombre fini d'atomes détectés [Santarelli 1999].

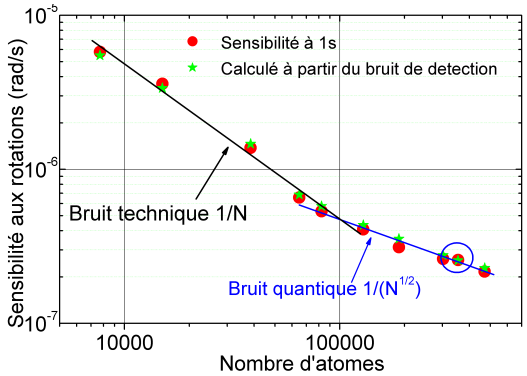

FIG. 3.20 : *Limite de la sensibilité aux rotations sur une seconde en fonction du nombre d'atomes. Les ronds rouges correspondent aux mesures interférométriques et les étoiles vertes à la limite calculée à partir du bruit de détection seul. Le cercle bleu indique les conditions expérimentales habituelles.*

Pour déterminer la limite due à la détection, nous avons mesuré son bruit en fonction du nombre d'atomes (voir figure 3.20). La première mesure a été réalisée dans les conditions d'une transition π contra-propageante donnant lieu à un taux de transition d'environ 50%, et la seconde correspond au signal de rotation. Les signaux issus des deux mesures ont ensuite été traités de façon similaire à ceux issus des interféromètres (normalisation par le contraste des interféromètres, demi-différence pour obtenir le signal de rotation). Le très bon accord, sur l'ensemble de la gamme de valeur, illustre clairement que les mesures de rotation sont effectivement limitées par la détection. De plus, pour un nombre élevé d'atomes, la variation du rapport signal à bruit est en $1/N^{1/2}$, caractéristique du bruit de projection quantique.

Dans le cas général de deux sources atomiques aillant un nombre différent d'atomes, respectivement N_F et N_V, mais un contraste identique C, la limite, sur le signal de rotation ou d'accélération, due au bruit de projection quantique peut s'exprimer simplement en fonction du nombre déduit d'atomes $N = \frac{N_F N_V}{N_F+N_V}$ et vaut :

$$\sigma_\Phi = \frac{1}{4C\sqrt{N}} \tag{3.9}$$

Pour les paramètres typiques de l'expérience : un nombre d'atomes $N_V \simeq N_F = 3,5.10^5$ et un contraste $C = 30\%$, le bruit de détection équivalent est de 5,5 mrad par coup, limitant la stabilité sur le signal de rotation à 2,4.10^{-7} rad.s^{-1} sur une seconde.

Limites à la stabilité à long terme

La stabilité à long terme s'explique par la dérive des biais liés aux défauts de front d'onde. Nous avons étudié différentes sources de biais et de dérives (effet Zeeman, déplacement lumineux à un et deux photons...) dont il est possible de trouver les détails dans [Gauguet thèse, Gauguet 2009]. Seul l'effet des fluctuations de trajectoires couplées aux défauts de front d'onde des faisceaux Raman peut expliquer ces dérives. Pour quantifier l'impact de cet effet, nous avons déplacé volontairement les positions relatives des deux nuages d'atomes au niveaux de la zone interférométrique. Nous avons simplement décalé (avancé ou retardé) la séquence temporelle, conduisant à un déplacement relatif de $\pm 400\mu m$ suivant la direction x (voir Fig. 3.21).

La pente correspond à une variation du déphasage de rotation de 1,1.10^{-9}rad.s^{-1}/μm. Les fluctuations typiques de positions initiales des sources atomiques et des vitesses des nuages (40 μm.s^{-1} à 1000 s, voir figure 3.16) peuvent toutes les deux donner lieu à des fluctuations en position de l'ordre de 10 μm après un temps de vol jusqu'à l'interféromètre d'environ 250 ms, et donc expliquer les dérives du signal de rotation au niveau de 10^{-8} rad.s^{-1}.

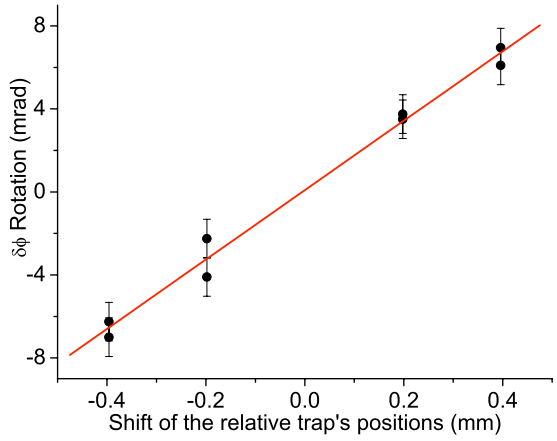

FIG. 3.21 : *Variation du déphasage de rotation en fonction du décalage des sources atomiques suivant la direction horizontale.*

3.3.4 Facteur d'échelle et biais : mesure de la rotation de la terre

L'utilisation d'un gyromètre atomique nécessite de connaître très précisément la valeur du biais mais également le facteur d'échelle, ces deux quantités étant nécessaires pour déduire la valeur de la vitesse de rotation à partir du déphasage atomique. Ces mesures peuvent être réalisées simplement dans le cas d'un gyromètre d'axe d'entré horizontal. En effet, il suffit de tourner l'ensemble de l'expérience autour de l'axe vertical pour faire varier la projection de la vitesse de rotation de la Terre sur l'axe d'entrée du gyromètre. La figure 3.22 montre les variations du déphasage de rotation en fonction de l'orientation de l'axe d'entrée du gyromètre par rapport à la direction pointant vers l'ouest. L'ajustement des points expérimentaux par une sinusoïde de période 360° connue permet d'en déduire d'un part le biais 28,3 mrad $\pm$ 0,7 mrad correspondant à une vitesse de rotation de 1,87.10^{-6} rad.s^{-1} et à un facteur d'échelle de 15124 $\pm$ 12 rad /(rad.s^{-1}). L'analyse des données en fonction de la vitesse de rotation (linéarisation de l'axe X) montre une très bonne linéarité, avec un terme quadratique inférieur à 10^{-5} du facteur d'échelle dans la gamme de vitesses de rotation explorées.

Compte tenu de la très bonne linéarité du capteur, il est possible de déterminer le biais et le facteur d'échelle uniquement à partir des données à $\pm 90°$ (le biais sur la demi-somme et le facteur d'échelle à partir de la demi-différence). La figure 3.23 présente les variations du facteur d'échelle et du biais, issus de la différence des signaux à $\pm 90°$, en fonction de la durée T entre deux impulsions Raman successives.

Nous constatons un excellent accord avec la variation en T^2 attendue (à mieux que 10^{-4}). Le biais augmente rapidement pour les temps d'interrogations élevés, ce qui peut s'expliquer

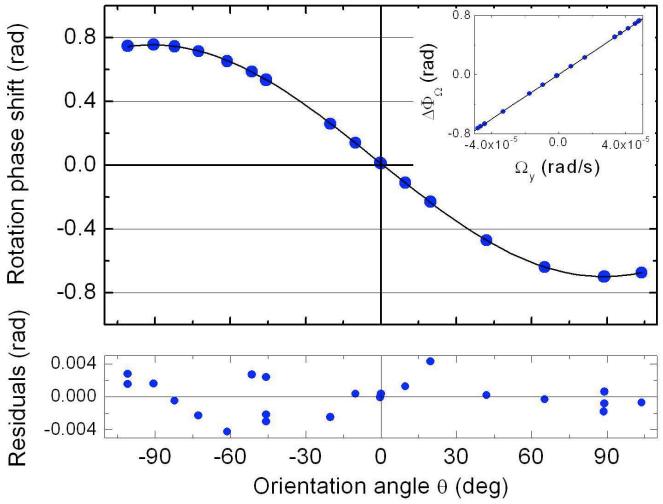

FIG. 3.22 : *Variation du déphasage de rotation en fonction de l'orientation de l'axe d'entrée du gyromètre dans le plan horizontal et par rapport à la direction ouest. La courbe correspond à un ajustement par une fonction sinusoïdale. Le résidu de l'ajustement est tracé sur le graphe du bas. L'encart correspond aux mêmes données pour lesquelles l'axe horizontal est linéarisé.*

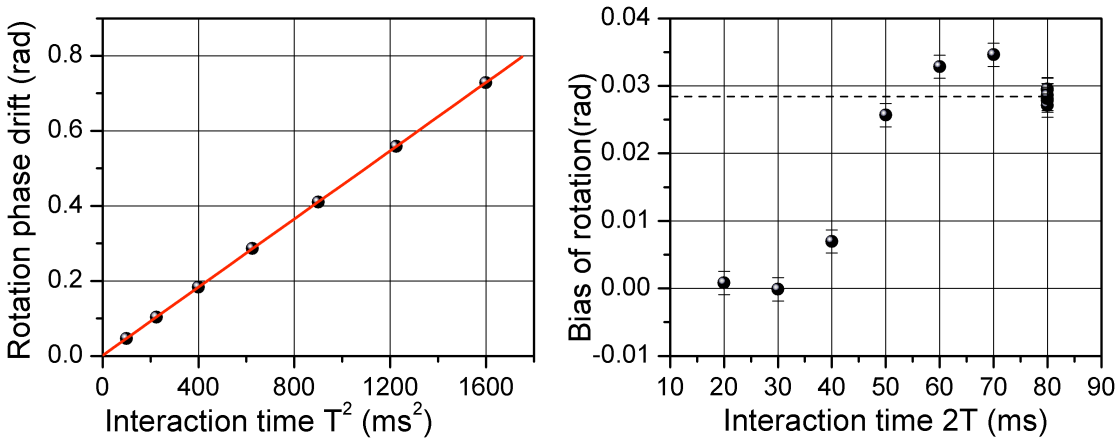

FIG. 3.23 : *Variation du facteur d'échelle (gauche) et du biais (droite) en fonction de la durée T entre deux impulsions successives.*

par la présence d'aberrations optiques plus importantes sur les bords des faisceaux Raman, liées aux contraintes mécaniques sur les bords des hublots, de la lame $\lambda/4$ ou du miroir de rétro-réflexion [Fils thèse].

3.3.5 Interféromètre à quatre impulsions : mesures de la rotation avec une seule source atomique

Il est possible d'avoir accès aux composantes de rotation suivant une direction horizontale en utilisant une nouvelle configuration à quatre impulsions $\pi/2 - \pi - \pi - \pi/2$ à l'aide de faisceaux horizontaux [Yver Leduc thèse, Canuel 2006], séparées respectivement d'un intervalle de temps T/2, T et T/2. En tirant profit de l'accélération de la gravité qui replie les trajectoires atomiques, cette configuration à quatre impulsions devient sensible à la composante de rotation horizontale et orthogonale à la direction des lasers Raman. L'interféromètre a alors une forme en aile de papillon dans lequel les deux demi-interféromètres ont des aires orientées dont les projections sur le plan horizontal s'annulent alors qu'elles s'ajoutent sur le plan vertical (voir figure 3.13) :

$$\Delta\Phi = \frac{1}{2}(\mathbf{k} \times \mathbf{g}).\Omega \mathrm{T}^3. \tag{3.10}$$

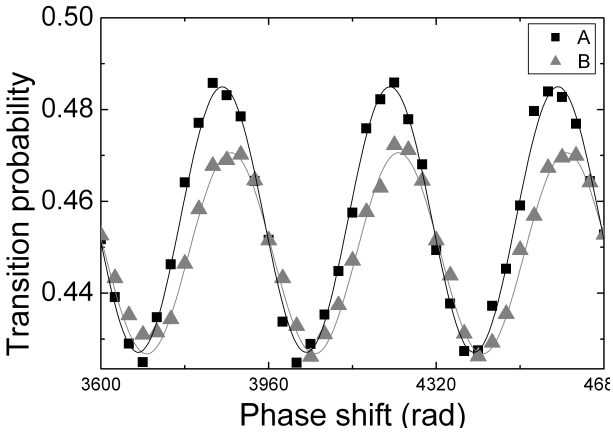

FIG. 3.24 : *Interférogrammes obtenus dans la configuration à quatre impulsions lasers pour un temps total d'interrogation de 60 ms.*

Il est important de noter que la dépendance du facteur d'échelle avec la vitesse initiale des atomes est remplacée par le changement de vitesse moyenne entre le premier et le deuxième demi-interféromètre, c'est à dire le produit de l'accélération due à la gravité g par la durée T. La figure 3.24 montre les interférogrammes obtenus pour les deux sources atomiques pour un temps d'interrogation total 2T= 60 ms.

Dans cette configuration les interféromètres sont insensibles à l'accélération continue, sauf à travers le facteur d'échelle. En effet, les deux demi-interféromètres ont une sensibilité opposée pour l'accélération, pour les fréquences petites devant 1/T. Il n'est donc pas nécessaire de disposer de deux sources atomiques mais d'une seule.

3.4 Conclusion

Il est intéressant de constater que ces deux gyromètres, bien qu'utilisant des sources de vitesse très différentes et des modes de fonctionnement différents (spatial ou temporel), donnent finalement des performances très proches sur le long terme (respectivement 5.10^{-9} et 10^{-8} rad.s^{-1}). L'expérience sur jet a l'avantage d'être plus simple à réaliser et permet de limiter les effets d'échantillonnages sur la mesure de la rotation, qui peuvent empêcher son utilisation à certaines applications, et notamment en navigation inertielle. Dans le cas du gyromètre à atome froids, les performances peuvent être notablement améliorées. En effet, les limites à la stabilité, que ce soit à court ou à long terme, sont clairement identifiées, ne sont pas fondamentales, et peuvent donc être réduites [Gauguet 2009]. Les défauts de front d'onde peuvent premièrement être réduits par plus d'un ordre de grandeur (notamment ceux dus aux hublots). De plus, l'aire de l'interféromètre, et donc sa sensibilité aux rotations, peut être augmentée notablement, diminuant d'autant les biais en terme de rotation. Les problèmes liés aux défauts de fronts d'onde existent de la même façon pour les interféromètres à jets et peuvent expliquer les dérives à long terme observées dans le gyromètre à jets atomiques et qui ne sont pas clairement expliquées [Durfee 2006].

Plusieurs directions doivent permettre d'améliorer de manière significative les performances d'un gyromètre à atomes froids. La première consiste à augmenter la vitesse longitudinale des atomes en utilisant des trajectoires plus tendues et en gardant des temps de vol similaires à ceux de la première expérience. Une augmentation d'un ordre de grandeur (vitesse horizontale de l'ordre de 3 m.s^{-1}) peut être réalisée avec les mêmes méthodes de préparation des sources atomiques et permet de gagner autant sur l'aire de l'interféromètre. Une contrainte supplémentaire vient de la nécessité de réaliser trois paires de faisceaux lasers séparées spatialement et donc de contrôler très précisément leurs directions relatives. Cette voie est suivie par l'équipe de E. Rasel à l'université d'Hanovre [Müller 2009].

La seconde voie consiste à utiliser la nouvelle configuration à quatre impulsions. A l'aide d'une configuration en fontaine, il est alors possible d'augmenter de manière drastique l'aire de l'interféromètre ($\times$ 300) : jusqu'à 11 cm^2 pour un temps d'interrogation de 800 ms, tout en gardant une taille totale de l'interféromètre raisonnable (< 1 m) et en n'utilisant qu'une seule source d'atomes. Comme pour la première solution, il est possible d'augmenter la sensibilité en améliorant la stabilité à long terme puisque l'augmentation de la sensibilité est plus rapide que l'augmentation des biais liés aux fluctuations de trajectoires et aux fronts d'onde.

Une dernière voie n'a pas été explorée pour l'instant et pourrait donner lieu à un compromis intéressant en terme de sensibilité et de simplicité par rapport aux deux "extrêmes" présentés dans ce document. Un gyromètre utilisant deux jets lents (de 10 à 30 m.s^{-1} issus

de MOT et mélasses 2D) peut permettre d'obtenir une aire importante avec un flux d'atomes élevés. Deux difficultés existent néanmoins, d'une part éviter les déplacements lumineux dus à la lumière émise lors du refroidissement (par exemple par un système mécanique comme dans [Füzesi 2007]), et d'autre part réaliser des séparatrices Raman ayant un très grand rapport d'aspect pour limiter la sélectivité en vitesse (hauteur 10 mm pour une largeur inférieure à 100 μm).

3.5 Articles gyromètre

Les deux premiers articles reproduits présentent d'une part l'état d'avancement du gyromètre à jets de Césium collimatés lors de mon départ de l'université de Yale en août 1999 (CQG 2000), et d'autre part la première caractérisation du gyromètre à atomes froids réalisée au SYRTE (PRL 2006). Le dernier présente le problème des défauts de fronts d'onde à la mesure des vitesses de rotation (EPJD 2005).

Class. Quantum Grav. **17** (2000) 2385–2398. Printed in the UK PII: S0264-9381(00)50380-3

Rotation sensing with a dual atom-interferometer Sagnac gyroscope

T L Gustavson†, A Landragin‡ and M A Kasevich
Physics Department, Yale University, PO Box 208120, New Haven, CT 06520-8120, USA

Received 24 March 2000

Abstract. We reports improvements to our Sagnac effect matter-wave interferometer gyroscope. This device now has a short-term rotation-rate sensitivity of 6×10^{-10} rad s^{-1} over 1 s of integration, which is the best publicly reported value to date. Stimulated Raman transitions are used to coherently manipulate atoms from counterpropagating thermal beams, forming two interferometers with opposite rotation phase shifts, allowing rotation to be distinguished from acceleration and laser arbitrary phase. Furthermore, electronically compensating the rotation-induced Doppler shifts of the Raman lasers allows operation at an effective zero rotation rate, improving sensitivity and facilitating sensitive lock-in detection readout techniques. Long-term stability is promising but not yet fully characterized. Potential applications include inertial navigation, geophysical studies and tests of general relativity.

PACS numbers: 0375D, 0630G, 3280L, 3920, 4250V

(Some figures in this article appear in colour in the electronic version; see `www.iop.org`)

1. Introduction

Gyroscopes based on the Sagnac effect measure a rotation rate relative to an inertial reference frame, based on a rotationally induced phase shift between two paths of an interferometer. Sensitive gyroscopes have potential applications in navigation, geophysics and general relativity. This paper presents improvements to our atom-interferometer gyroscope apparatus, including a factor of 30 increase in short-term sensitivity over our previously published work [1], which now exceeds that achieved by other matter-wave gyroscope experiments by a factor of 6000. Other major improvements include implementation of counterpropagating atomic beams and electronic rotation rate compensation. Preliminary studies of long-term stability are also discussed.

Sagnac effect rotation rate sensors have been constructed using light [2], neutrons [3], neutral atoms [1, 4, 5] and electrons [6]. The phase shift for an interferometer rotating at an angular velocity Ω can be written for either photons or massive particles as follows:

$$\Delta\Phi = \frac{4\pi \boldsymbol{\Omega} \cdot \boldsymbol{A}}{\lambda v}. \tag{1}$$

Here v is the velocity of the particle and λ is its wavelength, which for a massive particle is the de Broglie wavelength $\lambda_{\mathrm{dB}} = h/mv$ (h is Planck's constant and m is the mass of the

† Present address: Department of Physics and Research Laboratory of Electronics, Massachusetts Institute of Technology, Cambridge, MA 02139, USA.
‡ Present address: Laboratoire de l'Horloge Atomique, Université Paris XI, Bat. 220, 91405 Orsay Cedex, France.

0264-9381/00/122385+14$30.00

particle). The phase shift depends on the enclosed area $\boldsymbol{A}$ of the loop but is independent of its shape. Comparing atom- and light-based interferometers with the same area, one finds that the intrinsic sensitivity is larger by a factor of $mc^2/\hbar\omega = 6 \times 10^{10}$ for caesium atoms compared with a HeNe laser, motivating the atom-interferometry approach described here. Indeed, since atom interferometers with spatially separated trajectories were first achieved in 1991, atom interferometry has proven to be a useful precision measurement technique. However, the intrinsic sensitivity advantage of the atom-interferometer gyroscope is diminished by the much larger areas currently obtainable with a light-based interferometer. Better beamsplitters are available for light than for atoms, and the effective area can be increased by high finesse mirrors in a ring-laser gyro or multiple fibre turns in a fibre-optic gyro. Nonetheless, the short-term sensitivity of our atom-interferometer gyroscope is now 6×10^{-10} rad s^{-1} Hz$^{-1/2}$ compared with the 1.3×10^{-9} rad s^{-1} Hz$^{-1/2}$ sensitivity reported for a 1 m^2 ring laser gyroscope [2, 7]. Eventually, advances in atom optics are likely to result in much larger enclosed areas for atom interferometers.

1.1. Outline

The remainder of this paper is organized as follows. Section 2 describes some of the primary applications for high-performance gyroscopes, and section 3 describes the gyroscope interferometer configuration and experimental apparatus used. Section 4 outlines the procedure for calculating interferometer phase shifts, explains the advantages of counterpropagating atomic beams and discusses electronic methods for modulating the effective rotation rate. Synchronous detection techniques and their application to absolute rotation measurements are also discussed. Section 5 characterizes the performance of the apparatus. It describes short-term sensitivity and signal-to-noise ratio, systematic errors (and reduction thereof), and preliminary long-term stability results. Finally, section 6 gives a summary and discusses possible plans for the future.

2. Applications

One application for sensitive gyroscopes is inertial navigation, which is the determination of the current position relative to a known starting point through the continual monitoring of angular orientation and accelerations without referring to external landmarks. Accurate gyroscopes and accelerometers are required because small measurement errors can quickly become large position errors. Inertial navigation systems can be used to supplement the global positioning system (GPS) as well as for applications for which GPS is impractical (for example, due to poor satellite visibility).

Geophysicists are interested in precise rotation sensors for studying rotational motion of tectonic plates during seismic events. In addition, improved models of the Earth's composition and dynamics may result from studying variations in the Earth's rotation rate that are on the order of $\sim 10^{-8}\Omega_{\mathrm{E}}$ on time scales of a few days. Here $\Omega_{\mathrm{E}} \simeq 7.292 \times 10^{-5}$ rad s^{-1} is the rotation rate of the Earth about its axis. Furthermore, local measurements made by gyroscopes would complement the distributed measurements made by very-long baseline interferometry (VLBI).

Torsion pendulum measurements of the gravitational constant G may ultimately be limited by knowledge of local rotational noise from seismic and cultural sources [8]. Rotational noise at the pendulum oscillation rate (typical periods are between 100 and 1000 s) will give a systematic offset in the determination of G, which potentially could be corrected using a gyroscope like the one described here.

To test general relativity, one could measure the precession of a gyroscope (defining a locally non-rotating reference frame) relative to a reference frame defined by the distant stars. This precession arises from parallel propagating a vector through curved spacetime around a massive rotating body such as the Earth, and therefore applies equally to different types of gyroscopes. The effect can be divided into two parts: the geodetic effect is due to motion around a massive body that is not rotating, and the Lense–Thirring effect [9] arises due to the rotation of a massive body. For a gyroscope in orbit, the total precession rate is given by the sum of the two effects

$$\boldsymbol{\Omega}_{\text{geo}} = \frac{3}{2}\frac{GM}{c^2 r^3}(\boldsymbol{r} \times \boldsymbol{v}) \tag{2}$$

$$\boldsymbol{\Omega}_{\text{LT}} = \frac{GI}{c^2 r^3}\left[\frac{3\boldsymbol{r}}{r^2}(\boldsymbol{\omega} \cdot \boldsymbol{r}) - \boldsymbol{\omega}\right], \tag{3}$$

where $\boldsymbol{\Omega}_{\text{geo}}$ and $\boldsymbol{\Omega}_{\text{LT}}$ are the geodetic and Lense–Thirring precessions, respectively; $\boldsymbol{r}$ and $\boldsymbol{v}$ are the current position and velocity of the gyroscope; M, I, and $\boldsymbol{\omega}$ are the mass, moment of inertia and rotation rate of the Earth. For a 650 km polar orbit around the Earth, one finds $\boldsymbol{\Omega}_{\text{geo}} = 1 \times 10^{-12}$ rad s^{-1} and $\boldsymbol{\Omega}_{\text{LT}} = 6.45 \times 10^{-15}$ rad s^{-1}. The Lense–Thirring effect has recently been measured to 20% precision by Ciufolini *et al*, as described in [10] and elsewhere in these proceedings. The effect was observed by monitoring the orbital parameters of two satellites in polar orbits, and data extraction required detailed modelling of the Earth's mass distribution and gravitational field. The Gravity Probe B (GPB) satellite gyroscope test is designed to measure the geodetic effect to one part in 10^4 and the Lense–Thirring effect to within 2% [11]. GPB will measure the precession of spinning superconducting spheres in a cryogenic environment within a drag-free satellite†. Measuring the Lense–Thirring effect tests a unique aspect of general relativity, and might prove to be one of only a few tests that are within experimentally achievable limits. Because the atom-interferometer sensitivity improves as the interferometer length squared, a large instrument could make a ground-based test of general relativity feasible [13]. For example, increasing the length of our present 2 m long apparatus by a factor of 10 should yield a 100-fold improvement in sensitivity.

3. Apparatus

Much of our apparatus has been described previously. Results obtained with a single atom-interferometer configuration are presented in [1], implementation of dual counter-propagating interferometers and improved atomic sources are described in [14] and a detailed treatment including our most recent work is given in [15]. A schematic view of the gyroscope apparatus interferometer configuration is shown in figure 1, and a brief description follows.

Two-photon stimulated Raman transitions are used as beamsplitters and mirrors to manipulate atoms [16, 17]. Two counterpropagating laser beams are required, with a frequency difference equal to the hyperfine splitting of the caesium $6S_{1/2}$ ground states ($F = 3$ and 4), namely the clock transition at 9.2 GHz. The transition produces a change of internal state accompanied by a corresponding momentum kick of $\hbar\boldsymbol{k}_{\text{eff}}$, where $\boldsymbol{k}_{\text{eff}} = \boldsymbol{k}_1 - \boldsymbol{k}_2$. Both lasers are detuned ~ 2 GHz from the atomic resonance with the $6P_{3/2}$ excited state, avoiding

† Since the GPB readout is expected to be limited by the shot noise of the readout current, its ability to determine angle improves like $t^{1/2}$. However, if the instrument is used to measure a constant rotation rate, then the angular displacement increases linearly with time. This leads to a rotation rate measurement that improves like $t^{3/2}$ for GPB, in contrast to the $t^{1/2}$ scaling of a shot-noise-limited Sagnac gyroscope. GPB has an expected sensitivity of 1 marcsec (4.85×10^{-9} rad) over a 4 h integration [12]. That implies an angle measurement of 5.8×10^{-7} rad in 1 s (or $\simeq 5.8 \times 10^{-7}$ rad s^{-1}), which is 970 times worse than the Yale gyro, but in 4 h, GPB should achieve 3.4×10^{-13} rad s^{-1}, which is 15 times better than the scaled Yale gyro performance.

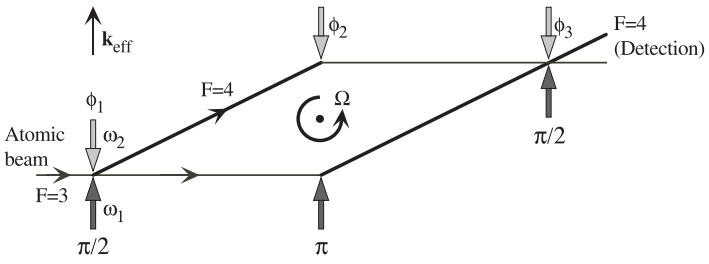

Figure 1. Interferometer configuration. Three pairs of Raman beams are used to divide, deflect and recombine atomic trajectories.

spontaneous emission. For Raman transitions, the RF laser frequency difference must be stable, but highly stable individual lasers are not required. Light beamsplitters for atoms have the advantage over mechanical gratings that they are more easily vibrationally isolated and do not clog. Because Raman beamsplitters transfer atoms between different ground states, a highly collimated atomic beam is not required as is the case for mechanical gratings or diffraction from standing waves, where diffracted orders must be resolved to distinguish a signal from background atoms. A disadvantage of Raman transition beamsplitters is that AC Stark shifts of the atomic energy levels due to off-resonant laser light can cause spurious interferometer phase shifts. Techniques used to minimize these shifts are described in section 5.2.

We generate the Raman laser frequencies from a master diode laser by using an acousto-optic modulator (AOM) operating at 4.6 GHz, and amplify the ± 1 diffraction orders by optical injection locking slave diode lasers [18]. Light from the two Raman lasers is combined with crossed polarizations on a beamsplitter cube and copropagates throughout the apparatus. The light is spatially filtered and then divided into three Raman pulses using plate beamsplitters. Raman transitions between copropagating beams (Doppler-insensitive configuration) are suppressed because the Raman detuning $\delta_{12} = \omega_1 - \omega_2$ is 160 MHz from the Raman transition resonance. After the Raman beams exit the vacuum chamber, the light is retroreflected through an AOM such that one pair of counterpropagating beams (Doppler-sensitive configuration) is on resonance.

To form the interferometer, a horizontal thermal beam of caesium atoms is transversely cooled and optically pumped into the $F = 3$ ground state before passing into a magnetically shielded interferometer region within a UHV vacuum chamber. The atoms pass through a sequence of three Raman laser interaction regions, with the lasers in a horizontal plane perpendicular to the atomic beam. The first beam ($\pi/2$) puts the atoms in a coherent superposition of the $F = 3$ and 4 ground states. This first pulse serves as a beamsplitter, causing the atomic wavepackets to divide into two trajectories. The second beam (π) acts as a mirror, exchanging the atomic states and momenta and deflecting the trajectories back towards each other. The third beam ($\pi/2$) acts as a beamsplitter and recombines the trajectories, forming a Mach–Zehnder-type interferometer. (The $\pi/2$–π–$\pi/2$ interferometer sequence we use is similar to that used to measure gravitational acceleration by Kasevich and Chu [19, 20], except that our interferometer uses spatially separated pulses rather than pulses in the time domain.) Rotation induces a phase shift between the two arms of the interferometer, and the interference signal is observed by measuring the number of atoms in the $F = 4$ state using a probe laser tuned to resonance and imaging the atomic fluorescence onto a photodiode. A magnetic bias field along the axis of the Raman beams shifts the transition frequencies corresponding to the different Zeeman m_F sublevels such that only the magnetic field insensitive $m_F = 0$ atoms are resonant with the Raman transitions and participate in the interferometer, minimizing phase

shifts due to inhomogeneities in the magnetic field.

4. Interferometer phase shifts

References to several viewpoints for calculating the Sagnac effect can be found in [2, 21]. The calculation may be performed in either the laboratory frame or in an inertial frame, as well as for time-domain or spatial-domain beamsplitters. Bordé *et al* have studied the theory of spatial-domain beamsplitters in detail (including effects of finite pulse width, which have been neglected here) in [22, 23] and references therein. To derive the interferometer phase shift, it is convenient to treat spatial propagation through the interferometer and interactions with the Raman lasers separately. The phase shift for our interferometer configuration was computed using this approach in [24], and a similar configuration was treated previously in [25]. Only a rough outline of the calculation will be presented here.

The spatial propagation phase shift can be computed using path integrals [26] of the Lagrangian. In classical mechanics, Hamilton's principle of least action states that a particle moving in an external potential $V(\boldsymbol{r})$ will travel along the path for which the integral

$$S_\Gamma \equiv \int_{t_a}^{t_b} L[\boldsymbol{r}(t), \dot{\boldsymbol{r}}(t)]\,\mathrm{d}t \tag{4}$$

is stationary, where the Lagrangian is defined as $L[\boldsymbol{r}, \dot{\boldsymbol{r}}] \equiv \frac{1}{2}m\dot{\boldsymbol{r}}^2 - V(\boldsymbol{r})$, and S_Γ is the *action* along the path Γ. Stationary means that the integral is extremal with respect to small variations in the path, that is, $\delta S_\Gamma = 0$. The classical action is denoted by

$$S_{\mathrm{cl}} \equiv S_{\mathrm{cl}}(\boldsymbol{r}_b, t_b; \boldsymbol{r}_a, t_a), \tag{5}$$

and represents the action evaluated along the classical path between the endpoints a and b, depending only on the endpoints. In our interferometer, atoms are treated classically with position and velocity corresponding to the centre of mass and group velocity of a spatially localized quantum mechanical wavepacket. The phase accumulated due to propagation between two points is

$$\Delta\phi = S_{\mathrm{cl}}/\hbar. \tag{6}$$

The phase shift due to a perturbation to the Lagrangian ΔL can be calculated to first order by integrating the perturbing potential over the unperturbed classical path, Γ_0. Therefore, the phase difference between the two interferometer arms is given by

$$\Delta\Phi = \frac{1}{\hbar}\oint_{\Gamma_0} \Delta L\,\mathrm{d}t. \tag{7}$$

In the rotating frame, Coriolis acceleration adds a perturbation $\Delta L = m\boldsymbol{\Omega}\cdot(\boldsymbol{r}\times\boldsymbol{v})$ to the free-particle Lagrangian.

The phase shift due to interaction with the laser light can be derived from the solution of the Raman transition equations given, for example, in [17]. At each vertex of the interferometer diagram corresponding to the atom receiving a momentum kick, an appropriate phase factor must be applied, namely

$$\exp(\pm\mathrm{i}[\boldsymbol{k}_{\mathrm{eff}}\cdot\boldsymbol{x} - (\omega_{\mathrm{eff}} - \omega_{eg} - \omega_r)t_0 - \phi_{\mathrm{eff}}]), \tag{8}$$

where $\omega_{\mathrm{eff}} = \omega_1 - \omega_2$, ω_{eg} is the caesium hyperfine splitting frequency, $\omega_r = \hbar k_{\mathrm{eff}}^2/2m$ is the recoil frequency, and the factor $\mathrm{e}^{\mathrm{i}\boldsymbol{k}_{\mathrm{eff}}\cdot\boldsymbol{x}}$ corresponds to the momentum of the absorbed photon. The arbitrary phase ϕ_{eff} is given by the difference of the individual Raman laser arbitrary phases, evaluated at the point of interaction with the atoms.

Our atom interferometer is sensitive to linear or Coriolis acceleration $\boldsymbol{a}$ along the Raman beam axis. Combining the phase shifts for spatial propagation and laser interactions, it can be shown that the total interferometer phase shift is

$$\Delta\Phi = -\boldsymbol{k}_{\text{eff}} \cdot \boldsymbol{a}\frac{L^2}{v^2} + \phi_1 - 2\phi_2 + \phi_3, \tag{9}$$

where ϕ_j represents the arbitrary phase from the jth Raman beam (evaluated at the point of interaction with the atoms). For rotation, $\boldsymbol{a}$ is the Coriolis acceleration

$$\boldsymbol{a}_{\text{Cor}} = -2\boldsymbol{\Omega} \times \boldsymbol{v}. \tag{10}$$

4.1. Counterpropagating atomic beams

Because the rotation phase shift depends on the Coriolis acceleration and thus the vector velocity, reversing the direction of the atomic beam yields a rotation phase shift with opposite sign. Our rotation rate measurement approach depends fundamentally on this phase shift reversal.

In the limit of perfect contrast, the probability for an atom exiting the interferometer in the $F = 4$ state used for detection is equal to

$$P(F = 4) = \tfrac{1}{2}[1 - \cos(\Phi_\Omega + \phi_{\text{arb}})], \tag{11}$$

where Φ_Ω is the Sagnac phase shift, and $\phi_{\text{arb}} = \phi_1 - 2\phi_2 + \phi_3$ is the sum of acceleration and the arbitrary laser phase. Therefore, the gyroscope signals corresponding to counterpropagating atomic beams have the form

$$S_{\text{north}} \sim \cos(\Phi_\Omega + \phi_{\text{arb}}) \tag{12}$$

$$S_{\text{south}} \sim \cos(-\Phi_\Omega + \phi_{\text{arb}}), \tag{13}$$

where S represents the detected signal of the north or south atomic beam (north and south are arbitrary labels for the counterpropagating atomic beams), and Φ_Ω represents the Sagnac phase shift. Using trigonometric identities, one can rearrange these equations as follows:

$$S_{\text{north}} - S_{\text{south}} \sim \sin(\Phi_\Omega)\cos(\phi_{\text{arb}}). \tag{14}$$

Due to the sine factor, the difference signal has a zero crossing for zero rotation rate, and the amplitude factor (cosine) can be maximized by adjusting the arbitrary phase. Therefore, this method allows precise determination of the zero rotation rate relative to the non-rotating inertial frame, and does not depend on knowledge of the gyroscope area or arbitrary phase.

To implement the counterpropagating atomic beams, caesium sources were mounted at each end of the vacuum chamber and aligned to overlap spatially so that the beams would sample the same magnetic bias field (collisions are negligible). The atoms from each atomic beam are transversely cooled in two dimensions using red-detuned laser light, and are optically pumped into the $F = 3$ ground state before passing through the detection laser for the opposing atomic beam. Since the detection light is tuned to the $F = 4 \rightarrow F' = 5$ resonance, the only atoms detected are those that end up in the $F = 4$ state after the interferometer interaction pulses. To enhance common-mode rejection, the interferometers share all laser sources, including light for state preparation, Raman beams and detection.

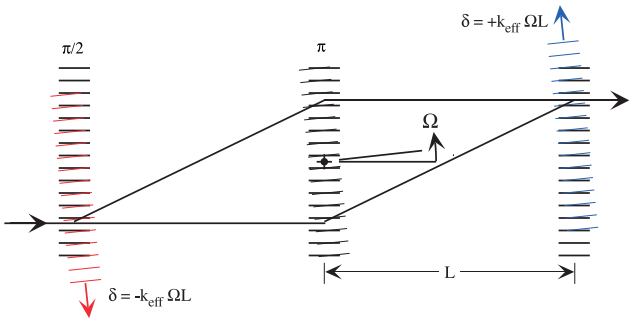

Figure 2. Rotation-induced Doppler shifts. The wavefronts of the three Raman pulses are drawn in their initial positions and after rotation of the apparatus about the centre of the π pulse. Small rotations leave the π pulse essentially unchanged, but Doppler shift the $\pi/2$ pulses by $\pm k_{\rm eff}\Omega L$. For clarity, only one Sagnac loop has been drawn, but the shifts are the same for each. The wavefronts and Sagnac loop are not drawn to scale.

4.2. Doppler shifts

In an inertial frame, rotation about the centre of the π pulse appears as a Doppler shift of the $\pi/2$ beams of magnitude

$$\delta = k_{\rm eff}\Omega L, \tag{15}$$

with opposite signs for the north and south $\pi/2$ beams. Figure 2 illustrates the Doppler shifts due to rotation. The interferometer phase shift can be interpreted as arising from the rotation induced Doppler shifts, and can be shown (to a first-order approximation) to result in a phase shift of

$$\Delta\Phi \simeq 2\delta L/v = 2k_{\rm eff}\Omega L^2/v, \tag{16}$$

where v is the longitudinal velocity of the atomic beam. The Earth's rotation rate causes a Doppler-shift of $\delta f = \delta/2\pi = 108.8$ Hz for our horizontally oriented instrument at Yale's latitude, measured by GPS to be 41:19:02.661N ($\sin(\phi_{\rm lat}) = 0.660$). The single interferometer phase shift due to the Earth's rotation rate would be 6.8 rad, and the projection at Yale's latitude is 4.5 rad.

4.3. Electronic rotation compensation

The AOMs used in the Raman beam retroreflections make it possible to tune the Raman transition frequency independently for each of the three pulses. In particular, shifting the frequencies of the $\pi/2$ beams by $\pm\delta f = 108.8$ Hz compensates for the Doppler shifts induced by the rotation rate of the Earth, described in the previous section. Because the Doppler shift depends only on the interferometer geometry and laser wavelength, the compensation works for both atomic beams and is independent of the velocity distribution of the atoms. To calibrate the frequency shifts in terms of rotation rate, we measured the separation between Raman beams, $L = 96.842 \pm 0.015$ cm, using a pinhole attached to a precision caliper. With the DC rotation compensated, we recover the maximum fringe contrast—as obtained for zero rotation rate in the absence of compensation. The contrast decreases for non-zero rotation rates due to averaging over longitudinal velocities in the atomic beam, since the phase shift depends on the velocity.

Rather than simply cancelling the bias due to the Earth's rotation rate, one could servo δf so that the rotation signal always reads zero, and accurately determine the rotation rate from the frequency offset δf. A closed loop rotation readout could improve the instrument's linearity by ensuring that the gyroscope is always operating near an effective zero rotation rate. Also, the dynamic range of measurable rotation rates could be increased, since servoing δf would keep the signal within the contrast envelope even for large rotation rates.

To avoid introducing unnecessary phase noise when adding the AOMs in the Raman retroreflections, the frequency-shifted light in the Raman retroreflection was phase-locked to the unshifted light (compared as close to the vacuum chamber as possible). This was accomplished by comparing the ∼160 MHz beatnote on a photodiode with a stable RF reference and servoing the AOM frequency using a voltage-controlled oscillator (VCO). A separate phase-locked loop is required for each of the three Raman retroreflection beams.

4.4. Frequency modulation

The electronic rotation compensation scheme described above can also be used to simulate the rotation of the optical table by scanning δf, avoiding the vibration and calibration uncertainties of mechanically rotating the table. (Previously, we had rotated the table with a piezo-electric transducer attached to a vibration-isolated massive column, and measured the velocity with a seismometer.) We also implemented a frequency modulation detection scheme in which we scanned δf with a triangle modulation which spanned the entire contrast envelope, acquiring multiple samples per scan. The rotation phase shift was computed for each scan after using a nonlinear curve-fitting routine to fit the data from both atomic beams. Such synchronous detection schemes are useful for reducing sensitivity to technical noise outside the modulation frequency band (for example, variations in atomic flux). To minimize phase noise, a single RF synthesizer was used to sweep $+\delta f$ or $-\delta f$ for the two $\pi/2$ beams, and this synthesizer output was mixed with two additional synthesizers to generate the RF references for each of the three Raman retroreflections. The synthesizers were combined in a symmetric fashion that exploited the interferometer laser arbitrary phase dependence $\phi_1 - 2\phi_2 + \phi_3$ such that slow phase drifts of any synthesizer cancelled in the interferometer signal.

4.5. Phase modulation

Adding a frequency offset to the π Raman beam causes the interferometer phase shift to increase linearly in time, which means that the number of atoms detected in the $F = 4$ state oscillates sinusoidally in time (see equation (11)). This can be seen in the time-domain picture by substituting the appropriate frequencies and times for the Raman laser arbitrary phases. Suppose the $\pi/2$ Raman lasers are at frequency ω_{eff}, the π pulse is at frequency $\omega_{\text{eff}} + \epsilon$, and an atom entering the interferometer at time t_0 takes a time $T = L/v$ to travel the distance L between pulses. Then we find

$$\Delta\Phi = \phi_1 - 2\phi_2 + \phi_3 = \omega_{\text{eff}} t_0 - 2(\omega_{\text{eff}} + \epsilon)(t_0 + T) + \omega_{\text{eff}}(t_0 + 2T) \tag{17}$$

$$= -2\epsilon t_0 - 2\epsilon T. \tag{18}$$

The first term of equation (18) increases linearly with time, and the second term corresponds to a constant acceleration. We used modulation frequencies between 3 and 48 Hz with 10 samples per period and determined the phase by fitting the sine waves using a nonlinear curve-fitting routine as a post-processing step. By subtracting and adding the phase for the north and south atomic beams, we recovered the rotation phase (modulo 2π) and the arbitrary phase (including acceleration). This linear phase modulation technique proved to be a convenient and robust

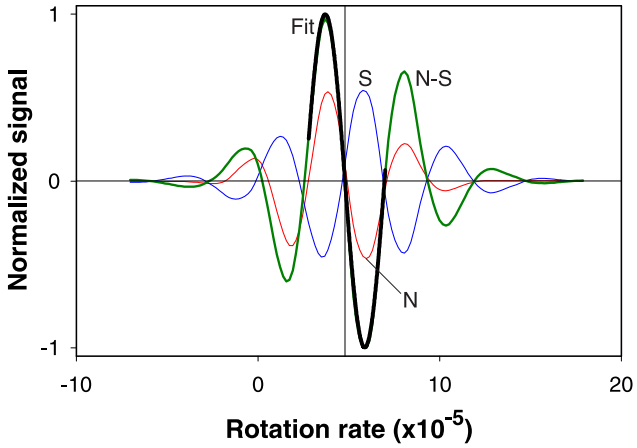

Figure 3. Earth rotation rate measurement (preliminary). The north and south rotation fringes are the symmetric signals shown with thin curves, the difference north − south is labelled N-S, and the fit to the centre of the difference curve is shown with a heavy black curve. The arbitrary phase was chosen so that the north and south signals have opposite sign, maximizing the contrast of the difference signal. From the fit, we determine $\Omega_E = 7.24 \times 10^{-5}$ rad s^{-1} (after compensating for latitude).

way to acquire rotation rate data. By combining four RF synthesizers, we were able to add an offset ϵ to the π pulse or shift the $\pi/2$ pulses by δf for electronic rotation compensation and modulation. However, the low-frequency phase noise does not cancel for the four-synthesizer configuration as it did for the frequency modulation scheme.

4.5.1. Earth rotation measurement. To test the technique of using the difference between the north and south atomic beams to determine the absolute rotation zero, we measured the Earth rotation rate. We used the frequency modulation technique to electronically scan the effective rotation rate. The Doppler shift correction frequency δf was swept 400 Hz over 10 s, and the signal was phase modulated at 48 Hz so lock-in demodulation could be used for detection. The results are shown in figure 3. The time-varying frequency shift δf was converted to an equivalent rotation rate based on the Doppler shift, using equation (15). We took the difference of the north and south normalized signals, and fit the centre of the curve to a sine wave. The point where the fitting curve crossed $y = 0$ was determined to be the zero rotation rate. (At this point, δf cancelled the Earth rotation rate.) We measured the Earth rotation rate to be $\Omega_E = 7.24 \times 10^{-5}$ rad s^{-1}, after correcting for Yale's latitude, compared with the expected value of $\Omega_E = 7.29 \times 10^{-5}$ rad s^{-1}. The dominant source of error was AC Stark shifts due to Raman laser misalignment. This and other systematic effects are discussed in section 5.2 along with experimental modifications that have dramatically reduced susceptibility to systematic errors.

5. Performance and results

This section discusses the performance of the instrument in different regimes. Short-term sensitivity measures the ability to detect small rotations over short time scales for which slow drifts of the apparatus are unimportant, and depends on interferometer area and signal-to-noise ratio. We used a rotation-independent method to determine the signal-to-noise ratio because

we have no independent means to characterize the rotational noise of the laboratory, which we expected to be above the intrinsic sensitivity of the gyroscope. Gyroscope test facilities exist; however, the difficulty of transporting our current apparatus precluded their use. For long-term stability, dimensional stability of the apparatus and pointing stability of the laser beams are critical, though stability is greatly improved by the use of counterpropagating atomic beams. Nonetheless, common-mode rejection cannot completely remove the effect of dimensional drift (i.e. thermal expansion) to the extent that it occurs during the time of flight of the atoms.

5.1. Short-term sensitivity

The improvement in short-term sensitivity over our previous work came from several factors. First, the atom flux was increased from 6×10^{8} to 1×10^{11} atom/s (detected in the interferometer region after transverse cooling) by replacing the caesium sources with a recirculating design and increasing the nozzle aperture to 4.5 mm diameter. The most probable velocity of the detected atoms was 290 m s^{-1}, with a transverse velocity spread of ±10 cm s^{-1} after transverse cooling. Second, the Raman transition linewidth was broadened by using spatially narrower Raman beams, resulting in ~5 times more atoms participating in the interferometer due to the wider range of transverse velocities addressed. Cylindrical optics were added to reshape the Raman beams, resulting in a beam size of 0.5 mm horizontally by 1.5 cm vertically ($1/e^2$ radius beam waist) at the plane of the atomic beams. Third, the detection noise for the atomic beam was reduced by narrowing the linewidth of the master laser diode used to derive the frequencies for transverse cooling and detection (referenced to a caesium vapour cell by saturated absorption). To narrow the linewidth, the distributed Bragg reflector (DBR) master laser with 3 MHz linewidth was optically injection locked to light from a grating-stabilized diode laser with 200 kHz linewidth. Retroreflecting the detection probe beam was found to prevent atoms from acquiring a net transverse momentum change during the detection pulse that would Doppler-shift the atoms off resonance. Keeping the atoms resonant with the probe light reduced the sensitivity to frequency fluctuations of the detection laser. Finally, sensitivity to air current fluctuations was reduced by placing tubes around cooling and detection beams, and building an enclosure around the optical table. To reduce the effect of air currents and mirror vibrations on the Raman beams, the Raman lasers were reconfigured to be copropagating as described in section 3.

We used two techniques to measure the interferometer signal-to-noise ratio independently from the rotational noise of the laboratory. First, we used the electronic rotation compensation technique of section 4.3 to set the effective rotation rate outside the bandwidth of the instrument, in the flat tails of the contrast envelope where there is no rotation sensitivity. We measured a signal-to-noise ratio of 33 000:1 for 1 s of integration, from which we determine a short-term sensitivity of 6×10^{-10} rad s^{-1} $Hz^{-1/2}$, or $8\times10^{-6}\Omega_E$. Second, we reconfigured the interferometer to have drastically reduced enclosed area. By using copropagating Raman beams (rather than counterpropagating ones as in the gyroscope configuration), the interferometer enclosed area and sensitivity to rotation and acceleration are reduced by a factor of $k_{\mathrm{eff}}/k_{\mathrm{RF}}\simeq1.3\times10^{-5}$. However, the sensitivity to many other sources of technical noise is unchanged; for example, phase shifts due to Zeeman shifts from changing magnetic fields, Raman pulse area or phase fluctuations, atomic beam flux and AC Stark shifts. With the null-area configuration, we obtained a signal-to-noise ratio of 50 000:1. Note that for both of the above techniques, we used a lock-in amplifier to remove low-frequency drifts by demodulating at 30 Hz, as we would have done in a rotation sensitive geometry. We compared the power spectral densities of the null-area interferometer with that of a single π pulse to measure the phase noise added by the interferometer sequence. The interferometer noise spectrum

(including rotation, acceleration and technical noise) had a minimum at about 3 Hz, which we subsequently used as the modulation frequency when doing long-term stability measurements, for which a high-frequency response is unnecessary.

5.2. Systematics

We investigated the sensitivity of the apparatus to possible sources of spurious phase shifts by acquiring dual-interferometer data using the phase modulation technique (described in section 4.5) while varying different parameters. First, we studied the stability of the applied magnetic bias fields, including the interferometer bias and the Helmholtz coils used to cancel the magnetic field in the cooling regions. In the worst case, we measured a phase shift of $\leqslant 3 \times 10^{-5}\Omega_{\mathrm{E}}$ mA^{-1}, and since the current supplies have 7×10^{-3} mA RMS ripple in 1 s, the bias field stability is not a limitation.

Next we studied the sensitivity to the detuning of the free-running Raman master laser, which could cause a phase shift due to changes in the AC Stark shift. We measured a phase-shift dependence of $3 \times 10^{-5}\Omega_{\mathrm{E}}$ MHz^{-1}, which indicated that a servo lock was needed for the master laser frequency. We used a high-speed counter interfaced to a computer to monitor a 2 GHz beatnote between the master Raman laser and the detection laser, which is locked to the $F = 4 \rightarrow F' = 5$ transition, and controlled the master laser current with a digital servo. The locked master laser had a 1.2 MHz RMS frequency error in 1 s, but because the detuning fluctuations are at high frequency and the average is locked precisely, detuning fluctuations are no longer a concern for long-term data acquisition.

The parameter that caused the largest systematic shifts was the horizontal overlap of the Raman beams, causing a phase shift of 1 rad for 100 μm relative displacement, which could occur due to beam-pointing instabilities or imperfect alignment through the spatial filter. To solve this problem, both lasers were coupled into one polarization-maintaining fibre. The fibre enforced spatial overlap between the Raman beams and reduced phase drift due to alignment-dependent AC Stark phase shifts. A Raman laser intensity servo was added to stabilize the power of the two lasers after exiting the fibre, preventing fluctuations due to etalon effects within the fibre. We retroreflected both lasers for the three Raman beams, which minimized AC Stark shifts due to Raman beam misalignments, since the intensity ratio between the beams was chosen such that the AC Stark shifts approximately cancel†.

In addition to the effects mentioned above, we investigated the dependence on the transverse cooling alignment, misalignment of the incident or retroreflected Raman beams, Raman injection, room temperature, and atomic source flux and velocity distribution. Sensitivity to certain systematic effects such as Raman beam misalignment must be rechecked now that the Raman beam delivery has been improved by the addition of the fibre and the two-beam retroreflection. We observed a correlation between the phase drift and atomic beam parameters that is not yet understood and requires further study.

We measured the rotational noise of the optical table for different methods of suspension. With the table floating on pneumatic vibration isolation legs (Newport #I-2000), it had a pronounced rotational resonance at 1.7 Hz, and when resting on unfloated legs, this was replaced by rotational noise at $\sim$12 Hz. The best performance for long-term studies was obtained by removing the legs from the optical table and resting the table close to the floor on ~ 5 cm high machined blocks sandwiched by 3 mm thick neoprene rubber sheets. This increased vertical vibration, but greatly reduced rotational noise and angular drift.

† Note that perfect AC Stark shift cancellation cannot be achieved both before and after the retroreflection AOM shift, since the intensity ratio needed for cancellation depends on the global detuning.

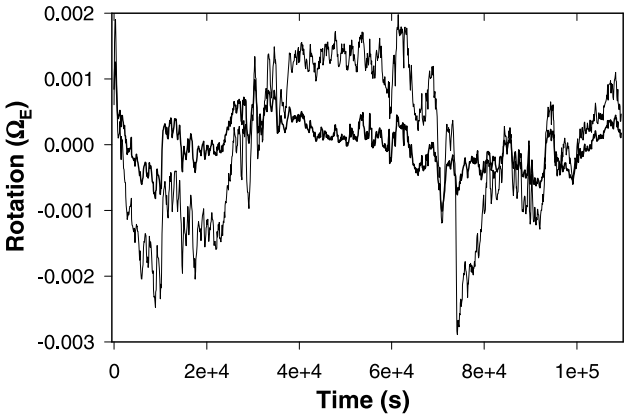

Figure 4. Preliminary long-term stability results. The Raman beams were fibre coupled with active intensity stabilization, and the optical table was resting on the floor. Phase modulation at 3.2 Hz was used with 100 samples per period, and the rotation phase was extracted using nonlinear curve fits. Each point plotted represents 60 s of data. The raw data are plotted as a thin curve. The thicker curve is the same data after normalizing by the oven flux, which was correlated to the rotation phase shift for reasons not fully understood. (The oven flux is determined by the amplitude of the phase modulation oscillations.)

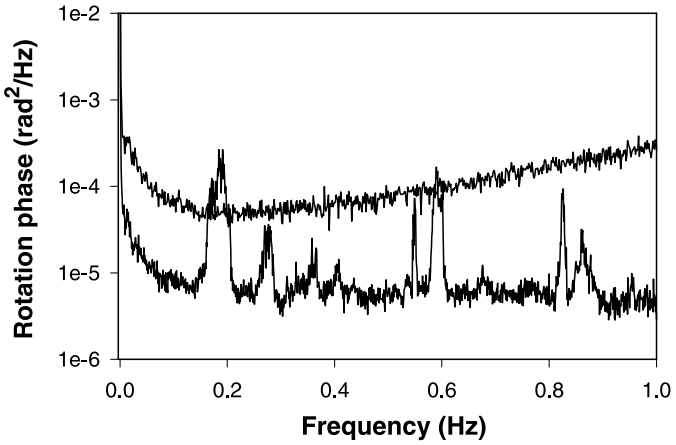

Figure 5. Power spectral density of rotation phase data. The bottom trace corresponds to the data of figure 4, taken with fibre-coupled and intensity-stabilized Raman lasers, with the optical table resting on the floor and 3.2 Hz phase modulation for data acquisition. The top trace shows previous data taken with the optical table floating, without fibre-coupling or intensity stabilization for the Raman beams, and using 48 Hz phase modulation for data acquisition. The increasing slope of the top trace is due to the floating table rotational resonance at 1.7 Hz.

5.3. Long-term stability results

The characterization of the long-term stability of the instrument is still underway, and we believe that a significant improvement can be made by identifying correlations between the rotation phase drift and various atomic beam and laser alignment parameters. Preliminary long-term stability data are shown in figure 4. These data were taken with the fibre-optic Raman delivery and intensity stabilization described in section 5.2. Also, on multiple runs, we observed a correlation between the rotation phase shift and the amplitude of the phase

modulated signal from one atomic beam. The phase modulation amplitude is proportional to the oven flux, but may coincide with other changes in the velocity distribution and therefore requires further study. These data represent worst-case instrument performance, since we have no independent knowledge of the rotational stability of our laboratory. We plan to acquire data for longer times to test for environmental disturbances with 24 h periodicity. Figure 5 compares the Fourier power spectral density of the data before and after implementing the stability improvements described in the previous section.

6. Conclusion

In summary, we have constructed a gyroscope using atom interferometry that has a short-term sensitivity of 6×10^{-10} rad s^{-1} Hz$^{-1/2}$. The device uses counterpropagating atomic beams to distinguish rotation from acceleration, determine absolute zero rotation rate, and for common-mode rejection. Adding independent frequency shifts to the Raman beams allows rotation compensation and synchronous detection schemes. Long-term stability testing is still underway, and we expect substantial improvements can be made with modest changes to our apparatus.

One approach to improving long-term performance is to periodically reverse the interferometer area. Switching the direction of the Raman k-vectors reverses the direction of the momentum kick to the atoms as well as the sign of the vector area associated with the loop. Although the Sagnac phase shift changes sign, many other potential sources of systematic shifts remain unchanged. This scheme is currently being implemented.

In the near future, we hope to reduce instrument noise to achieve shot-noise-limited performance, yielding a factor of three improvement in sensitivity. Multiple-pulse beamsplitting schemes could also be used to increase the enclosed area and sensitivity of the interferometer. With improved sensitivity, we hope to increase the integration time and observe fluctuations in the Earth's rotation rate. Long-term plans include the development of a compact and portable apparatus suitable for field use. Adding two Raman π pulses to our present apparatus would allow switching to and from a figure-of-eight interferometer geometry, in which case the apparatus could also measure gravity gradients. Finally, construction of a longer interferometer could make poorly known Earth rotation fluctuations at the $1 \times 10^{-9}\Omega_{\mathrm{E}}$ level accessible, and might be used for a test of general relativity.

Acknowledgments

This work has been funded by grants from NASA, NIST, NSF and ONR.

References

[1] Gustavson T L, Bouyer P and Kasevich M A 1997 *Phys. Rev. Lett.* **78** 2046–9
[2] Stedman G E 1997 *Rep. Prog. Phys.* **60** 615–87
[3] Werner S A, Staudenmann J L and Colella R 1979 *Phys. Rev. Lett.* **42** 1103–6
[4] Riehle F, Kisters T, Witte A, Helmcke J and Bordé C J 1991 *Phys. Rev. Lett.* **67** 177–80
[5] Lenef A *et al* 1997 *Phys. Rev. Lett.* **78** 760–3
[6] Hasselbach F and Nicklaus M 1993 *Phys. Rev.* A **48** 143–51
[7] Rowe C H *et al* 1999 *Appl. Opt.* **38** 2516–23
[8] Boynton P and Newman R 1999 *Symp. on Experimental Gravitation (Uzbekistan)*
[9] Lense J and Thirring H 1918 *Phys. Z.* **19** 156
[10] Ciufolini I, Pavlis E, Chieppa F, Fernandes-Vieira E and Pérez-Mercader J 1998 *Science* **279** 2100–3
[11] Everitt C W F 1987 *Near Zero: New Frontiers of Physics* (San Francisco, CA: Freeman) p 570

[12] Buchman S *et al* 1996 *Class. Quantum Grav.* A **13** 185–91
[13] Cerdonio M, Prodi G A and Vitale S 1988 *Gen. Rel. Grav.* **20** 83–7
[14] Gustavson T L, Bouyer P and Kasevich M A 1998 *Methods for Ultrasensitive Detection* (*Proc. SPIE* **3270**) ed B L Fearey pp 62–9
[15] Gustavson T L 2000 Precision rotation sensing using atom interferometry *PhD Thesis* Stanford University
[16] Kasevich M *et al* 1991 *Phys. Rev. Lett.* **66** 2297–300
[17] Young B, Kasevich M and Chu S 1997 *Atom Interferometry* ed P R Berman (New York: Academic) pp 363–406
[18] Bouyer P, Gustavson T L, Haritos K G and Kasevich M A 1996 *Opt. Lett.* **21** 1502–4
[19] Kasevich M and Chu S 1991 *Phys. Rev. Lett.* **67** 181–4
[20] Kasevich M and Chu S 1992 *Appl. Phys.* B **54** 321–32
[21] Neutze R and Hasselbach F 1998 *Phys. Rev.* A **58** 557–65
[22] Bordé C J 1997 *Atom Interferometry* ed P R Berman (New York: Academic) pp 257–92
[23] Bordé C J and Lämmerzahl C 1999 *Ann. Phys., Lpz.* **8** 83–110
[24] Storey P and Cohen-Tannoudji C 1994 *J. Physique II* **4** 1999–2027
[25] Bordé C J 1992 *Laser Spectroscopy X* ed M Ducloy, E Giacobino and G Camy (Singapore: World Scientific) pp 239–45
[26] Feynman R P and Hibbs A R 1965 *Quantum Mechanics and Path Integrals* (New York: McGraw-Hill)

Six-Axis Inertial Sensor Using Cold-Atom Interferometry

B. Canuel, F. Leduc, D. Holleville, A. Gauguet, J. Fils, A. Virdis,* A. Clairon, N. Dimarcq, Ch. J. Bordé, and A. Landragin†
LNE-SYRTE, CNRS UMR 8630, Observatoire de Paris, 61 avenue de l'Observatoire, 75014 Paris, France

P. Bouyer
Laboratoire Charles Fabry, CNRS UMR 8501, Centre Scientifique d'Orsay, Bâtiment 503, Boîte Postale 147, 91403 Orsay, France
(Received 14 March 2006; published 7 July 2006)

We have developed an atom interferometer providing a full inertial base. This device uses two counterpropagating cold-atom clouds that are launched in strongly curved parabolic trajectories. Three single Raman beam pairs, pulsed in time, are successively applied in three orthogonal directions leading to the measurement of the three axis of rotation and acceleration. In this purpose, we introduce a new atom gyroscope using a butterfly geometry. We discuss the present sensitivity and the possible improvements.

DOI: 10.1103/PhysRevLett.97.010402 PACS numbers: 03.75.Dg, 06.30.Gv, 39.20.+q

Since its proof of principle in 1991 [1,2], atom interferometry has demonstrated, in particular, great sensitivity to accelerations [3,4] and rotations [5,6]. Among beautiful applications [7], these experiments offer attractive perspectives for application in inertial navigation, geophysics, or tests of fundamental physics [8], where the ability of cold-atom interferometry to give stable and accurate measurements can bring a real improvement compared to standard technologies, as is already the case for atomic clocks [9]. Nowadays, best performances are achieved by interferometers using optical transitions [10,11], based on a sequence of three Raman pulses ($\pi/2 - \pi - \pi/2$) first introduced by Kasevich and Chu [2]. The pulses couple the two hyperfine ground states ($|6S_{1/2}, F = 3, m_F = 0>$ and $|6S_{1/2}, F = 4, m_F = 0>$ in the case of Cesium atoms), which split apart when using counterpropagating Raman lasers [12]. The $\pi/2$ and π pulses realize, respectively, the beam splitters and mirrors of the interferometer. This configuration allows measurement of acceleration along the direction of propagation of the Raman lasers. When the geometrical area included in the interferometer is nonzero, it also gives access to the rotation around the axes perpendicular to the oriented area. Up to now, atom interferometers have only been proven to be sensitive to a single inertial quantity (e.g., acceleration or rotation along one single axis), although intrinsically sensitive to at least both acceleration and rotation. In order to get full inertial monitoring, all six axes (3 rotations and 3 accelerations) must be measured, as needed for inertial navigation, geophysics measurements, or some tests of fundamental physics [8]. In the past, this was achieved by implementing multiple inertial sensors, as proposed in [8], and the ability of using a single "proof mass" for measuring all inertial axis has not yet been achieved. This represents a real challenge for inertial measurement such as the possibility of monitoring gravity and the 3 components of the earth rotation at the same position.

In this Letter we describe a new setup which is sensitive along six axes of inertia. The two key features of our setup are the use of a single Raman beam pair pulsed in time and the choice of a strongly curved parabolic trajectory. This allows successive use of three configurations of Raman lasers that interact with two counterpropagating atomic clouds, giving access to all components of rotation and acceleration. For one of these components, we use a new butterfly configuration based on a four-pulse sequence ($\pi/2 - \pi - \pi - \pi/2$). In addition, we introduce an original Raman configuration to reduce the systematic effect introduced by wave front distortions.

In our experiment, about 10^7 Cesium atoms are trapped from a vapor in magneto-optical traps during 125 ms, and cooled down to 3 μK. The Cesium clouds are launched along parabolic trajectories using moving molasses at 2.4 $m \cdot s^{-1}$, with an angle of 8° with respect to the vertical direction. Then the atoms are prepared in the state $|6S_{1/2}, F = 3, m_F = 0>$ before entering the interferometer zone at the top of their trajectory, where they interact with the Raman lasers. In the following, $\mathbf{k}$ denotes the effective wave vector of the Raman transition, and φ_l the difference of phase between the two lasers. The interrogation sequence is achieved with a single pair of Raman beams covering the entire interrogation zone. The beams are switched on during 20 μs to realize the Raman pulses, which provides an easy way to change the pulse sequence. The atomic velocity and the Raman beam size, 30 mm diameter ($1/e^2$), set the maximum interrogation time to 80 ms. At the exit of the interferometer, the transition probability depends on the inertial forces through the phase difference accumulated between the two arms of the interferometer [13]. Raman transitions enable detection of the internal states of the atoms by fluorescence imaging.

We now present the description of the 6 axis inertial sensor principle. The direction of sensitivity of the setup is defined by the direction of the Raman interrogation laser with respect to the atomic trajectory. As illustrated in Fig. 1, with a classical three pulses sequence ($\pi/2 - \pi - \pi/2$), a sensitivity to vertical rotation Ω_z and to horizontal acceleration a_y is achieved by placing the Raman lasers

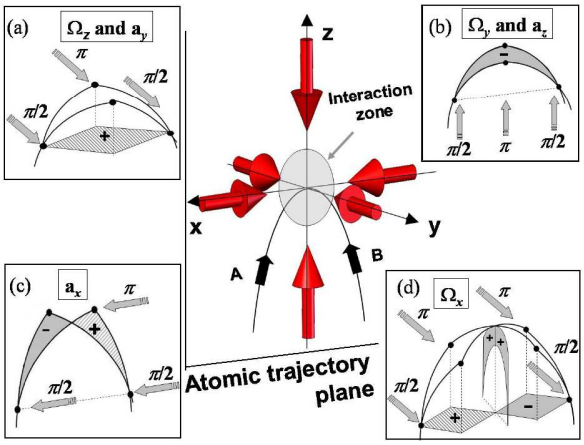

FIG. 1 (color online). Six-axis inertial sensor principle. The atomic clouds are launched on a parabolic trajectory, and interact with the Raman lasers at the top. The four configurations (a)–(d) give access to the 3 rotations and the 3 accelerations. In the three pulses configuration, the Raman beams direction can be horizontal or vertical, creating the interferometer in a horizontal (a) or vertical (b),(c) plane. With a butterfly four-pulse sequence of horizontal beams (d), the rotation Ω_x can be measured.

horizontal and perpendicular to the atomic trajectory [5] [Fig. 1(a)]. The same sequence, using vertical lasers, leads to the measurement of horizontal rotation Ω_y and vertical acceleration a_z [Fig. 1(b)]. Thanks to our specific setup, we also have access to the other components of acceleration and rotation which lie along the horizontal direction of propagation of the atoms (x axis). The use of cold atoms in strongly curved trajectories allows us to point the Raman lasers along the x direction, offering a sensitivity to acceleration a_x and no sensitivity to rotation [Fig. 1(c)]. We also have an easy access to the horizontal rotation Ω_x by changing the pulse sequence to 4 pulses: $\pi/2 - \pi - \pi - \pi/2$ [Fig. 1(d)]. We detail in the following the two configurations: the classical three pulses sequence (a) and our new butterfly four-pulse sequence (d).

The first pulse sequence that we study here is a standard three pulses ($\pi/2 - \pi - \pi/2$). The phase shift depends on the acceleration $\mathbf{a}$ and on the rotation rate $\mathbf{\Omega}$ through [11]:

$$\Delta\Phi = \mathbf{k}[\mathbf{a} - 2(\mathbf{\Omega} \times \mathbf{v})]T^2. \quad (1)$$

The scale factor depends only on $\mathbf{k}$, $2T$ the total interrogation time and $\mathbf{v}$ the mean velocity in the laboratory frame, which are well controlled. In the following, $\mathbf{k}$ is horizontal and along the y axis, as we see in Fig. 1(a). The surface delimited by the two arms of the interferometer is curved and the projection of the oriented area on the two vertical planes cancels out. Therefore it gives access to accelerations along this direction and to rotations around the vertical axis. To discriminate between acceleration and rotation, we use two counterpropagating cesium atomic clouds leading to an opposite velocity in Eq. (1) [14].

In our setup, we have developed a new method to reduce the variations of the local wave vector $\mathbf{k}$, which induce perturbations that can be read as inertial phase shifts [15]. In this method the Raman beams propagate in the same optical system with orthogonal circular polarizations, pass through the atomic trajectories, and are retroreflected through a quarter-wave plate [16]. In this case, the aberrations are common and compensated most of the time: until the lasers cross the atoms. With circular polarizations, the atoms can experience two diffraction processes with opposite $\mathbf{k}$ vectors. In order to select a single diffraction process, we tilt the laser beams by 6° in the horizontal plane (Fig. 2), and compensate the Doppler effect by an additional frequency difference between the Raman lasers [17]. Since the two atom clouds are counterpropagating, their Doppler detunings are opposite, which means that each atomic cloud is resonant with a different Raman pair, and this results in an opposite effective wave vector for the two interferometers. Therefore, the rotation and the acceleration parts are, respectively, obtained by the sum and the difference of the phases measured by the two interferometers (A and B).

We show in Fig. 3 the scan of the fringes of both interferometers by changing the phase φ_l between the first and the second Raman pulse. With our interrogation time of $2T = 60$ ms, the fringe contrasts are, respectively, 14.4% and 10.6% for A and B. The low contrast values can be explained by the sizes of the clouds after ballistic expansion (3.3 mm rms radius) and by the Gaussian intensity profile of the laser beams. In addition, mismatch between the trajectories A and B requires a compromise for the diffraction efficiency that leads to a reduction of the contrast by a factor of about 2.

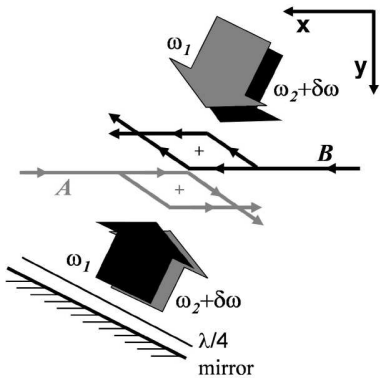

FIG. 2. The orthogonally polarized copropagating Raman beams are tilted with respect to the atom trajectories. They are retroreflected by a mirror through a quarter-wave plate so that the atoms interact with counterpropagating beams at frequency ω_1 and $\omega_2 + \delta\omega$ with $\omega_1 - \omega_2 \approx 9.2$ GHz. The detuning $\delta\omega$ compensates for the Doppler shift so that each of the two counterpropagating atom clouds can interact with only one pair of beams. Interferometer areas are shown in the case of a three-pulse interferometer.

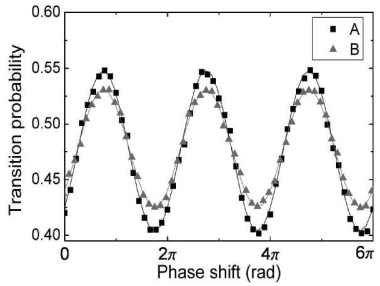

FIG. 3. Fringes obtained with the two interferometers A and B, for an interrogation time of $2T = 60$ ms and a cycling time of 560 ms without averaging.

To reach the maximum sensitivity to inertial forces, we operate the interferometer on the side of a fringe. To realize this condition for the two interferometers together, we align the Raman laser in the horizontal plane and compensate the rotational phase with an appropriate change of φ_l. In addition, by using two different values of φ_l, the interferometers can sit alternately on each side of a fringe [9], which allows rejection of long-term drifts of the contrast and of the offset of the fringe patterns. Figure 4 shows the time recordings of vertical rotation Ω_z and horizontal acceleration a_y extracted from the half sum and half difference of the two interferometers' phase shifts.

These results were obtained using an isolation platform (nano-K 350BM-1) to reduce the level of vibration in order to reach the maximum sensitivity [18]. However, this system introduces long-term tilt fluctuations which yield some acceleration fluctuations through the projection of $\mathbf{g}$ on the direction of $\mathbf{k}$. To limit this effect, we have developed a servo-lock of the platform tilt. The residual oscillation of this system at 0.03 Hz can be identified on the acceleration signal. Since this oscillation completely disappears on the rotation signal, it gives a clear validation of

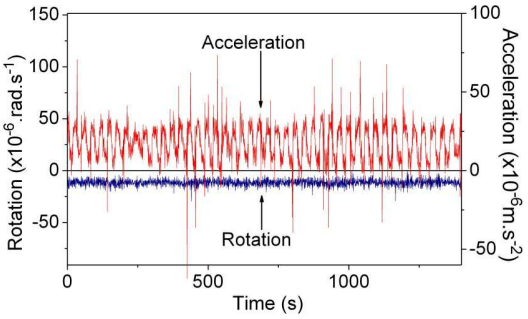

FIG. 4 (color online). Acceleration and rotation signals extracted from the half sum and half difference of the phase shifts of interferometers A and B. To obtain the actual value of the rotation, the phase φ_l has to be taken into account. dc offset on the acceleration signal is due to the residual contribution of gravitational acceleration. The acceleration dispersion on the acceleration signal comes from oscillations of the isolation platform.

the discrimination concept. We estimate the performances of our setup from the Allan standard deviation of these measurements. The signal-to-noise ratio from shot to shot (0.56 s) is 12 for the acceleration and 39 for the rotation leading to a respective sensitivity of 4.7×10^{-6} m $\cdot$ s^{-2} and 2.2×10^{-6} rad $\cdot$ s^{-1} for 1 s averaging time. For both measurements, the Allan standard deviation (Fig. 5) approaches the typical white noise behavior for long integration times. The sensitivity reaches 6.4×10^{-7} m $\cdot$ s^{-1} for acceleration and 1.4×10^{-7} rad $\cdot$ s^{-1} for rotation after 10 min of averaging time.

We have performed the measurement of the Earth's rotation rate with our cold-atom interferometer: $5.50 \pm 0.05 \times 10^{-5}$ rad $\cdot$ s^{-1}, in which the error bar corresponds to statistical uncertainty. This measured value for the projection along the vertical axis was found in good agreement with the expected value at Paris latitude ($\lambda = 48^{\circ}50'08''$): 5.49×10^{-5} rad $\cdot$ s^{-1}.

We now turn to the butterfly configuration [Fig. 1(d)], which was first proposed to measure the gravity gradient [19]. It can be used to measure rotations with the same Raman beams as in the previous configuration (y axis) but in a direction (x axis) that cannot be achieved with a standard 3 pulses sequence. Four pulses, $\pi/2 - \pi - \pi - \pi/2$, are used, separated by times $T/2$-T-$T/2$, respectively. The atomic paths cross each other leading to a twisted interferometer. The horizontal projection of the oriented area cancels out so that the interferometer is insensitive to rotation around the z axis. In contrast, the vertical projection now leads to a sensitivity to rotation around the x axis:

$$\Delta\Phi = \frac{1}{2}[\mathbf{k} \times (\mathbf{g} + \mathbf{a})]\Omega T^3. \quad (2)$$

This sensitivity to rotation appears from a crossed term with acceleration and is no longer dependent on the launching velocity. This configuration is not sensitive to dc accelerations along the direction of the Raman laser, but remains sensitive to fluctuations of horizontal and vertical acceleration. With our isolation platform, the remaining fluctuations are negligible compared to $\mathbf{g}$, which does not

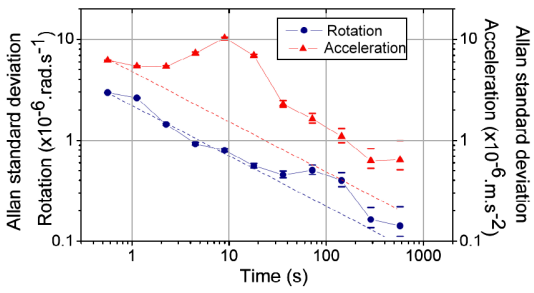

FIG. 5 (color online). Allan standard deviations of acceleration (triangles) and rotation (circles) measurements. Dashed lines corresponds to the $-1/2$ slope expected for a white noise. The peak near 10 s averaging time on the acceleration signal is due to the residual oscillations of the isolation platform tilt.

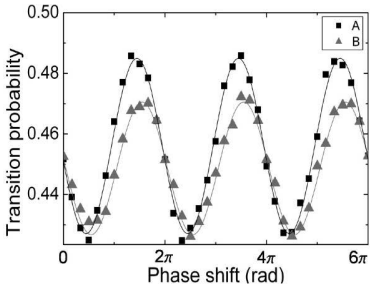

FIG. 6. Fringes obtained with both interferometers A and B in the four-pulses butterfly configuration for a total interrogation time of $2T = 60$ ms.

compromise the stability of the scaling factor. The sensitivity to rotation is comparable with that of configurations (a) and (b). With $2T = 60$ ms, this configuration leads to a interferometer area reduced by a factor 4.5, but it scales with $T^2$and thus would present a higher sensitivity for longer interrogation times.

The atomic fringe patterns are presented in Fig. 6 and show contrasts of 4.9% and 4.2% for interferometer A and B, respectively. By operating the interferometer on the fringe side, as explained before, we obtain a signal-to-noise ratio from shot to shot of 18 limited by the residual vibrations. The sensitivity to rotation is equal to 2.2×10^{-5} rad $\cdot$ s^{-1} in 1 s, decreasing to 1.8×10^{-6} rad $\cdot$ s^{-1} after 280 s of averaging time.

To summarize, we have presented the ability to measure the 6 inertial axis with the same setup. This shows the advantage of using cold atoms combined with a single laser beam pulse in the time domain. A first measurement, in three pulses interferometer, has demonstrated a sensitivity of 1.4×10^{-7} rad $\cdot$ s^{-1} to rotation and 6.4×10^{-7} m $\cdot$ s^{-2} to acceleration in 10 min averaging time. We have measured the Earth's rotation rate with an accuracy of 1%. Many improvements, such as the cold-atom sources, will allow us to increase the sensitivity by a factor of 50 on rotation and 10 on acceleration [20].

We plan to improve the cooling system in order to increase the total number of atoms, to get a lower temperature (≈ 1 μK), and to obtain a good superposition of the atomic trajectories.

In addition, we have demonstrated the butterfly configuration, which uses four pulses and which is sensitive to rotation around the axis parallel to the direction of propagation of the atoms at the top of their trajectory. This configuration is especially well adapted to trajectories close to those of an atomic fountain, in which a single source of atom is launched vertically. Since the interferometer area scales with T^3, this opens the possibility of a cold-atom gyroscope reaching a sensitivity of 10^{-9} rad $\cdot$ s^{-1} in 1 s.

The authors would like to thank the Déléguation Générale pour l'Armement, the Centre National d'Etudes Spaciales, the SAGEM, the European Union (FINAQS), and the Ile de France region (IFRAF) for their financial supports, Pierre Petit and Christophe Salomon for their contributions to the early stage of the experiment, and Robert Nyman for careful reading of the manuscript.

*Present address: SAGEM Défense et sécurité, Groupe SAFRAN, URD11, 72-74 rue de la Tour Billy, Boîte Postale 72-95101 Argenteuil Cedex, France.
†Corresponding author.
Electronic address: arnaud.landragin@obspm.fr

[1] O. Carnal and J. Mlynek, Phys. Rev. Lett. **66**, 2689 (1991); D. W. Keith, C. R. Ekstrom, Q. A. Turchette, and D. E. Pritchard, Phys. Rev. Lett. **66**, 2693 (1991); F. Riehle, Th. Kister, A. Witte, J. Helmcke, and Ch. Bordé, Phys. Rev. Lett. **67**, 177 (1991); F. Shimizu, K. Shimizu, and H. Takuma, Phys. Rev. A **46**, R17 (1992).
[2] M. Kasevich and S. Chu, Phys. Rev. Lett. **67**, 181 (1991).
[3] A. Peters, K. Y. Chung, and S. Chu, Metrologia **38**, 25 (2001).
[4] J. M. McGuirk, G. T. Foster, J. B. Fixler, M. J. Snadden, and M. A. Kasevich, Phys. Rev. A **65**, 033608 (2002).
[5] T. L. Gustavson, P. Bouyer, and M. A. Kasevich, Phys. Rev. Lett. **78**, 2046 (1997).
[6] A. Lenef, T. D. Hammond, E. T. Smith, M. S. Chapman, R. A. Rubenstein, and D. E. Pritchard, Phys. Rev. Lett. **78**, 760 (1997).
[7] *Atom Interferometry*, edited by R. Paul Berman (Academic, London, 1997), and references therein.
[8] R. Bingham *et al.*, Assessment Study Report, ESA-SCI (2000) 10, and references therein.
[9] A. Clairon, Ph. Laurent, G. Santarelli, S. Ghezali, S. N. Lea, and M. Bahoura, IEEE Trans. Instrum. Meas. **44**, 128 (1995).
[10] Ch. J. Bordé, Phys. Lett. A **140**, 10 (1989).
[11] Ch. J. Bordé, in *Laser Spectroscopy X*, edited by M. ducloy, E. Giacobino, and G. Camy (World Scientific, Singapore, 1991), Vol. 239.
[12] M. Kasevich, D. S. Weiss, E. Riis, K. Moler, S. Kasapi, and S. Chu, Phys. Rev. Lett. **66**, 2297 (1991).
[13] Ch. J. Bordé, Gen. Relativ. Gravit. **36**, 475 (2004).
[14] T. L. Gustavson, A. Landragin, and M. A. Kasevich, Classical Quantum Gravity **17**, 2385 (2000).
[15] J. Fils, F. Leduc, P. Bouyer, D. Holleville, N. Dimarcq, A. Clairon, and A. Landragin, Eur. Phys. J. D **36**, 257 (2005).
[16] A. Landragin and P. Featonby, French Patent No. FR 02-15454.
[17] With cold atoms, the Doppler width is small enough so that atoms can only feel the effect of a single Raman pair.
[18] Without the platform, the fluctuations could induce phase shifts higher than 2π [3], which would compromise the discrimination process.
[19] T. Gustavson, Ph.D. thesis, Stanford University, 2000.
[20] P. Cheinet, F. Pereira Dos Santos, T. Petelski, J. Le Gouët, K. T. Therkildsen, A. Clairon, and A. Landragin, physics/0510261 (to be published).

Eur. Phys. J. D **36**, 257–260 (2005)
DOI: 10.1140/epjd/e2005-00255-9

THE EUROPEAN PHYSICAL JOURNAL D

Influence of optical aberrations in an atomic gyroscope

J. Fils[1], F. Leduc[1,a], P. Bouyer[2], D. Holleville[1], N. Dimarcq[1], A. Clairon[1], and A. Landragin[1]

[1] BNM-SYRTE, UMR 8630, Observatoire de Paris, 61 avenue de l'Observatoire, 75014 Paris, France
[2] Laboratoire Charles Fabry, UMR 8501, Centre Scientifique d'Orsay, bâtiment 503, BP 147, 91403 Orsay, France

Received 5 March 2004 / Received in final form 20 June 2005
Published online 20 September 2005 –

Abstract. In atom interferometry based on light-induced diffraction, the optical aberrations of the laser beam splitters are a dominant source of noise and systematic effect. In an atomic gyroscope, this effect is dramatically reduced by the use of two atomic sources. But it remains critical while coupled to fluctuations of atomic trajectories, and appears as a main source of noise to the long term stability. Therefore we measure these contributions in our set-up, using cold cesium atoms and stimulated Raman transitions.

PACS. 03.75.Dg Atom and neutron interferometry – 42.15.Fr Aberrations – 32.80.Pj Optical cooling of atoms; trapping

1 Introduction

Since the pioneering demonstrations of interferometry with de Broglie atomic waves using resonant light [1,2] and nanofabricated structures [3] as atomic beam splitters, a number of new applications have been explored, including measurements of atomic and molecular properties, fundamental tests of quantum mechanics, and studies of various inertial effects [4]. Using atom interferometers as inertial sensors is also of interest for geophysics, tests of general relativity [5], and inertial guidance systems.

Atom interferometers based on light-induced beam splitters have already demonstrated considerable sensitivity to inertial forces. Sequences of optical pulses generate the atom optical elements (e.g., mirrors and beam splitters) for the coherent manipulation of the atomic wave packets [6]. The sensitivity and accuracy of light-pulse atom interferometer gyroscopes [7], gravimeters [8] and gravity gradiometers [9] compare favorably with the performances of state-of-the-art instruments. Furthermore, this type of interferometer is likely to lead to a more precise direct determination of the fundamental constant α from the measurement of $\hbar/M$ [10]. In the case of rotation measurements, the sensitivity reaches that of the best laboratory ring laser gyroscope [11]. Indeed the Sagnac phase shift, proportional to the total energy of the interfering particle, is much larger for atoms than for photons. This compensates for the smaller interferometer area and the lower flux.

In this paper, we focus on the effect of the fluctuations of the atomic trajectory, which might affect the long term stability of atomic gyroscopes when coupled with local phase variations induced by optical aberrations. We will introduce this problem in Section 2 and illustrate it quantitatively in the case of our set-up in Section 3.

Our experiment consists in an almost complete inertial measurement unit [12], using cold cesium atoms that enable for a drastic reduction of the apparatus dimensions while reaching a sensitivity of 30 $\mathrm{nrad\,s^{-1}\,Hz^{-1/2}}$ to rotation and 4×10^{-8} $\mathrm{m\,s^{-2}\,Hz^{-1/2}}$ to acceleration. Its operation is based on recently developed atom interference and laser manipulation techniques. Two interferometers with counter-propagating atomic beams discriminate between rotation and acceleration [13]. Thanks to the use of a single pair of counter-propagating Raman laser beams, our design is intrinsically immune to uncorrelated vibrations between the three beam splitters, usually limiting such devices. This configuration is made possible by the use of a reduced launch velocity, inducing a reasonable interaction time between the pulses. However, as any atomic gyroscope, our sensor's scheme remains sensitive to local phase variations, a limitation that has already been encountered in optical atomic clocks [14].

2 Principle

We first briefly review the basic light-pulse method in the case of a symmetric Ramsey-Bordé interferometer scheme [15], where three travelling-wave pulses of light resonantly couple two long-lived electronic states.The two-photon stimulated Raman transitions between ground state hyperfine levels are driven by two lasers with opposite propagation vectors $\mathbf{k}_e$ and $\mathbf{k}_g$ ($\mathbf{k}_e \simeq -\mathbf{k}_g$). First,

[a] e-mail: florence.leduc@obspm.fr

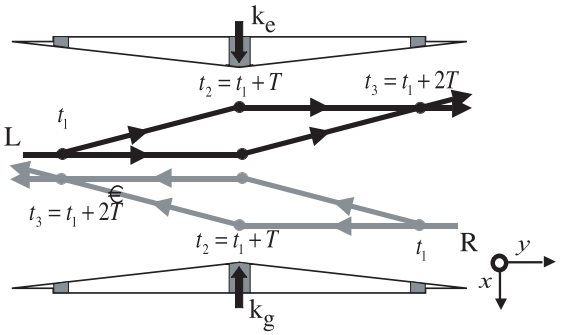

Fig. 1. Time-pulsed Ramsey-Bordé atom interferometer using stimulated Raman transitions induced by two counter-propagating laser beams of wave vectors $\mathbf{k}_e$ and $\mathbf{k}_g$. Cesium atoms are launched on the same trajectory but in opposite directions with velocities $\mathbf{v}^{L,R} = \{0, \pm v_y, v_z\}$, from right to left (R) and left to right (L). The interactions with light pulses occur at times $t_{i=1,2,3}$ at three different locations. The detection consists in measuring the probability of presence in each output port after the last pulse.

at $t = t_1$ a beam splitting pulse puts the atom into a coherent superposition of its two internal states. Because of conservation of momentum during the atom-light interaction, this pulse introduces a relative momentum $\hbar\mathbf{k}_{\text{eff}} = \hbar\mathbf{k}_g - \hbar\mathbf{k}_e$ between the atomic wave packets corresponding to each state. These wave packets drift apart for a time T, after which a mirror pulse is applied at $t_2 = t_1 + T$ to redirect the two wave packets. After another interval of duration T, the wave packets physically overlap, and a final beam splitting pulse recombines them at $t_3 = t_1 + 2T$. The measurement of the probabilities of presence in both internal states at the interferometer output leads to the determination of the difference of accumulated phases along the two paths. In general, atoms are launched with a velocity $\mathbf{v}$ so that each stimulated Raman transition occurs at a particular position $\{x_i, y_i, z_i\}_{i=1,2,3}$ that can be evaluated from the classical trajectories associated with the atomic wave packets [16], as shown Figure 1. In our set-up, Raman laser beams propagate in the (Ox) direction and atoms are launched in the (y, z)-plane. We define $\mathbf{u}_i = \{y_i, z_i\}$ the atomic cloud positions in this plane at time t_i.

In the absence of any external forces, atoms initially prepared in a particular state ($^6S_{1/2}$, $F = 3$, $m_F = 0$ in the present set-up) will return to this state with unit probability. A uniform external acceleration or rotation induces a relative phase shift between the interfering paths. This phase shift modifies the transition probability between the two cesium internal states $^6S_{1/2}$, $F = 3$, $m_F = 0$ and $^6S_{1/2}$, $F = 4$, $m_F = 0$ (noted $|3\rangle$ and $|4\rangle$ in the following). Hence the transition probability measurement leads to the determination of the phase shift and finally the evaluation of the perturbing forces.

It can be shown that the only contribution to the phase shift results from the interaction with the laser light fields [16]. In the limit of short, intense pulses, the atomic phase shift associated with a transition $|3\rangle \rightarrow |4\rangle$ (resp. $|4\rangle \rightarrow |3\rangle$) is $+\phi_i$ (resp. $-\phi_i$), where ϕ_i is the phase difference between the two Raman laser beams. We then find that the transition probability from $|3\rangle$ to $|4\rangle$ at the exit of the interferometer is simply $\frac{1}{2}[1 - \cos(\Delta\phi)]$ where $\Delta\phi = \phi_1 - 2\phi_2 + \phi_3$. The three quantities correspond to the phase imparted to the atoms by the initial beam splitting pulse, the mirror pulse, and the recombining pulse where $\phi_i = \phi_g(u_i, t_i) - \phi_e(u_i, t_i) = k_{\text{eff}} x_i + \Phi(\mathbf{u}_i)$. The sensitivity to rotation and acceleration arises from the first term $k_{\text{eff}} x_i$ and simplifies to $\Delta\phi_{\text{acc}} = a_x k_{\text{eff}} T^2$ and $\Delta\phi_{\text{rot}} = -2k_{\text{eff}} v_y \Omega_z T^2$ for the present set-up. The phase $\Phi(\mathbf{u}_i)$ for the pulse at time t_i corresponds to the local phase in the (y, z)-plane due to wavefront distortions of both laser beams[1]. It induces a residual phase error at the exit of the interferometer $\delta\Phi = \Phi(\mathbf{u}_1) - 2\Phi(\mathbf{u}_2) + \Phi(\mathbf{u}_3)$.

Acceleration cannot be discriminated from rotation in a single atomic beam sensor, as stated above. This limitation can be circumvented by installing a second, counter-propagating, cold atomic beam (Fig. 1) [13]. When both atomic beams perfectly overlap, the area vectors for the resulting interferometer loops have opposite directions. The corresponding rotational phase shifts $\Delta\phi_{\text{rot}}$ have opposite signs while the acceleration phase shifts $\Delta\phi_{\text{acc}}$ are identical. Consequently, acceleration is calculated by summing the two interferometer's phase shifts: $\Delta\phi_+ \sim 2\Delta\phi_{\text{acc}}$; while taking the difference rejects the contribution of uniform accelerations so that $\Delta\phi_- \sim 2\Delta\phi_{\text{rot}}$. In addition, the residual phase error $\delta\Phi$ vanishes in $\Delta\phi_-$, but remains in $\Delta\phi_+$ as an absolute phase bias $2\delta\Phi$.

However, an imperfect overlapping of the two counter-propagating wavepackets trajectories might lead to an imperfect common mode rejection of the residual phase error in $\Delta\phi_-$. Thus, a phase bias $\delta\Phi_- = \delta\Phi^L - \delta\Phi^R$ will appear, where the notations ^{L} and ^{R} concern the left and right atom interferometers. While the phase bias $\delta\Phi_+ \simeq 2\delta\Phi$ depends on the local value of the phase at the average position $\mathbf{r}_i = (\mathbf{u}_i^L + \mathbf{u}_i^R)/2$, the phase bias $\delta\Phi_-$ depends on the local phase gradient at the average position $\mathbf{r}_i$ with the position offset $\delta\mathbf{r}_i = \mathbf{u}_i^L - \mathbf{u}_i^R$:

$$\delta\Phi_- = \nabla\Phi(\mathbf{r}_1)\delta\mathbf{r}_1 - 2\nabla\Phi(\mathbf{r}_2)\delta\mathbf{r}_2 + \nabla\Phi(\mathbf{r}_3)\delta\mathbf{r}_3. \quad (1)$$

Equation (1) shows that uncorrelated fluctuations of the wavepackets trajectories from shot to shot causes fluctuations of the phase bias, which amplitude depends on the local wavefront slope of the phase. If we consider a perfect control of the launch velocity[2], fluctuations of trajectories are only due to fluctuations of the initial positions of the atomic clouds. Consequently, we can consider $\delta\mathbf{r}_1 = \delta\mathbf{r}_2 = \delta\mathbf{r}_3$. The phase fluctuation is then simply proportional to the product of the fluctuations of the cloud initial position (y_0, z_0) with the phase gradients $\Delta\Phi_i$. As

[1] The interferometer is also sensitive to time fluctuations of the Raman laser phases [12]. These fluctuations are identical for the two interferometers and disappear from the rotation signal. They will be neglected in this paper.

[2] We can reach a stability of 10^{-4} m s^{-1} or better from shot to shot thanks to the moving molasses technique [17].

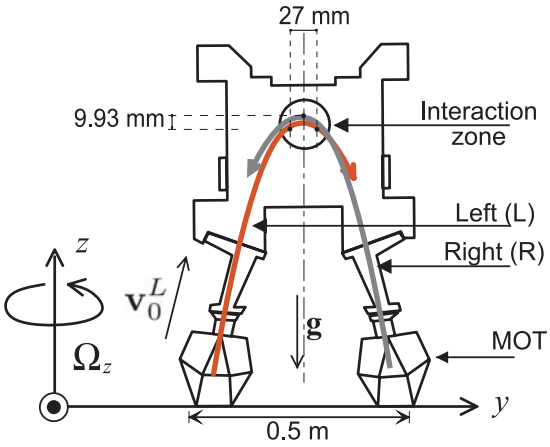

Fig. 2. Front view of our gyroscope; the interaction zone is located near the top of the atomic trajectories. Atoms are launched symmetrically at initial velocity $v_0 = 2.4\ \mathrm{m\,s^{-1}}$, making an angle of 82° with the horizontal axis. The enclosed oriented areas are equivalent to their projections on the (Oxy)-plane.

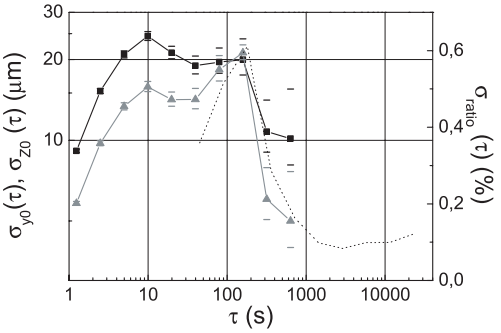

Fig. 3. Allan standard deviations of the horizontal (black squares) and vertical (grey triangles) MOT positions as a function of the integration time τ, plotted in log-log scale. On the right axis the Allan standard deviation of the intensity ratio of MOT cooling lasers is plotted in dashed line as a function of the integration time τ.

the phase gradients are time-independent, the Allan variance of the phase $\sigma^2_{\delta\Phi\_}$ is simply:

$$\sigma^2_{\delta\Phi\_} = \sigma^2_{y_0}\left[\partial_y\left(\Phi\left(\mathbf{r}_1\right) - 2\Phi\left(\mathbf{r}_2\right) + \Phi\left(\mathbf{r}_3\right)\right)\right]^2 + \sigma^2_{z_0}\left[\partial_z\left(\Phi\left(\mathbf{r}_1\right) - 2\Phi\left(\mathbf{r}_2\right) + \Phi\left(\mathbf{r}_3\right)\right)\right]^2 \quad (2)$$

where $\sigma^2_{y_0}$ and $\sigma^2_{z_0}$ are the Allan variances of the initial horizontal and vertical positions. Equation (2) shows that the fluctuations of the clouds initial positions, as well as the wavefront quality of the Raman beams, have to be systematically investigated in atomic gyroscopes in order to estimate how it affects its performances.

3 Experimental results

In our set-up, the atomic sources are clouds of cesium atoms, cooled in magneto-optical traps and launched with a parabolic flight (Fig. 2). As the initial angle reaches 82°, and the launch velocity 2.4 $\mathrm{m\,s^{-1}}$, the horizontal velocity v_y is 0.3 $\mathrm{m\,s^{-1}}$. The single pair of Raman laser beams propagates along the x-axis and is switched on three times at the top of the atomic trajectories. If the three pulses are symmetric with respect to the trajectory apogees, the interferometer oriented enclosed areas are equivalent to their flat horizontal projections: the oriented vertical projection is naught. The time delay between pulses is typically 45 ms. The positions of the atoms during the three Raman pulses are given in Figure 2.

In order to investigate the fluctuations of the atomic initial positions from shot to shot, we image one of the two clouds. The cycling sequence takes about 1.3 s and consists on a trap phase of 500 ms, a molasses phase of 20 ms, a launching phase of 2 ms and a waiting time phase of 800 ms needed to process the image: download of the image, subtraction of a background image and determination of the cloud barycenter position in y- and z-axes. The image is taken just after turning off the trap magnetic field, at the end of the molasses phase. We calculate the Allan standard deviations [18] of the barycenter horizontal and vertical positions (Fig. 3) from a one hour acquisition. Two peaks, appearing after 10 s and 150 s of integration time, are characteristic of fluctuations of periods equal to 20 s and 300 s. After about 10 min integration (630 s), the position standard deviations reach 10 μm and 5 μm in the horizontal and vertical directions respectively. This dissymmetry is consistent with the magnetic field gradient configuration, which is twice higher on the Z-direction. The long-term variations are due to fluctuations of the MOT cooling lasers intensity ratio, which Allan standard deviation is plotted in Figure 3. We see again the oscillation of period 300 s, appearing for 150 s integration time. We analyze this as the period of the air conditioning, creating temperature variations on the fibre splitters delivering the cooling lasers.

This result has to be coupled to the optical aberrations of the Raman lasers. The main contribution to these aberrations comes from the vacuum windows used for the Raman laser beams, which clear diameter is 46 mm. They have been measured with a Zygo wavefront analyzer, which gives the laser phase distortion created by the windows. This distortion is projected on the Zernike polynomial base [19]. As our atomic clouds are about 2 mm wide, the decomposition is pertinent only up to the 36th polynomial. Indeed, the upper numbers correspond to high spatial frequencies, so that their effect will be smoothed by averaging on the atomic cloud dimensions. To reduce the stress on the vacuum windows, essentially due to the mounting, they were glued in place. Thanks to this method, the wavefront quality reaches $\lambda/50$ rms over the whole clear diameter of 42 mm.

The wavefront measurement allows for evaluation of the atomic phase shift fluctuations due to the coupling between aberrations and position fluctuations using equation (2) assuming that the two sources are uncorrelated.

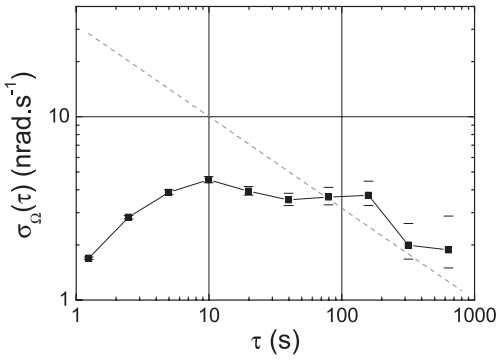

Fig. 4. Allan standard deviation of the rotation measurement, taking into account the optical aberrations when coupled with position fluctuations. The dashed curve shows the quantum projection noise limit, indicating that the optical aberrations may affect the gyroscope performances at long term.

Their relative position fluctuations are $\sqrt{2}$ times greater than these observed for one source. The contribution of this phase fluctuations to the Allan standard deviation of the rotation rate measurement is shown in Figure 4. We compare it with the ultimate stability of our gyroscope, given by the quantum projection noise. It is estimated to $30/\sqrt{\tau}$ nrad s^{-1} (τ is the integration time) from the ultimate signal-to-noise ratio obtainable with 10^6 atoms.

The rotation noise induced by position fluctuations has a significant contribution for integration times larger than 100 s. At the present stage of the experiment, this limitation is due to the high temperature sensitivity of the fibre splitters. This could be the main limitation of the gyroscope performances.

4 Conclusion

In the present paper we studied the stability of a cold atom gyroscope based on two symmetrical Ramsey-Bordé interferometers, with respect to optical phase inhomogeneity. Instability due to aberrations is not a specific problem induced by Raman transitions, but concerns every type of atom interferometer using light beam splitters. We showed that the coupling between wavefront distortions of these lasers and fluctuations of the atomic trajectory becomes predominant at long term, despite a wavefront quality of $\lambda/50$ rms obtained thanks to glued windows. In our set-up, atomic trajectory fluctuations are mainly due to fluctuations of the intensity ratio of the MOT cooling lasers, induced by the fibre splitters used for their generation.

However several improvements may render their contribution negligible:

- reduce the atomic trajectory fluctuations, by using discrete optical couplers for the MOT instead of the present fibre splitters,
- minimize the number of optics which contribute to the interferometer instability. This can be done by including the Raman laser beam imposition optics in the vacuum chamber, in order to remove the aberrations due to the vacuum windows, or by minimizing the number of non-common optics for the two Raman lasers, since only the phase difference between the lasers is imprinted on the atomic phase shift.

Such techniques open large improvement possibilities, which will be confirmed directly on the long-term stability measurement of the atomic signal in our interferometer set-up.

The authors would like to thank DGA, SAGEM and CNES for supporting this work, Pierre Petit for the early stage of the experiment and Christian Bordé for helpful discussions. They also thank Thierry Avignon and Lionel Jacubowiez from SupOptique for their help in the wavefront measurement.

References

1. F. Riehle, T. Kisters, A. Witte, J. Helmcke, Ch.J. Bordé, Phys. Rev. Lett. **67**, 177 (1991); M. Kasevich, S. Chu, Phys. Rev. Lett. **67**, 181 (1991)
2. E.M. Rasel, M. Oberthaler, H. Batelaan, J. Schmiedmayer, A. Zeilinger, Phys. Rev. Lett. **75**, 2633 (1995); D.M. Giltner, R.W. McGowan, S.A. Lee, Phys. Rev. Lett. **75**, 2638 (1995)
3. D.W. Keith, C. Ekstrom, Q.A. Turchette, D.E. Pritchard, Phys. Rev. Lett. **66**, 2693 (1991)
4. *Atom Interferometry*, edited by P.R. Berman (Academic Press, London, 1997)
5. R. Bingham et al., Assessment Study Report, ESA-SCI 10 (2000)
6. Ch.J. Bordé, *Laser Spectroscopy X*, edited by M. ducloy, E. Giacobino, G. Camy (World Scientific, 1991), p. 239
7. T.L. Gustavson, A. Landragin, M.A. Kasevich, Class. Quant. Grav. **17**, 1 (2000)
8. A. Peters, K.Y. Chung, S. Chu, Nature **400**, 849 (1999)
9. J.M. McGuirk, M.J. Snadden, M.A. Kasevich, Phys. Rev. Lett. **85**, 4498 (2000)
10. A. Wicht, J.M. Hensley, E. Sarajlic, S. Chu, in *Proceedings of the 6th Symposium on Frequency standards and metrology*, edited by P. Gill (World Scientific, 2001), p. 193
11. K.U. Schreiber, A. Velikoseltsev, M. Rothacher, T. Klügel, G.E. Stedman, D.L. Wiltshire, J. Geophis. Res. **60**, 615 (1997); K.U. Schreiber, A. Velikoseltsev, M. Rothacher, T. Klügel, G.E. Stedman, D.L. Wiltshire, J. Geophis. Res. **109** (2004); doi:10.1029/2003JB002803
12. F. Yver-Leduc, P. Cheinet, J. Fils, A. Clairon, N. Dimarcq, D. Holleville, P. Bouyer, A. Landragin, J. Opt. B: Quant. Semiclass. Opt. **5**, S136 (2003)
13. T.L. Gustavson, P. Bouyer, M.A. Kasevich, Proc. SPIE **3270**, 62 (1998)
14. T. Trebst, T. Binnewies, J. Helmcke, F. Riehle, IEEE Trans. Inst. Meas. **50**, 2165 (2001)
15. Ch.J. Bordé, in *Advances in the Interplay between Quantum and Gravity Physics*, edited by V. de Sabbada (Kluwer, Academic Publisher, 2001)
16. C. Antoine, Ch.J. Bordé, Phys. Lett. A **306**, 277 (2003)
17. A. Clairon, C. Salomon, S. Guellati, W. Phillips, Europhys. Lett. **16**, 165 (1991)
18. D.W. Allan, Proc. IEEE **54**, 221 (1966)
19. M. Born, E. Wolf, *Principles of Optics*, fifth edition (Pergamon Press, 1975)

Chapitre 4

Gravimètre à atomes froids

4.1 Introduction

Le projet de gravimètre absolu est lié à celui de balance du watt du Laboratoire National de Métrologie et d'Essais, dont le but est de proposer une nouvelle définition de l'unité de masse [Bordé 2005]. Dès le début, ce projet a pris en compte les problématiques liées à l'exactitude de la mesure de la gravité et à sa fiabilité afin de réaliser les mesures nécessaires au suivi de l'évolution de la gravité sur le site de Trappes, où sera finalement basée l'expérience. Ces acquisitions de la valeur de la gravité devront être évidemment réalisées de façon continue et simultanée avec les comparaisons de force effectuées sur de la balance. Enfin, pour démontrer pleinement l'intérêt de ce type de gravimètre par rapport aux instruments classiques, il sera nécessaire de réaliser des comparaisons, soit sur le site de Trappes, soit dans le cadre de campagnes de comparaisons internationales avec des gravimètres à coin de cube en chute libre. Ces contraintes ont orienté la conception du gravimètre vers un appareil relativement compact. Il est également important de noter que la sensibilité à court terme des gravimètres atomiques est intrinsèquement très élevée. Il suffit d'intégrer le signal pendant un temps relativement court (de 5 à 10 minutes) pour obtenir une exactitude au niveau de l'état de l'art et nécessaire pour l'expérience de balance du watt. Limiter volontairement le temps d'interrogation, et donc la sensibilité court terme, pour améliorer la compacité ou l'exactitude n'est donc pas pénalisant.

4.1.1 Etat de l'art des gravimètres

Gravimètres relatifs

Pour mesurer les variations de g, il est possible d'utiliser un ressort tendu sous le poids d'une masse. Les variations de position de la masse rendent compte des variations de l'accélération terrestre g. Un tel système présente cependant une résonance qui complique la mesure. La première méthode de montage permettant d'obtenir une grande sensibilité a été réalisée par La Coste et Romberg : elle consiste à maintenir la masse par des ressorts dits de longueur effective nulle, montés avec un angle de 45°. La période d'oscillation tend alors vers l'infini et ne gêne plus la mesure. Un bon contrôle de la température et l'utilisation de ressorts en silice fondue a permis la construction de gravimètres de très grande sensibilité (3.10^{-8} g.Hz$^{-1/2}$) malgré un retour à une géométrie verticale. Ces instruments sont affectés d'une dérive importante de quelques 10^{-8} g par jour, liée au vieillissement des ressorts et à la dérive de leur constante de raideur. Pour connaître la valeur de la gravité terrestre en un point avec ce type d'appareils, il faut au préalable réaliser un étalonnage à l'aide d'un gravimètre absolu ou d'une plateforme d'étalonnage [Riccardi 2002]. Par contre, la simplicité du principe de mesure a permis de rendre ces appareils très compacts et transportables.

Une technologie plus récente de gravimètre relatif s'est développée avec l'apparition des matériaux supra-conducteurs. Une sphère supraconductrice est mise en lévitation dans un champ magnétique généré par des bobines dont on contrôle l'alimentation. Un asservissement est réalisé sur la position de la sphère en réagissant sur le courant des bobines. Le signal d'erreur de l'asservissement donne alors les variations de l'attraction terrestre. Cette méthode offre une sensibilité exceptionnelle de l'ordre de 10^{-12}g.Hz$^{-1/2}$. De plus la dérive observée est extrêmement faible et vaut typiquement quelques 10^{-9}g par an [Hinderer 2002]. Elle est liée à l'instabilité des courants persistant dans les bobines supraconductrices et des variations de géométrie. La contrepartie à cette sensibilité exceptionnelle est la nécessité d'une enceinte cryogénique. De plus, tout déplacement requiert d'arrêter la lévitation et impose un ré-étalonnage de l'appareil.

Gravimètre commercial FG5

Un gravimètre est qualifié d'absolu lorsqu'il mesure g sans besoin d'étalonnage. Actuellement le gravimètre absolu le plus exact disponible dans le commerce (FG5, Microg Solutions) est fondé sur un interféromètre optique de Michelson [Faller 1967, Marson 1986]. L'un des miroirs est un coin de cube en chute libre, tandis que le miroir immobile joue le rôle de référence spatiale. En sortie de l'interféromètre, le déplacement du coin de cube fait défiler les franges d'interférences (fig. 4.1). La différence de chemin optique entre les deux bras de l'interféromètre est donnée par l'équation du mouvement du miroir en chute libre, et le signal

reçu sur la photodiode rapide varie comme :

$$I(t) = I_0 \cos\left(\frac{2\pi}{\lambda_l}\left(\frac{1}{2}gt^2 + v_0 t\right) + \Phi\right) \tag{4.1}$$

où la durée t de la chute est mesurée par une horloge atomique au Rubidium. Il suffit alors d'ajuster le signal à la fonction 4.1 pour connaître l'accélération de pesanteur locale.

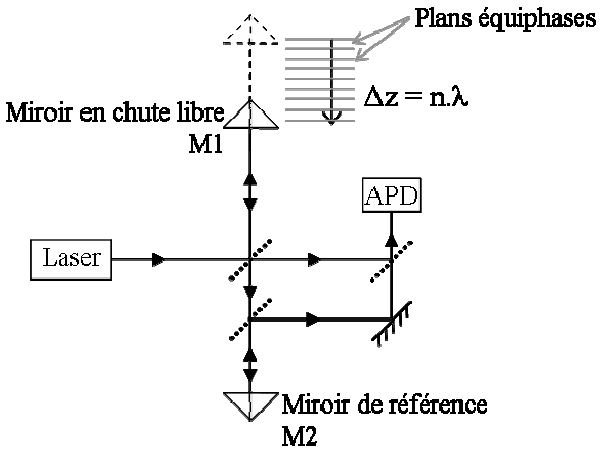

FIG. 4.1 : *Principe du gravimètre absolu à coin de cube en chute libre. La chute du miroir le long des plans équiphases fait varier la différence de chemin optique par rapport au miroir de référence comme* $\frac{1}{2}gt^2$*. Le défilement des franges est mesuré par une photodiode à avalanche (APD).*

Après correction des effets systématiques tels que le désalignement du faisceau laser, les gradients de gravité le long de la chute, les effets de marées terrestres et océaniques, de l'atmosphère, et du déplacement de l'axe de rotation de la Terre, l'exactitude annoncée est de $\delta g \approx 2\,10^{-9} g$, soit aussi 2 μGal (1 Gal =1 cm/s^2). Ses performances sont suffisantes pour l'objectif de la balance du watt, et cet instrument a donc été choisi dans les balances américaine, anglaise, et suisse. Cependant, d'une part les interféromètres atomiques se révèlent être plus sensibles et d'autre part ils permettent d'effectuer des mesures de g par des méthodes tout à fait différentes de celles des gravimètres à coin de cube, permettant d'identifier d'éventuels effets systématiques.

Interférométrie atomique

La première mesure de l'accélération de pesanteur par un interféromètre atomique a été réalisée en 1992 à Stanford, dans le groupe de Steven Chu [Kasevich 1992]. La manipulation cohérente des atomes de Césium était réalisée par des transitions Raman stimulées, dont le

principe a été rappelé au chapitre 2.2. Le schéma est similaire à celui de l'interféromètre de Mach-Zehnder en optique : une première transition sépare les paquets d'ondes, une seconde les redirige l'un vers l'autre, et une dernière recombine les paquets d'ondes des deux chemins pour faire interférer les états d'impulsions identiques (fig. 4.2). La source est un nuage d'atomes froids, dont la dispersion en vitesse étroite assure un bon contraste et un temps d'interrogation élevé. Les deux états de sortie de l'interféromètre sont identifiés par leur niveau d'énergie électronique, ce qui permet une détection simple par fluorescence [Bordé 1989].

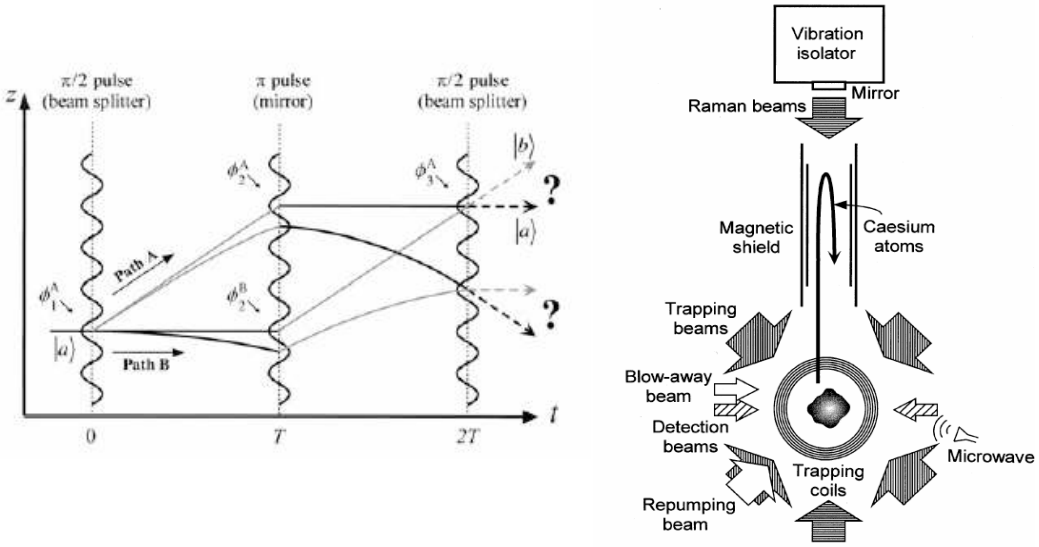

FIG. 4.2 : *Gauche : schéma de l'interféromètre à ondes de matière obtenu avec des transitions Raman. L'accélération g déforme les trajectoires par rapport aux surfaces d'ondes lasers. La mesure de g est déduite de la probabilité de transition d'un état d'impulsion à l'autre. Droite : fontaine atomique utilisée pour le gravimètre de Stanford. (Images tirées de [Peters 1999])*

La sensibilité croissant comme T^2 justifie l'intérêt des atomes froids pour ces expériences : le flux d'atomes élevé dans une distribution en impulsion étroite permet d'augmenter la durée $2T$ de l'interféromètre tout en conservant un bon rapport signal à bruit. Une configuration de fontaine atomique a été choisie, dans l'expérience de Stanford, pour augmenter encore la durée de l'interféromètre et la sensibilité. Comme nous le détaillons plus loin, les atomes de notre expérience sont simplement lâchés, ce qui réduit certes la sensibilité pour une mesure, mais permet de réduire l'encombrement de l'enceinte à vide, d'augmenter le taux de répétition et de réduire les effets systématiques liés aux défauts de trajectoires atomiques lors du lancement. Nous verrons également qu'en améliorant le rapport signal à bruit, les sensibilités obtenues sont finalement similaires.

Différents effets systématiques peuvent entâcher les gravimètres atomiques : des erreurs d'origine mécanique (alignements), liées aux défauts de trajectoires atomiques (sensibilité à la rotation et aux aberrations optiques), aux interactions atome-photon (effet Zeeman, déplacement lumineux) ou atome-atome. Le bilan d'exactitude du gravimètre de Stanford, achevé en 1999, donne une erreur relative sur g de $3\ 10^{-9}$ [Peters 1999, Peters 2001]. Une comparaison entre la mesure de ce gravimètre atomique et celle d'un FG5 sur le même site avait donné des résultats compatibles, aux incertitudes de mesure et de comparaison près. Néanmoins, l'effet des défauts de fronts d'onde des faisceaux lasers Raman n'a pas été pris en compte et représente, sans doute, une des sources principales de biais. Nous aborderons ce point par la suite. A cette occasion, l'interféromètre atomique avait montré une sensibilité sur une seconde 4 fois meilleure que celle de l'interféromètre optique dans les conditions particulières de vibrations du laboratoire. Ce gain était en grande partie dû au taux de répétition plus élevé du gravimètre atomique. En effet, pour le FG5, il faut attendre une dizaine de secondes entre deux mesures, avant que les vibrations causées par la chute du coin de cube ne s'estompent. En augmentant le temps d'interrogation à 2T = 800 ms, la sensibilité a été un peu améliorée [H-Müller 2008] pour atteindre $8\ 10^{-9}g$ sur une seconde . Le gravimètre atomique est ainsi apparu comme un bon candidat pour les expériences de balance du watt.

D'autre type d'interféromètres atomiques ont été proposés pour mesurer l'accélération de la gravité, en utilisant les transitions à deux photons dans le régime de Kapitza-Dirac [Cahn 1997, Weel 2006], ou en utilisant des transitions dans le régime de Bragg ou Raman [Impens 2006, Impens 2008, Hughes 2009].

4.1.2 Applications

La mesure absolue de l'accélération locale de la pesanteur est essentielle dans de nombreux domaines, de la géophysique à la métrologie. C'est ainsi par exemple qu'a été mis en évidence ce qui fut désigné comme "l'anomalie de Bouguer". Au cours de l'expédition qu'il mena au Pérou avec La Condamine de 1735 à 1743, afin d'y mesurer un degré de méridien à l'équateur, Pierre Bouguer procéda à des relevés de l'accélération de pesanteur g en utilisant un pendule. Bien qu'il prît en compte le gradient de gravité et l'influence des reliefs voisins, ses mesures rapportées à l'ellipsoïde de référence révélèrent des valeurs de g plus faibles au sommet des montagnes que dans les plaines, alors que l'on attendait au contraire que la masse de roche souterraine augmentât l'attraction terrestre. Ces observations ont été ensuite généralisées, jusqu'à être obtenues aujourd'hui par des satellites. L'anomalie de Bouguer s'interprète, à présent, comme une diminution de l'épaisseur de la croûte terrestre sous les reliefs.

Depuis, la gravimétrie est notamment mise à profit pour la prospection minière [Marson 1986]. En établissant un réseau de stations de mesures autour d'un site où une valeur absolue de g est connue, la cartographie des anomalies permet de détecter d'éventuels gisements, en tenant compte de multiples corrections : latitude (forme de la Terre et force centripète), gradient de gravité, correction de Bouguer, reliefs voisins...

En géophysique, le calcul du géoïde [Novak 2003] nécessite la connaissance absolue de l'accélération terrestre sur un très grand nombre de stations réparties sur la surface du globe, complétées par des mesures aériennes et plus récemment spatiales. En vulcanologie, les études sismiques permettent d'étudier l'activité d'un site, la composition de la croûte terrestre, sa délimitation avec le manteau ou leurs mouvements respectifs [Battaglia 1999, Mantovani 2001].

Notre gravimètre est quant à lui destiné à fournir une mesure absolue de g pour une mesure dans la balance du watt. L'expérience, décrite dans le paragraphe suivant, permettra de proposer une nouvelle définition du kilogramme. L'exactitude relative visée pour la mesure de masse étant de 10^{-8}, celle de notre gravimètre est de $\frac{\delta g}{g} = 10^{-9}$. Ainsi, après transfert entre les deux positions du gravimètre et de la balance, séparées de typiquement 10 m, l'erreur sur la connaissance de la gravité reste négligeable dans le bilan d'erreur total.

4.1.3 Application à la balance du watt : redéfinition du kilogramme

Le Kilogramme est la dernière unité du système international dont la définition repose sur un artefact matériel, et malgré tout le soin dont il fait l'objet, il s'use lors des comparaisons. Les comparaisons avec les copies du prototype international ont ainsi montré une dérive moyenne relative de l'ordre de $3\ 10^{-8}$ en 30 ans. La dérive absolue du kilogramme ne peut cependant pas être connue, tant que l'unité de masse est matérielle. La définition de la masse de référence du prototype international a donc été arrêtée comme sa masse immédiatement après son nettoyage-lavage selon une méthode bien spécifique.

L'unité de masse du système international varie, et avec elle les définitions connexes de l'ampère et d'autres grandeurs électriques ainsi que la valeur de la constante de Planck. Deux méthodes sont actuellement proposées afin d'établir une nouvelle définition du kilogramme. L'une consiste à produire une sphère de silicium, où le nombre d'atomes serait déduit de la maille cristalline et du volume de la sphère (mesuré par spectrométrie). Cette méthode démontre une exactitude relative de la constante d'Avogadro de $3\ 10^{-7}$ avec une composition isotopique naturelle, et pourrait atteindre $2\ 10^{-8}$ avec une sphère de ^{28}Si pur à 99,99% [Borys 2007]. Une autre méthode est la balance du watt, qui consiste à mesurer la constante de Planck h à partir du kilogramme actuel. La nouvelle définition de l'unité de masse serait alors

fondée sur cette mesure. Le gravimètre décrit ici a été développé pour participer au projet français de la balance du watt, piloté par le LNE [Geneves 2005].

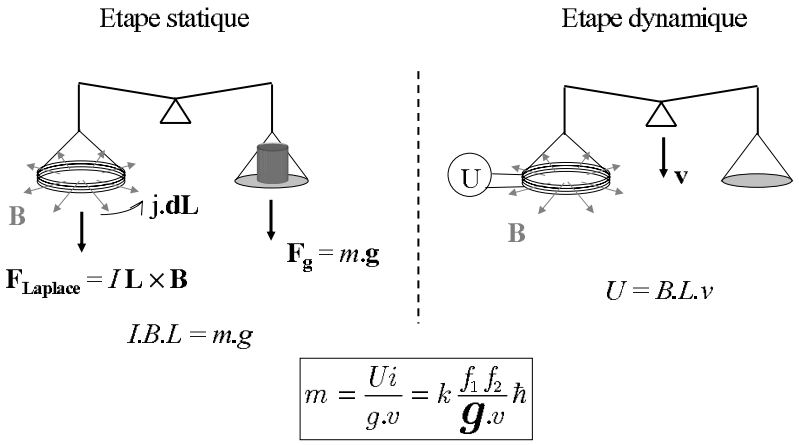

FIG. 4.3 : *Schéma du principe de la balance du watt. La première étape (statique) sert à déterminer la force égale au poids de l'étalon de référence. La deuxième étape (dynamique) permet de mesurer la valeur du produit $B.L$. Il est alors possible de déterminer avec exactitude la valeur de la masse de référence.*

Une mesure de masse avec la balance du watt est effectuée en deux étapes (fig. 4.3). La première est une phase statique : à un bras du fléau est fixée la masse de référence, et à l'autre se trouve une bobine de circonférence L dans laquelle circule un courant de charge $\mathbf{j}$. Un aimant produit un champ magnétique $\mathbf{B}$ dans une géométrie isotrope, de sorte que la force de Laplace résultante équilibre le poids de l'étalon de référence : $mg = IBL$. Le courant I équilibrant les deux forces est mesuré avec une grande exactitude à l'aide d'étalons de tension à effet Josephson et d'étalons de résistance fondés sur l'effet Hall quantique. La valeur du champ magnétique produit par l'aimant, et celle de la circonférence de la bobine sont difficilement mesurables avec la même exactitude. Aussi, dans une seconde étape, la bobine est déplacée dans le champ de l'aimant à une vitesse constante v. La tension induite $U = BLv$ aux bornes de la bobine et la vitesse v sont déterminées respectivement par effet Josephson et par interférométrie optique. L'ensemble des deux mesures permet de comparer une puissance électrique $U.i$ à une puissance mécanique $mg.v$ (d'où l'appellation de balance du watt), puis d'en déduire la relation entre la masse et la constante de Planck, qui s'écrit finalement :

$$m = k\frac{f_1 f_2}{gv}\hbar$$

où f_1 et f_2 sont les fréquences d'irradiation des étalons à effet Josephson lors de la mesure de la tension U et du courant i, via la résistance étalonnée par effet Hall quantique.

L'objectif de la balance du watt du LNE est d'atteindre une exactitude relative de 10^{-8} sur la mesure de la constante de Planck. La valeur de g sera mesurée dans une pièce à coté de la balance : il est donc nécessaire de faire le lien entre la valeur mesurée au niveau du gravimètre et au niveau précis où sera positionnée la masse de référence. Un travail exhaustif de mesure de g dans l'ensemble des deux salles a été réalisé, et permettra de faire ce raccordement [Merlet 2008]. La valeur de g, ainsi que les autres grandeurs mises en jeu, doivent donc être mesurées avec une meilleure exactitude, et l'objectif pour notre gravimètre est d'atteindre une exactitude relative de l'ordre de 10^{-9}.

4.2 Description générale du gravimètre

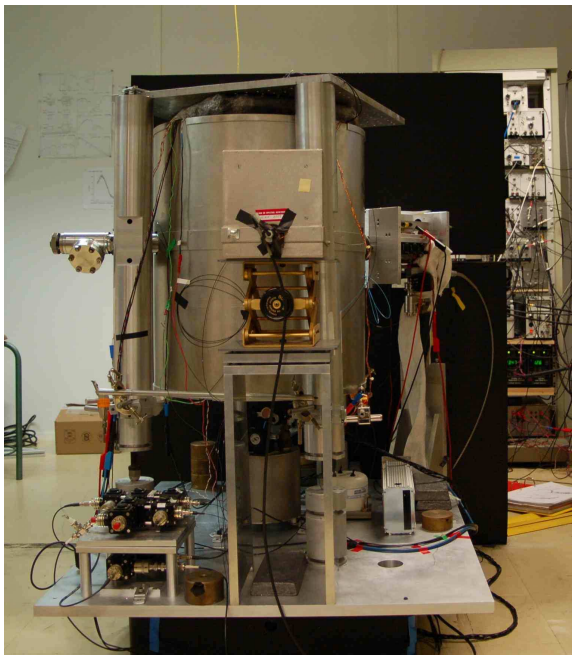

FIG. 4.4 : *Photographie du gravimètre. L'ensemble du système à vide est posé sur une plateforme d'isolation des vibrations. Les composants du piège 3D, interféromètre et détection sont à l'intérieur du blindage magnétique cylindrique. L'expérience est ensuite mise dans une boîte habillée de mousse, isolant des vibrations acoustiques (une des parois en noir est visible).*

Le gravimètre utilise une source d'atomes froids de Rubidium (^{87}Rb). Cette source est réalisée en chargeant un piège magnéto-optique à 3D par un jet ralenti issu d'un piège magnéto-optique à 2 dimensions. Le choix de cet atome est principalement lié à ses propriétés collisionnelles. D'une part, le déphasage, dû aux collisions entre atomes froids, est beaucoup plus

faible que pour le Césium [Sortais 2000], et d'autre part c'est un des atomes les moins difficiles à condenser [Anderson 1995]. Or il est prévu d'utiliser une source ultra-froide d'atomes dans ce gravimètre (voir paragraphe 4.5). Deuxièmement, il a été fait le choix, dès le début, de ne pas lancer les atomes comme dans une fontaine atomique par souci de simplicité du banc laser et de contrôle des trajectoires atomiques. Enfin, le chargement par un piège 2D permet d'une part un taux de cycle élevé limitant les effets des vibrations parasites et d'autre part de réduire très fortement la pression résiduelle de Rb dans l'enceinte à vide principale, garantissant que l'effet d'indice est négligeable dans la connaissance du vecteur d'onde effectif de la transition Raman.

Les résultats présentés dans ce manuscrit ont été réalisés avec une enceinte à vide préliminaire qui est en cours de remplacement. Cette enceinte ne permet pas d'atteindre le niveau d'exactitude nécessaire à l'expérience de balance du watt, mais a été utilisée pour permettre d'identifier clairement les problèmes expérimentaux afin de concevoir un système définitif compatible avec les exigences du projet.

4.2.1 Source atomique

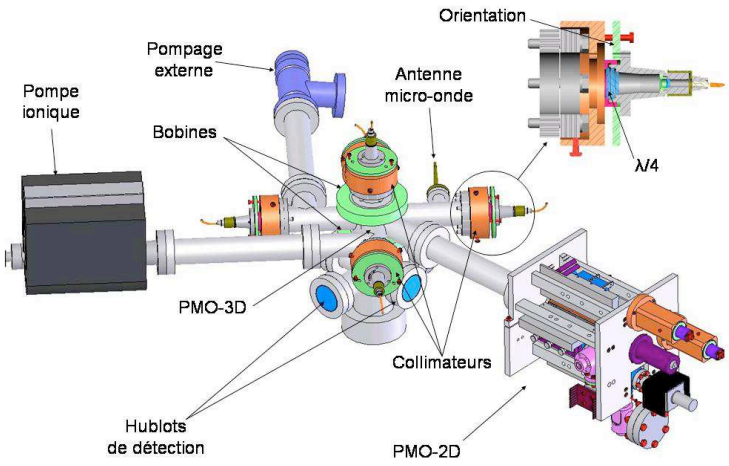

FIG. 4.5 : *Schéma de l'expérience.*

La source atomique est réalisée à partir d'un piège magnéto-optique à 3D chargé par un jet ralenti d'atomes issus d'un piège magnéto-optique à 2D [Dieckmann 1998, Cheinet thèse]. L'utilisation du chargement par un piège 2D permet de garder une pression de vapeur résiduelle faible dans l'enceinte à vide tout en ayant un chargement rapide du piège à 3D. Ce point est important pour assurer une fréquence de cycle élevée (typiquement 4 Hz) permettant de

moyenner efficacement les bruits de vibration. Un taux de chargement de 3.10^9 at.s^{-1} permet de charger jusqu'à 2.10^9 at dans le piège en environ 1s. En fonctionnement habituel, le temps de chargement est donc réduit à 50 ms pour limiter les temps morts tout en garantissant un nombre élevé d'atomes dans le piège. Après la phase mélasse, permettant de refroidir l'échantillon à 2,5 μK dans le niveau F = 2, les atomes sont préparés dans l'état F = 1, M_F = 0 à l'aide d'une impulsion micro-onde et d'un faisceau pousseur. Une sélection de la vitesse verticale (largeur $V_{rec}/2$) des atomes est alors réalisée à l'aide d'une seconde impulsion micro-onde qui repompe les atomes dans F = 2, M_F = 0 suivie d'une impulsion Raman qui retransfert uniquement les atomes ayant la vitesse sélectionnée dans l'état F = 1, M_F = 0 puis du faisceau pousseur.

4.2.2 Principe de la mesure de g

L'interféromètre est réalisé par une succession de trois impulsions Raman séparées respectivement d'un temps T pouvant allez jusqu'à 50 ms. Les atomes étant accélérés suivant la direction du faisceau Raman, il est nécessaire de changer la différence de fréquence entre les lasers Raman entre chaque impulsion Raman pour rester à résonance. Comme nous l'avons décrit dans le chapitre 2, le déphasage d'accélération correspond à l'accélération de la différence de phase (rampe de fréquence) entre les lasers Raman vue dans le référentiel en chute libre avec les atomes. En générant une rampe de fréquence α de signe opposé, il est possible de compenser le déphasage d'accélération :

$$\Delta\Phi = (\mathbf{a}.\mathbf{k_{eff}} - \alpha)T^2$$

Par ailleurs, en changeant la pente de la rampe de fréquence, il est possible de faire défiler les franges d'interférence. La rampe de fréquence $\alpha_\mathbf{0}$ qui compense exactement l'effet de la gravité peut être trouvée en changeant le temps d'interrogation de l'interféromètre. En effet, seule cette rampe correspond à un déphasage nul pour tous les temps d'interrogation (figure 4.6) :

$$\alpha_\mathbf{0} = \mathbf{g}.\mathbf{k_{eff}}$$

Une fois la frange centrale identifiée, nous effectuons des mesures à flanc de frange de façon alternée des deux cotés de la frange centrale. En comparant, les signaux des deux cotés, il est possible d'extraire un signal d'erreur qui permet d'asservir la fréquence moyenne de la frange pour suivre les variations de la gravité. Cette méthode a l'avantage de garantir une sensibilité maximale à flanc de frange d'une part et de s'affranchir d'éventuelles variations du contraste. L'expérience permet alors des acquisitions continues pendant des durées longues (figure 4.7) et donc de visualiser les effets des marées luni-sololaires.

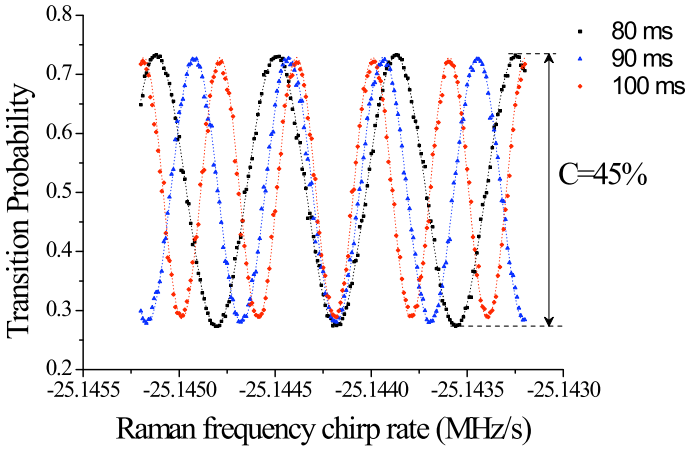

FIG. 4.6 : *Interférogrammes réalisés en changeant la rampe de fréquence appliquée sur la différence de fréquence entre les faisceaux lasers Raman.*

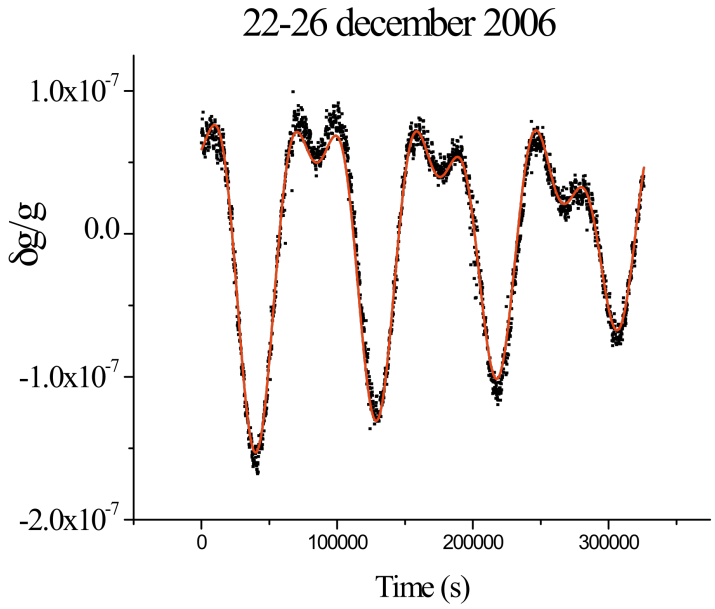

FIG. 4.7 : *Acquisition continue du signal d'accélération du 22 au 26 décembre 2006. Les données correspondent à une moyenne sur 25 s. La courbe représente la modélisation des effets de marée pendant cette même période.*

4.3 Sensibilité

Nous avons vu au chapitre 2 que l'interféromètre est sensible aux accélérations relatives entre les référentiels liés au centre de masse des atomes et celui aux équi-phases des lasers Raman. Dans le gravimètre, les lasers étant en configuration rétro-réfléchie, les équi-phases lasers sont donc étroitement liées à la position du miroir de rétro-réflexion (au terme près de délai de rétro-réflexion, voir article reproduit au paragraphe 2.4). D'un point de vue pratique, les deux sources principales de bruit correspondent, d'une part aux fluctuations temporelles de la différence de phase des faisceaux Raman et d'autre part aux vibrations parasites du miroir de rétro-réflexion. Un bilan de ces différentes sources de bruit est détaillé dans [Le Gouët thèse] et [Le Gouët 2008], qui est reproduit en fin du chapitre 4.

4.3.1 Bruits de phase des lasers Raman

Le même banc laser sert successivement au refroidissement, à l'interféromètre, puis à la détection et est décrit dans [Cheinet 2006] (reproduit en fin de chapitre, paragraphe 4.6). Les faisceaux lasers Raman sont réalisés à l'aide de deux lasers à cavité étendue, qui on été réalisés au laboratoire [Baillard 2006]. Le premier est asservi en fréquence proche de la transition D_2 du Rubidium ($F = 2$ vers $F' = 1, 2, 3$) via des techniques d'absorption saturée et de battement de fréquence. Le second est asservi en phase par rapport au premier via une rétroaction sur le courant de la diode laser avec une bande passante de plus de 4 MHz. Le bruit total de phase résulte des contributions dues aux résidus de phase de l'asservissement (principalement bruit aux fréquence supérieures à la bande d'asservissement), du bruit de la référence de fréquence micro-onde, aux bruits de propagation dans la fibre optique Raman (propagation dans la même même fibre mais suivant les deux axes propres de polarisation orthogonaux) et au délai de propagation couplé au bruit de fréquence du laser maître [Le Gouët 2007]. L'impact de ces différentes sources de bruit peut être étudié séparément grâce à la fonction de sensibilité (paragraphe 2.3). L'impact total est estimé à 3.5 mrad par coup, donnant une limite à la sensibilité de 4.10^{-9} g en une seconde, bien en dessous de la contribution liée aux vibrations parasites. De plus, les deux termes principaux peuvent être notablement réduits : le bruit de phase hors de la bande de l'asservissement, par exemple en augmentant la bande grâce à un modulateur électro-optique intra-cavité [Le Gouët 2009], et le bruit dû au délai de rétro-réflexion en améliorant l'asservissement de fréquence du laser maître. Il est donc possible de réduire l'ensemble des contributions pour atteindre un niveau de bruit permettant d'atteindre une sensibilité au niveau de 10^{-9} g en une seconde tout en gardant un interféromètre de temps d'interrogation réduit (2T = 100 ms).

4.3.2 Vibrations parasites

La deuxième source de bruit est liée aux vibrations parasites qui ont deux origines : les vibrations du sol et l'acoustique. Seules les sources de bruit à hautes fréquences (comparables à la fréquence de cycle ou supérieures) ont un réel impact, puisque les variations à basses fréquences peuvent être mesurées et moyennées : elles constituent le signal. Par ailleurs, l'interféromètre étant sensible aux positions des équi-phases au moment des trois impulsions, la sensibilité aux accélérations hautes fréquences f (au dessus de la fréquence de mesure 1/(2T) = 10 Hz) décroît donc comme f^{-2}. La gamme de fréquence pertinente des vibrations parasites, qui ont ont une influence, se situe donc typiquement entre 1 et 100Hz. Il est possible de calculer facilement la fonction de transfert de sensibilité aux vibrations à partir celle à la phase (voir eq. 2.32) en considérant d'une part qu'un saut de position et de phase sont équivalent, à un facteur k_{eff} près, et que l'accélération est la dérivée seconde de la position. A basse fréquence $\omega << \Omega_R$, la fonction de transfert de puissance d'accélération s'écrit :

$$|H_a(\omega)^2| = 16\frac{k^2}{\omega^4} sin^2(\frac{\omega T}{2}) \tag{4.2}$$

La sensibilité est constante en basse fréquence, puis décroît en ω^4 à haute fréquence avec des zéros aux harmoniques de $1/T$. Il est possible d'en déduire la limite de la sensibilité à un coup due aux vibrations parasites de densité spectrale de bruit $S_a(\omega)$ et pour un temps de cycle T_c comme étant la somme des harmoniques de fréquence de cycle $f_c = 1/T_c$:

$$\sigma_\Phi^2 = \frac{k_{eff}^2}{T_c} \sum_{n=1}^{\infty} |H_a(2\pi n f_c)|^2 S_a(2\pi n f_c) \tag{4.3}$$

Les vibrations acoustiques sont efficacement filtrées par l'utilisation d'une boîte tapissée à l'intérieur de mousse acoustique. Les vibrations du sol sont liées d'une part au fond sismique et d'autre part aux activités humaines à l'intérieur du laboratoire (climatisation, mezzanine, déplacement dans le laboratoire...) et à l'extérieur (passage du RER B sous le boulevard Denfert-Rochereau). L'impact de ces sources de bruit est notablement réduit par l'utilisation d'une plateforme anti-vibration passive (Minus-K) qui filtre efficacement le bruit au dessus de 1 Hz. En utilisant uniquement cette plateforme, les performances à court terme dépendent notablement de l'environnement extérieur, variant de 7.10^{-8} g.Hz$^{-1/2}$ en pleine journée à $1.4.10^{-8}$ g.Hz$^{-1/2}$ la nuit avec la climatisation éteinte.

4.3.3 Corrélation avec un sismomètre

Pour filtrer efficacement de façon active les vibrations à haute fréquence, il faut pouvoir les mesurer indépendamment au même niveau de sensibilité et de manière corrélée avec l'ac-

quisition de l'interféromètre. Pour cela, nous utilisons un sismomètre (GURALP T40) dont la bande passante (0,03 à 50 Hz) est adaptée à notre expérience. Le signal peut être utilisé pour réaliser un asservissement actif de la plateforme anti-vibration [Hensley 1999] ou plus simplement pour corriger des déphasages parasites. C'est cette dernière voie que nous avons testée de deux façons différentes.

La première méthode consiste en une acquisition simultanée avec l'interféromètre (figure 4.8), utilisée à postériori pour corriger le résultat issu du déphasage atomique. La seconde méthode consiste à modifier l'asservissement de phase en lui ajoutant un bruit de phase opposé à celui correspondant aux vibrations. Ces deux méthodes ont donné des résultats équivalents. Nous utilisons principalement la première méthode qui a l'avantage de la simplicité d'utilisation. Ces deux méthodes permettent d'obtenir une sensibilité de 2,5 à 3.10^{-8} g.Hz$^{-1/2}$ de façon très reproductible (de jour comme de nuit).

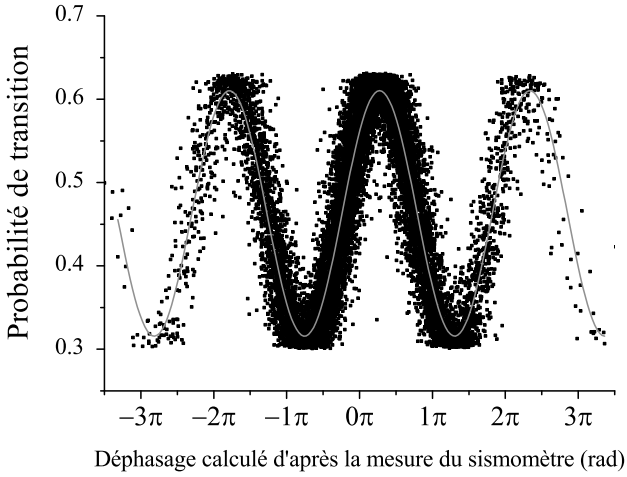

FIG. 4.8 : *Interférogramme en bloquant la plateforme anti-vibration. L'abscisse est déterminée en calculant le déphasage atomique attendu à partir du signal issu du sismomètre.*

La limite à cette méthode de corrélation de signaux est liée à la non linéarité du sismomètre et principalement à son filtre passe-bas qui déphase son signal aux fréquences supérieures à quelques Hz. Nous avons pu améliorer la corrélation à l'aide d'une méthode de filtrage numérique du signal issu du sismomètre, permettant d'obtenir une sensibilité de 2.10^{-8} g.Hz$^{-1/2}$, le bruit résiduel étant principalement dû aux couplages avec les axes horizontaux du sismomètre.

4.3.4 Mesures sans isolation des vibrations

Un des intérêts de la méthode de corrélation est de permettre de s'affranchir complètement de la plateforme d'isolation des vibrations, relativement encombrante en utilisant le gravimètre directement posé au sol. Sans cette méthode, le temps d'interrogation doit être limité à T = 10 ms afin que le déphasage reste inférieur à $\pi/2$ et d'éviter le problème d'ambiguïté de phase [Merlet 2009] (article reproduit à la fin du chapitre, paragraphe 4.6). Grâce à l'utilisation des signaux corrélés du sismomètre et de l'interféromètre, il est possible d'obtenir des sensibilités de $1{,}8.10^{-7}$ g.Hz$^{-1/2}$ le jour et de $5{,}5.10^{-8}$ g.Hz$^{-1/2}$ la nuit lorsque les sources de bruit dans la gamme 1 à 10 Hz sont nettement réduites. Enfin, en modifiant l'algorithme d'asservissement sur la frange centrale il est également possible de mesurer des variations très rapides des signaux comme, par exemple, ceux issus de tremblement de Terre (figure 4.9), démontrant la possibilité de travailler dans des environnements très bruités.

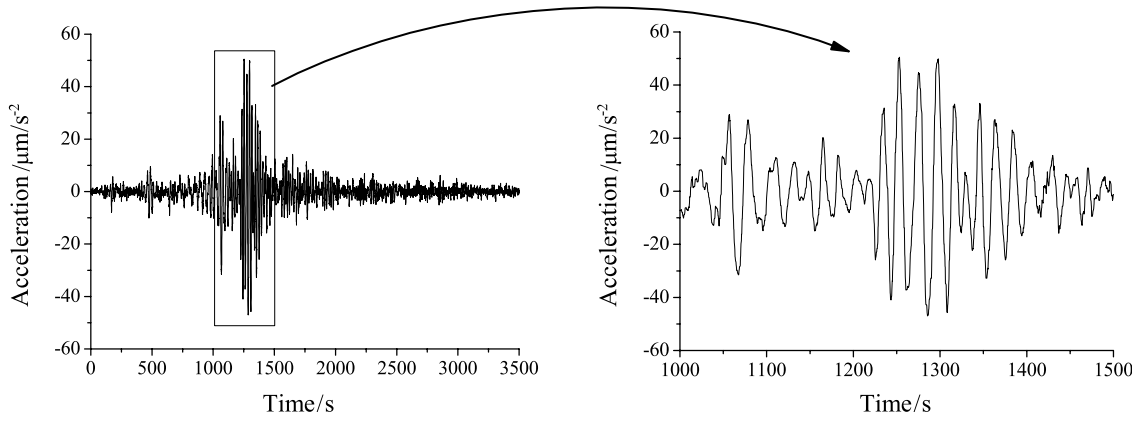

FIG. 4.9 : *Fluctuation du signal de gravité lors du tremblement de terre survenu en Chine le 20 mars 2008 et de magnitude 7,7. Les mesures ont été effectuées avec le gravimètre directement posé au sol. Les déphasages dépassent alors 2π, mais l'utilisation simultanée du sismomètre permet de lever l'ambiguïté de phase.*

4.4 Effets systématiques

L'objectif est d'atteindre une exactitude relative de 10^{-9} sur la mesure de la gravité. Or nous pouvons constater sur la figure 4.7 que les fluctuations à long terme (écart entre les données et le modèle) sont supérieures à cette valeur (de l'ordre de 10^{-8}). Les améliorations de la stabilité à long terme et de l'exactitude sont limitées par l'utilisation de l'enceinte à vide provisoire (magnétisme, défaut de surface d'onde des hublots...). Néanmoins, les études déjà me-

nées nous ont permis de tester les différentes stratégies pour les réduire [Mehlstäubler 2007]. Les effets systématiques peuvent être séparés en deux catégories suivant qu'ils dépendent ou non de $\mathbf{k_{eff}}$. S'ils en sont indépendants, ces effets ne changent pas de signe lorsque l'on alterne des mesures avec des vecteurs d'onde de directions opposées. Il est alors possible de les séparer du signal d'accélération en faisant la différence des résultats sans perdre en sensibilité. Si l'effet systématique change de signe avec $\mathbf{k_{eff}}$, il est nécessaire de mettre en place des méthodes de réduction plus complexes ou des étalonnages.

4.4.1 Effets indépendants de $\mathbf{k_{eff}}$

Trois termes, indépendants de la direction de $\mathbf{k_{eff}}$, contribuent principalement au biais de mesure : le déphasage lié au défaut de rampe de fréquence, le déplacement lumineux à un photon et l'effet Zeeman.

Rampe de fréquence

Le premier terme est dû à des défauts de linéarité de la rampe de fréquence et à la bande passante limitée de l'asservissement de phase des lasers Raman qui se traduit par un décalage entre la différence de fréquence réelle vue par les atomes et celle fixée par la référence microonde. Or ce décalage change pendant la rampe et se traduit par un déphasage parasite. Ce terme est identique pour deux rampes de sens opposés et ayant les mêmes fréquences initiales et finales.

Déplacement lumineux à un photon

Le second terme provient du déplacement lumineux à un photon Δ_{AC}. Il est possible de choisir le rapport de puissance [Weiss 1994] entre les deux faisceaux lasers Raman qui annule ce terme. Néanmoins ce rapport évolue dans le temps et est difficile à contrôler. Le déphasage qui en résulte s'écrit comme la différence de deux termes à la première et à la dernière impulsion :

$$\Delta\Phi_{AC} = \left(\frac{\Delta_{AC}^{(3)}}{\Omega_{\text{eff}}^{(3)}} - \frac{\Delta_{AC}^{(1)}}{\Omega_{\text{eff}}^{(1)}} \right) \tag{4.4}$$

De plus, ce terme s'annule à la sortie de l'interféromètre si les atomes voient la même intensité laser, et donc le même déplacement lumineux, pendant les trois impulsions. Mais comme les atomes ont une vitesse résiduelle transverse et que les faisceaux lasers Raman ont une forme gaussienne de taille finie ($\omega_0 = 12$ mm), ils voient une intensité différente à chaque impulsion. A cause de ces trajectoires transverses, nous avons mesuré une sensibilité de 5.10^{-9} g par % de rapport d'intensité et une réjection par la méthode différentielle de mieux que 99% qui nous garantit une réjection à bien mieux que 10^{-9} g.

Gradient de champ magnétique

Le troisième terme provient du gradient de champ magnétique. Bien que nous utilisions des atomes dans les sous-niveaux magnétiques $M_F = 0$, ils subissent un déplacement Zeeman au deuxième ordre. L'interféromètre étant symétrique du point de vue des états internes (les atomes passent autant de temps dans chaque état et dans chaque bras), il est insensible aux fluctuations long terme du biais de champ magnétique. Par contre l'interféromètre est sensible au gradient de champ magnétique le long de la trajectoire des atomes. A nouveau, la méthode différentielle permet de réduire cet effet à condition que les trajectoires des atomes soient identiques dans les deux cas à $\pm\mathbf{k}_{\mathbf{eff}}$. Pour cela, nous utilisons une impulsion micro-onde supplémentaire afin de débuter l'interféromètre dans les deux états internes différents pour les deux directions de diffraction comme indiqué sur la figure 4.10. Dans ces conditions, nous avons mesuré une réjection du biais de champ magnétique de 99,7% par rapport à des champs ajoutés de façon volontaire.

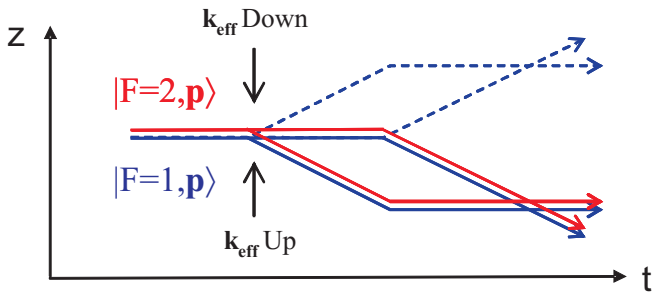

FIG. 4.10 : *Trajectoires atomiques dans le référentiel en chute libre en fonction du temps. Renverser la direction de* $\mathbf{k}_{\mathbf{eff}}$ *change la trajectoire moyenne des atomes. Par contre en changeant au préalable l'état interne, les trajectoires des deux interféromètres à* $\pm\mathbf{k}_{\mathbf{eff}}$ *sont identiques, garantissant la réjection du gradient de champ magnétique.*

4.4.2 Effets dépendants de $\mathbf{k}_{\mathbf{eff}}$

Quatre sources d'effets systématiques changent de signe avec le vecteur d'onde effectif et nécessitent d'être étudiées de façon systématique.

Alignement vertical

Le premier terme correspond à l'alignement de la direction de propagation des faisceaux lasers Raman suivant la verticale. Pour obtenir une exactitude relative de 10^{-9}, il est nécessaire d'aligner la verticale à mieux que 45 μrad. Ce terme peut être rendu négligeable en utilisant

directement le signal atomique et en répétant les mesures de g pour différentes valeurs d'inclinaison. La verticale correspondant au maximum de la valeur de g (variation parabolique).

Déplacement lumineux à deux photons

Le second terme correspond au déplacement lumineux à deux photons [Gauguet 2008] (article reproduit au paragraphe 4.6), lié à l'utilisation de la configuration rétro-réfléchie. Dans cette configuration, le désaccord Raman est ajusté pour annuler l'effet Doppler pour une paire de faisceaux Raman, alors que l'autre est décalée de deux fois l'effet Doppler. Cette transition à deux photons non résonante produit des déplacements lumineux de signes opposés pour les deux états couplés par la transition résonnante, qui croissent avec l'intensité des faisceaux laser Raman et décroissent avec l'effet Doppler (noté δ_D). Ce déplacement induit un déphasage parasite sur l'interféromètre s'il est différent pour la première et la dernière impulsion :

$$\Delta\Phi_{TPLS} = \frac{\Omega_R^{(1)}}{4\delta_D^{(1)}} - \frac{\Omega_R^{(3)}}{4\delta_D^{(3)}} \tag{4.5}$$

Pour le gravimètre, le déphasage est notamment dû à l'effet Doppler qui augmente avec le temps de chute entre la première et la dernière impulsion (figure 4.11).

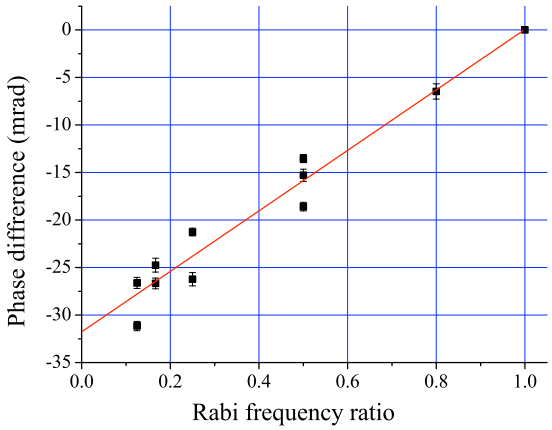

FIG. 4.11 : *Variation du déplacement lumineux à deux photons en fonction de la puissance des faisceaux lasers Raman. Les mesures ont été réalisées de façon différentielle par rapport à la puissance maximale.*

Par rapport à un gravimètre en fontaine dans lequel les atomes sont lancés verticalement, cet effet est relativement important (typiquement 32 mrad) pour notre gravimètre puisque l'effet Doppler à la première impulsion est relativement faible (temps de chute de 17 ms).

Néanmoins en alternant des mesures à forte et faible puissance, il est possible d'extrapoler cet effet à mieux que 1 mrad correspondant à 4.10^{-9} g. Pour améliorer encore la résolution de cet effet pour atteindre 10^{-9} g, une méthode consiste à baisser la puissance des faisceaux lasers Raman, quitte à réaliser une sélection en vitesse plus importante dans la direction verticale.

Rotation de la terre

Le troisième effet est lié à la sensibilité aux vitesses de rotation lorsque l'aire de l'interféromètre n'est pas parfaitement nulle. Cela peut, soit provenir d'un défaut de verticalité des faisceaux Raman, soit de la présence d'une vitesse horizontale résiduelle des atomes à la fin de la phase mélasse, soit d'un défaut de symétrie de la détection, favorisant plus une classe de vitesse transverse que les autres. L'aire orientée ainsi créée rend l'interféromètre sensible à une composante horizontale de la rotation Ω_H. Dans le cas d'une vitesse horizontale transverse dans la direction Est/West δV_{EW}, le déphasage parasite correspond à une accélération équivalente :

$$\delta_a = 2\Omega_H.\delta V_{EW}$$

Pour que cet effet ait une contribution plus faible que 10^{-9} g, il faut annuler la vitesse horizontale des atomes à mieux que 100 μm.s^{-1}, soit cent fois moins que la distribution en vitesse. Ce contrôle n'est pas possible avec cette enceinte à vide mais il le sera avec le nouveau dispositif. De plus, une façon indépendante de contrôler cet effet est de tourner l'expérience autour de l'axe vertical. Projection de composante horizontale de la vitesse de rotation de la terre est alors modulée de façon sinusoïdale et peut être mesurée.

Défauts de front d'onde

Le dernier effet est lié aux défauts de front d'onde. Il dépend également de la trajectoire des atomes dans le plan orthogonal à la direction de propagation des faisceaux lasers Raman (plan horizontal). A nouveau, avec l'enceinte préliminaire, cet effet est important car la qualité des hublots n'est pas suffisante. De plus, même si la vitesse moyenne des atomes est nulle dans le plan horizontal, un déphasage parasite apparaît à cause de la température résiduelle (expansion du nuage pendant la chute) et peut conduire à un biais important. En prenant le cas le plus simple d'une courbure des équi-phases Raman, il est possible de calculer que le biais augmente comme la température des atomes T_{at} et la courbure $1/R$ [Landragin 2009] :

$$\Delta\phi = 2\frac{k_{eff}}{R}\frac{k_B T_{at}}{m}T^2 \tag{4.6}$$

Pour un échantillon à 2,5μK et pour garder le biais inférieur à 10^{-9} g, il faut que le rayon de courbure soit supérieur à 16 km, soit à mieux que $\lambda/400$ sur un diamètre de 20 mm.

4.5 Conclusions

Avec un temps de cycle de seulement 250 ms et pour un temps d'interrogation de 100 ms (une distance de chute de quelques cm seulement) la sensibilité actuelle sur la mesure de g est de 2.10^{-8} g sur 1s, comparable à l'état de l'art en gravimétrie absolue. Elle est meilleure que celle des gravimètres commerciaux à coin de cube dans les mêmes conditions expérimentales ($3{,}5.10^{-8}$ g.Hz$^{-1/2}$). La sensibilité actuelle est principalement limitée par les vibrations parasites résiduelles du dispositif expérimental. Ces performances sont obtenues grâce à l'utilisation d'une plate-forme d'isolation passive et d'une correction de la mesure atomique par une mesure indépendante du bruit de vibration résiduel, réalisée à l'aide d'un sismomètre bas bruit. Ce niveau de sensibilité à court terme est tout à fait suffisant pour son application à la balance du watt puisque qu'il permet d'atteindre une stabilité relative de 10^{-9} en seulement 7 minutes de mesure. Le travail expérimental sur la stabilité à court terme permet également d'extrapoler ces résultats dans le cadre des projets spatiaux [Wolf 2009, Ertmer 2009].

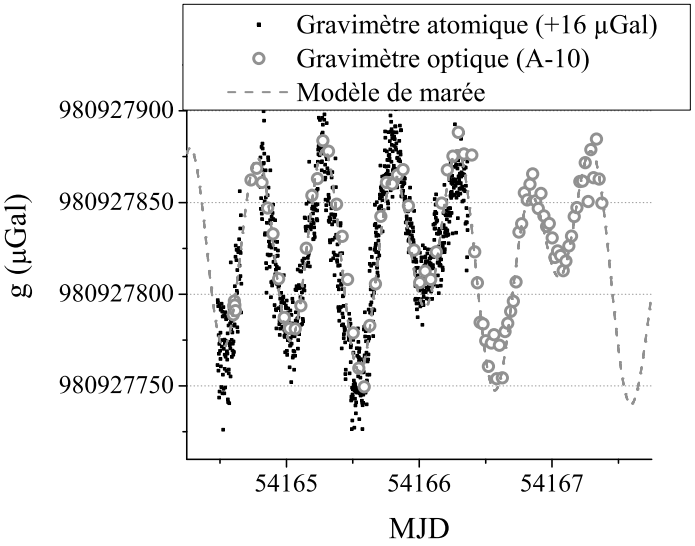

FIG. 4.12 : *Marées luni-solaires de la gravité mesurées par le A10 de l'IPGP et le gravimètre du SYRTE (mesures décalées de 16μGal)*

L'étude en cours des effets systématiques montre les limites imposées par le premier dispositif utilisant une enceinte à vide préliminaire : gradient de champ magnétique trop élevé, défaut d'homogénéité de la détection, aberrations sur les fronts d'onde des faisceaux lasers, manque d'accès optiques, absence de contrôle des trajectoires atomiques… La comparaison de notre instrument avec des gravimètres à coin de cube de type A10 donne un écart de

16.10^{-9} g (figure 4.12), que nous attribuons aux effets d'accélération de Coriolis et d'aberrations du front d'onde que nous ne sommes pas en mesure de quantifier précisément dans ce premier dispositif. Néanmoins, cette étude préliminaire des effets systématiques a mis en évidence la nécessité d'un meilleur contrôle des trajectoires transverses des atomes et l'intérêt d'utiliser des atomes plus froids. Elle a également mis clairement en évidence les problèmes liés aux défauts de front d'onde jusqu'alors négligés ou sous-estimés.

Il a été, par ailleurs, montré que l'exploitation du signal complémentaire d'un sismomètre mécanique permet également d'obtenir une excellente sensibilité dans un environnement beaucoup plus bruité, voire sans aucune isolation des vibrations. Pour cela, nous avons développé une méthode de traitement numérique du signal du sismomètre qui adapte le filtre de correction en fonction de l'environnement, ce qui ouvre la voie vers la réalisation de capteurs compacts et transportables fondés sur ces techniques d'interférométrie atomique. L'utilisation de gravimètres atomiques compacts pourrait remplacer avantageusement les gravimètres relatifs à ressorts pour les mesures de terrain en géophysique, pour lesquel il est nécessaire de réaliser des boucles afin de limiter l'impact des dérives.

4.6 Articles relatifs à l'expérience de gravimètre atomique

Quatre articles relatifs au gravimètre atomique sont reproduits ici. Le premier (Appl. Phys. B 2006) décrit en détail la réalisation du banc laser compact utilisé pour réaliser l'interféromètre et notamment le système d'asservissement en phase des lasers Raman. Le second (Appl. Phys. B 2008) détaille les différentes limites à la sensibilité à court terme du gravimètre. Le troisième (Metrologia 2009) décrit le fonctionnement de l'interféromètre couplé au sismomètre et dans un environnement donnant lieu à des déphasages supérieurs à la zone de linéarité. Le dernier article (Phys. Rev. A 2008) décrit les études de l'effet systématique dû au déplacement lumineux à deux photons, qui ont été réalisées à l'aide des deux expériences gravimètre et gyromètre.

Appl. Phys. B 84, 643–646 (2006)
DOI: 10.1007/s00340-006-2266-2

Applied Physics B
Lasers and Optics

Compact laser system for atom interferometry

P. CHEINET
F. PEREIRA DOS SANTOS✉
T. PETELSKI
J. LE GOUËT
J. KIM*
K.T. THERKILDSEN**
A. CLAIRON
A. LANDRAGIN

Lne-Syrte, CNRS UMR8630, Observatoire de Paris, 61 avenue de l'Observatoire, 75014 Paris, France

Received: 24 March 2006
Published online: 20 May 2006 •

ABSTRACT We describe an optical bench in which we lock the relative frequencies or phases of a set of three lasers in order to use them in a cold atom interferometry experiment. As a new feature, the same two lasers serve alternately to cool atoms and to realize the atomic interferometer. This requires a fast change of the optical frequencies over a few GHz. The number of required independent laser sources is then only three, which enables the construction of the whole laser system on a single transportable optical bench. Recent results obtained with this optical setup are also presented.

PACS 32.80.Pj; 42.50.Vk; 39.20.+q

1 Introduction

Within the last decades, atom interferometers have developed into a highly competitive tool for precision measurements [1]. Atomic fountains used as atomic clocks are the best realization of the time unit [2]. Atom interferometry also promises sensors that will be highly sensitive to inertial forces [3–6]. The use of stimulated Raman transitions to manipulate the atomic wave packet has proven to be an efficient way to obtain high accuracy devices [5, 6].

These techniques are now used to realize reliable instruments, with potential applications in inertial navigation, gravity field mapping, metrology, and fundamental tests in space.

In this letter, we describe a robust, compact and versatile laser system for atom interferometers using alkali atoms. Such experiments basically need two different optical frequencies, whose difference remains close to the hyperfine transition frequency. When they are tuned close to the D2 transitions, they are used to cool and repump the atoms in a magneto–optical trap (MOT). When far detuned, and phase locked, they are used to induce stimulated Raman transitions for the interferometer [7]. Since the lasers are not used simultaneously for trapping and Raman transitions, we have implemented a technique to use the same two lasers for both functions. It allowed us to build the whole laser setup on a $60 \times 90\ \mathrm{cm}^2$ optical bench. This setup has been developed for a transportable atomic gravimeter [8], whose present sensitivity is comparable to state of the art instruments.

✉ Fax: 33 1 4325 5542, E-mail: franck.pereira@obspm.fr
**Present address*: Department of Physics, Myongji University, Yongin, 449-728, Korea
***Present address*: Niels Bohr Institute, University of Copenhagen, Universitetsparken 5, 2100 Copenhagen, Denmark

2 Laser setup

Our laser setup is shown in Fig. 1. A first laser L1 is locked on an atomic transition, using FM-spectroscopy [9] on a saturated absorption signal. This laser constitutes an optical frequency reference and is used in our experiment to detect or push the atoms. A second laser L2 is alternately used as a repumper or as the master Raman laser. Part of the outputs of L1 and L2 are superimposed on a fast photodetector (PD_{12}) (Hamamatsu G4176) and the frequency of the beat note is servo locked by using a frequency to voltage converter. A third laser L3 is used alternately as a cooling or as a slave Raman laser. The frequency difference between L2 and L3 is measured with a second optical beat note on PD_{23}. Finally, both L2 and L3 beams are superimposed and directed through an acousto-optical modulator either to realize the magneto-optical trap or the atomic interferometer.

Both frequency locks of L2 and L3 use the same scheme which is shown in Fig. 2. The optical beat note issued from the photodetector is mixed with a reference oscillator, down to an intermediate frequency (IF). For the L2 lock, this reference is a YIG oscillator, which can be tuned between 3 and 7 GHz.

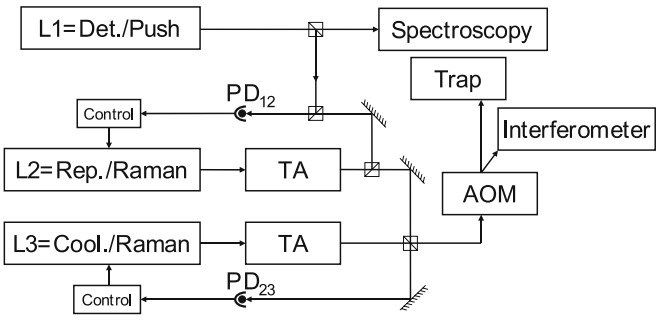

FIGURE 1 Laser setup. The detection laser L1 is locked on a spectroscopy signal. The repumper laser L2 frequency is compared to the detection laser frequency with an optical beat note and is frequency locked. A similar lock is used for the cooling laser L3. Two tapered amplifiers (TA) are used on the repumper and cooling lasers, before they are combined on a polarizing beam splitter cube and sent alternately to the trap or to the interferometer using an acousto-optical modulator (AOM)

Whereas for L3 we use a fixed 7 GHz frequency obtained by the multiplication of a low phase noise 100 MHz quartz oscillator. The IF signal is then sent into a digital frequency divider in order to fit into the working frequency range (0–1 MHz) of a frequency to voltage converter (FVC) (AD650). A computer controlled offset voltage V_{Set} is subtracted from the output voltage of the FVC. The obtained error signal is integrated once and added to the laser diode current. This correction signal is integrated again and added to the piezoelectric (PZT) voltage which controls the cavity length. To change the laser frequency, one can change V_{Set} for fine tuning or the YIG frequency for larger frequency changes. In addition, computer controlled feed-forward current I_{C} and voltage V_{C} are added to the current and PZT drivers to help the lock while changing the laser frequency.

For the phase lock of L3 a second path is implemented. The IF frequency is divided by 2 and compared, in a digital phase and frequency detector (DPFD) [10] (MCH12140), to the signal of a local oscillator at 82.6 MHz which is generated by a direct digital synthesiser (DDS) (AD9852) clocked at 300 MHz. The DPFD delivers an error signal which is added through a high bandwidth servo system (~ 4 MHz) to the laser current. It is also added to the PZT error signal before its last integration. Moreover some switches can be activated so that either the frequency lock loop or the phase lock loop is closed.

3 Atom interferometer

Our interferometer is an atomic gravimeter which measures the acceleration of freely falling ^{87}Rb atoms. Its sensitivity is given by: $\Delta\Phi = k_{\mathrm{eff}} g T^2$, where $\Delta\Phi$ is the interferometric phase, k_{eff} is the effective wave vector of the Raman transition, g is the Earth's gravity acceleration and T is the time between the interferometer's Raman pulses.

This frequency locking system is versatile and enables dynamic controlling of the frequency of the two lasers, over the whole experimental sequence. It is possible to first frequency lock the lasers to the frequencies required to cool ^{87}Rb atoms in a MOT. By dividing the total available laser power between a 2D-MOT [11] and a 3D-MOT, the loading rates of 3×10^9 atoms s^{-1} are obtained. Then we turn the magnetic field off and further cool the atoms with σ^+–σ^- molasses down to a temperature of 2.5 μK.

Once the atoms have been released from the molasses, a frequency ramp is applied on the YIG oscillator. This ramp induces a detuning Δ of up to 2 GHz on both L2 and L3 to get the Raman laser frequencies. We also add a ramp on the PZT voltages V_{C} to induce a 2 GHz sweep so that the laser frequencies stay inside the locking range. Since the PZT mode-hop free tuning range is close to ± 0.6 GHz, it is necessary to change the current setting point of the laser during the sweep. Thus, we also apply a simultaneous feed-forward ramp to the laser injection currents I_{C}, so that the laser frequencies remain in the middle of the free tuning range. When the servo loop is closed, the lasers stay locked during the whole sequence.

In Fig. 3 the response of the servo system to a frequency ramp of 2 GHz in 2 ms, in open and closed loop configurations is shown. The black curve corresponds to the error signal of L2 in open loop operation. It reflects the difference between the lasers frequency difference and the YIG frequency. The L2 laser frequency remains within 100 MHz from the locking point during the whole 2 GHz ramp. The voltage ramp does not compensate exactly for the sweep because of thermal effects due to the change in the laser current. When the servo loop is closed, the remaining frequency deviation is compensated for. The gray curve shows the residual frequency error of L2 during the sweep, and reveals residual damped oscillations of the PZT.

We then switch L3 to the phase-locked loop (PLL) after the end of the frequency ramp. We aim at obtaining an accuracy of 10^{-9} g which implies that the differential phase between the two Raman lasers remains on average below 0.3 mrad over the duration of the interferometer 2 T [8]. We display in Fig. 4 this phase difference as a function of the de-

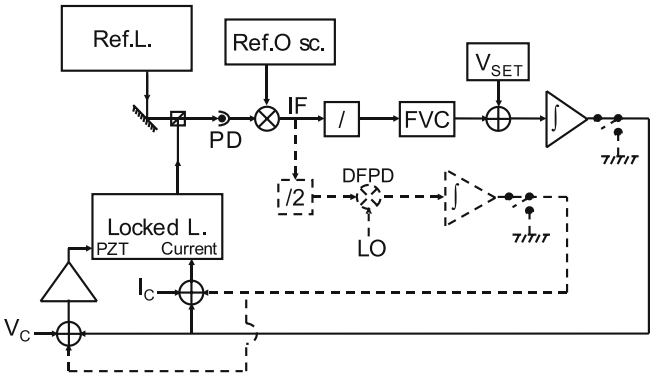

FIGURE 2 Locking electronics. Frequency lock scheme (*solid line*). The optical beat note is mixed with a reference oscillator to an intermediate frequency (IF). The IF is divided and converted to a voltage signal and another voltage V_{Set} is subtracted to obtain the error signal of the lock. This error signal is integrated and then sent to the current driver. It is integrated once more and sent to the PZT driver. Feed-forward corrections I_{C} and V_{C} are added to the diode current and to the PZT voltage during the sweep. A phase lock scheme is added to L3 (*dotted line*). The IF is compared to a local oscillator (LO) in a digital phase and a frequency detector (DPFD) delivering the phase error signal. Two switches select which loop is closed

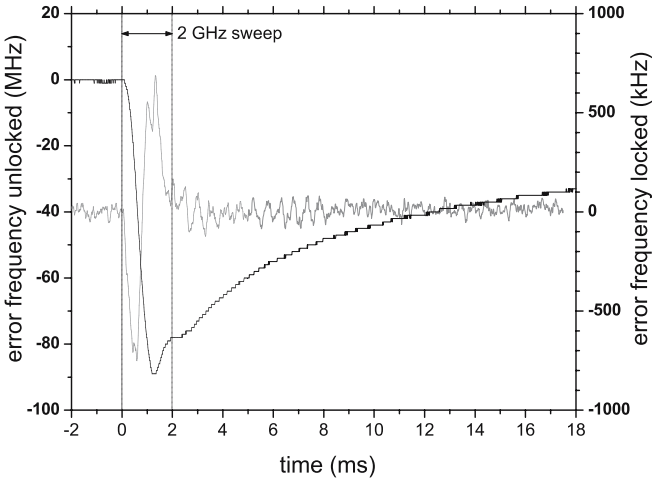

FIGURE 3 L2 frequency error during a 2 GHz sweep imposed in 2 ms. The *black trace* displays the frequency error when the servo loop is opened, and shows a sharp transient edge during the sweep, followed by an exponential like decay. The *gray trace* displays the frequency error when the servo loop is closed

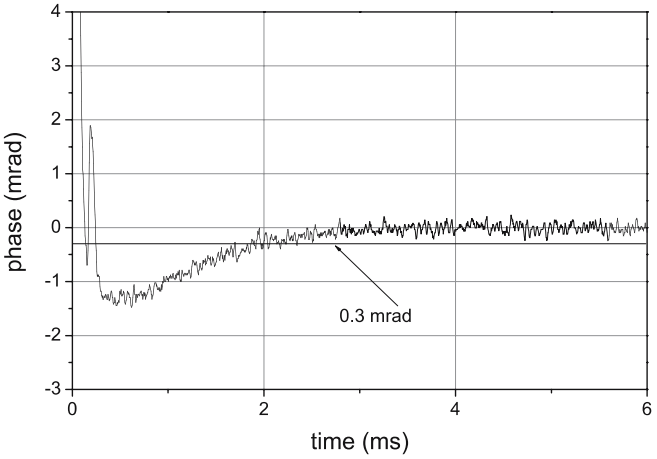

FIGURE 4 Differential phase between the Raman lasers. The PLL is closed at $t = 0$ after the 2 GHz sweep. After 0.5 ms, the phase difference is exponentially decreasing with a time constant of 2 ms

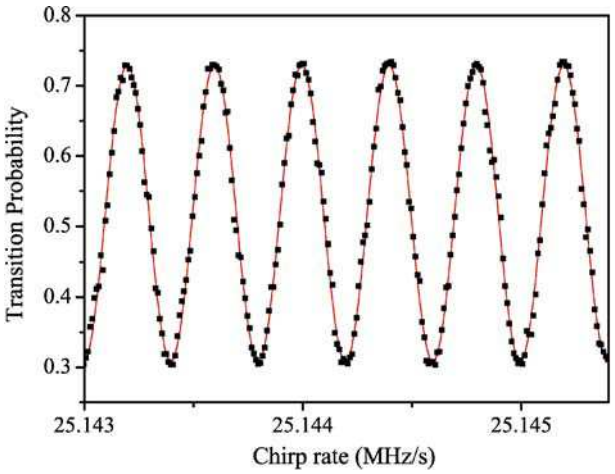

FIGURE 5 Atomic interferometer fringes obtained by scanning the Raman detuning chirp rate during the interferometer. The time between the Raman pulses is $T = 50$ ms. The *solid line* is a sinusoidal fit of the experimental points displayed in *black squares*

lay after enabling the PLL. At the start, the DPFD delivers an error signal proportional to the frequency difference between the divided IF and the LO. This makes the loop behave as a frequency lock loop, with a time constant of a few hundreds of μs. Once the frequency of the divided IF matches with the LO frequency, the DPFD detects the phase difference between them, which makes the loop behave as a phase lock loop. 0.5 ms after the loop is closed, the phase reaches a steady state with a 2 ms time constant exponential decay. The 0.3 mrad criterion is then reached in about 2 ms. We have measured its spectral phase noise density in the steady state [8]. When weighted by the transfer function of the atom interferometer, which acts as a low pass filter, and integrated over an infinite bandwidth, we calculated a total contribution of 0.56 mrad rms of phase noise in the atomic interferometer. This gives a limit to the sensitivity at a level of $6 \times 10^{-10}\,\mathrm{g\,Hz^{-1/2}}$.

We want to emphasize that the Raman detuning Δ can be changed at will and other sweeps can be added in the cycle. This enables realizing of a velocity selective Raman pulse (~ 35 μs), with a detuning of 2 GHz.

This pulse coherently transfers 20% of the atoms from one hyperfine state to the other. The vertical temperature of the selected atoms is then about 1 μK. Spontaneous emission during the selection pulse adds up an incoherent background of atoms, distributed in the original broader velocity distribution. This contribution, small with respect to the initial number of atoms (a fraction of a %), can become significant with respect to the number of selected atoms, especially when the selection is very severe. Increasing the detuning allows reduction of the amount of spontaneous emission. With a 2 GHz detuning, the atoms transferred by spontaneous emission represent about 2% of the selected atoms. After the selection pulse, the detuning is swept back to 1 GHz for the interferometer itself. This allows achievement of a larger Rabi frequency, and thus a better transfer efficiency.

Finally, the phased-locked Raman lasers are used to realize the interferometer. Due to the Doppler effect, the Raman detuning has to be chirped to compensate for the increasing vertical velocity of the atomic cloud. This chirp α, obtained by sweeping the DDS frequency, induces an additional phase shift. The total interferometric phase is then given by: $\Delta\Phi = (k_{\mathrm{eff}}g - \alpha)T^2$. Figure 5 displays the interferometric fringes obtained by scanning the chirp rate. The duration between the Raman pulses is $T = 50$ ms, and the repetition rate is 4 Hz. Compensation of g corresponds to a chirp rate of 25.144 MHz/s, for which the transition probability is minimum. The central fringe thus appears in the interference pattern as a "black fringe". The contrast of the fringes is 42%, and the signal to noise ratio about 35. This corresponds to a sensitivity of $7 \times 10^{-8}\,\mathrm{g\,Hz^{-1/2}}$, limited by residual vibrations of the apparatus. This sensitivity can be improved by a factor of 2 by measuring the acceleration noise with a low noise seismometer (Güralp T40), and then subtracting the phase shift induced by the vibrations to the output phase of the interferometer.

As the value of g is varying due to the earths tides, its measurement can be performed by tracking the position of the central fringe. We apply here a method very similar to the technique used in atomic clocks to lock the interrogation frequency to the atomic transition. A modulation is applied to the chirp rate in order to induce an additional

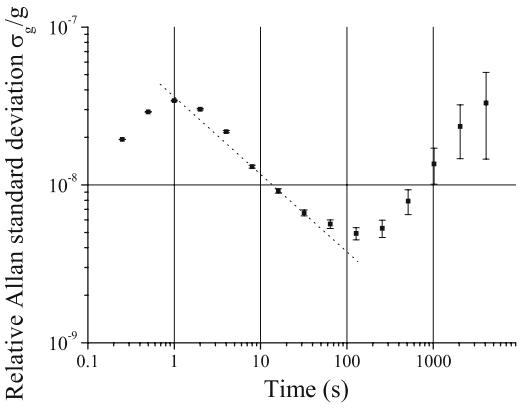

FIGURE 6 Allan standard deviation of the relative fluctuations of g. The time between the Raman pulses is $T = 50$ ms. The *dash line* corresponds to a sensitivity of $3.5 \times 10^{-8}\,\mathrm{g\,Hz^{-1/2}}$

phase shift of $\pm 90°$, to probe the interference pattern alternatively on the left and on the right side of the central fringe. From the measurements of the transition probability on both sides, we compute an error signal to lock the (unmodulated) chirp rate to the central fringe using a digital servo loop.

Figure 6 displays the Allan standard deviation of the relative fluctuations of g, σ_g/g. After a few seconds, which correspond to the time constant of the lock loop, σ_g/g decreases as $1/\tau^{1/2}$, where τ is the measurement time. This corresponds to a sensitivity of $3.5 \times 10^{-8}\,\mathrm{g\,Hz^{-1/2}}$, as indicated in the figure by the dashed line. For measurement times larger than 100 s, σ_g/g increases due to the variation of g induced by the earths tides.

4 Conclusion

To conclude, this locking technique allowed us to build with only three lasers, an optical bench providing the required frequencies to cool ^{87}Rb atoms in a 3D-MOT and to realize an atomic interferometer with far detuned Raman lasers.

The system is compact and low power, which can be necessary for transportable or space-based instruments. Moreover, our laser setup is robust and versatile since the lasers routinely stay locked for days and we can change the detuning of the Raman transitions at will.

Our goal for the gravimeter experiment is to reach an accuracy of $10^{-9}\,\mathrm{g}$ and a sensitivity of a few $10^{-9}\,\mathrm{g\,Hz^{-1/2}}$. Thanks to its compactness, the gravimeter will be transportable to compare it with other absolute gravimeters. It will also be moved close to the LNE watt balance experiment, which aims at measuring Planck's constant and redefining the kilogram [12].

ACKNOWLEDGEMENTS This work was in part supported by the "Institut Francilien de Recherche sur les Atomes-Froids" (IFRAF), and the EU through the project FINAQS "Future Inertial Atomic Quantum Sensors". The authors P. C. and J.L. G. thank the DGA for its financial support. The author K.T. T. also thanks the "Fondation Danoise" for its support.

REFERENCES

1 C.J. Bordé, Metrologia **39**, 435 (2002)
2 A. Clairon, P. Laurent, G. Santarelli, S. Ghezali, S.N. Lea, M. Bahoura, IEEE Trans. Instrum. Meas. **44**, 128 (1995)
3 F. Riehle, T. Kisters, A. Witte, J. Helmcke, C.J. Bordé, Phys. Rev. Lett. **67**, 177 (1991)
4 A. Lenef, T.D. Hammond, E.T. Smith, M.S. Chapman, R.A. Rubenstein, D.E. Pritchard, Phys. Rev. Lett. **78**, 760 (1997)
5 T.L. Gustavson, A. Landragin, M. Kasevich, Class. Quantum Grav. **17**, 1 (2000)
6 A. Peters, K.Y. Chung, S. Chu, Metrologia **38**, 25 (2001)
7 M. Kasevich, S. Chu, Phys. Rev. Lett. **67**, 181 (1991)
8 P. Cheinet, B. Canuel, F. Pereira Dos Santos, A. Gauguet, F. Leduc, A. Landragin, IEEE Trans. Instrum. Meas., unpublished, http://fr.arxiv.org/abs/physics/0510197
9 J.L. Hall, L. Hollberg, T. Baer, H.G. Robinson, Appl. Phys. Lett. **39**, 680 (1981)
10 G. Santarelli, A. Clairon, S.N. Lea, G.M. Tino, Opt. Commun. **104**, 339 (1994)
11 K. Dieckmann, R.J.C. Spreeuw, M. Weidemüller, J.T.M. Walraven, Phys. Rev. A **58**, 3891 (1998)
12 G. Genevès, P. Gournay, A. Gosset, M. Lecollinet, F. Villar, P. Pinot, P. Juncar, A. Clairon, A. Landragin, D. Holleville, F. Pereira Dos Santos, J. David, M. Besbes, F. Alves, L. Chassagne, S. Topçu, IEEE Trans. Instrum. Meas. **54**, 850 (2005)

Appl. Phys. B 92, 133–144 (2008)
DOI: 10.1007/s00340-008-3088-1

Applied Physics B
Lasers and Optics

Limits to the sensitivity of a low noise compact atomic gravimeter

J. LE GOUËT
T.E. MEHLSTÄUBLER*
J. KIM**
S. MERLET
A. CLAIRON
A. LANDRAGIN
F. PEREIRA DOS SANTOS✉

LNE-SYRTE, CNRS UMR 8630, UPMC, Observatoire de Paris, 61 avenue de l'Observatoire, 75014 Paris, France

Received: 21 December 2007 / Revised version: 6 May 2008
Published online: 27 June 2008 •

ABSTRACT A detailed analysis of the most relevant sources of phase noise in an atomic interferometer is carried out, both theoretically and experimentally. Even a short interrogation time of 100 ms allows our cold atom gravimeter to reach an excellent short term sensitivity to acceleration of $1.4 \times 10^{-8} g$ at 1 s. This result relies on the combination of a low phase noise laser system, efficient detection scheme and good shielding from vibrations. In particular, we describe a simple and robust technique of vibration compensation, which is based on correcting the interferometer signal by using the ac acceleration signal measured by a low noise seismometer.

PACS 32.80.Pj; 42.50.Vk; 39.20.+q

1 Introduction

Over the last fifteen years, atom interferometry techniques [1] have been used to develop novel inertial sensors, which now compete with state of the art "classical" instruments [2]. After the first demonstration experiments in the early 90's [3, 4], the performance of this technology has been pushed and highly sensitive instruments have been realized. As the inertial phase shifts scale quadratically with the interrogation time, high sensitivity can be reached using either cold atoms along parabolic trajectories [3, 5], such as in microwave fountain clocks, or very long beam machines. Best short term sensitivities to acceleration of 0.8–1.1×10^{-7} m s^{-2} at 1 s, and to rotations of 6×10^{-10} rad s^{-1} at 1 s have been reached in the experiments developed by Chu [6, 7] and Kasevich [8]. Moreover, a key feature of these instruments is to provide an absolute measurement with improved long term stability compared to other sensors, due to the intrinsic stability of their scale factor and a good control of the environment of the atomic samples.

Applications of these kinds of inertial interferometers are growing, from the measurement of fundamental constants, such as the gravitational constant G [9, 10], to the development of transportable devices for navigation, gravity field mapping, detection of underground structures and finally for space missions [11], where ultimate performances can be met, thanks to the absence of gravity and a low vibration environment.

We are currently developing a cold atom gravimeter, within the frame of the watt balance project, conducted by the Laboratoire National de Métrologie et d'Essais (LNE) [12]. A watt balance allows linking of the unit of mass, the kilogram, to electrical units and providing a measurement of the Planck constant. Watt balances developed at NIST and NPL presently reach relative accuracies of a few parts in 10^8 [13, 14]. During one of the phases of this experiment, the weight of a test mass is balanced with an electric force. An absolute measurement of gravity experienced by the test mass is thus required, which will be realized with our atom interferometer with a targeted relative accuracy of 1 ppb.

In this paper, we describe the realization of this sensor, which has been designed to be relatively compact, in order to be easily transportable. Our gravimeter reaches, despite rather small interaction times, a sensitivity of $1.4 \times 10^{-8} g$ at 1 s, better than state of the art "classical" gravimeters, and comparable to much larger atomic fountain gravimeters [6, 7].

In this paper, we first describe our experimental setup, and we investigate in detail in the next sections the contributions of the different sources of noise which affect the sensitivity. In particular, we describe in Sect. 3.4 an original, simple and efficient technique of vibration compensation, which allows improvement of the sensitivity of our measurement by rejecting residual vibrational noise with the help of a low-noise seismometer [15].

2 Experimental setup

The principle of the gravimeter is based on the coherent splitting of matter-waves by the use of two-photon Raman transitions [3]. These transitions couple the two hyperfine levels $F = 1$ and $F = 2$ of the $^5S_{1/2}$ ground state of the ^{87}Rb atom. A scheme of the experimental set-up is displayed in Fig. 1. The experiment is realized in a stainless steel vacuum chamber, shielded from magnetic field fluctuations with two layers of mu metal. An intense beam of slow atoms is first produced by a 2D-MOT, realized in a dedicated titanium chamber, connected to the side. Out of this beam which enters the main chamber through a 1.5 mm hole, about 10^7 atoms are loaded within 50 ms into a 3D-MOT and subsequently

✉ Fax: +33 1 4325 5542, E-mail: franck.pereira@obspm.fr
*Present address: Physikalisch-Technische Bundesanstalt (PTB), Bundesallee 100, 38116 Braunschweig, Germany
**Present address: Department of Physics, Myongji University, Yongin, 449-728, Korea

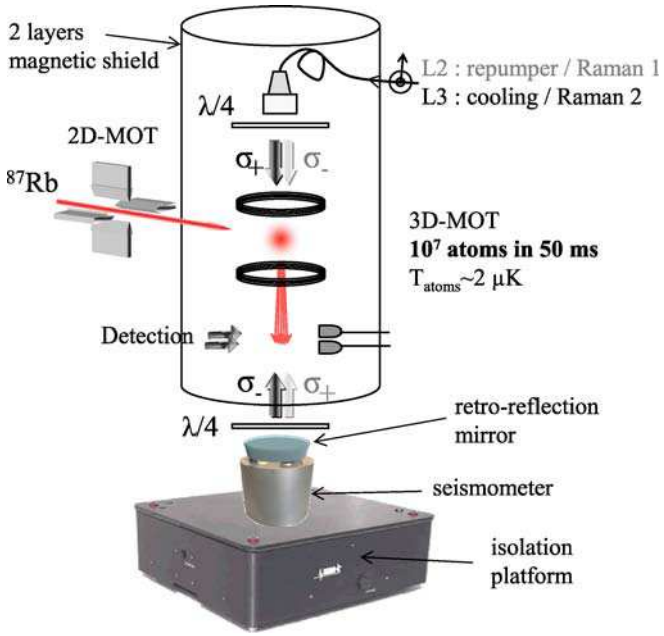

FIGURE 1 Scheme of the experimental set-up. The interferometer is realized in a stainless steel vacuum chamber, shielded from magnetic field fluctuations with two layers of mu-metal. The chamber is sustained with three legs onto a passive isolation platform (Minus-K BM). Atoms are first trapped in a MOT, cooled with optical molasses and released. The interferometer is then realized during their free fall, with vertical Raman laser beams, which enter the vacuum chamber from the top, and are retro-reflected on a mirror located below. This mirror is attached to a low noise seismometer. Finally, the populations in the two hyperfine states are measured by fluorescence, which allows to determine the interferometer phase shift

cooled in a far detuned (-25Γ) optical molasses. The lasers are then switched off adiabatically to release the atoms into free fall at a final temperature of 2.5 μK. Both lasers used for cooling and repumping are then detuned from the atomic transitions by about 1 GHz to generate the two off-resonant Raman beams. For this purpose, we have developed a compact and agile laser system that allows us to rapidly change the operating frequencies of these lasers, as described in [16]. Before entering the interferometer, atoms are selected in a narrow vertical velocity distribution ($\sigma_v \leq v_r = 5.9$ mm/s) in the $|F = 1, m_F = 0\rangle$ state, using a combination of microwave and optical Raman pulses.

The interferometer is created by using a sequence of three pulses ($\pi/2, \pi, \pi/2$), which split, redirect and recombine the atomic wave packets. Thanks to the relationship between external and internal state [1], the interferometer phase shift can easily be deduced from a fluorescence measurement of the populations of each of the two states. Indeed, at the output of the interferometer, the transition probability P from one hyperfine state to the other is given by the well-known relation for a two wave interferometer: $P = \frac{1}{2}(1 + C\cos\Delta\Phi)$, where C is the interferometer contrast, and $\Delta\Phi$ the difference of the atomic phases accumulated along the two paths. The difference in the phases accumulated along the two paths depends on the acceleration $\boldsymbol{a}$ experienced by the atoms. It can be written as $\Delta\Phi = \varphi(0) - 2\varphi(T) + \varphi(2T) = -\boldsymbol{k}_{\text{eff}}\boldsymbol{a}T^2$ [17], where $\varphi(0, T, 2T)$ is the difference of the phases of the lasers, at the location of the center of the atomic wavepackets, for each of the three pulses. Here $\boldsymbol{k}_{\text{eff}} = \boldsymbol{k}_1 - \boldsymbol{k}_2$ is the effective wave vector (with $|\boldsymbol{k}_{\text{eff}}| = k_1 + k_2$ for counter-propagating beams), and T is the time interval between two consecutive pulses.

The Raman light sources are two extended cavity diode lasers based on the design of [18], which are amplified by two independent tapered amplifiers. Their frequency difference is phase locked onto a low phase noise microwave reference source. The two Raman laser beams are overlapped with a polarization beam splitter cube, resulting in two orthogonal polarized beams. First, a small part of the overlapped beams is sent onto a fast photodetector to measure the optical beat. This beat-note is mixed down with the reference microwave oscillator, and compared to a stable reference rf frequency in a digital phase frequency detector. The phase error signal is then used to lock the laser phase difference at the very position where the beat is recorded. The phase lock loop reacts to the supply current of one of the two lasers (the "slave" laser), as well as to the piezo-electric transducer that controls the length of its extended cavity. Finally, the two overlapped beams are injected in a polarization maintaining fiber, and guided towards the vacuum chamber, entering the chamber from the top (see Fig. 1). We obtain counter-propagating beams by placing a mirror and a quarterwave plate at the bottom of the experiment. Four beams are actually sent onto the atoms, out of which only two will drive the counter-propagating Raman transitions, due to conservation of angular momentum and the Doppler shift induced by the free fall of the atoms.

3 Short term sensitivity

3.1 *Detection noise*

The transition probability is deduced from the population in each of the two hyperfine states, which are measured by fluorescence. Ultimately, noise on this measurement is limited by the quantum projection noise $\sigma_P = 1/2\sqrt{N}$ [19], where σ_P is the standard deviation of the transition probability, and N the number of detected atoms. Other sources of noise, such as electronic noise in the photodiodes, laser frequency and intensity noise, will affect the measurement, and might exceed the quantum limit depending on the number of atoms [20].

3.1.1 Basic scheme. The detection system implemented at first in the gravimeter is similar to the one developed for atomic fountain clocks. It consists of three separated horizontal sheets of light. The first detection zone consists of a laser beam circularly polarized, tuned on the cycling transition ($F = 2 \rightarrow F = 3$). This beam is retro-reflected on a mirror, in order to generate a standing wave. It allows measurement of the number of atoms in the $F = 2$ state by fluorescence. The atoms which have interacted with the laser light are then removed by a pusher beam, obtained by blocking the lower part of the retro-reflected beam. The second zone is a repumper beam tuned on the ($F = 1 \rightarrow F = 2$), which pumps the atoms in $F = 1$ into $F = 2$. The last zone is a standing wave tuned on the cycling transition, which allows measurement of the number of atoms initially in $F = 1$. The fluorescence emitted in the upper and lower zones is detected by two distinct photodiodes that collect 1% of the total fluorescence. Using a $\pi/2$ microwave pulse, the noise

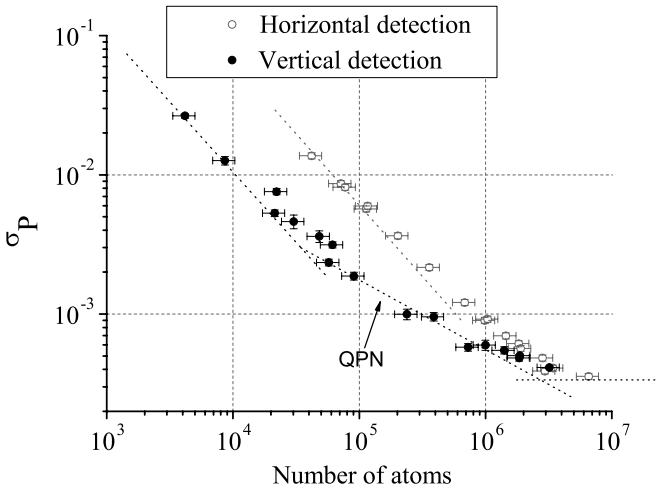

FIGURE 2 Allan standard deviation of the excitation probability σ_P for both methods described. *Open circles* correspond to horizontal detection, *full circles* to vertical detection. QPN is the quantum projection noise limit. The phase noise introduced onto the atom interferometer is $\sigma_\varphi = 2/C \times \sigma_P$

on the measurement of the transition probability at mid-fringe ($P = 0.5$) has been measured in the gravimeter as a function of the number of atoms, see Fig. 2. The saturation parameter at the center of the detection beams is close to 1. For less than 10^6 atoms, the detection noise is limited by the noise of the photodiodes and the electronics. The standard deviation of the fluctuations of the transition probability σ_P is then inversely proportional to the number of atoms. The detection noise is equivalent to about 900 atoms per detection zone. For atom number larger than 5×10^6, technical noise, arising from intensity and frequency noise of the detection laser, limits σ_P to about 3×10^{-4}. The noise in the measured transition probability σ_P converts into phase noise $\sigma_\varphi = 2/C \times \sigma_P$, with C being the contrast of the interferometer. A sensitivity close to 1 mrad per shot for the interferometer measurement can thus be obtained for the interferometer when the number of atoms is larger than 5×10^6.

3.1.2 Improved scheme. In our experiment, the same laser system is used for the Raman interferometer and for the atom trapping. After the interferometer sequence the lasers are brought back close to resonance in order to trap the atoms during the beginning of the next experimental cycle. In principle, they can also be used to detect the atoms by pulsing the vertical beam, when the atoms are located in the detection region.

The detection sequence we use has been inspired by the detection system [21] of the gradiometer of [22].

1. When the atoms are located in front of the top photodiode, a low intensity pulse, slightly red detuned to the cycling transition is induced in order to stop the $F = 2$ atoms.
2. One then waits for the atoms in $F = 1$ to reach the position in front of the bottom photodiode.
3. A second pulse (10 ms long) is then applied at full power. Cooling and repumper beams are both present during this pulse.
4. A third pulse, 10 ms later, finally serves for background substraction of stray light.

The areas of the fluorescence signals collected by the two photodiodes are thus proportional to the number of atoms in each of the two hyperfine states. This detection scheme has several advantages. First, the intensity in the vertical beam is much higher than in the standard detection beam, the saturation parameter being close to 50. Atoms will thus remain resonant despite the heating induced by photon recoils. Second, atoms spend a longer time in front of the photodiodes. Finally, the repumper is present on both clouds during the whole duration of the detection pulse. With this scheme, the detection noise is now equivalent to only 150 atoms per zone, thanks to the increase of the fluorescence signal, see Fig. 2. The detection is at the quantum projection noise limit with about 10^5 atoms. The same limit of $\sigma_P \approx 3 \times 10^{-4}$ is found for large number of atoms. This detection scheme is thus more efficient for low number of atoms, for instance when using Bose–Einstein condensates or narrower velocity selection. Limits to the signal to noise ratio for large numbers of atoms still have to be identified. They could arise from laser intensity and frequency fluctuations, as well as fluctuations of the normalization. In principle, the second detection scheme should be insensitive to laser fluctuations, which are common mode for the two populations, as the measurements are performed simultaneously.

3.2 *Phase noise*

In our interferometer, the noise in the phase difference of the two Raman lasers induces fluctuations of the interferometer phase. In a previous publication [23], we have introduced a useful tool to calculate the influence of the different sources of noise onto the stability of the interferometer phase measurement, the sensitivity function, $g(t)$ [24, 25]. Though this function has already been described in detail in [23], we recall here for completeness its definition and its expression, as well as the formulas one has to use to calculate the impact of the phase noise onto the sensitivity of the interferometer.

This function quantifies the influence of a relative laser phase shift $\delta\varphi$ occurring at time t onto the phase of the interferometer $\delta\Phi(\delta\varphi, t)$. It can be written as:

$$g(t) = \lim_{\delta\varphi \to 0} \frac{\delta\Phi(\delta\varphi, t)}{\delta\varphi} \,. \tag{1}$$

The interferometer phase shift Φ induced by fluctuations of φ is then given by:

$$\Phi = \int_{-\infty}^{+\infty} g(t) \frac{\mathrm{d}\varphi(t)}{\mathrm{d}t} \mathrm{d}t \,. \tag{2}$$

With a sequence of three pulses $\pi/2$, π, $\pi/2$ of duration τ_R, $2\tau_R$, τ_R and a time origin chosen at the center of the π pulse, g is an odd function whose expression was first derived in [23]:

$$g(t) = \begin{cases} \sin \Omega_R t & \text{for } 0 < t < \tau_R \\ 1 & \text{for } \tau_R < t < T + \tau_R \\ -\sin \Omega_R (T - t) & \text{for } T + \tau_R < t < T + 2\tau_R \end{cases} , \tag{3}$$

where Ω_R is the Rabi frequency.

The noise of the interferometer is characterized by the Allan variance of the interferometric phase fluctuations, $\sigma_\Phi^2(\tau)$, defined as:

$$\sigma_\Phi^2(\tau) = \frac{1}{2}\left\langle \left(\delta\bar{\Phi}_{k+1} - \delta\bar{\Phi}_k\right)^2 \right\rangle \tag{4}$$

$$= \frac{1}{2}\lim_{n\to\infty}\left\{\frac{1}{n}\sum_{k=1}^{n}\left(\delta\bar{\Phi}_{k+1} - \delta\bar{\Phi}_k\right)^2\right\}. \tag{5}$$

Here $\delta\bar{\Phi}_k$ is the average value of $\delta\Phi$ over the interval $[t_k, t_{k+1}]$ of duration τ. The Allan variance is equal, within a factor of two, to the variance of the differences in the successive average values $\delta\bar{\Phi}_k$ of the interferometric phase. Our interferometer operates sequentially at a rate $f_c = 1/T_c$, where τ is a multiple of T_c: $\tau = mT_c$. Without loosing generality, we can choose $t_k = -T_c/2 + kmT_c$.

For large averaging times τ, the Allan variance of the interferometric phase is given by [23]:

$$\sigma_\Phi^2(\tau) = \frac{1}{\tau}\sum_{n=1}^{\infty}|H(2\pi n f_c)|^2 S_\varphi(2\pi n f_c)\,. \tag{6}$$

The transfer function is thus given by $H(\omega) = \omega G(\omega)$, where $G(\omega)$ is the Fourier transform of the sensitivity function:

$$G(\omega) = \int_{-\infty}^{+\infty} \mathrm{e}^{-\mathrm{i}\omega t} g(t)\,\mathrm{d}t\,. \tag{7}$$

Equation (6) shows that the sensitivity of the interferometer is limited by an aliasing phenomenon similar to the Dick effect in atomic clocks [24, 25]: only the phase noise at multiples of the cycling frequency appears in the Allan variance, weighted by the Fourier components of the transfer function.

3.2.1 Reference oscillator. The previous formalism is used to analyze the specifications required for the reference microwave frequency [23]. We choose to generate the reference microwave signal by multiplication of an ultra-stable quartz. Assuming perfect multiplication of state of the art ultra-stable quartz oscillators, we find that their phase noise at low frequency will limit the sensitivity of the interferometer phase measurement at the mrad per shot level, for our total interferometer time of $2T = 100$ ms. A noise of 1 mrad/shot corresponds to a sensitivity to acceleration of $1.2 \times 10^{-9} g$ at 1 s, for a repetition rate of 4 Hz and interaction time $2T = 100$ ms.

Moreover, the relatively short duration of the Raman pulses makes the interferometer particularly sensitive to high frequency noise. If we consider a Raman pulse duration of 10 μs, a white noise floor of the reference microwave source, with a PSD of -120 dB rad^2/Hz, contributes to the interferometer phase noise at the level of 1 mrad/shot.

As already stated in a previous publication [26], the required phase noise specifications for such a reference oscillator cannot be met both at low and high frequency by a single quartz, but can be achieved by phase locking two quartz oscillators. We therefore use a combination of two quartz: a ultra low noise 10 MHz quartz (Blue Top from Wenzel) is multiplied up to 100 MHz, to which a 100 MHz SC Premium (Wenzel) is phase locked with a bandwidth of about 400 Hz. This system, whose performance is indicated as trace (a) in Fig. 4, was realized by Spectradynamics. Measurements performed in our laboratory on two independent such systems confirmed these specifications. If this oscillator is multiplied to 6.8 GHz without any degradation – see trace (b) in Fig. 4 – we calculate that its phase noise degrades the sensitivity of the interferometer at the level of 1.2 mrad per shot.

3.2.2 Microwave frequency synthesis. The microwave chain generates the 6.834 GHz reference signal, used to lock the laser to the Raman transition, out of a stable reference quartz (see Fig. 3). Details of this synthesis and its performance have been published in [26]. We briefly recall its architecture in the following paragraph.

In a first stage the 100 MHz output of the quartz system is multiplied by 2. Then, the 200 MHz output is amplified and sent to a step recovery diode, which generates a comb of multiples of 200 MHz. The 35th harmonic is selected with a passive filter, and compared in a mixer with a dielectric resonator oscillator (DRO) operating at 7.024 GHz. The 24 MHz intermediate frequency is mixed again with a direct digital synthesizer (DDS) using a digital phase/frequency detector. Using the phase error signal, the DRO is finally phase locked onto the comb with an offset frequency controlled by the DDS (DDS2 on Fig. 3). Figure 4 displays the phase noise power spectral density of the microwave chain, which has been measured by comparing the outputs of two identical chains, that shared a common 100 MHz input. The degradation generated by the system on the phase noise has been measured. It contributes to 0.6 mrad/shot to the sensitivity of the interferometer measurement.

A phase noise level at high frequency lower than presented above (and already reported in [26]) is obtained when replacing the digital phase detector by an analog mixer. Figure 4 displays the phase noise obtained in that case, which allows reaching of a lower white phase noise floor. Still, we currently use the digital phase detector, as the lock loop is then more robust, the DRO stays locked even if the DDS frequency is changed rapidly by several MHz.

3.2.3 Laser phase lock. The phase difference between the two Raman lasers is locked onto the phase of the reference microwave signal with an electronic phase lock loop (PLL) [27]. We have experimentally measured the residual phase noise power spectral density of our phase lock system. The measurement was performed by mixing the intermediate signal at 190 MHz and the local oscillator DDS1 onto an independent rf mixer, whose output phase fluctuations were analyzed with a FFT analyzer (for frequencies less than 100 kHz) and a rf spectrum analyzer (for frequencies above 100 kHz). The result of this measurement is displayed in Fig. 5. Careful optimization of the signal levels at the input of the phase comparator allowed reaching a phase noise level slightly lower than previously reported in [23]. The phase noise decreases at low frequencies down to a minimum value of -121 dB rad^2/Hz at about 30 kHz. At this frequency, we found that the residual noise was not limited by the finite gain of the PLL, but by the intrinsic noise of the PLL circuit. Above 60 kHz, the noise increases up to -90 dB rad^2/Hz at 3.5 MHz, which is the natural frequency of our servo loop. The contribution of

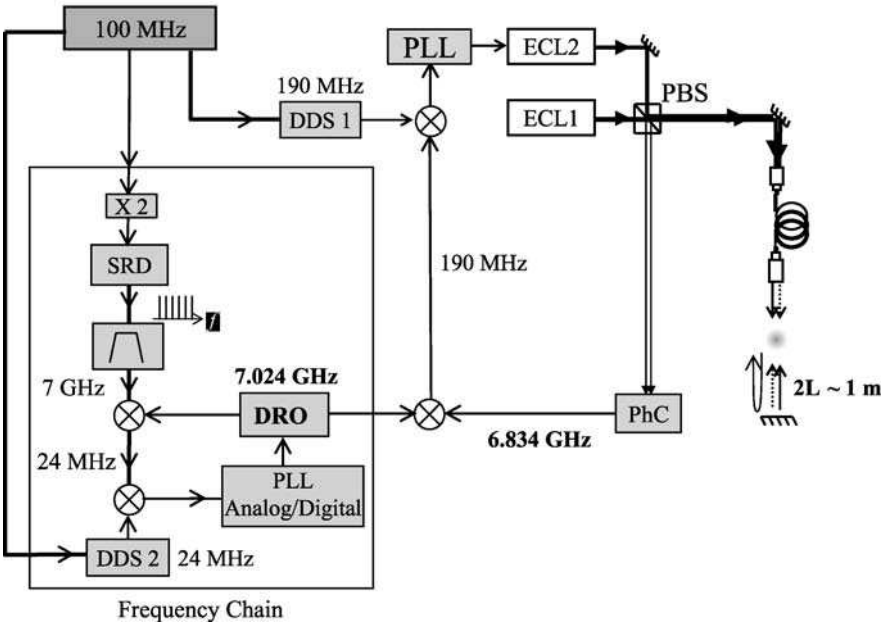

FIGURE 3 Scheme of the microwave synthesis and phase locked lasers. The 100 MHz quartz signal enters a frequency chain which generates the reference microwave frequency. Its microwave output is mixed with the lasers beatnote, and the IF is compared with a DDS signal. The error signal is used to phase lock the Raman lasers. ECL – extended cavity laser; DDS – direct digital synthesizer; PhC – photoconductor; SRD – step recovery diode; PBS – polarizing beam splitter; DRO – dielectric resonator oscillator

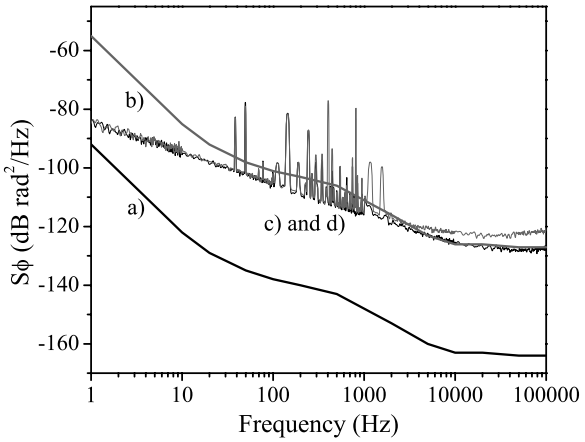

FIGURE 4 Power spectral density of phase fluctuations of the reference 100 MHz oscillator at 100 MHz (trace a) and at 6.8 GHz (trace b) assuming no degradation. (c) and (d) display the power spectral density of the phase noise generated by the synthesis, with a digital PLL (trace c, in *grey*) and analog PLL (trace d, in *black*)

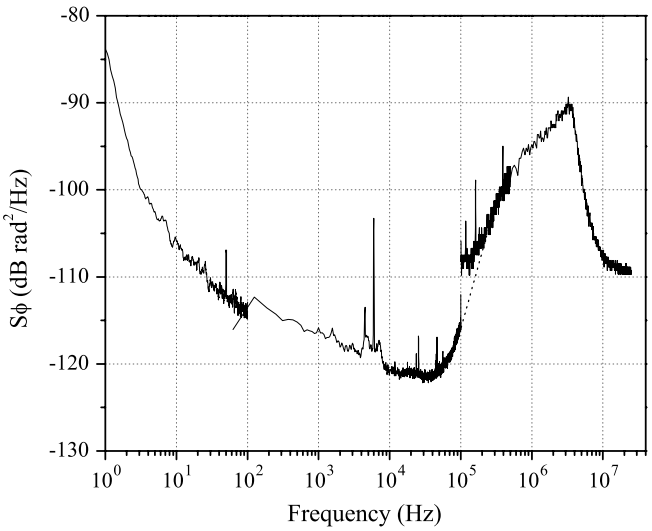

FIGURE 5 Power spectral density of laser phase noise. The measurement is performed by comparing the laser phase with respect to the reference oscillator, with a FFT analyzer below 100 kHz, and with a spectrum analyzer above. Note that the intrinsic phase noise of our spectrum analyzer is about $-110\,\mathrm{dB\,rad^2/Hz}$ at 100 kHz, which is above the lasers phase noise. The bandwidth of the PLL is 3.5 MHz

the residual noise is dominated by this high frequency part. We calculate a contribution to the interferometer phase noise of 1.5 mrad/shot.

3.2.4 Propagation in the fiber. In our experiment, the Raman beams are generated by two independent laser sources. The beams are finally overlapped by mixing them on a polarizing beam splitter cube, so the beams have orthogonal polarizations. A small fraction of the total power is sent to one of the two exit ports of the cube, where a fast photodetector detects the beat frequency. The beat note is compared with the reference signal produced by the microwave chain, in order to phase lock the lasers. The laser beams, sent to the atoms, are diffracted through an acousto-optical modulator, used as an optical shutter to produce the Raman pulses. During the interferometer, the total power is diffracted in the first order to produce the vertical Raman beams. Both beams are guided towards the atoms with a polarization maintaining fiber. Since the Raman beams have orthogonal polarization, any fiber length fluctuation will induce phase fluctuations, due to its birefringence. We measured the phase noise induced by the propagation in the fiber by comparing the beat signal measured after the fiber with the one we use for the phase lock. Figure 6 displays the power spectral density of the phase noise induced by the propagation, which is dominated by low frequency noise due to acoustic noise and thermal fluctuations. This source of noise was reduced by shielding the fiber from the air flow of the air conditioning, surrounding it with some packaging foam. The calculated contribution to the interferometer phase noise is 1.0 mrad/shot. This source of noise can be suppressed by using two identical linear polarizations for the Raman beams.

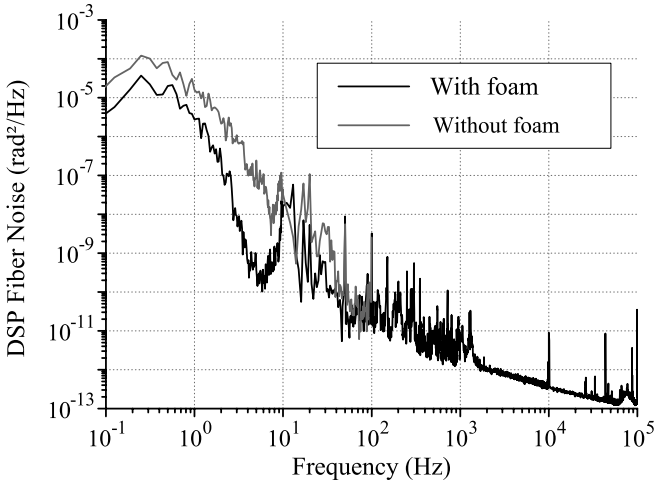

FIGURE 6 Power spectral density of phase fluctuations induced by the propagation in the fiber, with foam (*black trace*) and without (*grey foam*). The two Raman lasers travel with two orthogonal polarizations in the same polarization maintaining fiber. The noise, dominated by low frequency noise due to acoustic noise and thermal fluctuations, gets significantly reduced by shielding the fiber with foam

3.2.5 Retro-reflection delay. The phase lock loop guaranties the stability of the phase difference between the two Raman lasers at the particular position, where their beatnote is measured on the fast photodetector. Between this position and the atoms, this phase difference is affected by fluctuations of the respective paths of the two beams over the propagation distance. In our experiment, the influence of path length variations is minimized by overlapping the two beams, and making them propagate as long as possible over the same path. However, for the interferometer to be sensitive to inertial forces, the two beams need to be counter-propagating. The two overlapped beams are thus directed to the atoms and finally retro-reflected on a mirror. As a consequence, the reflected beam is delayed with respect to the other one. The phase difference at the atoms position is then affected by the phase noise of the lasers accumulated during this reflection delay. This effect has been described in detail in [28], where the influence of the frequency noise of the Raman lasers onto the interferometer phase was studied quantitatively. From the measurement of the power spectral density of the laser frequency fluctuations, we derived a contribution of this effect of 2.0 mrad/shot. This effect can be significantly reduced by reducing the linewidth of the reference laser, and/or reducing the delay by bringing the mirror closer to the atoms.

3.2.6 Overall laser phase noise contribution. Adding all the laser phase noise contributions described above, leads to a sensitivity of 3 mrad/shot, which corresponds to an acceleration sensitivity of $3.7 \times 10^{-9} g/\mathrm{Hz}^{1/2}$, for our interrogation time of $2T = 100$ ms.

3.3 *Short term fluctuations of frequency dependent shifts*

Due to its intrinsic symmetry, the phase of the interferometer is not sensitive to a shift of the resonance frequency $\delta\nu$ as long as this shift is constant. On the contrary, a time dependent frequency shift will in general lead to a phase shift of the interferometer. For instance, sensitivity to acceleration can be seen as arising from a time dependent Doppler shift. Such frequency shifts are also caused by Stark shifts, Zeeman shifts, cold atom interactions. The formalism of the sensitivity function can be used to determine the influence of these effects [29], as (2) can be written as

$$\Phi = \int_{-\infty}^{+\infty} g(t) 2\pi\delta\nu(t)\,\mathrm{d}t\,. \tag{8}$$

In this section we detail the effects of the dominant contributions: ac Stark shifts and quadratic Zeeman shift.

3.3.1 Light shifts. Each of the Raman lasers, as they are detuned with respect to the electronic transition $^5S_{1/2} \rightarrow {}^6P_{3/2}$, induces a light shift on the two-photon Raman transition. This one-photon light shift (OPLS) can be expressed as a linear combination of the laser intensities, $\delta\nu = \alpha I_1 + \beta I_2$. For a detuning $\Delta\nu$ smaller than the hyperfine transition frequency, the OPLS can be cancelled by adjusting the ratio between the two laser beams: $\alpha I_{10} + \beta I_{20} = 0$ [30]. Still, intensity fluctuations occurring on times scales shorter than the interferometer duration $2T$ can lead to noise in the interferometer phase, given by

$$\Phi = \int_{-\infty}^{+\infty} g(t) h(t) 2\pi(\alpha I_1(t) + \beta I_2(t))\,\mathrm{d}t\,, \tag{9}$$

where $h(t) = 1$, during the Raman pulses, and 0 during free evolution times.

Following the same formalism as used in [23], the degradation of the sensitivity can be expressed as

$$\sigma_\Phi^2(\tau) = \frac{1}{\tau}(2\pi\alpha I_{10})^2 \sum_{n=1}^{\infty} \left|G'(2\pi n f_\mathrm{c})\right|^2 \times \left(S_{I1/I1_0}(2\pi n f_\mathrm{c}) + S_{I2/I2_0}(2\pi n f_\mathrm{c})\right), \tag{10}$$

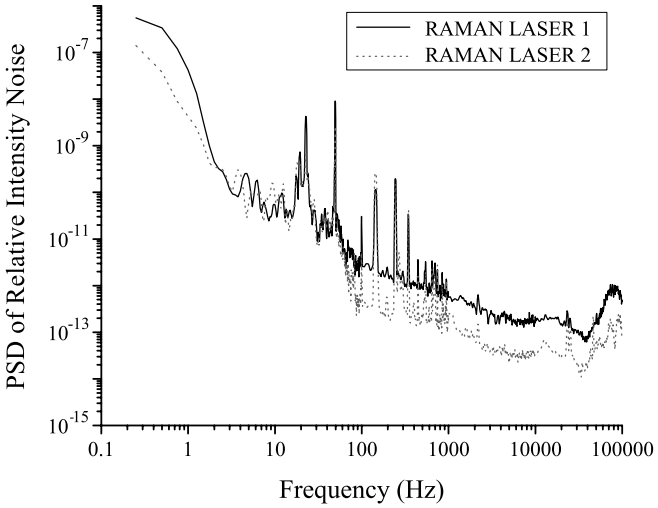

FIGURE 7 Power spectral density of relative intensity noise (RIN) of the Raman lasers measured at the output of the fiber

where G' is the Fourier transform of $g(t)h(t)$ and S_{Ii/Ii_0} is the power spectral density of relative intensity fluctuations of the i-th laser [29].

We measured the relative intensity noise (RIN) of both laser beams at the output of the optical fiber. The power spectral densities of the lasers RINs are displayed in Fig. 7. From the measurement of the resonance condition as a function of laser intensities, we determined $\alpha I_{10} = 70\,\text{kHz}$, from which we finally calculate a contribution of 0.8 mrad per shot.

In the geometry of our experiment, where a pair of co-propagating beams is retro-reflected in order to generate the counter-propagating laser beams, another frequency shift occurs due to non-resonant two photons transitions. The main contribution arises from the two-photons transition with inverted k_{eff}, additional contributions are also present from co-propagating and magnetic field sensitive transitions, $\Delta m = 2$. This two photons shift, as detailed in [29, 31], can be expressed as

$$\Phi_{\text{TPLS}} = \int_{-\infty}^{+\infty} g(t)h(t) \sum_i \frac{\hbar\Omega_i^2}{4\delta_i}\,, \tag{11}$$

where Ω_i and δ_i are the Rabi frequency and detuning with respect to the two photons transition. Here again, fluctuations in the intensities will induce noise on the interferometer phase. As δ_i increases with time due to the increasing Doppler shift, the influence of the second and third Raman pulse can be neglected, and (11) approximated by

$$\Phi_{\text{TPLS}} = \frac{1}{\Omega} \sum_i \frac{\hbar\Omega_i^2}{4\delta_i}\,. \tag{12}$$

As Ω_i, $\Omega \propto \sqrt{I_1 I_2}$, this leads to

$$\delta\Phi_{\text{TPLS}} = \Phi_{\text{TPLS}} \left(\frac{\delta I_1}{2I_1} + \frac{\delta I_2}{2I_2}\right). \tag{13}$$

As this effect scales linearly with the Rabi frequency, it is measured with a differential measurement, alternating measurements with two different Rabi frequencies. We find $\Phi_{\text{TPLS}} = 40\,\text{mrad}$. Shot to shot fluctuations of the relative intensity are measured to be 3×10^{-4}. The contribution is thus about 0.1 mrad/shot.

3.3.2 Magnetic fields. In order to reduce the sensitivity to magnetic field fluctuations, the atoms are selected in the $m_F = 0$ state. Still, the Raman resonance condition exhibits a quadratic Zeeman shift of $\delta\nu = KB^2$ where B is the amplitude of the magnetic field and $K = 575\,\text{Hz/G}^2$. Magnetic field gradients will thus induce a shift of the interferometer phase given by

$$\Phi = \int_{-\infty}^{+\infty} g(t) 2\pi K B(t)^2 \,\mathrm{d}t\,. \tag{14}$$

In our experiment we observe a large magnetic field gradient induced by residual magnetization of the vacuum chamber, which is made out of stainless steel. It causes a constant phase shift of 320 mrad in our interferometer, which we reject at a level of 1 per 300 by consecutive differential measurements with reversed k_{eff}-vectors. For it's influence on the short term stability, we determine the stability of the magnetic fields by recording fluctuations of the resonance condition of a field-sensitive transition. The relative stability of the field is 10^{-4} per shot, which induces a negligible phase shift fluctuation of 3×10^{-2} mrad per shot.

3.4 *Vibrations*

As the interferometer phase shift is a measurement of the relative acceleration between free falling atoms and the "optical ruler" attached to the phase planes of the Raman lasers, vibrations of the experimental setup will add noise to the measurement. With the retro-reflected geometry, the phase difference between the laser beams depends only on the position of a single element, the retro-reflecting mirror. For optimal performances, it is thus mandatory to shield this element from external vibrational noise.

The degradation of the sensitivity due to parasitic vibrations can easily be derived from (6), by replacing $S_\varphi(\omega)$ by $k_{\text{eff}}^2 S_z(\omega) = k_{\text{eff}}^2 \frac{S_a(\omega)}{\omega^4}$, where S_z and S_a are power spectral densities of position and acceleration fluctuations. The transfer function of the interferometer thus acts as a second order low pass filter, which reduces drastically the influence of high frequency noise. The sensitivity of the interferometer is finally given by:

$$\sigma_\Phi^2(\tau) = \frac{k_{\text{eff}}^2}{\tau} \sum_{n=1}^{\infty} \frac{|H(2\pi n f_c)|^2}{(2\pi n f_c)^4} S_a(2\pi n f_c)\,. \tag{15}$$

3.4.1 Isolation of the vibration noise. We tested two different vibration isolation tables and compared their performances. The tables were loaded up to their nominal load with lead bricks. Acceleration noise on the platforms were measured with a low noise seismometer Guralp T40. Figure 8 displays

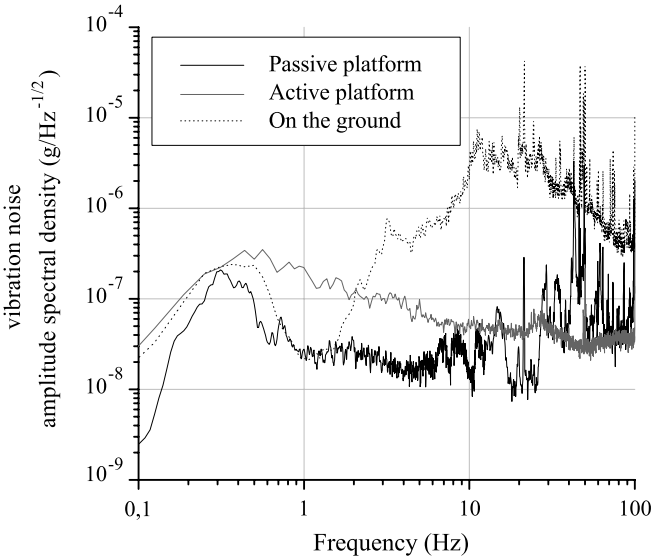

FIGURE 8 Comparison of the performance of two isolation platforms. We found the passive platform behaves better in the low frequency range, where our interferometer is most sensitive to vibrations

the PSD of the residual vibration noise, compared to the noise measured directly on the ground. We finally selected the passive platform (Minus K BM), which displays a better noise between 0.5 and 50 Hz, where our interferometer is most sensitive. The experimental setup was then assembled on it. With respect to the spectrum of Fig. 8, the vibration noise of the experiment increased at frequencies higher than 50 Hz, due to several structural resonances excited by acoustic noise. We therefore enclosed the experimental setup with a wooden box, whose walls were covered with dense isolation acoustic foam. The gain on the vibration power spectrum was about 20 dB above 50 Hz. The contribution of residual vibrations to the interferometer can be calculated by weighting the vibration spectrum with the transfer function of the interferometer [23]. We then foresee a sensitivity of $6.5 \times 10^{-8} g$ at 1 s. Vibrations are typically less during the night (from 1 to 5 AM) when there is no underground traffic, and the sensitivity is then $5 \times 10^{-8} g$ at 1 s. Measurements of the interferometer phase noise are in excellent agreement with the inferred vibration noise, which surpasses all other sources of phase noise.

3.4.2 Seismometer correction. To further improve the sensitivity of the sensor, we use the signal of the seismometer to correct the interferometer phase from the fluctuations induced by the vibration noise. An efficient rejection requires that the seismometer measures the vibrations of the retro-reflecting mirror as accurately as possible. We placed the mirror directly on top of the seismometer, which is underneath the vacuum chamber. Figure 9 displays the measured transition probability as a function of the phase shift calculated from the seismometer output signal. To obtain large variations of the interferometer phase, we deliberately increased for this measurement the vibrational noise by having the passive platform non-floating. This figure illustrates the good correlation between the seismometer signal and the interferometer phase. In the conditions of minimal noise, with a floating isolation platform, the correlation coefficient between seismometer acceleration noise and interferometer phase noise is found to be as high as 0.94.

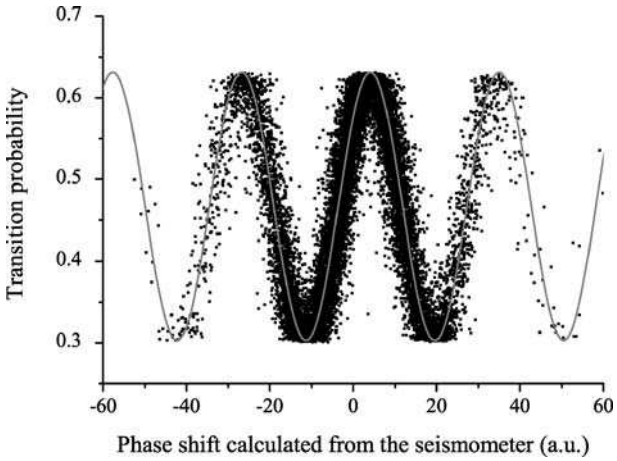

FIGURE 9 Interferometer signal as a function of the phase shift calculated from the seismometer signal with the passive isolation platform down. Experimental determination of the transition probabilities are displayed as dots. The *line* displays a sinusoidal fit to the data, with a constrained amplitude

We then studied two types of vibration compensation. The first one is a post-correction: the velocity signal from the seismometer is recorded during the interferometer, and we subtract from the measured interferometer phase the calculated phase shifts due to the recorded vibrations. As the correction is applied to the transition probability, the interferometer should be measuring at mid-fringe, in order to have a simple (linear) relationship between the change in the transition probability and the fluctuation of the interferometer phase. This technique requires that peak to peak phase noise fluctuations remain less than a few tens of degrees and that the contrast remains constant.

The second method is a real time compensation, where the seismometer velocity signal is amplified and integrated by an analog circuit. The integrated signal is subtracted from the phase error signal at the output of the comparator in the phase lock loop of the Raman laser system. In this feed-forward loop, the laser phase difference counterbalances vibrational noise, so that in the inertial frame, the laser phase planes are steady. A scheme of the setup is displayed on Fig. 10.

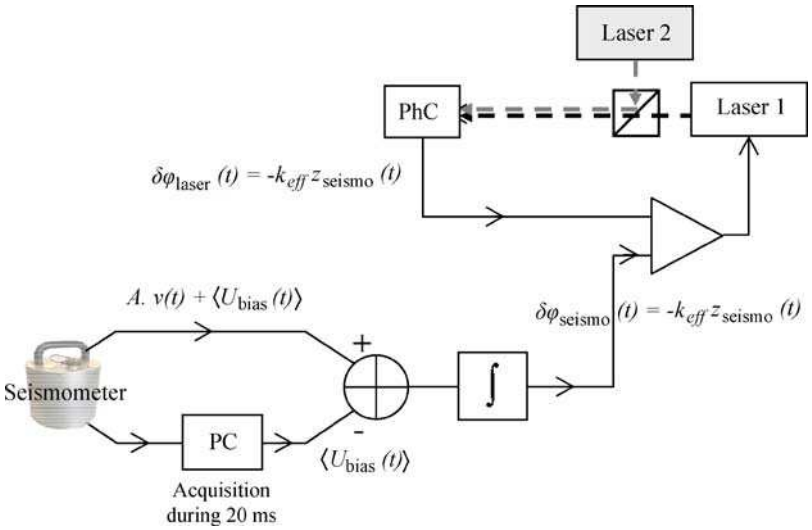

FIGURE 10 Scheme of the real-time compensation set-up. The phase shift induced by vibrations is subtracted from the phase error signal at the output of the phase comparator. The laser phase difference counterbalances vibrational noise, so that in the inertial frame, the laser phase planes are steady. PhC – photoconductor

In principle, the digital phase detector ensures the linearity of its voltage output with respect to the input phase difference. Here, a maximum voltage output values ± 0.5 V corresponds to $\pm 2\pi$ input phase difference. For the phase lock loop to remain active, the voltage at the output of the integrator has to correspond to a phase that remains within this range. This was ensured by resetting the integrator at each cycle and by compensating the intrinsic offset of the seismometer output. As this offset fluctuates, due to either electronic noise or low frequency vibrations, the compensation is realized by

i) acquiring the seismometer signal with a digital card at the end of the previous measurement cycle,
ii) calculating its average value,
iii) outputting it with an analog voltage board at the beginning of the next cycle, and
iv) subtracting this last value from the seismometer signal before being integrated.

Despite all these precautions, the range of the phase compensation had to be increased by a factor of 2 (dividing the intermediate frequency signal by 2 before the phase comparator), in order for the phase lock loop to remain active.

In principle, this last technique is more powerful, as it remains efficient even if the contrast changes, and can compensate large phase fluctuations, if the effective dynamic of the mixer is large enough. In practice we found that the digital phase detector had two drawbacks.

i) The residual non-linearity of the output signal is enough to induce a large bias to the interferometer phase (the linearity should be at the mrad level for typical phase excursions of about 1 rad over 100 ms.)
ii) Operation far from null output increases the phase noise.

To circumvent these problems, the phase compensation could be performed in the phase lock loop of a second quartz onto the 100 MHz signal, with an analog mixer. This increases the dynamics by more than one order of magnitude and guarantees the linearity. But, as on our platform, the vibration noise is low, we finally chose the post-correction method, which is simpler and more robust.

In both cases, the rejection efficiency was limited to a factor of 3, corresponding to a typical sensitivity of $2 \times 10^{-8} g$ at 1 s.

3.4.3 Seismometer response function. In order to study the transfer function between the seismometer and the retro-reflecting mirror, we induce a platform oscillation at given frequencies (by running ac-currents through a loaded loudspeaker placed onto the isolation platform) and record simultaneously the atomic and seismometer signals. The excitation frequencies f_{exc} were chosen close but not exactly equal to multiple of the cycling frequency $f_{\mathrm{exc}} = k f_{\mathrm{c}} + \delta f$, so that the transition probability and its correction calculated from the seismometer signal were modulated in time, at an apparent frequency controlled by δf. The seismometer transfer function can be determined from the ratio of the amplitudes of the modulation of the two signals and their phase difference. The measured transfer function is displayed in Fig. 11. It corresponds very well to the response of the seismometer. This response, which is provided by the manufacturer, and can also be retrieved by the user using an internal measurement protocol, see solid lines in Fig. 11. As one can see from these curves, the seismometer has a built-in low pass filter to cut mechanical resonances, which occur typically above 450 Hz. This filter has a 3 dB cut-off frequency of 50 Hz. This adds some phase shifts to the calculated correction with respect to the real perturbation for higher frequencies. This corrupts the rejection efficiency and eventually adds noise. To improve the rejection, we would either need to flatten the transfer function, or to cut frequencies at which the rejection process degrades the sensitivity.

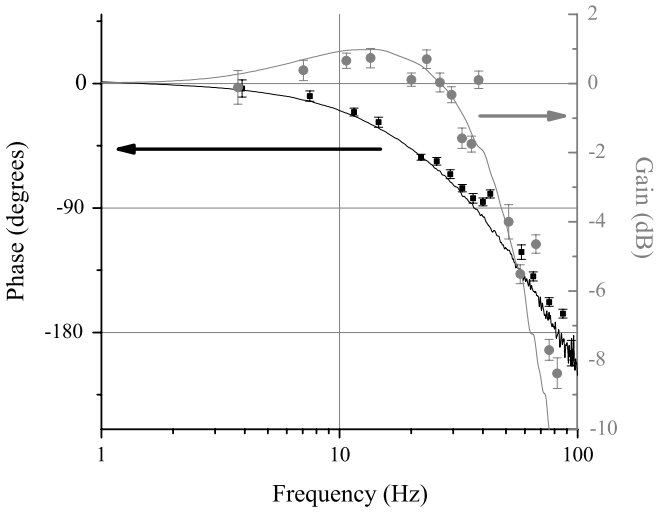

FIGURE 11 Transfer function between the acceleration measured with the interferometer and the seismometer. The transfer function agrees well with the response function of the seismometer (*solid lines*)

3.4.4 Digital filtering. We apply a digital filter to the seismometer signal to compensate for attenuation and phase shifts. In the ideal situation, where the transfer function would be made perfectly flat, meaning that the efficiency of the rejection would be 100% for each frequency. The limitation of the vibration rejection would arise from the intrinsic noise of the seismometer, which strongly depends on the frequency. When taking this noise into account, it appears useless to literally flatten the seismometer response. We numerically found that a simple first order digital filter compensates the response function well enough to reach a sensitivity of $5 \times 10^{-9} g$ at 1 s, despite the high order of the internal low pass filter of the seismometer. As for the noise spectrum given by the manufacturer, we calculated that its limitation to the interferometer sensitivity would amount to $2 \times 10^{-9} g$ at 1 s.

Since the vibration signal is processed with the computer, a digital filtering seems very favorable. We use a recursive infinite impulse response (IIR) filter with the following shape: a unity gain below the lower frequency f_0, an increasing slope of 20 dB/decade from f_0 to f_1, and a constant gain above f_1. We also take benefit of the post-correction process to implement a non-causal low-pass filter (NCLPF). Such a filtering consists in processing the sampled data in a forward and backward sense with respect to time. A positive phase shift induced by the direct reading will be canceled by the reversed one, whereas the attenuation is applied twice. In our case, the NCLPF prevents the IIR filter from amplifying the intrinsic noise of the seismometer at high frequencies, without affect-

ing the phase advance needed to improve the rejection. More precisely, the corner frequency of the NCLPF corresponds to the frequency above which the seismometer signal doesn't carry any useful information.

After combining the IIR and low-pass non causal filter and before implementing them during the interferometer measurement, we checked their effect on the amplitude and the phase shift of the vibration signal, by exciting the platform again and comparing the seismometer signal, with and without filter. Excellent agreement with the expected behavior was found.

As the atomic signal was also recorded during this measurement, the influence of the filter on the efficiency of the vibration phase correction could be demonstrated directly on the interferometer signal. To illustrate the gain on the rejection, the modulation of the interferometer signal is displayed in Fig. 12 (left) for an excitation frequency of 14 Hz in the different cases:

i) we apply no correction,
ii) the correction without filter and
iii) the correction with the digital filtering.

The rejection efficiencies are displayed on Fig. 12 (right) as a function of the excitation frequency. They are obtained by calculating the ratio between the amplitudes with and without correction, for the two cases where the digital filter is used or not.

We then implemented the digital filtering in the interferometer phase correction and operated the interferometer with the nominal vibration noise. First measurements with the interferometer showed a resolved influence of the filter, but the rejection was improved by only 15%. By putting neoprene rubber below the seismometer legs, the vibrations above 30 Hz are well damped, so that the signal above this frequency reaches the seismometer intrinsic noise. This way, we reduce the contribution of the "high" frequencies, for which it is difficult to sufficiently compensate for the response of the seismometer. Nevertheless, the filter does not improve the rejection efficiency by more than 25%, whereas the calculation predicts an improvement by a factor of 3.

At night and with air conditioning switched off, the sensitivity reaches its best level. Considering the standard deviation at one shot, we deduce an equivalent noise of $1.4 \times 10^{-8} g$ at 1 s (see Fig. 13). Deviation from the expected $\tau^{-1/2}$ behavior could be due to the crosstalk with the horizontal directions (see Sect. 3.4.5), or to fluctuations of the systematics, most probably to intensity fluctuations. In this situation, with low environmental noise, we find that the filter has no influence, which seems to indicate that the sensitivity is not limited anymore by vibrational noise.

This sensitivity corresponds to phase fluctuations of 11 mrad/shot, which exceeds the level obtained when summing (quadratically) all other contributions (4 mrad). As the measurements of laser phase noise were performed in steady state condition, one cannot exclude differences in the noise spectra when the interferometer is operated sequentially, as laser frequencies undergo abrupt changes and sweeps and Raman lasers are pulsed. Intrinsic noise of the seismometer, if higher than rated by the manufacturer, could also be responsible for the observed higher noise level.

3.4.5 Seismometer intrinsic noise. First, since coils are used as actuators inside the seismometer, excess noise could be due to magnetic field fluctuations. We therefore measured the seismometer response to magnetic field fluctuations, by modulating the current in a coil placed around it. Having then measured the PSD of ambient magnetic field fluctuations in the laboratory, we finally calculated the equivalent vibration noise, and found less than $1 \times 10^{-9} g/\mathrm{Hz}^{-1/2}$, which rules out magnetic field fluctuations.

We then tried to measure the intrinsic noise of the seismometer, by stacking up two such devices and subtracting their output signals with a low noise differential amplifier. Figure 14 displays the result of this differential measurement, as well as the vibration noise measured by the sensors and the intrinsic noise given by the manufacturer. The rejection efficiency at high frequency (above 10 Hz) is poor, as expected, due to the difference between the transfer functions of the two sensors, which prevents reaching their intrinsic noise. More surprisingly, we find around 2 Hz a poor rejection (only 14 dB) and a broad structure in the spectrum of the differential signal. The output signals from both seismometers being in phase at low frequency and the difference in their scale factor being less than 1%, the rejection efficiency should reach about 40 dB. The same broad peak also appears in the horizontal acceleration noise spectrum on the platform,

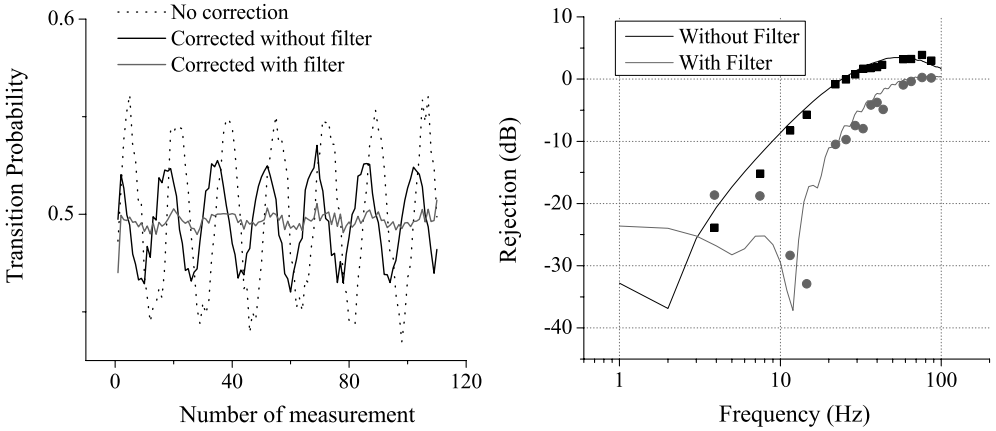

FIGURE 12 *Left*: modulation of the transition probability for an excitation frequency of 14 Hz, without correction, with correction, with and without a filter. *Right*: measured rejection efficiencies versus frequency, with and without a digital filter

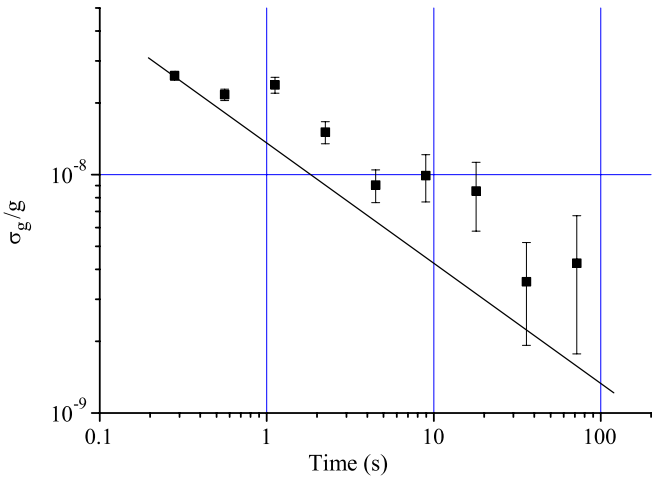

FIGURE 13 Allan standard deviation of the interferometer phase fluctuations. The seismometer signal is filtered before calculating the phase correction. The air conditioning is switched off

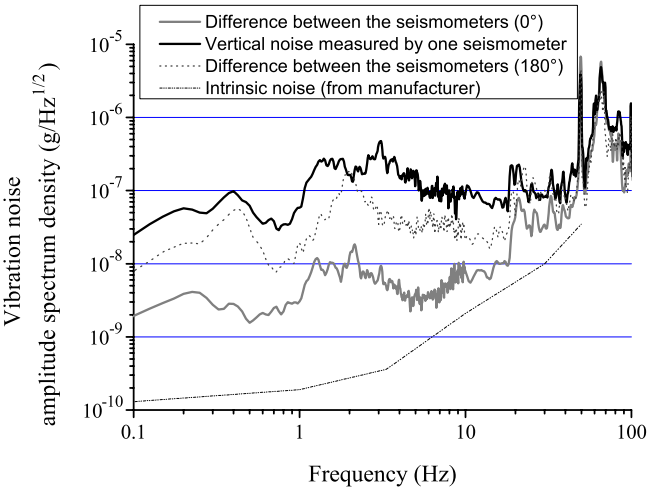

FIGURE 14 Differential measurements between two seismometers. The *grey thick curve* displays the difference between seismometers (with identical orientations in the horizontal plane)and the *black curve* the signal from one of the two seismometers. The *dotted curve* displays the differential signal for a relative orientation of 180 degrees. The *dotted line* displays the intrinsic noise of the sensor, as given by the manufacturer

about 30 times higher, up to $6 \times 10^{-7} g\,\mathrm{Hz}^{-1/2}$ at 2 Hz. We thus attribute this residual noise to crosstalk (at the level of a few %) between horizontal and vertical directions. This assumption was further confirmed by noticing that the rejection was considerably spoiled when positioning the sensors with different orientations in the horizontal plane: see Fig. 14 the differential signal for an angle between the horizontal axes of the two devices of 180°. Still, this parasitic contribution to the vertical acceleration noise at 0° is probably partially rejected in the difference, but not completely, due to a difference in the amplitude of the crosstalk, or to the fact that the two devices not being at the same position don't see exactly the same horizontal acceleration. This crosstalk could then constitute the limit in the efficiency of any 1D vibration compensation scheme. A quantitative evaluation of the impact of this effect deserves further studies, and would require the determination of the crosstalk amplitude and transfer function.

3.5 *Other contributions related to transverse displacement*

Many other effects can affect the interferometer phase. In particular, the most important systematic shifts are related to Coriolis acceleration and wavefront aberrations.

The Coriolis acceleration leads to a Sagnac effect. If the atoms are released from the molasses with a transverse velocity as low as 100 μm/s, the shift on the interferometer signal leads to a bias as large as $10^{-9} g$. If the velocity distribution is symmetric and centered around zero, then this effect is canceled when detecting the atoms, provided the detection efficiency is homogeneous across the whole cloud. Experimental inhomogeneities will in general lead to a residual shift. We have measured the fluctuations of the mean velocity of the atomic sample in the horizontal plane by performing absorption imaging at two different delays after releasing the atoms. We found short term fluctuations on the order of 10 μm/s shot. The equivalent noise is 0.03 mrad/shot, which is negligible with respect to the other effects studied above.

Wavefront aberrations induce an interferometer phase shift that depends on the trajectories of the atoms. A quantitative evaluation of this effect was performed in [32]. Short term fluctuations of the positions (and velocities) of atoms released from a moving molasses were found to limit the sensitivity of their gyro-accelerometer at the level of 0.2 mrad/shot. This limit depends on the details of the wavefront distortions and of the atomic trajectories. It is expected to be different in our geometry, as free falling atoms remain at the center of the laser beam during the interferometer. We have investigated the influence of the velocity fluctuations on the interferometer phase by unbalancing the power in the molasses beams. We found phase shifts of 0.4 mrad per percent change in the intensity ratio, which corresponds to a 40 μm/s velocity change. Velocity fluctuations thus induce phase instability at the level of 0.1 mrad/shot.

4 Conclusion

We have extensively studied the different sources of noise in an atom interferometer, and their influence on the short term sensitivity of gravity measurement.

We have demonstrated that a very high sensitivity can be achieved even with a moderate interrogation time of only 100 ms. This requires an excellent control of laser phase fluctuations and efficient detection schemes. We have also shown that the sensitivity can be efficiently improved by compensating the phase shifts induced by vibrations, using the signal of a low noise seismometer, down to a level limited by intrinsic noise of the sensor and/or by crosstalk between the different measurement axes.

Our best sensitivity at 1 s is $1.4 \times 10^{-8} g$, which is more than twice better than "classical" corner-cube gravimeters. The measurement at the same location, and in the same vibration environment, with the FG5#206 the from Institut de Physique du Globe de Strasbourg showed an equivalent sensitivity at 1 s of $4 \times 10^{-8} g$.

More generally, the work presented here allows quantification of the performances of atom interferometers as a function of the interaction time, cycling rate, and sources of per-

turbations. The same formalism can be used for the design of ultimate sensitivity instruments (such as a space interferometer for instance [26]), as well as for the realization of lower level compact instruments. In particular, the compensation technique that we have demonstrated in this paper is particularly attractive for the development of a simple and compact instrument, which could reach high sensitivities without vibration isolation.

ACKNOWLEDGEMENTS We would like to thank Patrick Cheinet for his contribution in the early stage of the experiment, David Holleville for his help with the mechanics and optics design, the Institut Francilien pour la Recherche sur les Atomes Froids (IFRAF) and the European Union (FINAQS) for financial support. J.L.G. thanks the DGA for supporting his work.

REFERENCES

1 C.J. Bordé, Phys. Lett. A **140**, 10 (1989)
2 T.M. Niebauer, G.S. Sasagawa, J.E. Faller, R. Hilt, F. Klopping, Metrologia **32**, 159 (1995)
3 M. Kasevich, S. Chu, Phys. Rev. Lett. **67**, 181 (1991)
4 F. Riehle, T. Kisters, A. Witte, J. Helmcke, C.J. Bordé, Phys. Rev. Lett. **67**, 177 (1991)
5 B. Canuel, F. Leduc, D. Holleville, A. Gauguet, J. Fils, A. Virdis, A. Clairon, N. Dimarcq, C.J. Bordé, A. Landragin, P. Bouyer, Phys. Rev. Lett. **97**, 010 402 (2006)
6 A. Peters, K.Y. Chung, S. Chu, Metrologia **38**, 25 (2001)
7 H. Mueller, S. Chiow, S. Herrmann, S. Chu, K.Y. Chung, Phys. Rev. Lett. **100**, 031 101 (2008)
8 T.L. Gustavson, A. Landragin, M.A. Kasevich, Class. Quantum Grav. **17**, 2385 (2000)
9 J.B. Fixler, G.T. Foster, J.M. McGuirk, M.A. Kasevich, Science **315**, 74 (2007)
10 G. Lamporesi, A. Bertoldi, L. Cacciapuoti, M. Prevedelli, G.M. Tino, Phys. Rev. Lett. **100**, 050 801 (2008)
11 Special Issue: "Quantum Mechanics for Space Application: From Quantum Optics to Atom Optics and General Relativity" Appl. Phys. B **84** (2006)
12 G. Genevès, P. Gournay, A. Gosset, M. Lecollinet, F. Villar, P. Pinot, P. Juncar, A. Clairon, A. Landragin, D. Holleville, F. Pereira Dos Santos, J. David, M. Besbes, F. Alves, L. Chassagne, S. Topçu, IEEE Trans. Instrum. Meas. **54**, 850 (2005)
13 R.L. Steiner, E.R. Williams, R. Liu, D.B. Newell, IEEE Trans. Instrum. Meas. **56**, 592 (2005)
14 I. Robinson, B.P. Kibble, Metrologia **44**, 427 (2007)
15 F. Yver-Leduc, P. Cheinet, J. Fils, A. Clairon, N. Dimarcq, D. Holleville, P. Bouyer, A. Landragin, J. Opt. B **5**, S136 (2003)
16 P. Cheinet, F. Pereira Dos Santos, T. Petelski, J. Le Gouët, J. Kim, K.T. Therkildsen, A. Clairon, A. Landragin, Appl. Phys. B **84**, 643 (2006)
17 C.J. Bordé, C.R. Acad. Sci. Paris, t. 2, Série IV 509 (2001)
18 X. Baillard, A. Gauguet, S. Bize, P. Lemonde, P. Laurent, A. Clairon, P. Rosenbusch, Opt. Commun. **266**, 609 (2006)
19 W.M. Itano, J.C. Bergquist, J.J. Bollinger, J.M. Gilligan, D.J. Heinzen, F.L. Moore, M.G. Raizen, D.J. Wineland, Phys. Rev. A **47**, 3554 (1993)
20 G. Santarelli, Ph. Laurent, P. Lemonde, A. Clairon, A.G. Mann, S. Chang, A.N. Luiten, C. Salomon, Phys. Rev. Lett. **82**, 4619 (1999)
21 J.M. McGuirk, G.T. Foster, J.B. Fixler, M.A. Kasevich, Opt. Lett. **26**, 364 (2001)
22 J.M. McGuirk, G.T. Foster, J.B. Fixler, M.J. Snadden, M.A. Kasevich, Phys. Rev. A **65**, 033 608 (2002)
23 P. Cheinet, B. Canuel, F. Pereira Dos Santos, A. Gauguet, F. Leduc, A. Landragin, IEEE Trans. Instrum. Meas. **57**, 1141 (2008)
24 G.J. Dick, Local Ocillator induced instabilities, In: Proc. 19th Annual Precise Time and Time Interval, pp. 133–147 (1987)
25 G. Santarelli, C. Audoin, A. Makdissi, P. Laurent , G.J. Dick, A. Clairon, IEEE Trans. Ultrason. Ferroelectr. Freq. Control **45**, 887 (1998)
26 R.A. Nyman, G. Varoquaux, F. Lienhart, D. Chambon, S. Boussen, J.-F. Clément, T. Müller, G. Santarelli, F. Pereira Dos Santos, A. Clairon, A. Bresson, A. Landragin, P. Bouyer, Appl. Phys. B **84**, 673 (2006)
27 G. Santarelli, A. Clairon, S.N. Lea, G. Tino, Opt. Commun. **104**, 339 (1994)
28 J. Le Gouët, P. Cheinet, J. Kim, D. Holleville, A. Clairon, A. Landragin, F. Pereira Dos Santos, Eur. Phys. J. D **44**, 419 (2007)
29 Benjamin Canuel, http://tel.archives-ouvertes.fr/tel-00193288/fr/
30 D.S. Weiss, B.C. Young, S. Chu, Appl. Phys. B **59**, 217 (1994)
31 P. Cladé, E. de Mirandes, M. Cadoret, S. Guellati-Khélifa, C. Schwob, F. Nez, L. Julien, F. Biraben, Phys. Rev. A **74**, 052 109 (2006)
32 J. Fils, F. Leduc, P. Bouyer, D. Holleville, N. Dimarcq, A. Clairon, A. Landragin, Eur. Phys. J. D **36**, 257 (2005)

IOP PUBLISHING METROLOGIA
Metrologia **46** (2009) 87–94 doi:10.1088/0026-1394/46/1/011

Operating an atom interferometer beyond its linear range

S Merlet[1], J Le Gouët[1], Q Bodart[1], A Clairon[1], A Landragin[1], F Pereira Dos Santos[1] and P Rouchon[2]

[1] LNE-SYRTE, CNRS UMR 8630, UPMC, Observatoire de Paris, 61 avenue de l'Observatoire, 75014 Paris, France
[2] Mines ParisTech, Centre Automatique et Systèmes, 60, bd Saint-Michel, 75272 Paris Cedex 06, France

E-mail: franck.pereira@obspm.fr

Received 30 May 2008, in final form 22 October 2008
Published 6 January 2009
Online at stacks.iop.org/Met/46/87

Abstract
In this paper, we show that an atom interferometer inertial sensor, when associated with the auxiliary measurement of external vibrations, can be operated beyond its linear range and still keep a high acceleration sensitivity. We propose and compare two measurement procedures (fringe fitting and non-linear lock) that can be used to extract, without adding any bias, the mean phase of the interferometer when the interferometer phase fluctuations exceed 2π. Despite operating in the urban environment of inner Paris without any vibration isolation, the use of a low noise seismometer for the measurement of ground vibrations allows our atom gravimeter to reach at night a sensitivity as good as $5.5 \times 10^{-8} g$ at 1 s. Robustness of the measurement to large vibration noise is also demonstrated by the ability of our gravimeter to operate during an earthquake with excellent sensitivity. For such low vibration frequency though, high pass filtering of the seismometer degrades its correlation with the interferometer signal, so that low frequency seismic vibrations appear on the gravity measurement. Nevertheless, our high repetition rate allows for efficient sampling of these perturbations, ensuring proper averaging. Such techniques open new perspectives for applications in other fields, such as navigation and geophysics.

(Some figures in this article are in colour only in the electronic version)

1. Introduction

Atom interferometers [1] are used to develop highly sensitive inertial sensors, which compete with state of the art 'classical' instruments [2]. Applications of such interferometers cover numerous fields, from fundamental physics [3–7] to navigation and geophysics. For instance, transportable devices are being developed with foreseen applications in the fields of navigation, gravity field mapping, detection of underground structures etc.

In most of these experiments, atomic waves are separated and recombined using two-photon transitions, induced by a pair of counterpropagating lasers. The inertial force is then derived from the measurement of the relative displacement of free-falling atoms with respect to the lasers' equiphase, which provide a precise ruler. As the inertial phase shift scales quadratically with the interrogation time, very high sensitivities can be reached using cold atoms along parabolic trajectories [8, 9], provided that the experiments are carefully shielded from ground vibrations. In the usual geometry where the laser beams are retroreflected on a mirror, the position of this mirror sets the position of the lasers' equiphase, so that only this 'reference' optical element is to be shielded from ground vibrations. Such an isolation can be realized either with an active stabilization scheme, using a long period superspring [2, 10, 11], or by using a passive isolation platform [12]. For instance, the use of a superspring allowed the interaction time to be increased to 800 ms and permitted a best short term sensitivity to acceleration of $8 \times 10^{-8}\,\mathrm{m\,s^{-2}}$ at 1 s [13]. An alternative technique, which we study in this paper, does not require any vibration isolation, but exploits an independent measurement of ground vibrations, realized by a low noise accelerometer, in order to correct for their impact on the gravity measurement. This technique is based on a simple idea: any measurement corrupted by parasitic vibrations can in principle be efficiently corrected from them, providing these vibrations

are measured and the transfer function of vibrations on the quantity of interest is known. It could thus be applied to light interferometers or to lasers stabilized on high finesse cavities, for instance. A technique based on the same principle has already been used with a 'classical' corner cube gravimeter [14, 15] and allowed its sensitivity to be improved by a factor of 7 [15].

In this paper, we investigate the limits to the sensitivity of an atomic gravimeter when operating without vibration isolation. This transportable gravimeter is developed within the frame of the watt balance project led by the Laboratoire National de Métrologie et d'Essais (LNE) [16, 17]. We first briefly describe our experimental setup and recall the usual procedures for measuring the mean phase of the interferometer. We then introduce and compare two measurement schemes (fringe fitting and non-linear lock) that allow the sensor to be operated in the presence of large vibration noise and show how phase measurements can be performed even though the interferometer phase noise amplitude exceeds 2π. These schemes, which use an independent measurement of vibration noise with a low noise seismometer, allow good sensitivities to be achieved without vibration isolation. In particular, we reach a sensitivity as good as $5.5 \times 10^{-8} g$ at 1 s during night measurements, in the urban environment of inner Paris. Finally, the robustness of these measurement schemes versus changes in the vibration noise is illustrated by the capability of our instrument to operate and measure large ground accelerations induced by an earthquake.

2. Limits due to vibration noise in a conventional setup

2.1. Experimental setup

The experimental setup, which we briefly recall here, has been described in detail in [12, 18]. About 10^7 ^{87}Rb atoms are first loaded in a 3D-MOT (magneto-optical trap) within 50 ms, and further cooled down to 2.5 µK before being dropped in free fall. Before creating the interferometer, a narrow vertical velocity distribution of width about 1 cm s^{-1} is selected in the $|F = 1, m_F = 0\rangle$ state, using several microwave and optical Raman pulses.

The interferometer is then created using Raman transitions [8] between the two hyperfine levels $F = 1$ and $F = 2$ of the $^5S_{1/2}$ ground state, which are induced by two vertical and counterpropagating laser beams of frequencies ω_1, ω_2 and wavevectors $\vec{k}_1$, $\vec{k}_2$. A sequence of three Raman pulses ($\pi/2 - \pi - \pi/2$) allows one to split, redirect and recombine the atomic wave packets. The relationship between external and internal state [1] allows one to measure the interferometer phase shift from a fluorescence measurement of the populations of each of the two states. At the output of the interferometer, the transition probability P from one hyperfine state to the other is given by $P = a + b \cos \Delta\Phi$, where $2b$ is the interferometer contrast, and $\Delta\Phi$, the difference in the atomic phases accumulated along the two paths, is given by $\Delta\Phi = -\vec{k}_{\text{eff}} \cdot \vec{g} T^2$ [19]. Here $\vec{k}_{\text{eff}} = \vec{k}_1 - \vec{k}_2$ is the effective wave vector (with $|\vec{k}_{\text{eff}}| = k_1 + k_2$ for counterpropagating beams), T is the time interval between two consecutive pulses and g is the acceleration of gravity.

The Raman light sources are two extended cavity diode lasers based on the design of [20], which are amplified by two independent tapered amplifiers. Their frequency difference, which is phase locked onto a low phase noise microwave reference source, is swept according to $(\omega_2 - \omega_1)(t) = (\omega_2 - \omega_1)(0) + \alpha t$ in order to compensate for the gravity-induced Doppler shift. This adds αT^2 to the interferometer phase shift, which eventually cancels it for a perfect Doppler compensation, for which $\alpha_0 = \vec{k}_{\text{eff}} \cdot \vec{g}$.

2.2. Conventional measurement procedures

Maximal sensitivity to phase fluctuations is achieved when operating the interferometer at mid-fringe, which corresponds to $\Delta\Phi = \pm\pi/2$. In this case, though, variations in the offset a can be interpreted as fluctuations of the interferometer phase. A standard technique [10] then consists in recording a full fringe, by measuring the transition probability as a function of a controlled phase shift induced on the interferometer. Fitting this fringe then allows g to be measured. This technique degrades the short term sensitivity as measurements performed at the top or bottom of the fringes are not sensitive to phase fluctuations. An alternative way consists of using a method inspired by microwave atomic clocks. The phase is modulated by $\pm\pi/2$ so that the measurement is always performed at mid-fringe, alternatively to the right and to the left side of the central fringe. From two consecutive measurements P_i and P_{i+1}, the phase error can be estimated. In practice, a correction $G \times (P_i - P_{i+1})$ is added at each cycle to α, in order to steer the chirp rate onto the central fringe. This realizes an integrator, whose time constant can be set to a few cycles by adjusting the gain G. This locking technique has the advantage of rejecting offset and contrast fluctuations, while preserving maximal sensitivity to phase fluctuations.

2.3. Influence of vibration noise

In the case where the duration of the Raman pulses can be neglected, the phase shift $\Delta\Phi$ induced by vibrations is given by

$$\begin{aligned}\Delta\Phi &= k_{\text{eff}}(z_g(-T) - 2z_g(0) + z_g(T)) \\ &= k_{\text{eff}} \int_T^{-T} g_s(t) v_g(t)\, \mathrm{d}t, \end{aligned} \tag{1}$$

where z_g and v_g are the position and velocity of the experimental setup, and g_s is the sensitivity function [21], given by

$$g_s(t) = \begin{cases} -1 & -T < t < 0, \\ 1 & 0 < t < T. \end{cases} \tag{2}$$

The expected sensitivity of the interferometer to g fluctuations of the interferometer is then given by a weighted sum of the vibration noise at the harmonics of the cycling rate f_c [21]:

$$\sigma_g^2(\tau) = \frac{1}{\tau} \sum_{k=1}^{\infty} \left(\frac{\sin(\pi k f_c T)}{\pi k f_c T} \right)^4 S_a(2\pi k f_c), \tag{3}$$

where $\sigma_g(\tau)$ is the Allan standard deviation of acceleration fluctuations for an averaging time τ and S_a is the power spectral density of acceleration fluctuations.

Figure 1 displays the power spectral densities of vibrations, measured with a low noise seismometer (Guralp CMG-40T, response option 30 s) on the platform which is either floating (ON) (day time) or put down (OFF) (day time and night time). In the case where the platform is OFF, the spectrum is similar to the spectrum measured directly on the ground. For our typical parameters, $2T = 100$ ms and $f_c = 3.8$ Hz, we calculate using equation (3) sensitivities at $\tau = 1$ s of $2.9 \times 10^{-6} g$ during the day and $1.4 \times 10^{-6} g$ during the night with the platform OFF. With the platform ON, the sensitivity is expected to be $7.6 \times 10^{-8} g$.

3. Vibration noise correction

3.1. Correlation between atomic and seismometer signals

The signal of the seismometer can be used to determine the phase shift of the interferometer due to residual vibrations, as measured by the seismometer, $\phi^S_{\rm vib}$, which is given by

$$\phi^S_{\rm vib} = k_{\rm eff} \int_T^{-T} g_{\rm s}(t) v_{\rm s}(t)\, {\rm d}t = k_{\rm eff} K_{\rm s} \int_T^{-T} g_{\rm s}(t) U_{\rm s}(t)\, {\rm d}t, \tag{4}$$

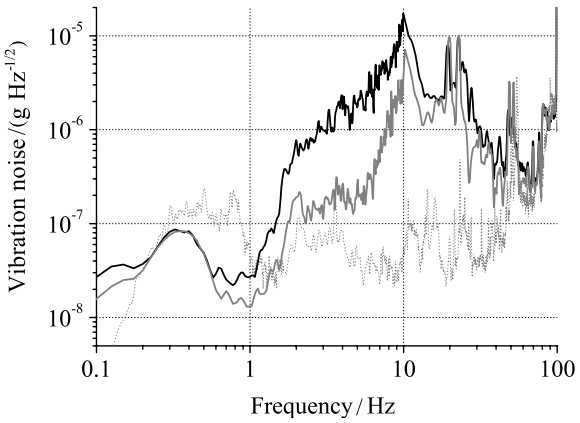

Figure 1. Amplitude spectral densities of vibration noise. The black (respectively, grey) thick curve displays the vibration noise with the isolation platform down (OFF) at day time (respectively night time), while the dotted curve displays the vibration noise with the floating platform (ON) at day time.

where $U_{\rm s}$ is the seismometer voltage (velocity) output and $K_{\rm s} = 400.2\ {\rm V\,m^{-1}\,s^{-1}}$ is the velocity output sensitivity of the seismometer.

Figure 2 displays the measured transition probability as a function of $\phi^S_{\rm vib}$, in the two cases of platform ON and OFF, for an interferometer time $2T = 100$ ms. The noise is low enough in the ON case (figure 2(*b*)) for the interferometer to operate close to mid-fringe, while in the OFF case (figure 2(*a*)) interferometer phase noise is larger than 2π, and the interferometer signal jumps from one fringe to another. Figure 2 shows the good correlation between measured and calculated phase shifts. In the ON case, we find a correlation factor as high as 0.94.

The calculated $\phi^S_{\rm vib}$ can thus be used to significantly improve the sensitivity of the measurement, by applying a post-correction on the transition probability measured at mid-fringe. This correlation is not perfect though due to the response function of the seismometer, which is not flat, and behaves like a low-pass filter with a cut-off frequency of 50 Hz. This response function thus limits the efficiency of the vibration rejection. Figure 3 displays as a continuous black line the rejection efficiency as a function of frequency, which is calculated from the seismometer transfer function.

3.2. Digital filtering

We implemented a numerical filtering of the seismometer signal to compensate for the phase lag of the seismometer at intermediate frequencies. The design of the filter is described in detail in [12]. It consists of the product of a recursive infinite impulse response (IIR) filter, with corner frequencies f_0 and f_1, and a non-causal low-pass filter. The IIR filter compensates the phase shift of the seismometer signal and the non-causal filter prevents the IIR filter from amplifying the intrinsic noise of the seismometer at high frequencies, without affecting the phase advance needed to improve the rejection. The total transfer function of the filter is given by

$$F(f) = \frac{1 + jf/f_0}{1 + jf/f_1} \frac{1}{1 + (f/f_{\rm c})^2}, \tag{5}$$

where f_0, f_1 and $f_{\rm c}$ are then optimized in order to reach the best sensitivity. This digital filtering significantly improves

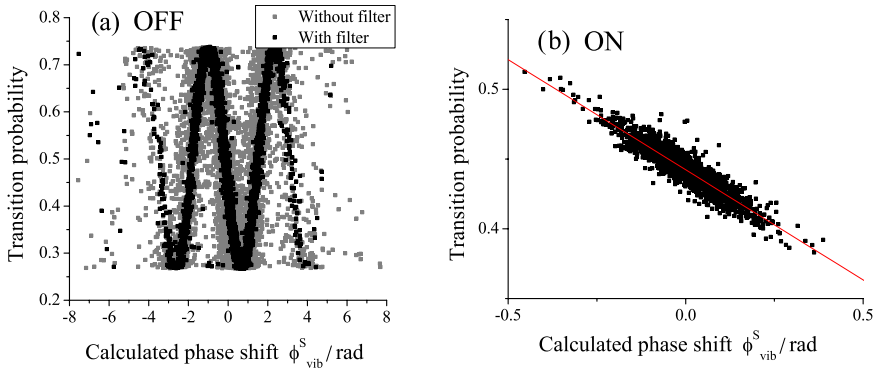

Figure 2. Correlation between the transition probability of the interferometer and the phase shift calculated from the seismometer data, for $2T = 100$ ms. (*a*) The isolation platform is OFF. Grey points: without digital filter, black points: with digital filter. (*b*) The isolation platform is ON. Black points: with digital filter. Line: fit to the data, with correlation factor of 0.94.

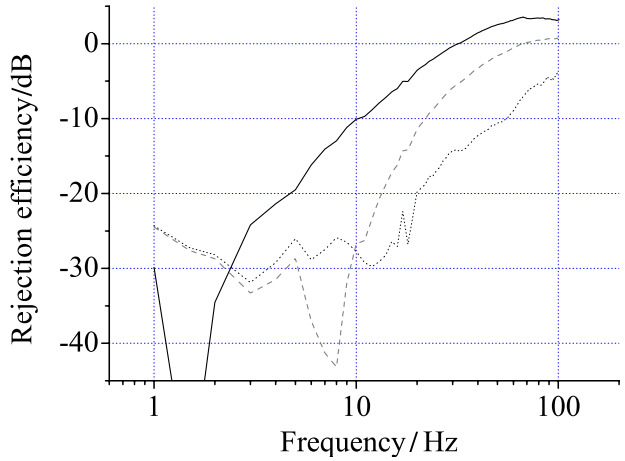

Figure 3. Efficiency of the vibration rejection as a function of frequency without any processing (black straight line), with a digital filter (dashed line), with a compensation of a delay of 4.6 ms (dotted line).

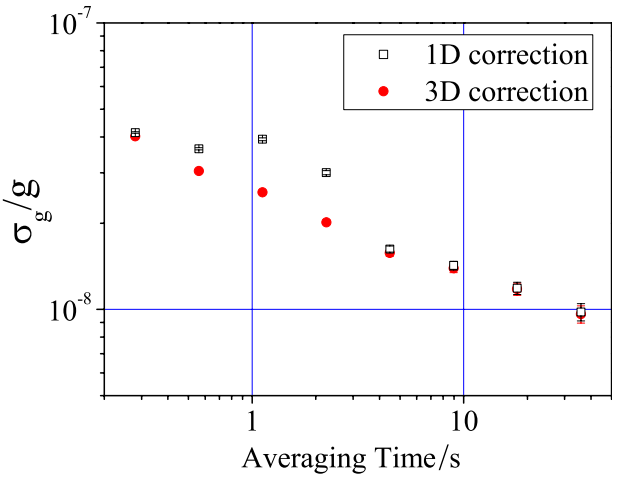

Figure 4. Sensitivity to g with 1D and 3D corrections. The measurement was realized during the day, with a floating platform.

the rejection efficiency, as can be seen in figure 3, where it is displayed as a dashed line, for the frequencies $f_0 = 30$ Hz, $f_1 = 180$ Hz and $f_c = 29$ Hz. Despite this increase in the rejection efficiency, the gain in the sensitivity, when implementing this filter in the ON mode, was limited to 25% only [12], which we attributed to excess noise of the seismometer arising from coupling between the horizontal and the vertical axes.

3.3. Cross couplings

In order to detect these couplings, we recorded simultaneously the seismometer outputs along the three directions, calculated three corrections, one along each axis (only the vertical correction was numerically filtered though) and fitted the transition probability measured at mid-fringe with a linear combination of the three corrections. The result of this fit showed couplings of 4% and 5% with the horizontal axes. We finally determined the influence of these couplings on the sensitivity of the measurement, by comparing the Allan standard deviation of the phase fluctuations in the case where the correction is performed only with the vertical correction (1D) or with the optimal combination of the three (3D). The results are shown in figure 4, where the sensitivity is expressed relative to g.

Using the three corrections allows one to remove a bump that appears when using the 1D correction. This indicates that horizontal vibration noise, as also appears in the vertical seismometer signal, adds noise when performing a 1D correction.

3.4. Efficiency of the filter without vibration isolation

The digital filter is much more efficient in the OFF mode, as one can see in figure 2(*a*) where the noise on the interferometer fringes is significantly reduced when seismometer data are processed with the digital filter. In that case, the dominant contribution of the vibration noise to the degradation of the sensitivity corresponds to frequencies around 10 Hz, for which the effect of the filter improves the rejection efficiency from 10 dB to about 30 dB [12].

3.5. Case of a pure delay

We later noticed that the phase lag of the seismometer signal varies almost linearly with respect to the frequency in the 1 Hz to 100 Hz band, with a slope corresponding to a delay of about 5 ms. The phase shift of the seismometer can thus be compensated for, by simply shifting the acquisition of the seismometer data by this delay. We measured the correlation factor as a function of the delay, with the platform OFF, and found an optimal delay of 4.6 ms. The rejection efficiency for this optimal delay is displayed as a dotted line on figure 3. Surprisingly, we find a correlation similar to the optimal digital filter, despite a significantly different behaviour of the rejection efficiency versus frequency.

4. Measurement protocols

4.1. Standard procedures

The standard measurement protocols described above need phase fluctuations to remain significantly smaller than 2π. This requires the interferometer duration in the OFF mode to be reduced to $2T \leqslant 20$ ms. For $2T = 20$ ms, the integrator scheme described above allows one to reach sensitivities of $1 \times 10^{-5} g$ at 1 s when applying no correction to the measured transition probability, $5 \times 10^{-6} g$ when correcting without filtering and $1.5 \times 10^{-6} g$ when correcting with digital filtering. The simple post-correction (without filter) thus improves the sensitivity by a factor 2, and the digital filter improves it further by a factor 3.5. Better performances are expected with large interrogation time for which the transfer function of the interferometer filters high frequency vibration noise more efficiently. In order to operate the interferometer with large interrogation times despite excess noise, we propose two alternative measurement procedures described in the following subsections. Both are based on the combination of measurements of the transition probability and of $\phi^S_{\rm vib}$ by the

seismometer. Though developed for the case of large vibration noise, these techniques can be extended to low vibration noise by adding a well controlled phase modulation.

4.2. Fringe fitting

The first technique simply consists of fitting fringes, as in [10], except that here the phase of the interferometer is now scanned randomly by vibration noise. The signal displayed in figure 2 and obtained when plotting the transition probability versus $\phi^S_{\rm vib}$, calculated with the digital filter, can be fitted by the function $P = a + b\cos(\eta\phi^S_{\rm vib} + \delta\phi)$, where a, b, η and $\delta\phi$ are free parameters. Due to the influence of the seismometer transfer function, η will in general differ from 1. In practice, we operate the interferometer close to the central fringe, which corresponds to a small phase error $\delta\phi$. Every 20 points, we perform a fit of the signal and extract a value for the phase error $\delta\phi_m$. We then calculate the Allan standard deviation of the $\delta\phi_m$ in order to determine the sensitivity of the measurement. Note that this fitting procedure is not very efficient if the noise amplitude is significantly less than 2π, because the interferometer signal remains close to the bottom of the central fringe. An additional and perfectly controlled phase modulation of $\pm\pi/2$ is thus applied in order to optimize the sensitivity of the interferometer to phase fluctuations. Moreover, the sensitivity improves by about 50% when taking cross couplings of the seismometer into account, which can be realized by adjusting the data with a linear combination of the corrections along three directions $\Sigma\eta_j\phi^S_{{\rm vib},j}$, where $j = x, y, z$ and $\phi^S_{{\rm vib},j}$ is the phase shift calculated from the filtered seismometer data along axis j.

4.3. Non-linear lock

The lock procedure described in section 2.2 can be adapted in the case where the phase noise exceeds 2π. Let us consider the measurement at cycle i of the transition probability P_i

$$\begin{aligned} P_i &= a - b\cos((k_{\rm eff}g - \alpha)T^2 + S_i) \\ &= a - b(\cos e\cos S_i - \sin e\sin S_i), \end{aligned} \tag{6}$$

where $e = (k_{\rm eff}g - \alpha)T^2$ is the phase error and S_i is the phase shift induced by residual vibrations, estimated from the seismometer signal. We assume here that the phase error e varies slowly, so that we can consider it as constant between three consecutive measurements. Eliminating a and $\cos e$ from the following three equations

$$\begin{aligned} P_{i-1} &= a - b(\cos S_{i-1}\cos e - \sin S_{i-1}\sin e), \\ P_i &= a - b(\cos S_i\cos e - \sin S_i\sin e), \\ P_{i+1} &= a - b(\cos S_{i+1}\cos e - \sin S_{i+1}\sin e) \end{aligned}$$

gives

$$bB_i\sin e = A_i$$

with

$$\begin{aligned} A_i &= (\cos S_{i+1} - \cos S_i)(P_{i-1} - P_i) \\ &\quad - (\cos S_{i-1} - \cos S_i)(P_{i+1} - P_i), \\ B_i &= (\cos S_{i+1} - \cos S_i)(\sin S_{i-1} - \sin S_i) \\ &\quad - (\cos S_{i-1} - \cos S_i)(\sin S_{i+1} - \sin S_i). \end{aligned}$$

In order to steer the chirp rate onto the Doppler shift rate, an iterative correction is applied to α according to

$$\alpha_{i+2} = \alpha_{i+1} + K\frac{2B_i}{1 + B_i^2}A_i, \tag{7}$$

where K is a positive gain. Here $\frac{2B_i}{1+B_i^2}$ is used as a pseudo-inverse of bB_i with $b \approx 1/2$, in order to prevent the correction from diverging when B_i is close to zero. Choosing $K < 1/T^2$ guarantees the stability of the servo loop.

4.4. Adaptation of the non-linear lock

When phase fluctuations are significantly less than 1 rad, B_i becomes much smaller than 1 (note that B_i is null in the absence of vibration noise, which implies that the lock scheme does not work, as it is not able to steer the chirp rate), so that $\frac{B_i}{1+B_i^2}$ is not a good pseudo-inverse of B_i. This decreases the effective gain of the loop, which can be compensated for either by increasing K or by replacing $\frac{B_i}{1+B_i^2}$ with $\frac{B_i}{\sigma_B^2+B_i^2}$, where σ_B is the standard deviation of the B_is.

The scheme is then to be modified by adding extra phase shifts in order to increase the sensitivity to phase fluctuations. A simple phase modulation of $\pm\pi/2$, which implies that the interferometer operates alternately at the right and left sides of the central fringe, is not sufficient, as in that case B_i is still null for null vibration noise. With a three-phase modulation $(-\pi/2, 0, \pi/2)$, $B_i = 1$ for null vibration noise, and replacing $\frac{B_i}{1+B_i^2}$ with $\frac{B_i}{\sigma_B^2+B^2+B_i^2}$, with B the mean of B_is, guarantees the full efficiency of the lock, whatever the amplitude of vibration noise.

The lock technique can be further modified to first determine and servo the vibration phase coefficients η_j. The phase of the interferometer is $e + S_i + \delta\phi_i$, where $\delta\phi_i$ is a controlled additional phase shift (alternately $-\pi/2, 0, \pi/2$), and the vibration phase S_i is (best approximated by) $\Sigma\eta_j\phi^S_{{\rm vib},j}$, where $j = x, y, z$ and $\phi^S_{{\rm vib},j}$ is the phase shift calculated from the seismometer data along axis j. At the ith measurement, S_i is calculated by $\sum_{j=1}^3 \eta_{j,i}\phi^S_{{\rm vib},j,i}$, where $\eta_{j,i} = \eta_j - \delta\eta_{j,i}$. P_i is thus given by

$$P_i = a - b\cos\left(\delta\phi_i + \sum_{j=1}^3 \eta_{j,i}\phi^S_{{\rm vib},j,i} + e + \sum_{j=1}^3 \delta\eta_{j,i}\phi^S_{{\rm vib},j,i}\right),$$

$$P_i = a - b\left(\cos S_i - \left(e + \sum_{j=1}^3 \delta\eta_{j,i}\phi^S_{{\rm vib},j,i}\right)\sin S_i\right),$$

where $S_i = \delta\phi_i + \sum_{j=1}^3 \eta_{j,i}\phi^S_{{\rm vib},j,i}$.

Generalizing the algebra above, one gets

$$b\left(B_i e + \sum_{j=1}^3 C_{j,i}\delta\eta_{j,i}\right) = A_i, \tag{8}$$

where

$$\begin{aligned} C_{j,i} &= (\cos S_{i+1} - \cos S_i)(\phi^S_{{\rm vib},j,i-1}\sin S_{i-1} - \phi^S_{{\rm vib},j,i}\sin S_i) \\ &\quad - (\cos S_{i-1} - \cos S_i)(\phi^S_{{\rm vib},j,i+1}\sin S_{i+1} \\ &\quad - \phi^S_{{\rm vib},j,i}\sin S_i). \end{aligned}$$

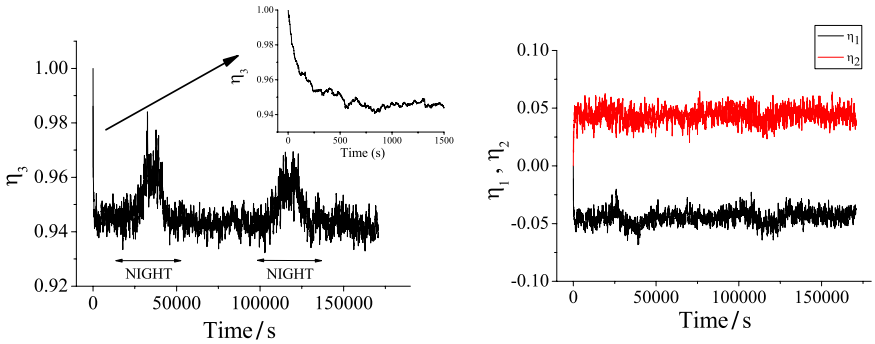

Figure 5. Evolution of the vibration phase coefficients, during a measurement realized using the non-linear lock scheme, with initial settings $\eta_{j,0} = (0, 0, 1)$. The graph on the left (respectively, right) displays the vertical (respectively, horizontal) phase coefficient(s).

Chirp rates and vibration phase coefficients are then corrected according to

$$\alpha_{i+2} = \alpha_{i+1} + K \frac{B_i}{\sigma_B^2 + B^2 + B_i^2} A_i,$$

$$\eta_{j,i+2} = \eta_{j,i+1} + L_j \frac{C_{j,i}}{\sigma_{C_j}^2 + C_{j,i}^2} A_i,$$

where L_j is the gain for direction j. Such non-linear feedback and estimation algorithms are inspired from Lyapounov stability theory, for the main loop given by equation (7), and adaptive techniques, for the estimation of parameters η_j (see [22] for a tutorial presentation of such techniques and [23] for a more advanced one).

Figure 5 displays the evolution of the vibration phase coefficients during a two-day measurement. The time constant of the lock is about 200 s (see inset). Note that the vertical phase coefficient η_3 differs significantly from 1 and is different at day and night times, which can be attributed to a change in the vibration noise PSD. Moreover, the lock converges towards horizontal phase coefficients of about 5%, in agreement with the values previously determined with the fit.

4.5. Comparison of the two techniques

Figure 6 displays the Allan standard deviation of g fluctuations for $2T = 100$ ms, with the two techniques described above (fringe fitting and non-linear lock), during day and night times. The vibration phase shifts were calculated from the 3D signals, using the optimal delay of 4.6 ms.

We obtain equivalent sensitivities at 1 s of $2.7 \times 10^{-7} g$ (respectively $1.8 \times 10^{-7} g$) with the non-linear lock (respectively fringe fitting) technique during the day and $8.5 \times 10^{-8} g$ (respectively $5.5 \times 10^{-8} g$) during the night. We find that the fit of the fringes is slightly better than the lock technique, by about 50%. The efficiency in removing vibration noise from the gravimeter signal can be calculated from the ratio of the sensitivities obtained here with the calculated contribution of the vibration noise (see section 2.3). A gain from 11 to 25 is obtained depending on the technique and noise conditions.

Best sensitivities are obtained during night measurements, as the vibration noise in the 1 Hz to 10 Hz band is significantly lower. We reach at best an equivalent sensitivity as low as

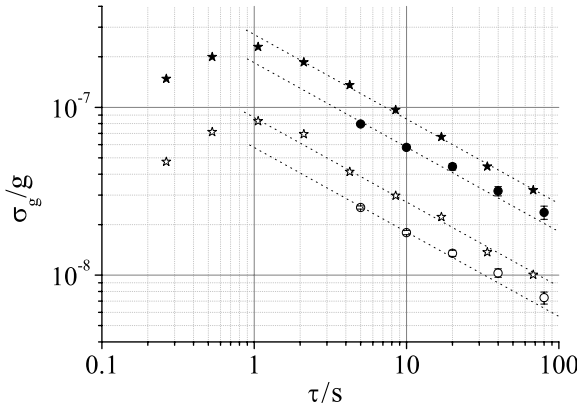

Figure 6. Allan standard deviation of g fluctuations versus averaging time. Measurements with the non-linear lock technique at day (respectively, at night) are displayed as full stars (respectively, open stars). Measurements with the fringe fitting technique at day (respectively, at night) are displayed as full circles (respectively, open circles).

$5.5 \times 10^{-8} g$ at 1 s when fitting fringes, which is only 4 times worse than our best reported value with the platform floating [12] and only twice as large as the sensitivity obtained in our laboratory with a commercial FG-5 corner cube gravimeter [2] in the same vibration noise conditions.

These two techniques were also compared in a numerical simulation, where the phase of the interferometer was generated randomly as the sum of two independent terms $\phi = \phi_1 + \phi_2$, with Gaussian distribution of standard deviations σ_1 and σ_2. ϕ_1 simulates the vibration phase noise measured by the seismometer ϕ_{vib}^S and ϕ_2 the phase difference between the real vibration phase noise and ϕ_{vib}^S. We then implemented the two techniques with such simulated data, with $\sigma_2 = 0.02$ rad and with σ_1 ranging from 0.06 rad to 30 rad. For each technique, we find the corresponding sensitivity of the interferometer at 1 shot σ_Φ and calculate a normalized sensitivity by dividing σ_Φ with σ_2. We verified that this normalized sensitivity does not depend on σ_2. The results of the simulations are displayed in figure 7 and for both techniques the normalized sensitivity exhibits the same behaviour. It increases for vibration noise larger than a few hundred millirads, for which linear approximation of the transition probability is no longer valid, and finally saturates for large vibration noise. This degradation is due to the non-linearity of the transition probability versus interferometer

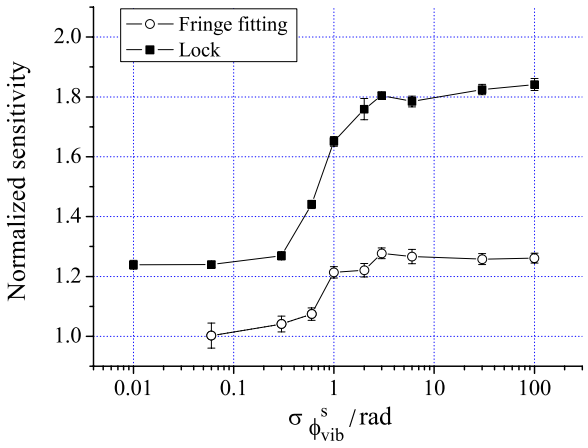

Figure 7. Numerical simulation of the normalized sensitivity of the interferometer as a function of the vibration noise standard deviation. Black squares (respectively, open circles) display the sensitivity degradation for the non-linear lock (respectively, fringe fitting) technique.

phase: measurements at top and bottom of the fringes have no sensitivity to phase fluctuations. The simulation confirms that this degradation is higher for the lock technique than for the fringe fitting technique, as observed in the measurements. In particular, for $\sigma_2 = 3$ rad, which corresponds roughly to day conditions, we find normalized sensitivities of 1.28 and 1.80 for the fringe fitting and lock techniques. The ratio of the sensitivities is thus 1.4, in reasonable agreement with the measurements.

4.6. Investigation of systematic effects

It is important to verify that the techniques presented here provide an accurate measurement of the interferometer phase, free from any bias. The lock procedure, which is intrinsically non-linear, could in principle induce such a bias. The numerical simulation indicates that neither of the two techniques suffers from such systematics. This was confirmed experimentally by performing differential measurements, alternating the standard integration technique described in section 2.2 with the lock procedure described in section 4.4, in the case where the platform was ON and thus the noise level low. The difference between the two techniques was found to be 0.3 µGal ± 0.8 µGal, which is consistent with no bias. Moreover, the two techniques were compared together during the day with the platform OFF, which corresponds to a noise level of $\sigma_{\phi^s_{\rm vib}} = 3$ rad. The difference for a 6 h measurement was found to be −2 mrad ± 4 mrad, which corresponds to −5 µGal ± 10 µGal, which is also consistent with no bias.

4.7. Interest of the non-linear lock procedure

The main advantage of the non-linear lock scheme is a better time resolution. Indeed, the time constant of the lock loop can be reduced to a few cycles only, so that a time constant $\leqslant$1 s can be reached. In comparison, fitting the fringes requires to fit data in packets of at least 20 cycles for optimal sensitivity, which reduces the time resolution to about 5 s. Both techniques can operate with low vibration noise. Indeed, the fit of the fringes can also be adapted by modifying the phase modulation to add measurements performed at the top and bottom of the interferometer, in order to constrain the sinusoidal fit (in doing so sensitivity will as well be degraded because these measurements are not sensitive to phase fluctuations). We finally illustrate the efficiency of the lock algorithm by demonstrating its robustness versus large changes in the vibration noise. Figure 8 displays the measurement during an earthquake of magnitude 7.7 that occurred in China on 20 March 2008. The gravimeter efficiently detects the occurrence of seismic waves, of period about 20 s. As our seismometer, of long period 30 s only, measures these vibrations with a large phase lag of about 1 rad, they are not efficiently removed from the gravimeter phase shift by the lock algorithm. They thus appear as a clear and well-resolved signal in the gravimeter data. This demonstrates the robustness of our system versus large excitations, which is not the case for traditional absolute corner cube gravimeters, which have neither adequate repetition rate (usually about 0.1 Hz) nor sufficient dynamic range, due to the finite range of the superspring mechanism. Note that the use of a longer period seismometer would in principle allow removal of these low frequency vibrations from the gravimeter data.

5. Conclusion

In this paper, we demonstrate that an atom interferometer can reach high sensitivities without vibration isolation, when using an independent measurement of vibrations by a low noise seismometer. We develop here several measurement protocols that allow determination of the mean phase of the interferometer, even when the interferometer phase noise amplitude exceeds 2π. In particular, fitting the fringes scanned by vibration noise allows one to reach a sensitivity as low as $5.5 \times 10^{-8} g$ at 1 s during night measurements. This performance is obtained with a rather short interaction time ($2T = 100$ ms), for which the vertical length of the interferometer corresponds to a few centimetres only.

The techniques presented here are of interest for the realization of a portable atom gravimeter, with potential application to geophysics and gravity measurements in noisy environments. A compact gravimeter associated with a good ac accelerometer and operating at a high repetition rate would reach fairly high sensitivities, without much hardware isolation against ground vibrations. Moreover, in contrast to other classical instruments, such as ballistic corner cube gravimeters, a high sensitivity would still be reached in the presence of earthquakes, if using a long period seismometer (100 s) to measure vibration noise. The technique demonstrated here could, for instance, be of interest for applications of atom interferometers to mobile gravimetry, in strap-down configuration.

More generally, these techniques can be extended to differential measurements with atom interferometers, such as gradiometers and cold atom gyroscopes. In particular, the phase difference can easily be extracted from the fits of the

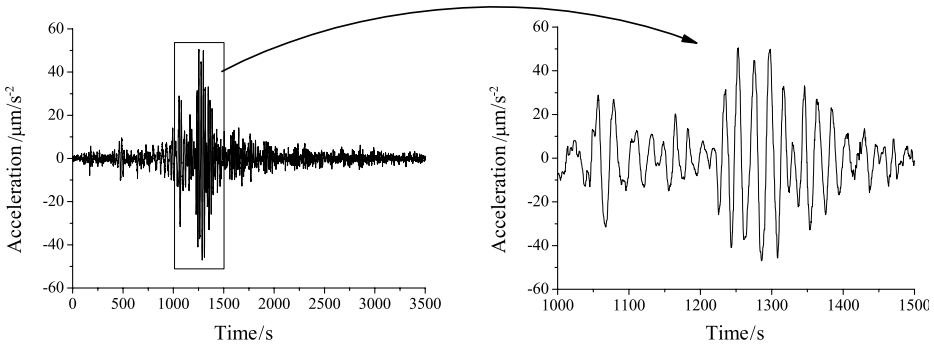

Figure 8. Fluctuations of the gravimeter signal during the earthquake of magnitude 7.7 that occurred in China on March 20, 2008. Data were obtained with the non-linear lock procedure.

two interference patterns. Much interest in these techniques lies in the ability to extend the dynamic range of the sensors and to extract the inertial phase without bias.

Acknowledgments

We would like to thank the Institut Francilien pour la Recherche sur les Atomes Froids (IFRAF) and the European Union (FINAQS) for financial support. QB and JLG, respectively, thank CNES and DGA for supporting their work.

References

[1] Bordé Ch J 1989 Atomic interferometry with internal state labeling *Phys. Lett.* A **140** 10
[2] Niebauer T M, Sasagawa G S, Faller J E, Hilt R and Klopping F 1995 A new generation of absolute gravimeters *Metrologia* **32** 159–80
[3] Fixler J B, Foster G T, McGuirk J M and Kasevich M A 2007 Atom interferometer measurement of the Newtonian constant of gravity *Science* **315** 74–7
[4] Lamporesi G, Bertoldi A, Cacciapuoti L, Prevedelli M and Tino G M 2008 Determination of the Newtonian gravitational constant using atom interferometry *Phys. Rev. Lett.* **100** 050801
[5] Wicht A, Hensley J M, Sarajlic E and Chu S 2002 A preliminary measurement of the fine structure constant based on atom interferometry *Phys. Scr.* **T102** 82–8
[6] Cladé P, de Mirandes E, Cadoret M, Guellati-Khélifa S, Schwob C, Nez F, Julien L and Biraben F 2006 Determination of the fine structure constant based on bloch oscillations of ultracold atoms in a vertical optical lattice *Phys. Rev. Lett.* **96** 033001
[7] Jacquey M, Büchner M, Trénec G and Vigué J 2007 First measurements of the index of refraction of gases for lithium atomic waves *Phys. Rev. Lett.* **98** 240405
[8] Kasevich M and Chu S 1991 Atomic interferometry using stimulated Raman transitions *Phys. Rev. Lett.* **67** 181–4
[9] Canuel B, Leduc F, Holleville D, Gauguet A, Fils J, Virdis A, Clairon A, Dimarcq N, Bordé Ch J, Landragin A and Bouyer P 2006 Six-axis inertial sensor using cold-atom interferometry *Phys. Rev. Lett.* **97** 010402
[10] Peters A, Chung K Y and Chu S 2001 High-precision gravity measurements using atom interferometry *Metrologia* **38** 25–61
[11] Hensley J M, Peters A and Chu S 1999 Active low frequency vertical vibration isolation *J. Sci. Instrum.* **70** 2735–41
[12] Le Gouët J, Mehlstäubler T E, Kim J, Merlet S, Clairon A, Landragin A, Pereira Dos Santos F 2008 Limits to the sensitivity of a low noise compact atomic gravimeter *Appl. Phys.* B **92** 133–44
[13] Müller H, Chiow S, Herrmann S, Chu S and Chung K Y 2008 Atom-interferometry tests of the isotropy of post-Newtonian gravity *Phys. Rev. Lett.* **100** 180405
[14] Canuteson E, Zumberge M and Hanson J 1997 An absolute method of vertical seismometer calibration by reference to a falling mass with application to the measurement of the gain *Bull. Seismol. Soc. Am.* **87** 484–93
[15] Brown J M, Niebauer T M and Klingele E 2001 Towards a dynamic absolute gravity system *Gravity, Geoid, and Geodynamics 2000, Int. Assoc. Geodesy (Banff, Canada, 31 July–4 August 2000)* vol 123 pp 223–8
[16] Genevès G *et al* 2005 The BNM Watt balance project *IEEE Trans. Instrum Meas.* **54** 850–3
[17] Merlet S, Kopaev A, Diament M, Genevès G, Landragin A and Pereira Dos Santos F 2008 Micro-gravity investigations for the LNE watt balance project *Metrologia* **45** 265–74
[18] Cheinet P, Pereira Dos Santos F, Petelski T, Le Gouët J, Kim J, Therkildsen K T, Clairon A and Landragin A 2006 Compact laser system for atom interferometry *Appl. Phys.* B **84** 643–6
[19] Bordé Ch J 2001 Theoretical tools for atom optics and interferometry *C.R. Acad. Sci. Paris, Série IV* **2** 509–30
[20] Baillard X, Gauguet A, Bize S, Lemonde P, Laurent Ph, Clairon A and Rosenbusch P 2006 Interference-filter-stabilized external-cavity diode lasers *Opt. Commun.* **266** 609–13
[21] Cheinet P, Canuel B, Pereira Dos Santos F, Gauguet A, Leduc F and Landragin A 2008 Measurement of the sensitivity function in a time-domain atomic interferometer *IEEE Trans. Instrum. Meas.* **57** 1141–8
[22] Slotine J J E and Li J W 1991 *Applied Nonlinear Control* (Englewood Cliffs, NJ: Prentice Hall)
[23] Khalil H K 1992 *Nonlinear Systems* (London: MacMillan)

Off-resonant Raman transition impact in an atom interferometer

A. Gauguet, T. E. Mehlstäubler,* T. Lévèque, J. Le Gouët,† W. Chaibi, B. Canuel,‡ A. Clairon, F. Pereira Dos Santos, and A. Landragin§

LNE-SYRTE, UMR 8630 CNRS, Observatoire de Paris, UPMC, 61 avenue de l'Observatoire, 75014 Paris, France

(Received 29 August 2008; published 29 October 2008)

We study the influence of off-resonant two-photon transitions on high-precision measurements with atom interferometers based on stimulated Raman transitions. These resonances induce a two-photon light shift on the resonant Raman condition. The impact of this effect is investigated in two highly sensitive experiments using a gravimeter and a gyroscope-accelerometer. We show that it can lead to significant systematic phase shifts, which have to be taken into account in order to achieve the best performances in terms of accuracy and stability.

DOI: 10.1103/PhysRevA.78.043615 PACS number(s): 03.75.Dg, 37.10.Vz, 37.25.+k, 06.30.Gv

I. INTRODUCTION

In the field of atom interferometry, the improving sensitivity of inertial sensors [1–4] is paving the way for many new applications in geophysics, navigation, and tests of fundamental physics. Most of these experiments are based on Raman transitions [5] to realize beam splitters and mirrors, which manipulate the atomic wave packets. Among others, this technique has the advantage of internal state labeling of the exit ports of the interferometer [6], enabling efficient detection methods. Moreover, the atoms spend most of their time in free fall, with very small and calculable interactions with the environment. The inertial forces are then determined by the relative displacement of the atomic sample with respect to the equiphases of the laser beams, which realize a very accurate and stable ruler. This makes this technique suitable for high-precision measurements, as required for instance for inertial sensors and for the determination of fundamental constants [7–11].

A limit to the accuracy and the long-term stability of these sensors comes from wave-front distortions of the laser beams. This wave-front distortion shift appears directly on the signal of an interferometer when the atoms experience different wave fronts at each Raman pulse. This effect thus depends on the actual trajectories of the atoms, so that a precise control of the initial position, velocity, and temperature of the atomic clouds is required [12,13]. A convenient technique to reduce this bias is to minimize the number of optical components in the shaping of the two Raman laser beams and by implementing them in a retroreflected geometry [1,3,14]. Indeed, as long as the two beams travel together, wave-front aberrations are identical for the two beams and thus have no influence on their phase difference. This geometry also provides an efficient way to use the **k** reversal technique, which allows the atomic wave packets to be diffracted in one direction or the opposite one and thus to separate the effects of many major systematic errors such as gradients of magnetic fields or light shifts [15]. The main drawback of this geometry arises from the presence of off-resonant Raman transitions, which induce a light shift on the resonant Raman transition and thus a phase shift of the atom interferometer.

In the following, we investigate this effect, called the two-photon light shift (TPLS) [16]. We first show that the TPLS arises from several off-resonant transitions and evaluate each contribution. We then derive the impact on the phase of an atom interferometer and use our gravimeter and gyroscope-accelerometer for quantitative comparisons. In particular, we measure the systematic shifts and we investigate the influence on the long-term stability. The study demonstrates that the precise control of experimental parameters, in particular the Raman laser intensities and polarizations, is needed to reduce the influence of this effect for such interferometers.

II. LIGHT SHIFT DUE TO OFF-RESONANT RAMAN TRANSITIONS

A. Raman Spectroscopy

The two experiments use different alkali-metal atoms: ^{87}Rb in the case of the gravimeter and ^{133}Cs in the case of the gyroscope. As the hyperfine structures, transition selection rules, and Raman laser setups are similar (see Fig. 1), their results can be compared easily. The Raman transitions couple the two hyperfine ground states of the alkali-metal atom (labeled $|g\rangle$ and $|e\rangle$) via an intermediate state (labeled $|i\rangle$) and two lasers with frequencies (labeled ω_1 and ω_2) detuned by Δ_i to the red of the D_2 line. During the interferometer sequence, a bias magnetic field is applied along the direction of propagation of the Raman laser beam to lift the degeneracy of the magnetic sublevel manifold. The two Raman lasers are overlapped with orthogonal linear polarizations and delivered within the same polarization-maintaining optical fiber to the vacuum chamber. After the fiber, the Raman beams pass through a quarter-wave plate to convert the initial linear polarizations into circular polarizations, denoted σ_1^{i+} for the Raman laser at frequency ω_1 and σ_2^{i-} for the

*Present address: Physikalisch-Technische Bundesanstalt, Bundesallee 100, D-38116 Braunschweig, Germany.

†Present address: Optical and Quantum Communications Group, MIT, Rm 36-479, Cambridge, MA 02139, USA.

‡Present address: European Gravitational Observatory, Via E. Amaldi, 56021 S. Stefano a Macerata—Cascina (PI), Italy.

§arnaud.landragin@obspm.fr

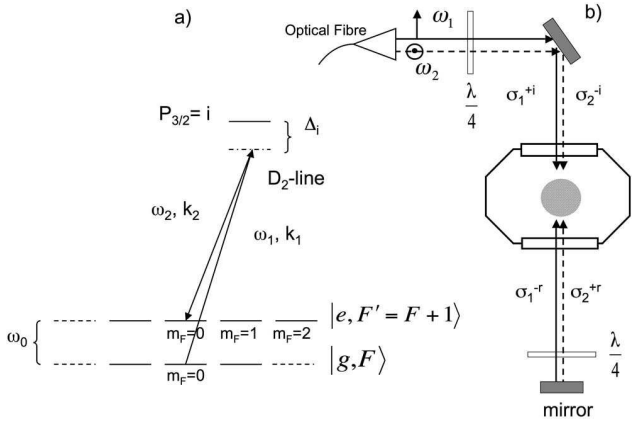

FIG. 1. Scheme of our Raman laser setup. (a) Scheme of the Raman transition between the two hyperfine ground states of an alkali-metal atom. (b) Implementation of the Raman laser beams. The two Raman lasers of orthogonal polarizations are guided to the experiment through the same polarization-maintaining fiber. The two lasers are represented, respectively, by the solid and dashed lines. The lasers go through a first quarter-wave plate ($\lambda/4$), cross the experiment, and are reflected by a mirror, crossing a second quarter-wave plate twice. The wave plates are set in such a way that counterpropagating Raman transitions are allowed but copropagating Raman transitions are forbidden.

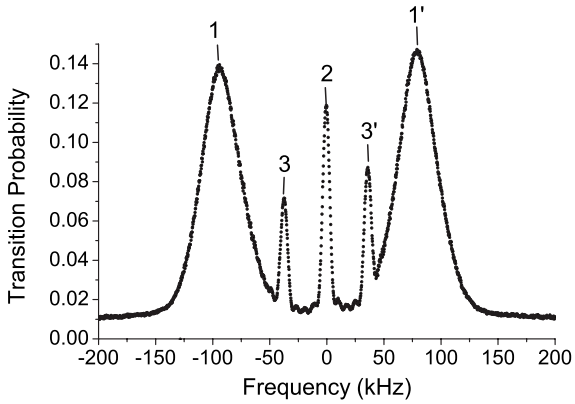

FIG. 2. Transition probability as a function of the frequency difference between the two Raman lasers when the atoms have a nonzero velocity in the direction of propagation of the Raman laser beams. The frequency is referenced to the microwave hyperfine transition (ω_0). The data have been recorded with laser parameters corresponding to a π pulse of 135 μs duration. Lines $1,1'$ correspond to the two counterpropagating transitions, line 2 to the copropagating transition between the two $m_F=0$ states, and lines $3,3'$ to the copropagating magnetic sensitive transitions.

orthogonal polarization at ω_2. These beams are then retroreflected through a quarter-wave plate to rotate the polarization of each beam into its orthogonal polarization (σ_2^{+r}, σ_1^{-r}).

For $m_F=0$ to $m_F=0$ transitions, there are two pairs of beams (σ^+-σ^+ and σ^--σ^-), that can drive counterpropagating Raman transitions with effective wave vectors $\pm\mathbf{k}_{\text{eff}} = \pm(\mathbf{k}_1-\mathbf{k}_2)$. Then, the ground state $|g,\mathbf{p}\rangle$ is coupled with the excited state $|e,\mathbf{p}+\hbar\mathbf{k}_{\text{eff}}\rangle$ by the pair of Raman lasers (σ_1^{+i}-σ_2^{+r}) and to the excited state $|e,\mathbf{p}-\hbar\mathbf{k}_{\text{eff}}\rangle$ with the pair of Raman lasers (σ_2^{-i}-σ_1^{-r}).

We use the Doppler effect to lift the degeneracy between the two resonance conditions. Indeed, if the atoms have a velocity in the direction of propagation of the Raman lasers, the Doppler shifts are of opposite sign for the two counterpropagating transitions. The resonance condition for each of these couplings is $\Delta\omega_{\text{laser}}=\omega_0+\omega_r\pm\omega_D$, where ω_0 is the hyperfine transition frequency, $\hbar\omega_r=\hbar k_{\text{eff}}^2/2m$ the recoil energy, and $\omega_D=-\mathbf{k}_{\text{eff}}\cdot\mathbf{v}$ the Doppler shift due to the atomic velocity $\mathbf{v}$ in the reference frame of the apparatus. Consequently, the detuning between the two resonances is $2\omega_D$; therefore we can discriminate between the two transitions when the Doppler shift is large enough compared to the linewidth of the Raman transition. This linewidth is characterized by the effective Rabi frequency Ω_{eff}, which depends on the product of the two Raman lasers intensities and inversely on the Raman detuning Δ_i [15].

In this first part, we use the gyroscope-accelerometer experiment described in detail in [3]. The experiment was performed with a cloud of cold cesium atoms (1.2 μK) prepared initially in the $|F=3,m_F=0\rangle$ state. The atoms are launched at 2.4 m s^{-1} with an angle of 8° with respect to the vertical direction. The Raman lasers are implemented in the horizontal plane with a 6° angle with the normal of the atomic flight direction. Thus, to select only one Raman transition for the interferometer, the frequency difference between the two Raman lasers can be tuned to be resonant with either the $+k_{\text{eff}}$ or the $-k_{\text{eff}}$ transition.

Figure 2 shows the transition probability as a function of the detuning of the Raman transition with respect to the hyperfine transition frequency. One can identify the two velocity-selective counterpropagation transitions (labeled 1 and $1'$), whose widths reflect the velocity distribution of the atomic cloud. In addition to the counterpropagating transitions, we observe transitions due to residual copropagating Raman coupling, also detuned from resonance by a Zeeman shift (lines 2, 3, and $3'$). When the frequency difference of the Raman lasers is tuned to be resonant with one of the counterpropagating transitions, the second counterpropagating transition and the copropagating ones induce a light shift (the TPLS) on the selected Raman transition used for the interferometer.

B. Frequency shift due to the second pair of Raman laser beams

The TPLS is the differential shift between the two atomic levels corresponding to the atomic states $|g,\mathbf{p}\rangle$ and $|e,\mathbf{p}\pm\hbar\mathbf{k}_{\text{eff}}\rangle$ involved in the atomic interferometer. The energy of the state $|g,\mathbf{p}\rangle$ is shifted by ε_g by the off-resonant $|g,\mathbf{p}\rangle\leftrightarrow|e,\mathbf{p}\mp\hbar\mathbf{k}_{\text{eff}}\rangle$ transition detuned by $\pm2\omega_D$ [Eq. (1)], while the energy of the state $|e,\mathbf{p}\pm\hbar\mathbf{k}_{\text{eff}}\rangle$ is shifted by ε_e by the off-resonant $|e,\mathbf{p}\pm\hbar\mathbf{k}_{\text{eff}}\rangle\leftrightarrow|g,\mathbf{p}\mp2\hbar\mathbf{k}_{\text{eff}}\rangle$ transition detuned by $\hbar(\mp2\omega_D+4\omega_r)$ [Eq. (2)]. The two levels are shifted in opposite directions as illustrated in Fig. 3, here for the case of a Raman transition resonant with $+\mathbf{k}_{\text{eff}}$.

TPLS corrections are calculated from fourth-order perturbation theory. In the case of our system, the level shifts ε_g and ε_e for a $\pm k_{\text{eff}}$ interferometer are given by

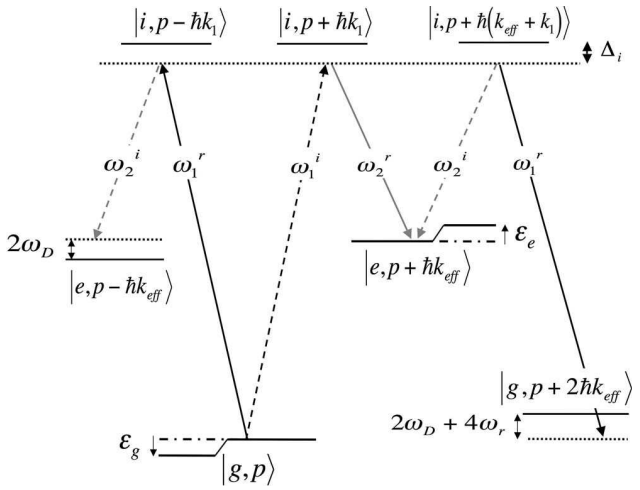

FIG. 3. Scheme of levels $|g,\mathbf{p}\rangle$ and $|e,\mathbf{p}+\hbar\mathbf{k}_{\mathrm{eff}}\rangle$ involved in the atomic interferometer. The two states are coupled together through the selected Raman transition (+**k** in this particular case). But each state is also coupled to another one, through an off-resonant Raman transition of opposite wave vector.

$$\varepsilon_g = \mp\hbar\frac{\Omega_{\mathrm{eff}}^2}{4(2\omega_D)}, \tag{1}$$

$$\varepsilon_e = \hbar\frac{\Omega_{\mathrm{eff}}^2}{4(\pm 2\omega_D + 4\omega_r)}, \tag{2}$$

where Ω_{eff} is the effective Rabi frequency corresponding to counterpropagating Raman transitions. Thus, the shift of the resonance condition depends on the sign of direction of the selected Raman laser pair (i.e., $\pm k_{\mathrm{eff}}$), quadratically on the Rabi frequency and inversely to the Doppler detuning,

$$\delta\omega_{(\mathrm{TPLS}\pm)} = \frac{1}{\hbar}(\varepsilon_e - \varepsilon_g) = \frac{\Omega_{\mathrm{eff}}^2}{\pm 8\omega_D} + \frac{\Omega_{\mathrm{eff}}^2}{4(\pm 2\omega_D + 4\omega_r)}. \tag{3}$$

1. Variation with Ω_{eff}

The frequency shift is measured from fits of the spectral lines, as displayed in Fig. 2, with different Raman intensities (Ω_{eff}^2 is proportional to the product of the intensity of the two lasers). Note that we discriminate it from the shifts independent of $\mathbf{k}_{\mathrm{eff}}$, like the quadratic Zeeman effect or ac Stark shift, by alternating measurements $+k_{\mathrm{eff}}$ and $-k_{\mathrm{eff}}$, leading to a differential determination of the effect. The difference in the resonance condition $\Delta\omega = 2k_{\mathrm{eff}}v + 2\delta\omega_{(\mathrm{TPLS})}$ depends only on the TPLS and the Doppler effect. The Doppler effect does not depend on the Rabi frequency and can be determined by extrapolating $\Delta\omega$ to $\Omega_{\mathrm{eff}}=0$. The results of these measurements are displayed in Fig. 4 as a function of Ω_{eff}^2. The curve clearly shows the quadratic dependence of the frequency shift with Ω_{eff}. For this experimental configuration the Doppler shift was 85 kHz, and the value of $\delta\omega_{(\mathrm{TPLS})}$ for the largest Ω_{eff} ($2\pi\times 27$ kHz at the center of the beam) is 2.1 kHz, in good agreement with the expected 2.4 kHz.

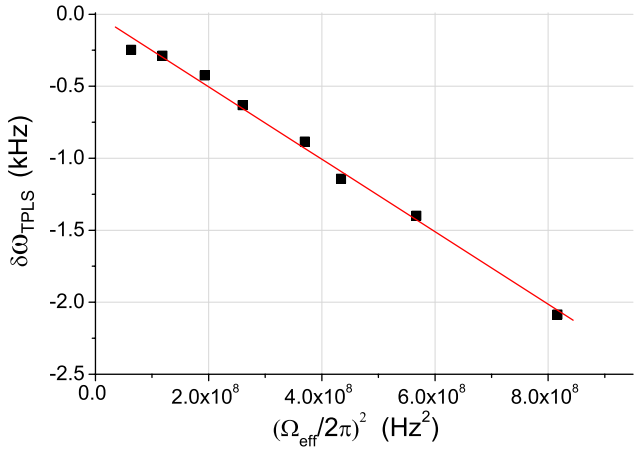

FIG. 4. (Color online) Variation of the frequency shift of the counterpropagating Raman transition versus the square of the Rabi frequency. The Rabi frequency is controlled by changing the Raman laser intensities.

2. Position dependence in the Raman laser beams

The laser beams have a Gaussian shape, with a 15 mm waist (radius at $1/e^2$ in intensity). In order to evaluate the phase shift, we first measure the TPLS for different atomic positions by scanning the resonance along their trajectory. As the Raman beams are horizontal, the Doppler shift is constant for the three pulses and the TPLS varies only with the Raman laser intensity. Figure 5 displays the measured TPLS, proportional to the laser intensity, which follows exactly the Gaussian profile of the laser beams.

C. Frequency shift due to the copropagating transitions

In an ideal experiment, with perfect circular polarization and a Raman detuning Δ_i large compared to the hyperfine structure of the intermediate state (201 MHz in the case of the cesium atom), copropagating transitions are forbidden. In

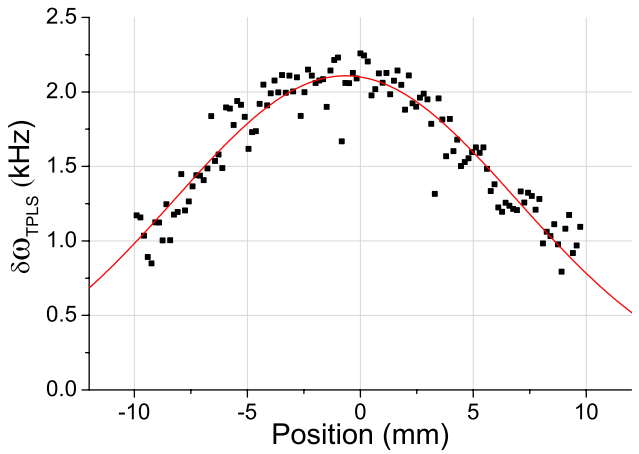

FIG. 5. (Color online) Variation of the two-photon light shift with the position in the Gaussian beam of the Raman lasers. The dots correspond to the measurement of the shift and the line to the fit of the data by a Gaussian function.

a real experiment, with imperfect polarization and/or finite Raman detuning, copropagating transitions are slightly allowed, and will lead to an additional TPLS.

1. TPLS induced by $m_F=0$ to $m_F=0$ copropagating transitions

Imperfect polarization leads to a residual combination of σ_1^+-σ_2^+ and σ_1^--σ_2^- in the copropagating beams and allows coupling between $m_F=0$ states. As the momentum exchange $\hbar\mathbf{k}_{\text{eff}}=\hbar(\mathbf{k}_1-\mathbf{k}_2)\simeq\mathbf{0}$, the Doppler and recoil effect are negligible and the resonance condition is $\Delta\omega_{\text{laser}}=\omega_0$ (line 2 of Fig. 2). The Rabi frequency corresponding to the transition $\Delta m_F=0$ is determined experimentally using the residual copropagating transition probability, $P=0.1$ at full Raman laser power. It gives $\Omega_{\text{eff}}/\Omega_{00}=5$, which can be explained by an error of linear polarization of one of the Raman laser of 2% in power. The detuning of this transition, compared to the two counterpropagating transitions, depends on the Doppler and recoil shift:

$$\delta\omega^{00}_{(\text{TPLS}\pm)} \simeq \frac{1}{4}\frac{\Omega_{00}^2}{\pm\omega_D+\omega_r}. \tag{4}$$

For $\omega_D=2\pi\times 85$ kHz and $\Omega_{\text{eff}}\simeq 2\pi\times 27$ kHz we find an effect due to this coupling smaller than 100 Hz.

2. TPLS induced by $m_F=0$ to $m_F=\pm 2$ copropagating transitions

The second source of residual copropagating transitions stems from the coupling of $|F,m_F=0\rangle\leftrightarrow|F',m_{F'}=\pm 2\rangle$ by the copropagating Raman laser pairs (σ_1^+,σ_2^-) and (σ_1^-,σ_2^+). Because of the hyperfine splitting in the intermediate state, there are two paths for the Raman transition. Both transitions interfere destructively when the detuning compared to the intermediate state Δ_i is larger than the hyperfine splitting of the intermediate state, and so in this case the transition strength is zero. However, in our experimental setup, with $\Delta_i\simeq 2\pi\times 780$ MHz and $\Delta_{\text{HFS}}=2\pi\times 201$ MHz, the ratio between the Rabi frequency of counterpropagating transitions Ω_{eff} and the Rabi frequency of the copropagating $\Delta m_F=\pm 2$ transition Ω_{02} is 6.1, leading to a transition probability of 6.4%, in good agreement with the experimental value (see Fig. 2). These transition resonance conditions depend on the magnetic field amplitude as $\Delta\omega_{\text{laser}}=\omega_0\pm 2\alpha B$, where $\alpha=2\pi\times 350$ kHz/G for cesium. With a calculation similar to the one used to obtain Eq. (3), we deduce the two-photon light shifts $\delta\omega^{02}_{(\text{TPLS}\pm)}$ induced by the magnetically sensitive transitions for the $\pm k_{\text{eff}}$ case to be

$$\delta\omega^{02}_{(\text{TPLS}\pm)}=\frac{\Omega_{02}^2}{4}\left(\frac{1}{\pm\omega_D+\omega_r+2\alpha B}+\frac{1}{\pm\omega_D+\omega_r-2\alpha B}\right). \tag{5}$$

The first term in Eq. (5) is due to the coupling with $|F',m_{F'}=+2\rangle$ whereas the second term is induced by the coupling with $|F',m_{F'}=-2\rangle$. It is clear from Eq. (5) that a residual magnetic contribution appears in the half difference and creates a magnetic sensitivity in addition to the standard quadratic Zeeman effect. This contribution to the two-photon light shift is measured by changing the bias field in the Raman interaction zone. Using the differential method previously described, we show in Fig. 6 the variation of the total TPLS with the bias field. The resonance around 130 mG corresponds to the case where a magnetic copropagating transition and the counterpropagating transition are resonant simultaneously. Previous measurements have been performed with a 31 mG magnetic field bias.

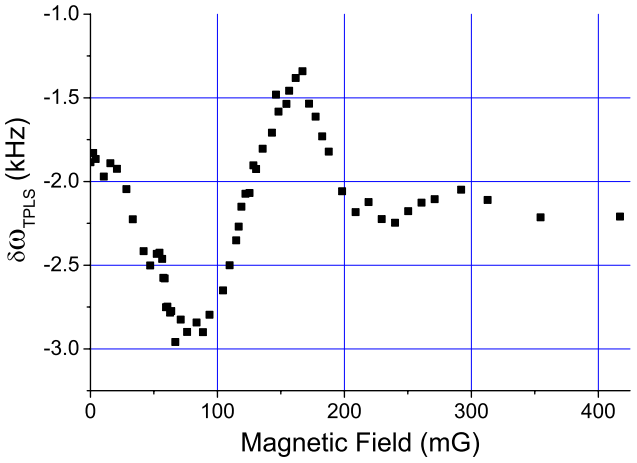

FIG. 6. (Color online) Variation of the two-photon light shift versus the bias magnetic field. A resonance appears when the Zeeman shift equals the Doppler shift.

III. IMPACT ON THE INTERFEROMETER PHASE SHIFT

A. Theoretical derivation of the phase shift

In the following we will consider interferometers constituted of three Raman pulses in a $\pi/2$-π-$\pi/2$ sequence. If the TPLS is constant during the interferometer it is equivalent to a fixed frequency shift of the Raman transition. In that case, it is well known that no phase shift is introduced in the interferometer. On the contrary, a fluctuation of the TPLS during the interferometer sequence leads to a phase shift given by:

$$\Phi_{\text{TPLS}}=\int_{-\infty}^{+\infty} g(t)\,\delta\omega_{\text{TPLS}}(t)dt, \tag{6}$$

where $g(t)$ is the sensitivity function of the atom interferometer, defined in [17].

1. Case $\Omega_{\text{eff}}\tau=\pi/2$

In the case where the interaction pulses are short enough that one can neglect the variation of the TPLS during the pulses, and that the area of the first and last pulse satisfies the $\Omega_{\text{eff}}\tau=\pi/2$ condition, the two-photon interferometer phase shift can be approximated by

$$\Phi_{\text{TPLS}}=\left(\frac{\delta\omega^{(1)}_{\text{TPLS}}}{\Omega^{(1)}_{\text{eff}}}-\frac{\delta\omega^{(3)}_{\text{TPLS}}}{\Omega^{(3)}_{\text{eff}}}\right), \tag{7}$$

where $\omega^{(i)}_{\text{TPLS}}$ and $\Omega^{(i)}_{\text{eff}}$ are the TPLS and the Rabi frequencies of the ith pulse, respectively. One might notice that the frequency shift during the π pulse does not contribute to the interferometer phase shift. Moreover, as all components of

the TPLS, counterpropagating and copropagating terms, increase as the square of the Rabi frequencies, the interferometer phase shift scales linearly with the Raman laser power.

In the limit where the copropagating transitions are negligible (perfect polarization and very large Raman detuning) and the dominant source of TPLS is due to the counterpropagating transition, the phase shift of the interferometer can be simplified as

$$\Phi_{\mathrm{TPLS}}^{\mathrm{counter}} = \left(\frac{\Omega_{\mathrm{eff}}^{(1)}}{4\delta_D^{(1)}} - \frac{\Omega_{\mathrm{eff}}^{(3)}}{4\delta_D^{(3)}} \right), \tag{8}$$

where δ_D^i is the Doppler shift for the ith pulse.

2. Case $\Omega_{\mathrm{eff}}\tau \neq \pi/2$

More generally, the interferometer phase shift can be calculated when the $\pi/2$ pulse condition is no longer satisfied. This appears when the Rabi frequency drifts due to changes in power or polarization of the Raman lasers. Generalization of the formalism of the sensitivity function to the case where $\Omega_{\mathrm{eff}}\tau \neq \pi/2$ allows derivation of the interferometer phase shift:

$$\Phi_{\mathrm{TPLS}} = \frac{\delta\omega_{\mathrm{TPLS}}^{(1)}}{\Omega_{\mathrm{eff}}^{(1)}} \tan\left(\frac{\Omega_{\mathrm{eff}}^{(1)}\tau^{(1)}}{2} \right) - \frac{\delta\omega_{\mathrm{TPLS}}^{(3)}}{\Omega_{\mathrm{eff}}^{(3)}} \tan\left(\frac{\Omega_{\mathrm{eff}}^{(3)}\tau^{(3)}}{2} \right). \tag{9}$$

Usually, the Rabi frequencies and pulse durations can be taken equal for the first and the last pulses; the expression of the interferometer shift is then

$$\Phi_{\mathrm{TPLS}} = \frac{(\delta\omega_{\mathrm{TPLS}}^{(1)} - \delta\omega_{\mathrm{TPLS}}^{(3)})}{\Omega_{\mathrm{eff}}} \tan\left(\frac{\Omega_{\mathrm{eff}}\tau}{2} \right). \tag{10}$$

As before, for a dominant counterpropagating transition, the previous expression can be simplified to

$$\Phi_{\mathrm{TPLS}}^{\mathrm{counter}} = \Omega_{\mathrm{eff}} \left(\frac{1}{4\delta_D^{(1)}} - \frac{1}{4\delta_D^{(3)}} \right) \tan\left(\frac{\Omega_{\mathrm{eff}}\tau}{2} \right). \tag{11}$$

An other aspect of the influence of the TPLS on the atomic phase shift concerns the stability of the experiment versus the experimental parameters fluctuations, in particular the Raman laser power. As Rabi frequency fluctuations are small in relative values (typically smaller than 10%), we can develop Eq. (11) to first order in $\delta\Omega_{\mathrm{eff}}$ close to the usual conditions $\Omega_{\mathrm{eff}}\tau = \pi/2$ and find

$$\delta\Phi_{\mathrm{TPLS}} = \left(1 + \frac{\pi}{2} \right) \frac{\delta\Omega_{\mathrm{eff}}}{\Omega_{\mathrm{eff}}} \Phi_{\mathrm{TPLS}}. \tag{12}$$

Similar calculations may be derived to extract the dependence on the duration of the pulse or the Doppler detuning. As the stability of the latter parameters is much better controlled in cold atom interferometers, no measurable influence on the short-term stability of the interferometer is expected.

B. Case of a gravimeter

We first consider the case of the gravimeter developed at our laboratory SYRTE (Systèms de référence Temps-Espace) and described in detail in [14,18]. In this compact experimental setup, cold ^{87}Rb atoms are trapped in a three-dimensional magneto-optical trap in 60 ms and further cooled during a brief optical molasses phase before being released by switching off the cooling lasers. During their free fall over a few centimeters, the interferometer is created by driving the Raman laser in the vertical direction, with pulses separated by free evolution times of $T=50$ ms. The first Raman pulse occurs 17 ms after releasing the atoms. The Doppler shift at the first pulse is thus relatively small, about 400 kHz, and gets large, about 3 MHz, for the last pulse. With a Rabi frequency of 40 kHz, this leads to a TPLS of about 22 mrad for counterpropagating transitions. Following the method of Sec. II C, we find 11 mrad for copropagating ones. This corresponds to a large shift for the gravity measurement of about $8.10^{-8}g$.

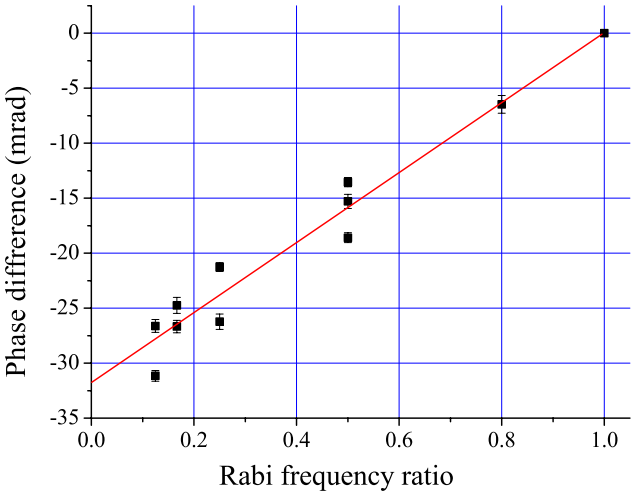

FIG. 7. (Color online) Variation of the gravimeter phase shift due to the two-photon light shift versus the Rabi frequency ratio, keeping the pulse area constant. To remove drifts from other sources, the phase shift is measured in a differential way by changing the Rabi frequency up to 40 kHz, which is the maximum available. The dotted line is a linear fit of the shifts.

To measure the bias on the atomic interferometer phase due to TPLS, we exploit its dependence on the Rabi frequency. The principle of this measurement is based on a differential method, where one performs an alternating sequence of measurements of the interferometer phase with two different Rabi frequencies Ω_{eff} and Ω'_{eff}, but keeping the areas of the pulses constant by changing the duration of the pulses τ. The Rabi frequency is modulated with the power of the Raman lasers. In practice, the differential measurement is performed by alternating sequences of measurements with four different configurations $(\Omega_{\mathrm{eff}}, +k_{\mathrm{eff}})$, $(\Omega_{\mathrm{eff}}, -k_{\mathrm{eff}})$, $(\Omega'_{\mathrm{eff}}, +k_{\mathrm{eff}})$, and $(\Omega'_{\mathrm{eff}}, -k_{\mathrm{eff}})$. After averaging for 5 min, we extract the difference of the TPLS between the two Rabi frequencies with an uncertainty below 1 mrad. This measurement was repeated for various Ω'_{eff}, keeping Ω_{eff} fixed. The phase differences are displayed in Fig. 7 according to the ratio of the Rabi frequencies $\Omega'_{\mathrm{eff}}/\Omega_{\mathrm{eff}}$. The results clearly demonstrate the linear dependence of the phase shift with the Rabi frequency. The fit of the data allows a 32 mrad shift to

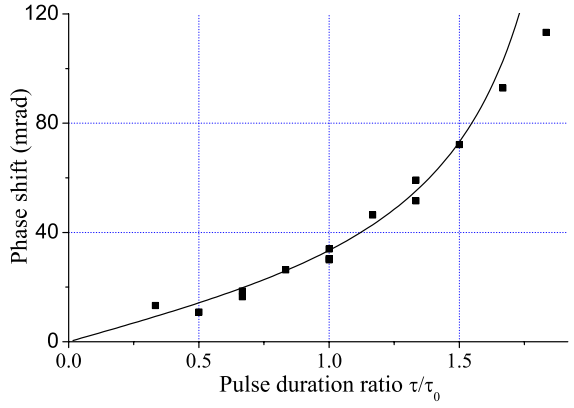

FIG. 8. (Color online) Variation of the gravimeter phase due to the two-photon light shift versus the pulse duration ratio, with the Rabi frequency constant (40 kHz). To remove drifts from other sources, the phase shift is measured in a differential way with respect to the optimum pulse duration (6 μs). The line corresponds to the calculated shift.

be extracted, in very good agreement with the expected value (33 mrad), deduced from Eq. (7). Deviations from the linear behavior and discrepancies (up to $\pm 10\%$) between different measurements that correspond to the same ratio cannot be explained by uncontrolled fluctuations in the Rabi frequencies, as the simultaneous monitoring of the laser intensities showed stability at the percent level during the course of the measurements. We demonstrated that these fluctuations were correlated with changes of the polarization of the Raman beams, which modulate the contribution to the phase shift of the undesired copropagating transitions.

We perform a complementary measurement by changing the duration of the first and last pulse simultaneously, while keeping Ω_{eff} constant. The acquisition is performed with a similar differential method than previously, but now alternating between different pulse durations and a pulse duration of 6 μs, when the $\pi/2$ pulse condition is satisfied. The data are then shifted by the bias deduced from previous measurements with $\tau=6$ μs (result of Fig. 7) and displayed in Fig. 8. Using Eq. (10), the fit of the data gives a Rabi frequency of 39 kHz, in very good agreement with the expected value (42 kHz). A small deviation appears for long pulse durations when the areas of each of the two pulses are close to π.

In the case of our gravimeter, where cold atoms are dropped from rest, the TPLS is very large, almost two orders of magnitude above the pursued accuracy. In principle, this effect can be measured accurately by alternating measurements with different Rabi frequencies. But, it seems desirable to decrease the effect by operating with lower Rabi frequencies, the drawback being an increased velocity selectivity of the Raman pulses. A more stringent velocity selection, or smaller temperatures, are then required in order to preserve a good fringe contrast. In the case of a fountain gravimeter, where the atoms are launched upward at a few m/s, the Doppler shift at the first and last pulses is much larger, considerably reducing this effect. For the parameters of the Stanford gravimeter [1] (long pulse duration of 80 μs and time between pulses of 160 ms), we find a phase shift of 0.8 mrad, which corresponds to $2\times 10^{-10}g$.

C. Case of a gyroscope-accelerometer

In the case of the gyroscope-accelerometer, the mean velocity of the wave packet is not collinear with the effective Raman wave vector. Consequently, the atomic phase shift measured with the interferometer is sensitive to the rotation rate Ω in addition to the acceleration **a**. As in the case of the gravimeter, the atomic phase is shifted by the TPLS and by other systematics (labeled Φ_0), for instance the phase shift induced by the laser wave-front distortions [12]. The total phase shift is expressed by

$$\Phi = \mathbf{k}_{\text{eff}} \cdot \mathbf{a}T^2 + 2\mathbf{k}_{\text{eff}} \cdot \mathbf{V} \times \mathbf{\Omega} T^2 + \Phi_0 + \Phi_{\text{TPLS}}. \quad (13)$$

Our gyroscope-accelerometer uses a double interferometer with two atomic clouds following the same trajectory but with opposite directions to discriminate between acceleration and rotation phase shifts. Moreover, our experiment is designed to measure different axis of rotation and acceleration according to direction of propagation of the Raman laser beams. We will illustrate the impact of the TPLS on the interferometer in the configuration where the Raman lasers are directed along the vertical direction.

The measurement is realized in the same way than for the gravimeter experiment by comparing atomic phases with high and low Rabi frequency, changing the Raman laser power but keeping the pulse duration constant to 7.6 μs. In order to enhance the TPLS signal we decrease the time between pulses to 20 ms. Indeed, the Doppler effect is reduced and the available laser power on the side of the Gaussian laser profile is increased. The first pulse occurs 15 ms before the apogee and the third 25 ms after the apogee, corresponding, respectively, to a Doppler shift of about $\omega_D^{(1)}=2\pi \times 344$ kHz and $\omega_D^{(3)}=2\pi\times 574$ kHz. The Rabi frequency for each pulse is approximately 33 kHz; then the TPLS expected from Eq. (7) is about 38 mrad for each interferometer. As this shift is similar for the two interferometers when the two atomic clouds perfectly overlap and experience the same TPLS, it biases the acceleration signal only. Figure 9 displays the variation of the acceleration and rotation signals with the Rabi frequency. The acceleration shift (squares) varies in good agreement with the expected shift (continuous curve) calculated from Eq. (9). The rotation shift (circles) shows no dependence on the Rabi frequency and illustrates that the rejection from the acceleration signal is efficient. Nevertheless, fluctuations from the expected behavior are clearly resolved and repeatable. We attribute these deviations to wave-front distortions of the Raman laser beams. Indeed, when the atomic trajectories do no perfectly overlap, a residual bias appears on the rotation due to unperfected cancellation. This bias depends on the details of the wave-front distortions weighted by the actual atomic cloud distributions, and is modified when the Rabi frequency is changed. In the usual conditions, with interrogation time of 80 ms, the acceleration shift is reduced to about 12 mrad thanks to the increase of the Doppler shift and reduction of the Rabi frequency on the side of the Gaussian Raman beams.

We finally estimate the impact of the Raman laser power fluctuations on the stability of the rotation signal in usual conditions (interrogation time of 80 ms). We performed a

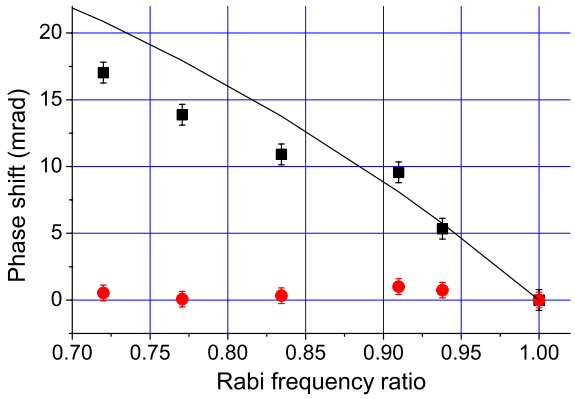

FIG. 9. (Color online) Variation of the rotation and acceleration phases (circles and squares, respectively) due to the two-photon light shift versus the Rabi frequency ratio, with constant pulse duration (7.6 μs). Acquisitions have been recorded for a total interaction time between the first and the last pulse of 40 ms. To remove drifts from other sources, the phase shift is measured in a differential way with respect to the maximum Rabi frequency available at the location of the $\pi/2$ pulses (33 kHz). The line shows the calculated shift for acceleration signal.

complementary measurement by recording the interferometer signal and the Raman laser power at the same time when a modulation of the laser powers of 10% is applied. The modulation is applied by attenuating the radio-frequency signal sent to the acousto-optic modulator used to generate the Raman pulses. The power of the lasers was recorded during the third pulse thanks to a photodiode measuring the intensity on the edge of the laser beams. We found a small dependence of the rotation signal on the power fluctuation of 6×10^{-9} rad $s^{-1}/\%$ of the Raman laser beams intensity, which can limit the long-term stability of the gyroscope. As no dependence was expected, we attribute it again to nonperfect superimposition of the two atomic clouds trajectories, leading to a different Rabi frequencies experienced by the two clouds.

IV. CONCLUSION

We have shown that the use of retroreflected Raman lasers in atom interferometers induces off-resonant Raman transitions, which have to be taken into account in order to achieve best accuracy and stability of interferometers. We have first quantitatively evaluated the effect on the resonance condition for each off-resonant line: the other counterpropagating transition, which cannot be avoided in the retroreflected design, and copropagating transitions arising mainly from imperfections in the polarization. Then we measured the impact of this two-photon light shift on the phase of two atom interferometers: a gravimeter and a gyroscope. In particular, we show that this shift is an important source of systematic errors for acceleration measurements. Nevertheless, it can be measured accurately by modulating the Raman laser power and/or the pulse durations. Our study has also shown that it can impact the stability of the two sensors if the polarization and/or the power of the Raman lasers fluctuate.

The TPLS appears as a drawback of using retroreflected Raman laser beams. But, as it can be well controlled, it does not reduce the benefit from this geometry, whose key advantage is to drastically limit the bias due to wave-front aberrations, which is larger and more difficult to extrapolate to zero.

This study can be extended to other possible polarization configurations, when using linear instead of circular polarizations. Moreover, when using this retroreflected geometry, the same effect holds for Bragg-type transitions in the case where the Doppler effect lifts the degeneracy of the two opposite diffraction gratings. If the signal is generated from the subtraction of the phase shifts of two independent atomic clouds, e.g., gradiometers or gyroscopes, perfect common mode rejection is required to suppress this effect. In our case this means a perfect overlap of atomic trajectories.

Finally, the two-photon light shift can be drastically reduced by increasing the Doppler effect and/or using colder atoms, allowing the Rabi frequency to be reduced during the Raman pulses. By contrast, for a setup with an intrinsic small Doppler effect, as for space applications [13,19], this effect becomes extremely large and has to be taken into account in the design of the experiment.

ACKNOWLEDGMENTS

We express our gratitude to F. Biraben for pointing out this effect and to P. Cheinet for earlier contributions to the gravimeter experiment. We would like to thank the Institut Francilien pour la Recherche sur les Atomes Froids (IFRAF), the European Union (FINAQS contract), the Délégation Générale pour l'Armement (DGA), and the Centre National d'Études Spatiales (CNES) for financial support. B.C., J.L.G., and T.L. thank DGA for supporting their work.

[1] A. Peters, K. Y. Chung, and S. Chu, Metrologia **38**, 25 (2001).
[2] T. L. Gustavson, A. Landragin, and M. A. Kasevich, Class. Quantum Grav. **17** 1 (2000).
[3] B. Canuel, F. Leduc, D. Holleville, A. Gauguet, J. Fils, A. Virdis, A. Clairon, N. Dimarcq, Ch. J. Bordé, A. Landragin, and P. Bouyer, Phys. Rev. Lett. **97**, 010402 (2006).
[4] J. M. McGuirk, G. T. Foster, J. B. Fixler, M. J. Snadden, and M. A. Kasevich, Phys. Rev. A **65**, 033608 (2002).
[5] M. Kasevich, D. S. Weiss, E. Riis, K. Moler, S. Kasapi, and S. Chu, Phys. Rev. Lett. **66**, 2297 (1991).
[6] Ch. J. Bordé, Phys. Lett. A **140**, 10 (1989).
[7] J. B. Fixler, G. T. Foster, J. M. McGuirk, and M. A. Kasevich, Science **315** 74 (2007).
[8] G. Lamporesi, A. Bertoldi, L. Cacciapuoti, M. Prevedelli, and G. M. Tino, Phys. Rev. Lett. **100**, 050801 (2008).
[9] A. Wicht, J. M. Hensley, E. Sarajlic, and S. Chu, Phys. Scr., T

102, 82 (2002).

[10] P. Cladé, E. de Mirandes, M. Cadoret, S. Guellati-Khélifa, C. Schwob, F. Nez, L. Julien, and F. Biraben, Phys. Rev. Lett. **96**, 033001 (2006), Sec. VI F 2.

[11] G. Genevès *et al.*, IEEE Trans. Instrum. Meas. **54**, 850 (2005).

[12] J. Fils, F. Leduc, P. Bouyer, D. Holleville, N. Dimarcq, A. Clairon, and A. Landragin, Eur. Phys. J. D **36**, 257 (2005).

[13] A. Landragin and F. Pereira Dos Santos, e-print arXiv:0808.3837, in, *Atom Optics and Space Physics*, Proceedings of the Enrico Fermi International School of Physics "Enrico Fermi," Course CLXVIII, Varenna, 2007, edited by E. Arimondo, W. Ertmer, E. M. Rasel, and W. P. Schleich-(Elsevier, Amsterdam, 2008).

[14] P. Cheinet, F. Pereira Dos Santos, T. Petelski, J. Le Gouët, J. Kim, K. T. Therkildsen, A. Clairon, and A. Landragin, Appl. Phys. B: Lasers Opt. **84**, 643 (2006).

[15] D. S. Weiss, B. C. Young, and S. Chu, Appl. Phys. B: Lasers Opt. **59**, 217 (1994).

[16] See P. Cladé, E. de Mirandes, M. Cadoret, S. Guellati-Khélifa, C. Schwob, F. Nez, L. Julien, and F. Biraben, Phys. Rev. A **74**, 052109 (2006), Sec. VI F 2.

[17] P. Cheinet, B. Canuel, F. Pereira Dos Santos, A. Gauguet, F. Leduc, and A. Landragin, IEEE Trans. Instrum. Meas. **57**, 1141 (2008).

[18] J. Le Gouët, T. E. Mehlstäubler, J. Kim, S. Merlet, A. Clairon, A. Landragin, and F. Pereira Dos Santos, Appl. Phys. B: Lasers Opt. **92**, 133 (2008).

[19] See, for instance, *Quantum Mechanics for Space Application: From Quantum Optics to Atom Optics and General Relativity*, edited by Phillipe Bouyer and Alexande Bresson, special issue of Appl. Phys. B: Lasers Opt. **84** (2006); P. Wolf *et al.*, e-print arXiv:0711.0304v5, Exp. Astron. (to be published); W. Ertmer *et al.* (unpublished), and references therein.

Chapitre 5

Perspectives

Les activités de recherche en interférométrie atomique peuvent être orientées dans deux directions, qui sont en continuité avec les travaux précédents : pousser les performances des interféromètres à sources atomiques standard et utiliser les sources ultra-froides. Ces deux directions sont complémentaires et peuvent être envisagées en parallèle ou simultanément en fonction des architectures d'interféromètre.

La première direction a pour but de pousser à leurs limites les performances des capteurs inertiels fondés sur des sources atomiques conventionnelles (voire paragraphe 5.1). Cette activité de recherche bénéficiera directement des résultats obtenus ces dernières années et notamment de l'identification des limites principales liées aux fluctuations de trajectoires atomiques et aux défauts de fronts d'onde. Le nouveau gravimètre, spécialement conçu pour améliorer la stabilité à long terme et l'exactitude, doit permettre de dépasser les performances des capteurs traditionnels en améliorant l'environnement magnétique et les contrôles des trajectoires atomiques et des défauts de fronts d'onde des lasers Raman (paragraphe 5.1.1). Une exactitude meilleure que 10^{-9} g est attendue. Pour le gyromètre (paragraphe 5.1.2), une nouvelle expérience sera mise en place qui permettra d'augmenter l'aire de l'interféromètre d'un facteur 300, ouvrant la voie à des performances bien au delà de celles des gyromètres optiques commerciaux, et notamment pour des mesures sur des temps longs (plus de quelques heures). Par ailleurs, l'utilisation des séparatrices atomiques plus efficaces, utilisant des transitions Raman multiples pour augmenter significativement l'aire des interféromètres, est également envisagée (paragraphe 5.1.3).

La seconde direction consiste à étudier les possibilités offertes par les sources atomiques ultra-froides (paragraphe 5.2). La meilleure définition du mode spatial atomique de ces sources doit permettre d'améliorer l'exactitude dans des interféromètres fondés sur les concepts standard, utilisant des transitions à deux photons. Dans ce type d'expérience, il n'est pas néces-

saire, voire pas souhaitable, d'utiliser une source cohérente. L'intérêt de ces sources est alors directement lié à la stabilité en position et en vitesse initiale, ainsi que la réduction de la dispersion en vitesse, qui permet de limiter les effets systématiques et notamment ceux liés aux défauts de front d'onde. L'utilisation de piège dipolaire, pour le refroidissement évaporatif, est une solution élégante pour ce type d'interféromètre. Par ailleurs, de nouveaux concepts, utilisables uniquement avec des atomes ultra-froids sont très prometteurs mais soulèvent de nombreuses questions. Ils concernent notamment la réalisation d'interféromètres avec des atomes confinés, soit dans des pièges dipolaires, soit dans des pièges magnétiques réalisés sur puce [Madison 2000, Schumm 2005, Lemonde 2005, Wang 2005, Garcia 2006, Jo 2007, Wu 2007, Impens 2006, Arnold 2006, Hughes 2009]. Un autre aspect, qu'il est souhaitable d'explorer, est la possibilité de réaliser une mesure de la phase atomique en-dessous de la limite standard imposée par le nombre fini de particules. Le nombre d'atomes ultra-froids étant toujours relativement faible (1000 à 10^5 at), une telle démonstration contournerait cette limite importante.

En plus de ces deux directions de recherche, le domaine est suffisamment mûr pour envisager dès maintenant un transfert vers le monde industriel, que ce soit à travers des démonstrations de principe avec des expériences de laboratoire, à l'aide d'expériences transportables ou dans le cadre de développements conjoints avec des industriels pour des instruments de terrain. Par exemple, il est possible de réaliser un gravimètre atomique très compact (volume de la partie physique inférieur à 2l) avec des performances proches de l'état de l'art (mieux que 10^{-7} g sur la seconde). Ces développements concerne également les applications dans l'espace, pour lesquelles l'interférométrie atomique est très prometteuse, notamment pour des tests de physique fondamentale.

5.1 Performances ultimes des capteurs inertiels à atomes froids

5.1.1 Gravimètre à source atomique conventionnelle

Le nouveau gravimètre atomique permettra de mieux contrôler les biais limitant l'exactitude de la mesure. Les deux effets systématiques principaux, l'accélération de Coriolis et l'influence des aberrations optiques, sont liés aux trajectoires transverses des atomes. Par exemple, l'accélération de Coriolis subie par un atome de vitesse transverse résiduelle de seulement 0,1 mm.s^{-1} est de 10^{-9} g. Pour une température de l'ordre de 2 μK à l'issue de la phase de mélasse sub-Doppler, la vitesse rms des atomes est de l'ordre de 1 cm.s^{-1} , soit 100

fois supérieure. Il est pourtant envisageable d'atteindre une bonne exactitude car ce biais dépend du signe de la vitesse, et se moyenne en principe sur l'ensemble du nuage. Avec une telle température, il faut, pour espérer atteindre 10^{-9} d'exactitude relative, garantir une distribution en vitesse symétrique à mieux que 1% près, une vitesse moyenne inférieure à 100 μm.s^{-1}, et une homogénéité de la détection sur l'ensemble du nuage meilleure que le pour-cent.

La nouvelle expérience bénéficiera de nouveaux moyens de contrôle de la vitesse et des trajectoires des atomes (mesure de la distribution en vitesse horizontale, de la position des atomes, asservissement de la puissance des faisceaux de mélasse ...). L'utilisation d'une sélection en vitesse transverse, à l'aide d'une transition Raman, permettra de réduire la largeur de la distribution en vitesse, mais aussi de contrôler la vitesse moyenne. Un nouveau système de détection doit permettre de garantir l'homogénéité, à mieux que 1%, de l'efficacité de collection du signal de fluorescence sur le volume du nuage. Il permettra de s'affranchir d'une part de l'inhomogénéité spatiale des photodiodes utilisées, et d'autre part, de la dépendance de l'ouverture numérique à la position des atomes en symétrisant l'optique de collection de la lumière. Enfin, le montage sous vide des optiques Raman critiques (miroir de rétro-réflexion et lame quart d'onde) permettra de limiter au maximum l'impact des défauts de front d'onde.

FIG. 5.1 : *Photographie de la nouvelle enceinte à vide du gravimètre*

Le développement du nouveau gravimètre doit permettre d'atteindre une exactitude relative meilleure que 10^{-9} sur la mesure de g, qui sera mise à profit dans le cadre de la balance du watt. Ces performances ouvrent également un champ d'application important en géophysique ainsi qu'en physique fondamentale, où ils peuvent servir à des tests de la relativité générale [H-Müller 2008].

5.1.2 Gyromètre de très grande sensibilité

La nouvelle expérience de gyromètre permettra de pousser les limites des gyromètres atomiques utilisant des sources atomiques conventionnelles, fondées sur l'utilisation de pièges magnéto-optiques. La sensibilité à la rotation des interféromètres étant liée à l'effet Sagnac, le déphasage de l'interféromètre est proportionnel à son aire. Grâce à la nouvelle configuration à quatre impulsions lasers, nous obtiendrons une aire beaucoup plus grande que dans la configuration habituelle à trois impulsions (l'aire augmentant comme le cube du temps d'interrogation au lieu du carré pour une configuration habituelle à trois impulsions). Dans cette nouvelle expérience, l'aire pourra être augmentée d'un facteur 300 par rapport à celle de l'expérience actuelle et de plus d'un facteur 30 par rapport à celle d'une expérience à trois impulsions de taille similaire, comme celle en cours de réalisation dans l'équipe de E. Rasel à Hanovre (Allemagne). L'aire de l'interféromètre atteindra donc une taille de près de 11 cm^2. De plus, cette nouvelle expérience est conçue pour limiter l'impact des défauts de fronts d'onde, qui étaient la limite de la première expérience.

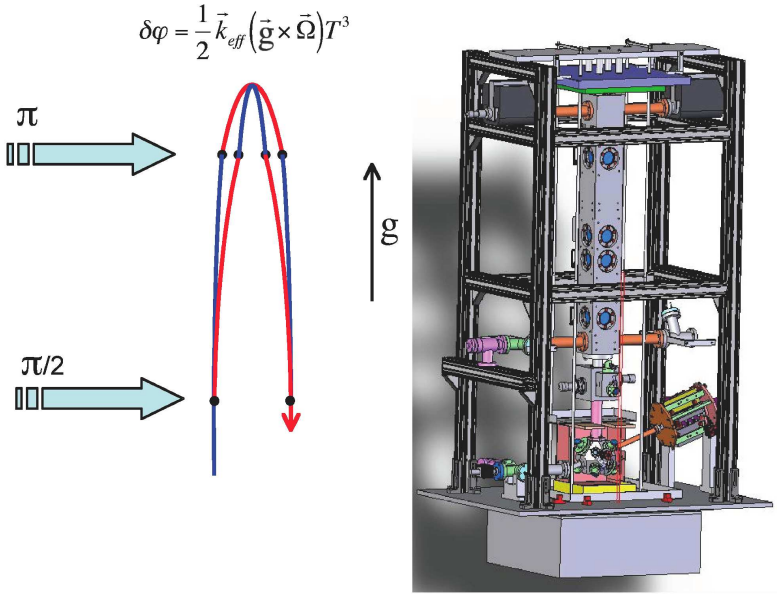

FIG. 5.2 : *Schéma du nouveau gyromètre à quatre impulsions.*

Dans cette expérience, les atomes sont issus d'une seule source et lancés verticalement à une vitesse de 5 $m.s^{-1}$. Les faisceaux lasers Raman sont orientés horizontalement et sont appliqués à quatre reprises (voir figure 5.2) pour réaliser un interféromètre en forme de huit replié (temps d'interrogation total 2T maximal de 800 ms). L'interféromètre n'est pas sensible à l'accélération continue car les deux demi-interféromètres ont des sensibilités opposées. Par

contre, grâce à la gravité qui replie l'interféromètre, les sensibilités à la rotation des deux boucles s'ajoutent. Cette expérience sera intrinsèquement moins sensible aux effets systématiques liés aux défauts de fronts d'onde qui limitent la première expérience. Ces effets dépendent des différences de phase vues dans chaque paire de faisceaux Raman entre l'impulsion à la montée et celle à la descente. Premièrement, l'appareil devient donc insensible aux fluctuations de position initiale et donc seules les fluctuations de vitesse de lancement peuvent avoir encore un impact. Deuxièmement, les déphasages parasites n'augmentent que comme le temps de vol entre le lancement et la fin de l'interféromètre (accroissement d'un facteur 3 entre l'ancienne et la nouvelle expérience) alors que la sensibilité augmente comme l'aire (facteur 300). Troisièmement, l'utilisation du centre des hublots permettra de gagner également sur le défaut de front d'onde (un ordre de grandeur).

Les études précédentes ont également montré qu'une des limites importantes à l'utilisation des capteurs inertiels à atomes froids, notamment en navigation inertielle, est l'échantillonnage des vibrations parasites et notamment l'influence du temps mort entre deux mesures. L'utilisation d'un fonctionnement quasi-continu peut être mise en place et testée. Pour cela, il sera nécessaire d'utiliser en permanence un nuage d'atomes froids dans l'interféromètre en préparant un nouveau nuage pendant la mesure avec le nuage précédent. Dans le cas d'un gyromètre à quatre impulsions (temps d'interrogation total 2T), il faut lancer un nuage tous les intervalles de temps T : un nuage, indicé n, réalise sa troisième impulsion alors que le nuage suivant (n+1) réalise sa deuxième impulsion, puis réalise sa quatrième impulsion alors que le nuage indicé n+2 réalise sa première impulsion. Ce mode de fonctionnement permet de moyenner très efficacement les bruits qui apparaissent de manière similaire (mais de signe opposé) pour les deux nuages car ils interagissent simultanément avec la même paire de faisceaux Raman. C'est notamment le cas des bruits de vibrations (accélération et rotation) ou de phase des faisceaux lasers... Il est possible de montrer à l'aide de la fonction de sensibilité que l'effet d'échantillonnage est pratiquement annulé (à un rapport τ/T près) à basse fréquence ($2\pi f << \Omega_{Rabi}$). La difficulté expérimentale consiste à isoler la zone où est réalisé l'interféromètre de la lumière parasite issue du piège. Il est possible d'utiliser une méthode similaire à celle développée pour les jets ralentis [Füzesi 2007] fondée sur l'utilisation d'obturateurs mécaniques. Cette méthode est très générale et peut également être utilisée pour les mesures d'accélération (gravité) ou pour les gradiomètres.

Les performances attendues devraient nettement dépasser celles des gyromètres commerciaux optiques ou mécaniques, notamment sur les temps longs (stabilité de 10^{-10} rad.s^{-1} pour des temps de 1000 à 10000 s), et par là même démontrer clairement l'intérêt de ce type d'interféromètres pour les applications en géophysique (mesure des fluctuations de la rotation de la Terre) et en navigation inertielle (voir paragraphe 3.1.3).

5.1.3 Séparatrices optiques de plus grande efficacité

En réalisant des transitions optiques multiples il est possible d'augmenter la sensibilité des interféromètres, soit en réalisant des interféromètres à ondes multiples [Cahn 1997, Hinderthür 1999, Aoki 2001] soit en augmentant la séparation entre les paquets d'ondes atomiques. Cette dernière voie a été depuis longtemps proposée mais commence seulement à être explorée. Des séparations correspondant à quatre ou six photons ont bien été démontrées [McGuirk 2000], mais les techniques utilisées ne permettent pas leur extrapolation à des séparations beaucoup plus grandes. De nouvelles méthodes ont récemment été démontrées pour réaliser des séparatrices plus efficaces, soit en réalisant des transitions avec $2n\hbar k$ [H-Müller 2008b], soit en utilisant des oscillations de Bloch [Cladé 2009, H-Müller 2009] et qui pourraient également être utilisée dans nos expériences. De notre côté, nous avons testé une autre méthode permettant de réaliser directement une séparation correspondant au recul dû à quatre puis huit photons optiques et pouvant donner lieu facilement à une augmentation importante de la séparation entre paquets d'ondes (séparations correspondant à des multiples de celle pour quatre photons) [Lévèque 2009]. Des investigations supplémentaires seront réalisées sur la nouvelle expérience de gyromètre qui disposera des accès optiques nécessaires pour ces études.

5.2 Utilisation de sources atomiques cohérentes

5.2.1 Utilisation de sources atomiques ultra-froides

La première étape pour tirer profit des possibilités offertes par les atomes ultra-froids consiste à les utiliser dans des configurations d'interféromètres similaires à celles utilisant des atomes froids classiques, mais en bénéficiant de sa meilleure définition spatiale de la source et de sa température réduite (plus faible dispersion en vitesse). La difficulté consiste à limiter l'effet des interactions entre atomes froids. Un inconvénient provient de l'augmentation du temps de cycle due à la durée de préparation importante de l'échantillon, mais qui peut être compensée par l'augmentation du temps de mesure. Ce type de source a un intérêt particulier pour atteindre une grande exactitude et pour les expériences en micro-gravité, où la réduction de la température permet une augmentation importante du temps d'interrogation et donc de la sensibilité (voir paragraphe 5.5).

Gravimètre : source atomique ultra-froide

Outre les modifications concernant l'enceinte à vide et le contrôle des trajectoires, une seconde approche, pour améliorer l'exactitude du gravimètre consiste à transférer les atomes dans un piège dipolaire, engendré par un laser à fibre de puissance et très désaccordé. La possibilité de réaliser un refroidissement évaporatif très efficace et de condenser des atomes de rubidium dans un piège dipolaire croisé à 1,5 μm ayant été récemment démontré [Cément 2009], nous utiliserons ce type de dispositif pour étudier les performances de l'interféromètre avec un échantillon plus dense, mieux défini spatialement et plus froid.

L'utilisation d'atomes ayant une dispersion en vitesse plus faible doit permettre d'améliorer l'exactitude de la mesure : l'influence des aberrations du front d'onde, des gradients de déplacements lumineux ou de l'accélération de Coriolis sera plus faible. Un autre intérêt du piège dipolaire est qu'il constitue un piège de nature différente, non dissipatif, pour le lâcher des atomes. Lors de l'extinction du piège dipolaire, il n'y pas de transfert d'impulsion dans une direction privilégiée et donc pas de déphasage parasite dû à l'effet Coriolis.

L'utilisation d'un piège dipolaire, permettant d'obtenir un condensat de Bose-Einstein par des méthodes purement optiques, semble préférable aux pièges magnétiques pour des instruments de grande exactitude, parce qu'il peut être coupé rapidement sans engendrer de perturbations. Cependant, pour des échantillons très denses, le déphasage lié aux interactions entre les atomes pourra affecter la mesure de l'accélération de la pesanteur. Nous étudierons cet effet qu'il est important de bien maîtriser pour envisager l'utilisation des atomes ultra-froids à des mesures de précision et comparer les mérites respectifs des atomes ultra-froids non condensés et condensés.

5.2.2 Nouveaux concepts : Condensation de Bose-Einstein et Interférométrie Atomique dans un Résonateur Optique de Grande Finesse (BIARO)

En utilisant des atomes piégés (piège dipolaire ou magnétique), il est possible d'envisager un temps d'interrogation notablement plus grand (supérieur 1s) tout en restant très compact, mais également des conceptions très différentes bénéficiant des particularités de ce type de source [Impens 2008]. Dans ce type d'interféromètre, la difficulté principale est liée au contrôle des interactions avec le piège et aux interactions entre atomes froids, qui déplacent les niveaux d'énergie et génèrent des déphasages parasites.

L'expérience BIARO vise à utiliser un résonateur optique de haute finesse pour obtenir un condensat de Bose-Einstein de façon tout optique (piège dipolaire), qui servira ensuite pour des expériences d'interférométrie atomique. Cette expérience est réalisée en collaboration avec Philippe Bouyer du laboratoire Charles Fabry de l'Institut d'Optique de Palaiseau. L'utilisation d'une cavité de haute finesse apporte plusieurs avantages. Le premier provient du fait que la cavité permet d'amplifier l'intensité laser et donc de réaliser un piège très confinant nécessaire à l'obtention d'atomes ultra-froids, tout en utilisant une source laser de faible puissance (de l'ordre de 100 mW au lieu de 100 W). En utilisant une cavité à quatre miroirs, l'échantillon est alors à une position bien définie au croisement de deux bras, ce qui est un avantage certain pour le contrôle des effets systématiques (problèmes de défauts de front d'onde des faisceaux lasers Raman).

La cavité devrait également être utilisée pour réaliser une mesure de déphasage atomique en dessous de la limite standard due au bruit de projection quantique (en $1/N^{1/2}$). La détection non destructive de l'état de spin des atomes permet de créer des états intriqués macroscopiques qui peuvent être utilisés dans l'interféromètre. La cavité permet à la fois d'obtenir le nuage ultra-froid, mais assure également la superposition du mode atomique et optique pour la détection non-destructive et un gain sur l'efficacité de cette détection non-destructive (comme la racine carrée de la finesse qui est attendue supérieure à 10 000 à 780 nm).

Ce type de méthode est particulièrement adapté aux sources d'atomes ultra-froids. Premièrement, l'épaisseur optique de l'échantillon est très élevée, ce qui est nécessaire pour obtenir une détection faiblement destructive. Deuxièmement, le nombre d'atomes étant typiquement faible dans ces sources ultra-froides (typiquement de 1000 à 10^5 at), la limite standard représente effectivement une limite pratique à la sensibilité. L'intérêt de cette méthode dépasse son utilisation en interférométrie atomique et peut par exemple être également utilisée pour les horloges atomiques. Les premières démonstrations de mesures non-destructives, fondées sur des méthodes similaires, ont été publiées à l'automne 2008 dans les équipe E. Polzik [Appel 2009] à Copenhague et de Vuletic au MIT [Schleier-Smith 2009].

5.3 Des capteurs inertiels pour les applications spatiales

5.3.1 Tests des lois de la gravité à l'aide de l'interférométrie atomique

Depuis leurs débuts, les interféromètres à ondes de matière sont envisagés pour réaliser des sondes très précises des forces gravito-inertielles [Clauser 1988, Bordé 1994b]. Leur développement rapide et leurs performances en font des candidats prometteurs pour tester la gravité [Lämmerzahl 2000, Bordé 2002, Fray 2004, Dimopoulos 2007]. Ce type de capteur a

été proposé pour tester la relativité générale en mesurant l'effet Lense-Thirring [Lense 1918, Gustavson 2000, ESA-SCI 2000, Angonin 2006], pour tester le principe d'équivalence en comparant la chute de deux corps de compositions différentes (deux atomes de natures différentes) [Nyman 2006, Ertmer 2009], pour détecter les ondes gravitationnelles [Bordé 1994b, Delva 2006, Lamine 2006, Tino 2007b, Dimopoulos 2008] ou encore pour tester les lois de la gravité à très faibles distances ($\sim 10\mu m$) [Dimopoulos 2003, Harber 2005, Wolf 2007, Sorrentino 2008, Pereira 2009] ou très grandes distances comme à l'échelle du système solaire [Wolf 2009]. D'autres applications, hors du champ de la physique fondamentale, sont également envisagées et notamment pour les nouvelles générations de gradiomètres dans l'espace [Yu 2006].

Pour la plupart de ces propositions, l'utilisation de la micro gravité permet de bénéficier d'un environnement permettant de décupler les performances de ce type de capteur grâce à un environnement vibratoire plus calme (fond sismique, bruit gravitationnel...) et à l'augmentation du temps d'interrogation. Cet avantage a déjà été mis en avant pour les horloges et notamment dans le cadre du projet ACES [Cacciapuoti 2007] incluant comme charge utile l'horloge à atomes froids PHARAO [Laurent 2006]. Il est encore plus net pour les capteurs inertiels car, d'une part la sensibilité augmente comme le carré du temps d'interrogation, et d'autre part le passage dans l'espace peut, dans certaines conditions, permettre de réduire très significativement les vibrations parasites.

Des applications des capteurs inertiels ont déjà été proposés ou même mises en pratique à l'aide de capteurs macrosopiques [Everitt 2008, Touboul 2001, Tapley 2004]. L'intérêt de l'interférométrie atomique repose sur la possibilité de réaliser des appareils sans biais (ou très peu) et avec une très bonne stabilité sur les temps longs.

5.3.2 HYPER : mesure de l'effet Lense-Thirring

La mesure de l'effet Lense-Thirring était le but principal de la proposition de mission spatiale HYPER. L'effet Lense-Thirring est un effet relativiste qui conduit à la précession du référentiel d'inertie local, matérialisé par des gyromètres, par rapport à un référentiel non local, réalisé en pointant une étoile lointaine fixe. La précession due à l'effet Lense-Thirring s'écrit [Lense 1918] :

$$\Omega_{LT} = \frac{G\,I}{c^2}\frac{3(\omega \times \mathbf{r}).\mathbf{r} - \omega r^2}{r^5}$$

où G est la contante gravitationnelle, I et ω sont respectivement le moment d'inertie et la vitesse de rotation de la terre, et $\mathbf{r}$ la position par rapport au centre de la terre.

La très grande sensibilité de l'interféromètre atomique à l'effet Sagnac doit permettre de mesurer la modulation de la précession due à l'effet Lense-Thirring lorsque le satellite tourne

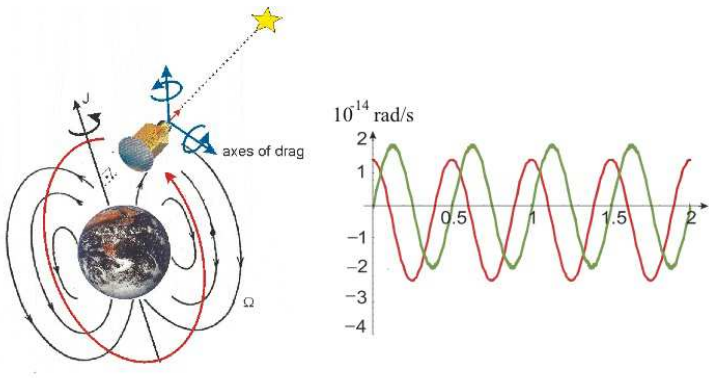

FIG. 5.3 : *Diagramme schématisant la mesure de l'effet Lense-Thirring. Les lignes noires visualisent les lignes de champ de l'effet d'entraînement de la Terre. Les axes d'entrée des gyromètres pointent dans deux directions orthogonales à la direction de pointé du télescope. La direction de l'effet d'entraînement varie au cours de l'orbite du satellite par rapport aux axes d'entrée des gyromètres.*

en orbite autour de la Terre. Sur une orbite synchrone avec le soleil, à une altitude de 700 km, HYPER peut mesurer l'effet d'entraînement sur une trajectoire quasi-polaire en fonction de sa latitude :

$$\begin{pmatrix} \Omega_x \\ \Omega_y \end{pmatrix} \alpha \frac{3}{2} \begin{pmatrix} sin(2\theta) \\ cos(2\theta) - \frac{1}{3} \end{pmatrix} \tag{5.1}$$

où e_x et e_y définissent le plan orbital, avec le moment d'inertie de la Terre **J** parallèle à e_y et $\theta = arcos(\mathbf{r}.\mathbf{e_x})$.

La charge utile de HYPER est constituée de deux gyromètres atomiques dont les axes d'entrée sont orthogonaux entre eux. Un télescope de très grande sensibilité est utilisé comme pointeur d'étoile pour donner la référence d'angle (10^{-9}rad dans la gamme de fonctionnement de 0,3 à 3 Hz). Les deux gyromètres peuvent mesurer les deux composantes de la vitesse de rotation dans le plan orthogonal à la direction de pointé du télescope, dirigé vers l'étoile de référence. A cause de l'effet Lesne-Thirring, les vitesses de rotation mesurées par les deux gyromètres varient à une fréquence double de celle de révolution du satellite autour de la Terre (voir eq. 5.1). Les deux signaux suivant les deux axes ont la même amplitude de modulation (3,75.10^{-14} rad.s^{-1}) mais évoluent en quadrature. La sensibilité de chaque gyromètre est de 3.10^{-12} rad.s^{-1} pour un temps d'interrogation de trois secondes. En répétant la mesure toutes les trois secondes, chaque gyromètre atteint une sensibilité de 7.10^{-14} rad.s^{-1} après une orbite (90 minutes) et 2.10^{-15} rad.s^{-1} en un an, soit un vingtième de l'effet mesuré.

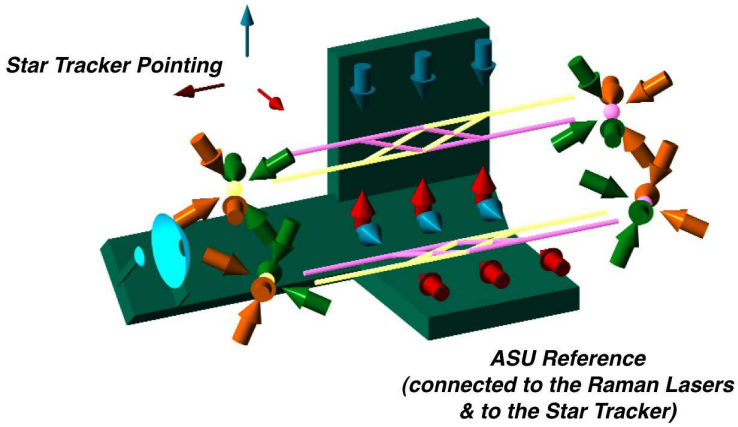

FIG. 5.4 : *Schéma de principe de la charge utile de HYPER. Les deux gyromètres sont basés sur le même principe de fonctionnement que celui décrit au paragraphe 3.3. Chaque gyromètre utilise deux sources d'atomes lancées suivant des directions opposées. Les deux gyromètres donnent accès aux deux composantes de la vitesse de rotation dans le plan orthogonal à la direction de pointé du télescope, qui est monté de façon solidaire avec les deux gyromètres.*

Bien que cette proposition de mesurer l'effet Lense-Thirring ne soit plus d'actualité, la proposition de ce projet en 2000, ainsi que l'étude de faisabilité industrielle qui l'a suivi, ont permis de montrer la faisabilité et les potentialités de l'interférométrie dans l'espace pour tester les lois de la gravité mais également d'envisager des applications spatiales en gravimétrie terrestre par exemple. De plus, après le vol de la mission Gravity Probe B, l'analyse des données [Everitt 2008] n'a permis de mesurer directement cet effet avec la résolution espérée (une fraction de %). Ce test est donc toujours d'actualité.

Mais surtout, cette première étude a permis d'ouvrir une nouvelle thématique de test de la physique fondamentale dans l'espace à l'aide d'interféromètres atomiques. Deux autres projets ont été proposés à l'ESA lors de l'appel "COMSIC vision 2007" et sont maintenant envisagés. Premièrement, en comparant la chute de deux nuages d'atomes ultra-froids de Rubidium et de Potassium, il a été proposé de tester le principe d'équivalence à mieux que 10^{-15} en bénéficiant pleinement de l'augmentation du temps d'interaction en apesanteur (typiquement 10 s), grâce à l'utilisation d'atomes ultra-froids (mission MWXG [Ertmer 2009]). Une deuxième proposition, baptisée SAGAS [Wolf 2009], a plusieurs objectifs de physique fondamentale et d'étude du système solaire, par exemple un test de la relativité générale et une exploration de la ceinture de Kuiper. La mission consiste à lancer ensemble de capteurs atomiques (horloge optique, accéléromètre, et lien optique) sur une trajectoire s'échappant du système solaire. L'accéléromètre, fondé sur des concepts très proches de ceux du gravimètre,

permet distinguer les forces inertielles de force non-inertielles (par exemple la pression de radiation du soleil) lors du voyage.

5.3.3 ICE : Interférométrie Cohérente pour l'Espace

Ce projet est développé en collaboration avec le laboratoire Charles Fabry de l'Institut d'Optique de Palaiseau (Philippe Bouyer) et l'ONERA (Alexandre Bresson) depuis 2005. Il a pour but de tester le principe d'universalité de la chute des corps entre deux espèces d'atomes (Rubidium et Potassium). A terme, l'expérience consistera en un double interféromètre à sources cohérentes et fonctionnant dans l'avion zéro-g du CNES. L'un des intérêts de cette expérience est la possibilité de disposer de longs temps d'interrogation, inaccessibles au sol à cause de la gravité. Cette expérience a également un but de démonstration de faisabilité pour les projets spatiaux fondés sur l'utilisation de l'interférométrie atomique.

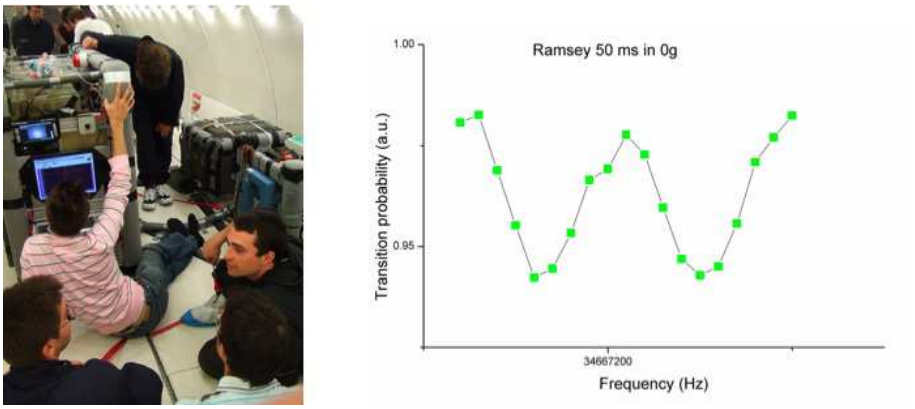

FIG. 5.5 : *A gauche : installation de l'expérience dans l'avion. A droite : franges de Ramsey obtenues en micro-gravité pendant la campagne d'octobre 2008 à l'aide de transitions Raman co-propageantes.*

Bien qu'encore en développement, une partie de l'expérience a déjà volé en zéro-g, démontrant la validité des choix technologiques réalisés en terme de source laser, qui est fondée sur des lasers à 1,5 μm doublés en fréquence pour le piégeage et les faisceaux Raman. Cette technologie a l'intérêt de bénéficier des développements importants des composants entièrement fibrés réalisés pour les applications telecom. Le piégeage et le refroidissement des atomes ainsi que des franges de Ramsey ont été obtenus dans l'avion en zéro-g. L'expérience sera d'abord testée en tant qu'interféromètre à source froide conventionnelle, avec des atomes de Rubidium, puis avec les deux espèces atomiques simultanément. Enfin, l'utilisation des sources ultra-froides sera mise en place pour obtenir les performances ultimes. La tempéra-

ture plus froide des échantillons atomiques permettra de bénéficier pleinement de l'augmentation du temps d'interrogation accessible en micro-gravité. Le refroidissement évaporatif sera réalisé à l'aide d'un piège dipolaire utilisant un laser de puissance également à 1,5 μm. Son utilisation commune pour les deux espèces atomiques garantit la superposition spatiale des trajectoires atomiques nécessaire pour limiter l'effet des défauts de front d'onde sur la mesure différentielle.

Il est important de noter que, même si l'expérience est conçue pour fonctionner en micro-gravité, elle fonctionne également au sol (temps d'interrogation réduit), ce qui permet d'effectuer des tests préliminaires et d'améliorer sa fiabilité. Le niveau de vibrations très élevé dans l'avion brouille les franges d'interférences. Néanmoins, il est possible de récupérer le signal utile en utilisant des méthodes de corrélation de signaux, issus des deux interféromètres [Stockton 2007] et d'un accéléromètre mécanique embarqué de façon solidaire. Cette méthode est similaire à celle déjà utilisée pour le gravimètre [Merlet 2009].

Un projet relativement similaire est en cours de développement en Allemagne (coopération entre plusieurs laboratoires) [Vogel 2006]. Ce projet, nommé QUANTUS, utilise une puce atomique pour générer le condensat et réalise les mesures dans la tour de chute libre de Brême.

5.4 Articles relatifs aux applications des capteurs inertiels atomiques

Trois articles sont reproduits dans ce paragraphe. Le premier est un article de vulgarisation des applications de l'interférométrie atomique à la réalisation de capteurs inertiels (Physics-Wolrd 2007). Les deux suivants concernent le projet ICE. Le premier donne une description générale du projet (Appl. Phys. B 2006) et le second (EPJD 2009) donne des résultats préliminaires dans lesquels des franges de Ramsey ont été obtenues à l'aide de transition Raman co-propageante en micro-gravité.

Getting the measure of atom interferometry

Interferometers that exploit the wave nature of atoms, rather than light, are being turned into precise inertial sensors for vehicle guidance systems. As **Franck Pereira Dos Santos** and **Arnaud Landragin** explain, such matter-wave interferometers also allow precise tests of fundamental physics

Franck Pereira Dos Santos and **Arnaud Landragin** are at the SYRTE laboratory, Observatoire de Paris, France, e-mail franck.pereira@obspm.fr

Since the beginning of the 20th century, physicists have known that light must be considered as both a wave and a particle. Some properties of light – such as diffraction – can only be explained by treating it as waves, while others – like the photoelectric effect – can only be explained by treating it as particles. In the 1920s Louis de Broglie suggested that this wave–particle duality, which lies at the heart of the counterintuitive laws of quantum mechanics, could be extended to massive particles. In other words, electrons, atoms and molecules should diffract and interfere just like light does.

The wave nature of particles was first demonstrated in 1927, when George Paget Thomson – the son of J J Thomson, who discovered the electron in 1897 – found that a narrow beam of electrons produced an interference pattern after passing through a diffraction grating made from a thin metal film. Three years later, Immanuel Estermann and Otto Stern found that helium atoms generated a similar pattern when they were reflected from the surface of a crystal, which has a periodic structure like a grating does. Since then, a variety of tools have been developed to split these so-called matter waves into different parts as prisms and mirrors do for light. Unlike these optical elements, however, devices capable of manipulating matter waves need exotic structures such as mechanical and laser gratings. Armed with such devices, we can build a matter-wave interferometer.

At a Glance: Atom interferometry

- According to quantum mechanics, atoms and molecules can also be treated as waves, which means that they can be made to reflect, diffract and interfere
- Matter-wave interferometers are similar to optical interferometers but instead of using a solid beam splitter, such as a prism, to control light, the atomic wave packets are split, redirected and recombined using lasers
- The phase of a matter wave is significantly affected by rotations and accelerations, which means that atomic interferometers can be used as highly sensitive inertial sensors
- Inertial sensors are primarily used in guidance systems for planes, submarines and spacecraft, but conventional technologies quickly lose accuracy
- Atomic inertial sensors can also be used to determine certain fundamental constants and test gravity at both very small and very large scales

Interferometers are a vital tool in physics. By analysing the interference pattern produced when two or more waves that have travelled along different paths interfere, an interferometer can reveal information about the physical environments of those paths or "arms" (figure 1). In an optical interferometer, for example, the separation of fringes in such an interference pattern depends on the relative phases of – and thus the distances travelled by – the waves in each arm of the device. Most interferometers use electromagnetic waves, but the principle is the same for sound and matter waves too. The latter, for instance, experience a phase shift that depends on the refractive index of the medium they are travelling through.

The crucial difference between a matter-wave and an optical interferometer, however, is that matter waves have mass while photons are massless. As a result, the phase of a matter wave is affected by gravity to a much greater extent, thereby offering a highly accurate way to test Newtonian gravity on very small scales and to measure certain fundamental constants (see box on page 37).

But atom interferometers also have much more practical applications. In particular, they can provide an absolute measure of rotation and acceleration, and have recently been used to build inertial sensors with an accuracy that rivals traditional devices. Indeed, it may not be long before such atom interferometers are used to guide aircraft, submarines and even spacecraft.

Separating states

The first matter-wave interferometer was built in the 1950s by Norman Ramsey, who shared the 1989 Nobel Prize for Physics for the work. Ramsey and his colleagues set out to measure the resonance frequency of an electronic transition in hydrogen molecules – the principle on which atomic clocks are based. To do so, they constructed an interferometer using two separated microwave cavities.

In the first cavity a cloud of hydrogen molecules was put into a quantum superposition of different energy states by firing a microwave pulse at it. When a molecule or atom in its ground state absorbs a photon with the right energy, it moves to an excited state, where it

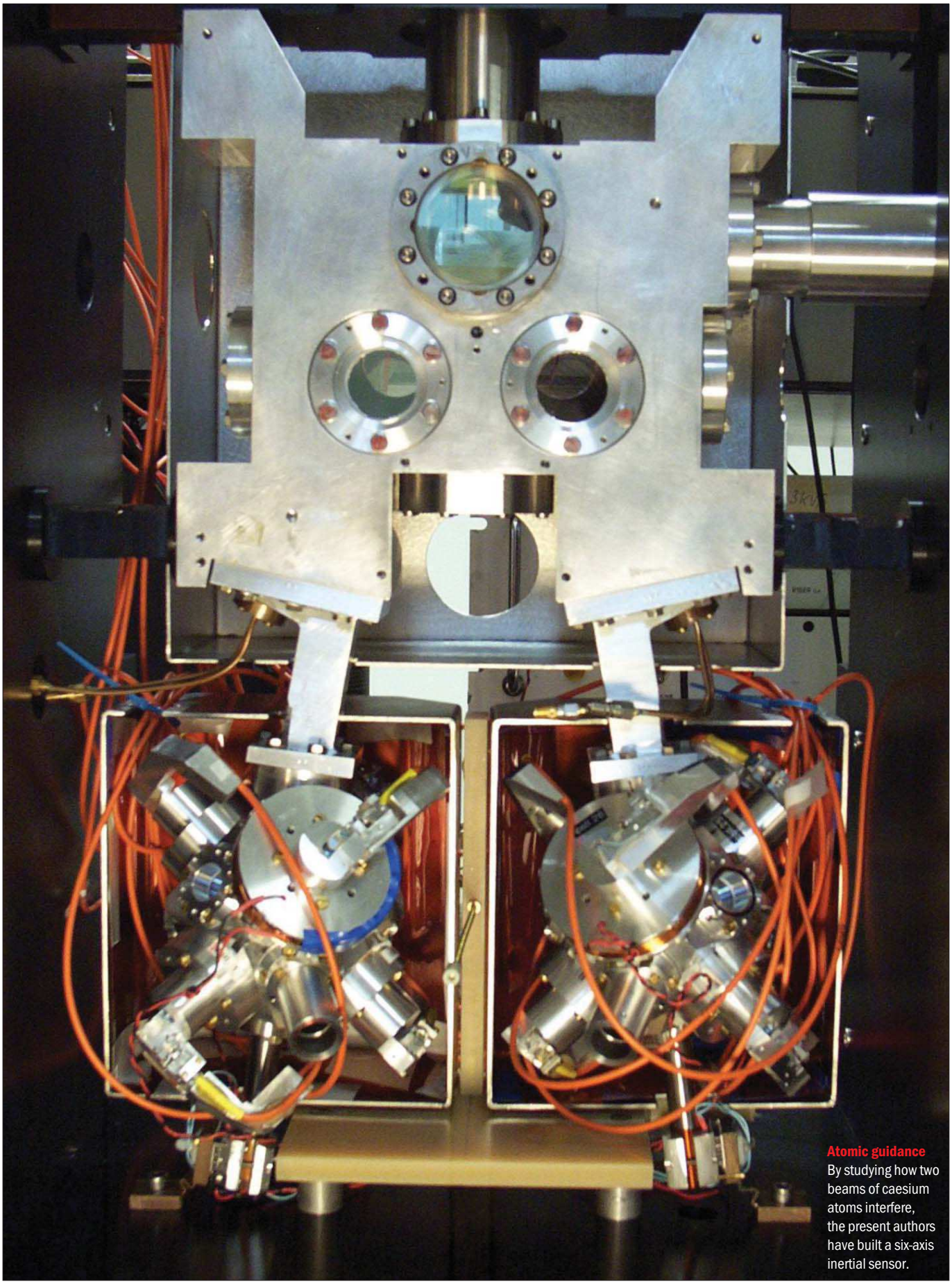

Atomic guidance
By studying how two beams of caesium atoms interfere, the present authors have built a six-axis inertial sensor.

1 Interferometry matters

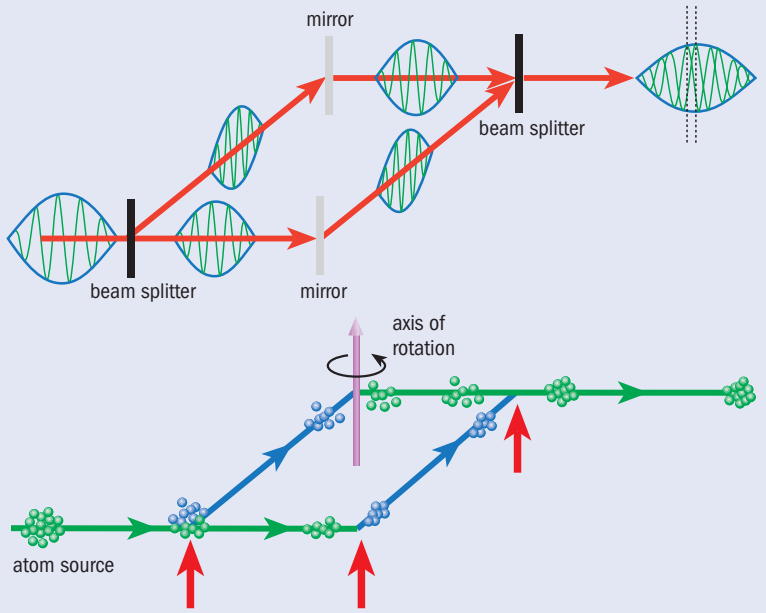

In an optical "Mach–Zehnder" interferometer (top) a partially reflecting mirror splits a beam of light so that it travels along two different paths. Any difference in the physical properties of these paths – for instance if one is slightly longer than the other – causes the two beams to acquire different phase shifts, so that when they are recombined, they produce an interference pattern that contains information about those properties. Since particles can also be considered as waves, the same principle can be used to build a "matter-wave" interferometer (bottom) in which clouds of cold atoms are manipulated using lasers rather than mirrors. First a laser pulse (red arrow) places the atomic wave packets into a superposition of two partial wave packets with different momenta (green and blue) so that they follow two separate paths. A second laser forces the wave packets to converge, while a third recombines them to generates the interference pattern. Because atoms are massive particles, matter-wave interferometers with this geometry are sensitive to acceleration along the direction of diffraction and to rotations about an axis perpendicular to the atomic paths. The larger the separation of the two paths, the better the sensitivity to inertial forces.

may remain or return to its ground state by re-emitting a photon. By adjusting the duration and/or the amplitude of the microwave pulse, Ramsey was able to split the "wave packet" of individual hydrogen molecules into two partial wave packets that together made up a coherent superposition of the ground and excited states.

These partial wave packets were then made to travel to the second microwave cavity, each incurring a phase shift the size of which depends on its energy. In the second cavity another microwave pulse recombined the two partial wave packets, which generated an interference pattern. Because the difference between the phase shifts accumulated by the matter waves along each path is proportional to the difference between the energies of the two states, and since the energy of a photon is directly proportional to its frequency, Ramsey's interferometer allowed him to determine the resonance frequency of electronic transitions in molecular hydrogen.

Since atoms are massive particles, their energy is affected by inertial forces, so that a matter-wave interferometer of a similar type also provides a natural inertial or motion sensor. Inertial sensors measure the displacement of an object with respect to an inertial (i.e. non-accelerating) reference frame. Gyroscopes, for example, measure the angle or rotation rate of a rotating body either mechanically or optically, while accelerometers – which are usually microelectromechanical devices that measure the deflection of a cantilever – are sensitive to accelerations.

Spacecraft, missiles, submarines and modern aircraft are all equipped with inertial-measurement units that detect acceleration as well as changes in rotation in 3D (i.e. its "pitch", "roll" and "yaw"). With the help of a computer, the geographic position can then be tracked using a process known as dead reckoning. The Global Positioning System (GPS) is designed specifically for navigation purposes, but it relies on communicating with external satellites. Inertial-measurement units, on the other hand, are closed systems with much faster response times and are not affected by storms or other disturbances that can interrupt the GPS signal.

In fact, interferometry is already used in conventional inertial-measurement units in the form of optical gyroscopes. These devices contain a coil of optical fibre, along which two light beams propagate in opposite directions. If the coil rotates in the plane of the beams, then the beam travelling against the rotation experiences a slightly shorter path than the other, which induces a phase shift between the beams – known as the Sagnac effect. The interference that results when the beams are recombined therefore provides a direct measure of the rotation rate.

Because matter waves travel much slower than light waves, however, rotation sensors based on atom interferometry are potentially much more sensitive than optical gyroscopes because the matter waves spend more time in the interferometer and hence accumulate greater phase shifts. Furthermore, matter-wave interferometers provide absolute measurements of the displacement of the atoms and therefore eliminate the instrumental bias that limits the accuracy of conventional inertial sensors. This is because the lasers used to send the atoms along different paths define perpendicular planes in which the phase of the light waves is constant. Since these planes are fixed with respect to the rest of the instrument, and are separated by increments equal to the wavelength of the laser, they provide a precise reference ruler against which to measure the displacement of the atoms. This also means that matter-wave interferometers can only measure accelerations in the direction of propagation of the lasers.

Gathering inertia

Inertial sensors based on atom interferometers were first demonstrated in 1991 by Steven Chu's group at Stanford University in the US and by Jürgen Helmcke's group at the Physikalisch-Technische Bundesanstalt (PTB) in Braunschweig, Germany. These early devices were sensitive to acceleration due to gravity and to rotation rate. For example, in the PTB interferometer the wave packets of calcium atoms were put into a superposition of states with different momenta using a laser, similar to the way Ramsey used microwaves to manipulate the electronic states of hydrogen molecules. As in the case of an optical gyroscope, rotating the PTB apparatus introduced a phase shift between the two beams of partial wave packets that was proportional to the rotation rate.

Since this experiment was carried out, researchers have improved the sensitivity and accuracy of matter-

DHD Multimedia Gallery

In a spin
Conventional mechanical gyroscopes use the forces on a spinning flywheel to measure rotations.

2 The six-axis inertial sensor

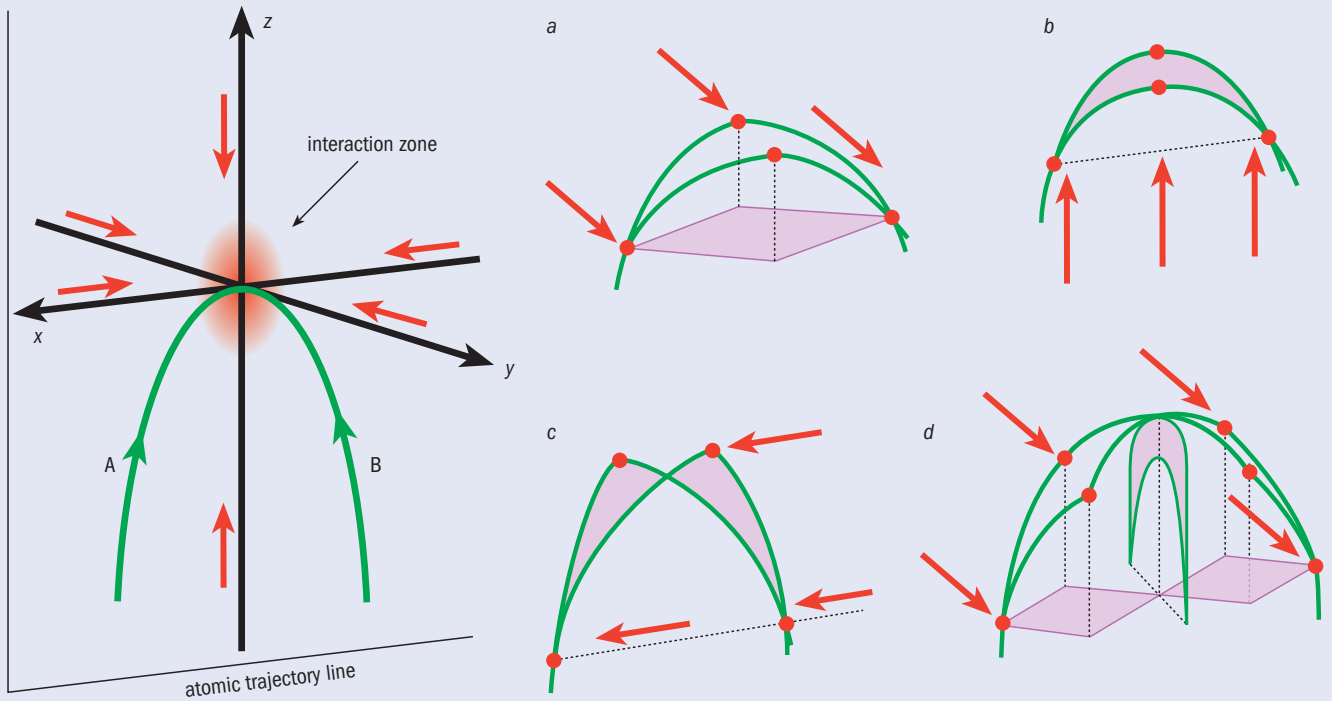

Since atoms (unlike photons) have mass, atomic or matter-wave interferometers make ideal inertial-motion sensors. For example, the present authors have recently built a six-axis inertial sensor based on a double interferometer in which two counter-propagating atomic clouds follow parabolic trajectories (A and B) and are split into partial wave packets at the apogee of these trajectories using lasers (red arrows). In order to measure all three components of rotation, Ω, and acceleration, $\boldsymbol{a}$, the set-up requires the successive use of four different laser configurations. Configurations *a*, *b*, and *c* use Mach–Zehnder three-pulse configurations with the lasers propagating along the *y*-, *z*- and *x*-axes, respectively; while in configuration *d*, four pulses cause the atomic wave packets to follow a figure-of-eight-shaped path. In each case the interferometer is sensitive to accelerations along the direction of propagation of the lasers and rotations around the axis perpendicular to the purple shaded area. This area is the projection of the atom paths onto the plane of interest.. As a result, configurations *a* and *b* each measure one component of acceleration and one of rotation (Ω_z and $\boldsymbol{a}_y$; and Ω_y and $\boldsymbol{a}_z$, respectively). Configuration *c* only measures acceleration along the *x*-axis ($\boldsymbol{a}_x$) and has no sensitivity to rotation (since the purple areas cancel out), while configuration *d* measures rotation around the *x*-axis (Ω_x) without being sensitive to acceleration.

wave inertial sensors beyond what can be achieved by classical instruments. In our laboratory at the Observatoire de Paris, for instance, we are currently developing an inertial sensor that can measure all three rotation and all three acceleration components, and hence simultaneously function as a gyroscope and an accelerometer for navigation applications. In contrast, previous atomic gyroscopes – such as that built by Mark Kasevich, then at Yale University, and co-workers in the late 1990s – were designed to measure the vertical component of rotation and the horizontal component of acceleration only. Our six-axis sensor is thus a key step towards a practical navigation instrument, for which one needs to measure motion along all possible directions.

In fact, our device consists of a double interferometer in which two clouds of cooled caesium atoms follow parabolic trajectories in opposite directions (figure 2). We use infrared lasers to launch the atoms along the parabolic trajectories, split the atomic wave packets into partial wave packets with different energies, and to recombine them again in order to generate the interference patterns. As both atomic samples share the same lasers, this allows us to tell which contribution to the resulting interference patterns comes from the rotation and which comes from the acceleration. The rotation signal changes from positive to negative when the atoms change direction; but the acceleration signal does not, which means that we can extract the acceleration and rotation from the sum and difference of the signals from the two interferometers, respectively.

We chose caesium atoms because they can be cooled very efficiently, which means that since they are moving so slowly, they spend longer in the interferometer, thus making it more sensitive. The other key feature of our device is the highly curved parabolic trajectories of the atoms. These let us measure all the components of acceleration and rotation because it means we can arrange the apparatus in many different configurations without equipment getting in the way of the lasers or atoms. Three of these configurations use a "Mach–Zehnder" set-up with three laser pulses forming the interferometers, while a fourth configuration uses four laser pulses and makes the atomic wave packets follow a figure-of-eight-shaped path. So far we have measured the Earth's rotation rate and the tidal effect resulting

Matter-wave interferometers eliminate the instrumental bias that limits the accuracy of conventional inertial sensors

3 Detecting earthquakes

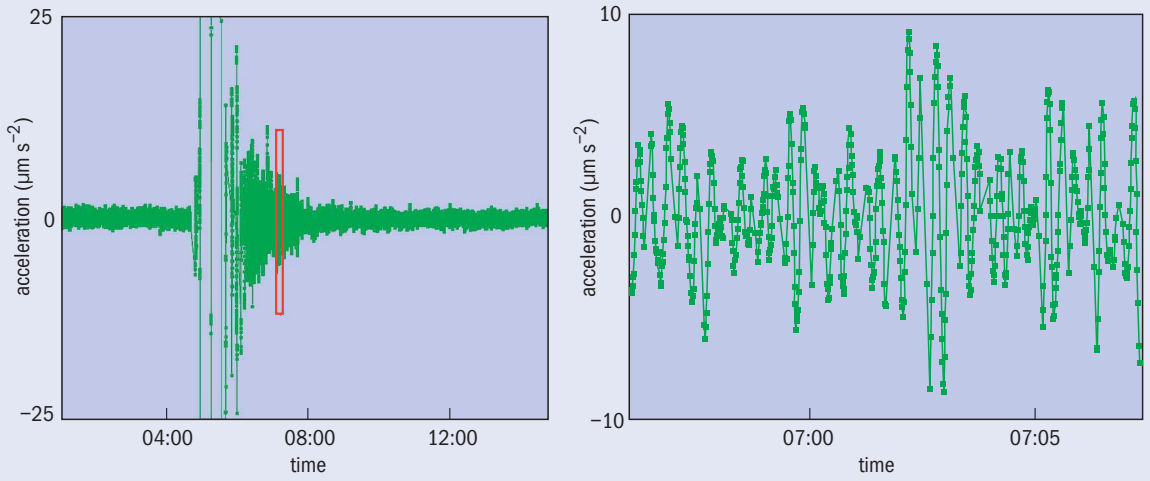

Matter-wave interferometers allow us to measure accelerations very accurately. For example, an "atomic gravimeter" can provide an accurate measure of the acceleration due to gravity, *g*, by allowing researchers to study clouds of cold atoms in free fall. This is particularly important for "watt balance" experiments that attempt to redefine the kilogram in terms of only fundamental constants (see box on page 37), but such a device is so sensitive that it can detect vibrations originating from the other side of the planet. For example, on 13 January the atomic gravimeter in our lab at the Observatoire de Paris detected an earthquake of magnitude 8.1 on the Richter scale in the Kuril Islands between Russia and Japan about 15 minutes after it occurred (left). Unlike standard absolute gravimeters, the high (4 Hz) repetition rate of the instrument clearly resolves the long-period ground oscillations (right).

from the gravitational interaction between the Earth, Sun and Moon with sensitivities of 2×10^{-7} rad s^{-1} for rotation and 4×10^{-7} m s^{-2} for acceleration, both for a 1 s measurement time. This is competitive with the best commercial optical gyroscopes, but we hope to improve the sensitivity in the near future.

One way to achieve better sensitivities is to use atom interferometers that measure rotation around just one axis. Ernst Rasel and Wolfgang Ertmer at the University of Hanover in Germany, for example, are currently developing an experiment that will push the sensitivity of atom interferometers to their limits (expected to be about 10^{-8} rad s^{-1}) on Earth and allow the technology to be tested for possible applications in the guidance systems in spacecraft. Their set-up is a Mach–Zehnder configuration in which the atoms travel 10 times faster than they do in our six-axis sensor, thus increasing the area of the interferometer and so making it more sensitive to rotation. Since the resulting trajectories are almost horizontal, the interferometer is sensitive to at most two components of rotation and two components of acceleration.

Atom interferometers could potentially distinguish between the predictions of general relativity and those of alternative gravity theories

The outer limits

A matter-wave inertial sensor in space would provide an important test of fundamental physics. For example, atom interferometers can be used to measure gravity both over microscopic distances and at the very large scale of the solar system, which means that they could potentially distinguish between the predictions of general relativity and those of alternative gravity theories such as modified Newtonian dynamics. In particular, matter-wave interferometers allow a test of the weak equivalence principle, which states that the trajectory of a falling test body depends only on its initial position and velocity, and is independent of its composition.

The absence of gravity and the low level of vibrations in space allows the measurement time to be increased 10-fold, which improves the sensitivity of an atomic inertial sensor by several orders of magnitude. Since 2000 the European Space Agency has been considering a project called HYPER (hyper-precision cold-atom interferometry in space), which would involve sending interferometers into space to test the gravitomagnetic "frame-dragging" effect of the Earth that is predicted by general relativity and to measure the fine-structure constant. Although HYPER is not scheduled for launched, it has shown that such sensors are feasible, and in the past couple of years more space missions have been proposed (see *Physics World* September 2006 p7).

For example, researchers in our laboratory (together with several other institutions) have proposed a project called SAGAS (Search for Anomalous Gravitation using Atomic Sensors). This would send an atom interferometer to the far reaches of the solar system in order to test whether the trajectories of the Pioneer probes – which were launched in the 1970s and appear to be experiencing an anomalous acceleration towards the Sun – are indeed due to a real gravitational effect. When this or a similar mission successfully gets off the ground – which could take up to 20 years – it will open the door for many more space-based applications of atom interferometry.

Back on Earth, many research teams have now developed reliable matter-wave interferometers for geophysics and geodesy (figure 3). These instruments can detect tiny changes in the Earth's gravitational field, which can reveal features such as underground structures or the presence of oil. As for navigation applications, vehicles equipped with atomic instruments should be able to evaluate their positions much more accurately than is possible with conventional inertial sensors. This is because atomic accelerometers have an intrinsically stable "scale factor", which relates the

Atom interferometry for fundamental physics

As well as providing accurate navigation systems, sensors based on atom interferometers can also be used to measure atomic quantities, to test Einstein's general theory of relativity and to determine fundamental constants. The gravitational constant, G, for example, can be determined by measuring the accelerations of two vertically separated clouds of atoms in free fall (each of which constitutes a separate interferometer). By adding and removing a control mass between the two interferometers, researchers can deduce the differential acceleration induced by this mass, which is proportional to G. Since each interferometer experiences the same platform vibrations, this approach is potentially much more sensitive than traditional methods used to determine G, for example those based on torsion balances, because the vibrations cancel out. The first experiment of this kind was performed at Stanford University by Mark Kasevich's team in the early 2000s, which led to a relative uncertainty of just 5×10^{-3}. Another team at Firenze University in Italy expects to achieve a relative uncertainty of 1×10^{-4} soon. (The smallest relative uncertainty achieved with a torsion balance experiment is about 1×10^{-5}.)

Atom interferometers also have an important role to play in redefining the kilogram – the last SI unit to be defined by an artefact. In an effort to redefine the kilogram in terms of only fundamental constants, thus bringing it in line with other SI units such as the metre and the second, researchers have turned to an instrument known as a watt balance (see *Physics World* May 2004 pp31–35). In such a device the gravitational force on an object (i.e. which has a nominal mass of 1 kg) is balanced with the electromagnetic force produced by a current-carrying coil in a magnetic field. Once the balancing condition is met, the weight of the object can be determined in terms of the Josephson effect and the quantum Hall effect, which relate it back to Planck's constant and the charge on the electron.

To then find out the object's mass, it is necessary to know the local value of g – the acceleration due to gravity – very accurately, and this is where atom interferometry comes in. As part of the a watt-balance project being undertaken at the Laboratoire National de Métrologie et d'Essais in France, for example, the present authors are developing an atom interferometer in which cold rubidium atoms are dropped from a magneto-optical trap and then made to interact with three laser pulses that cause the wave packets to split, converge and then recombine during their fall. Since the atomic trajectories and the direction of propagation of the beam splitters both lie along the vertical direction, the interferometer is only sensitive to accelerations, not rotations, and the set-up should yield a relative uncertainty of 1×10^{-9}.

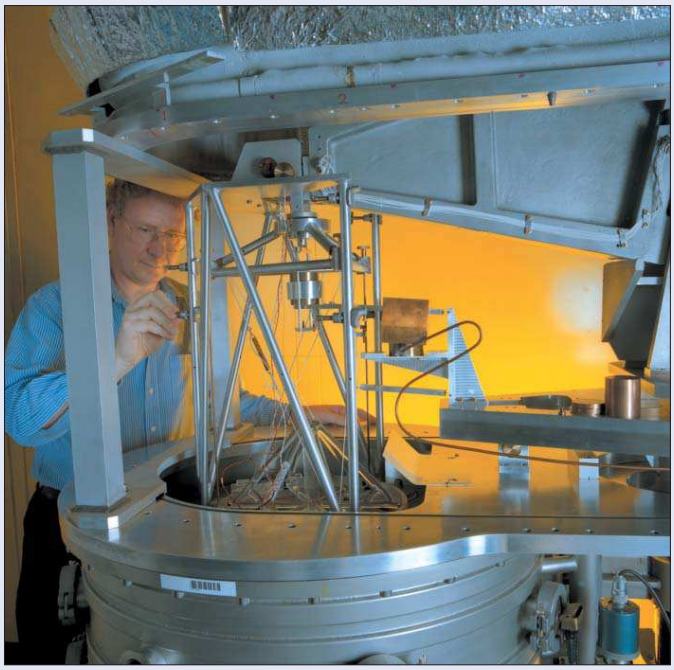

NPL

Well balanced Using a watt balance, like this one at the National Physical Laboratory in the UK, requires a precise knowledge of the local acceleration due to gravity.

Such a high accuracy is possible because the main source of uncertainty in measurements of g is vibrations induced by human activity, and atomic interferometers perform considerably better in noisy environments than conventional absolute gravimeters based on optical interferometers. Firstly, they have a high repetition rate (4 Hz), which allows better averaging of the vibrational noise. Secondly, atom interferometers are more stable over time than conventional instruments, so they can provide the continuous measurements that are needed for the watt-balance project. These attributes also make gravimeters based on atomic interferometers useful for applications in geophysics, where changes in Earth's gravitational field in different regions over time can help determine the structure of the planet.

output signal of the interferometer (say phase or voltage) with the actual quantity of interest, e.g. acceleration. In conventional optical gyroscopes, thermal instabilities cause the scale factor to change over time, which means the devices have to be frequently recalibrated. Such recalibration is not a major problem for aircraft but it could be for submarines and spacecraft, which must spend long periods of time out of contact with the outside world.

However, several technical challenges still need to be overcome before inertial sensors based on atom interferometry can equip actual planes, spacecraft or submarines. Current atom interferometers are several cubic metres in volume, so the technology needs to be made significantly more compact and able to operate in noisy environments. We also need to develop robust optical components, such as lasers and optical fibres, so that devices are able to run for several years without major maintenance.

A few years ago Mark Kasevich, now at Stanford University, began development work aimed at achieving onboard instruments. Kasevich is working with the US military and has a large team of researchers and a budget of millions of dollars to develop a practical device that can be used in military planes and submarines. The French aerospace lab ONERA has also now started similar work.

Much of this research is secret, so it is difficult to say what progress has been made so far. But it is hoped that we will have operational matter-wave interferometer systems within the next decade. We will then have a system that turns one of the most intangible and bizarre concepts in physics – the wave-like behaviour of matter – into one of the most useful. ■

More about: Atom interferometry

B Canuel *et al.* 2006 6-axis inertial sensor using cold-atom interferometry *Phys. Rev. Lett.* **97** 010402
J B Fixler *et al.* 2007 Atom interferometer measurement of the Newtonian constant of gravity *Science* **315** 74–77
A Miffre *et al.* 2006 Atom interferometry *Phys. Scr.* **74** C15–C23
www.ice-space.fr

Appl. Phys. B 84, 673–681 (2006)
DOI: 10.1007/s00340-006-2395-7

Applied Physics B
Lasers and Optics

I.C.E.: a transportable atomic inertial sensor for test in microgravity

R.A. NYMAN[1,✉]
G. VAROQUAUX[1]
F. LIENHART[2]
D. CHAMBON[3]
S. BOUSSEN[2]
J.-F. CLÉMENT[1]
T. MÜLLER[4]
G. SANTARELLI[3]
F. PEREIRA DOS SANTOS[3]
A. CLAIRON[3]
A. BRESSON[2]
A. LANDRAGIN[3]
P. BOUYER[1]

[1] Laboratoire Charles Fabry de l'Institut d'Optique, Centre National de la Recherche Scientifique et Université Paris Sud 11, Bât. 503, Campus Universitaire d'Orsay, 91403 Orsay Cedex, France
[2] Office National d'Etude et de Recherches Aérospatiales, Chemin de la Hunière, 91761 Palaiseau, France
[3] LNE-SYRTE, UMR8630, Observatoire de Paris, 61 avenue de l'Observatoire, 75014 Paris, France
[4] Institute for Quantum Optics, University of Hannover, Welfengarten 1, 30167 Hannover, Germany

Received: 2 May 2006/Revised version: 15 June 2006
Published online: 16 August 2006 •

ABSTRACT We present the construction of an atom interferometer for inertial sensing in microgravity, as part of the I.C.E. (Interférométrie Cohérente pour l'Espace) collaboration. On-board laser systems have been developed based on fibre-optic components, which are insensitive to mechanical vibrations and acoustic noise, have sub-MHz line width, and remain frequency stabilised for weeks at a time. A compact, transportable vacuum system has been built, and used for laser cooling and magneto-optical trapping. We will use a mixture of quantum degenerate gases, bosonic ^{87}Rb and fermionic ^{40}K, in order to find the optimal conditions for precision and sensitivity of inertial measurements. Microgravity will be realised in parabolic flights lasting up to 20 s in an Airbus. We investigate the experimental limits of our apparatus, and show that the factors limiting the sensitivity of a long-interrogation-time atomic inertial sensor are the phase noise in reference-frequency generation for Raman-pulse atomic beam splitters and acceleration fluctuations during free fall.

PACS 06.30.Gv; 39.20.+q; 42.60.By

1 Introduction

Intense research effort has focussed on the study of degenerate quantum gases and macroscopic matter waves since their first observation in 1995. Atom interferometers benefit from the use of trapped ultra-cold atomic gases, gaining good signal-to-noise ratios due to the high atomic densities and the coherence required for the visibility of interference patterns due to the low temperatures [1]. The sensitivity limit of an interferometric measurement scales with the square root of the number of detected particles; it also increases with the interrogation time, the time between beam splitters. For atom interferometers, during the interrogation time, the atoms are usually allowed to evolve free of external potentials, to minimise the effects of inhomogeneities. The interrogation time is thus limited both by the free fall of the atomic cloud, requiring tall vacuum chambers, and by its free expansion, demanding extra-sensitive detection systems for extremely dilute clouds. The use of ultra-cold gases alleviates the limits due to expansion of the cloud, and current experiments are limited by the achievable free-fall times.

In conceiving the next generation of extreme-precision atom interferometers, there is much to be gained by performing experiments in microgravity [2, 3]. Free-fall heights of more than 100 m, corresponding to durations of 5 s or more, are available either in a drop tower (e.g. ZARM Bremen, Germany) or in a parabolic flight in an aeroplane. Laboratory experiments are limited to about 300 ms of free fall. The sensitivity of an interferometric accelerometer increases quadratically with time, and thus one can expect to gain more than two orders of magnitude with a transportable, drop-compatible device.

There remain questions over the best method to perform atom interferometry. Bosons suffer from interaction shifts [4] leading to systematic errors such as the clock shift, a problem not apparent with ultra-cold fermions [5, 6]. However, degenerate fermions have an intrinsically broad momentum distribution due to Pauli blocking, limiting the visibility of interference patterns. Furthermore, to achieve quantum degeneracy, fermions must be cooled using a buffer gas, typically an ultra-cold gas of bosons, thus complicating experiments using fermions. Pairs of fermions (molecules or Cooper pairs [7]) can be created by applying homogeneous magnetic fields (Feshbach resonances [8, 9]), offering yet more possible candidate species for atom interferometers.

A further bonus in a free-fall environment is the possibility of using weaker confining forces for the atoms, since gravity need not be compensated with additional levitation forces [10]. Temperatures achieved by evaporative cooling and adiabatic expansion are lowered as the trapping potential is reduced. Not only can the sensitivity of an interferometric measurement benefit, but also new phases of matter may be observed if the kinetic energy can be made smaller than the interatomic potential. A reduced-gravity environment will permit study of new physical phenomena, e.g. spin dynamics and magnetic ordering (see for example [11] and references therein).

✉ Fax: +33 (0) 1 69 35 87 00, E-mail: robert.nyman@institutoptique.fr

This article presents our design for a transportable, boson–fermion mixture, atom interferometer, compatible with a parabolic flight in an aeroplane. We describe our laser systems: a temporary bench for ground-based development, and the rack-mounted transportable system, based on frequency-doubled telecommunications lasers. We then explain our vacuum system and optics for atomic manipulation, and the accompanying support structure. Finally, we describe the Raman-transition-based atom-interferometric accelerometer. We characterise the expected sensitivity of our interferometer, and show that the limits to in-flight performance are vibrations (acceleration fluctuations) and phase noise on the Raman laser frequency difference.

1.1 *Overview of the experiment*

The central components of this project are the atomic-physics vacuum system, the optics, and their supports. The atomic manipulation starts with alkali-metal vapour dispensers for rubidium and potassium [12]. A slow jet of atoms is sent from the collection chamber by a dual-species, two-dimensional, magneto-optical trap (2D MOT) to the trapping chamber, for collection and cooling in a three-dimensional magneto-optical trap (3D MOT). Atoms are then transferred to a conservative, far-off-resonance optical-dipole trap (FORT) for further cooling towards degeneracy. The sample will then be ready for coherent manipulation in an atom interferometer. Raman two-photon transitions will be used as atomic beam splitters and mirrors. Three-pulse sequences ($\pi/2 - \pi - \pi/2$) will be used for accelerometry.

All light for the experiment arrives by optical fibres, making the laser sources independent of the vacuum system. Transportable fibre laser sources for laser cooling and trapping have been fabricated with the required frequency stability. The techniques for mechanically stable power distribution by free-space fibre couplers function according to specifications. The vacuum chamber is compatible with the constraints of microgravity in an Airbus parabolic flight. Such a flight permits total interrogation times up to 7 s giving a potential sensitivity of better than 10^{-9} m s^{-2} per shot, limited by phase noise on the frequency reference for the Raman transitions, or by residual acceleration noise.

2 Laser systems

2.1 *Ground-based laser diodes for potassium and rubidium cooling*

Our test laser system is not intended to fly, but nonetheless represents several technical achievements, detailed in [13]. All of the lasers and optical amplifiers for trapping and cooling light are built around commercial semiconductor elements (Eagleyard) with home-made mounts and drive electronics. Semiconductor technology is one of the candidates for atomic-physics lasers in microgravity experiments: the chips are small, lightweight, and robust, with low power consumption.

Extended-cavity grating-diode lasers (based on a design by Arnold et al. [14]) are locked to atomic transitions (the hyperfine structure of the D2 lines of ^{87}Rb and ^{39}K, as appropriate), frequency shifted by acousto-optical modulators, injected into tapered amplifiers, and then input to the optical fibres. We produce more than 200 mW of useful light (out of the fibres) for trapping and cooling each species for both the 2D MOT and the 3D MOT.

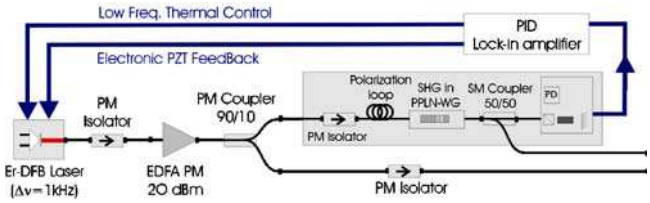

FIGURE 1 Transportable laser set-up schematic. A double-loop feedback system is used for frequency control: the first loop returns a saturated-absorption signal to the piezoelectric transducer; the second loop compensates thermal drifts of the fibre laser when the error signal of the first loop becomes large

One major difficulty was in making the master oscillator at 766.5 nm (potassium D2 transition, wavelength in air). Semiconductor lasers at 780 nm (rubidium D2 line) have been available for some time [15], but are less easily found at short wavelengths. We pulled a 780-nm diode to 766.5 nm using very weak feedback, by anti-reflection coating the output face, and ensuring low reflectance from the grating (which was optimised for UV, not visible light). Decreasing the feedback increases the threshold current, which increases the number of carriers in the active region, increasing the energy of the lasing transitions, and thus giving gain at relatively short wavelengths. The tapered amplifiers we use work equally well for the two wavelengths.

2.2 *Continuous-wave fibre-laser source at* 780 nm *for rubidium cooling*

An entirely pigtailed laser source is particularly appropriate in our case as it does not suffer from misalignments due to environmental vibrations. Moreover, telecommunications laser sources in the C-band (1530–1570 nm) have narrow line widths ranging from less than 1 MHz for laser diodes, down to a few kHz for erbium-doped fibre lasers. By second-harmonic generation (SHG) in a nonlinear crystal, these 1.56-μm sources can be converted to 780-nm sources [16–18]. Such devices avoid the need for extended cavities, as their line widths are sufficiently narrow to satisfy the requirements of laser cooling.

Our laser set-up is sketched in Fig. 1. A 1560-nm erbium-doped fibre laser is amplified by a 500-mW polarisation-maintaining (PM) erbium-doped fibre amplifier (EDFA). A 90/10 PM fibre coupler directs 10% of the pump power to a pigtailed output. 90% of the light is then sent into a periodically poled lithium-niobate waveguide (PPLN-WG). This crystal is pigtailed on both sides with single-mode PM fibres. The input fibre is installed in a polarisation loop system in order to align the electric field with principal axes of the crystal. A fibre coupler which is monomode at 780 nm filters pump light after the crystal and sends half of the 780-nm light into a saturated-absorption spectroscopy device for frequency servo control. The other half is the frequency-stabilised pigtailed output. The whole device, including the frequency-control electronics, was implemented in a rack for ease of transport. Typical output from the first-generation device was 500 μW of 780-nm light, with more than 86 dB attenuation of

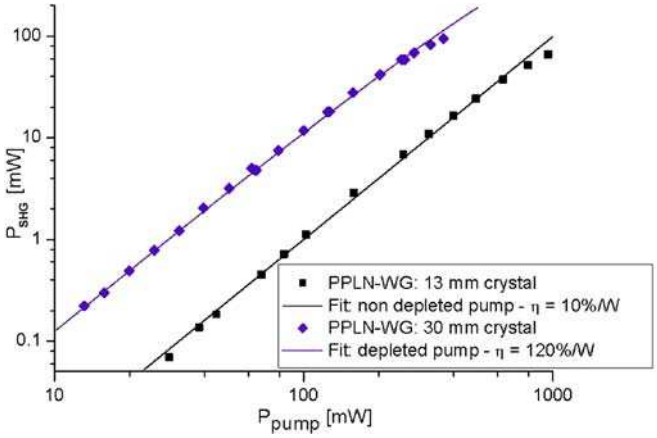

FIGURE 2 Second-harmonic generation as a function of pump power. Two crystals (13 mm, 30 mm) were tested. Fits to non-depleted pump (13-mm crystal, 10%/W efficiency, *squares*) and depleted pump (30-mm crystal, 120%/W, *lozenges*) are shown

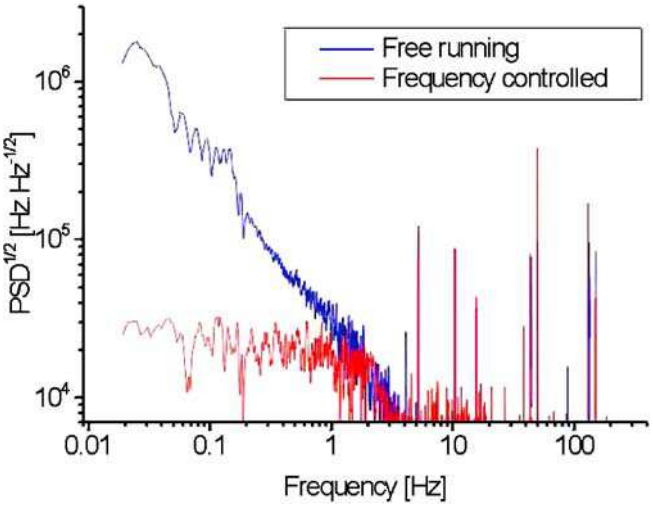

FIGURE 3 Power spectral density of the laser frequency noise in open- and closed-loop configurations. The data are derived from the error signal of the frequency-control system

1560-nm light after 3 m of monomode fibre. A more recent version (> 50 mW) has been used to power a magneto-optical trap.

Two PPLN-WGs from HC-Photonics were tested, with poling periods appropriate for SHG at 780 nm. They have the same quasi-phase-matching temperature of 63 °C. The first is 13-mm long, doped with 1% MgO, and is used in our laser source. The second is 30-mm long and doped with 5% MgO. Figure 2 gives the output power as a function of the pump power. The 13-mm-long crystal has a fibre-to-fibre efficiency of 10%/W. The fit curve corresponds to the non-depleted pump regime. Photorefractive effects appear when there is more than 10 mW of 780-nm light. In practice, the laser is run with 100-mW pump power. Power fluctuations in this crystal are due to two phenomena: first, the input fibre does not maintain polarisation, and polarisation fluctuations lead to a variation of the output power. Secondly, the output fibre of the crystal is not single mode at 780 nm. Thus, the power distribution in the fundamental mode varies with time, leading to power fluctuations when the crystal is pigtailed to a single-mode fibre at 780 nm. The second crystal has a fibre-to-fibre efficiency of 120%/W for low pump power. The fit curve corresponds to a depleted regime. The photorefractive threshold is estimated to be around 60 mW of the second harmonic. The input fibre is not polarisation maintaining, leading to output power drifts, but the output fibre is PM and single mode at 780 nm, which greatly reduces power fluctuations.

2.2.1 Frequency stabilisation. A Doppler-free saturated-absorption spectroscopy system with no polarisation-sensitive elements provides the frequency reference signal. The frequency stability of the laser is assured by locking to a peak in the Rb spectrum. We drive oscillations of the laser frequency of amplitude a few 100 kHz by modulating the piezoelectric element of the fibre Bragg grating of the pump laser. The modulation frequency is 1.3 kHz, permitting long-term drifts to be compensated without significantly broadening the laser line width. The spectroscopic signal is demodulated by phase-sensitive detection and fed back to the piezoelectric element. Figure 3 presents the spectral density of noise with and without frequency stabilisation. Noise is attenuated up to 1.6 Hz, a frequency corresponding to the low-pass-filter bandwidth of the demodulation. Points below 7 kHz/$\sqrt{\text{Hz}}$ are not represented because they are below the measurement noise. The r.m.s. frequency excursion in the band 0–20 Hz is less than 200 kHz.

The laser remains frequency locked even with strong mechanical disturbances (hand claps, knocks on the rack, and so on), but cannot withstand even small variations of the ambient temperature. The fibre source at 1560 nm, though temperature controlled, suffers frequency drifts due to temperature changes of the fibre. Small fluctuations are compensated by the frequency-stabilisation loop but long-term drifts are beyond the range of the piezoelectric element, so the laser jumps off lock. We developed an integrated circuit based on a PIC 16F84 micro-controller: the output voltage of the regulator is monitored by the micro-controller and, when fixed boundaries are exceeded, the set temperature of the laser controller is adjusted. This additional loop prevents the frequency control from unlocking without modifying the frequency properties of the source. The laser typically stays locked for three weeks.

2.3 *Fibre power splitters*

The optical bench and the vacuum chamber are not rigidly connected to each other, and laser light is transported to the vacuum chamber using optical fibres. Stability of trapping and coherent atom manipulation are assured by using only polarisation-maintaining fibres. Six trapping and cooling laser beams are needed for the 3D MOT and five for the 2D MOT, with relative power stability better than a few percent. We have developed fibre beam splitters based on polarising cubes and half-wave plates with one input fibre and the relevant number of output fibres. The stability of the beam splitters has been tested by measuring the ratio of output powers between different outputs as a function of time. Fluctuations are negligible on short time scales (less than 10^{-4} relative intensity over 1 s), and very small over typical periods of ex-

perimental operation (less than 1% over a day). Even over months, drifts in power distribution are only a few percent, which is sufficient for this experiment.

3 Mechanical and vacuum systems

The mechanical construction of the apparatus is critical to any free-fall experiment. Atomic-physics experiments require heavy vacuum systems and carefully aligned optics. Our design is based around a cuboidal frame of foam-damped hollow bars with one face being a vibration-damped optical breadboard: see Figs. 4 and 5. The outside dimensions are 1.2 m × 0.9 m × 0.9 m, and the total weight of the final system is estimated to be 400 kg (excluding power supplies, lasers, control electronics, and air and water flow). The frame provides support for the vacuum system and optics, which are positioned independently of one another. The heavy parts of the vacuum system are rigged to the frame using steel chains and high-performance polymer slings under tension, adjusted using turnbuckles, most of the equipment being available as standard components from recreational sailing or climbing suppliers. The hollow bars have precisely positioned grooves which permit optical elements to be rigidly fixed (bolted and glued) almost anywhere in the volume within the frame. An adaptation for transportability will be to enclose the frame in a box, including acoustic and magnetic shielding, temperature control, and air overpressure (dust exclusion), as well as ensuring safety in the presence of the high-power lasers.

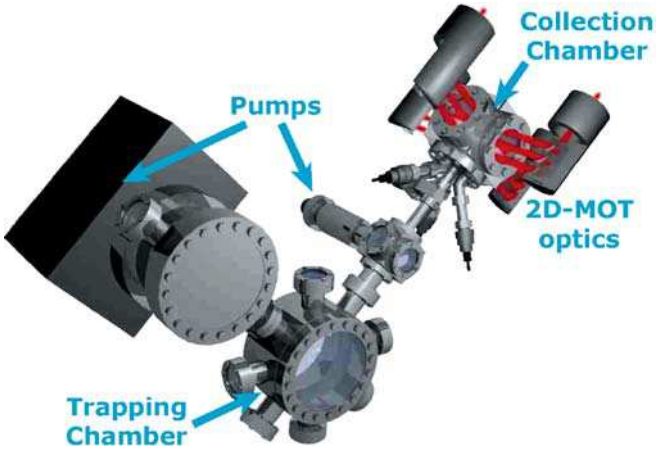

FIGURE 4 Artist's impression of the vacuum system. Atoms are transferred from the collection chamber, using a 2D MOT, to the trapping chamber, where they are collected in a 3D MOT. The trapping chamber has large optical accesses for the 3D MOT, optical-dipole trap (FORT), imaging, and interferometry. There is a getter pump between the two chambers to ensure a large pressure difference. The other pump is a combined ion pump–titanium sublimation pump

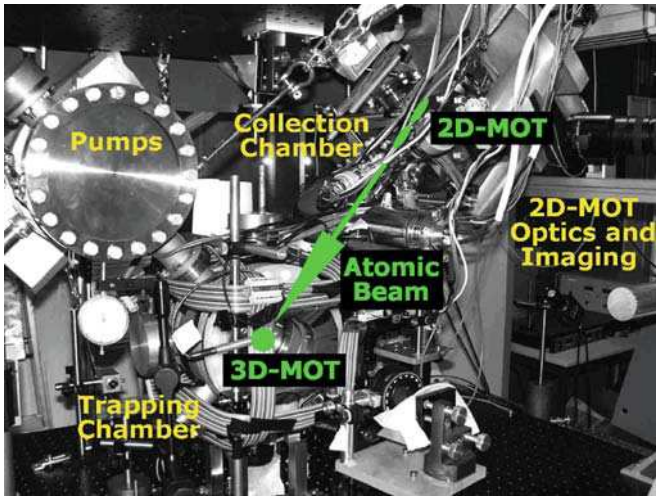

FIGURE 5 Photograph of the vacuum chamber, the support structure, and the optics for magneto-optical traps

The vacuum chamber has three main parts: the collection chamber (for the 2D MOT), the trapping chamber (for the 3D MOT and the FORT), and the pumps (combined ion pump and titanium sublimation pump). Between the collection and trapping chambers there is an orifice and a getter pump, allowing for a high differential pressure, permitting rapid collection by the 2D MOT (pressure pulsed up to 10^{-6} mbar) but low trap losses in the 3D MOT and FORT (background pressure below 10^{-10} mbar). The magnetic coils for the 2D MOT are under vacuum, and consume just 5 W of electrical power.

The main chamber has two very large viewports as well as seven side windows (and one entry for the atoms from the 2D MOT). Thus, there is plenty of optical access for the 3D MOT, the FORT, imaging, and interferometry. To preserve this optical access, the magnetic coils are outside the chamber, although this markedly increases their weight and power consumption.

To avoid atomic heating due to vibrations in the FORT optics, or measurement uncertainties due to vibrations of the imaging system, the trapping chamber is as close to the breadboard as possible. For laboratory tests, the breadboard is lowest, and the 2D MOT is at 45° to the vertical, leaving the vertical axis available for addition of light for interferometry, e.g. a standing light wave. Around the main chamber, large electromagnet coils in Helmholtz configuration will be added, to produce homogeneous, stable fields up to 0.12 T (1200 G), or gradients up to 0.6 T/m (60 G/cm).

3.1 *2D MOT*

The 2D MOT is becoming a common source of cold atoms in two-chamber atomic-physics experiments [19], and is particularly efficient for mixtures of ^{40}K and ^{87}Rb [20], if isotopically enriched dispensers are used. Briefly, a 2D MOT has four sets of beams (two mutually orthogonal, counter-propagating pairs) transverse to the axis of the output jet of atoms, and a cylindrical-quadrupole magnetic field generated by elongated electromagnet pairs (one pair, or two orthogonal pairs). Atoms are cooled transverse to the axis, as well as collimated. They then pass through an orifice. Implicitly, only slow atoms spend enough time in the 2D MOT to be collimated, so the output jet is longitudinally slow. The number of atoms in the jet can be increased by the addition of the push beam, running parallel to the jet: a 2D MOT$^+$. Typically the output jet has a mean velocity below 30 m s^{-1}, with up to 10^{10} at s^{-1} of ^{87}Rb and 10^8 at s^{-1} of ^{40}K.

Our design uses 40 mW per species for each of the four transverse beams, each divided into two zones of about 20 mm using non-polarising beam-splitter cubes, corresponding to about three times the saturation intensity for the trapping

transitions. The push beam uses 10 mW of power, and is about 6 mm in diameter. Each beam comes from an individual polarisation-maintaining optical fibre, with the light at 766.5 nm and 780 nm being superimposed on entry to the fibres. The 2D MOT is seen as two bright lines of fluorescence in the collection chamber.

At the time of writing we do not have much quantitative data for the performance of our ^{87}Rb 2D MOT. One interesting test we have performed is spectroscopy of the confined cloud, using a narrow probe beam parallel to the desired output jet (replacing the push beam): see Fig. 6. We detect a significant number of atoms in the 2D MOT with velocities at or below 20 m s^{-1} (the output jet should have a similar velocity distribution). More sensitive spectroscopy is difficult, since the probe beam must be smaller than the transverse dimension of the atom cloud (less than 0.5 mm) and much less than saturation intensity (1.6 mW cm^{-2}), so as not to excessively perturb the atoms. We used a lock-in detection (modulation–demodulation–integration) method, averaging over many spectra. A saturated-absorption spectroscopy signal was used for calibration. We have not yet tested a ^{39}K or ^{40}K 2D MOT.

3.2 *3D MOT and optical-dipole trap*

The atomic jet from the 2D MOT is captured by the 3D MOT in the trapping chamber. We have observed that the transfer and capture of atoms is significantly increased by the addition of the push beam [21]. The 3D MOT uses one polarisation-maintaining fibre input per species. Beams are superimposed and split into six arms (on a small optical breadboard fixed near one face of the frame) for the three, orthogonal, counter-propagating beam pairs. Once enough atoms are collected in the 3D MOT, the 2D MOT is to be turned off, and the 3D MOT optimised for transfer to the FORT.

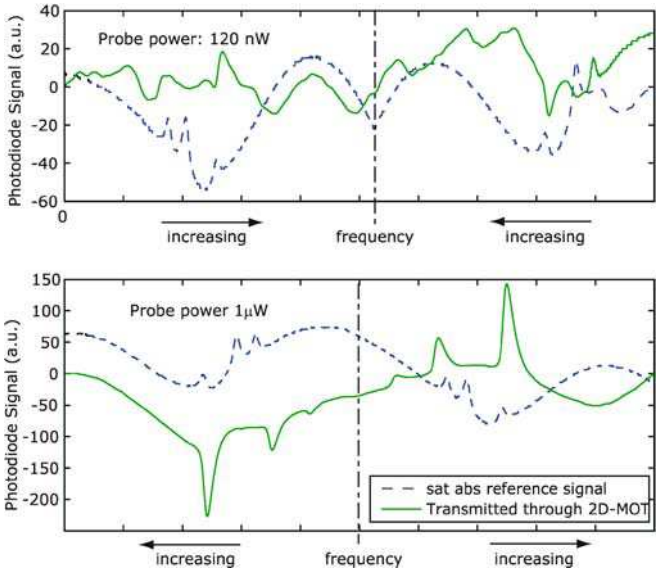

FIGURE 6 Absorption spectrum of atoms in the 2D MOT in the collection chamber (*green solid line*) and a reference saturated-absorption spectroscopy signal (*blue dotted line*). 120 nW corresponds to about $I_{sat}/15$; 1 μW is equivalent to $I_{sat}/2$. (I_{sat} is the saturation intensity.) Features with line widths around 20 MHz (equivalent to Doppler broadening of atoms moving at 20 m s^{-1}) are seen for the lowest probe powers, indicating a large density of slow atoms in the 2D MOT. For higher probe powers, resonant light destroys the trapping in about 2 ms, so the velocity distribution is not resolved. Note that the inversion of absorption peaks is an artefact of the modulation–demodulation detection method

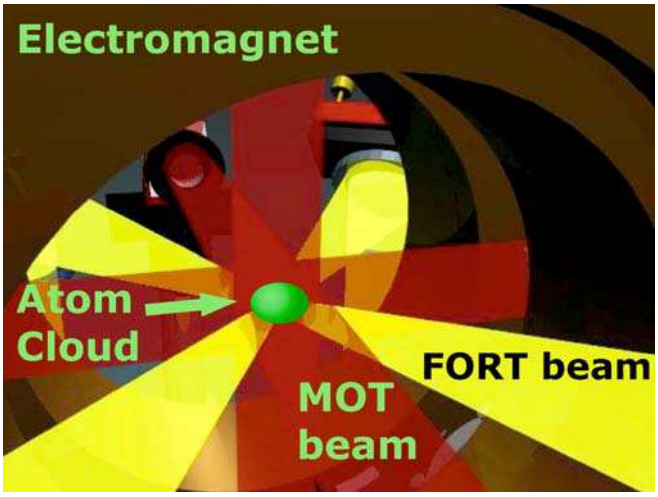

FIGURE 7 Artist's impression of the 3D MOT (*dark red beams and the electromagnets*) and the far-off-resonance optical-dipole trap (*pale yellow beams*)

The FORT will consist of two nearly orthogonal (70°) beams making a crossed dipole trap using 50 W of light at 1565 nm: see Fig. 7. We will have rapid control over intensity using an electro-optical modulator, and beam size using a mechanical zoom, after the design of Kinoshita et al. [22]. Optimisation of transfer from the 3D MOT to the FORT, and the subsequent evaporative cooling, will require experiments. Strong, homogeneous, magnetic fields will be used to control interspecies interactions via Feshbach resonances [8, 9], to expedite sympathetic cooling of ^{40}K by ^{87}Rb.

We can expect to load the 3D MOT during less than 5 s, and then cool to degeneracy in the optical-dipole trap in around 3–10 s. Thus, we will be able to prepare a sample for interferometry in less than the free-fall time of a parabolic flight (around 20 s).

4 Performance

4.1 *Coherent Raman-pulse interferometer*

The acceleration measurement is based on an atomic interferometer using light pulses as beam splitters [23, 24], a technique which has the demonstrated best performance of all atomic inertial sensing techniques. Three Raman pulses ($\pi/2 - \pi - \pi/2$) generate respectively the beam splitter, the mirror, and the beam re-combiner of the atom interferometer. Two counter-propagating lasers (Raman lasers) drive coherent transitions between the two hyperfine ground states of the alkaline atoms. Two partial wave-packets are created with differing momenta, due to the absorption and stimulated emission of photons in the Raman lasers. The differences in momenta correspond to velocity differences of 1.2 cm s^{-1} for ^{87}Rb and 2.6 cm s^{-1} for ^{40}K, for Raman lasers tuned close to the D2 lines. Finally, detection by fluorescence gives a measurement of the transition probability from one hyperfine level to the other, given by $P = 1/2(1 - \cos(\Phi))$, where Φ is the in-

terferometric phase difference. It can be shown [25] that the interferometric phase difference depends only on the phase difference between the Raman lasers at the classical position of the centre of the atomic wave-packets at the time of the pulses. In the case of an experiment in free fall, with an initial atomic velocity of zero, the interferometric phase depends only on the average relative acceleration of the experimental apparatus with respect to the centre of mass of the free-falling atoms, taken along the direction of propagation of the Raman lasers. We neglect here the effects of gradients of gravity on expanding and separating wave-packets, which cause small changes to the final fringe visibility.

As the measurement is performed in the time domain with pulses of finite duration $\tau_R - 2\tau_R - \tau_R$ separated by a free evolution time T, it is also sensitive to fluctuations of the relative phase of the Raman lasers between pulses. Moreover, as the measurement is not continuous but has dead time, the sensitivity of the interferometer is limited by an aliasing effect similar to the Dick effect in atomic clocks [26]. Thus, the sensitivity of the interferometer also depends on vibrations and on the phase noise on the beat note between the Raman lasers at multiples of the cycling frequency T_c. The effects of these noise sources are calculated [27] using the sensitivity function which gives the influence of the fluctuations of the Raman phase on the transition probability, and thus on the interferometric phase.

4.2 *Influence of phase noise*

The sensitivity of the interferometer can be characterised by the Allan variance of the interferometric phase fluctuations, $\sigma^2(\tau)$, defined by

$$\sigma_\Phi^2(\tau) = \frac{1}{2}\left\langle \left(\delta\bar{\Phi}_{k+1} - \delta\bar{\Phi}_k\right)^2 \right\rangle = \frac{1}{2}\lim_{n\to\infty}\left\{\frac{1}{n}\sum_{k=1}^{n}\left(\delta\bar{\Phi}_{k+1} - \delta\bar{\Phi}_k\right)^2\right\}, \quad (1)$$

where $\delta\Phi$ is the fluctuation of the phase measured at the output of the interferometer and $\delta\bar{\Phi}_k$ is the average value of $\delta\Phi$ over the interval from t_k to t_{k+1} (of duration τ). For an interferometer operated repeatedly at a rate $f_c = 1/T_c$, τ is a multiple of T_c: $\tau = mT_c$.

When evaluating the stability of the interferometric phase Φ, one should take into account the fact that the measurement is pulsed. The sensitivity of the interferometer is limited by the phase noise at multiples of the cycling frequency weighted by the Fourier components of the transfer function. For large averaging times ($\tau \gg T_c$), the Allan variance of the interferometric phase is given by

$$\sigma_\Phi^2(\tau) = \frac{1}{\tau}\sum_{n=1}^{\infty}|H(2\pi n f_c)|^2 S_\phi(2\pi n f_c), \quad (2)$$

where S_ϕ is the spectral power density of the phase difference between the Raman lasers.

Assuming square Raman pulses, the transfer function $H(f)$ of the Raman laser phase fluctuations to the interferometric phase is given by [27]

$$|H(f)|^2 = \left| -\frac{4\Omega\omega}{\omega^2 - \Omega^2}\sin\left(\omega\frac{T+2\tau_R}{2}\right) \times \left(\sin\left(\omega\frac{T+2\tau_R}{2}\right) + \frac{\Omega}{\omega}\sin\left(\omega\frac{T}{2}\right)\right)\right|^2, \quad (3)$$

where $\omega = 2\pi f$ and Ω is the Rabi oscillation frequency, with the Raman π pulses having the ideal transfer efficiency: $\Omega = \pi/2\tau_R$. The transfer function is characterised by zeroes at multiples of $1/(T+2\tau_R)$ and decreases as $1/\Omega^2$ for frequencies higher than the Rabi frequency, as illustrated in Fig. 8.

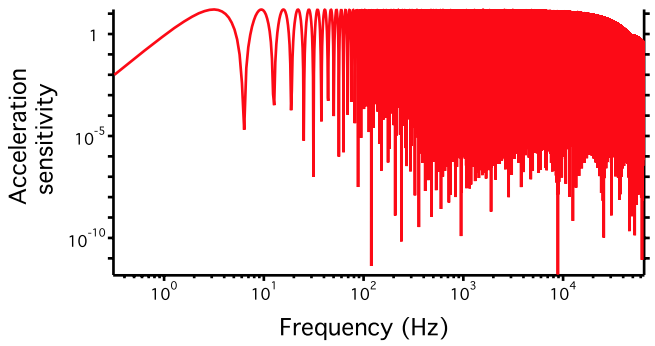

FIGURE 8 Transfer function from amplitude of phase fluctuations to interferometric phase. The curve has been calculated for $T = 0.5$ s between pulses, and pulse duration $\tau_R = 50\,\mu$s

For white phase noise S_ϕ^0, to first order in τ_R/T, the phase stability is given by

$$\sigma_\Phi^2(\tau) = \frac{\pi\Omega}{2}S_\phi^0\frac{T_c}{\tau}. \quad (4)$$

Thus, we see that the transfer function filters noise for frequencies greater than the Rabi frequency: the shorter the pulse duration τ_R, and thus the greater the Rabi frequency, the greater the interferometer noise. However, longer-duration pulses interact with fewer atoms (smaller velocity distributions) leading to a pulse duration around 10 µs. More quantitatively, a desired standard deviation of interferometer phase below 1 mrad per shot, with pulse duration $\tau_R = 10\,\mu$s, demands white phase noise of 4×10^{-12} rad^2/Hz or less.

4.3 *Generation of a stable microwave source for atom interferometry*

4.3.1 The 100-MHz *source oscillator.* The frequency difference between the Raman beams needs to be locked to a very stable microwave oscillator, whose frequency is close to the hyperfine transition frequency, $f_{MW} = 6.834$ GHz for ^{87}Rb and 1.286 GHz for ^{40}K. The reference frequency will be delivered by a frequency chain, which transposes a rf source (typically a quartz oscillator) into the microwave domain, retaining the low level of phase noise. With degradation-free transposition the phase noise power spectral density of the rf oscillator, of frequency f_{rf}, is multiplied by $(f_{MW}/f_{rf})^2$.

No single quartz oscillator fulfils the requirement of very low phase noise over a sufficiently large frequency range. We present in Fig. 9 the specifications of different high-stability quartz oscillators: a Premium 10 MHz-SC from Wenzel, a BVA OCXO 8607-L from Oscilloquartz, and a Premium

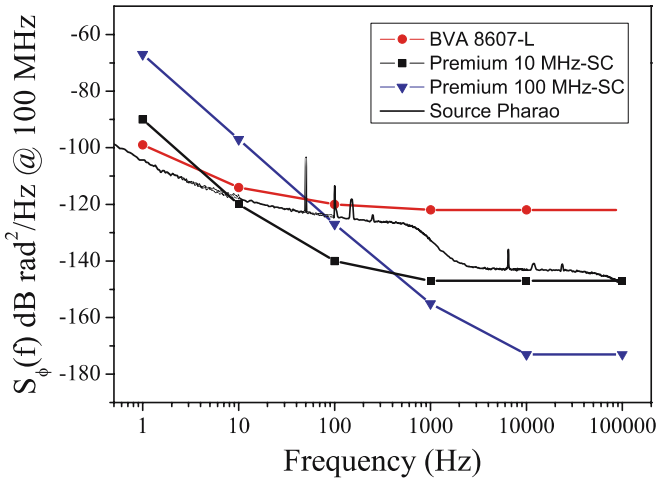

FIGURE 9 Specifications for the phase noise spectral power density of different quartz oscillators, transposed to 100 MHz. The phase noise of the source developed for the PHARAO project is also displayed as a *solid black line* (courtesy of CNES)

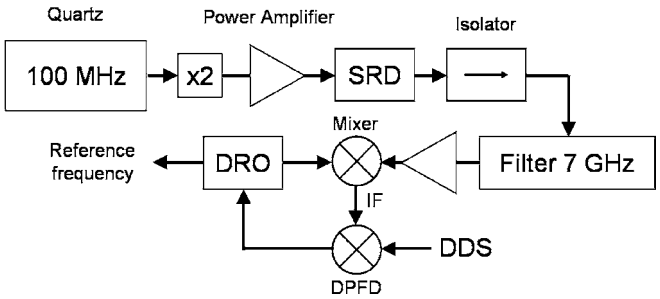

FIGURE 10 Synthesis of the microwave reference signal. SRD: step recovery diode, DDS: direct digital synthesis, DRO: dielectric resonator oscillator, DPFD: digital phase–frequency detector, IF: intermediate frequency

100 MHz-SC quartz from Wenzel. The phase noise spectral density is shown as transposed to 100 MHz, for fair comparison of the different oscillators.

The 100-MHz source we plan to develop for the I.C.E. project will be a combination of two phase-locked quartz oscillators: one at 100 MHz locked onto one of the above-mentioned high-stability 10-MHz reference oscillators. The desired bandwidth of the lock corresponds to the frequency below which the phase noise of the reference oscillator is lower than the noise of the 100-MHz oscillator.

The phase noise properties of such a combined source can be seen in Fig. 10, where we also show (solid line) the performance of the 100-MHz source developed by THALES for the PHARAO space clock project. This combined source has been optimised for minimal phase noise at low frequency, where it reaches a level of noise lower than any commercially available quartz oscillator. An atomic clock is indeed mostly limited by low-frequency noise, so the requirements on the level of phase noise at higher frequency ($f > 1$ kHz) are less stringent than the requirement for an atom interferometer. A medium-performance 100-MHz oscillator is thus sufficient.

Using a simple model for the phase-lock loop, we calculated the phase noise spectral power density of the different combined sources we can make by locking the Premium 100 MHz-SC to the Premium 10 MHz-SC (source 1), the BVA (source 2), or even the PHARAO source (source 3). We then estimated the impact on the interferometer of the phase noise of the 100-MHz source, assuming that we are able to transpose the performance of the source at 6.8 GHz without degradation. The results presented in Table 1 were calculated using (2) for the Allan standard deviation of the interferometric phase fluctuations for the different configurations and various interferometer parameters.

For short interrogation times, such as $2T = 100$ ms (the maximum interrogation time possible when the experiment is tested on the ground), source 1 is best, whereas for long interrogation times, where the major contribution to the noise comes from the lowest frequencies (0.1–10 Hz), sources 2 and 3 are better.

We are currently using a source based on the design of source 1 for the gravimeter experiment at SYRTE [28]. Its performance is about 10% better than predicted, as the reference oscillator phase noise level is lower than the specifications. Considering that the interferometer is intended for a zero-g environment, we plan to build a source based on source 2.

We have assumed here that for any source, the phase noise below 1 Hz is accurately described as flicker noise, for which the spectral density scales as $S_\phi(f) = S_\phi(1\,\text{Hz})/f^3$. If the phase noise behaves as pure flicker noise over the whole frequency spectrum, the Allan standard deviation of the interferometer phase scales as T. We note that the observed behaviour of the gravimeter is consistent with Table 1.

The sensitivity of the accelerometer improves with the square of the interrogation time, T^2. For example, for $2T = 10$ s and $T_c = 15$ s, the phase noise of source 3 would limit the acceleration sensitivity of the interferometer to 4.6×10^{-11} m s^{-2} per shot for ^{87}Rb. As the hyperfine splitting of ^{40}K is five times smaller, the transposed phase noise is lower, and the measurement limit with ^{40}K is just 8.7×10^{-12} m s^{-2} per shot.

4.3.2 The frequency chain. The microwave signal is generated by multiplication of the 100-MHz source. We have developed a synthesis chain whose principle is shown in Fig. 10.

The source is first frequency doubled; the 200-MHz output is filtered, amplified to 27 dB m, and sent to a step recovery

TABLE 1 Contribution of the 100-MHz source phase noise to the interferometric phase fluctuations (σ_Φ) and to the acceleration sensitivity (σ_a). The calculation has been performed for a ^{87}Rb interferometer, for each of the three different sources assuming pulse duration $\tau_R = 10\,\mu$s. T_c is the cycle time for measurements, $2T$ is the total interrogation time (source 1: Premium; source 2: BVA; source 3: PHARAO)

T_c (s)	$2T$ (s)	Source 1 σ_Φ (T_c) (mrad)	Source 2 σ_Φ (T_c) (mrad)	Source 3 σ_Φ (mrad)	Best source σ_a (T_c) (m s^{-2}/shot)	Best source σ_a (1 s) (m s^{-2} Hz$^{-1/2}$)
0.25	0.1	1.2	3.5	2.2	3×10^{-8}	1.5×10^{-8}
10	2	22	8.8	4.7	1.1×10^{-9}	3.6×10^{-9}
10	5	55	20	10	9.9×10^{-11}	3.1×10^{-10}
15	10	110	37	19	4.7×10^{-11}	1.8×10^{-10}

diode (SRD), which generates a comb of frequencies, at multiples of 200 MHz. An isolator is placed after the SRD in order to prevent back reflections from damaging the SRD. The 35th harmonic (7 GHz) is then filtered (passed) using a passive filter. A dielectric resonator oscillator (DRO) is then phase locked onto the 7-GHz harmonic, with an adjustable offset frequency provided by direct digital synthesis. A tunable microwave source is thus generated which copies the phase noise of the 7-GHz tooth of the comb, within the bandwidth of the DRO phase-lock loop (about 500 kHz). The noise added by the frequency chain, including the DRO, was measured by mixing the outputs of two identical chains, with a common 100-MHz source; this noise is weaker than the noise due to the 100-MHz source.

The derived contribution to the phase noise of a ^{87}Rb interferometer is 0.6 mrad per shot for $\tau_R = 10\,\mu s$, $2T = 10\,s$, and $T_c = 15\,s$. The sensitivity limit due to the frequency synthesis is almost negligible for ^{40}K. In conclusion, the limit to sensitivity comes predominantly from the phase noise of the low-frequency oscillator. This contribution could be further reduced by the use of a cryogenic sapphire oscillator [29].

4.4 *Zero-gravity operation*

In this section, we estimate the possible limitations of the interferometer when used in a parabolic flight, by calculating the effect of residual acceleration in the Airbus (the proposed test vehicle for this experiment) during a parabola. During a typical flight the residual acceleration can be of the order of $0.1\,m\,s^{-2}$, with fluctuations of acceleration of the same order (Fig. 11).

To determine the influence of environmental noise on the acceleration measurement, one uses the transfer function $H(f)$ for the phase (3). Phase noise is equivalent to position noise, since the phase of the Raman beams is $\Delta\varphi = k_L \delta z$, where k_L is the wave-vector of the laser, Δz the position difference along the laser path, and position is the second integral of acceleration over time. The variance of the fluctuation of the phase shift at the output of the interferometer is

$$\sigma^2 = \left\langle |\delta(\Delta\varphi)|^2 \right\rangle = k_L^2 \int_0^\infty S_a(f)\,|H(f)|^2/\omega^4\,\mathrm{d}f\,, \qquad (5)$$

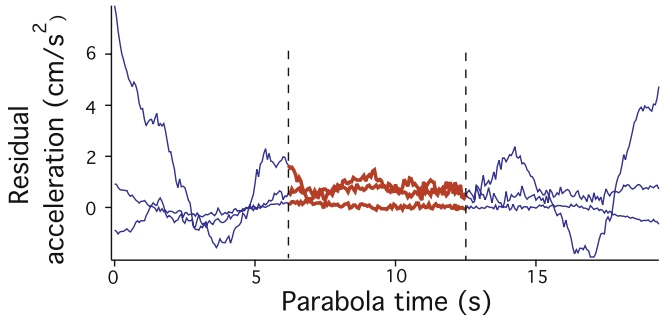

FIGURE 11 Typical residual acceleration along three orthogonal axes during a parabolic flight. The period when an experiment can be performed in conditions of very low residual acceleration is highlighted. During this period (from 7 to 14 s, between the *dotted lines*) the apparatus may be allowed to float freely

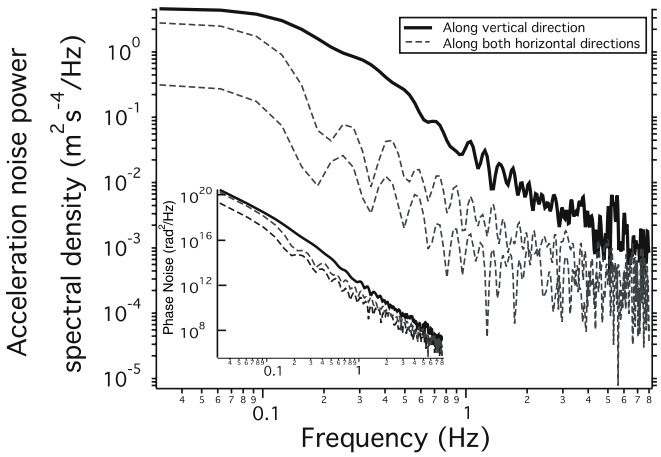

FIGURE 12 Typical acceleration noise power spectral density during the quiet part of the zero-gravity parabola. The three curves represent the noise along three directions (vertical being the noisiest). *Inset:* the corresponding phase noise which should be taken into account in the actual interferometer performance

where $S_a(f)$ is the acceleration noise power density, which corresponds to the Fourier transform of the temporal fluctuation.

From the residual acceleration curves for the Airbus, one can deduce the acceleration noise power in a bandwidth from 0.05 to 10 Hz, giving an estimation of the noise on the measurement of acceleration. A spectral acceleration–noise power density curve for the useful low-noise part of a parabola is shown in Fig. 12, and is converted to interferometric phase noise power spectral density by multiplication by $k_L^2|H|^2/\omega^4$.

The vibration noise results in a substantial residual phase noise, which is incompatible with the operation of the accelerometer. Calculating the variance of the fluctuations from (5), one obtains a variance $\sigma_\Phi \sim 10^7$ rad, which corresponds to acceleration noise $\sigma_a \sim 1\,m\,s^{-2}$, where $\sigma_\Phi = k_L \sigma_a T^2$ with $T = 1$ s. Thus, a vibration-isolation system will be required, reducing the noise by 60–80 dB around 0.5 Hz, about 40 dB at 50 Hz, and less than 10 dB beyond 1 kHz. The situation can be more favourable if one restricts the measurements to the middle of the parabola, as indicated in Fig. 11. By letting the apparatus fly almost free of mechanical constraints during the 7-s quiet period, one could expect to achieve such noise reduction.

5 Conclusions

We have shown our design for a transportable atom interferometer for parabolic flights in an Airbus. The device is built in two main parts, the laser systems and the atomic-physics chamber. We have made major technical advances: high-stability frequency synthesis for coherent atom manipulation, flight-compatible laser sources and fibre power splitters, as well as a rugged atomic-physics chamber.

We have analysed the possibility of using this device in the microgravity environment of a parabolic flight, as a high-precision accelerometer, taking advantage of the long interrogation times available to increase the sensitivity to acceleration. We conclude that the limits to measurement under such conditions come from acceleration fluctuations and from

phase noise in the frequency synthesis, and thus both aspects are to be minimised. Sensitivity of better than $10^{-9}\,\mathrm{m\,s^{-2}}$ per shot is predicted. Under such conditions our interferometers will limited not by the interrogation time, but by technical noise. Comparisons of acceleration measurements made using two different atomic species (K and Rb) are possible.

ACKNOWLEDGEMENTS The I.C.E. collaboration is funded by the CNES, as is RAN's fellowship. Further support comes from the European Union STREP consortium FINAQS.

REFERENCES

1 P.R. Bermann (eds.), *Atom Interferometry* (Academic, Boston, MA, 1997)
2 T. Sleator, P.R. Berman, B. Dubetsky, arXiv: physics/9905047 (1999)
3 K. Bongs, K. Sengstock, Rep. Prog. Phys. **67**, 907 (2004)
4 Y. Le Coq, J.A. Retter, S. Richard, A. Aspect, P. Bouyer, e-print cond-mat/0501520 (2005)
5 S. Gupta, Z. Hadzibabic, M.W. Zwierlein, C.A. Stan, K. Dieckmann, C.H. Schunck, E.G.M. van Kempen, B.J. Verhaar, W. Ketterle, Science **300**, 1723 (2003)
6 M.W. Zwierlein, Z. Hadzibabic, S. Gupta, W. Ketterle, Phys. Rev. Lett. **91**, 250 404 (2004)
7 C.A. Regal, M. Greiner, D.S. Jin, Phys. Rev. Lett. **92**, 040 403 (2004)
8 G. Ferrari, M. Inguscio, W. Jastrzebski, G. Modugno, G. Roati, Phys. Rev. Lett. **89**, 053 202 (2002)
9 F. Ferlaino, C. D'Errico, G. Roati, M. Zaccanti, M. Inguscio, G. Modugno, Phys. Rev. A **73**, 040 702 (2006)
10 A.E. Leanhardt, T.A. Pasquini, M. Saba, A. Schirotzek, Y. Shin, D. Kielpinski, D.E. Pritchard, W. Ketterle, Science **301**, 1513 (2003)
11 H. Schmaljohann, M. Erhard, J. Kronjäger, K. Sengstock, K. Bongs, Appl. Phys. B **79**, 1001 (2004)
12 Natural-abundance dispensers are available from SAES Getters. We are interested in the isotopes ^{87}Rb and ^{40}K, which are respectively 28% and 0.012% naturally abundant. We will be investing in isotopically enriched ^{40}K (about 5%) dispensers in the near future
13 R.A. Nyman, G. Varoquaux, B. Villier, D. Sacchet, F. Moron, Y. Le Coq, A. Aspect, P. Bouyer, Rev. Sci. Instrum. **77**, 033 105 (2006)
14 A.S. Arnold, J.S. Wilson, M.G. Boshier, Rev. Sci. Instrum. **69**, 1236 (1998)
15 C.E. Wieman, L. Hollberg, Rev. Sci. Instrum. **62**, 1 (1991)
16 V. Mahal, A. Arie, M.A. Arbore, M.M. Fejer, Opt. Lett. **21**, 1217 (1996)
17 R.J. Thompson, M. Tu, D.C. Aveline, N. Lundblad, L. Maleki, Opt. Express **11**, 1709 (2003)
18 J. Dingjan, B. Darquié, J. Beugnon, M.P.A. Jones, S. Bergamini, G. Messin, A. Browaeys, P. Grangier, Appl. Phys. B **82**, 47 (2006)
19 K. Dieckmann, R.J.C. Spreeuw, M. Wiedemüller, J.T.M. Walraven, Phys. Rev. A **58**, 3891 (1998)
20 C. Ospelkaus, S. Ospelkaus, K. Sengstock, K. Bongs, Phys. Rev. Lett. **96**, 020401 (2006)
21 Our current measurements suggest 10^8–10^9 atoms in the cloud. Loading to nearly the maximum atom number takes less than 5 s
22 T. Kinoshita, T.R. Wenger, D.S. Weiss, Phys. Rev. A **71**, 01 162(R) (2005)
23 M. Kasevich, S. Chu, Phys. Rev. Lett. **67**, 181 (1991)
24 C.J. Bordé, in *Laser Spectroscopy X*, ed. by M. Ducloy, E. Giacobino, G. Camy (World Scientific, Singapore 1991), p. 239
25 C. Antoine, C.J. Bordé, J. Opt. B **5**, 199 (2003)
26 G.J. Dick, Local oscillator induced instabilities. In *Proc. Nineteenth Annual Precise Time and Time Interval Applications Planning Meet.*, 1987, pp. 133–147
27 P. Cheinet, B. Canuel, F. Pereira Dos Santos, A. Gauguet, F. Leduc, A. Landragin, e-print physics/0510197 (2005)
28 P. Cheinet, F. Pereira Dos Santos, T. Petelski, J. Le Gouët, J. Kim, K.T. Therkildsen, A. Clairon, A. Landragin, e-print physics/0510261 (2005)
29 A. Mann, C. Sheng, A. Luiten, IEEE Trans. Instrum. Meas. **50**, 519 (2001)

Eur. Phys. J. D **53**, 353–357 (2009)
DOI: 10.1140/epjd/e2009-00150-5

THE EUROPEAN PHYSICAL JOURNAL D

Regular Article

Light-pulse atom interferometry in microgravity

G. Stern[1,2], B. Battelier[1], R. Geiger[1], G. Varoquaux[1], A. Villing[1], F. Moron[1], O. Carraz[3], N. Zahzam[3], Y. Bidel[3], W. Chaibi[2], F. Pereira Dos Santos[2], A. Bresson[3], A. Landragin[2], and P. Bouyer[1,a]

[1] Laboratoire Charles Fabry de l'Institut d'Optique, Centre National de la Recherche Scientifique et Université Paris Sud 11, Institut d'Optique Graduate School, RD 128, 91127 Palaiseau Cedex, France
[2] LNE-SYRTE, CNRS UMR 8630, UPMC, Observatoire de Paris, 61 avenue de l'Observatoire, 75014 Paris, France
[3] Office National d'Étude et de Recherches Aérospatiales, Chemin de la Hunière, 91761 Palaiseau, France

Received 19 March 2009 / Received in final form 21 April 2009
Published online 16 May 2009 –

Abstract. We describe the operation of a light pulse interferometer using cold ^{87}Rb atoms in reduced gravity. Using a series of two Raman transitions induced by light pulses, we have obtained Ramsey fringes in the low gravity environment achieved during parabolic flights. With our compact apparatus, we have operated in a regime which is not accessible on ground. In the much lower gravity environment and lower vibration level of a satellite, our cold atom interferometer could measure accelerations with a sensitivity orders of magnitude better than the best ground based accelerometers and close to proven spaced-based ones.

PACS. 37.25.+k Atom interferometry techniques – 03.75.Dg Atom and neutron interferometry

Atom interferometry is one of the most promising candidates for ultra-accurate measurements of gravito-inertial forces [1], with both fundamental [2–5] and practical (navigation or geodesy) applications. Atom interferometry is most often performed by applying successive *coherent* beam-splitting and -recombining processes separated by an interrogation time T to a set of particles [6]. Understanding matter wave interferences phenomena follows from the analogy with optical interferometry [7,8]: the incoming wave is separated into two wavepackets by a first beam-splitter; each wave then propagates during a time T along a different path and accumulates a different phase; the two wavepackets are finally recombined by a last beam-splitter. To observe the interferences, one measures the two output-channels complementary probability amplitudes which are sine functions of the accumulated phase difference $\Delta\phi$. This phase difference increases with the paths length, i.e. with the time T between the beam-splitting pulses.

When used as inertial sensors [9,10], the atoms are usually left free to evolve during the interrogation time T so that the interferometer is only sensitive to gravito-inertial effects. In particular, one avoids residual trapping fields that would induce inhomogeneities or fluctuations and would affect the atomic signal. The interrogation time T is consequently limited by, on the one hand, the free expansion of the atomic cloud, and, on the other hand, the free fall of the atomic cloud. The limitation of expansion

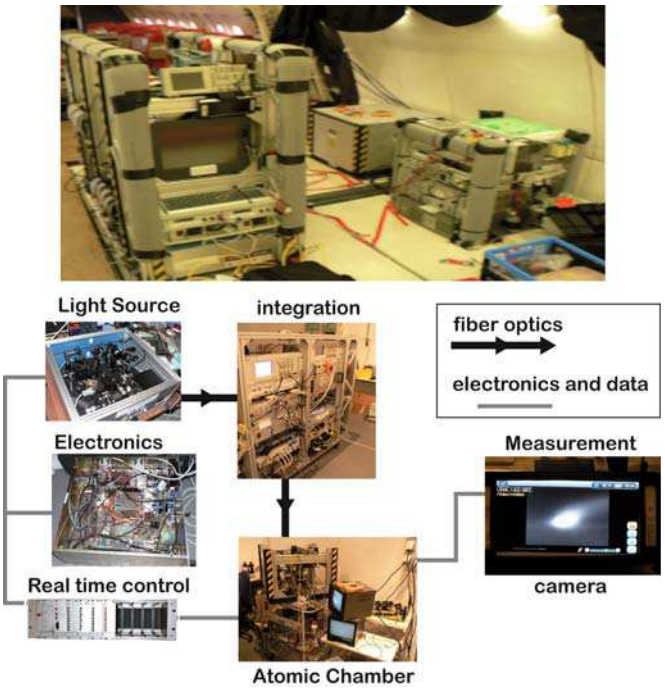

Fig. 1. (Color online) Top: the atom interferometer assembled in the Airbus. The main rack on the left houses the laser sources and the control electronics. The rack on the front right contains the uninterruptable power-supply, the electrical panel and the high-power laser part. The rack on the back right hosts atom-optics part of the experiment. Bottom: the architecture of the atom interferometer.

[a] e-mail: philippe.bouyer@institutoptique.fr

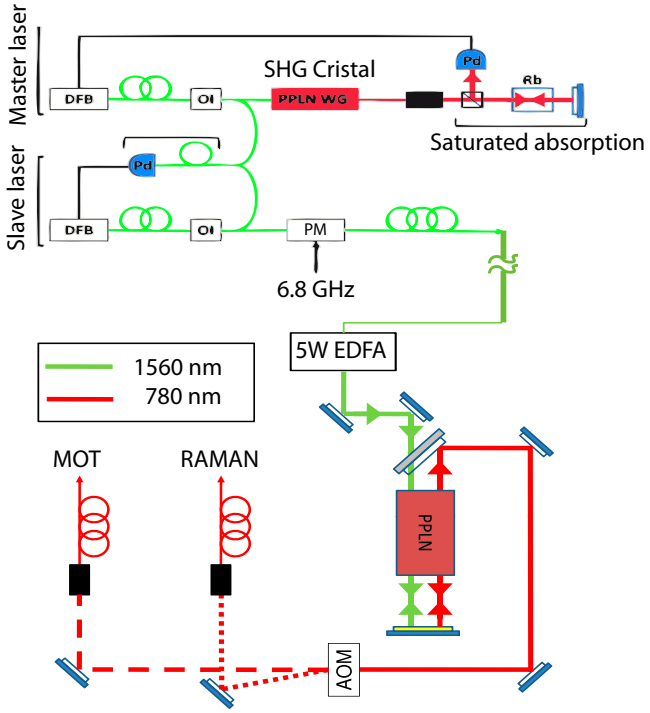

Fig. 2. (Color online) Diagram of the laser system. The master laser (linewidth of 1 MHz) is a monolithic semiconductor element: a 1560 nm distributed feed-back (DFB) fiber laser is frequency doubled in a PPLN waveguide; the resulting 780 nm light is then sent into a saturated-absorption spectroscopy setup for frequency locking on a ^{85}Rb transition; the slave is a 80 mW DFB laser diode at 1560 nm and is frequency-locked on the master laser by measuring the frequency of their beat-note recorded on a fibered fast photodiode. Frequency control of the lasers is achieved via feedback to their supply current. After amplification through a 5W-erbium-doped fiber amplifier (EDFA), the slave laser is frequency doubled in free space with a bulk PPLN crystal; we obtain about 0.3 W at 780 nm.

is alleviated by the use of ultracold gases [11,12], but, due to free-fall distance, long-interrogation-time experiments require tall vacuum chambers [13]. Laboratory experiments are typically limited to about 300 ms of free fall with a 1 m-tall apparatus if the atoms are simply released, or twice by launching them upward as in atomic fountains. This can be increased on much larger apparatuses: a 10 m-high atom interferometer is currently under construction at Stanford [3], giving access to 1.4 s of interrogation time. Free-fall heights of more than 100 m, corresponding to durations of about 5 s are also available in a drop tower (ZARM Bremen, Germany [14]). Another solution consists in performing the experiments in microgravity achieved during parabolic flights provided by an aeroplane, as for the PHARAO prototype [15]. In the I.C.E. (Interférometrie Cohérente pour l'Espace) collaboration [16,17] that we present here, we are conducting cold-atom interferometry experiments in such an airplane (the A-300 0-G Airbus of Novespace), which carries out ballistic flights. Microgravity is obtained via 20 s-long parabolas by steering the plane to cancel drag and follow free fall. The residual acceleration is of the order of 10^{-2} g ($\sim$10 cm s^2). With 90 parabolas per flight session, we have access to 30 min total of reduced gravity. In this letter, we present a first validation of our 0-g setup by obtaining Ramsey fringes with copropagating Raman transitions during parabolas, the interrogation times being longer than those we could obtain on Earth with the same configuration.

Transferring a laboratory-bound cold atoms interferometer into an automated experiment suitable for microgravity use poses many technical challenges [14,16,18,19]. We assembled a prototype atomic source suitable for inertial-sensing in an airplane from the I.C.E. collaboration components [16] (see Fig. 1). The atom interferometer is made of 4 elements: a vacuum chamber with optics; lasers sources for cooling and coherent manipulation of atoms; a stable oscillator (in our case a microwave frequency source at about 6.8 GHz [16]) which is a frequency reference for the Raman lasers; and an autonomous real-time controller for the experimental sequence and data calculations. For the interferometric measurement, we prepare clouds of cold ^{87}Rb in a magneto-optical trap (MOT) and release them for interrogation during their free fall.

Moving away from extended-cavity-laser-diode-based systems, as developed in the PHARAO project [20], we have designed laser sources at 780 nm for cooling and coherently manipulating the atoms that rely on telecom technologies and second harmonic generation [21,22]. This allows to use fiber-optics components and offers a reliable, robust and compact system, quite insensitive to the environmental perturbations encountered in the airplane. These novel laser sources are very similar to the ones described in details in [23] so we limit here to outlining the successful design. A first reference DFB 1560 nm pigtailed laser diode (linewidth $\sim$ 1 MHz) is frequency doubled in a PPLN waveguide and locked on a ^{85}Rb transition through a saturated absorption setup (see Fig. 2). A slave DFB 1560 nm pigtailed diode, similar to the first one, is locked to the first laser at a frequency difference monitored through the beat note signal, as measured by a fibered fast photodiode. The frequency offset can be adjusted so that the slave DFB is red detuned from the resonance of the $F = 2 \rightarrow F = 3$ transition of ^{87}Rb with a detuning ranging from 0 to 1.1 GHz. A 1560 nm fibered phase modulator is then used to generate two sidebands $\sim$6.8 GHz apart. One of these sidebands acts either as the repumping laser during the cooling phase, or as the second Raman laser during coherent manipulation of the atoms, depending on the applied frequency.

The microwave reference has been simplified compared to [16] in order to make it more reliable in the plane environment. It's based on a direct multiplication of a 10 MHz quartz oscillator to 6.8 GHz without any intermediate oscillator or phase lock loop. The ultra-stable quartz has been chosen to be a good compromise to achieve low phase noise at low and high frequencies simultaneously (see Fig. 3), as in [15]. The multiplication is done in three steps: a first multiplication by 10 to 100 MHz (commercial Wenzel system), then multiplication by 2 and finally

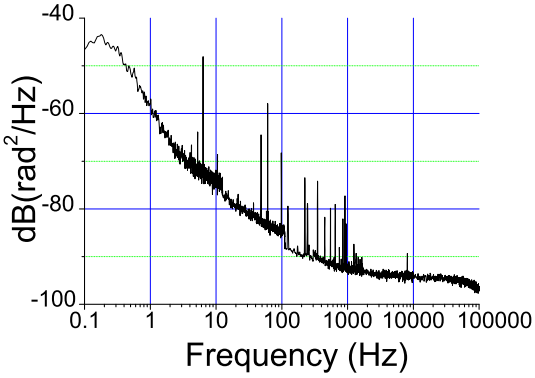

Fig. 3. (Color online) Spectral density of the phase noise at 6.8 GHz of the quartz recorded by comparison with other ultra-stable quartz oscillators phase-locked on H-Maser of the SYRTE.

to 6.8 GHz by a comb generator (non-linear transmission line, Wenzel model 7100). Two direct digital synthesis (DDS) are used to adjust the cooling/repumping frequency difference and the Raman beams frequency difference respectively.

After amplification through a 5W erbium-doped fiber amplifier (EDFA), the slave laser is frequency doubled in free space with a double-pass in a 4 cm bulk PPLN crystal. We typically obtain ∼300 mW at 780 nm. A 80 MHz acousto-optical modulator (AOM) is used to switch between the MOT configuration (in which the non diffracted order of the AOM is used) and the Raman configuration (in which the first diffraction order is used, see Fig. 2). The use of the first order of the AOM for the Raman beam enables to create ultra-short pulses of light (10 μs typically). Additional mechanical shutters ensure a total extinction of the beams. Two optical fibers finally bring the MOT and the Raman beams to the science chamber.

The fibers deliver the light to the vacuum-chamber module [17]. The MOT fiber is sent to a 1-to-3 fiber beam-splitter[1] which delivers three beams which are then retroreflected and produce the MOT. The circularly-polarized Raman beam has a 25 mm diameter and is aligned with the horizontal plane. A 300 mG horizontal magnetic field is aligned with the Raman beam to raise the Zeeman degeneracy of the hyperfine sub-levels. The intensity of the lasers can be up to 20 times the saturation intensity of rubidium, which allows for short Raman pulses with weak velocity selection. The Raman detuning is about 700 MHz. The effective Rabi pulsation Ω_{eff} is about $2\pi \times 12.5$ kHz. Finally, a magnetic shield around the science chamber prevents from changes of the Earth's magnetic field directions during parabolas [17].

The science chamber in which we operate our atom interferometer is shown in Figure 4. We load about 10^9 atoms in the MOT from a rubidium vapor in 500 ms. We release the atoms from the MOT and further cool them down below 100 μK during a brief phase of optical molasses. Then, we prepare the atoms in the lower hyperfine

[1] From Schäfter und Kirchhoff: http://www.sukhamburg.de/

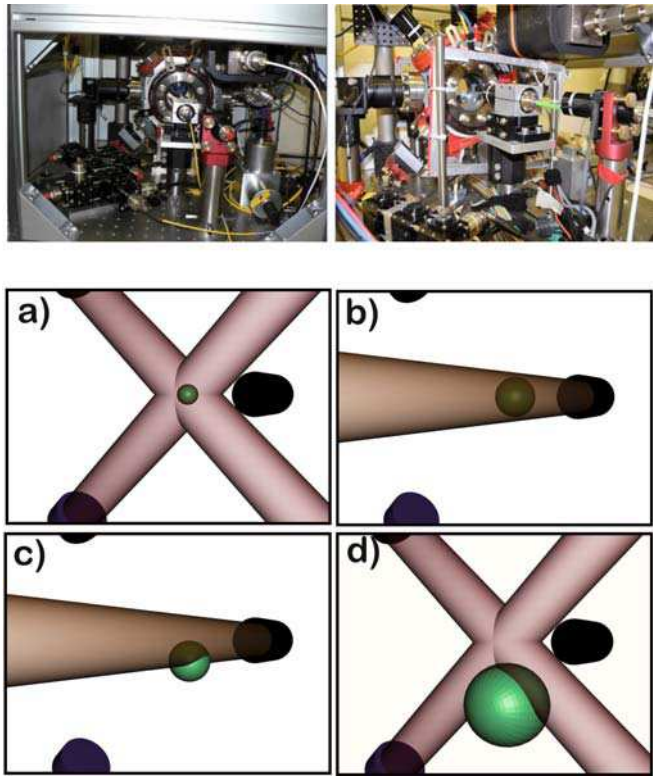

Fig. 4. (Color online) Up: inside the atom-optics rack (the vacuum chamber and the free-space optics). Down: 3D schematics showing the beams configuration and the interferometer sequence. (a) Atom cooling and trapping (MOT, the horizontal retroreflected MOT beam is not shown for clarity), (b) first Raman interrogation pulse colinear to the horizontal retroreflected MOT beam, (c) second Raman interrogation pulse and (d) detection with the MOT beams. The atomic cloud is represented as falling under gravity.

state $F = 1$ using optical pumping. After the extinction of the MOT beams, we shine the atoms with two Raman light pulses separated by a time T. The duration τ of these pulses is chosen such that $\Omega_{\text{eff}} \times \tau = \frac{\pi}{2}$ (splitting of the matter wave). The Raman lasers are copropagating so that a nearly zero momentum is transfered during the Raman transition. In this configuration, the two successive $\frac{\pi}{2}$ pulses enable us to record optically induced Ramsey fringes that are the signature of the matter wave interferences between the two interferometer paths [24,25]. After the Raman pulses, the MOT beams are switched on at resonance and a photodiode monitors the fluorescence which is proportional to the number of atoms. During a few milliseconds, the microwave source is first turned off (absence of the repumping laser) to record the number N_2 of atoms in $F = 2$. Second, we switch on the microwave source (presence of the repumping sideband) and the photodiode detects the total number of atoms N. Plotting the ratio N_2/N with respect to the frequency of the Raman transitions sideband, we thus obtain Ramsey fringes, corresponding to the proportion of atoms having undergone coherent transfer between the two states $|F = 1, m_F = 0\rangle$ and $|F = 2, m_F = 0\rangle$ (see Fig. 5).

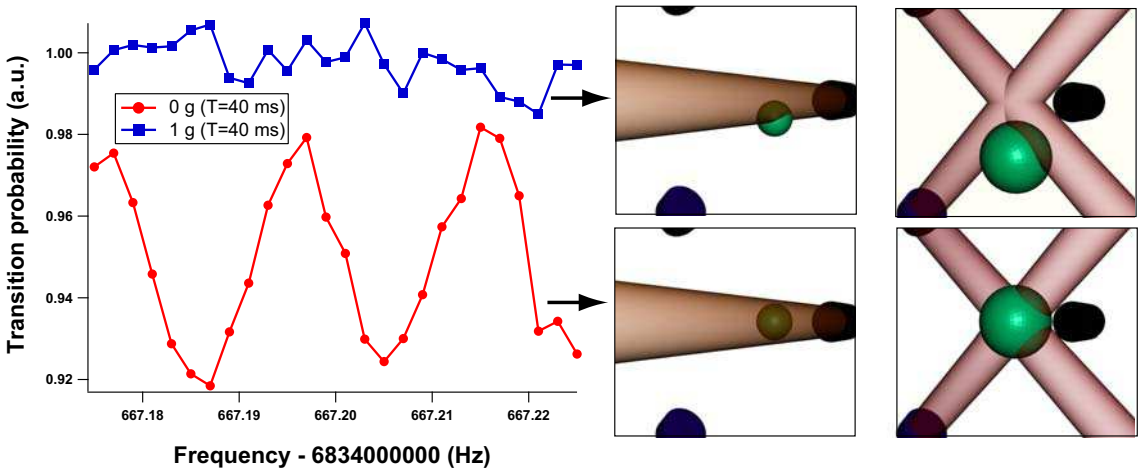

Fig. 5. (Color online) Comparison of fringes with or without gravity. In the presence of gravity (upper curve and pictures), the atoms, when released from the trap fall down, and eventually exit the Raman pulse region and the recapture volume. The atomic signal then drops and no fringes are visible. In the absence of gravity (lower curve and pictures), even for longer times, the atoms stay in the Raman pulse region and recapture area. The detection limit is eventually set by the temperature induced expansion of the atomic cloud.

The total duration of the sequence is about $T + 10$ ms from the end of the molasses phase until the detection. In the lab, i.e. in a 1-g environment, we can typically detect atoms until $T = 20$ ms. Above this limit, the free fall of the atoms is too important and the atoms exit both the area of the Raman beams and the detection volume, as shown in the schematics of Figure 5. However, T can be much longer during parabolas where the residual acceleration is of the order of 10^{-2} g. Figure 5 clearly illustrates the advantage of such a reduced gravity environment: with $T = 40$ ms, we have recorded fringes which could not be observed on ground; we could operate at a largest pulse time interval of $T = 75$ ms (see Fig. 6) which represents a fringe period of $1/T \sim 14$ Hz. We are prone to believe that the main limitation for longer values of T is due to the cloud temperature: the spatial extension of the cloud increases, and the Rabi frequency is then not the same for all the atoms, depending on the laser intensity at their position. It can explain the decrease of the fringes amplitude when T is longer. This effect is enhanced by the residual acceleration -4×10^{-2} g during about 100 ms leads to motion amplitudes of 2 mm which is enough to reduce the Raman beams efficiency. Atoms also exit the detection area, and this makes the signal-to-noise ratio drop.

The vibration noise in the plane does not enable us to use the Raman beams in a velocity selective configuration yet [26], and thus we could not render this interferometer sensitive to inertial effects. Consequently, the residual acceleration noise has been measured with accelerometers locally anchored to the experimental apparatus. This noise corresponds to large residual accelerations ($\sim$10 cm/s^2) that will Doppler shift the resonance and thus hinder it. Different techniques can be used to reduce the influence of these spurious accelerations: active stabilization of the retroreflecting mirror [27], post-corrections or feed-forward from an accelerometer signal on the Raman phase [28], or combination of vibrations measurements

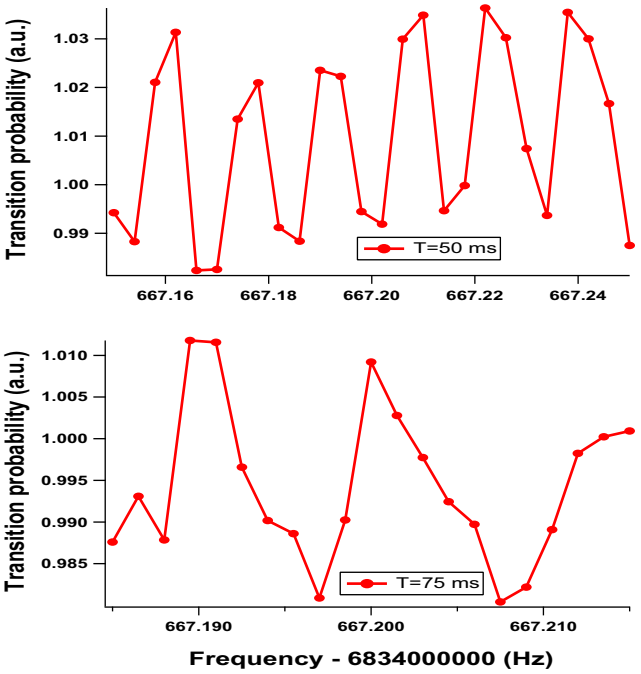

Fig. 6. (Color online) Optical Ramsey fringes obtained in micro gravity for $T = 50$ ms and $T = 75$ ms (corresponding to respectively 18 mm and 35 mm of free fall under gravity). The x-axis is the frequency of the Raman transition sideband delivered by the hyperfrequency source and the y-axis represents the non-normalized ratio N_2/N.

by a seismometer and the measured transition probabilities [29]. With the use of an appropriate vibration isolation, it will allow interrogation of the freely-falling atoms during several seconds, and reach high-precision not yet achieved with ground based atom inertial sensors. When implemented in space, with a residual noise lower than 10^{-6} g, the sensibility can reach that of the best spaced-based accelerometers [30].

To conclude, we have successfully tested a cold atom light pulse interferometer in aircraft parabolic flights. Our preliminary results show that laboratory experiments can be adapted for this new experimental platform and used to develop the future generation of air/spaceborn atom inertial sensors. Our experimental set-up offers an unprecedented platform for development of future fundamental physics instruments to test general relativity of gravitation. Unlike orbital platforms, development cycles on ground-based facilities (either in a plane or in a drop tower) can be short enough to offer rapid technological evolution for these future sensors. In the future, high-precision drag-free space-born applications will require further progress to achieve longer interrogation times using ultra-low velocity atoms. New-generation of degenerate atomic source design are currently under study for that purpose [14,16].

The I.C.E. collaboration is funded by the Centre National d'Études Spatiales, as are GS, and RG. This work is also supported by the European Space Agency under the "Space Atom Interferometry" program. Further support comes from the RTRA "triangle de la physique" and the European Union STREP consortium FINAQS. Laboratoire Charles Fabry, ONERA and SYRTE are all members of IFRAF[2].

References

1. B. Dubetsky, M.A. Kasevich, Phys. Rev. A **74**, 023615 (2006)
2. S. Dimopoulos, P.W. Graham, J.M. Hogan, M.A. Kasevich, Phys. Rev. Lett. **98**, 111102 (2007)
3. S. Dimopoulos, P.W. Graham, J.M. Hogan, M.A. Kasevich, Phys. Rev. D **78**, 042003 (2008)
4. W. Ertmer et al., Exp. Astron. **23**, 611 (2009)
5. P. Wolf et al., Exp. Astron. **23**, 651 (2009)
6. C.J. Bordé, Phys. Lett. A (1989)
7. P. Storey, C. Cohen-Tannoudji, J. Phys. II France **4**, 1999 (1994)
8. C.J. Bordé, C.R. Acad. Sci. Sér. IV **2**, 509 (2001)
9. M. Kasevich, S. Chu, Phys. Rev. Lett. **67**, 181 (1991)
10. T.L. Gustavson, P. Bouyer, M.A. Kasevich, Phys. Rev. Lett. **78**, 2046 (1997)
11. A. Leanhardt, T. Pasquini, M. Saba, A. Schirotzek, Y. Shin, D. Kielpinski, D. Pritchard, W. Ketterle, Science **301**, 1513 (2003)
12. Y. Le Coq, J. Retter, S. Richard, A. Aspect, P. Bouyer, Appl. Phys. B **84**, 627 (2006)
13. A. Clairon, C. Salomon, S. Guelatti, W. Phillips, Europhys. Lett. **16**, 165 (1991)
14. A. Vogel et al., Appl. Phys. B **84**, 663 (2006)
15. P. Laurent, P. Lemonde, E. Simon, G. Santarelli, A. Clairon, N. Dimarcq, P. Petit, C. Audoin, C. Salomon, Eur. Phys. J. D **3**, 201 (1998)
16. R.A. Nyman et al., Appl. Phys. B **84**, 673 (2006)
17. G. Varoquaux in *Proceedings of the XLIInd Rencontres de Moriond, Gravitational Waves and Experimental Gravity*, edited by J. Dumarchez and J.T.T. Vân (2007), p. 335, arXiv:physics/0705.2922
18. T. Könemann et al., Appl. Phys. B **89**, 431 (2007)
19. N. Yu, J.M. Kohel, J.R. Kellogg, L. Maleki, Appl. Phys. B **84**, 647 (2006)
20. P. Laurent et al., Appl. Phys. B **84**, 683 (2006)
21. A. Bruner, V. Mahal, I. Kiryuschev, A. Arie, M.A. Arbore, M.M. Fejer, Appl. Opt. **37**, 6410 (1998)
22. R.J. Thompson, M. Tu, D.C. Aveline, N. Lundblad, L. Maleki, Opt. Express **11**, 1709 (2003)
23. F. Lienhart, S. Boussen, O. Carraz, N. Zahzam, Y. Bidel, A. Bresson, Appl. Phys. B **89**, 177 (2007)
24. C. Antoine, C.J. Bordé, J. Opt. B: Quantum. Semiclass. Opt. **5**, S199 (2003)
25. C.J. Bordé, Metrologia **39**, 435 (2002)
26. M. Kasevich, D.S. Weiss, E. Riis, K. Moler, S. Kasapi, S. Chu, Phys. Rev. Lett. **66**, 2297 (1991)
27. J. Hensley, A. Peters, S. Chu, Rev. Sci. Instrum. **70**, 2735 (1999)
28. J.L. Gouët, T. Mehlstäubler, J. Kim, S. Merlet, A. Clairon, A. Landragin, F. Pereira Dos Santos, Appl. Phys. B **92**, (2008)
29. S. Merlet, J.L. Gouët, Q. Bodart, A. Clairon, A. Landragin, F. Pereira Dos Santos, P. Rouchon, Metrologia **46**, 87 (2009)
30. B. Christophe et al., Exp. Astron. **23**, 529 (2009)

[2] Institut Francilien de Recherche en Atomes Froids: http://213.251.135.217/ifraf/

Bibliographie

[Altshuler 1966] S. Altshuler, L.M. Frantz, and S. Braunstein, "Reflexion of atoms from standing light waves." Phys. Rev. Lett. **17**, 231 (1966).

[Anderson 1994] R. Anderson, H. R. Bilger, G. E. Stedman, "Sagnac effect : A century of Earth Rotated interferometers." Am. J. Phys. **62**(11) (1994).

[Anderson 1995] M. H. Anderson, J. R. Ensher, M. R. Matthews, C. E. Wieman and E. A. Cornell, 'Observation of Bose-Einstein Condensation in a dilute Atomic Vapor", Science **269**, 198 (1995).

[de Angelis 2009] M. de Angelis, A. Bertoldi, L. Cacciapuoti, A. Giorgini, G. Lamporesi, M. Prevedelli, G. Saccorotti, F. Sorrentino and G. M. Tino, "Precision gravimetry with atomic sensors", Meas. Sci. Technol. Topical Review **20**, 022001 (2009).

[Angonin 2006] M.-C. Angonin, P. Tourrenc, and P. Delva " Cold atom interferometer in a satellite : orders of magnitude of the tidal effect" Appl. Phys. B **84** (4), 579 (2006).

[Antoine 2003a] Ch. Antoine, Ch. J. Bordé, "Exact phase shifts for atom interferometry" Phys. Lett. A **306**, 277 (2002).

[Antoine 2003b] Ch. Antoine, Ch. J. Bordé, "Quantum theory of atomic clocks and gravito-inertial sensors : an update", J. Opt. B : Quantum Semiclass. Opt., **5**, pp. 199-207, (2003).

[Antoine 2006] Ch. Antoine, "Matter wave beam splitters in gravito-inertial and trapping potentials : generalized ttt scheme for atom interferometry", Appl. Phys. B, **84**, 691 (2006).

[Antoine 2007] Ch. Antoine, "Rotating matter-wave beam splitters and consequences for atom gyrometers", Phys. Rev. A, **76**, 033609 (2007).

[Aoki 2001] T. Aoki, K. Shinohara, A. Morinaga, "High-finesse atomic multiple-beam interferometer comprised of copropagating stimulated Raman-pulse fields", Phys. Rev. A **63**, 063611 (2001).

[Appel 2009] J. Appel, P. J. Windpassinger, D. Oblak, U. B. Hoff, N. Kjærgaard, and E. S. Polzik, "Quantum noise squeezing and entanglement on the atomic clock transition", arXiv :0810.3545v1 (2009).

[Arndt 2001] M. Arndt, O. Nairz, J. Petschinka, and A. Zeillinger, "High contrast interference with C-60 and C-70" Compt. Rend. Acad. Sci. Serie IV **2**(4), 581.

[Arnold 2006] A.S. Arnold, C.S. Garvie, and E. Riis, "Large magnetic ring for Bose-Einstein condensates" Phys. Rev. A **73**, 041606(R) (2006).

[Baillard 2006] X. Baillard, A. Gauguet, S. Bize, P. Lemonde, Ph. Laurent, A. Clairon, P. Rosenbusch, "Interference-filter-stabilized external-cavity diode lasers", Optics Communications, **266**-2, 609-613, (2006).

[Battaglia 1999] M. Battaglia, C. Roberts, and P. Segall, "Magma intrusion beneath long valley caldera confirmed by temporal changes in gravity". Science **285**(5436), 2119–2122 (1999).

[Berman 1997] *Atom Interferometry* (ed. Paul R. Berman, London : Academic Press) (1997) and references therein.

[Bertoldi 2006] A. Bertoldi, G. Lamporesi, L. Cacciapuoti, M. de Angelis, M. Fattori, T. Petelski, A. Peters, M. Prevedelli, J. Stuhler and G. M. Tino, " Atom interferometry gravity-gradiometer for the determination of the Newtonian gravitational constant G" Euro. Phys. J. D **40**(2), 271 (2006).

[Bertoldi 2008] G. Lamporesi, A. Bertoldi, L. Cacciapuoti, M. Prevedelli and G. M. Tino, " Determination of the Newtonian Gravitational Constant Using Atom Interferometry " Phys. Rev. Lett. **100** 050801 (2008).

[Bordé 1989] Ch. J. Bordé, "Atomic interferometry with internal state labelling", Physics Letters A **140**, 10-12 (1989).

[Bordé 1991] Ch. J. Bordé, "Atomic interferometry and laser spectroscopy", *Laser Spectroscopy X* (ed. M. ducloy, E. Giacobino, G. Camy, World Scientific) 239-245 (1991).

[Bordé 1994a] Ch.J. Bordé, N. Courtier, F. du Burck, A.N. Goncharov, M. Gorlicki "Molecular interferometry experiments", Physics Letters A **188**, 187 (1994).

[Bordé 1994b] Ch.J. Bordé, A. Karasiewicz and Ph. Tourrenc "General relativistic framework for atom interferometry", International Journal of modern Physics D **3**, 157-161 (1994).

[Bordé 2001] Ch.J. Bordé, "Theoretical tools for atom optics and interferometry", C. R. Acad. Sci. Paris, t. 2, Série IV, p. 509–530, (2001).

[Bordé 2002] Ch.J. Bordé, "Atomic clock and inertial sensors" Metrologia **39**, 435 (2002).

[Bordé 2005] Ch. J. Bordé "Base Units of the SI, Fundamental Constants and Modern Quantum Physics", Phil. Trans. Roy. Soc. A **363**, 2177-2201 (2005).

[Bordé 2008] Ch.J. Bordé, "5D optics for atomic clocks and gravito-inertial sensors" Eur. Phys. J. Special Topics **163**, 315–332 (2008).

[Borys 2007] M. Borys, M. Gläser, and M. Mecke, "Mass determination of silicon spheres used for the Avogadro project", Measurement **40**, 785-790 (2007).

[de Broglie 1923] L. de Broglie, "Waves and Quanta", Nature **112**, 540 (1923)

[Bouyer 1996] P. Bouyer, T. L. Gustavson, K. G. Haritos, andM. A. Kasevich, "Micro-wave signal generation with optical injection locking", OpticsLetters **21**, pp. 1502–4, 1996.

[Cacciapuoti 2007] L. Cacciapuotia, N. Dimarcq, G. Santarelli, P. Laurent, P. Lemonde, A. Clairon, P. Berthoud, A. Jornod, F. Reina, S. Feltham and C. Salomon, "Atomic Clock Ensemble in Space : Scientific Objectives and Mission Status", Nuclear Physics B - Proceedings Supplements textbf166, 303-306 (2007)

[Cadoret 2008] M. Cadoret, E. de Mirandes, P.Cladé,S. Guellati-Khélifa, C. Schwob, F. Nez, L. Julien, and F. Biraben, "Combination of Bloch Oscillations with a Ramsey-Bordé Interferometer : New Determination of the Fine Structure Constant", Phys. Rev. Lett. **101**, 230801 (2008).

[Cahn 1997] S. B. Cahn, A. Kumarakrishnan, U. Shim, and T. Sleator, "Time-Domain de Broglie Wave Interferometry", Phys. Rev. Lett. **79**, 784 (1997).

[Canuel 2006] B. Canuel, F. Leduc, D. Holleville, A. Gauguet, J. Fils, A. Virdis, A. Clairon, N. Dimarcq, Ch. J. Borde, A. Landragin, P. Bouyer, "Six-Axis Inertial Sensor Using Cold-Atom Interferometry", Pyys. Rev. Lett. **97**, 010402 (2006).

[Canuel thèse] B. Canuel , "Etude d'un gyromètre à atomes froids", thèse de doctorat de l'université Paris-Sud XI, (2007), HAL : tel-00193288.

[Carnal 1991] O. Carnal, J. Mlynek, "Young s double-slit experiment with atoms : A simple atom interferometer ", Phys. Rev. Lett., **66**, 2689 (1991).

[Chapman 1995] M. S. Chapman, C. R. Ekstrom, T. D. Hammond, R. Rubenstein, J. Schmiedmayer, S. Wehinger, and D. E. Pritchard, " Optics and interferometry with Na_2 molecoles", Phys. Rev. Lett.**74**, 4783 (1995).

[Chao 1997] B.F. Chao and R.D. Ray, "Oceanic tidal angular momentum and Earth's rotation variations." Prog. Oceanog. **40**, 399 (1997).

[Cheinet thèse] P. Cheinet , "Conception et réalisation d'un gravimètre à atomes froids", thèse de doctorat de l'université Pierre et Marie Curie Paris VI, (2006), HAL : tel-00070861.

[Cheinet 2006] P. Cheinet, F. Pereira Dos Santos, T. Petelski, J. Le Gouët, J. Kim, K.T. Therkildsen, A. Clairon, A. Landragin, "Compact laser system for atom interferometry", Appl. Phys. B **84**, 643–646 (2006).

[Cheinet 2008] P. Cheinet, B. Canuel, F. Pereira Dos Santos, A. Gauguet, F. Leduc, A. Landragin, "Measurement of the sensitivity function in time-domain atomic interferometer", IEEE *Trans. on Instr. and Meas.* **57**, 1141 (2008).

[Cladé 2006] P.Cladé, E. de Mirandes, M. Cadoret, S. Guellati-Khélifa, C.Schwob, F. Nez, L. Julien, F. Biraben, "Determination of the Fine Structure Constant Based on Bloch Oscillations of Ultracold Atoms in a Vertical Optical Lattice", Phys. Rev. Lett. **96**, 033001 (2006).

[Cladé 2009] Pierre Cladé, S.Guellati-Khélifa, F. Nez, and F. Biraben, "Large Momentum Beamsplitter using Bloch Oscillations", Phys. Rev. Lett. **102**, 240402 (2009).

[Clauser 1988] J. F. Clauser "Ultra high sensitivity accelerometers and gyroscopes using neutral atom matter wave interferometry" Physica B **151**, 262 (1988).

[Cément 2009] J.-F. Clément, J.-P. Brantut, M. Robert de Saint Vincent, R.A. Nyman, A. Aspect, T. Bourdel, and P. Bouyer, "All-optical runaway evaporation to Bose-Einstein condensation", Physical Review A **79**, 061406(R) (2009).

[Colella 1975] R. Colella, A. W. Overhauser, S. A. Werner, "Observation of Gravitationally Induced Quantum Interference", Phys. Rev. Lett. **34**, 1472 - 1474 (1975).

[Davisson 1927] C. Davisson, H. Germer, "The Scattering of Electrons by a Single Crystal of Nickel", Nature **119**, 558-560 (1927).

[Delva 2006] P. Delva, M.-C. Angonin and P. Tourrenc, "A comparison between matter wave and light wave interferometers for the detection of gravitational waves", Physics Lett. A **357**, 249-254 (2006).

[Dick 1987] G. J. Dick, "Local Oscillator induced instabilities in trapped ion frequency standards" in *Proc. Nineteenth Annual Precise Time and Time Interval*, pp. 133-147 (1987).

[Dieckmann 1998] K. Dieckmann, R. J. C. Spreeuw, M. Weidemüller and J. T. M. Walraven, "Two-Dimentional Magnetooptical Trap as a source of slow atoms", Physical Review A **58**, 3891 (1998).

[Dimopoulos 2003] S. Dimopoulos and A. A. Geraci, "Probing submicron forces by interferometry of Bose-Einstein condensed atoms", Phys. Rev. D 68, 124021 (2003).

[Dimopoulos 2007] S. Dimopoulos, P. W. Graham, J. M. Hogan, and M. A. Kasevich, "Testing General Relativity with Atom Interferometry" Phys. Rev. Lett. **98**, 111102 (2007).

[Dimopoulos 2008] S. Dimopoulos, P. W. Graham, J. M. Hogan, M. A. Kasevich and S. Rajendran, "Atomic gravitational wave interferometric sensor" Phys. Rev. D **78**, 22002 (2008)

[Durfee 2006] D. S. Durfee, Y.K. Shaham, M.A. Kasevich, "Long-Term Stability of an Area-Reversible Atom-Interferometer Sagnac Gyroscope" Phys. Rev. Lett. **97**, 240801 (2006).

[Ekstrom 1995] C.R. Ekstrom, J. Schmiedmayer, M.S. Chapman, T.D. Hammond, D. Pritchard, "Measurement of the electric polarizability of sodium with atom interferometer", Phys. Rev. A **51**, 3883 (1995).

[Ertmer 2009] W. Ertmer, C. Schubert, T. Wendrich, M. Gilowski, M. Zaiser, T. v. Zoest, E. Rasel, Ch. J. Bordé, A. Clairon, A. Landragin, P. Laurent, P. Lemonde, G. Santarelli *et al.* "Matter wave explorer of gravity (MWXG)", Exp Astron **23**, 611–649 (2009).

[ESA-SCI 2000] HYPER, Hyper-precision cold atom interferometry in space Assessment Study Report ESA-SCI (2000).

[Everitt 2008] C. W. F. Everitt *et al.* "Gravity Probe B data analysis status and potential for improved accuracy of scientific results", Class. Quantum Grav. **25**, 114002 (2008).

[Faller 1967] J.E. Faller, "Precision measurement of the acceleration of gravity". Science **158**, 60–67 (1967).

[Fattori03] M. Fattori, G. Lamporesi, T. Petelski, J. Stuhler, G. M. Tino, Towards an atom interferometric determination of the Newtonian gravitational constant, Phys. Lett. A **318**, 184 (2003).

[Fils thèse] J. Fils, "Réalisation et caractérisation d'un gyromètre à ondes de Broglie", thèse de doctorat de l'université Paris-Sud XI, (2002).

[Fils 2005] J. Fils, F. Leduc, P. Bouyer, D. Holleville, N. Dimarcq, A. Clairon and A. Landragin, "Influence of optical aberrations in an atomic gyroscope", Eur. Phys. J. D **36**, 257-260 (2005).

[Fixler 2007] J. B. Fixler, G. T. Foster, J. M. McGuirk, M. A. Kasevich, "Atom Interferometer Measurement of the Newtonian Constant of Gravity" Science **315**, 74-77 (2007).

[Fray 2004] S. Fray, C.A. Diez, T.W. Hänsch, and M. Weitz, "Atomic interferometer with amplitude gratings of light and its applications to atom based test of the equivalence principle", Phys. Rev. Lett. **93**, 210404 (2004).

[Frede 2000] V. Frede, "Dynamical analysis of the atmospheric angular momentum short-term fluctuations. Comparison with the Earth" Journal of geodesy **73**, 660 (2000).

[Freimund 2001] D.L. Freimund, K. Aflatooni, and H. Batelaan "Observation of the Kapitza-Dirac effect", Nature **413**, 142 (2001).

[Füzesi 2007] F. Füzesi, A. Jornod, P. Thomann, M. Plimmer, G. Dudle, R. Moser, L. Sache, and H. Bleuler, "An electrostatic glass actuator for ultra-high vacuum : Arotating light trap for continuous beams of laser-coolled atoms", Rev. Sci. Instr. **78**, 102109 (2007).

[Garcia 2006] O. Garcia, B. Deissler, K. J. Hughes, J. M. Reeves, and C. A. Sackett, "Bose-Einstein-condensate interferometer with macroscopic arm separation" Phys. Rev. A **74** 031601(R) (2006).

[Gauguet 2008] A. Gauguet, T. E. Mehlstäubler, T. Lévèque, J. Le Gouët, W. Chaibi, B. Canuel, A. Clairon, F. Pereira Dos Santos, et A. Landragin, "Off-resonant Raman transition impact in an atom interferometer", Phys. Rev. A **78**, 043615 (2008).

[Gauguet 2009] A. Gauguet, B. Canuel, T. Lévèque, W. Chaibi and A. Landragin, "Characterization and limits of a cold atom Sagnac interferometer", arXiv :0907.2580v1.

[Gauguet thèse] A. Gauguet , "Gyromètre à atomes froids : Etude de la stabilité limite et des effets systématiques liés aux séparatrices lasers", thèse de doctorat de l'université Pierre et Marie Curie Paris VI, (2008), HAL : tel-00322150.

[Geneves 2005] G. Genevès, P. Gournay, A. Gosset, M. Lecollinet, F. Villar, P. Pinot, P. Juncar, A. Clairon, A. Landragin, D. Holleville, F. Pereira Dos Santos, J. David, M. Besbes, F. Alves, L. Chassagne and S. Topcu "The BNM Watt Balance Project" IEEE transaction on Instrumentation and Measurement **54**, 850-853 (2005).

[Gilowski 2008] M. Gilowski, T. Wendrich, T. Müller, Ch. Jentsch, W. Ertmer, E. M. Rasel, and W. P. Schleich, "Gauss Sum Factorization with Cold Atoms", Phys. Rev. Lett. **100**, 030201 (2008).

[Giltner 1995] D.M. Giltner, R.W. McGowan, and S.A. Lee, "Atom interferometer based on Bragg scattering fron standing light waves", Phys. Rev. Lett. **75**, 2638 (1995).

[Gustavson 1997] T. L. Gustavson, P. Bouyer, M. A. Kasevich "Precision Rotation Measurements with an Atom Interferometer Gyroscope ", Phys. Rev. Lett. **78** 2046 (1997).

[Gustavson 1998] T. L. Gustavson, P. Bouyer, M. A. Kasevich, " A dual atomic beam matter-wave gyroscope", Proc. SPIE **3270**, 62 (1998).

[Gustavson 2000] T. L. Gustavson, A. Landragin, M. A. Kasevich, "Rotation sensing with a dual atom-interferometer Sagnac gyroscope", Class. Quantum Grav. **17**, 1-14 (2000).

[Harber 2005] D. M. Harber, J. M. Obrecht, J. M. McGuirk, and E. A. Cornell, "Measurement of the Casimir-Polder force through center-of-mass oscillations of a Bose-Einstein condensate", Phys. Rev. A 72, 033610 (2005).

[Hensley 1999] J. M. Hensley, A. Peters, and S. Chu, "Active low frequency vertical vibration isolation", Rev. of Scien. Inst. **70** (6), 2735-2741 (1999).

[Hinderer 2002] J. Hinderer, N. Florsch, J. Makinen, H. Legros J.E. and Faller, "On the calibration of a superconducting gravimeter using absolute gravity measurements". Geophys. J. Int., **106**, 491–497 (2002).

[Hinderthür 1999] H. Hinderthür, F. Ruschewitz, H.-J. Lohe, S. Lechte, K. Sengstock, and W. Ertmer, "Time-domain high-finesse atom interferometry", Phys. Rev. A **59**, 2216 (1999).

[Holleville thèse] D. Holleville, "Conception et réalisation d'un gyromètre à atomes froids fondé sur l'effet Sagnac pour les ondes de matière", thèse de doctorat de l'université Paris-Sud XI, (2001). HAL : tel-00001098

[Hughes 2009] K. J. Hughes, J. H. T. Burke and C.A. Sackett, "Suspension of atoms and gravimetry using a pulsed standing wave", Phys. Rev. Lett. **102**, 150403 (2009).

[Hurst 2009] R. B. Hurst, G. E. Stedman, K. U. Schreiber, R. J. Thirkettle, R. D. Graham, N. Rabeendran and J.-P. R. Wells, "Experiments with an 834 m^2 ring laser interferometer", Journal of Applied Physics **105**, 113115 (2009).

[Impens 2006] F. Impens, P. Bouyer and C.J. Bordé, " Matter-wave cavity gravimeter", Appl. phys. B, **84**, 603 (2006).

[Impens 2008] F. Impens, and C.J. Bordé, "Space-time sensors using multiple-wave atom interferometry", arXiv :0808.3380.

[Igel 2007] H. Igel, A. Cochard, J. Wassermann, A. Flaws, U. Schreiber, A. Velikoseltsev and N. P. Dinh, "Broad-band observations of earthquake-induced rotational ground motions", Geophys. J. Int. **168**, 182-196 (2007).

[Jacquey 2007] M. Jacquey, M. Büchner, G. Trénec, and J. Vigué, " Measurement of the electric polarizability of lithium by atom interferometry", Phys. Rev. Lett. **98**, 240405 (2007).

[Jo 2007] G.-B. Jo, Y. Shin, S. Will, T. A. Pasquini, M. Saba, W. Ketterle, and D. E. Pritchard, M. Vengalattore and M. Prentiss "Long Phase Coherence Time and Number Squeezing of Two Bose-Einstein Condensates on an Atom Chip", Phys. Rev. Lett. **98** 030407 (2007).

[Kapitza 1933] L.P. Kapitza, and P.A.M. Dirac, "The reflection of electrons from standing light waves." Proc. Camb. Phil. Soc. **29**, 297 (1933)

[Kasevich 1991a] M. Kasevich, D.S. Weiss, E. Riis, K. Moler, S. Kasapi and S. Chu "Atomic velocity selection using stimulated Raman transitions", Phys. Rev. Lett. **66** 2297 (1991).

[Kasevich 1991b] M. Kasevich, S. Chu "Atomic interferometry using stimulated Raman transitions", Phys. Rev. Lett. **67** 181 (1991).

[Kasevich 1992] M. Kasevich, S. Chu, "Measurement of the gravitational acceleration of an atom with a light-pulse atom interferometer". Appl. Phys. B **54**, 321-332 1992.

[Keith 1991] D. W. Keith, Christopher R. Ekstrom, Quentin A. Turchette, David E. Pritchard, "An interferometer for atoms ", Phys. Rev. Lett., **66**, 2693 (1991).

[Kornack 2005] T.W. Kornack, R. K. Ghosh, and M.V. Romalis, " Nuclear Spin Gyroscope Based on an Atomic Comagnetometer ", Phys. Rev. Lett. **95** 230801 (2005).

[Lambeck 1980] K. Lambeck, "The Earth's Variable Rotation : Geophysical Causes and Consequences" Cambridge Univ. Press, (1980).

[Lamine 2006] B. Lamine, R. Hervé, A. Lambrecht, and S. Reynaud, "Ultimate Decoherence Border for Matter-Wave Interferometry", Phys. Rev. Lett. **96**, 050405 (2006).

[Lämmerzahl 2000] C. Lämmerzahl and Ch. J. Bordé, dans "Gyros, Clocks and interferometers : testing relativistic gravity in space", édité par C. Lämmerzahl, C.W.F. Everitt and F.W. Hehl (Springer Verlag, Berlin, 2000).

[Landragin 1996a] A. Landragin, J.Y. Courtois, G. Labeyrie, N. Vansteenkiste, C. I. Westbrook, A. Aspect, "Measurement of the van der Waals force in an atomic mirror ", Phys. Rev. Lett. **77** 1464 (1996).

[Landragin 1996b] A. Landragin, G. Labeyrie, C. Henkel, R. Kaiser, N. Vansteenkiste, C. I. Westbrook, A. Aspect, "Specular versus diffuse reflection of atoms from an evanescent wave mirror ", Phil. Trans. Optics Letters, **21**, 1591 (1996).

[Landragin 1997] A. Landragin, L. Cognet, G.Zs.K. Horvath, C.I. Westbrook, N. Westbrook, A. Aspect, "A reflection grating for atoms at normal incidence", Europhys. Lett., **39**, 485 (1997).

[Landragin 2009] A. Landragin et F. Peirera Dos Santos, "Accelerometer using atomic waves for space applications", in Atom Optics and Space Physics, Proceedings of the Enrico Fermi International School of Physics "Enrico Fermi," Course CLXVIII, Varenna, 2007, edited by E. Arimondo, W. Ertmer, E. M. Rasel, and W. P. Schleich (IOS press) p337-350 (2009), arXiv :0808.3837.

[Landragin thèse] A. Landragin, "Réflexion d'atomes sur un miroir à onde évanescente : mesure de la force de van der Waals et diffraction atomique", thèse de doctorat de l'université Paris-Sud XI, (1997), HAL : tel-00400765.

[Laurent 2006] Ph. Laurent *et al.* "Design of the cold atom PHARAO space clock and initial test results", Appl. Phys. B textbf84, 683–690 (2006).

[Le Gouët 2007] J. Le Gouët, P. Cheinet, J. Kim, D. Holleville, A. Clairon, A. Landragin, and F. Pereira Dos Santos " Influence of lasers propagation delay on the sensitivity of atom interferometers", Eur. Phys. J. D, **44**, 419–425 (2007).

[Le Gouët 2008] J. Le Gouët, T.E. Mehlsäubler, J. Kim, S. Merlet, A. Clairon, A. Landragin, and F. Pereira Dos Santos, "Limits to the sensitivity of a low noise compact atomic gravimeter", Appl. Phys. B **92**, 133–144 (2008).

[Le Gouët 2009] J. Le Gouët, J. Kim, C. Bourassin-Bouchet, M. Lours, A. Landragin, and F. Pereira Dos Santos, "Wide bandwidth phase-locked diode laser with an intra-cavity electro-optic modulator", Opt. Commun. **282**, 977–980 (2009).

[Le Gouët thèse] J. Le Gouët, "Etude des performance d'un gravimètre atomique absolu : sensibilité limite et exactitude préliminaire", thèse de doctorat de l'université Paris-Sud XI, (2008), HAL : tel-00311422.

[Lemonde 2005] P. Lemonde et P. Wolf, "Optical lattice clock with atoms confined in a shallow trap", hys. Rev. A **72**, 033409 (2005).

[Lenef 1997] A.Lenef, T. D. Hammond, E. T. Smith, M. S. Chapman, R.A. Rubenstein, and D. E. Pritchard, "Rotation Sensing with an Atom Interferometer", Phys. Rev. Lett. **78**, 760 (1997).

[Lense 1918] J. Lense, H. Lense, Phys. Zeit. **19**, 156 (1918).

[Lévèque 2009] T. Lévèque, A. Gauguet, F. Michaud, F. Pereira Dos Santos and A. Landragin, "Enhancing the area of a Raman atom interferometer using a versatile double-diffraction technique", Phys. Rev. Lett., **103**, 080405 (2009).

[Lodge 1893] O. Lodge, Philosophical Transaction of the Royal Society of London, **184**, p. 727 (1893).

[Madison 2000] K. W. Madison, F. Chevy, W. Wohlleben and J. Dalibard, " Vortex Formation in a Stirred Bose-Einstein Condensate", Phys. Rev. Lett., **84**, 806-809 (2000).

[Mantovani 2001] M. S. M. Mantovani, S. R. C. de Freitas, and W. Shukowsky, "Tidal gravity anomalies as a tool to measure rheological properties of the continental lithosphere : application to the south american plate", J. of South Am. Earth Sci. **14**(1), 1–14 (2001).

[Marton 1952] L. Marton , "Electron Interferometer", Phys. Rev., **85**, 1057, (1952).

[Marson 1986] I. Marson and J. E. Faller. g - the acceleration of gravity : its measurement and its importance. J. Phys. E, 19 :22–32, 1986.

[McGuirk 2000] JJ. M. McGuirk, M. J. Snadden, and M. A. Kasevich, "Large Area Light-Pulse Atom Interferometry" Phys. Rev. Lett. **85**(21), 4498 (2000).

[McGuirk 2002] J.M. McGuirk, G.T. Foster, J.B. Fixler, M.J. Snaden, and M.A. Kasevich "Sensitive absolute-gravity gradiometry using atom interferometry" Phys. Rev. A **65**(3), 033608 (2002).

[Merlet 2008] S. Merlet, A. Kopaev, M. Diament, G. Geneves, A. Landragin et F. Pereira Dos Santos, "Micro-gravity investigations for the LNE watt balance project", Metrologia **45**, 265 (2008).

[Merlet 2009] S. Merlet, J. Le Gouët, Q. Bodart, A. Landragin et F. Pereira Dos Santos, P. Rouchon "Operating an atom interferometer beyond its linear range", Metrologia **46**, 87-94 (2009).

[Mehlstäubler 2007] T. E. Mehlstäubler, J. Le Gouët, S. Merlet, D. Holleville, A. Clairon, A. Landragin, F. Pereira Dos Santos, "Systematic phase shit in cold atom gravimeter", Proceedings of the XLII-th Rencontres de Moriond « Gravitational waves and experimental gravity ». Edited by J. Dumarchez and J. Trân Thanh Vân, Thê' Gió'i Publishers (Vietnam), 323-333 (2007).

[Michelson 1925] A.A. Michelson, H.G. Gale, "", Astrophys. J. **61**, 137 (1925).

[Miffre 2006a] A Miffre, M Jacquey, M Büchner, G Trénec and J Vigué, "Atom Interferometry", Phys. Scr. **74**, C15–C23 (2006).

[Miffre 2006b] A. Miffre, M. Jacquey, M. B¸chner, G. Trénec, and J. Vigué, " Measurement of the electric polarizability of lithium by atom interferometry", Phys. Rev. A **73**, 011603(R) (2006).

[Moler 1992] K. Moler, D.S. Weiss,M.A. Kasevich, and S. Chu, "Theoretical analysis of velocity-selective Raman transitions", Phys. Rev. A **45** 342 (1992).

[Moskowitz 1983] P.E. Moskowitz, P.L. Gould, S.R. Atlas, and D.E. Pritchard, "Diffraction of an atomic Beam by Standing-Wave Radiation." Phys. Rev. Lett. **51**, 370 (1983).

[Müller 2007] T. Müller, T. Wendrich, M. Gilowski, C. Jentsch, E.M. Rasel, and W. Ertmer "Versatile compact atomic source for high resolution dual atom interferometry" Phys. Rev. A **76**, 063611 (2007).

[Müller 2009] T. Müller, M. Gilowski, M. Zaiser, T. Wendrich, W. Ertmer, and E.M. Rasel, "A compact dual atom interferometer gyroscope based on laser-cooled rubidium", Eur. Phys. J. D **53**, 273-281 (2009).

[H-Müller 2008] H. Müller, S.-W. Chiow, S. Herrmann, S. Chu "Atom-interferometry tests of the isotropy of post-newtonian gravity ", Phys. Rev. Lett. **100**, 031101 (2008).

[H-Müller 2008b] H. Mülle, S.-W. Chiow, Q. Long, S. Herrmann, and S. Chu, "Atom Interferometry with up to 24-Photon-Momentum-Transfer Beam Splitters", Phys. Rev. Lett. **100**, 180405 (2008).

[H-Müller 2009] H. Müller, S.-W. Chiow, S. Herrmann, S. Chu "Atom interferometers with scalable enclosed area", Phys. Rev. Lett. **102**, 240403 (2009).

[Novak 2003] P. Novak, M. Kern, K. P. Schwarz, M. G. Sideris, B. Heck, S. Ferguson, Y. Hammada and M. Wei, "On geoid determination from airborne gravity", J. Geod., **76**, 510 (2003).

[Nyman 2006] R.A. Nyman, G. Varoquaux, F. Lienhart, D. Chambon, S. Boussen, J.-F. Clément, T. Müller, G. Santarelli, F. Pereira Dos Santos, A. Clairon, A. Bresson, A. Landragin et P. Bouyer, "I.C.E. : a Transportable Atomic Inertial Sensor for Test in Microgravity" Appl. Phys. B **84**, 673 (2006).

[Pereira 2007] F. Pereira Dos Santos, and A. Landragin "Getting the measure of atom interferometry", Physics World, November 2007, 32-37 (2007).

[Pereira 2009] F. Pereira Dos Santos, P. Wolf, A. Landragin, M.-C. Angonin, P. Lemonde, S. Bize, and A. Clairon, "Measurement of short range forces using cold atoms", Proceeding of the 7th International Symposium on Frequency Standard and Metrology, ed. by L. Maleki (World Scientific), 44-52 (2009),

[Peters 1997] A. Peters, K. Y. Chung, B. Young, S. Chu, "Precison atom interferometry", Phil. Trans. R. Soc. Lond. A, **355**, 2223-2233 (1997).

[Peters 1999] A. Peters, K. Y. Chung, S. Chu, "Measurements of gravitational acceleration by dropping atoms", Nature, **400**, 849-852 (1999).

[Peters 2001] A. Peters, K. Y. Chung, S. Chu, "High-precision gravity measurements using atom interferometry", Metrologia, **38**, 25-61 (2001).

[Post 1967] E. J. Post, "Sagnac Effect", Rev. Mod. Phys. **39**, 475-93 (1967).

[Quessada 2003] A. Quessada, R. P. Kovacich, I. Courtillot, A. Clairon, G. Santarelli and P. Lemonde, "The Dick effect for an optical frequency standard", J. Opt. B : Quantum Semiclass. Opt. **5**, S150-S154 (2003).

[Rasel 1995] E. M. Rasel, M. K. Oberthaler, H. Batelaan, J. Schmiedmayer, and A. Zeilinger, "Atom Wave Interferometry with Diffraction Grating of Light " Phys. Rev. Lett. **75** 2633 (1995).

[Rauch 1974] H. Rauch, W. Treimer, "Test of a single crystal neutron interferometer", Physics Letters A, **47**, 369-371 (1974).

[Riccardi 2002] U. Riccardi, G. Berrino and G. Corrado, "Changes in instrumental sensitivity of some feedback systems used in LaCoste-Romberg gravimeters", Metrologia **39**(5), 509–515 (2002).

[Riehle 1991] F. Riehle, Th. Kisters, A. Witte, J. Helmcke, Ch. J. Bordé, "Optical Ramsey spectroscopy in a rotating frame : Sagnac effect in a matter-wave interferometer " Phys. Rev. Lett. **67**, 177 (1991).

[Rizzi 2003] G. Rizzi et M.L. Ruggierro, "Relativity in Rotating Frames : Relativistic Physics in Rotating Reference Frames" Springer (2003). ou G. Rizzi et M.L. Ruggierro "The relativistic Sagnac effect : two derivations" arXiv :gr-qc/0305084v4 (2003)

[Sagnac 1913] M.G. Sagnac, Compte rendus de l'académie des sciences, **157**, 708-1410, (1913).

[Santarelli 1998] G. Santarelli, C. Audoin, A. Makdissi, Ph. Laurent, J.G. Dick, and A. Clairon, "Frequency stability degradation of an oscillator slaved to a periodically interrogated atomic resonator", I.E.E.E. Trans. Ultrason. Ferroelect. Control. **45**, 887 (1998).

[Santarelli 1999] G. Santarelli, Ph. Laurent, P. Lemonde, A. Clairon, A.G. Mann, S. Chang, A.N. Luiten, C. Salomon, "Quantum Projection Noise in an Atomic Fountain : A High Stability Cesium Frequency Standard", Phys. Rev. Lett. **82**, 4619 (1999).

[Schleier-Smith 2009] M. H. Schleier-Smith, I. D. Leroux, and V. Vuletic, "Reduced-Quantum-Uncertainty States of an Ensemble of Two-Level Atoms", arXiv :0810.2582v2 (2009).

[Schmiedmayer 1995] J. Schiedmayer, M.S. Chapman, C.R. Ekstrom, T.D. Hammond, S. Wehinger, and D. Pritchard, "Index of Refraction of Various Gases for Sodium Matter Waves", Phys. Rev. Lett. **74**, 1043 (1995).

[Schöllkopf 2004] W. Schöllkopf, R.E. Grisenti, and J.P. Toennies, " Time-of-flight resolved transmission-grating diffraction of molecular beams", Eur. Phys. J. D. **28**, 215 (2004).

[Schreiber 2006] K.U. Schreiber, G.E. Stedman, H. Igel, A. Flaws. "Ring Laser Gyroscopes as Rotation Sensors for Seismic Wave Studies." Earthquake Source Asymmetry, Structural Media and Rotation Effects, 377 (2006).

[Schreiber 2008] K.U. Schreiber, J.-P. R. Wells and G. E. Stedman "Noise process in large ring lasers", Gen. relativ. Gravit. **40**, 935-943 (2008).

[Schumm 2005] T. Schumm, S. Hofferberth, L. M. Andersson, S. Wildermuth, S. Groth, I. Bar-Joseph, J. Schmiedmayer, P. Kruger, " Matter wave interferometry in a double well on an atom chip" Nature Physics **1**, 57 (2005).

[Shimizu 1992] F. Shimizu, K. Shimizu and T. Takuma, "Double-slit interference with ultracold metastable neon atoms", Phys. Rev. A **55**, R17 (1992).

[Snadden 1998] M. J. Snadden, J. M. McGuirk, P. Bouyer, K. G. Haritos, and M. A. Kasevich, "Measurement of the Earth's Gravity Gradient with an Atom Interferometer-Based Gravity Gradiometer", Phys. Rev. Lett. **81** 971 (1998).

[Sorrentino 2008] F. Sorrentino, A. Alberti, G. Ferrari, V. V. Ivanov, N. Poli, M. Schioppo, G.M. Tino, "A quantum sensor for atom-surface interactions below 10 μm", arXiv :0811.0878 (2008).

[Sortais 2000] Y. Sortais, S. Bize, C. Nicolas, A. Clairon, C. Salomon, C. Williams, "Cold Collision Frequency Shifts in a 87Rb Atomic Fountain", Phys. Rev. Lett. **85** 3117 (2000).

[Stedman 2007] G.E. Stedman, R.B. Hursta and K.U. Schreiberb, "On the potential of large ring lasers." Optics Com. **279**(1), 124 (2007).

[Stern 2009] G. Stern, B. Battelier, R. Geiger, G. Varoquaux, A. Villing, F. Moron, O. Carraz, N. Zahzam, Y. Bidel, W. Chaibi, F. Pereira Dos Santos, A. Bresson, A. Landragin, and P. Bouyer, "Light-pulse atom interferometry in microgravity", Eur. Phys. J. D **53**, 353–357 (2009).

[Stockton 2007] J. K. Stockton, X. Wu, and M. A. Kasevich, "Bayesian estimation of differential interferometer phase", Phys. Rev. A **76**, 033613 (2007).

[Storey 1994] P. Storey , C. Cohen Tannoudji, "The feynmann path integral approach to atomic interferometry : A tutorial", J. Phys. II **4**, 1999(1994).

[Szriftgiser 1996] P. Szriftgiser, D. Guéry-Odelin, M. Arndt, and J. Dalibard, "Atomic Wave Diffraction and Interference Using Temporal Slits", Phys. Rev. Lett. **77**, 4-7 (1996).

[Tapley 2004] B. D. Tapley, S. Bettadpur, M. Watkins, C. Reigber, "The gravity recovery and climate experiment : Mission overview and early results", Geo. Res. Lett. **31**, L09607 (2004).

[Tino 2007] G.M. Tino, L. Cacciapuoti, K. Bongs, Ch.J. Bordé, P. Bouyer, H. Dittus, W. Ertmer, A. Görlitz, M. Inguscio, A. Landragin, P. Lemonde, C. Lammerzahl, A. Peters,

E. Rasel, J. Reichel, C. Salomonk, S. Schiller, W. Schleich, K. Sengstock, U. Sterr and M. Wilken, "Atom interferometers and optical atomic clocks : New quantum sensors for fundamental physics experiments in space." Nucl. Phys. B **166**, 159 (2007).

[Tino 2007b] G.M. Tino and F. Vetrano, "Is it possible to detect gravitational waves with atom interferometers ?", Class. Quantum Grav. **24**, 2167–2178 (2007).

[Touboul 2001] P. Touboul and M. Rodrigues, "The MICROSCOPE space mission", Class. Quantum Grav. **18**, 2487–2498 (2001).

[Vali 1976] V. Vali, R.W. Shorthill, "", Appl. Opt. **15**, 1099 (1976).

[L. Vitushkin] L. Vitushkin, "Measurement standards in gravimetry", dans *Proceedings of the international symposium on terrestrial gravimetry : static and mobile measurement*, Saint Petersburg, Russia, 98 (2007).

[Vogel 2006] A. Vogel *et al.*, "Bose–Einstein condensates in microgravity", Appl. Phys. B **84**, 663–671 (2006).

[Wang 2005] Y.-J. Wang, D. Z. Anderson, V. M. Bright, E. A. Cornell, Q. Diot, T. Kishimoto, M. Prentiss, R. A. Saravanan, S. R. Segal, and S. Wu "Atom Michelson Interferometer on a Chip Using a Bose-Einstein Condensate", Phys. Rev. Lett. **94** 090405 (2005).

[Wang 2007] P. Wang, R.-B. Li, H. Yan, J. Wang, M.-S. Zhan "Demonstration of a Sagnac -type cold atom interferometer with stimulated Raman transitiosn" Chin. Phys. Lett. **24**, 27-30 (2007).

[Weel 2006] M. Weel, I. Chan, S. Beattie, A. Kumarakrishnan, D. Gosset, and I. Yavin. "Effect of a magnetic field gradient and gravitational acceleration on a time- domain grating-echo interferometer", Phys. Rev. A, **73**, 063624 (2006).

[Weiss 1994] M. Weiss, B. C. Young, and S. Chu, " Atomic Interferometer Based on Adiabatic Population Transfer", Phys. Rev. Lett. **73**, 2563 (1994).

[Weitz 1994] M. Weitz, B. C. Young, and S. Chu, " Atomic Interferometer Based on Adiabatic Population Transfer", Phys. Rev. Lett. **73**, 2563 (1994).

[Werner 1979] S.A. Werner, J.L. Staudenmann, and R. Colella, "Effect of Earth's Rotation on the Quantum Mechanical Phase of the Neutron", **42**, 1103 (1979).

[Wicht 2002] A. Wicht, J.M. Henlsey, E. Sarajlic, S. Chu, "A preliminary measurement of the fine structure constantebased on atom interferometry", Physica Scripta **102**, 82-82 (2002).

[Will 2006] C. M. Will, Living Reviews in Relativity 9 (2006), URL http ://www.livingreviews.org/lrr-2006-3.

[Wolf 1999] P. Wolf, and P. Tourrenc, "Gravimetry using atom interferometers : Some systematic effects", Phys. Lett. A **251**, 241–246 (1999).

[Wolf 2007] P. Wolf, P. Lemonde, A. Lambrecht, S. Bize, A. Landragin, A. Clairon, "From optical lattice clocks to the measurement of forces in the Casimir regime", Phys. Rev. A **75**, 063608 (2007).

[Wolf 2009] P. Wolf, Ch. J. Bordé, A. Clairon, L. Duchayne, A. Landragin, P. Lemonde, G. Santarelli *et al.* "Quantum physics exploring gravity in the outer solar system", Exp Astron **23**, 651-687 (2009).

[Wu 2007] S. Wu, E. Su, and M. Prentiss, "Demonstration of an Area-Enclosing Guided-Atom Interferometer for Rotation Sensing", Phys. Rev. Lett. **99** 173201 (2007).

[Yu 2006] N. Yu, J. M. Kohel, J. R. Kellogg, L. Maleki, " Development of an atom-interferometer gravity gradiometer for gravity measurement from space" Appl. Phys. B **84**, 647-652 (2006).

[Yver Leduc thèse] F. Yver Leduc , "Caractérisation d'un capteur inertiel à atomes froids", thèse de doctorat de l'université Paris-Sud XI, (2004). HAL : tel-00007729

[Yver-Leduc 2005] F. Yver-Leduc, P. Cheinet, J. Fils, A. Clairon, N. Dimarcq, D. Holleville, P. Bouyer, A. Landragin, "Reaching the quantum noise limit in a high-sensitivity cold-atom inertial sensor", J. Opt. B : Quantum Semiclass. Opt. **5**, S136-S142 (2003).

[Zimmerman 1965] J. E. Zimmerman and J. E. Mercereau "Compton Wavelength of Superconducting Electrons", Phys. Rev. Lett. **14**, 887 (1965).

Chapitre 6

Curriculum Vitae

Arnaud Landragin
Né le 1^{er} octobre 1969
Marié, 3 enfants

E-mail : arnaud.landragin@obspm.fr

Laboratoire SYRTE
Observatoire de Paris
61, av de l'Observatoire
75014 Paris
Tél : 01 40 51 23 92

Position actuelle

Chargé de recherche CNRS 1^{ere} classe affecté au Laboratoire SYRTE
Responsable de l'Equipe "Interférométrie Atomique et Capteurs Inertiels"

Expérience professionnelle

2006 Début du projet BIARO (Condensat de Bose-Einstein et Interférométrie atomique dans une cavité de haute finesse) en collaboration avec le LCFIO.

2005 Début du projet ICE (Interférométrie Cohérente pour l'Espace) en collaboration avec le LCFIO, L'ONERA et le CNES.

2002 Responsable de l'équipe "Capteurs inertiels et interférométrie atomique".

2002 Initiation de l'expérience du gravimètre absolu à atomes froids dans le cadre du projet balance du Watt du Bureau National de Métrologie.

2000-2003	Co-responsable scientifique du "projet Fleximission" ESA HYPER. Expert scientifique auprès de l'ESA pour l'étude industrielle de la mission HYPER.
1999	Poste de **chargé de recherche** au Laboratoire de l'Horloge Atomique. Réalisation d'un gyromètre-accéléromètre à atomes froids.
1998-1999	Séjour **post-doctoral** à l'université de Yale (USA) dans le groupe de M. Kasevich. Etude et optimisation d'un gyromètre atomique à jet thermique de Césium.
1994-1997	Travaux de **thèse** de réalisation et d'étude d'un miroir atomique à onde évanescente : mesure de la force de van der Waals entre un atome dans l'état fondamental et une paroi diélectrique et diffraction atomique.
1993-1994	Service militaire dans le **contingent scientifique**. Réalisation d'un laser titane saphir continu de 5 W, monomode et accordable sur une plage de 40 nm autour de 780 nm.
1993	Stage de fin d'étude à l'Institut d'optique : étude d'un laser titane saphir continue à 780 nm.
1993	Stage de deuxième année au Commissariat à l'Energie Atomique (Saclay) : doublage de fréquence non critique en angle d'un laser Nd:Yag dans un cristal de LBO.

Formation Académique

1997	**Thèse de doctorat** en Sciences Physiques à l'Institut d'Optique (Université d'Orsay, Paris XI), sous la direction de A. Aspect : "Réflexion d'atomes sur un miroir à onde évanescente : mesure de la force de van der Waals et diffraction atomique".
1993	DEA **optique et photonique** de l'Université d'Orsay, Paris XI.
1990-1993	**Ecole Supérieure d'Optique** à Orsay. Obtention du diplôme d'Ingénieur de l'Ecole Supérieure d'Optique.
1987-1990	Classes préparatoires aux Grandes Ecoles aux lycées Clémenceau et Roosevelt à Reims.
1987	Baccalauréat série C.

Bourses et Prix

2009 Prix "Lamb" de l'académie des sciences.

1998 Bourse de séjour post-doctorale de la Direction Générale de l'Armement du ministère de la défense.

1994 Bourse de Docteur Ingénieur du CNRS, allocation de recherche DRET/CNRS.

Expérience pédagogique

1994-1996 Enseignements de travaux pratiques d'optique à l'Ecole Supérieure d'optique.

1988-1992 Enseignement privé de Mathématiques et de Sciences Physiques.

Encadrement

Depuis 1999, j'ai co-encadré 8 **thèses** dans le cadre de mon activité de recherche au SYRTE

- **David Holleville** (1999-2001). Taux d'encadrement 50%. Le sujet de thèse de David a porté sur la conception et la réalisation d'un gyromètre à atomes froids fondé sur l'effet Sagnac. Sa thèse est disponible sur http ://tel.archives-ouvertes.fr/tel-00001098/fr/. David a été recruté comme Ingénieur de Recherche au CNRS en 2001.
- **Jérôme Fils** (1999-2002). Taux d'encadrement 50%. Le sujet de thèse de Jérôme a porté sur la réalisation et la caractérisation d'un gyromètre à ondes de matière. Jérôme a effectué un stage post-doctoral au CEA (Bordeaux) et est maintenant Ingénieur de Recherche au GSI Helmholtz Centre for Heavy Ion Research en Allemagne.
- **Florence Yver-Leduc** (2001-2004). Taux d'encadrement 100%. Le sujet de thèse de Florence a porté sur la première caractérisation d'un gyromètre à ondes de matière et la démonstration de la possibilité de mesurer l'ensemble des axes d'inertie sur le même dispositif. Sa thèse est disponible sur http ://tel.archives-ouvertes.fr/tel-00007729/fr/. Florence a passé l'agrégation de physique et est maintenant enseignante dans le secondaire.
- **Patrick Cheinet** (2002-2006). Taux d'encadrement 50%. Patrick a débuté l'expérience de gravimètre atomique et a permis d'obtenir sa première évaluation. Sa thèse est disponible sur http ://tel.archives-ouvertes.fr/tel-00070861/. Patrick a effectué un séjour post-doctoral dans le groupe d'Immanuel Bloch à Mayence, et est actuellement post-

doc au Laboratoire Charles Fabry de l'Institut d'Optique, dans l'équipe de Philippe Bouyer et Alain Aspect.

- **Benjamin Canuel** (2003-2007). Taux d'encadrement 100%. Benjamin a réalisé une étude détaillée du fonctionnement du gyromètre à atomes froids et notamment des différentes sources de bruit pouvant limiter sa stabilité. Sa thèse est disponible sur http ://tel.archives-ouvertes.fr/tel-00193288/fr/. Depuis sa thèse, Benjamin est "applied physicist" à l'EGO (European gravitational observatory).
- **Julien Le Gouët** (2004-2008). Taux d'encadrement 20%. Julien a participé aux mesures de caractérisation des performances du gravimètre en terme de sensibilité et d'exactitude. Il a notamment réalisé les études du filtrage numérique du signal du sismomètre. Sa thèse est disponible sur http ://tel.archives-ouvertes.fr/tel-00311422/. Julien a effectué un séjour post-doctoral au Research Laboratory For Electronics du MIT, dans l'équipe de Shapiro et Wong. Julien a été recruté au service Temps-Fréquence du CNES (Toulouse).
- **Alexandre Gauguet** (2004-2008). Taux d'encadrement 100%. Alexandre a participé à l'étude de la stabilité limite et des effets systématiques liés aux séparatrices lasers dans le gyromètre-accéléromètre. Sa thèse est disponible sur http ://tel.archives-ouvertes.fr/tel-00322150/fr/. Alexandre a ensuite effectué un service d'ATER à l'Institut Galilée sous la direction A. Amy-Klein. Il est actuellement en séjour post-doctoral à l'université de Durham (UK) sous la direction de C. Adams.
- **Thomas Lévèque** (depuis 2007). Taux d'encadrement 100%. Thomas a participé à la caractérisation complète du gyromètre, et notamment à celle du facteur d'échelle. Il participe à la conception d'un nouveau gyromètre de très grande aire, pour lequel il a participé à la démonstration d'un nouveau type de séparatrices atomiques plus efficaces.

J'ai également supervisé le travail de trois **post-doctorants** et de deux **ingénieurs** en CCD

- **Franck Pereira Dos Santos** (2002-2004). Franck est arrivé comme post-doctorant quelques mois après le début du projet de gravimètre. Il a été recruté sur un poste de CR2 au CNRS, affecté au SYRTE dans l'équipe "Capteurs inertiels" en 2004.
- **Walid Chaibi** (2006-2007). Walid a travaillé comme post-doctorant sur l'expérience de gyromètre-accéléromètre à atomes froids. Il a été recruté sur un poste de CR2 au CNRS, affecté au laboratoire ARTEMIS (Nice) en 2008.
- **Franck Michaud** (2008-2009). Franck a participé comme post-doctorant à l'expérience de gyromètre-accéléromètre. Il est actuellement post-doctorant au laboratoire LASIM (Lyon).

- **Bertrand Venon** (2007-2008). Bertrand a travaillé un an en CDD ingénieur d'étude en conception mécanique à la conception du nouveau gyromètre de très grande aire.
- **Raphaël Lambert** (2008-2009). Raphaël a travaillé un an en CDD ingénieur d'étude à la réalisation de références de fréquence micro-onde très bas bruit pour l'interférométrie atomique dans le cadre de coopérations européennes FINAQS et SAI.

Liste de publications et de conférences

1/ Revues à comité de lecture

1. T. LEVEQUE, A. GAUGUET, F. MICHAUD, F. PEREIRA DOS SANTOS, AND A. LANDRAGIN, Phys. Rev. Lett. **103** (2009), 080405, « Enhancing the area of a Raman atom interferometer using a versatile double-diffraction technique ».

2. G. STERN, B. BATTELIER, R. GEIGER, G. VAROQUAUX, A. VILLING, F. MORON, O. CARRAZ, N. ZAHZAM, Y. BIDEL, O. CHAIBI, F. PEREIRA DOS SANTOS, A. BRESSON, A. LANDRAGIN, AND P. BOUYER, Eur. Phys. J. D **53**, 353–357 (2009), « Light-pulse atom interferometry in microgravity ».

3. J. LE GOUËT, J. KIM, C. BOURASSIN-BOUCHET, M. LOURS, A. LANDRAGIN, F. PEREIRA DOS SANTOS, Opt. Commun. **282** (2009), 977–980, « Wide bandwidth phase-locked diode laser with an intra-cavity electro-optic modulator ».

4. P. WOLF, CH. J. BORDE, A. CLAIRON, L. DUCHAYNE, A. LANDRAGIN, P. LEMONDE, G. SANTARELLI *et al.*, Exp Astron **23** (2009), 651-687, « Quantum physics exploring gravity in the outer solar system ».

5. W. ERTMER, C. SCHUBERT, T. WENDRICH, M. GILOWSKI, M. ZAISER, T. V. ZOEST, E. RASEL, CH. J. BORDE, A. CLAIRON, A. LANDRAGIN, P. LAURENT, P. LEMONDE, G. SANTARELLI et al., Exp Astron **23** (2009), 611–649, « Matter wave explorer of gravity (MWXG) ».

6. S. MERLET, J. LE GOUËT, Q. BODART, A. CLAIRON, A. LANDRAGIN, F. PEREIRA DOS SANTOS, P. ROUCHON, Metrologia **46** (2009), 87–94, « Operating an atom interferometer beyond its linear range ».

7. A. GAUGUET, T. E. MEHLSTÄUBLER, T. LEVEQUE, J. LE GOUËT, W. CHAIBI, B. CANUEL, A. CLAIRON, F. PEREIRA DOS SANTOS, ET A. LANDRAGIN, Phys. Rev. A **78** (2008), 043615 « Off-resonant Raman transition impact in an atom interferometer ».

8. J. LE GOUËT, T. E. MEHLSTÄUBLER, J. KIM, S. MERLET, A. CLAIRON, A. LANDRAGIN, F. PEREIRADOS SANTOS, Appl. Phys. B **92** (2008), 133–144, « Limits in the sensitivity of a compact atomic interferometer ».

9. S. MERLET, A. KOPAEV, M. DIAMENT, G. GENEVES, A. LANDRAGIN ET F. PEREIRA DOS SANTOS, Metrologia **45** (2008), 265, « Micro-gravity investigations for the LNE watt balance project».

10. P. CHEINET, B. CANUEL, F. PEREIRA DOS SANTOS, A. GAUGUET, F. LEDUC, A. LANDRAGIN, IEEE Trans. on Instrum. Meas. 57 (2008), 1141, « Measurement of the sensitivity function in time-domain atomic interferometer ».

11. F. PEREIRA DOS SANTOS, J. LE GOÜET, T. E. MEHLSTÄUBLER, S. MERLET, D. HOLLEVILLE, A. CLAIRON, A. LANDRAGIN, Revue Française de Métrologie n°13, Vol 2008-1, 33-40, « Gravimètre à atomes froids ».

12. A. LANDRAGIN, B. CANUEL, A. GAUGUET ET P. TUCKEY, Revue Française de Métrologie **10** (2007), 11-16, «Capteur inertiel six axes fondé sur l'interférométrie atomique».

13. J. LE GOUËT, P. CHEINET, J. KIM, D. HOLLEVILLE, A. CLAIRON, A. LANDRAGIN, F. PEREIRA DOS SANTOS, Eur. Phys. J. D. **44** (2007) , 419-425, « Influence of lasers propagation delay on the sensitivity of atom interferometers».

14. P. WOLF, P. LEMONDE, A. LAMBRECHT, S. BIZE, A. LANDRAGIN, A. CLAIRON, Phys. Rev. A **75** (2007), 063608, « From optical lattice clocks to the measurement of forces in the Casimir regime».

15. P. CHEINET, F. PEREIRA DOS SANTOS , T. PETELSKI, J. LE GOUËT, J. KIM, K.T. THERKILDSEN, A. CLAIRON AND A. LANDRAGIN, Appl. Phys. B **84** (2006), 643, « Compact laser system for atom interferometry».

16. R.A. NYMAN, G. VAROQUAUX, F. LIENHART, D. CHAMBON, S. BOUSSEN, J.-F. CLEMENT, T. MÜLLER, G. SANTARELLI, F. PEREIRA DOS SANTOS, A. CLAIRON, A. BRESSON, A. LANDRAGIN ET P. BOUYER, Appl. Phys. B **84** (2006), 673, « I.C.E.: a transportable atomic inertial sensor for test in microgravity ».

17. B. CANUEL, F. LEDUC, D. HOLLEVILLE, A. GAUGUET, J. FILS, A. VIRDIS, A. CLAIRON, N. DIMARCQ, CH. J. BORDE, A. LANDRAGIN ET P. BOUYER, Phys. Rev. Lett. **97** (2006), 010402, « Six-axis inertial sensor using cold-atom interferometry »

18. J. FILS, F. LEDUC, PH. BOUYER, D. HOLLEVILLE, N. DIMARCQ, A. CLAIRON AND A. LANDRAGIN, Eur. Phys. J. D. **36** (2005), 257-260, « Influence of optical aberrations in an atomic gyroscope ».

19. G. GENEVES, P. GOURNAY, A. GOSSET, M. LECOLLINET, F. VILLAR, P. PINOT, P. JUNCAR, A. CLAIRON, A. LANDRAGIN, D. HOLLEVILLE, F. PEREIRA DOS SANTOS, J. DAVID, M. BESBES, F. ALVES, LUC CHASSAGNE AND S. TOPÇU, IEEE transaction on Instrumentation and Measurement **54** (2005) 850-853, « The BNM Watt Balance Project».

20. I. COURTILLOT, A. QUESSADA, R.P. KOVACICH, J.J. ZONDY, A. LANDRAGIN, A. CLAIRON AND P. LEMONDE, Opt. Lett. **28** (2003) 468, « Efficient cooling and trapping of Stontium atoms».

21. F. YVER-LEDUC, P. CHEINET, J. FILS, A. CLAIRON, N. DIMARCQ, D. HOLLEVILLE, P. BOUYER, A. LANDRAGIN, J. Opt.B : Quantum Semiclas. Opt. **5** (2003) S136-S142, « Reaching the quantum noise limit in a high-sensitivity cold-atom inertial sensor ».

22. I. COURTILLOT, A. QUESSADA, R.P. KOVACICH, A. LANDRAGIN, G. SANTARELLI, A. CLAIRON AND P. LEMONDE, IEEE transaction on Instrumentation and Measurement **52** (2003) 255-257, « Cold Stontium Atom for an Optical Frequency Standard».

23. T.L. GUSTAVSON, A. LANDRAGIN, M.A. KASEVICH, Class. Quantum. Gravity **17** (2000) 2385-2398. «Rotation sensing with a dual atom-interferometer Sagnac gyroscope».

24. N. WESTBROOK, C.I. WESTBROOK, A. LANGRAGIN, G. LABEYRIE, L. COGNET, V. SAVALLI, G. HORVATH, A. ASPECT, C. HENKEL, K. MOELMER, J.-Y. COURTOIS, W.D. PHILLIPS, R. KAISER, V. BAGNATO. Physica Scripta, vol **T78**, 7 (1998). «New physics with evanescent wave atomic mirrors: the van der Waals force and atomic diffraction».

25. A. LANDRAGIN, L. COGNET, G.Zs.K. HORVATH, C.I. WESTBROOK, N. WESTBROOK, A. ASPECT. Europhys. Lett. **39**, 485 (1997) «A reflection grating for atoms at normal incidence».

26. A. LANDRAGIN, J.Y. COURTOIS, G. LABEYRIE, N. VANSTEENKISTE, C. I. WESTBROOK, A. ASPECT. Phys. Rev Lett. **77**, 1464 (1996). « Measurement of the van der Waals force in an atomic mirror ».

27. A. LANDRAGIN, G. LABEYRIE, C. HENKEL, R. KAISER, N. VANSTEENKISTE, C. I. WESTBROOK, A. ASPECT. Optics Letters **21**, 1591 (1996). « Specular versus diffuse reflection of atoms from an evanescent wave mirror ».

28. G. LABEYRIE, A. LANDRAGIN, J. VON ZANTHIER, R. KAISER, N. VANSTEENKISTE, C. I. WESTBROOK, A. ASPECT. Quantum Semiclass. Opt. **8**, 603 (1996). « Detailed study of a high finesse planar wave-guide for evanescent wave atomic mirrors ».

29. A. LANDRAGIN., G. LABEYRIE.,J.-Y. COURTOIS, R. KAISER., N. VANSTEENKISTE, C.I. WESTBROOK, A. ASPECT. Quatrième Colloque sur les Lasers et l'Optique Quantique, Palaiseau, 6-8 novembre 1995. Ann. Phys. Fr. **20** 641-642. «Observation de la force de van der Waals dans le miroir à atomes ».

30. N. VANSTEENKISTE, A. LANDRAGIN, G. LABEYRIE, R. KAISER, C.I. WESTBROOK, A. ASPECT Quatrième Colloque sur les Lasers et l'Optique Quantique, Palaiseau, 6-8 novembre 1995 Ann. Phys. Fr. **20** 595-596. «Miroir à atomes : réflexion spéculaire ou réflexion diffuse ? ».

2/ Conférences invitées dans les congrès

1. A. LANDRAGIN and F. PEREIRA DOS SANTOS, The 39th Winter Colloquium on the Physics of Quantum Electronics, Snowbird, Utha USA, January 4-8, 2009, « Inertial sensors with cold atoms » (présentation orale).

2. A. LANDRAGIN, T. LEVEQUE, A. GAUGUET ET W. CHAIBI, 7th International Symposium on Frequency Standards and Metrology, Pacific Grove CA, USA, 4-8 October 2008 « Characterization of a cold atom gyroscope » (présentation orale).

3. A. LANDRAGIN *et al.*, International Conference on Space Optics (ICSO), Toulouse, France, 14-17 Octobre 2008 , « Towards a UFF test with dual cold atom interferometer ». (présentation orale)

4. A. LANDRAGIN, INTERNATIONAL SCHOOL OF PHYSICS "ENRICO FERMI", Varenna (Lake Como) - July 3rd to 13th 2007, « Accelerometer using atomic waves for space applications » (cours).

5. A. LANDRAGIN, From Quantum to Cosmos II, Bremen, Germany, 10-13 juin 2007, « Quantum sensors using atomic waves for space applications » (présentation orale).

6. A. LANDRAGIN, P. CHEINET, K. T. THERKILDSEN, J. LE GOUËT, F. PEREIRA DOS SANTOS, D. HOLLEVILLE, A. CLAIRON, XVII International Conference on Laser Spectroscopy, Cairngorms, Scotland, 19-24 Juin 2005, « Cold atom absolute gravimeter for the Watt Balance » (affiche)

7. A. LANDRAGIN, B. CANUEL, P. CHEINET, A. GAUGUET, J. FILS, F. LEDUC, CH. J BORDÉ, P. BOUYER, N. DIMARCQ, D. HOLLEVILLE, F. PEREIRA DOS SANTOS ET A. CLAIRON, QELS 2005, Baltimore USA, 23-28 mai 2005, « Results on inertial measurement with a Raman interferometer».(présentation orale)

8. A. LANDRAGIN ,B. CANUEL, F. LEDUC, D. HOLLEVILLE, N. DIMARCQ, A. CLAIRON, J. FILS, Ph. BOUYER, CH. BORDE, 35th COSPAR Scientific Assembly, Paris, France, 18-25 juillet 2004, « A cold atom interferometer for high precision inertial measurements ». (présentation orale)

9. A. LANDRAGIN, F. LEDUC, P. CHEINET, B. CANUEL, J. FILS, F. PEREIRA DOS SANTOS A. CLAIRON, N. DIMARCQ, D. HOLLEVILLE, P. BOUYER, CH.J. BORDE, Journées Scientifiques du CNFRS « Métrologie et Capteur en Electromagnétisme », Meudon, 29 et 30 mars 2004, « Capteurs inertiels à atomes froids : gyromètre et accéléromètre ». (présentation orale)

10. A. LANDRAGIN, F. LEDUC, J. FILS, A. CLAIRON, N. DIMARCQ, D. HOLLEVILLE, 16th International Conference On Laser Spectroscopy, Cairns, Australie, 13-17 juillet 2003, « Cold atom interferometry for precision measurement ». (affiche)

11. A. LANDRAGIN, F. YVER-LEDUC, P. CHEINET, J. FILS, A. CLAIRON, N. DIMARCQ, D. HOLLEVILLE, P. BOUYER, CH.J. BORDE, HYPER symposium, Paris, 5 novembre 2002, « a cold atom interferometric inertial sensor ». (présentation orale)

12. A. LANDRAGIN, Cours à l'Ecole « Optics and Astrophysics », Cargèse, France, 19 septembre 2002. « Atom Interferometry ». (présentation orale)

13. A. LANDRAGIN, *et al.* 7th International Conference on Advanced Technology and Particle Physics, Como, Italie, Octobre 2001. « HYPER : Atom Interferometry in Space ». (présentation orale)

14. A. LANDRAGIN, T.L. GUSTAVSON, M.A. KASEVICH. Fifth Workshop on atom optics and interferometry, 8-11 mars 1999. « Atomic gyroscope ». (présentation orale)

15. A. LANDRAGIN, T.L. GUSTAVSON, M.A. KASEVICH. Laser Spectroscopy, ICOLS 99 Innsbruck, 7-11 juin 99. « Precision atomique Gyroscope » (présentation orale)

3/ Actes de colloques à comité de lecture

1. A. LANDRAGIN, T. LEVEQUE, A. GAUGUET AND W. CHAIBI, Proceeding of the 7th International Symposium on Frequency Standards and Metrology, ed. by L. Maleki (World scientific) p 502-510 (2009) « Characterization of a cold atom gyroscope ».

2. F. PEREIRA DOS SANTOS, P. WOLF, A. LANDRAGIN, M.-C. ANGONIN, P. LEMONDE, S. BIZE, AND A. CLAIRON, Proceeding of the 7th International Symposium on Frequency Standards and Metrology, ed. by L. Maleki (World scientific) p 44-52 (2009) « Measurement of short range forces using cold atoms»,

3. A. LANDRAGIN ET F. PREIRA DOS SANTOS, *in Atom Optics and Space Physics*, Proceedings of the Enrico Fermi International School of Physics "Enrico Fermi," Course CLXVIII, Varenna, 2007, edited by E. Arimondo, W. Ertmer, E. M. Rasel, and W. P. Schleich (IOS press) p337-350 (2009), « Accelerometer using atomic waves for space applications », arXiv:0808.3837v1.

4. P. WOLF, CH. J. BORDE, A. CLAIRON, L. DUCHAYNE, A. LANDRAGIN, P. LEMONDE, G. SANTARELLI *et al.*, Proceedings of the Europeen Frequency and Time Forum 2008, « The SAGAS project ».

5. S. MERLET, J. LE GOUËT, Q. BODART, A. CLAIRON, P. ROUCHON, A. LANDRAGIN, AND F. PEREIRA DOS SANTOS, Proceeding GGEO2008 Symposium, IAG International Symposium on Gravity, Geoid & Earth Observation, in Chania Crete, 23-27 June 2008 « A cold atom gravimeter based on atom interferometry ».

6. S. MERLET, O. FRANCIS, V. PALINKAS, J. KOSTELECKY, N. LE MOIGNE, T. JACOBS, G. GENEVES, Proceedings Terrestrial Gravimetry : Static and Mobile Measurements, Saint Petersburg, Russia, (2007), « Absolute gravity measurements at LNE ».

7. T.E. MEHLSTÄUBLER, J. LE GOUËT, S. MERLET, D. HOLLEVILLE, A. CLAIRON, A. LANDRAGIN, F. PEREIRA DOS SANTOS, Proceedings of the XLII-th Rencontres de Moriond « Gravitational waves and experimental gravity ». Edited by J. Dumarchez and J. Trân Thanh Vân, Thê' Gió'i Publishers (Vietnam) 2007, 323-333 . « Systematic phase shit in cold atom gravimeter ».

8. G. VAROQUAUX, N. ZAZHAM, O. CHAIBI, J-F. CLEMENT O. CARRAZ, J-P. BRANTUT, R. A. NYMAN, F. PEREIRA DOS SANTOS, Y. BIDEL, A. BRESSON, A. LANDRAGIN AND P. BOUYER, Proceedings of the XLII-th Rencontres de Moriond « Gravitational waves and experimental gravity ». Edited by J. Dumarchez and J. Trân Thanh Vân, Thê' Gió'i Publishers (Vietnam) 2007, 335-343, « ICE: New transpotable atom inertial sensor for applications to space experiment ».

9. S. MERLET, A. KOPAEV, F. PEREIRA DOS SANTOS, M. DIAMENT, Proceedings of the Symposium on Terrestrial Gravimetry: Static and Mobile Measurements 2007, « Micro-gravity characterization in the laboratory of the LNE watt balance project ».

10. S. MERLET, J. LE GOUËT, T. MEHLSTÄUBLER, D. HOLLEVILLE, A. CLAIRON, A. LANDRAGIN, F. PEREIRA DOS SANTOS, Proceedings of the Symposium on Terrestrial Gravimetry: Static and Mobile Measurements 2007, « Atom interferometry at LNE-SYRTE for accurate measurement of gravity ».

11. G. TINO et al., Nuclear Physics B (Proc. Suppl.) **166** (2007) 159–165, « Atom interferometers and optical atomic clocks: New quantum sensors for fundamental physics experiments in space ».

12. F. IMPENS, P. BOUYER, A. LANDRAGIN ET CH. J. BORDE, J. Phys. IV France **135**, 311-312(2006), « Gravimètre à cavité d'ondes de matière ».

13. A. GAUGUET ., B. CANUEL, F. LEDUC, D. HOLLEVILLE, DIMARCQ N., CLAIRON A., LANDRAGIN A, J. Phys. IV France **135**, 357-358 (2006), « Caractérisation d'un gyromètre à atomes froids ».

14. J. LE GOUËT, P. CHEINET, K. THERKILDSEN, F. PEREIRA DOS SANTOS, A. LANDRAGIN, A. CLAIRON, J. Phys. IV France **135**, 213-214 (2006), « Premiers résultats d'un gravimètre atomique au LNE-SYRTE ».

15. F. LEDUC, D. HOLLEVILLE, J. FILS, A. CLAIRON, N. DIMARCQ, A. LANDRAGIN, P. BOUYER AND CH. J BORDE, Proceedings of the 16th International Conference On Laser Spectroscopy, Cairns, Australie, World Scientific, Ed. P. Hannaford, A. Sidorov, H. Bachor et K. Baldwin (2004) « Cold atom interferometric for precision measurement ».

16. G. BAGNASCO et al., Proceedings of « 52nd International Astronautical Congress», Toulouse, France, 1-5 October 2002, IAF-01-J.1.04. « High precision atom interferometry in space: the Hyper project ».

17. A. LANDRAGIN et al,. Proceedings of the « 7th International Conference on Advanced Technology and Particle Physics », Como, Italie, Octobre 2001 par World Scientific, pp16-22. « HYPER : Atom Interferometry in Space ».

18. A. LANDRAGIN, J. FILS, F. YVER, D. HOLLEVILLE, N. DIMARCQ, A, CLAIRON. Proceedings of the 6th Symposium on Frequency Standards and Metrology , Edited by P. Gill, World scientific, (St Andrew, UK) 2001, 532 pp. «Phase noise in atomic interferometer».

19. WOLF P., BIZE S., CLAIRON A., LANDRAGIN A., LAURENT P., LEMONDE P, CH. J. BORDE. Proceedings of the 6th Symposium on Frequency Standards and Metrology , Edited by P. Gill, World scientific, (St Andrew, UK) 2001, 593 pp. «Recoil effects in MICROWAVE atomic frequency standards: an update».

20. B. ANDERSON, T.L. GUSTAVSON, A. LANDRAGIN, J. McGUIRK, M. SNADDEN, M.A. KASEVICH. Proceedings of the XXXIVth rencontre de Moriond « Gravitational waves and experimental gravity ». Edited by J. Trân Thanh Vân, J. Dumarchez, S. Reynaud, C. salomon, S. Thorsett, J.Y. Vinet, World Publishers (Hanoi-Vietnam) 2000, 421pp . « Precision atom interferometry ».

21. A. LANDRAGIN, T.L. GUSTAVSON, M.A. KASEVICH. Laser Spectroscopy, 14th International Conference. ICOLS 99. World Scientific, Singapore; 1999; XXII 373 pp. « Precision atomic Gyroscope ».

22. T.L. GUSTAVSON, A. LANDRAGIN, J. MCGUIRK, M. SNADDEN, M. KASEVICH. Technical Digest. Summaries of papers presented at the Quantum Electronics and Laser Science Conference. Postconference Edition (cat. 99CH37012). Opt. Soc. America, Washington DC, USA; 1999; 283pp. « Atom interferometer inertial sensors »

23. C. HENKEL , A. ASPECT, J-Y. COURTOIS, R. KAISER, G. LABEYRIE, A. LANDRAGIN, K. MØLMER, N. VANSTEENKISTE, C.I. WESTBROOK Frühjahrstagung der Deutschen Physikalischen Gesellschaft, Jena, Allemagne, 11-15 mars 1996. Verhandl. DPG (VI) **31** 286 «Diffuse reflection of atoms at an evanescent wave mirror».

24. A. ASPECT., C. HENKEL., G. LABEYRIE, A. LANDRAGIN. International School of Physics 'Enrico Fermi', Course **CXXXI**, ed. par A Aspect, W. Barletta, R. Bonifacio (1995). «Coherent Atomic Mirrors».

4/ Publications dans des revues sans comité de lecture

1. F. PEREIRA DOS SANTOS, A. LANDRAGIN, Physics World, November 2007, 32-37, « Getting the measure of atom interferometry ».

2. P. BOUYER ET A. LANDRAGIN, Techniques de l'ingénieur **R1792** 1-10 (2005) « Le refroidissement des atomes et leurs applications aux horloges et aux senseurs inertiels».

3. A. LANDRAGIN, P. CHEINET, F. LEDUC ET P. BOUYER, in Optics and Astrophysics, NATO Science series II. Mathematics, Physics and Chemistry **198**, 359 (2005). « Atom interferometry »

4. A. LANDRAGIN ET P. BOUYER, proccedings of the 39th ESLAB Symposium, Eds. F. Favata and A. Gimenez, (2005), « Atom interferometry and coherent matter waves »

5. F. LEDUC, B ; CANUEL, D. HOLLEVILLE, N. DIMARCQ, A. CLAIRON, J. FILS, PH. BOUYER, CH. BORDE et A. LANDRAGIN, J. Phys. IV France, **119** , 225 (2004), « Interférométrie à atomes froids : vers un gyromètre-accélromètre de grande sensibilité».

6. P. CHEINET, F. PEIRERA DOS SANTOS, A. CLAIRON, N. DIMARCQ, D ; HOLLEVILLE et A. LANDRAGIN, J. Phys. IV France, **119** , 153 (2004), « Gravimètre à atomes froids».

7. P. CHEINET, F. PEREIRA D. S., A. CLAIRON, N. DIMARCQ, D. HOLLEVILLE AND A. LANDRAGIN, Proceeding de Métrologie 2003, Collège Français de Métrologie, N° ISBN: 2-915416-00-1 dépot légal Octobre 2003, « Gravimètre à atomes froids pour la balance du Watt ».

5/ Chapitres d'ouvrages

1. P. BOUYER, F.PEREIRA DOS SANTOS, A. LANDRAGIN AND CH. J. BORDE, in Lasers, Clocks, and Drag Free: Exploration of Relativistic Gravity in Space, ed by H. Dittus, C. Lämmerrzahl and S. Turyshev, Springer (2007), p 297, « Atom Interferometric Inertial Sensors for Space Applications ».

6/ Brevets

1. P. BOUYER, W GUERIN, J. BILLY, V. JOSSE ET A. LANDRAGIN, Brevet 08/305062.5 du 19 mars 2008 : « laser à atomes » déposé par IXSEA avec l'IOGS et l'Observatoire de Paris

2. P. BOUYER ET A. LANDRAGIN, Brevet FR 08/51599: « Capteurs interférométrie à atomes froids », déposé par le CNRS.

3. P. FEATONBY, A. VIRDIS, A. LANDRAGIN, B. CANUEL, F. LEDUC, brevet français n° FR02877430 déposé le 04-11-2004, Titulaire : SAGEM S.A. et Observatoire de Paris, France, publié le 05-05-2006 (BOPI2006-18) « Procédé et appareil de mesure de vitesse de rotation par interférométrie atomique ».

4. A. LANDRAGIN, P. FEATONBY, brevet français n° FR 02-15454 déposé le 06-12-02, Titulaire : SAGEM SA et Observatoire de Paris, Pays : France, publié le 11-06-04 Bulletin 04/24 «Procédé et appareil de mesure de vitesse de rotation par interférométrie atomique».

5. J.T. AUDREN, CH. BORDE, PH. BOUYER, A. CLAIRON, N. DIMARCQ, P. FEATONBY, J. FILS, D. HOLLEVILLE, A. LANDRAGIN, P. PETIT, ET CH. SALAMON, Brevet français déposé le 20 Juin 2001 sous le N° 01 08112, Titulaire : SAGEM SA, Pays : France, publié le 27-12-02 Bulletin 02/52. «Capteur Inertiel à Atomes Lents».

7/Autres

1. R. BINGHAM, C. BORDE, P. BOUYER, M. CALDWELL, A. CLAIRON, K. DANZMANN, N. DIMARCQ, W. ERTMER, J. HELMCKE, C. JENTSCH, B. KENT, C. LÄMMERZAHL, A. LANDRAGIN, I. PERCIVAL, E.M. RASEL, C. SALOMON, M. SANDFORD, W. SCHLEICH, P. TOURRENC, S. VITALE, P. WOLF, HYPER : «Hyper-Precision Cold Interferometry in Space », Assessment Study Report, ESA-SCI(2000)10.

Résumé

Ce manuscrit décrit l'étude et le développement de capteurs inertiels fondés sur l'utilisation de l'interférométrie atomique. Une introduction historique du domaine est suivie d'une description du principe de fonctionnement des interféromètres, fondés sur l'utilisation de transition Raman stimulées comme séparatrices atomiques d'une part et d'atomes refroidis par laser d'autre part. L'étude porte principalement sur trois systèmes expérimentaux : deux gyromètres et un gravimètre. Leurs performances respectives sont présentées et comparées à l'état de l'art des capteurs standard et mises en perpective des différents domaines d'application envisagés. Les limites expérimentales sont identifiées comme étant liées à l'interaction entre atomes et séparatrices lasers. Le manuscrit se termine par une présentation des perspectives en terme de performances ultimes et de nouveaux concepts, notamment fondés sur l'utilisation d'atomes ultra-froids, ainsi que d'un certain nombre de missions spatiales envisagées utilisant des capteurs inertiels par interférométrie atomique.

Summery

This manuscript describes the study and the development of inertial sensors based on atom interferometry. A historical introduction of the subject is given first. Then, the principle of the interferometer, based both on Raman transition and laser cooled atoms, is described. The mean part of the study concerns three experimental setups : two gyroscopes and one gravimeter. There respective performances are presented and compared to the state of the art of the standard sensors. Experimental limitations have been identified to be linked to the interaction between atoms and light beamsplitters. These results are presented in prospect to possible applications. Then, ultimate performances and new concepts, especially concerning the use of ultra-cold atoms, are presented. Prospects in possible space missions with atom interferometry based inertial sensors end the manuscript.